Multiple Star Formation

Thesis by

Adam L. Kraus

In Partial Fulfillment of the Requirements

for the Degree of

Doctor of Philosophy

California Institute of Technology

Pasadena, California

2010

(Defended July 13, 2009)

Acknowledgements

This thesis notwithstanding, I am a man of few words. However, I try to make them count when it matters. I owe my gratitude (and my completed degree) to the many people who have offered their advice, assistance, and encouragement since I began this journey.

First, I want to thank the mentors who have provided support and guidance over the past decade:

- Lynne Hillenbrand (my PhD advisor at Caltech) has offered advice when I needed it, but still gave me free rein to explore a wide range of research interests. As my sole collaborator for many projects, her scientific insight has been invaluable. Lynne also has read every word in this thesis multiple times, and marked up at least half of them in red ink; I hope that the resulting improvement in my scientific communication abilities is reflected in the subsequent pages.

- Russel White (formerly a Caltech postdoc and now faculty at Georgia State) provided crucial guidance in my early career at Caltech. My first two papers were written primarily in collaboration with Russel, and he worked tirelessly to help develop my scientific and writing skills. Many of my projects build on concepts that Russel discussed in his thesis, and many of my expeditions into the literature still lead back to his 2001 compendium on multiple star formation.

- Eric Craine, Mark Giampapa, and Roy Tucker (my collaborators on the GNAT project) gave me my first chance to grab an idea and run with it. The spirit of science is in discovery and creativity, and my "summer project" (which continues

to yield rewarding new science after eight years) left no doubt that scientific research was the only career for me.

- Barbara Anthony-Twarog, Bruce Twarog, Steve Shawl, and Steve Sanders (my astronomy and physics professors at KU) started me down the path of the scientist. I faced a choice between astrophysics and history, and I'm grateful to them for helping me choose wisely. Barb also supervised my first research project, a study of stellar populations in the LMC; I'm still working on stellar astronomy, and every one of my Fortran programs is distantly derived from some code she gave me in 2001.

Most of the good ideas in this thesis can be attributed to one or more of these people; all bad ideas are wholly my own.

I've also benefited from the support, advice, and friendship of many students and postdocs over the past six years. I was blessed with an amazing set of classmates: Brian, David, Karin, Dan, and Larry. We spent many late nights studying in the Robinson sub^n-basement, and their friendship and collaboration have carried us all through to the finish line. Many of the older students provided guidance in navigating science and life here at Caltech, and I learned to listen to their voices of experience. I'd especially like to thank fellow Jayhawk Stuartt Corder - even when I didn't need advice, we could still celebrate or complain about the sports teams back home. Finally, I've had the great fortune to collaborate with several postdocs in my later years here at Caltech. Mike Ireland, Kelle Cruz, and Greg Herczeg provided sage advice on science and careers, plus we have some really exciting results coming down the pipeline.

Of course, it really takes a village to observe a photon. Much of the data in this thesis came from the Keck and Palomar Observatories, and the observations only happen because of brilliant and tireless efforts by the engineers, support astronomers, telescope operators, and administrators. Similarly, the Caltech astronomy department would grind to a halt without everybody working behind the scenes to keep us observing.

Finally, I want to thank my family for their love and support. Look, Mom and Dad - I actually got a job before I turned 30! OK, barely...

Adam Kraus

August 2009

Abstract

In this thesis, I present a study of the formation and evolution of stars, particularly multiple stellar systems. Binary stars provide a key constraint on star formation because any successful model should reproduce the mass-dependent frequency, distribution of separations, and distribution of mass ratios. I have pursued a number of surveys for different ranges of parameter space, all yielding one overarching conclusion: binary formation is fundamentally tied to mass. Solar-mass stars have a high primordial binary frequency (50%–75%) and a wide range of separations (extending to >10,000 AU), but as the system mass decreases, the frequency and separation distribution also decrease. For brown dwarfs, binaries are rare ($\sim$10%–15%) and have separations of <5 AU. Inside of this outer separation cutoff, the separation distribution appears to be log-flat for solar-mass stars, and perhaps for lower-mass systems. Solar-mass binary systems appear to have a flat mass ratio distribution, but for primary masses <0.3 $M_\odot$, the distribution becomes increasingly biased toward similar-mass companions.

My results also constrain the binary formation timescale and the postformation evolutionary processes that sculpt binary populations. The dynamical interaction timescale in sparse associations like Taurus and Upper Sco is far longer than their ages, which suggests that those populations are dynamically pristine. However, binary systems in denser clusters undergo significant dynamical processing that strips outer binary companions; the difference in wide binary properties between my sample and the field is explained by the composite origin of the field population. I also have placed the individual components of young binary systems on the HR diagram in order to infer their coevality. In Taurus, binary systems are significantly more coeval

($\Delta\tau\sim$0.5 Myr) than the association as a whole ($\Delta\tau\sim$3–5 Myr).

Finally, my survey of young very-low-mass stars and brown dwarfs found no planetary-mass companions like the prototypical system 2M1207A+b. Modeling the population as either "super-Planets" or "failed binaries" indicates that the total frequency of companions with masses >1 M_{Jup} is $<1\%$–2%. My survey of young solar-mass stars found no brown dwarf companions; evidence in favor of the brown dwarf desert is marginal, but my results do not exclude its existence.

Contents

List of Figures

List of Tables

Chapter 1

Introduction

1.1 Multiplicity and Star Formation

The frequency and properties of multiple star systems offer powerful constraints on star formation and early cluster evolution. The semimajor axis of a binary system should correspond to the characteristic size of its progenitor core at the time of fragmentation, so the binary separation distribution constrains the range of sizes and the size evolution for cores. The overall binary frequency and the distribution of mass ratios also constrain the detailed physics of binary fragmentation, and each binary system's mass ratio will depend on the post-fragmentation accretion history. Finally, the relative positions of binary components in the HR diagram, and hence their apparent ages, offers a strong constraint on the duration and coevality of multiple star formation.

A successful model for star formation should be able to match the observed properties of the binary star population. The newest generation of theoretical models now match the slope and turnover of the IMF (e.g., Bate 2009a), but requiring simultaneous agreement with the frequency, separation distribution, and mass ratio distribution for binary systems is a far more demanding criterion, and one that has yet to be achieved. The apparent mass dependence of these properties adds yet another dimension for testing star formation models. Furthermore, any discrepancy with respect to observations will provide guidance in developing the next generation of models, marking the phenomena that might be lacking (i.e., radiative feedback or

magnetic fields; Bate 2009b; Offner et al. 2009; Price & Bate 2009) or overrepresented (dynamical interactions; Chapters 2 and 4).

The rewards from truly understanding stellar multiplicity have motivated a century of study, but the observational and theoretical challenges have stymied significant progress until the past twenty years. As I review in Section 2 of this introduction, technological advances have allowed our observational understanding of multiplicity and multiple star formation to surge ahead; my thesis represents the latest step in a long line of discoveries. However, as I summarize in Section 3 (and will reiterate in Chapter 8), observers have far outpaced the theoretical underpinnings for interpreting their results. The balkanization of observers and instrument builders by technique (imaging, astrometry, or RV), target set (field, cluster, or star-forming region), separation range (wide versus close), primary mass (high-mass stars, solar-mass stars, or low-mass stars and brown dwarfs), and companion mass (stellar, substellar, or planetary-mass companions) has further confused a complicated field.

The goal of my thesis is to present a singular view of the outcome of multiple star formation, encompassing as much parameter space as I could explore within six years. From this overarching picture, I extract a set of lessons that should guide future theoretical efforts; each of my surveys provides one or more concrete observables that should be replicated by any successful theoretical model. My goal is to motivate the advances that will bring models into agreement with reality.

1.2 A Brief History of Multiplicity Studies

1.2.1 Prehistory: Multiplicity Before 1990

One of the first and most influential large surveys is now approaching a century in age. Öpik (1924) compiled data from visual double-star catalogs on >1800 pairs of field stars (spanning 3/4 of the sky, and thus comprising a nominally unbiased sample) in order to characterize their binary properties. Öpik's most enduring conclusion (commonly dubbed "Öpik's Law") was that the semimajor axis distribution of binary

systems is approximately log-flat, with an equal number of companions per decade of separation. This conclusion has waxed and waned in popularity over the intervening decades, and modern studies (e.g., Duquennoy & Mayor 1991) suggest that it is not true for field stars. However, as I describe in Chapter 4, the separation distribution for dynamically pristine samples of young solar-type stars does indeed closely approximate Öpik's Law.

The next several decades saw a number of similar studies, including major works by Luyten (1930), Kuiper (1942), Jaschek & Jaschek (1957), and Petrie (1960); their results varied widely, yielding G star binary frequencies of 18%–54%. The next fundamental leap in binary studies did not come until Abt & Levy (1976) conducted the first large survey to simultaneously identify spectroscopic binaries, visual binaries, and common proper motion binaries among 135 F–G stars. Their completeness corrections have been shown to overcorrect an observed frequency of >50%, so their estimate of 1.4 companions per star was too high. However, the motivations and methods for achieving robust completeness have been emulated by many subsequent surveys.

Between 1970 and 1990, many long-term monitoring projects were launched; some of their results will be summarized below. Shorter-term studies also concentrated on characterizing the mass ratio distribution, including the first significant evidence that short-period binary systems might have a large population of twins, or pairs of nearly equal mass (Trimble 1978; 1990), and the significant evidence that binary systems do not have a twin population, but instead have a universal mass ratio distribution for both very close and very wide systems (Halbwachs 1987). These contradictory results illustrated the difficulty of achieving statistical rigor with samples that are incomplete, biased, or drawn from past catalogs; this lesson was finally addressed during the 1990s.

1.2.2 An Observational Renaissance: 1990–1997

The 1990s saw two developments that transformed our understanding of multiplicity. First, the discovery and characterization of large samples of young stars and nearby field stars allowed for systematic investigation of binary statistics. Second, the widespread adoption of high-resolution imaging techniques like speckle interferometry allowed for the study of binary systems inside the seeing limit. This benefit was not as useful for nearby bright stars since decade-long RV campaigns could identify most binary systems inside the seeing-limited regime. However, for more distant young stars, high-resolution imaging uncovered the core of the binary separation distribution (separations of 10–100 AU) that had previously been inaccessible.

1.2.2.1 Field Stars

The 1990s saw the publication of several synoptic multiplicity campaigns of statistically robust, volume-limited samples. The most influential of these campaigns, which remains the benchmark for solar-type multiplicity to this day, was a survey by Duquennoy & Mayor (1991; hereafter DM91) of 181 members of the Gliese catalog (Gliese 1969) with spectral types of F7–G9 and distances <22 pc that were accessible from northern observatories. The primary observational program for DM91 was a decade-long spectroscopic monitoring campaign, but the authors also considered all known common proper motion companions to their bright, very well-studied sample.

The solar-type multiplicity results of DM91 established the paradigm against which all other multiplicity surveys have been compared, and which theoretical models generally attempt to reproduce. First, they found a separation distribution which is apparently unimodal and log-normal, with a mean semimajor axis of ~30 AU and a standard deviation of ~1 dex. Second, they found a mass ratio distribution that is peaked at low masses ($q \sim 0.3$) and has few similar-mass companions, though their survey was not sensitive to most substellar companions and relied on significant completeness corrections for low-mass stellar companions. Finally, they found that $\sim60\%$ of solar-type stars have at least one binary companion.

The survey by Duquennoy & Mayor only concentrated on solar-mass stars, omitting the K and M stars that make up the nearby field star population. This gap was filled by a number of parallel and subsequent surveys, most notably that of Fischer & Marcy (1992; hereafter FM92). FM92 compiled multiplicity results for M0–M4 stars as determined by a number of different surveys from the late 1980s and early 1990s. They found that the separation distribution was broadly similar to that of DM91, with a unimodal and log-normal shape that peaked at separations of $\sim$3–30 AU. However, they found a mass ratio distribution which was linear-flat, with all mass ratios equally probable (albeit only to a completeness limit of $q \sim$0.4). They also found that the total binary frequency was somewhat lower, with a total frequency of $42\pm9\%$. These differences were the first indication that the frequency and properties of binary systems might depend on mass.

1.2.2.2 Young Stars

Corresponding advances for young stars were spurred by two simultaneous developments, one in observations and one in instrumentation. First, intensive study of nearby star-forming regions led to a significant increase in the number of well-characterized targets for follow-up observation; these studies culminated in the creation of the Herbig & Bell catalog (Herbig & Bell 1988) of emission-line stars and the census of Taurus-Auriga by Strom et al.(1989) and Kenyon & Hartmann (1995). Second, advances in infrared detectors allowed the first diffraction-limited observational campaigns using speckle interferometry and lunar occultations.

Speckle interferometry uses high-cadence observations, with individual exposure times of less than the atmospheric coherence time, to freeze out atmospheric seeing. This allows the recovery of diffraction-limited spatial information through either image stacking ("shift and add") or Fourier analysis. Ghez et al.(1993; hereafter G93) and Leinert et al.(1993; hereafter L93) used speckle interferometry to study young stars in Taurus-Auriga, Ophiuchus, and Sco-Cen, and found solar-type stars to have a significantly more binary companions than the field stars that were studied by DM91; G93 found a binary frequency of $60 \pm 17\%$ for separations of 16–250 AU, a factor of

four higher than the field binary frequency in that separation range. The inference, based on an extrapolation to unobserved separations, was that almost all young stars in these T associations formed with binary companions.

At the same time, experiments with lunar occulatation monitoring by Simon et al.(1995; hereafter S95) yielded higher resolution for those young stars in Taurus and Ophiuchus which fall along the moon's orbital path on the celestial sphere. These experiments offered a view inside the diffraction limit of 5m-class telescopes ($\sim$100 mas or $\sim$15 AU at K) and supported the high binary frequency found by speckle surveys. However, the sample size was fundamentally limited to the set of bright young stars that could be occulted by the Moon. The limits on very wide multiplicity were driven by the difficulty of distinguishing genuine companions from background stars (such as via common proper motion). I return to the topics of very wide or very close systems in Chapters 4 and 5, respectively.

Radial velocity surveys also continued to work in parallel with the results of Duquennoy & Mayor (1991), studying solar-type stars in the nearest open clusters (e.g., Mermilliod et al. 1992) and extending detection limits into the planetary mass regime (Mayor & Queloz 1995; Marcy & Butler 1996). The late 1990s saw a rapid increase in the rate of exoplanet discovery, but also revealed a paucity of brown dwarf companions to stars; this absence of companions was dubbed the "brown dwarf desert" (Marcy & Butler 2000) and spurred a number of followup studies.

Finally, the middle and end of this decade saw the debut of space-based imaging (with HST) and adaptive optics imaging. HST observations of known binaries allowed for the intensive study of their properties and ages (e.g., White et al. 1999; White & Ghez 2001), but HST did not provide significant impact for survey work until after the turn of the millenium. As I describe below, adaptive optics also did not achieve its promise for multiplicity surveys until the late 1990s and beyond. However, it has since become the method of choice, supplanting speckle techniques and lunar occultation due to its superior contrast limits at moderate separations (>2 λ/D) and HST due to its widespread availability and relatively low cost.

1.2.3 The Industrial Revolution: 1997–2004

Adaptive optics (AO) has revolutionized the study of multiplicity. AO uses light from a bright reference star to sense and correct wavefront aberrations introduced by atmospheric turbulence, restoring diffraction-limited image quality. AO surveys can achieve a high cadence, observing scores of targets in a single night, while also achieving far better contrast limits than earlier techniques. AO can also be used for much fainter targets, as faint as $R \sim 15$ with modern wavefront sensors. These advantages have led to rapid proliferation in the number and size of multiplicity surveys.

The first generation of large AO surveys concentrated on solar-type stars in open clusters, led by a survey of 144 Pleiades G–K stars by Bouvier et al. (1997). They found that the cluster binary population resembles that of similar-mass field stars in frequency and separation distribution, a result that was subsequently confirmed in surveys of other open clusters (Bouvier et al 2001; Patience et al. 1998, 2002). A similar survey in the young cluster IC348 (Duchêne et al. 1999) also found no evidence of a binary excess like was seen in young T associations. These results all indicated that the binary excess was tied to environment, due to either formation conditions or early dynamical evolution.

The discovery of the brown dwarf desert in the late 1990s also spurred a number of large surveys (conducted with seeing-limited imaging, AO, or HST) to verify its existence and further characterize its extent. McCarthy & Zuckerman (2004), Lowrance et al. (2005), Metchev & Hillenbrand (2004, 2009), and Carson et al. (2009) observed large samples of nearby field stars with high-contrast imaging techniques, discovering a small number of wide substellar companions. These discoveries indicated that the desert is not completely dry at very wide separations, and depending on the form of the stellar binary companion mass function, the desert even might not exist.

Finally, this era also saw the first series of HST imaging surveys of multiplicity in the substellar regime. A significant sample of field brown dwarfs was not established until the late 1990s (e.g., Kirkpatrick et al. 1999), and they lay beyond the reach of

most ground-based high-resolution imaging techniques, requiring multiplicity surveys to be conducted from space. The first surveys by Bouy et al.(2003) and Burgasser et al.(2003), supplemented by ground-based AO surveys of late-M stars by Close et al.(2003) and Siegler et al.(2005), revealed a very different paradigm for multiplicity in the very low-mass regime. Low-mass binaries tend to have very small separations, with almost no systems separated by >10–20 AU. The mass ratio distribution is also strongly biased toward equal-mass systems, unlike for higher mass stars. Finally, the overall frequency is also much lower, with only 10%–15% of targets having a binary companion at separations >2–4 AU. As I discuss in the next section and in Chapters 3 and 6, these discrepant features have driven most of the developments in brown dwarf formation models.

1.2.4   The Information Age: 2005 and Beyond

The past few years have seen a number of observational and instrumentational advances that finally might provide the necessary guidance for theory to match observations. Many of these developments have led to the projects that make up my thesis, so I will return to these themes throughout the rest of my thesis.

The first major advance was the identification of large samples of very low-mass stars and brown dwarfs in nearby star-forming regions by Ardila et al.(2000), Briceño et al.(2002), Preibisch et al.(2002), Luhman (2004, 2006), and Slesnick et al.(2006a, 2006b). Much like the discovery of young solar-type stars led to the groundbreaking surveys of G93, L93, and S95, the discovery of young brown dwarfs allowed me to pursue an HST imaging survey of young brown dwarfs to determine if they had a low binary frequency like for field brown dwarfs or a high excess of binary companions like for young solar-type stars; I describe this work in Chapter 3.

The second major advance was the implementation of laser guide star adaptive optics (LGSAO) at major observatories, and especially at Keck (Wizinowich et al. 2006). LGSAO uses a laser beacon to excite sodium atoms in the upper atmosphere, producing an artificial $V \sim 9$–10 guide star at any arbitrary point on the sky. The

ability to produce artificial guide stars allows for the observation of much fainter science targets, and since observations with HST are too expensive to justify a large survey, the ability to observe faint targets from the ground is critical for investigating detailed trends in binary properties. As I describe in Chapter 6, this allowed me to follow up my HST survey and determine the mass-dependent change in binary properties between the solar-mass regime and the substellar regime.

Finally, the last advance was the rapid proliferation of uniform, high-quality sky surveys like 2MASS (Skrutskie et al. 2006) and USNO-B1.0 (Monet et al. 2003). These surveys can be mined to search for extremely infrequent types of binary systems that would not be found in targeted surveys of discrete samples of stars. As I describe in Chapter 4, I have exploited 2MASS survey data to characterize the extremely wide binary population in several nearby star-forming regions. Similar surveys in the field, typically exploiting photometry from SDSS and proper motions from USNO-B1.0, have revealed that even very low-mass stars and brown dwarfs have an extremely small fraction of loosely bound wide binary systems, challenging the conclusion that low-mass binary systems must have very small separations. I return to this topic in both Chapters 4 and 6.

1.3 Theoretical Depictions of (Multiple) Star Formation

The modern picture of star formation can be traced back to an analytic description by Shu et al.(1987) that is popularly known as the Shu model. The Shu model stipulates that star formation proceeds in four main stages. First, a portion of a giant molecular cloud reaches the critical Jeans mass for collapse, forming a bound prestellar core. This core then condenses to form a central protostar that is embedded in a massive envelope; this envelope accretes onto the central protostar through a circumstellar disk. As the majority of the envelope accretes, stellar winds break through along the rotational axis and drive an outflow. Finally, the remaining material settles into a

circumstellar disk, and this disk is gradually dissipated through some combination of accretion, photoevaporation, and planet formation.

The past two decades have seen a flood of observations that largely support the validity of the Shu model, with a preponderance of the evidence coming from the Spitzer Space Telescope. The youngest star-forming regions boast a large number of bound cores, with varying fractions that are "starless" (i.e., have not yet differentiated into a star/envelope system) or that boast recognizeable protostars at their center (e.g., Enoch et al. 2009). Moderately older regions tend to have an increasing number of stars that no longer have any envelope, but merely host circumstellar disks with typical masses of $\sim$1%–10% of the host star's mass (Andrews & Williams 2005). Finally, regions older than $\sim$3–5 Myr tend to have few stars with optically thick protoplanetary disks, indicating that the processes of star formation and giant planet formation have ceased (Hernández et al. 2007; Currie et al. 2009).

However, as I will describe in the next two subsections, the Shu model does not completely describe star formation. The evolutionary process by which bound cores condense from a molecular cloud is complex and relies on several global macrophysical phenomena that are still poorly constrained; the vast majority of stars have a mass much lower than the typical Jeans mass in giant molecular clouds, and only a small fraction of the gas in any molecular cloud is ultimately formed into stars, so appealing to ambipolar diffusion as the timescale moderator probably is not sufficient. The Shu model also implicitly ignores multiple star formation by starting with (and maintaining) azimuthal symmetry in the bound core. Binary formation most likely occurs when an asymmetric cloud has sufficient angular momentum to collapse into two distinct cores, so it must be described with an asymmetric model.

1.3.1 The Big Picture: Quasi-static Collapse or Turbulent Fragmentation?

There are two competing paradigms for the large-scale star formation process that converts a giant molecular cloud into a stellar population. The quasi-static collapse

model, which is closer in spirit to the Shu model, stipulates that a molecular cloud will fragment into bound cores, and those cores will gradually approach and exceed Jeans criticality. In this model, core collapse is moderated by the interplay between compressive forces (gravitation and pressure confinement) and restorative forces (thermal energy, rotation, and magnetic fields) such that all cores maintain quasistable equilibrium near the Jeans limit for periods of $>10^6$ yr. In contrast, the turbulent fragmentation model (e.g., Bate et al. 2009a) stipulates that turbulent motions within the molecular cloud will overwhelm restorative forces and lead to the creation of bound stellar-mass cores that exceed the Jeans limit; these cores then promptly collapse to form stars on a timescale of $\sim 10^5$ yr. As I will describe throughout my thesis, each model has significant advantages and drawbacks in predicting the observed IMF, cluster properties, and binary properties.

Quasi-static collapse predicts the overall velocity dispersions ($v \sim c_s$) and spatial distributions that are seen in the nearest star-forming regions (e.g., Goodman et al. 1998), including the Pipe Nebula (Lada et al. 2008) and Taurus (Chapter 2). The overall duration of star formation in these regions (perhaps as much as ~ 5 Myr; Chapter 7) is also much more consistent with a slow, nearly steady-state process. However, quasi-static collapse might not work as well for very dense clusters like the Orion Nebula Cluster since the apparent velocity dispersions are higher (Tobin et al. 2009) and the interaction timescales for cores are much less than the quasi-static timescale. Quasi-static collapse also has difficulty producing objects with masses significantly less than the mean Jeans mass (~ 1 $M_\odot$ in a typical molecular cloud), whereas the IMF is dominated by lower-mass stars and brown dwarfs.

Turbulent fragmentation sports all of the opposite strengths and weaknesses. The resulting stellar densities and velocities are much higher ($V \sim 10c_s$) than those seen in Taurus and the Pipe Nebula, though the results are more consistent with denser clusters like the ONC. Also, the short interaction timescales that result from these velocities and densities should lead to the disruption of wide binary systems that are seen in low-density populations (Chapter 4), including the low frequency and small separations of substellar binary systems. The formation timescale is also quite short,

with most simulations concluding the formation epoch within $\sim$2–3 $\times$ 10^5 yr. How-
ever, the advantage of turbulent fragmentation is that interactions between turbulent
flows can create high overdensities with correspondingly small characteristic Jeans
masses; the prestellar cores that condense in these regions could then collapse to
form the low-mass stars and brown dwarfs that do not form easily under quasi-static
collapse.

The macrophysics of star formation must play a role in binary formation. The dis-
tribution of characteristic sizes for prestellar cores should be reflected in the maximum
size of binary systems, and the distribution of angular momentum should determine
the epoch and frequency of binary fragmentation. The overall stellar density and
velocity dispersion also play a key role in the dynamical evolution of binary sys-
tems after fragmentation and until the systems escape into the field. Conversely,
binary properties can provide constraints on the large-scale processes that occur in
star-forming regions. The existence and maximum size of wide binaries constrains
the rate of dynamical interactions, and the ages of binary systems can be used to
constrain the star formation history of a region.

1.3.2 Competing Models of Binary Formation

Most of the observational signatures of large-scale star formation (such as binary
properties, disk properties, and the IMF) will also be shaped by the detailed physics
of individual star formation. The framework of the Shu model suffices to describe
the formation of a single star, but in the absence of a credible explanation for binary
formation, any model which forms more than two stars at a time will remain funda-
mentally untested. Several models have been proposed as the primary mechanism for
multiple star formation; it is unclear how many of these models are relevant, what
their relative branching ratios are, and what ranges of parameter space they might
explain. The state of binary formation theory has been the subject of several reviews
over the past decade, most notably those of Bonnell (2001) and Tohline (2002), and
the following subsubsections summarize the topics that they discuss. There has been

little work specifically on binary theory since the beginning of this decade, with a few exceptions I list below, but most larger-scale formation models have begun to simulate smaller scales where they might be able to supplant dedicated binary formation models.

The reigning model is the prompt fragmentation of a bound prestellar core, either during or immediately after the stage of free-fall collapse (e.g., Bodenheimer & Burkert 2001). This model is the only compelling explanation for systems with sizes of $\gg$100 AU, but it does not seem to proceed efficiently at scales of $<$100 AU since the protostellar core becomes nonisothermal and heating of the gas causes it to resist compression. At smaller scales, the two models that have received most consideration are fission of the collapsing protostellar core (Tohline & Durisen 2001) and fragmentation in a circumstellar disk (e.g., Bonnell 2001). Both of these models have significant drawbacks, but disk fragmentation seems to be less flawed at present. Finally, a model that has now been largely discredited is capture, either via three-body interactions of stars or by two-body interactions in which circumstellar material (a disk or envelope) or the natal molecular cloud draws away kinetic energy, leaving a bound system (Clarke 1992; Ostriker 1994).

1.3.2.1 Prompt Fragmentation

The most probable model for the formation of wide ($>$100 AU) binary systems is by prompt fragmentation, during or just after the epoch where the prestellar core has become Jeans critical and begun free-fall collapse. This process typically is modelled using smoothed-particle hydrodynamic (SPM) simulations; the most recent simulations of larger-scale star formation implicitly include this process by extending down to much smaller angular scales ($\sim$5 AU). Analytic treatments of fragmentation have not fared well because collapsing systems are not expected to show any symmetries and because the collapse process tends to be highly nonlinear. In general, models can be divided into two categories: homologously collapsing systems where the system monolithically collapses to a flattened spheroid, and nonhomologous collapse where collapse occurs inside out and quickly forms a small core that can subsequently accrete

the remainder of the material.

Homologous collapse is expected to occur when a core's thermal energy is low compared to its gravitational energy, either because the core mass is significantly higher than the Jeans mass or because most of the energy is in rotation. The total collapse timescale is then the free-fall timescale, as collapse will continue until the core becomes nonisothermal and the increased pressure resists further collapse. The amount of rotational energy determines the shape of the resulting spheroid. Nonhomologous collapse is expected to occur in a slowly rotating core for which the thermal energy is similar to the gravitational energy, and thus the system is only marginally Jeans unstable. This process results in a steep density gradient between the center and edge of the core and quickly assembles a small central core onto which the surrounding material will then accrete.

Simulations of these processes suggest that fragmentation does not occur during free-fall collapse, but it could occur at the point when the cloud settles into a quasi-static, rotationally flattened state. This outcome appears to be more likely for homologous collapse, as it could allow for local fluctuations within which a Jeans mass will accumulate and grow. If a core had sufficient angular momentum, it could flatten sufficiently that initial small overdensities would become Jeans critical, collapsing to form binary companions. By contrast, the nonhomologous case for quick formation of a small core and subsequent gradual accretion of all remaining material, with limited rotational flattening that would seem to prohibit any large accumulations of material.

Finally, simulations show that prompt formation is less efficient for nonisothermal gas; that is, for gas that will heat up under compression and resist further collapse. A protostellar core is expected to remain isothermal only for sizes of >100 AU, so prompt fragmentation should become less prevalent at smaller scales.

1.3.2.2   Fragmentation in a Protostellar Disk

After a protostellar core undergoes sufficient collapse to form a central protostar, the remaining envelope accretes into a circumstellar disk and from the disk onto the star. If disks accumulate material from the envelope more quickly than that material can

accrete onto the star, then they could grow more massive and violate the Toomre stability criterion (Toomre 1964), fragmenting to form a bound companion. If there is sufficient material left in the disk and envelope, this bound companion would then accrete additional mass and grow into a stellar binary companion.

Observations suggest that the characteristic radius for a protostellar disk and for accretion onto it is ∼50–100 AU (Enoch et al. 2009; Watson et al. 2007), so disk fragmentation could explain binary formation at small scales where prompt fragmentation is not feasible. However, this process must occur early in the formation process; the rarity of substellar companions indicates that fragmentation only occurs while a significant amount of material is left to accrete onto the companion, driving its mass above the substellar boundary. This process is also quite unlikely to occur at ages of ∼1–2 Myr in protoplanetary disks, as most typically only contain ∼1%–5% of the primary stellar mass and would be unable to form stellar companions (Andrews & Williams 2005). Even much more massive stars, such as AB Aur, tend to have disk masses of only ∼10 M_{Jup} at ages of 1–2 Myr (Corder et al. 2005).

If this model explains the formation of close binary systems, then the properties of those systems would provide critical insight into the early evolution of protostars and protobinaries. Mass should preferentially accrete onto the secondary since it is not as deep in the system's potential well, a process which is seen in older systems like UZ Tau (Jensen et al. 2007), though the accretion rates are modified by the specific angular momentum of the material (Bate & Bonnell 1997). The distribution of mass ratios would therefore indicate the relative epochs for disk fragmentation and envelope accretion. The binary separation distribution should correspond to the distribution of radii at which disk fragmentation occurs, albeit potentially modified by subsequent migration. This distribution would then provide a fossil record of the initial structure of such disks.

1.3.2.3 Fission

Another suggested mode for multiple star formation is via fission of a young protostar or protostellar core. In contrast to fragmentation, fission is expected to occur after

a central core has condensed and begun nonisothermal evolution. This evolution is expected to occur on the Kelvin-Helmholtz timescale, which is much longer than the free-fall timescale, so subsequent evolution should be far slower than the free-fall collapse stage. This longer timescale would allow for significant evolution in the shape of the core.

Any core with nonzero rotational energy will flatten into an oblate spheroid; if it possesses sufficient angular momentum, it could then further deform into a triaxial bar. The fate of these bar-shaped deformations is uncertain, though. If it can further evolve without losing angular momentum, then it should undergo higher-order deformation to a pear or dumbbell shape; the deformed regions could then separately coalesce into individual stars (Cazes & Tohline 2000). However, Boss (1988) suggests that a bar-shaped core would rapidly dissipate angular momentum as material with high specific angular momentum (but low total mass) migrated to the tips of the bar, preventing coalescence of multiple bodies.

It has been suggested that processes that change the equation of state might encourage binary coalescence via fission. For example, molecular hydrogen should dissociate when the internal temperature of a core reaches $\sim$3000 K; this process should rapidly soften the equation of state until all molecular hydrogen has been destroyed (Goodwin et al. 2007). This process is expected to happen on a scale of $\sim$30 AU for solar-mass cores and $\sim$5–10 AU for substellar cores, so it provides an attractive explanation for the observed mass dependence of binary separations. However, this process must be studied in much more detail before it can be treated as a serious contender. Modern SPH simulations (e.g., Bate et al. 2009a) do not produce many (if any) binary systems via this process, so in the absence of new processes to encourage coalescence, it appears that fission does not contribute significantly to binary formation.

1.3.2.4 Capture

The final mode of multiple star formation that must be considered is capture, either via 3-body interactions or by 2-body interactions in a dissipative medium. Capture

and disruption (via 3-body interactions) have been suggested as the dominant forces for binary evolution in very dense environments like globular clusters (Portegies Zwart et al. 1997)), but most star-forming regions are much too sparse for capture to be relevant within ages of $<10^6$ yr (e.g., Clarke 1992). Two-body interactions seemed more promising for a time, as extended protoplanetary disks or the natal molecular cloud could dissipate extra kinetic energy and convert two unbound stars into a bound binary system. However, simulations suggest that the relative velocities are too large for disks to absorb the corresponding kinetic energy (Clarke & Pringle 1993; Ostriker 1994). As I will discuss further in Chapter 2, indirect studies of the internal kinematics of star-forming regions also suggest that the interaction rate is too low for even two-body interactions to be significant. As such, capture does not appear to be relevant.

1.3.3 Other Unconstrained Processes

Most models of (multiple) star formation are still incomplete, omitting physical processes that are poorly constrained, difficult to model, or thought to be insignificant. Conversely, some models also predict or rely on processes that observations have begun to rule out. In the following subsections, I will describe three processes that remain to be addressed: dynamical interactions in the natal environment, the effect of radiative feedback in damping star formation, and the role of magnetic fields.

1.3.3.1 Dynamical Interactions

Over the past century, dynamical formation and evolution of binary systems has been accepted or rejected numerous times. Early models suggested that binaries might form via 3- or even 2-body interactions, but as I described above, most evidence argues against this point. However, some models still explicitly invoke binary destruction to explain features in the observed binary population, especially the absence of wide substellar binaries. Early dynamical removal from small-N clusters has also been invoked as a possible formation mechanism for all brown dwarfs, and binary disruption

would be a key signpost of this process.

Binary disruption is likely to occur in very dense populations. For example, observations of the ONC suggest that binary systems with separations >200–300 AU are significantly less common than in sparser regions (Köhler et al. 2006), and observations of open clusters find a similar lack of binaries with separations >100–200 AU (Section 1.2). However, as I will describe in Chapter 2, the interaction timescale is much longer for unbound associations like Taurus and Upper Sco. Any binary features seen in these regions, including the paucity of wide brown dwarf binaries, must be considered a primordial outcome of the collapse of a protostellar core. As I will discuss in Chapter 4, this also has implications for the observed binary population in the field, which represents a composite of all possible star-forming environments.

The dynamical evolution of small-N clusters has also been invoked as a possible means of forming brown dwarfs, which are traditionally difficult to explain since their mass is much less than the characteristic Jeans mass of a molecular cloud. The "embryo ejection" model (Reipurth & Clarke 2001) suggests that a collapsing protostellar core might repeatedly fragment, yielding 5–10 substellar-mass objects. This minicluster would then evolve to a stable (hierarchically multiple) state, ejecting members in the process. As these members are ejected, they lose access to the surrounding envelope and cease accreting; this outcome would explain the range of wide range of masses seen at the bottom of the IMF, especially the absence of any binaries without very high binding energy. However, numerous observations have shown that the observed kinematics and disk and binary properties in these regions put a strict limit on the number and strength of ejection events. I will return to this topic throughout my thesis as I make my own arguments against embryo ejection.

1.3.3.2   Radiative Feedback

Radiative feedback is also expected to play a significant role in star formation, but it has only very recently been incorporated into star formation models. Feedback from very high-mass stars is likely to shut off star formation by eroding early-stage protostellar cores, affecting both global star formation and the early evolution of those

stars would could become bound. Feedback from lower-mass stars could also play a signficant role in shaping star formation on smaller scales, including the degree to which small-N clusters will subdivide and the evolution of protostellar disks.

One of the best examples of radiative feedback from high-mass stars is in the development of HII regions like that in the young cluster W5, which was recently studied by Koenig et al.(2008) using Spitzer observations with IRAC and MIPS. The cluster features a significant HII region centered on four bright O stars; surrounding this HII region is the remainder of a significant molecular cloud. The molecular cloud material has been ionized and driven outward by the O stars, and the low-mass stars inside of the cleared region appear to be older than those still embedded in the molecular cloud, indicating that triggered star formation might be occurring around the boundary of the cloud. The influence of high-mass stars can also be seen in the ONC, where UV flux from θ^1 Ori C appears to be photoevaporating the closest protoplanetary disks (e.g., Eisner et al. 2008; Mann & Williams 2009).

Recent simulations from Bate et al.(2009) and Offner et al.(2009) show that radiative feedback is also important for low-mass star formation. Their simulations suggest that radiative feedback from a protostar will inhibit fragmentation in the surrounding protostellar disks, preventing them from forming the large number of substellar and low-mass stellar companions that had formed in earlier simulations. This reduced efficiency for disk fragmentation should reduce the number of binary companions. Feedback also reduces the overall number of brown dwarfs formed; earlier simulations produced equal numbers of stars and brown dwarfs, while the updated simulations more closely match the observed IMF by producing $\sim$5 stars for every brown dwarf.

1.3.3.3 Magnetic Fields

Magnetic fields played a critical role in moderating collapse for the original Shu model of star formation, but recent simulations have largely neglected their role. Modelers omitted magnetic fields from binary formation models during the 1990s because it was expected that the higher-density gas of protostellar cores would rapidly become neutral due to recombination, and thus the vast majority of material would be unaf-

fected by magnetic fields. This assumption simplifies models considerably, so it has persisted. Very recent simulations by Price & Bate (2009) have revisited the role of magnetic fields, and they find that magnetic fields indeed have little effect on the formation of individual stars or binary systems. However, they suggest that magnetic fields are very important in guiding large-scale star formation since they can support low-density gas, delaying collapse and yielding a star formation rate of <10% per free-fall time.

1.4   Thesis Outline

My thesis is divided into four major observational programs and two major archival programs, each studying a different slice of parameter space (primary mass, companion mass, separation range). These ranges of parameter space were chosen by a combination of my expectation for an interesting result (i.e., high-resolution imaging to bridge the solar-mass and substellar binarity regimes) and the availability of new techniques for which I had some assurance of exclusivity (i.e., aperture-masking interferometry for young stars).

In Chapter 2, I study the spatial distributions of known young stars in two nearby star-forming regions by computing their two-point correlation functions. This analysis provides context for my subsequent work by inferring order-of-magnitude answers to three fundamental questions. First, what is the spatial structure of star-forming regions, and is there a universal structure seen across a range of environments? Second, below what characteristic spatial scale has that structure been averaged out, and what is the velocity dispersion corresponding to that characteristic spatial scale and the characteristic age of the stars in that association? Finally, can bound binary systems be distinguished from chance alignments of (spatially clustered) young stars, and what are the widest binary systems in sparse, unbound associations?

In Chapter 3, I present the first major observational program of my thesis, an HST imaging survey of young brown dwarfs and very low-mass stars. This survey confirmed that the binary frequency and properties seen in the field are broadly

consistent with those in dynamically pristine populations, and therefore that the tendency for infrequency, tightly bound, equal-mass binaries is a fundamental outcome of the substellar formation process. My observations also yielded the first uniform set of high-precision optical photometry for young low-mass objects, so I used these data to study their optical colors. I found that known accretors have a significant V band excess due to thermal emission from the accreting material, allowing direct measurement of the accretion rate.

In Chapter 4, I present a search for wide binary companions to 783 members of three nearby young associations: Taurus-Auriga, Chamaeleon I, and two subgroups of Upper Scorpius. For this program, I used archival 2MASS data to select candidate companions based on their JHK colors, then pursued an astrometric and spectroscopic campaign to confirm the youth and association of a complete subsample of these candidate wide companions in Taurus and Upper Sco. The total sample and the confirmed subsample both conform to only some expectations from field multiplicity surveys. Higher-mass stars have a higher frequency of wide binary companions, and there is a marked paucity of wide binary systems near the substellar regime. However, the separation distribution appears to be log-flat, rather than declining as in the field, and the mass ratio distribution is linear-flat, rather than increasing toward low mass ratios as in field. The maximum separation also shows no evidence of a limit at <5000 AU until the abrupt cessation of any wide binary formation at system masses of $\sim$0.3 $M_\odot$. I attribute this result to the post-natal dynamical sculpting that occurs for most field systems; my binary systems will escape to the field intact, but most field stars are formed in denser clusters and do not.

In Chapter 5, I present the results of a survey for stellar and substellar companions to 82 young stars in Upper Scorpius. My survey used nonredundant aperture-mask interferometry to achieve typical contrast limits of $\Delta K \sim$5–6 at the diffraction limit, revealing binary companions that lay below the detection limits of traditional high-resolution imaging. The overall frequency of binary companions ($\sim$35$^{+5}_{-4}$% at separations of 6–435 AU) appears to be equivalent to field stars of similar mass, but companions could be more common among lower-mass stars than for the field. The

companion mass function has statistically significant differences compared to several suggested mass functions for the field, and I suggest an alternate log-normal parameterization of the mass function. My survey limits encompass the entire brown dwarf mass range, but I only detected a single companion that might be a brown dwarf; this deficit resembles the so-called brown dwarf desert that has been observed by radial-velocity planet searches. Finally, my survey's deep detection limits extended into the top of the planetary mass function, reaching 8–12 M_{Jup} for half of our sample, but I did not identify any planetary companions.

In Chapter 6, I present the results of a large-scale survey of multiplicity at the bottom of the IMF in Taurus and Upper Sco; this program was meant to follow up the survey described in Chapter 3, studying the mass-dependent outcome of low-mass binary formation. I again confirmed the overall trend observed in the field for lower-mass binary systems to be less frequent and more compact, including a null detection for any substellar binary systems with separations wider than $\sim$7 AU. I also demonstrated that the binary frequency and binary separations decline between masses of 0.5 $M_{\odot}$ and 0.03 $M_{\odot}$, though I can not distinguish the form of this decline due to a degeneracy between the total binary frequency and the mean binary separation. I also show that the mass ratio distribution becomes progressively more concentrated at $q \sim$1 for declining masses, though a small number of systems appear to have unusually wide separations and low mass ratios for their mass. Finally, I found no wide planetary-mass companions in my survey, or in any previous survey that was sensitive to such low masses. Depending on the functional form of the companion mass distribution, my null result suggests an upper limit on the companion frequency of $\sim$1% at a 50% confidence level or $\sim$2%–3% at a 90% confidence level.

In Chapter 7, I study the binary population of the Taurus-Auriga association using the component positions in an HR diagram, in order to quantify the frequency and degree of coevality in young binary systems. Multiple star systems are commonly assumed to form coevally, so they provide the anchor for most calibrations of stellar evolutionary models. After identifying and rejecting the systems that are known to be affected by systematic errors (due to further multiplicity or obscuration by cir-

cumstellar material), I found that the overall dispersion in predicted relative binary ages, $\Delta \log \tau$, is 0.40 dex. For comparison, random pairs of Taurus members are coeval only to within 0.58 dex, indicating that Taurus binaries are indeed more coeval than the association as a whole. Based on the distribution of $\Delta \log \tau$, my sample appears to be composed of two populations, with $\sim 2/3$ appearing significantly more coeval ($\sigma_{\Delta \log \tau} \sim 0.16$ dex) and the other $\sim 1/3$ distributed in an extended tail with $\Delta \log \tau \sim 0.4$–0.9 dex. I suggest that the tail of the differential age distribution includes unrecognized hierarchical multiples, stars seen in scattered light, or stars with disk contamination; additional follow-up is required to rule out or correct for these explanations. I also find that the relative coevality of binary systems does not depend significantly on the system mass, mass ratio, or separation, but any pair of Taurus members wider than $\sim 10'$ (~ 0.7 pc) shows the full age spread of the association.

Finally, in Chapter 8, I synthesize all of the conclusions of my observational and archival programs into a series of "lessons" to guide future observational and theoretical work. Many of these lessons support the reigning ideas regarding multiple star formation, but I also cast significant doubt upon some concepts and convincingly debunk several more.

Bibliography

Abt, H. & Levy, S. 1976, ApJS, 30, 273

Andrews, S. & Williams, J. 2005, ApJ, 631, 1134

Allen, P. 2007, ApJ, 668, 492

Ardila, A., Martín, E., & Basri, G. 2000, AJ, 120, 479

Bate, M. 2009a, MNRAS, 392, 590

Bate, M. 2009b, MNRAS, 392, 1363

Bate, M. & Bonnell, I. 1997, MNRAS, 285, 33

Bodenheimer, P. & Burkert, A. 2001, in The Formation of Binary Stars, ed. H. Zinnecker & R. Mathieu (San Francisco, CA: ASP), 13

Bonnell, I. 2001, in The Formation of Binary Stars, ed. H. Zinnecker & R. Mathieu (San Francisco, CA: ASP), 23

Boss, A. 1988, ApJ, 331, 370

Bouvier, J., Duchêne, G., Mermilliod, J.-C., & Simon, T. 2001, A&A, 375, 989

Bouvier, J., Rigaut, F., & Nadeau, D. 1997, A&A, 323, 139

Bouy, H. et al. 2003, AJ, 126, 1526

Briceño, C. et al. 2002, ApJ, 580, 317

Burgasser, A. et al. 2003, ApJ, 125, 850

Carson, J., Hiner, K., Villar, G., Blaschak, M., Rudolph, A., & Stapelfeldt, K. 2009, AJ, 137, 218

Cazes, J. & Tohline, J. 2000, ApJ, 532, 1051

Clarke, C. 1992, Complementary Approaches to Double and Multiple Star Research, ed. H. McAlister & W. Hartkopf (San Francisco, CA: ASP), 176

Clarke, C. & Pringle, J. 1993, MNRAS, 261, 190

Close, L. et al. 2003, ApJ, 587, 407

Corder, S., Eisner, J., & Sargent, A. 2005, ApJ, 622, L133

Currie, T., Lada, C., Plavchan, P., Robitaille, T., Irwin, J., & Kenyon, S. 2009, ApJ, 698, 1

Duchêne, G., Monin, J.-L., Bouvier, J., & Menard, F. 1999, A&A, 351, 954

Duquennoy, A. & Mayor, M. 1991, A&A, 248, 485

Eisner, J., Plambeck, R., Carpenter, J., Corder, S., Qi., C., & Wilner, D. 2008, ApJ, 683, 304

Enoch, M., Evans, N., Sargent, A., & Glenn, J. 2009, ApJ, 692, 973

Fischer, D. & Marcy, G. 1992, ApJ, 396, 178

Ghez, A., Neugebauer, G., & Matthews, K.1993, AJ, 106, 2005

Gliese, W. 1969, Veröffentlichungen des Astronomishen Rechen-Instituts, Heidelberg, 22

Goodman, A., Barranco, J., Wilner, D., & Heyer, M. 1998, ApJ, 504, 223

Goodwin, S. & Kroupa, P. 2007, in Protostars and Planets V, ed. B. Reipurth, D. Jewitt, & K. Keil (Tucson: Univ. Arizona Press), 133

Halbwachs, J. 1987, A&A, 183, 234

Herbig, G. & Bell, K. 1988, Lick Obs. Bull., 1111, 1

Hernàndez, J. et al. 2007, ApJ, 662, 1067

Jaschek, C. & Jaschek, M. 1957, PASP, 69, 546

Jensen, E. et al. 2007, AJ, 134, 241

Kenyon, S. & Hartmann, L. 1995, ApJS, 101, 117

Kirkpatrick, J.D. et al. 1999, ApJ, 519, 802

Koenig, X., Allen, L., Gutermuth, R., Hora, J., Brunt, C., & Muzerolle, J. 2008, ApJ, 688, 1142

Köhler, R., Petr-Gotzens, M., McCaughrean, M., Bouvier, J., Duchêne, G., Quirrenbach, A., & Zinnecker, H. 2006, A&A, 458, 461

Kuiper, G. 1942, ApJ, 95, 201

Lada, C., Muench, A., Rathborne, J., Alves, J., & Lombardi, M. 2008, ApJ, 672, 410

Leinert, Ch. et al. 1993, A&A, 278, 129

Lowrance, P. et al. 2005, AJ, 130, 1845

Luhman, K. 2004, ApJ, 617, 1216

Luhman, K. 2006, ApJ, 645, 676

Luyten, W. 1930, Proc. Nat. Acad. Sci., 16, 257

Mann, R. & Williams, J. 2009, ApJ, 699, 55

Marcy, G. & Butler, R. 1996, ApJ, 464, 147

Marcy, G. & Butler, R. 2000, PASP, 112, 137

Mayor, M., & Queloz, D. 1995, Nature, 378, 355

McCarthy, C., & Zuckerman, B. 2004, AJ, 127, 2871

Mermilliod, J.-C., Rosvick, J., Duquennoy, A., & Mayor, M. 1992, A&A, 265, 513

Metchev, S. & Hillenbrand, L. 2004, ApJ, 617, 1330

Metchev, S. & Hillenbrand, L. 2009, ApJS, 181, 62

Monet, D. et al. 2003, AJ, 125, 984

Offner, S., Klein, R., McKee, C., & Krumholz, M. 2009, ApJ, in press

Öpik, E. 1924, Tartu Obs. Publ., 25, 6

Ostriker, E. 1994, ApJ, 424, 292

Patience, J., Ghez, A., Reid, I.N., & Matthews, K. 2002, AJ,123, 1570

Patience, J., Ghez, A., Reid, I.N., Weinberger, A., & Matthews, K. 1998, AJ, 115, 1972

Petrie, R., 1960, Ann. d'Ap., 23, 744

Portegies Zwart, S., Hut, P., McMillan, S., & Verbunt, F. 1997, A&A, 328, 143

Preibisch, T., Brown, A., Bridges, T., Guenther, E., & Zinnecker, H. 2002, AJ, 124, 404

Price, D. & Bate, M. 2009, MNRAS, 398, 33

Reid, I.N., Gizis, J., Kirkpatrick, J.D., & Koerner, D. 2001, AJ, 121, 489

Reipurth, B. & Clarke, C. 2001, AJ, 122, 432

Shu, F., Adams, F., & Lizano, S. 1987, ARA&A, 25, 23

Siegler, N., Close, L., Cruz, K., Martín, E., & Reid, I.N. 2005, ApJ, 621, 1023

Simon, M. et al. 1995, ApJ, 443, 625

Skrutskie, M. et al. 2006, AJ, 131, 1163

Slesnick, C., Carpenter, J., & Hillenbrand, L. 2006a, AJ, 131, 3016

Slesnick, C., Carpenter, J., Hillenbrand, L., & Mamajek, E. 2006b, AJ, 132, 2665

Strom, K., Strom, S., Edwards, S., Cabrit, S., & Skrutskie, M. 1989, AJ, 97, 1451

Tobin, J., Hartmann, L., Furesz, G., Mateo, M., & Megeath, S. 2009, ApJ, 697, 1103

Tohline, J. 2002, ARA&A, 40, 349

Tohline, J. & Durisen, R. 2001, in The Formation of Binary Stars, ed. H. Zinnecker & R. Mathieu (San Francisco, CA: ASP), 40

Toomre, A. 1964, ApJ, 139, 1217

Trimble, V. 1978, Observatory 98, 163

Trimble, V. 1990, MNRAS, 242, 79

Watson, D. et al. 2007, Nature, 448, 1026

White, R. & Ghez, A. 2001, ApJ, 556,265

White, R., Ghez, A., Reid, I.N., & Schultz, G. 1999, ApJ, 520, 811

Wizinowich, P. et al. 2006, PASP, 118, 297

Chapter 2

The Spatial Distributions of Young Stars

Abstract

We analyze the spatial distribution of young stars in Taurus-Auriga and Upper Sco, as determined from the two-point correlation function (i.e., the mean surface density of neighbors). The corresponding power-law fits allow us to determine the fractal dimensions of each association's spatial distribution, measure the stellar velocity dispersions, and distinguish between the bound binary population and chance alignments of members. We find that the fractal dimension of Taurus is $D \sim 1.05$, consistent with its filamentary structure. The fractal dimension of Upper Sco may be even shallower ($D \sim 0.7$), but this fit is uncertain due to the limited area and possible spatially-variable incompleteness. We also find that random stellar motions have erased all primordial structure on scales of $<0.07^o$ in Taurus and $<1.7^o$ in Upper Sco; given ages of ~ 1 and ~ 5 Myr, the corresponding internal velocity dispersions are ~ 0.2 km and ~ 1.0 km s^{-1}, respectively. Finally, we find that binaries can be distinguished from chance alignments at separations of $<120''$ (17,000 AU) in Taurus and $<75''$ (11,000 AU) in Upper Sco. The binary populations in these associations that we previously studied, spanning separations of $3''$–$30''$, is dominated by binary systems. However, the few lowest-mass pairs ($M_{prim}<0.3\ M_\odot$) might be chance alignments.

2.1 Introduction

The spatial distribution of young stars is a powerful diagnostic of their formation and early evolution. Young stars trace the gas distribution from which they formed, so the large-scale structure of a young association retains these primordial features after the gas has been accreted or dispersed. On intermediate scales, the absence of structure indicates the typical distance over which stars have randomly dispersed since their birth, and therefore the velocity dispersion for the association. Finally, the enhanced stellar density on small scales outlines the binary population, distinguishing bound binary systems from chance alignments between young stars. Some of these topics have been addressed in previous work on young star distributions (Gomez et al. 1993; Larson 1995; Simon 1997; Bate et al. 1998; Hartmann 2002), but the modern census of several key star-forming regions is more complete and extends to lower masses than a decade ago, so the analysis is worth revisiting.

The traditional tool for studying spatial distributions is the two-point correlation function (hereafter TPCF). The TPCF, $w(\theta)$, is defined as the number of excess pairs of objects with a given separation θ over the expected number for a random distribution (Peebles 1980). The TPCF is proportional to the mean surface density of neighbors, so it is often recast in terms of this more intuitive quantity: $\Sigma(\theta) = (N_*/A)[1 + w(\theta)]$, where A is the survey area and N_* is the total number of stars.

In this letter, we describe an updated relation for $\Sigma(\theta)$ in Taurus and present the first such analysis for Upper Sco, then we fit power laws for the different angular regimes. Finally, we interpret our results to address three questions: What is the primordial fractal dimension of star-forming regions, and how does it relate to their observed geometry? What is the primordial velocity dispersion suggested by each association's randomization? And what is a wide binary companion, and can it be distinguished from an unbound association member?
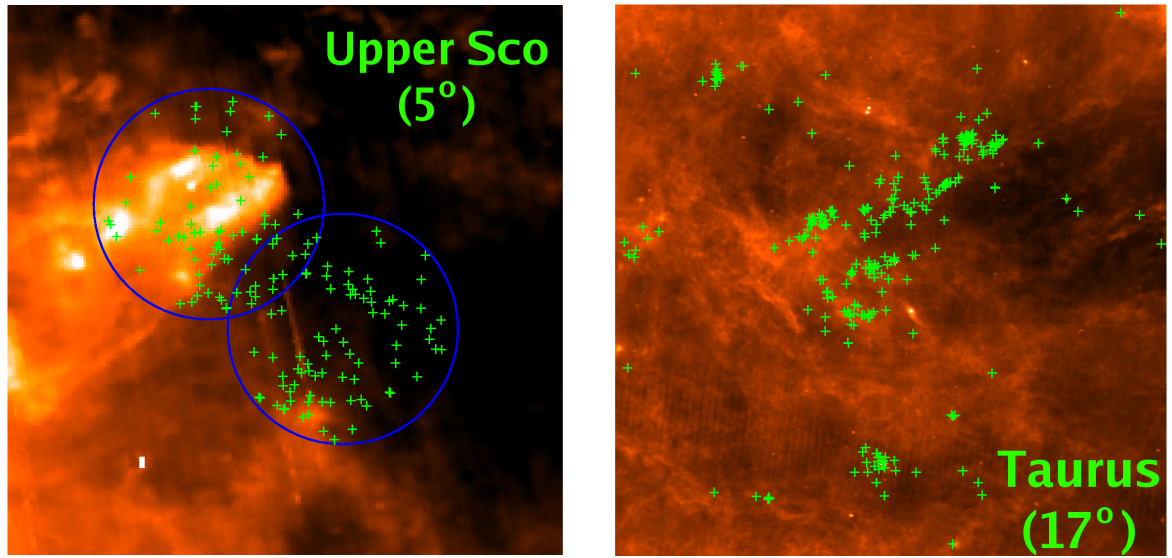
Figure 2.1 Locations of stars in Taurus and Upper Sco, superimposed on 60 μm IRAS images. Members are denoted by green crosses, while the sample fields in Upper Sco are denoted by blue circles. The field of view is 17° in Taurus and 5° in Upper Sco. Known members in Upper Sco outline the dusty clouds in the northern field, suggesting systematic incompleteness for extincted members.

Table 2.1.   Power Law Fits

Regime	Sep Range[a]	α	C (log deg^{-2})
		Upper Sco	
Binary	3″-30″	-1.44±0.41	2.98±0.12 (at 9.5″)
Intermediate	2.8′-1.5^o	-0.12±0.02	1.537±0.010 (at 16′)
Association	1.5^o-4.7^o	-1.31±0.09	1.174±0.011 (at 2.6^o)
		Taurus	
Binary	3″-30″	-1.53±0.32	3.28±0.10 (at 9.5″)
Intermediate	1.6′-5.0′	0.12±0.39	1.62±0.05 (at 2.8′)
Association	5.0′-4.7^o	-0.951±0.007	0.650±0.005 (at 1.2^o)

[a]There is a small range of separations between the binary and intermediate regimes where the data are consistent with our power law fits, but the uncertainties are too large for those data to contribute meaningfully to the fits.

2.2   The Correlation Functions of Taurus and Upper Sco

We compiled our Taurus sample from the member list in Kraus & Hillenbrand (2007a, 2008; hereafter KH07a and KH08), plus the Class 0/I sources that were compiled by Kenyon & Hartmann (1995). We omitted the latter sources from our multiplicity surveys because their stellar properties are uncertain, but we include them here because that information is not necessary for clustering analysis. We have also included the partial list of new sources identified in data from the Taurus Spitzer Legacy Project (Padgett et al. 2006) as described by Luhman et al.(2006). For separations of <30″, we have calculated the surface density of neighbors only among those sources included in our initial wide binary survey. We have neglected the Class 0/I and heavily embedded sources because only some have been surveyed for multiplicity in the mid-infrared wavelengths (e.g., Duchêne et al. 2004), and not with uniform sensitivity. Our full sample consists of 272 members, while the binary-regime sample consists of 226. The Taurus sample is almost certainly incomplete, as a number of additional

candidates have been identified in the Taurus Legacy Project (Padgett et al. 2006) and the XEST survey (Scelsi et al. 2007). However, preliminary reports suggest an increment of $<20\%$ in the total sample. Even if these new members do not trace the known distribution, their influence should be modest.

The census of Upper Sco across the full association is very incomplete, so we implemented our analysis for intermediate and large separations ($\theta > 30''$) using only members in two heavily studied fields observed by Preibisch et al.(2002), the 2dfE and 2dfW fields. The census of members in these fields is not complete, but we expect that it is the least incomplete. As for Taurus, we calculated the surface density of neighbors at $<30''$ using the full sample of our wide binary surveys; this choice maximizes our sample size for small separations (where the statistics are weakest). The 2dfE/2dfW and binary samples consist of 162 and 352 members.

In Figure 2.1, we plot the locations of our sample members superimposed on archival 60μm IRAS images. In Upper Sco, we see evidence of incompleteness for the northern field. Most of the known members outline the dusty regions, suggesting that any members in these regions were too extincted to have been identified. As we discuss later, this could affect the TPCF on scales of $>1^o$. In Taurus, the distribution traces the filamentary dust, though there are also many filaments that do not include any known members.

We directly measured $\Sigma(\theta)$ for Taurus because our sample spans the entire area of the association. However, for bounded subsets (as in Upper Sco), it is often easier to evaluate the TPCF via a Monte Carlo-based definition, $w(\theta) = N_p(\theta)/N_r(\theta) - 1$, where $N_p(\theta)$ is the number of pairs with separations in a bin centered on θ and $N_r(\theta)$ is the expected number of pairs for a random distribution of objects over the bounded area (Hewett 1982). The advantage is that this method does not require edge corrections, unlike direct measurement of $\Sigma(\theta)$. In both cases, we report our results as $\Sigma(\theta)$ since it is a more visually motivated quantity than $w(\theta)$. In Figure 2.2, we plot $\Sigma(\theta)$ for Upper Sco (top) and Taurus (bottom) spanning a separation range of $3''$ to 10°.

Based on the predicted time evolution of young associations (Bate et al. 1998),

we expect that $\Sigma(\theta)$ can be fit with a twice-broken power law, corresponding to structure on three scales. At small scales, bound binary systems yield a relatively steep power law. At large scales (and for young ages, <1 crossing time), intra-association clustering yields a shallower (but nonzero) power law that corresponds to the primordial structure of the association. Finally, at intermediate separations, the random motion of association members acts to smooth out the primordial structure and yield a constant surface density (and thus a slope near zero, according to the simulations of Bate et al. 1998). The first knee (transition between gravitationally bound multiplicity and a smooth randomized distribution) corresponds to the maximum angular scale for distinguishing binary systems, while the second knee (transition between a random distribution and primordial structure) corresponds to an angular scale that depends on the age since members were released from their natal gas clouds, τ, and the internal velocity dispersion, v_{int}, where $\theta \propto \tau v_{int}$. Hartmann (2002) suggested that this break also could indicate the mean spacing of cores along filaments (the Jeans length), which assumes that stars have randomized by a smaller angular scale and that the inferred value characteristic angular scale, the inferred value of v_{int} is an upper limit.

In Table 2.1, we summarize our weighted least-squares fits for the power law slope α and zero-point C in each regime. The binary regime was fit in the range probed in our survey of wide multiplicity ($3''$–$30''$), while the intermediate and association regimes were fit in the ranges where the error bars were <3%. We established the zero point of each fit at the logarithmic center of the angular range in order to minimize correlation between σ_α and σ_C. In Upper Sco, both the inner and middle power laws are clearly defined, but the fit for the outer regime is uncertain because the angular scale is similar to the size of the survey area ($\sim 2^o$–4°). In Taurus, the inner and outer power laws are clearly defined, but the fit for the intermediate regime is uncertain. The TPCF at separations of $2'$–$4'$ is flat and diverges from the fit for larger and smaller separations by 3σ–5σ, so we provisionally assume that this separation range represents the intermediate regime. The points at smaller separations also fall below the projection of the association-regime power law, while the points at larger

separations agree well with the overall fit, suggesting that our inferred value of v_{int} is at most an upper limit. The locations of the first knee, where the two power laws are equal, are $\theta_{1,USco} \sim 75''$ and $\theta_{1,Tau} \sim 120''$; the respective locations of the second knee are $\theta_{2,USco} \sim 1.7^o$ and $\theta_{2,Tau} \sim 0.07^o$. The formal uncertainties in these measurements are only $\sim$2-3%, but the errors are dominated by systematic uncertainties in the membership census and in the angular range over which to fit each regime.

2.3   Association Regime: The Fractal Dimension of Taurus

The primordial spatial distribution of young stars should trace the overdensities in the original gas distribution from which those stars formed (e.g., Hartmann 2002; Bate et al. 2003). Even if these gas distributions have dispersed, the remnants of primordial structure in the stellar distribution can still provide a key constraint to the distribution of overdensities during star formation. Early studies of TPCFs have suggested that current (and presumably primordial) stellar distributions are fractal in nature (e.g., Larson 1995; Simon 1997), with self-similar structure on a range of angular scales. Similar TPCFs can be reproduced (at least over a decade of separation) with simpler distributions like a finite number of non-fractal subclusters following a simple r^α profile (Bate et al. 1998). However, our TPCF for Taurus follows a single power law across >2 decades of separation, so it appears to be genuinely self-similar. The dimensionality D of a fractal distribution indicates the extent to which it fills space, such that the number of neighbors N within a distance θ goes as $N(\theta) \propto \theta^D$. This parameter is related to the surface density of neighbors; if $\Sigma(\theta) \propto \theta^\alpha$, then $D = \alpha + 2$ (Larson 1995).

The fractal dimension is a result of the turbulent fragmentation that leads to star formation, and most models yield filamentuary structure (i.e., a dimension near unity). As we showed in Section 2.2, the observed power-law slope for Taurus in the large-scale regime is $\alpha = -0.951 \pm 0.007$, indicating that the fractal dimension
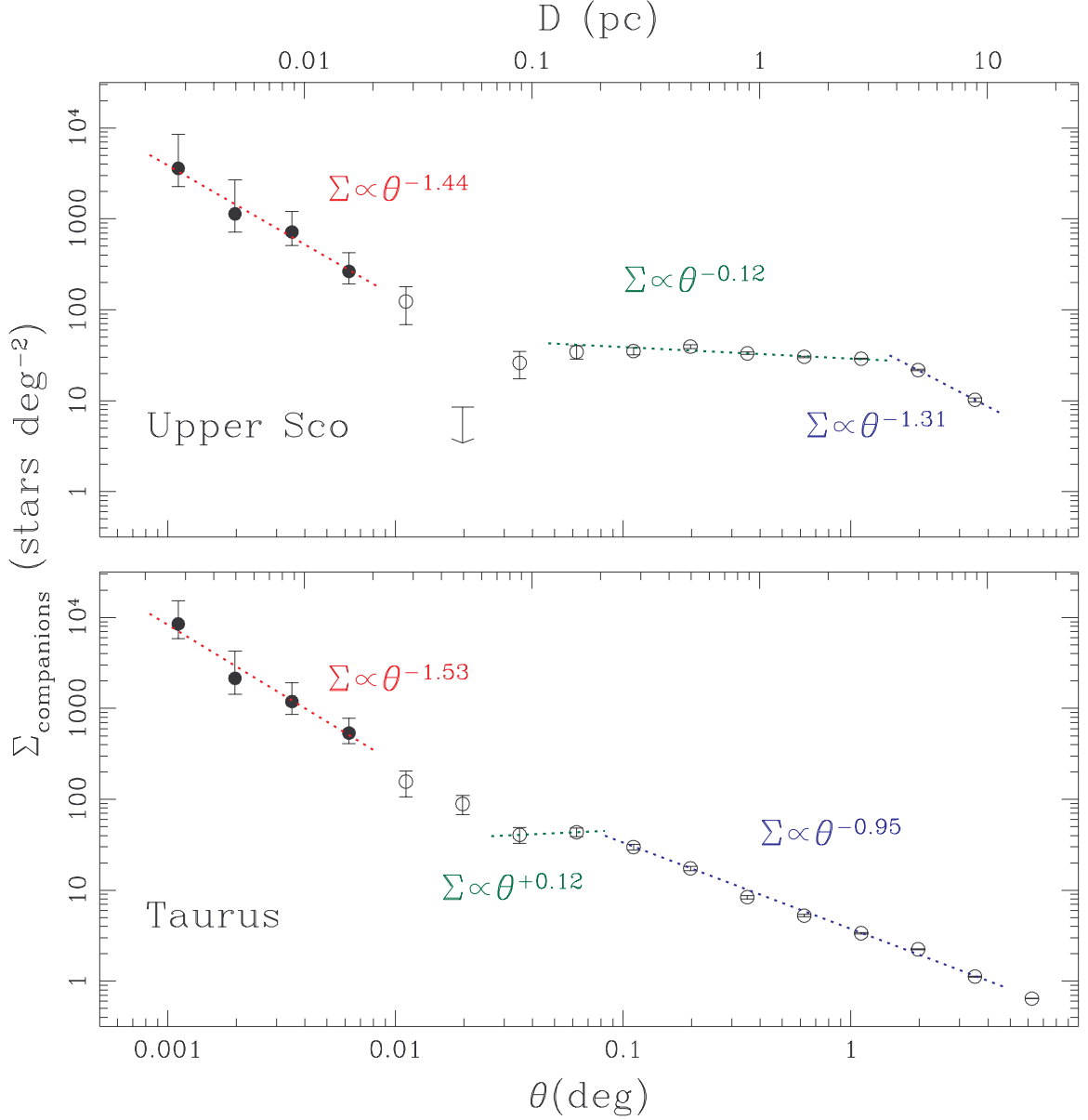
Figure 2.2 Two-point correlation functions for members of Upper Sco and Taurus. These plots show the surface density of neighbors as a function of separation, $\Sigma(\theta)$, with θ in degrees (bottom axis) or in parsecs (top axis). The observations are from our recent wide binary survey (KH08; filled circles) or membership surveys in the literature (open circles). For each association, we have fit power laws to the small-scale regime (red; binary systems), the large-scale regime (blue; association members distributed according to the primordial structure), and the intermediate regime (green; association members with a randomized spatial distribution).

($D = 1.049\pm0.007$) is indeed close to unity. This result is consistent with visual inspection of the stellar distribution, as well as with CO maps of the remaining gas distribution (e.g., Goldsmith et al. 2008). Our value is significantly lower than the fractal dimension suggested by Larson (1995) and Simon (1997), $D = 1.4$, but close to the more recent value suggested by Hartmann (2002). Our sample is significantly more complete than the older samples; based on our reconstruction of those samples, most of the new (typically low-mass) members are located near the major concentrations (e.g., Strom & Strom 1994; Briceño et al. 2002) rather than in the more distributed population (e.g., Slesnick et al. 2006). These members increase the surface density of neighbors at small separations, yielding a steeper slope for $\Sigma(\theta)$. However, the census is still incomplete (Section 2.2) and if the incompleteness is spatially variable, such as for heavily embedded brown dwarfs, then our updated power-law slope could be incorrect.

We are hesitant to estimate the fractal dimension in Upper Sco. The appropriate regime in the TPCF includes only two separation bins, so the choice of bin locations could significantly affect the slope. Incompleteness in the dusty northern region could also influence the inferred large-scale structure. However, if we adopt our power-law fit from Section 2.2 ($\alpha= -1.31\pm0.09$), we find that $D = 0.69\pm0.09$ on scales of $\sim2^o$.

2.4 Intermediate Regime: The Primordial Velocity Dispersion

The angular scales over which structure has been randomized, as indicated by the location of the second knee in $\Sigma(\theta)$, directly constrains the primordial velocity dispersion for each association (e.g., Bate et al. 1998). This constraint is particularly important for low-density associations like Taurus and Upper Sco because the expected velocity dispersion ($<$1-2 km s^{-1}; Frink et al. 1997) may be too low to be measured easily via a direct method (like high-resolution spectroscopy to determine radial velocities). OB and T associations are not bound once their unaccreted gas

is expelled (e.g., Lada et al. 1984), so the internal velocity dispersion is critical for determining how long they can persist as recognizable moving groups (like the β Pic, TW Hya, or μ Oph associations; Webb et al. 1999; Zuckerman et al. 2004; Mamajek 2006) and how long substructure can remain in these moving groups.

Allowing for projection effects, the angular scales of each TPCF's outer knee correspond to physical dispersion scales of ~ 0.23 pc in Taurus and ~ 6 pc in Upper Sco. Given the characteristic ages of each association (~ 1 Myr and ~ 5 Myr, respectively), the corresponding characteristic velocity dispersions are ~ 0.2 km s^{-1} and ~ 1.0 km s^{-1}. As we previously discussed, there is uncertainty in the fits, so this values should be taken with caution. We also note that these values represent the velocity dispersion with respect to other stars only within an angular distance of $\sim \theta_{knee}$. We can not rule out the possibility that larger substructures are moving coherently with a higher velocity dispersion, only that any substructure with angular size θ is not moving with sufficient speed ($\dot{\theta} \sim \theta/\tau$) that its angular displacement from birth is of order θ. This limit also suggests an explanation for the larger velocity dispersion in Upper Sco; even if the velocity dispersion within ~ 0.1-0.2 pc substructures is the same as in Taurus, the observed TPCF could be reproduced if the velocity dispersion between those substructures is ~ 1 km s^{-1}. A scale dependence in the velocity dispersion could also explain previous proper motion studies in Taurus, which found velocity dispersions within the major subclumps (on scales of ~ 1-3 pc; e.g., Jones & Herbig 1979) that were ~ 1 km s^{-1}.

A similar effect has been noted in locations like the ONC, where radial velocities show an overall north-south gradient of ~ 5 km s^{-1} in addition to the local velocity dispersion of 2-3 km s^{-1} (Fũrész et al. 2008). However, there is also observational evidence that small-scale velocity dispersions are higher in denser clusters; submillimeter observations of IRS1 in NGC 2264 (Williams & Garland 2002) found that six protostellar cores (spanning 0.44 pc) had a velocity dispersion of 0.9 km s^{-1}, which is much higher than the velocity dispersion that we find in Taurus, though also closer to the value for scales of 1-3 pc suggested by Jones & Herbig (1979).

Our results suggest that regions like Taurus and Upper Sco are even less dynami-

cally active, relative to the ONC, than their lower densities might imply. The velocity dispersions also provide a direct estimate of the virial velocity in the natal environment (before the removal of gas) and therefore jointly constrain the typical mass and size of a star-forming clump: $Mv^2 \sim (3GM^2)/(5R)$ or $M/R \sim (5v^2)/(3G)$, yielding $M/R \sim 15$ in Taurus and $M/R \sim 550$ in Upper Sco, where the mass is in solar masses and the radius is in parsecs. Thus, the primordial star-forming structures that are now dispersing with these characteristic velocities were smaller and/or more massive in Upper Sco than in Taurus.

2.5   Binary Regime: What is a Binary System?

The existence and properties of wide binary systems are critical for constraining multiple star formation in the limiting case of large separations and early times. If wide binaries form out of a single protostellar clump, then the maximum separation also constrains the maximum size of clumps that can collapse to become bound systems. As previous authors have suggested (e.g., Larson 1995), the outer edge of the young binary separation distribution is similar to the mean Jeans length for nearby molecular clouds. This limit is also similar to the maximum separation seen in the field (e.g., Duquennoy & Mayor 1991), suggesting that some wide binaries join the field without being subjected to significant dynamical interactions. However, study of young binaries is complicated by the difficulty of distinguishing gravitationally bound binary pairs from coeval, comoving association members that are aligned in projection. We addressed this issue for a single system in Upper Sco (UScoJ1606-1935; Kraus & Hillenbrand 2007b) by calculating the association's TPCF to determine the probability that it is a bound system; we now extend our analysis to the full known populations of Taurus and Upper Sco.

We find that the transition between the binary and intermediate regimes occurs at $\sim$11,000 AU in Upper Sco and $\sim$17,000 AU in Taurus. The binary population therefore extends at least to these angular scales, but we can not distinguish binary companions from chance alignments outside this limit. The difference between these

regimes is a result of the higher total wide binary frequency in Taurus (KH07a, KH08), as the overall surface density of "contaminant" co-association members is similar in both associations. The number statistics do not support any assertions regarding the outer maximum limit of binary formation, but this angular scale matches both the maximum binary separation seen in the field and the typical Jeans length, so we do not expect to find many binary systems with wider separations.

Candidate companions inside this limit could also be chance alignments, but the probability drops for progressively smaller separations. In Upper Sco, we expect $\sim$3.3 chance alignments with separations of 15-30″ from an intermediate- or high-mass member ($M_{prim} >$0.4 $M_\odot$), plus another $\sim$2.4 chance alignments of two low-mass members. The number of high-mass chance alignments is far lower than the total number of pairs, which suggests that the vast majority are bound binaries. However, our wide binary survey found only four wide pairs of low-mass companions, so it is unclear whether any are genuine binary systems. The contamination rate is moderately lower in Taurus, yielding <1 contaminant in either mass range, but the results are similar. Most of the high-mass pairs are binary systems, but the two low-mass pairs may or may not be bound binary systems.

Bibliography

Bate, M., Clarke, C., & McCaughrean, M. 1998, MNRAS, 297, 1163

Bate, M., Bonnell, I., & Bromm, V. 2003, MNRAS, 339, 577

Briceño, C., Luhman, K., Hartmann, L., Stauffer, J., & Kirkpatrick, J. 2002, ApJ, 580, 317

Duchêne, G., Bouvier, J., Bontemps, S., André, P., & Motte, F. 2004, A&A, 427, 651

Duquennoy, A. & Mayor, M. 1991, A&A, 248, 485

Frink, S., Roser, S, Neuhauser, R., & Sterzik, M. 1997, A&A, 325, 613

Fűrész, G., Hartmann, L., Megeath, S., Szentgyorgyi, A., & Hamden, E. 2008, ApJ, 676, 1109

Goldsmith, P., Heyer, M., Narayanan, G., Snell, R., Li, D., & Brunt, C. 2008, arXiv:0802.2206

Gomez, M., Hartmann, L., Kenyon, S., & Hewett, R. 1993, AJ, 105, 1927

Hartmann, L. 2002, ApJ, 578, 914

Hewett, P. 1982, MNRAS, 201, 867

Jones, B. & Herbig, G. 1979, AJ, 84, 1872

Kenyon, S. & Hartmann, L. 1995, ApJS, 101, 117

Kraus, A. & Hillenbrand, L. 2007a, ApJ, 662, 413 (KH07a)

Kraus, A. & Hillenbrand, L. 2007b, ApJ, 664, 1167

Kraus, A. & Hillenbrand, L. 2009, ApJ, in press

Lada, C., Margulis, M., Dearborn, D. 1984, ApJ, 285, 141

Larson, R. 1995, MNRAS, 272, 213

Luhman, K., Whitney, B., Meade, M., Babler, B., Indebetouw, R., Bracker, S., & Churchwell, E. 2006, ApJ, 647, 1180

Mamajek, E. 2006, AJ, 132, 2198

Padgett, D. et al. 2006, BAAS, 209, 3016

Peebles, J. 1980, The Large Scale Structure of the Universe (Princeton: Princeton Univ. Press)

Preibisch, T. et al. 2002, AJ, 124, 404

Scelsi, L. et al. 2007, A&A, 468, 405

Simon, M. 1997, ApJ, 482, 81

Slesnick, C., Carpenter, J., Hillenbrand, L., & Mamajek, E. 2006, AJ, 132, 2665

Strom, K. & Strom, S. 1994, ApJ, 424, 237

Webb, R., Zuckerman, B., Platais, I., Patience, J., White, R., Schwartz, M., & Mc-Carthy, C. 1999, ApJ, 512, 63

Williams, J. & Garland, C. 2002, ApJ, 568, 259

Zuckerman, B., Song, I., & Bessell, M. 2004, ApJ, 613, 65

Chapter 3

Multiplicity and Optical Excess Across the Substellar Boundary in Two Young Associations

Abstract

We present the results of a high-resolution imaging survey of 34 brown dwarfs and very-low-mass stars in the nearby ($\sim$145 pc) young ($\sim$1–5 Myr) star-forming regions Upper Sco and Taurus-Auriga. We obtained images with the Advanced Camera for Surveys/High Resolution Channel on HST through the $F555W$ (V), $F775W$ (i'), and $F850LP$ (z') filters. This survey found five binary systems, yielding binary frequencies of $9^{+10}_{-4}\%$ in Taurus and $25^{+16}_{-9}\%$ in Upper Sco. All systems are tight ($<$20 AU), and most have mass ratios near unity. The binary frequency and separations are consistent with low-mass binary properties in the field, but the mass ratio of V410-Xray3 is among the lowest known. We find that the binary frequency is higher for very-low-mass stars and high-mass brown dwarfs than for lower-mass brown dwarfs, implying either a decline in frequency or a shift to smaller separations for the lowest mass binaries. Combining these results with multiplicity statistics for higher-mass Taurus members suggests a gradual decline in binary frequency and separation toward low masses. The implication is that the distinct binary properties of very-low-mass systems are set during formation and that the formation process is similar to the

process which creates higher-mass stellar binaries, but occurs on a smaller scale. We combine the survey detection limits with models for planetary-mass objects to show that there are no planets or very-low-mass brown dwarfs with mass $> 3M_J$ (for Taurus) or $> 5M_J$ (for Upper Sco) at projected separations >40 AU orbiting any of the members in our sample, implying that planetary-mass companions at wide separations are rare. Finally, based on fits to the optical and near-infrared spectral energy distributions, we identify several BDs with significant (≥ 1 mag) V-band excesses. The excesses appear to be correlated with signatures of accretion, and if attributed to accretion luminosity, may imply mass accretion rates several orders of magnitude above those inferred from line-profile analyses.

3.1 Introduction

Brown dwarfs (BDs) are objects with masses between those of stars and planets, insufficient to maintain stable fusion reactions in their cores. BDs comprise a significant fraction of the total (sub)stellar content of the galaxy and are among our nearest neighbors (Reid et al. 2001); in the past decade, field surveys have discovered several hundreds of BDs in the solar neighborhood (e.g., Delfosse et al. 1997; Kirkpatrick et al. 1999; Leggett et al. 2000). Soon after BDs were discovered, it was found that many, like stars, are members of binary systems. However, the properties of binary systems near and below the substellar boundary ($M_{primary} < 0.2M_\odot$) appear to be fundamentally different from those of higher-mass stars ($0.3 < M_{primary} < 1.0M_\odot$). Multiplicity surveys of field T dwarfs (Burgasser et al., 2003), L dwarfs (Koerner et al., 1999; Close et al., 2003; Bouy et al., 2003; Gizis et al., 2003), and late M dwarfs (Siegler et al., 2005) have found lower binary frequencies ($\sim$15% vs 40%–55%) and smaller binary separations (<20 AU vs < 1000 AU) than for field stars (Duquennoy & Mayor 1991; Fischer & Marcy 1992; Halbwachs et al. 2003).

These results demonstrate that field binary properties depend on mass. Unfortunately, binary frequencies for field stars are only reported for broad mass ranges, so they do not place strong constraints on the functional form of this dependence. Var-

ious groups interpret the transition in binary properties as either a sharp break near the stellar/substellar boundary (Kroupa et al., 2003; Close et al., 2003) or a smooth mass dependence (Luhman, 2004b). Also, since field BD systems are typically old and possess lower binding energies than stellar binaries of equal separation, the results could be biased by the dynamical disruption of wide, low-mass systems. To begin testing this possibility, we performed a small multiplicity survey of low-mass stars and BDs in the nearby young OB Association Upper Scorpius (Kraus et al. 2005) and T Association Taurus (this work). In Upper Sco, we found several young binary systems, but the binary frequency, separations, and mass ratios were consistent with the field and somewhat ($\sim 2\sigma$) inconsistent with higher-mass members of Upper Sco (Kohler et al. 2000). This suggests that dynamical evolution after the T Tauri stage probably does not produce the unique binary parameters of BDs; instead, the implication is that the mechanism by which binaries form depends on mass.

Recent efforts to model low mass binary formation have typically assumed that a cluster of 5-10 protostellar embryos form from a single fragmenting cloud core (e.g., Kroupa 1995; Sterzik & Durisen 1998; Kroupa & Bouvier 2003; Kroupa et al. 2003; Delgado-Donate et al. 2003; Hubber et al. 2005); these embryos would then undergo dynamical evolution to form single stars and stable multiple systems. However, the frequency of multiple stellar systems ($M_{primary} > 0.3 M_\odot$) in the field (35-57%; Duquennoy & Mayor 1991; Reid & Gizis 1997) and in young associations (50-80%; Kohler et al. 2000; White et al. 2009) has been interpreted by Goodwin & Kroupa (2005) to mean that the collapse and fragmentation of a cloud core produces only 2 or 3 stars. Larger systems would eject more single stars and tight binaries than are observed. Reipurth & Clarke (2001) have suggested that evolution to a dynamically stable state could occur early in the formation process; the ejected embryos would then cease accretion and become BDs.

The ejection process would preferentially disrupt wide BD binary systems, causing the deficit of wide systems seen in low-mass field binaries. However, simulations by Bate et al. (2003) find that the corresponding binary frequencies and separations ($<5\%$ and <10 AU) are too low to be consistent with the field. Also, some wide

very-low-mass binaries have recently been discovered in the field (Gizis et al. 2000; Phan-Bao et al. 2005; Billeres et al. 2005). These systems are very weakly bound and most likely would not survive the ejection process, though recent simulations by Bate (2005) suggest that they could form via simultaneous ejection of previously-unbound objects. Finally, some models predict that ejection would alter other properties of BDs (spatial and velocity dispersion, disk lifetime, and accretion frequency). The preponderance of observations show that these properties are similar in the stellar and substellar regimes (White & Basri, 2003; Luhman, 2004b; White & Hillenbrand, 2004; Mohanty et al., 2005); the strong similarity between the two regimes suggests that brown dwarfs for in a manner similar to stars and thus that BD binaries form like stellar binaries, though possibly on a smaller scale. The implication is that all binaries share a common formation mechanism, fragmentation of a single collapsing cloud core, and that this mechanism features a mass dependence that remains unexplained by theoretical models.

Multiplicity surveys of the field and of nearby stellar populations (e.g., Kohler et al. 2000; Luhman et al. 2005a; White et al. 2009) have placed some constraints on the form of this mass dependence. In particular, White et al.(2006) studied the mass dependence of multiplicity in a speckle interferometry survey of the nearby ($\sim$145 pc) young ($\sim$1-2 Myr) T Association Taurus-Auriga. This survey included objects from 1.5 $M_\odot$ to the substellar boundary and found that the separation distribution and mass ratio distribution functions were mass dependent. Their results for the binary frequency were inconclusive, but suggested a possible slow decline with mass. Better statistics will be required for very-low-mass binaries in order to confirm this trend. In this chapter, we present the results of an complementary imaging multiplicity survey of very-low-mass stars and brown dwarfs to near the planetary mass regime in Upper Sco and Taurus-Auriga.

3.2 Observations and Data Reduction

3.2.1 Sample Selection

The Taurus-Auriga and Upper Scorpius associations have been the target of many recent wide-field surveys to detect new low-mass members (e.g., Briceno et al. 1998; Ardila et al. 2000; Martín et al. 2001; Briceno et al. 2002; Luhman et al. 2003a). These surveys identified candidate members based on their location on an optical or near-infrared color-magnitude diagram, and membership was then confirmed spectroscopically via the detection of lithium absorption, excess $H\alpha$ emission, or low surface gravity, all of which are indicators of youth.

In Taurus, the sample includes 18 members with spectral type later than M5.5 that were discovered by these surveys. Three additional targets (V410-Xray3, V410-Anon13, and GM Tau) were previously known Taurus members which have also been confirmed to possess spectral types in this range (Strom & Strom 1994; White & Basri 2003). Our final target (LH0419+15) was chosen from a survey for Hyades members by Reid & Hawley (1999); it is the only member of their survey with a spectroscopic detection of lithium, and they classify it as a likely Taurus member with spectral type M7 based on its apparent youth and distance.

In Upper Sco, the sample includes targets from the low-mass membership survey of Ardila et al.(2000). They identified 15 candidate members with spectral types of M5.5 or cooler, based on either low resolution spectra (10 objects) or $R - I_C$ colors (5 objects). Three of these 15 (USco 85, 114, 121) were determined to be likely non-members, based on low lithium abundance and radial velocities that are inconsistent with higher mass members (Muzerolle et al. 2003; White et al. 2009). The remaining 12 were observed in this program. Subsequently, membership for all but the faintest member of this sample, USco 137, has been confirmed with additional high resolution spectra (Mohanty et al. 2005). USco 137 has not yet been observed spectroscopically.

Finally, our targets include both very-low-mass stars and brown dwarfs, so we hereafter refer to them as very-low-mass objects, or VLMOs. We list these 34 VLMOs and their discovery or confirmation references in Table 3.1; this was a complete list of

known members of each association with spectral types later than M5.5 at the time the observations were proposed (January 2003).

3.2.2 Observations

The images were obtained with the Advanced Camera for Surveys/High Resolution Camera on the Hubble Space Telescope, which has a field of view of $2\text{arcsec}\times29''$ and distortion-corrected pixel size of 27 mas pix^{-1}. In Table 3.1, we summarize the exposure time and epoch of observation for each target (Program ID: 9853). Observations were made between July 2003 and January 2004 with the filters F555W (V), F775W (i'), and F850LP (z') at two dither positions near the center of the detector and with two exposures per position. Total integration times were 510, 300, and 200 seconds, respectively. The F555W exposure times for the brightest objects were reduced to 350 seconds to allow for additional short exposures in F775W and F850LP, which were close to the saturation limit in the full-length exposures and were saturated in the case of MHO-Tau-5 and MHO-Tau-8. Saturation was permitted in the full-length images to allow for comparable sensitivities to faint companions at wide separations. We chose the V band to maximize angular resolution (diffraction limit $\theta_{res,V} = 58$ mas) and the i' and z' bands to maximize sensitivity to very-low-mass companions.

The raw images were calibrated and distortion-corrected by the CALACS pipeline during on-the-fly reprocessing (Mack et al., 2003). Some cosmic rays remained, but their morphologies were substantially different from stellar PSFs, so they were easily identified by visual inspection.

3.2.3 Data Reduction

Potential point sources were identified with the IRAF task DAOPHOT/DAOFIND, which found all local brightness maxima with a significance of $> 5\sigma$ and a full-width at half-maximum (FWHM) near the expected value for the filter. We then measured aperture photometry and point-spread function (PSF) fitting photometry for

Table 3.1.   Observations

Target	Date[a]	Exposure Times (s)			Discovery
		F555W	F775W	F850LP	
CFHT-Tau-1	2904.3	510	300	200	Martín et al.(2001)
CFHT-Tau-2	2904.3	510	300	200	Martín et al.(2001)
CFHT-Tau-3	2901.5	510	300	200	Martín et al.(2001)
CFHT-Tau-4	2857.5	510	300	200	Martín et al.(2001)
GM Tau	2850.6	350	300/30	200/20	White & Basri (2003)
KPNO-Tau-1	2881.2	510	300	200	Briceno et al.(2002)
KPNO-Tau-2	2903.3	510	300	200	Briceno et al.(2002)
KPNO-Tau-3	2901.4	510	300	200	Briceno et al.(2002)
KPNO-Tau-4	2904.4	510	300	200	Briceno et al.(2002)
KPNO-Tau-5	2884.2	350	300/30	200/20	Briceno et al.(2002)
KPNO-Tau-6	3054.5	510	300	200	Briceno et al.(2002)
KPNO-Tau-7	2901.6	510	300	200	Briceno et al.(2002)
KPNO-Tau-8	2850.5	350	300/30	200/20	Briceno et al.(2002)
KPNO-Tau-9	3025.8	510	300	200	Briceno et al.(2002)
KPNO-Tau-12	3028.7	510	300	200	Luhman et al.(2003a)
KPNO-Tau-14	2897.5	350	300/30	200/20	Luhman et al.(2003a)
LH 0419+15	2901.0	510	300	200	Reid & Hawley (1999)
MHO-Tau-4	2893.5	350	300/30	200/20	Briceno et al.(1998)
MHO-Tau-5	3023.0	350	300/30	200/20	Briceno et al.(1998)
MHO-Tau-8	3028.5	350	300/30	200/20	Briceno et al.(1998)
V410 Anon13	2903.4	510	300	200	Strom & Strom (1994)
V410-Xray3	3029.4	350	300/30	200/20	Strom & Strom (1994)
USco-55	2849.9	350	300/30	200/20	Ardila et al.(2000)
USco-66	2862.6	350	300/30	200/20	Ardila et al.(2000)
USco-67	2849.0	350	300/30	200/20	Ardila et al.(2000)
USco-75	2859.7	350	300/30	200/20	Ardila et al.(2000)
USco-100	2867.0	510	300	200	Ardila et al.(2000)
USco-109	2864.6	510	300	200	Ardila et al.(2000)
USco-112	2871.6	510	300	200	Ardila et al.(2000)
USco-128	2870.6	510	300	200	Ardila et al.(2000)
USco-130	2887.8	510	300	200	Ardila et al.(2000)
USco-131	2863.6	510	300	200	Ardila et al.(2000)
USco-132	2888.8	510	300	200	Ardila et al.(2000)
USco-137	2888.9	510	300	200	Ardila et al.(2000)

[a]Observation Date: JD minus 2450000.

all objects in each field, and we report aperture photometry for all isolated objects and PSF photometry for all close binaries. PSF magnitudes were corrected to match aperture magnitudes based on results for the 29 targets that appeared isolated under visual inspection. Aperture photometry was carried out with the IRAF task DAOPHOT/PHOT with a 5-pixel aperture for faint objects and a 10-pixel aperture for bright objects, and the sky annulus had an inner radius of 200 pixels and width of 15 pixels. We used the finite aperture corrections of Sirianni et al.(2005).

Point-spread function (PSF) fitting photometry was carried out with the IRAF task DAOPHOT/ALLSTAR. A preliminary PSF for each filter was constructed from the 20 well-sampled VLMOs that appeared isolated under visual inspection. Since all of the targets were located near the center of the chip and have similar temperatures, image distortion and target color should not be important. There was some variation in the PSF FWHM from target to target ($\pm 5\%$), which we attribute to small orbit-to-orbit changes in focus. We investigated this by dividing our sample into two groups, based on whether the target PSF appeared to be narrower or wider than the average PSF, and constructing new average PSFs for each group. We then re-ran PSF photometry, but the modest decrease in the residuals did not reveal any companions which were not previously identified. Since it is not possible to determine which PSF is appropriate for blended binaries, we proceed using only the average PSF for the entire group. This choice could lead to systematic errors in the calculation of binary properties; we discuss these errors in more detail in Section 3.3.4.

Transformations to ground-based magnitudes (V, SDSS i', and SDSS z') were calculated with the IRAF task SYNPHOT/CALCPHOT, which convolves an input spectrum with transmission curves for HST's optics and filters or standard ground-based filters. Since SYNPHOT does not include transmission curves for the i' and z' filters, which are defined at the United States Naval Observatory 40-in telescope, they were obtained from the website for the Sloan Digital Sky Survey[1] and represent the filters and optics at the USNO-40 observing at 1.3 airmasses (Fukugawa et al., 1996). Based on transformations determined for a set of M0-M8 dwarfs and M5-M8 giants

---

[1]http://www.sdss.org/dr1/algorithms/standardstars/Filters/response.html

from the Bruzual-Persson-Gunn-Stryker Spectrophotometry Atlas (Bruzual et al., 1996), we find constant corrections that do not depend significantly on temperature or surface gravity: $m_{555} - m_V = -0.16 \pm 0.03$, $m_{775} - m_{i'} = +0.07 \pm 0.03$, and $m_{850} - m_{z'} = +0.03 \pm 0.03$. The uncertainties are estimated from the standard deviation between all tested objects. The transformed magnitudes[2] are listed in Table 3.2. The statistical uncertainties correspond to either the photon noise (for aperture photometry; typically <0.01 magnitudes) or the goodness of fit (for PSF-fitting photometry; 0.02-0.09 magnitudes). Systematic uncertainties in the magnitude transformations and aperture corrections are ∼0.03 magnitudes. The photometry calculated from short exposures was consistent with that from long exposures, so we report only the long exposures.

---

[2]The V flux for USco-112 appears to be anomalously bright. Based on its i' and z' magnitudes, it appears to be of similar brightness and color to USco-55 B. However, it is 0.88 ± 0.06 magnitudes brighter than USco-55 B in V. Exposures in both dither positions give consistent fluxes, so it is probably not the result of a cosmic ray hit on one exposure. We suggest that this is caused either by a transient optical brightening of the system (e.g., a flare or increased accretion) or by contamination from a spatially unresolved blue background object.

Table 3.2. Photometry of Very-Low-Mass Objects in Taurus

Name	V^a	i'^a	z'^a	J^b	H^b	K^b
CFHT-Tau-1	23.427±0.026	18.612±0.003	16.612±0.002	13.740±0.024	12.537±0.023	11.849±0.015
CFHT-Tau-2	22.520±0.014	18.112±0.002	16.307±0.002	13.754±0.021	12.762±0.021	12.169±0.017
CFHT-Tau-3	21.654±0.009	17.970±0.002	16.119±0.001	13.724±0.023	12.861±0.023	12.367±0.023
CFHT-Tau-4	21.556±0.008	16.920±0.001	14.951±0.001	12.168±0.020	11.008±0.019	10.332±0.016
KPNO-Tau-1	24.063±0.044	19.572±0.004	17.596±0.003	15.101±0.038	14.247±0.037	13.772±0.034
KPNO-Tau-2	21.376±0.007	17.670±0.002	16.074±0.001	13.925±0.022	13.241±0.027	12.753±0.020
KPNO-Tau-3	20.239±0.004	16.959±0.001	15.484±0.001	13.323±0.019	12.501±0.021	12.079±0.019
KPNO-Tau-4	24.722±0.071	20.072±0.006	17.897±0.004	14.997±0.033	14.025±0.037	13.281±0.031
KPNO-Tau-5	19.690±0.004	16.226±0.001	14.706±0.001	12.640±0.020	11.918±0.022	11.536±0.016
KPNO-Tau-6	22.292±0.012	19.097±0.003	17.301±0.003	14.995±0.028	14.197±0.038	13.689±0.036
KPNO-Tau-7	22.068±0.011	18.358±0.002	16.661±0.002	14.521±0.030	13.828±0.026	13.272±0.032
KPNO-Tau-8	19.261±0.003	16.147±0.001	14.863±0.001	12.946±0.018	12.367±0.019	11.985±0.020
KPNO-Tau-9	24.918±0.084	20.035±0.006	18.056±0.004	15.497±0.042	14.660±0.039	14.185±0.053
KPNO-Tau-12	23.228±0.023	20.781±0.009	18.998±0.006	16.305±0.085	15.483±0.096	14.927±0.092
KPNO-Tau-14	20.735±0.007	16.297±0.001	14.502±0.001	11.907±0.019	10.805±0.021	10.269±0.018
MHO-Tau-4	18.678±0.002	15.246±0.001	13.732±0.001	11.653±0.028	10.923±0.032	10.567±0.020
MHO-Tau-5	17.595±0.001	14.489±0.001	13.114±0.001	11.070±0.023	10.390±0.029	10.063±0.020
MHO-Tau-8	17.951±0.002	14.453±0.001	12.976±0.001	10.862±0.018	10.140±0.020	9.726±0.016
MHO-Tau-8 A	18.241±0.030	14.911±0.033	13.556±0.021	...	...	...
MHO-Tau-8 B	19.525±0.048	15.611±0.060	13.934±0.013	...	...	...
LH 0419+15	21.835±0.010	18.028±0.002	16.488±0.002	14.364±0.029	13.549±0.027	13.079±0.035
V410 Xray-3	18.319±0.002	15.046±0.001	13.629±0.001	11.544±0.018	10.817±0.021	10.446±0.017
V410 Xray-3 A	...	15.046±0.014	13.812±0.011	...	...	...
V410 Xray-3 B	...	20.032±0.446	15.658±0.028	...	...	...
V410 Anon-13	22.175±0.012	17.665±0.002	15.782±0.001	12.954±0.019	11.659±0.020	10.958±0.015
GM Tau	17.577±0.001	15.169±0.001	13.908±0.001	12.804±0.019	11.586±0.017	10.632±0.016
USco-55 A	18.73±0.04	15.92±0.012	14.81±0.09	...	...	...
USco-55 B	18.92±0.015	16.19±0.08	15.12±0.09	...	...	...
USco-66 A	18.92±0.021	16.36±0.016	15.41±0.012	...	...	...
USco-66 B	18.94±0.022	16.30±0.023	15.29±0.008	...	...	...
USco-67	18.47±0.002	15.52±0.001	14.32±0.001	12.543±0.026	11.908±0.022	11.568±0.026
USco-75	18.71±0.002	15.80±0.001	14.61±0.001	12.784±0.026	12.203±0.026	11.841±0.026
USco-100	19.09±0.002	15.99±0.001	14.73±0.001	12.840±0.022	12.182±0.023	11.827±0.026
USco-109 A	20.20±0.03	17.13±0.04	15.87±0.016	...	...	...
USco-109 B	21.21±0.076	18.07±0.08	16.92±0.04	...	...	...
USco-112	18.04±0.001^e	16.15±0.001	15.17±0.001	13.463±0.029	12.898±0.023	12.507±0.023
USco-128	21.29±0.007	17.79±0.002	16.34±0.002	14.395±0.035	13.614±0.041	13.207±0.035

Table 3.2 (cont'd)

Name	V^a	i'^a	z'^a	J^b	H^b	K^b
USco-130	21.39±0.008	17.80±0.002	16.30±0.002	14.204±0.032	13.482±0.032	13.075±0.034
USco-131	21.98±0.011	18.22±0.002	16.67±0.002	14.547±0.030	13.830±0.037	13.481±0.033
USco-132	22.11±0.013	18.31±0.002	16.59±0.002	14.260±0.035	13.556±0.041	13.039±0.029
USco-137	22.92±0.023	19.27±0.004	17.75±0.003	15.660±0.081	15.002±0.097	14.419±0.105

[a]Uncertainties are statistical only; systematic uncertainties due to aperture corrections and conversion to standard systems are ∼0.03 magnitudes.

[b]Near-infrared photometry is taken from the Two Micron All Sky Survey (Cutri et al. 2003). We quote total system magnitudes for the two binary systems.

3.3   Results

3.3.1   New VLMO Binaries in Upper Sco

In Figure 3.1, we present contour plots of three candidate binaries (USco-55, 66, and 109) and the apparently single star USco-67 in the F555W, F775W, and F850LP filters. The USco-55 and USco-66 systems are clearly resolved. The USco-109 system is not obviously resolved and was not initially reported as a double-source by ALL-STAR, but the PSF appears to be marginally elongated in the +x direction relative to the single VLMO USco-67.

One limitation in the ALLSTAR-based data reduction method is that binaries with very close ($\leq \lambda/D$) separations are often not identified, even when their combined PSF is elongated at a high confidence level. DAOFIND, the task which identifies potential objects in the images, only identifies point sources based on the presence of a distinct peak. Thus, automated photometry will be biased against the detection of very close binaries. This limitation can be overcome for known or suspected binaries by manually adding a second point source in approximately the correct location and letting ALLSTAR recenter it to optimize the fit; if it does not produce a statistically significant fit, ALLSTAR then discards it. We have done this for USco-109.

In Figure 3.2, we present plots for USco-109 and the next-brightest object in the same images, a likely background field star (Section 3.3.2). The first three columns show USco-109 and the residuals from fitting with one and then two point sources,

and the last two columns show the field star and its single-source fit. The maximum and minimum pixel values are also given to allow quantitative comparison of the residuals to the original images. The common position angle of the residuals in the single-source fit in all three filters seems to imply that this elongation is a real effect, and not simply noise. USco-109 appears elongated in the same direction relative to both its neighbor and USco-67; this extension is therefore unlikely to be an artifact due to excess jitter, which would affect the field star as well. USco-109 is better fit with two point sources in all three filters, and the fit reduces the residuals by factors of 2-8. Moreover, these fits independently find similar positions and flux ratios in all three filters, which further supports its classification as a binary system. Since the similar two-source residuals in each filter imply some remaining uncertainty in the fit and the separation is only ~1.3 pixels, followup observation of this system to confirm its multiplicity and properties should be a priority. However, we will proceed under the assumption that it is a binary system in our subsequent analysis.

We summarize the properties of these three systems in Table 3.3. The uncertainties in separation and position angle are determined from the standard deviations in the locations as reported by ALLSTAR for the three filters.

3.3.2   New VLMO Binaries in Taurus-Auriga

Our survey found no fully-resolved low-mass binaries among the subsample in Taurus. However, after implementing the method described above for USco-109, we found that two targets appear to be marginally-resolved binary systems. In Figures 3.3-3.5, we illustrate this technique with contour plots of the known VLMO binary MHO-Tau-8 (discovered by White et al. (2006) and independently rediscovered here), the new candidate VLMO binary V410-Xray3, and the apparently single VLMO MHO-Tau-4 in the F555W, F775W, and F850LP filters. Since the long exposures in i' and z' for MHO-Tau-8 were saturated, we show only the short exposures. Neither of the two candidate systems is obviously resolved and neither was consistently reported as a double-source by DAOFIND, but the PSF for MHO-Tau-8 is slightly elongated along
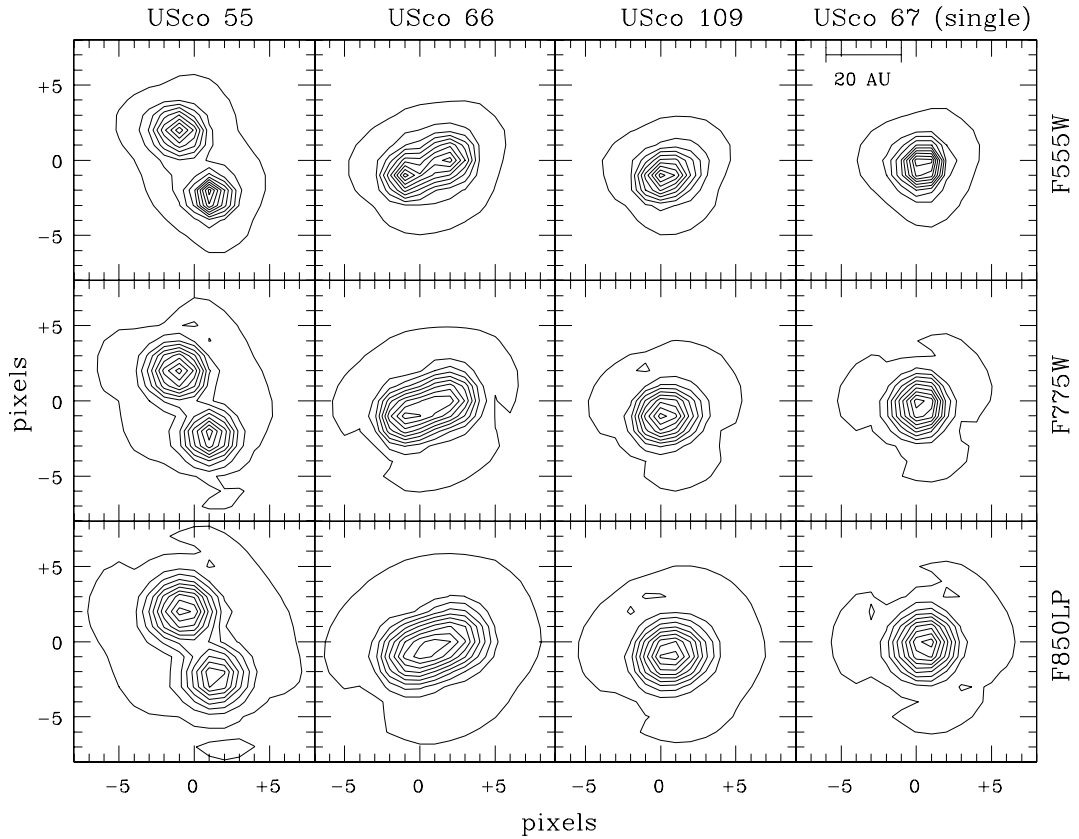
Figure 3.1 Contour plots of four targets: USco-55, USco-66, USco-109, and USco-67, respectively. Units are in pixels, and the projected physical scale at the distance of Upper Sco is shown in the upper right panel. Contours are drawn at 95% through 5% of the maximum pixel value, in increments of 10%. The field of view in each image is 432 mas, or ∼60 AU at 145 pc.

USco 109   Single Fit   Double Fit   Field Star   Single Fit

+5

0

−5

Max: 4238

Max: 560
Min: −1037

Max: 204
Min: −158

Max: 1500

Max: 58
Min: −133

F555W

+5

0

−5

pixels

Max: 32466

Max: 3254
Min: −6657

Max: 1208
Min: −3120

Max: 1119

Max: 29
Min: −27

F775W

+5

0

−5

Max: 23587

Max: 2283
Min: −3787

Max: 1012
Min: −958

Max: 298

Max: 10
Min: −9

F850LP

−5   0   +5   −5   0   +5   −5   0   +5   −5   0   +5   −5   0   +5

pixels
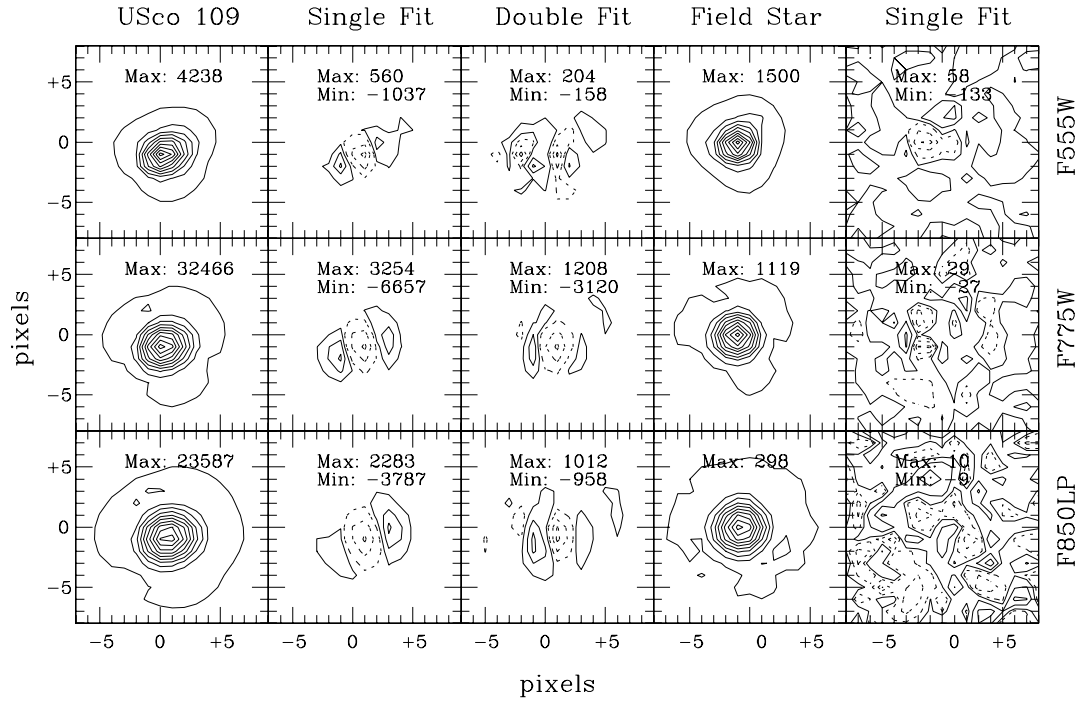
Figure 3.2 Contour plots of USco-109 and a background star in the same field for all three filters. The first three columns show USco-109 and the residuals from fitting with one and then two point sources, and the last two columns show the background star and the residuals from a single-source fit. For residuals, contours are drawn at the 90%, 50%, and 10% levels of maximum (solid lines) and minimum (dashed lines). The maximum and minimum pixel values are given to allow comparison of the residuals to the original images. The pixel values in the last column, where the sky background contours fill each panel and obscure the text, are (58,-133), (29,-27), and (10,-9), respectively.

the y-axis and that of V410-Xray3 is slightly elongated along the x-axis relative to MHO-Tau-4.

In Figure 3.3, we present contour plots of MHO-Tau-8 in each filter. The first column shows the original image, the second column shows the result from fitting with one point source, and the last column shows the result from fitting with two point sources. The maximum and minimum pixel values are also given to allow quantitative comparison of the residuals to the original images. The common position angle of the residuals in the single-source fit seems to imply that this elongation is a real effect, and not simply noise. Normal levels of jitter were reported in the observation log, so this is also unlikely to be a systematic effect. Unfortunately, there were no other bright objects in the field to serve as PSF references. However, as we summarize in Table 3.3, the system properties in each filter are consistent with previous observations and expected orbital motion (Section 3.5.3). Since MHO-Tau-8 was independently identified as a binary system by White et al.(2009), we regard it as a confirmed discovery.

In Figure 3.4, we present similar contour plots of V410-Xray3, showing both the long and short exposures in i' and z'. The residuals from the single-source fit are roughly aligned and the jitter levels were normal, as in the case of MHO-Tau-8, but the separations of the residuals are marginally lower, implying a smaller separation or larger flux ratio. ALLSTAR was unable to fit two point sources in the V image and the fit for the secondary in the i' images was not statistically significant, but the fit for the z' images appears consistent and statistically significant in both the short and long exposures. The number statistics for the i' and z' images are similar and the z' filter has lower resolution, therefore the superior fit for the z' images suggests that a possible companion may be much cooler and redder. We summarize the system parameters as calculated from each image in Table 3.3, though the results for the i' images should be used with caution.

The significant residuals in the double-source fit and the scatter in system properties suggests that even if V410-Xray3 is a binary, the measured parameters are not very reliable. Since there are no background stars for comparison and no other obser-

Table 3.3.   Binary Properties

Target	Date[a]	Separation (mas)	Position Angle(deg)	ΔSpT	q Δm (mag)
MHO-Tau-8	1143[b]	37	311	...	...
MHO-Tau-8	3029	44±8	270±2	0.6±0.1	0.75±0.07
V410-Xray3	3029[c]	44±2	336±2	1.7±0.2	0.47±0.07
USco-55	2850	121.6±0.6	307.7±0.4	0.5±0.1	0.86±0.04
USco-66	2863	70.3±0.5	31.7±0.2	0.0±0.1	0.94±0.03
USco-109	2865	34±2	302±3	1.5±0.2	0.59±0.04

[a]Observation Date: JD minus 2450000.

[b]White et al.(2009)

[c]System values for most targets are determined from the mean and standard deviation for all HST observations; values for V410-Xray3 are determined from the long and short z' observations only.

vations to support its multiplicity, we suggest its classification as a candidate binary. Followup observation to confirm its existence and properties should be a priority, since if confirmed, its small separation and corresponding short orbital period ($\sim$50 years for a circular orbit) could allow for a dynamical mass determination in less than a decade. Our subsequent analysis will consider V410-Xray3 as a candidate binary, but since its binarity has not been confirmed or disproved, our discussion will reflect both possibilities.[1]

In Figure 3.5, we illustrate the typical results for single stars with contour plots of MHO-Tau-4 and the residuals after fitting with a single point source. We could not obtain a statistically significant fit for two point sources, suggesting that there are no binary companions at separations $\geq$4 AU with mass ratio near unity.

One target VLMO, KPNO-Tau-14, was reported as a possible double-lined spectroscopic binary by Mohanty et al.(2005). We did not detect any PSF elongation for this target. Since the components of SB2s have similar brightness, the detection limits we find in Section 3.3.3 imply its separation is less than the inner detection limit ($\sim$4 AU). Since it falls inside the survey limits, we will not consider it as a binary in the discussion.

---

[1]Observations conducted in February 2006 with the Keck-II telescope and Laser Guide Star Adaptive Optics have confirmed this candidate and will be reported in a future publication.
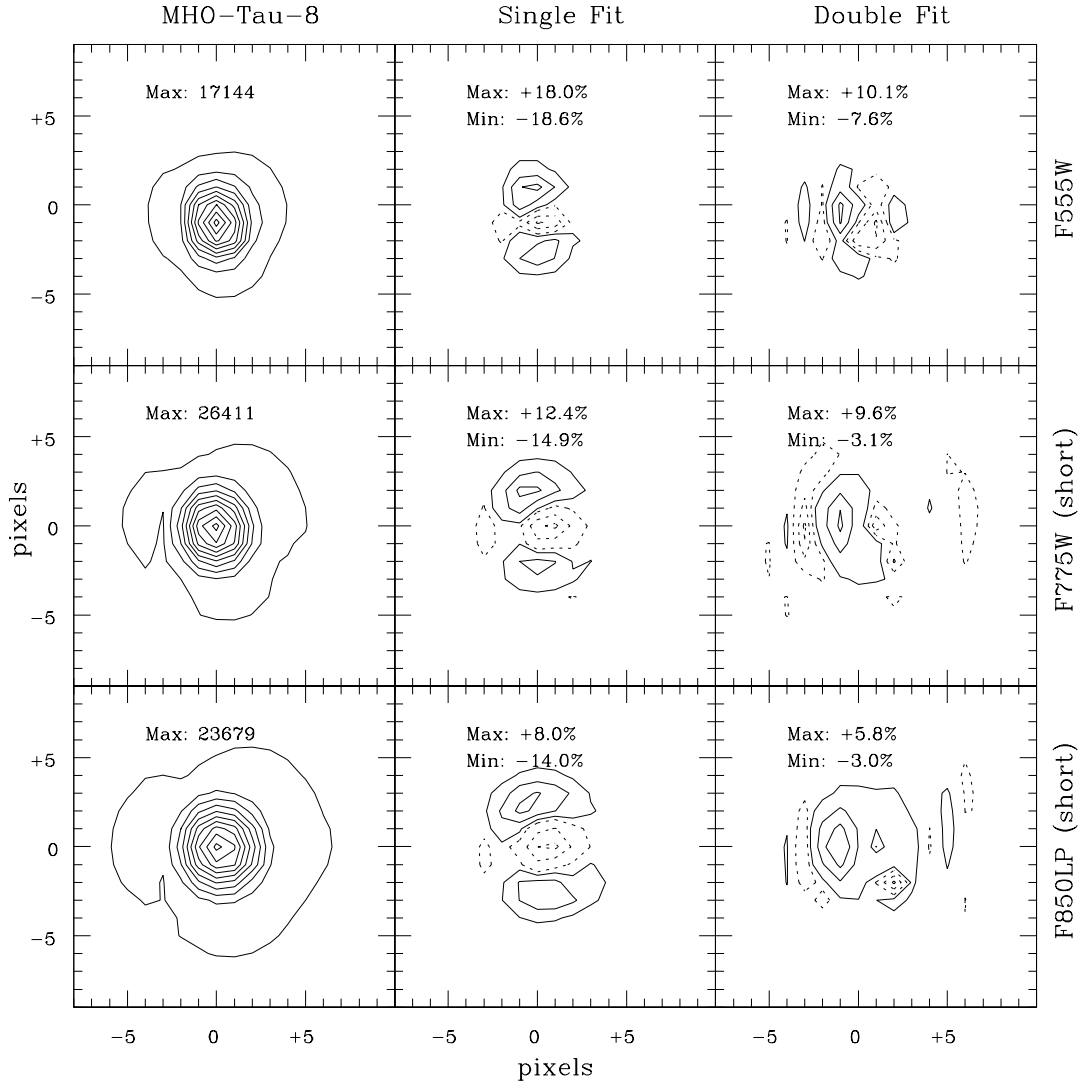
Figure 3.3 Contour plots of MHO-Tau-8 for all three filters. The first column shows MHO-Tau-8, the second column shows the residuals from fitting it with one source, and the last column shows the residuals from fitting it with two sources. For residuals, contours are drawn at the 90%, 50%, and 10% levels of maximum (solid lines) and minimum (dashed lines). The peak pixel value in each original image is shown; the positive and negative peaks of the residuals are reported as a percentage of the original peak value.

V410−Xray3   Single Fit   Double Fit
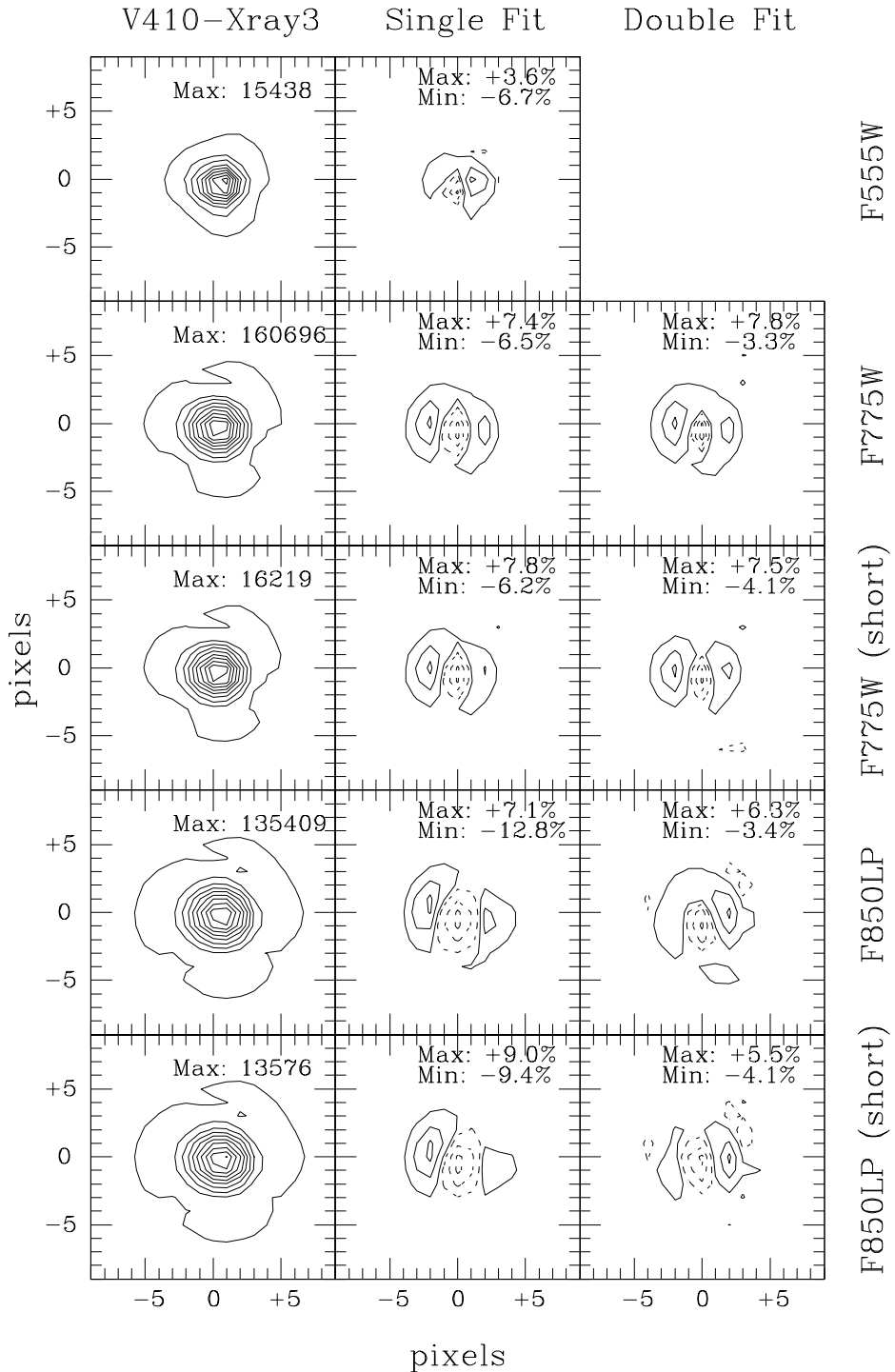
Figure 3.4 Contour plots of V410-Xray3 for all three filters. The first column shows V410-Xray3, the second column shows the residuals from fitting it with one source, and the last column shows the residuals from fitting it with two sources. For residuals, contours are drawn at the 90%, 50%, and 10% levels of maximum (solid lines) and minimum (dashed lines). The peak pixel value in each original image is shown; the positive and negative peaks of the residuals are reported as a percentage of the original peak value.

MHO−Tau−4   Single Fit

Max: 11334

Max: +5.5%
Min: −7.8%

F555W

Max: 143715

Max: +3.1%
Min: −1.1%

F775W

pixels

Max: 130614

Max: +1.8%
Min: −9.9%

F850LP

pixels
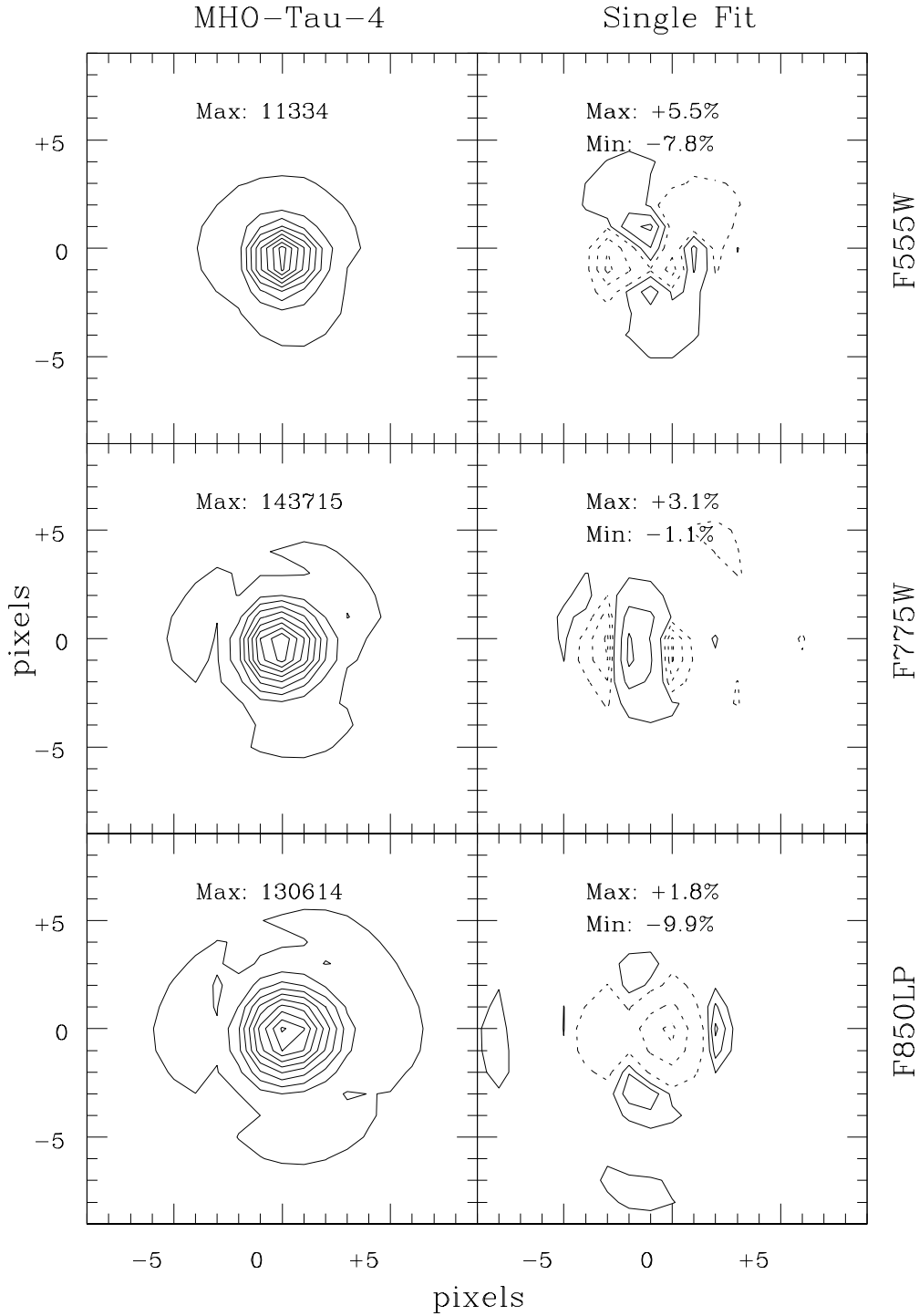
Figure 3.5 Contour plots of MHO-Tau-4 for all three filters. The first column shows MHO-Tau-4 and the second column shows the residuals from fitting it with one source. For residuals, contours are drawn at the 90%, 50%, and 10% levels of maximum (solid lines) and minimum (dashed lines). The peak pixel value in each original image is shown; the positive and negative peaks of the residuals are reported as a percentage of the original peak value.

3.3.3 VLMOs and Background Stars

In Figure 3.6, we present an i' versus $i' - z'$ color magnitude diagram of the 12 targets in Upper Sco (filled circles) and all other objects in those fields that were detected at the 5σ level in both filters. Objects within $5''$ (800 AU), which are statistically more likely to be physically associated, are shown as open circles while other objects are shown as crosses. Also shown are the average main sequence at the distance of Upper Sco (Hawley et al., 2002) and a 5 Myr isochrone based on the evolutionary models of Baraffe et al. (1998). The location of the isochrone is determined by converting the predicted I_C and J magnitudes to i' and z' magnitudes, using $I_C - i'$ colors derived using the methods described in Section 3.2 and $z' - J$ colors found from the SDSS field main sequence for older, more massive M dwarfs by Hawley et al. (2002). Although the $I_C - i'$ transformations should be accurate (Section 3.2), the $z' - J$ transformations may be more sensitive to surface gravity differences due to the larger difference in central wavelengths. Consequently, the $i' - z'$ color of the 5 Myr isochrone is somewhat uncertain.

In Figure 3.7, we present a corresponding i' versus $i' - z'$ color magnitude diagram for our Taurus targets showing the 20 apparently single VLMO targets (filled circles), the components of the two candidate binary systems (filled circles with error bars), and all other objects which were clearly resolved and detected at the 5σ level in both filters (open circles). The candidate secondary component of V410-Xray3 is well off the right side of the graph; its extremely red color ($i' - z' = 4.374$) is probably due to the high uncertainty in its i' fit (Section 3.3.1); since the secondary has an approximate spectral type of M7.7 (Section 3.4.3), we expect it to possess colors similar to those of CFHT-Tau-3: $i' - z' = 2$, and thus $i' = 17.5$. Also shown are the average main sequence at the distance of Taurus (Hawley et al., 2002), 1- and 2-Myr isochrones based on the evolutionary models of Baraffe et al. (1998), and a reddening vector based on the extinction relations reported in Schlegel et al.(1998). The isochrone was derived as for Figure 3.6.

In both figures, the binary components are located above the SDSS main sequence

and well above the background population, so they are most likely association members; based on their close proximity and the low density of association members we conclude that these are physically associated companions. All other detected objects fall well below the empirical main sequence and are most likely background stars. One target object, KPNO-Tau-12, appears to be somewhat underluminous compared to the other Taurus VLMOs. The discovery survey (Luhman et al. 2003a) also found KPNO-Tau-12 to be underluminous for its assumed age and distance, so this is most likely a genuine feature of the system.

3.3.4   Sensitivity Limits

We determined detection limits as a function of distance from the primary stars via a Monte Carlo simulation similar to that of Metchev et al. (2003). We used the IRAF task DAOPHOT/ADDSTAR and the average PSF to add artificial stars at a range of radial separations and magnitudes to the fields of GM Tau, KPNO-Tau-2, KPNO-Tau-7, and KPNO-Tau-4, which represent the full range of brightness in our sample. We then attempted to identify the artificial stars with the ALLSTAR PSF-fitting photometry package.

In Figure 3.8, we show the detection limits for the four representative targets in V and z', as a function of separation, at which we can detect $> 10\%$, 50%, and 90% of the companions. At small separations ($\leq$20 AU), the 50% detection thresholds roughly scale with the brightness of the primary; the survey limits are similar for all objects in terms of Δm. The detection limits converge to constant values at large separations; in the case where the noise is background-dominated, the 5σ detection limits are $z'=23.8$, $i' =25.1$, and $V=26.7$. The simulations demonstrate that we potentially could identify bright, equal-mass pairs as close as 1 pixel ($0.027''$; 4 AU; $\sim$0.5 λ/D) and binaries with mass ratio $q = 0.1$ ($\Delta z'=4$) at $\geq$10 AU. We also show the locations (in Δm and separation) of the companion to MHO-Tau-8 and the candidate companion to V410-Xray3 (for z' only). These results indicate that the probability of detecting close binary companions in the z' images is near unity for even the faintest systems,
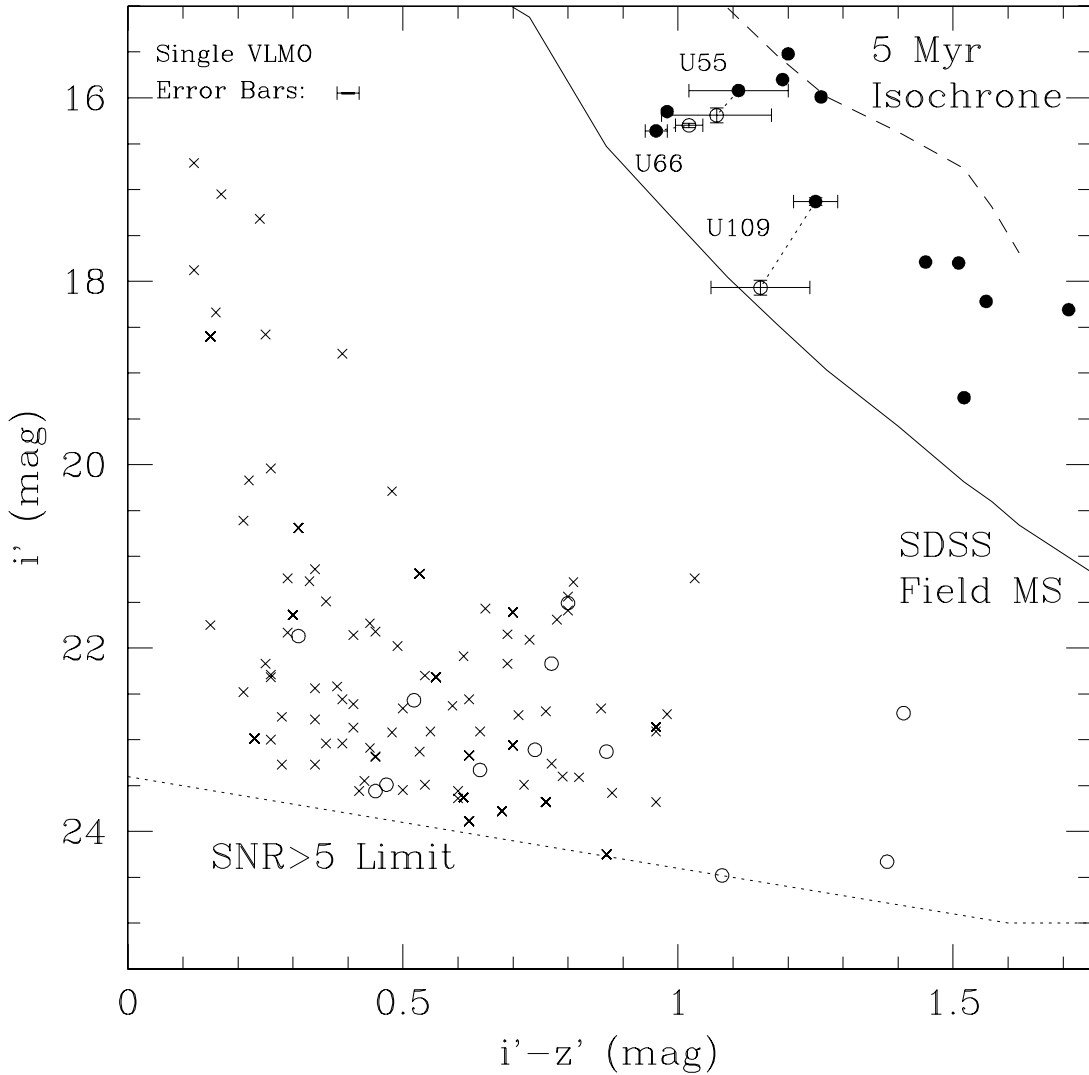
Figure 3.6 An i' vs $i' - z'$ color magnitude diagram for our observations in Upper Sco. Primary targets are shown as filled circles, neighbors within 5″ are shown as open circles, and widely-separated objects are shown as crosses. The SDSS field main sequence (solid line), a 5 Myr isochrone (dashed line), and the detection limits of the survey (dotted line) are also shown. Candidate binary VLMO pairs are connected with dotted lines and labeled. The error bars for binary components are associated with each point, and the error bars for single objects are shown in the upper left corner.
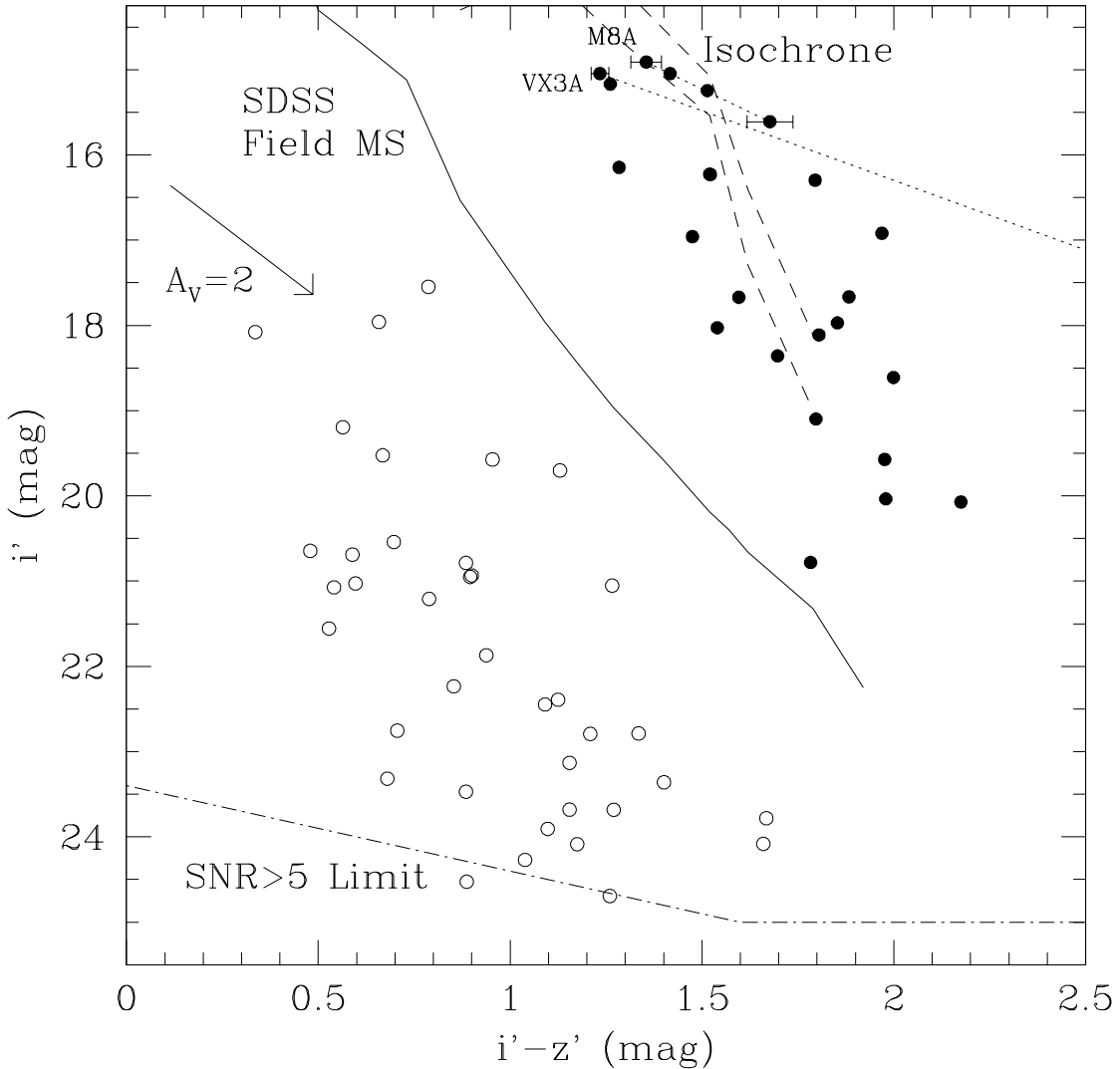
Figure 3.7 An i' vs $i' - z'$ color magnitude diagram. Taurus members are shown as filled circles; objects which are classified as background stars based on their position in this CMD are shown as open circles. The SDSS field main sequence (solid line), 1 and 2 Myr isochrones (dashed lines), and the detection limits of the survey (dot-dashed line) are also shown. The components of both binary systems are connected with a dotted line; the candidate secondary component of V410-Xray3 is well off the right side of the plot. The i' photometry for V410-Xray3 B is highly uncertain, so its $i' - z'$ color is not likely to be accurate. The statistical error bars for binary components are associated with each point; the error bars for single objects are smaller than the symbols, so they are not shown.

but the probability of detecting similar systems in the V filter declines rapidly for the faintest targets. This inability to resolve the V410-Xray3 system in the V band suggests a limit of $V > 20.3$ for the secondary component; the corresponding color limit ($V - z' > 4.7$) is consistent with the spectral type (M7.7) we determine in Section 3.4.3.

Our simulations suggest that it is not easier to resolve extremely red targets at shorter wavelengths; given the PSF stability of HST, the improved number statistics at redder bands outweigh the superior diffraction-limited resolution at bluer bands. However, the additional color information was useful in confirming the identify of association members. Also, this is the first large set of homogeneous observations of young VLMOs shortward of 6000 angstroms. As we describe in Section 3.4.3, this allows us to characterize a previously unexplored regime in their spectral energy distributions.

3.3.5 Uncertainties in Binary Properties

A similar Monte Carlo routine was used to test the uncertainties in the measurements of two of the marginally unresolved systems, MHO-Tau-8 and V410-Xray. We used ADDSTAR and the average PSF to construct 100 simulated images, given the positions and brightnesses reported for the primary and the secondary for the real images, and then used ALLSTAR to perform PSF-fitting photometry on these simulated images. The standard deviation in separation ($\sim$0.5 mas) reported for the simulated images of MHO-Tau-8 is consistent with that calculated from the standard deviation in separation between the three filters ($\sim$2 mas), and the standard deviation in the flux ratio Δm (0.04 magnitudes in each filter) is consistent with that determined from the magnitudes reported by ALLSTAR for each object. The uncertainties predicted by our simulations are generally lower than those observed, but this is likely due to the small variations in PSF width observed for each target (Section 3.2.2). We found similar results for the z'-band images of V410-Xray3 (0.5 mas, 0.03 magnitudes), but ALLSTAR only found a two-source fit for this object in 87% of the i'-band images,
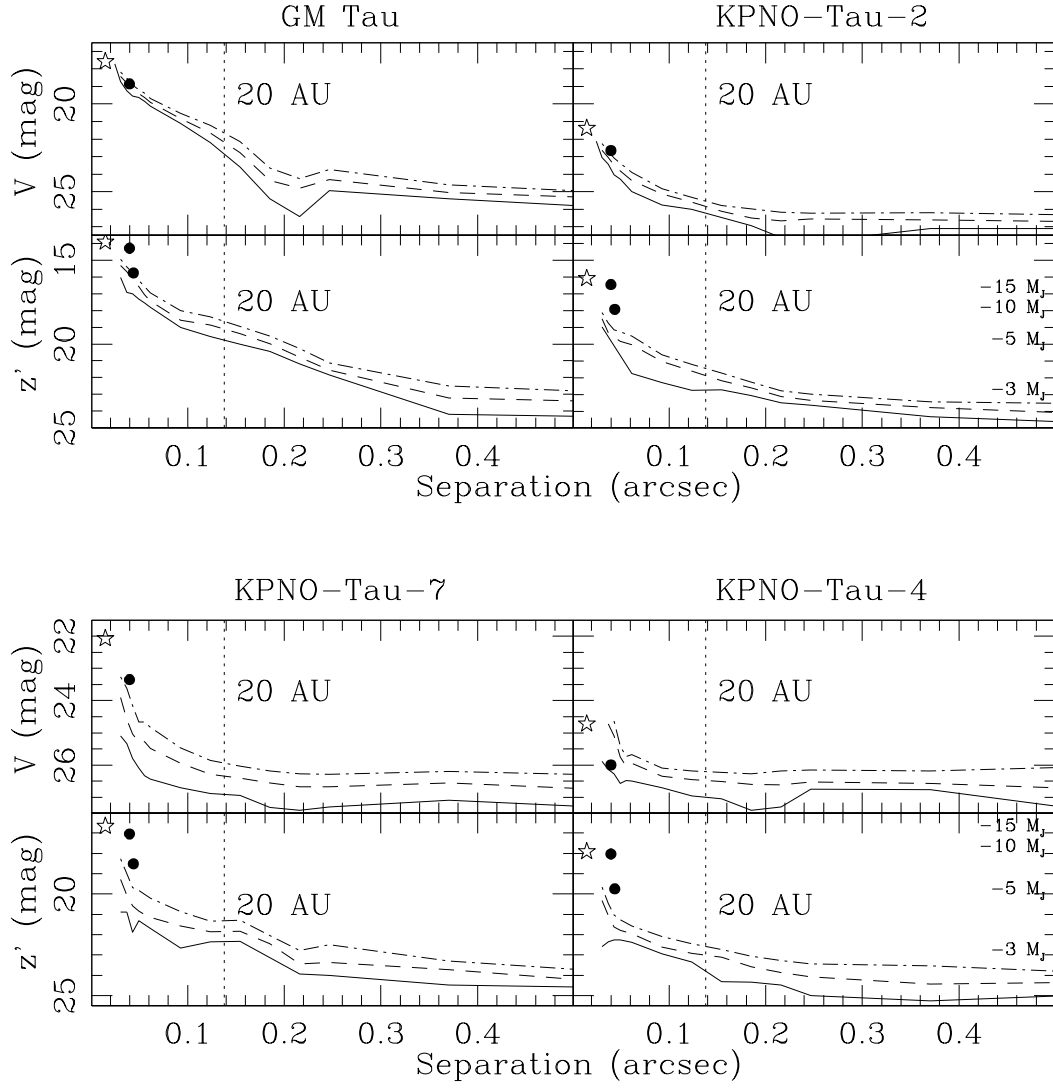
Figure 3.8 Five-sigma detection frequencies (10%: solid, 50%: dashed, and 90%: dash-dotted) as a function of separation in each filter for single VLMOs of maximum, intermediate, and minimum brightness: GM Tau, KPNO-Tau-2 and KPNO-Tau-7, and KPNO-Tau-4, respectively. Corresponding brightnesses of potential planetary-mass companions (assuming $A_V = 1.5$) are shown on the right for the z' plots. The brightness of the primary object is denoted with a star to allow conversion to Δm values, and the vertical dotted line indicates a separation of 20 AU at the distance of Taurus (145 pc). The filled circles mark the separation and Δm values for the binary companions to MHO-Tau-8 and V410-Xray3.

and the standard deviation among successful fits was much higher in both separation ($\sim$7 mas) and flux ratio (0.4 magnitudes). These uncertainties are dominated by the measurements of the secondary component, and match the uncertainties from the observations.

We also conducted Monte Carlo tests to determine the probability of mistakenly identifying a true single star as a binary. We constructed a series of simulated images (100 each for several objects spanning our sample's range of brightness), and then tried to fit each object with two point sources. We found that this never produced a successful fit, so the probability of an erroneous binary identification due to statistical errors appears to be low ($<$ 1%). However, since the PSF width varies between observations, there is also a systematic component to the uncertainty in binary values. We have used the average PSF for all fits, but since there are no other bright objects in either binary field, it is not possible to determine whether the wide or narrow PSFs might be more appropriate in a specific case. Experiments show that the separation and position angle for each binary are independent from the choice of template PSF, but the photometry is not. If we attempt to fit the binaries with the wider template PSFs, then ALLSTAR is unable to produce a significant fit. If we attempt to fit the binaries with the narrower template PSFs, ALLSTAR reports values for Δm which are systematically lower by $\sim$50%. This suggests that higher-resolution observations will be required to determine accurate component fluxes.

3.4   Analysis

3.4.1   VLMO Binary Frequency

For the 22 M5.75-M9.5 targets in Taurus, we have confirmed a previously-identified binary VLMO system and identified one new system, both with separations of $\sim$6 AU. The observed binary fraction is thus 9^{+10}_{-4}% for separations $\geq$4 AU. For the 12 M5.5-M7.5 targets in Upper Sco, we have detected three binary VLMO systems with projected separations of 4.9-17.6 AU, giving an observed binary fraction of 25^{+16}_{-9}%.

These values are very marginally inconsistent ($\sim 1.5\sigma$), but as we will describe further in Section 3.5.2, this could be a function of the samples' different mass ranges. The Taurus sample includes many more brown dwarfs and fewer very-low-mass stars.

As can be seen in Figure 3.8, the detection of faint companions is difficult at separations comparable to the PSF width (58 mas in V). Consequently, the total binary fraction in this separation range may be higher. However, studies of VLMO binaries in the field have found that companions preferentially have mass ratios $q > 0.6$ despite the surveys' sensitivity to companions with lower mass ratios (Close et al. 2003; Bouy et al. 2003), which corresponds to $\Delta z < 1$ according to the models of Baraffe et al.(1998). If Taurus VLMOs have a similar mass ratio distribution, then the detection thresholds in Figure 3.8 predict that we should identify all VLMO companions at separations ≥ 4 AU in at least z' and likely in the other filters as well. Even if these limits are optimistic, the identification of V410-Xray3 as a candidate binary near the minimum measurable separation, ~ 5 AU, implies that the survey should be complete to $\Delta z' = 2$ (q=0.45) for separations ≥ 4 AU. It is therefore unlikely that there are many additional binaries at separations ≥ 4 AU with $q > 0.45$ in this sample.

The intrinsically higher luminosity of binaries makes them easier to identify in membership surveys, which can also bias the binary frequency to larger values. However, all five binaries are substantially brighter than the detection limits of their discovery surveys and would have been easily detected without the additional flux of their companions, so this effect should not bias our multiplicity results.

3.4.2 Limits on Planetary-Mass Companions

The high dynamic range of our deep exposures would allow us to directly image wide planetary-mass companions. In Figures 3.8, we indicate the predicted brightness of some representative masses of planetary companions based on the DUSTY models of Chabrier et al. (2000). These values assume an extinction of $A_V \sim 0$ in Upper Sco and $A_V \sim 1.5$ in Taurus, typical values for both regions. The extremely red colors

predicted for planetary-mass objects imply that z' observations provide the strictest limits on planetary companions.

In Taurus, we conclude that there are no planetary companions with mass ≥ 3 M_J at projected separations larger than 280 mas (40 AU) for the brightest targets or 140 mas (20 AU) for the faintest targets. In Upper Sco, the corresponding limits are masses ≥ 5 M_J at projected separations larger than 280 mas (40 AU) or mass ≥ 10 M_J at projected separations larger than 140 mas (20 AU) among our sample. For comparison, these limits would have allowed for a significant detection of the planetary-mass companion to 2MASSWJ 1207334-393254, a substellar member of the TW Hya association, which has a projected separation of ~ 54 AU, a flux ratio of $\Delta z' \sim 7$, and a predicted mass of ~ 5 M_J (Chauvin et al., 2004). Other surveys in Cham I (12 targets; Neuhauser et al. 2002) and IC 348 (37 targets; Luhman et al. 2005a) which included VLMOs in the same mass range (≤ 0.12 $M_\odot$) also found no planetary-mass companions.

3.4.3 Inferred (Sub)stellar Properties

3.4.3.1 Masses and Spectral Types

In Table 3.4, we give the inferred spectral types and masses for all of the VLMOs in our sample. Spectral types for single VLMOs and for binary primaries in our sample are taken from the discovery sources listed in Table 3.1 and were determined via low- or intermediate-resolution spectroscopy. The masses for this sample are estimated from the 2-Myr or 5-Myr mass-magnitude-temperature relations of Baraffe et al. (1998) and the temperature-SpT relations of Luhman et al. (2003b), and range from 0.015 to 0.15 $M_\odot$. Large systematic errors may be present in these and all pre-main sequence models (e.g., Baraffe et al. 2002; Hillenbrand & White 2004; Close et al. 2005; Reiners et al. 2005), so they are best used for relative comparison only.

The models of Baraffe et al. (1998) predict that the mass ratio ($q = m_s/m_p$) and difference in component spectral types (ΔSpT) for young VLMO binaries are a function of the primary-to-secondary flux ratios Δm with only a minor mass dependence;

Table 3.4.   VLMO (Sub)Stellar Properties

Name	SpT[a]	M (M$_\odot$)[b]	A_V	L/L_{MS}	log L ($L_\odot$)	R ($R_\odot$)	Accretor?[c]	$E(V - V_{MS})$
CFHT-Tau-1	M7	0.055	4.8	54	-1.4	0.73	N	-0.59
CFHT-Tau-2	M7.5	0.04	2.7	35	-1.6	0.56	N	-0.35
CFHT-Tau-3	M7.75	0.035	1.8	29	-1.8	0.50	N	-0.71
CFHT-Tau-4	M7	0.055	4.4	210	-0.8	1.45	Y?	-0.61
KPNO-Tau-1	M8.5	0.02	1.5	10	-2.3	0.27	N	0.08
KPNO-Tau-2	M7.5	0.04	0.7	17	-2.0	0.39	N	-0.25
KPNO-Tau-3	M6	0.1	2.0	18	-1.6	0.47	Y	-0.74
KPNO-Tau-4	M9.5	0.01	4.0	31	-2.0	0.42	Y?	-1.18
KPNO-Tau-5	M7.5	0.04	0.3	51	-1.5	0.68	N	-0.35
KPNO-Tau-6	M8.5	0.02	0.7	9	-2.3	0.26	Y	-0.95
KPNO-Tau-7	M8.25	0.017	0.1	11	-2.2	0.29	Y	-0.12
KPNO-Tau-8	M5.75	0.11	0.7	15	-1.7	0.44	N	-0.02
KPNO-Tau-9	M8.5	0.02	1.7	7	-2.5	0.22	N	0.43
KPNO-Tau-12	M9	0.014	1.6	3	-2.8	0.14	Y	-2.15
KPNO-Tau-14	M6	0.1	4.2	123	-0.8	1.22	N	-0.42
MHO-Tau-4	M7	0.055	0.8	126	-1.1	1.12	N	-0.39
MHO-Tau-5	M7	0.055	0.3	191	-0.9	1.38	Y?	-0.39
MHO-Tau-8 AB	M6+M6.6	0.17	1.7	158	-0.7	1.38	N	-0.38
LH 0419+15	M7	0.055	1.2	12	-2.1	0.35	-	-0.22
V410 Xray-3 AB	M6+M7.7	0.14	1.5	81	-1.0	0.99	N	-0.54
V410 Anon-13	M5.75	0.11	5.6	60	-1.0	0.87	Y	-0.57
GM Tau	M6.5	0.08	0.2	49	-1.1	0.74	Y	-1.23
USco 55	M5.5	0.010	0.1	18	-1.5	0.49	N	0.18
USco 66	M6	0.07	-0.4	16	-1.7	0.44	N	-0.58
USco 67	M5.5	0.10	0.4	18	-1.5	0.49	N	0.25
USco 75	M6	0.07	0.2	19	-1.6	0.48	N	-0.43
USco 100	M7	0.05	-0.2	34	-1.6	0.58	N	-0.40
USco 109	M6	0.057	0.4	9.1	-1.9	0.33	N	-0.33
USco 112	M5.5	0.10	-0.2	6.8	-1.9	0.30	N	-0.63
USco 128	M7	0.05	0.5	10	-2.2	0.32	N	-0.28
USco 130	M7.5	0.04	0.4	12	-2.1	0.33	N	-0.28
USco 131	M6.5	0.06	1.3	6.7	-2.2	0.27	N	-0.08
USco 132	M7	0.05	1.9	14	-2.0	0.37	-	-0.40
USco 137	M7	0.05	1.0	3.3	-2.6	0.18	-	-0.28

[a]Spectral types for binary secondaries are inferred from photometry presented here; others are from their discovery source (Section 3.4.3)

[b]Masses are determined from the models of Baraffe et al. (1998).

[c]Muzerolle et al. 2003; Mohanty et al. 2005; Muzerolle et al. 2005.

we report these quantities as determined from the flux ratio $\Delta z'$ in Table 3.3 for the detected binary VLMOs. The models do not report z' magnitudes so we calculated these from the model I_C magnitudes, the $I_C - i'$ transformations determined in Section 3.2, and the $i' - z'$ colors for the appropriate spectral type. The uncertainties reflect the uncertainties in the flux ratios and the scatter in this relation in the models, but do not include any systematic uncertainties from the models. The values determined from ΔV and $\Delta i'$ for four of the binaries are roughly consistent with these results, but the values for $\Delta z'$ are the only reliable result for V410-Xray3, so we use $\Delta z'$ in all cases for uniformity.

3.4.3.2   Luminosities and Extinctions

Our results, in combination with other surveys, also allow us to determine the luminosity and extinction for each VLMO by fitting the observed spectral energy distribution (SED) with a reddened dwarf SED of the same spectral type. This allows us to test for potential optical excesses that previous observations at longer wavelengths would not have detected. The VLMO SEDs are constructed from $Vi'z'JHK$ photometry from this work and from the Two Micron All-Sky Survey (2MASS; Cutri et al. 2003). Our standard SEDs are constructed from the mean $i'z'JHK$ photometry for field stars in the SDSS (West et al. 2005) and 2MASS (Leggett et al. 2002), plus the mean $V - K$ colors reported for the field by Reid et al.(2003). Typical uncertainties are ≤ 0.05 magnitudes for our observations and ~ 0.1-0.2 magnitudes for the field star photometry. Any significant difference between a VLMO SED and the corresponding field SED should be a result of the intrinsically higher luminosity of our targets (pre-main sequence VLMOs have larger radii) or extinction due to obscuring material. These will result in a constant multiplication and a wavelength-dependent multiplication to the flux in each band, respectively. We solve for these constants, which correspond to L/L_{MS} and A_V, by a least-squares fit of the set of equations:

$$m_{i,VLMO} = m_{i,field} + \frac{A_i}{A_V}A_V - 2.5log\frac{L}{L_{MS}}$$

where i denotes five filters used in the fit (i'z'JHK) and the reddening coefficient for each band is taken from Schlegel et al.(1998). Variations in distance will also be included in the luminosity term, but if the depth is similar to the apparent width of Taurus-Auriga on the sky ($\sim$10 deg; 25 pc), these should be relatively minor.

We list the inferred luminosity ratio, total luminosity, radius, and extinction for each VLMO in Table 3.4. The total luminosity is determined from the K-band magnitude, corrected for extinction, and the bolometric corrections of Leggett et al.(2002), which are $BC_K \sim 3.1$ for mid to late M dwarfs. The radius is determined from the luminosity ratio ($L/L_{MS} \propto (R/R_{MS})^2$) and the main sequence mass-radius relations of Baraffe et al. (1998), which find that $R_{MS}/R_\odot \sim M_{MS}/M_\odot$ for M5-M9 dwarfs at ages >1 Gyr. We also performed some experiments in varying the spectral type of the field standard; these imply that the uncertainty in spectral type (typically half a subclass) corresponds to uncertainties of $\sim$0.5 in A_V, $\sim$20% in L/L_{MS}, and $\sim$10% in R. The uncertainty in the bolometric correction is typically $\sim$5% for spectral types later than M5 (Leggett et al. 2002). The statistical uncertainties from the fitting process are generally insignificant compared to these systematic uncertainties. These experiments also reveal a degeneracy in the determination of extinction and luminosity; fitting with an earlier or later spectral type yields systematically different extinctions and luminosities, but the goodness of fit does not decrease significantly for small changes ($\leq$1 subclass). The same fitting process has been applied to the binaries by considering the total system brightness in each filter and assigning it the spectral type of the primary fitting it with a field standard corresponding to the spectral type of the primary. However, since the observed spectrum is a composite of both objects' spectra, the results may be biased.

In Figure 3.9, we present SEDs for the 18 Taurus VLMOs which produced successful fits to the dwarf SEDs (within 2σ). Four stars could not be fit well and are discussed below. The solid lines and filled circles denote VLMO SEDs which have been corrected for extinction and the dashed lines denote the best fit dwarf SEDs which have been shifted upward by $log(L/L_{MS})$ to correct for their intrinsically lower luminosity. Typical uncertainties in the SED flux measurements are $\sim$0.02 dex for the

VLMO SEDs, $\sim$0.05 dex for the $r'i'z'JHK$ fluxes in the dwarf SEDs, and $\sim$0.15 dex for the V band fluxes in the dwarf SEDs. Since our results typically agree with the dwarf SEDs to within the uncertainties, the common assumption of dwarf colors for pre-main sequence objects appears to be valid for this age and mass regime. However, as we discuss in Section 3.4.3.3, the targets appear to be systematically brighter than equivalent dwarf SEDs in V, yielding bluer optical colors.

In Figure 3.10, we present SEDs for the four VLMOs with significant discrepancies in their fit: KPNO-4, KPNO-6, KPNO-12, and GM Tau. The first three objects deviate significantly only in their V band measurement, but the optical and near-infrared portions of the SED for GM Tau appear to be inconsistent; we can not produce a fit to its dwarf reference by any single combination of A_V and L/L_{MS}. Based on the slope of its NIR SED, GM Tau appears to have been significantly fainter and/or possessed a significant K-band excess during its epoch of observation in 2MASS. The excellent agreement between the optical and near-infrared values for all other objects, which were taken at different epochs, suggest that they are typically not variable at amplitudes of >0.2 magnitudes.

Finally, we note that all 12 of the Upper Sco members produced successful fits, so we have not plotted their SEDs.

3.4.3.3   Optical Excesses

Nine of the Taurus VLMOs in our sample have been observed to possess spectroscopic signatures of active accretion of circumstellar material by Muzerolle et al.(2003), Mohanty et al.(2005), and Muzerolle et al. (2005). Accreted material falling onto more massive T Tauri stars is typically heated to higher temperatures than the stellar photosphere, leading to an optical excess (Basri & Batalha 1990; Hartigan et al. 1991). However, since the rate of accretion appears to depend on system mass (e.g., Muzerolle et al. 2003), the low mass accretion rates of T Tauri VLMOs should not produce any significant excess. Nonetheless, as we note in Section 3.4.3.2, several VLMOs show signs of an optical excess which might be a result of accretion. In Table 3.4, we identify the known accretors and non-accretors and list the V-band excess
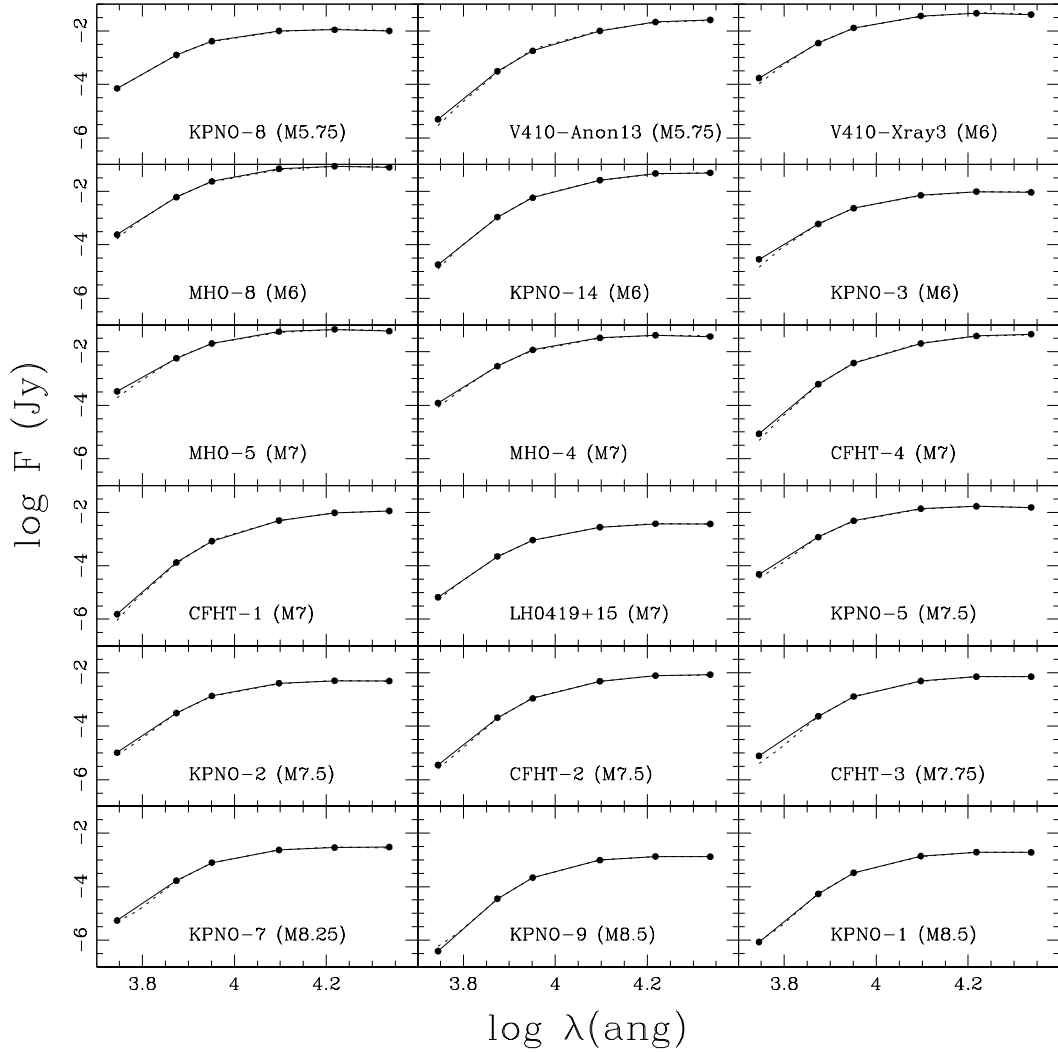
Figure 3.9 Spectral energy distributions for the VLMOs in the Taurus sample which produced successful fits. Solid lines and filled circles denote the target SEDs which have been corrected for extinction. Dashed lines denote field SEDs which have been corrected for the higher luminosity of our targets.
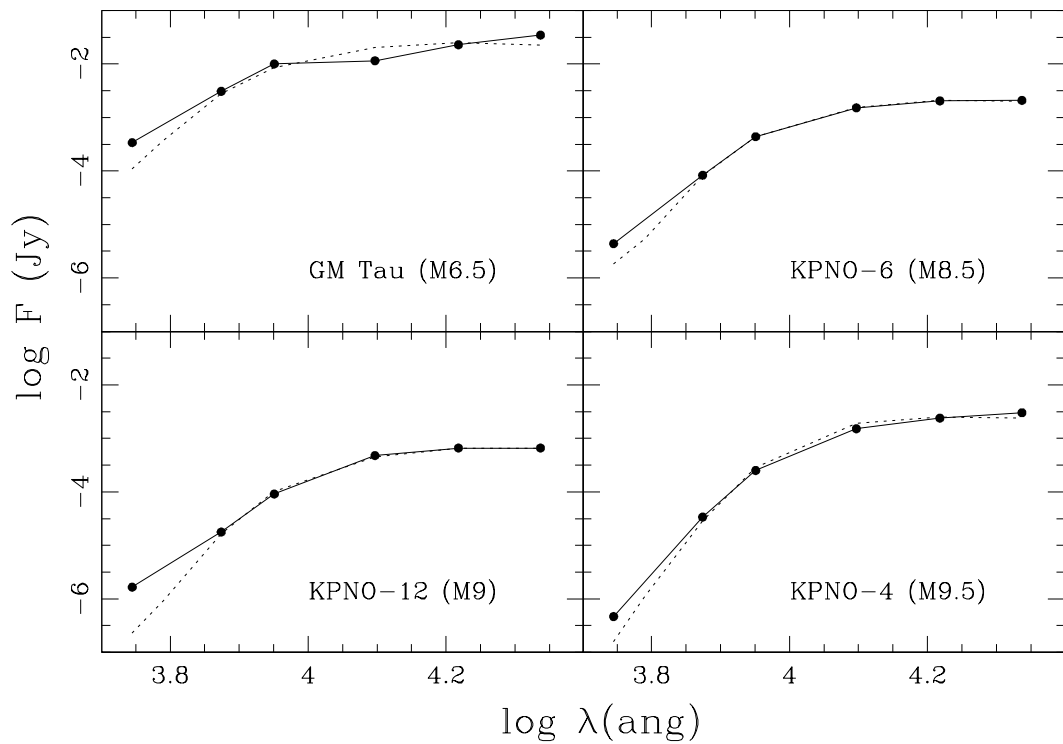
Figure 3.10 Spectral energy distributions for the four VLMOs in our sample which produced anomalous fits.

or deficit (in magnitudes) observed for each target. The four objects with the most significant V-band discrepancies are confirmed or probable accretors.

In Figure 3.11, we show a plot of the V-band excesses and deficits as a function of spectral type for each target. Filled circles denote Taurus VLMOs; symbols for known accretors (based on Hα or other line profile diagnostics) are larger than those of nonaccretors. Open circles denote Upper Sco VLMOs, none of which are known accretors. The dotted line denotes the V-band excess one would mistakenly infer if the color were influenced by surface gravity effects, estimated here using the intrinsically bluer $V - I$ colors of M5-M8 giants (Bessell & Brett 1988). Most of the known accretors sit preferentially higher in the plot relative to the non-accretors and relative to the giant locus, implying that they possess intrinsic excesses which are related to accretion or to the assessment of their accretion status.

Even non-accretors seem to possess small V-band excesses over typical dwarf colors, though they are not as high as typical giant excesses and do not depend significantly on spectral type; this suggests that young VLMOs tend to be bluer than dwarfs of the same spectral type. The mean and standard deviation for this discrepancy among known non-accretors are 0.28±0.33 magnitudes; in Figure 3.11, the mean value is denoted with a solid line and the $+2\sigma$ limit with a dashed line. If we regard this mean value as a measure of the true photospheric flux for young VLMOs, then the four objects identified earlier still possess excesses significant at $\geq+2\sigma$.

Finally, we note that there are no known accretors among our Upper Sco sample, and the mean V-band excess (0.27±0.08) is consistent with the mean excess for nonaccretors in Taurus (0.28±0.10). As we show in Figure 3.11, all Upper Sco VLMOs fall below the $+2\sigma$ criterion for a statistically significant optical excess over the nonaccretor value. This supports the suggestion that accretors may show optical excesses over nonaccretors, though the older age of Upper Sco may also play a role.
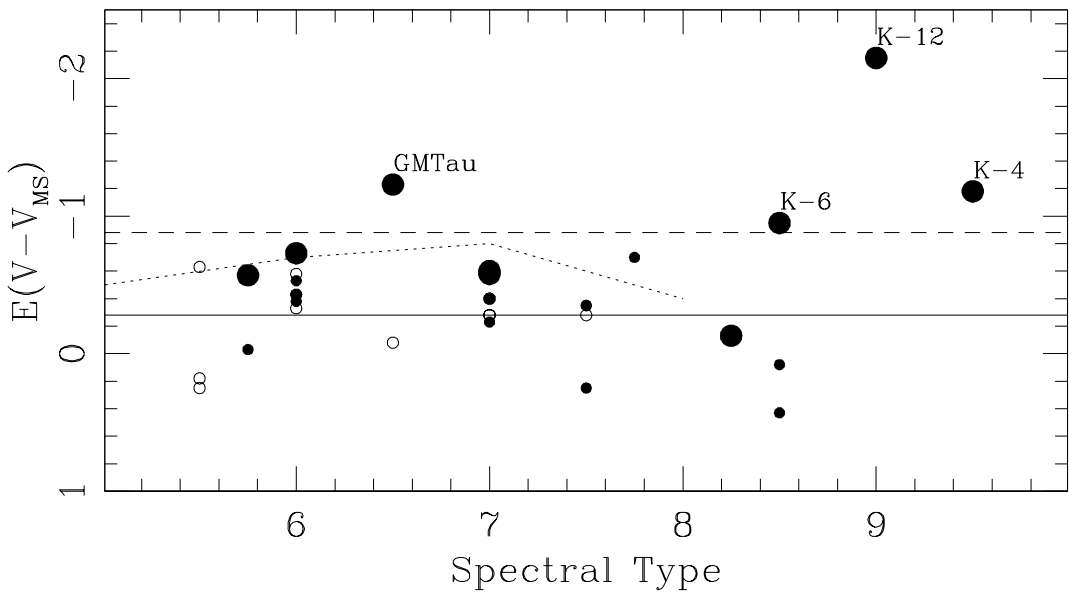
Figure 3.11 V-band excesses as a function of spectral type. Filled circles denote Taurus members, open circles denote Upper Sco members, and large symbols denote confirmed or probable accretors. A solid line shows the mean value for all non-accretors in our sample, and the dashed line shows the corresponding 2σ limit for the existence of significant optical excesses. The four objects with significant excesses are labeled.

Table 3.5. Results for Previous Multiplicity Surveys

Survey	SpTs	Minimum Sep (AU)	Binary Frequency
Close et al.(2003)	M8.0-L0.5	3	$15\pm7\%$
Bouy et al.(2003)	M8.0-L8.0	1	$18.8\pm3.7\%$
Burgasser et al.(2003)	T5.0-T8.0	1	$9^{+4}_{-3}\%$
Siegler et al.(2005)	M6.0-M7.5	3	$9^{+4}_{-3}\%$
Martín et al.(2003)	M6.0-M9.5[a]	7	$15^{+15}_{-5}\%$
Our Survey: USco	M5.5-M7.5[a]	5	$25^{+16}_{-9}\%$
Our Survey: Taurus	M5.75-M9.5[a]	5	$9^{+10}_{-4}\%$

[a]The surveys by Martin et al. (2003) and Kraus et al. (2005) observed BDs in the Pleiades and Upper Sco, respectively. Since these regions are young, the spectral type range corresponds to lower masses than in the field.

3.5   Discussion

3.5.1   (Sub)stellar Multiplicity

Multiplicity surveys of VLMOs have suggested a fairly uniform set of binary properties in the field (Close et al., 2003; Bouy et al., 2003; Burgasser et al., 2003; Siegler et al., 2005) and in the Pleiades (Martin et al., 2003). No companions with wide separations (>20 AU) or with unequal mass ratios ($q < 0.6$) were found, despite sufficient sensitivity for their detection. Several wider systems have been discovered serendipitously or during ongoing surveys (Gizis et al. 2000; Luhman 2004a, 2005c; Phan-Bao et al. 2005; Billeres et al. 2005). However, the corresponding survey statistics are not available, so it is difficult to determine a frequency for wide VLMO binaries. The binary fractions observed were also significantly lower than the binary fractions of 57% for field G-dwarfs (Duquennoy & Mayor, 1991) and 35-43% for field M-dwarfs (Reid & Gizis, 1997; Fischer & Marcy, 1992). We summarize these results in Table 3.5.

The study presented here is the first large survey of young VLMOs with sufficient resolution to identify binaries at separations seen for field VLMOs. Our binary fractions, $25^{+16}_{-9}\%$ in Upper Sco and $9^{+10}_{-4}\%$ in Taurus, are consistent with the range of results seen in the field. However, the field surveys are sensitive to companions with

separations as small as ~ 1 AU and found many companions within 4 AU that we could not have detected because of the larger distance to our targets. Our binary fraction for companions with $a \geq 4$ AU only sets a lower limit on the total binary fraction for VLMOs. The mass ratios and separations are also consistent with those seen in the field; V410-Xray3 has a mass ratio that is moderately low, but this result is based only on the z' observations and should be confirmed with followup observations.

The combined VLMO binary fraction (5/34 or $15^{+NN}_{-N}\%$) is also quite consistent with the field, though again, over a more restricted separation range than typical field surveys can observe. Our binary fraction for Taurus ($9\pm5\%$) is somewhat lower than that for Upper Scorpius ($25\pm16\%$), though the difference is not statistically significant ($<2\sigma$). However, larger surveys (particularly in Upper Sco) will be required to test whether the binary fraction depends on mass.

3.5.2   The Mass Dependence of Multiplicity

The distinct binary properties of field BDs, relative to those of stars, indicate that these properties are mass dependent. However, the form of this dependence is not known; Kroupa et al. (2003), Close et al. (2003), and Kraus et al. (2005) interpret current data as a sharp transition near the stellar/substellar boundary while Luhman (2004b) and White et al.(2009) argue for a smooth mass dependence. The field binary fraction appears to decrease from 57% for G dwarfs to 35-43% for M dwarfs (Duquennoy & Mayor 1991; Fischer & Marcy 1992; Reid & Gizis 1997), but the trend with mass is only marginally significant.

Our combined young VLMO sample for Taurus and Upper Scorpius is large enough to investigate a possible mass dependence in the VLMO binary frequency over the single order of magnitude mass range of our survey (0.015-0.15 $M_{\odot}$). All five binaries and candidate binaries were found among the 13 most massive VLMO targets ($M \geq 0.07\ M_{\odot}$); none were found among the 21 lower-mass VLMOs. If the probability of binarity is 5/34 for all members of our sample, then the probability that all five binaries will fall among the 13 most massive targets is $(13!/8!)/(34!/29!) \sim 0.005$.

The possible double-lined spectroscopic binary KPNO-Tau-14 (Mohanty et al. 2005) also falls in the upper mass range, though its separation is well inside our survey limit. The detection limits in Figure 3.8 demonstrate that bright binaries are more easily identified due to superior photon statistics, but at least the three high-confidence binaries in the combined sample (USco-55, USco-66, and MHO-Tau-8) could have been identified around even the faintest targets. Also, since this trend is seen at lower significance in both regions, it should be robust against variations in initial conditions. The implication is that the binary fraction may decline over the mass range, though a constant binary fraction combined with a shift toward smaller separations could produce the same effect in our resolution-limited sample.

We can further investigate the mass dependence of multiplicity in Taurus by combining our results with a binary census of more massive Taurus members by White et al.(2009). This speckle interferometry survey included 44 members of Taurus in the mass range $0.06 < M < 1.5$ $M_\odot$ and, in combination with previous results for 41 additional targets (Leinert et al. 1993; Ghez et al. 1993; Simon et al. 1995; Duchene 1999), identified 23 binaries with separations >27 mas (4 AU). The sample is reported to be complete for separations of 9-460 AU and mass ratios >0.1 (ΔK<2.75), which falls within the completeness range of our survey (Section 3.3.3). They report that the binary frequency appears to peak for stars with masses of 0.3-0.7 $M_\odot$ and decline toward lower masses, though the results are not statistically significant ($<2\sigma$). Our VLMO sample supports this mass dependence, since we found no binaries with separations in the completeness regime. However, a similar survey in Upper Scorpius by Kohler et al.(2000) found no evidence of a similar decline until immediately above the stellar/substellar boundary (0.1-0.2 $M_\odot$). This implies that the mass dependence of multiplicity could also have a regional dependence.

3.5.3   A Future Dynamical Mass for MHO-Tau-8?

Theoretical models of the mass-luminosity-temperature relation are still largely uncalibrated for low masses and young ages (e.g., Baraffe et al. 2002). Surface gravity

measurements for young brown dwarfs in Upper Sco (Mohanty et al., 2005) have provided some evidence that the theoretical models underestimate masses for very-low-mass stars and brown dwarfs and overestimate masses for the least massive brown dwarfs, but the measurement of dynamical masses for low-mass binaries will be required to directly calibrate the models. To date, this has been done only for three young VLMOs, the older ($\sim$50-100 Myr) brown dwarf AB Dor C (Close et al. 2005; Luhman et al. 2005b) and both components of the young substellar eclipsing binary 2MASS J05352184-0546085 (Stassun et al. 2006).

Relative to the speckle interferometry measurement by White et al.(2009), MHO-Tau-8 B has traced $\sim$40 degrees of its orbit around MHO-Tau-8 A within only $\sim$5 years; this suggests an orbital period of $\sim$45 years. If we assume a circular face-on orbit, then we estimate from Kepler's Law and the system parameters ($a \geq 6$ AU, $P \sim 45$ years) that the total mass of the system is $\geq$0.11 $M_\odot$, which is consistent with the total system mass implied by the models of Baraffe et al.(1998), $\sim$0.17 $M_\odot$. Since this lower limit is substantially lower than the predicted total mass, the orbit of the secondary is likely either inclined relative to the plane of the sky (implying a larger semi-major axis) or highly eccentric and near apastron. In either case, additional astrometric measurements for this system should yield precise orbital parameters and better limits on the dynamical masses of its components over the next decade.

3.5.4   VLMO Optical Excesses

The rate of (sub)stellar mass accretion onto T Tauri stars is typically estimated either by measuring the optical continuum excess or by modeling its effect on emission line features that result from outflows as accreting material impacts the photosphere. Previous observations of brown dwarfs and low- and intermediate-mass stars have found mass accretion rates that scale roughly as $\dot{M} \propto M^2$ for masses of 0.03-3.0 $M_\odot$ (Gulbring et al. 1998; White & Ghez 2001; Muzerolle et al. 2003; Calvet et al. 2004). Specifically, these surveys found mass accretion rates ranging from $\sim$10^{-7} $M_\odot$/yr for intermediate-mass T Tauri stars with mass 3 $M_\odot$ to $\sim$10^{-11} $M_\odot$/yr for T Tauri-age

brown dwarfs. Recent results from Mohanty et al.(2005) and Muzerolle et al.(2005), who measure accretion rates by modeling of Ca II and Hα emission respectively, support this trend. They found that many low-mass brown dwarfs (including KPNO-6, KPNO-12, and possibly KPNO-4) have apparent mass accretion rates of $\sim 5 \times 10^{-12}$ $M_\odot$/yr.

These low accretion rates would result in negligible optical excesses ($E(V-V_{MS}) <$ 0.01; e.g., Muzerolle et al. 2003); the very large excesses observed for our targets imply that either these objects have much higher accretion rates or the V-band excesses are not the result of accretion. The mass accretion rates that would be required for each known accretor to generate the optical excess can be calculated using the method described in Gullbring et al.(1998) whereby the excess V-band flux is converted to a total accretion luminosity. This luminosity is then assumed to result from mass infall from the inner edge of a circumstellar disk onto the surface of the star via magnetospheric accretion. Specifically, we assume that the radius of the inner disk edge is $5R_{VLMO}$ and the entire change in potential energy is radiated away via the optical excess. To correct our V-band excess luminosity to the total accretion luminosity, we adopt a bolometric correction factor of 10, which is 10% less than the bolometric correction adopted by White & Hillenbrand (2004) for a slightly redder, but narrower band-pass (0.60 - 0.65 μm). As emphasized by White & Hillenbrand, these bolometric corrections are still highly uncertain, but by adopting a value consistent with previous assumptions, we can minimize systematic errors in comparisons with previous calculations. Unfortunately, there are no photometric or spectroscopic data available at wavelengths shorter than 6000 angstroms for young BDs, so our results can not be directly compared to any in the literature.

The resulting mass accretion rates for the 4 stars with significant excesses (10^{-7} to 10^{-9} $M_\odot/yr$) are 3-4 orders of magnitude higher than the values found via other methods or inferred from the M-$\dot{M}$ relations observed for higher-mass T Tauri stars. Given this discrepancy, we consider the possibility that the excess results from our analysis methods or from other physical processes. However, it is statistically unlikely that 4/22 objects would possess $>+2\sigma$ excesses, or that KPNO-12 would possess a

6σ excess, if these accretors are part of a random distribution with the same mean and standard deviation as we observe for nonaccretors. Since 4/9 accretors possess excesses significant at $>+2\sigma$ and 8/9 possess excesses significant at $\geq+1\sigma$, it appears that the V-band excesses are related to accretion diagnostics. Since three of the outliers fall among the 5 latest objects, there could also be a gravity-based V-band excess inherent to all late-type young VLMOs. However, the corresponding trend for giants (which possess even lower surface gravity) appears to decline for spectral types later than M7 (Figure 3.11), and there is no sign of a similar excess for the two non-accreting late-type objects, KPNO-1 and KPNO-9. Finally, the possibility of erroneous spectral classifications cannot explain this result because there are significant discrepancies in the SED fits for errors of more than one subclass, and the degeneracy between spectral type, A_V, and L/L_{MS} that we note in Section 3.4.3.2 acts to preserve most of the inferred V-band excess under the assumption of a different spectral type.

One explanation that we cannot rule out is the presence of chromospheric activity or flaring. Stellar flares are characterized by transient regions with higher temperatures than the surrounding photosphere ($\geq 10^5$ K); they cause a temporary increase in the total luminosity, with much higher amplitude of variability at short wavelengths. Surveys for x-ray emission from young BDs (e.g., Preibisch et al. 2005) have found that 1/3 to 1/2 of all objects may possess significant activity. These regions also typically produce Hα emission; the width of the base of the Hα emission line is a typical test for accretion, so it is possible that a large flare or significant chromospheric activity could broaden the line base, mimicking the signature of accretion.

3.6 Conclusions

We present the results of a high-resolution imaging survey of 34 brown dwarfs and very-low-mass stars in the nearby young associations Taurus-Auriga and Upper Scorpius.

This survey confirmed the binarity of MHO-Tau-8 and four new binary systems,

resulting in a binary fraction of 15% at separations >4 AU. All binary systems are tight (<20 AU), and most of the systems appear to have mass ratios near unity ($q \geq 0.7$). The binary frequency and separations are consistent with very-low-mass binary properties in the field, but the mass ratio of V410-Xray3 is among the lowest known. The binary frequency and separations are also consistent with the trends in multiplicity statistics observed for higher-mass Taurus members, which suggest a gradual decline in both properties toward low masses; the implications are that the distinct binary statistics of low-mass systems are set in the formation process and that this formation process is similar to that which creates low-mass stars.

Our sample reveals another possible mass dependence of multiplicity; all five binaries and candidate binaries fall in the more massive half of the combined sample, implying either a decline in frequency or a shift to smaller separations for the lowest-mass binaries. We also combine the survey detection limits with the models of Chabrier et al.(2000) to show that there are no planets or very-low-mass brown dwarfs with separations $> 3M_J$ at projected separations >40 AU orbiting any of the Taurus members in our sample, implying that planetary-mass companions at wide separations like 2M1207b are found with frequency $\leq 5\%$. Finally, we observe significant optical excesses in the spectral energy distributions of most targets and conclude that the targets with spectroscopic signatures of accretion possess larger optical excesses than other young brown dwarfs and very-low-mass stars.

Acknowledgements

Bibliography

Ardila, D., Martin, E. L., & Basri, G. 2000, AJ, 120, 479

Baraffe, I., Chabrier, G., Allard, F. & Hauschildt, P.H. 1998, A&A, 337, 403

Baraffe, I., Chabrier, G., Allard, F. & Hauschildt, P.H. 2002, A&A, 382, 563

Basri, G., & Batalha, C. 1990, ApJ, 363, 654

Bate, M. 2005, MNRAS, 363, 363

Bessell, M., & Brett, J. 1988, PASP, 100, 1134

Billéres, M., Billéres, M., Delfosse, X., Beuzit, J.-L., Forveille, T., Marchal, L., & Martín, E. L. 2005, A&A, 440, L55

Bouy, H. et al. 2003, AJ, 126, 1526

Briceno, C., et al. 1998, AJ, 115, 2074

Briceno, C., et al. 2002, ApJ, 580, 317

Bruzual, G., Persson, E., Gunn, J. & Stryker, L. 1996, Bruzual-Persson-Gunn-Stryker
    Spectrophotometry Atlas

Burgasser, A., et al. 2003, ApJ, 586, 512

Chabrier, G., Baraffe, I., Allard, F., & Hauschildt, P. 2000, ApJ, 542, 464

Chauvin, G. et al. 2004, A&A, 425, L29

Close, L. M., Siegler, N., Freed, M., & Biller, B. 2003, ApJ, 587, 407

Close, L. M., et al. 2005, Nature, 433, 286

Cutri, R. M., et al. 2003, 2MASS Point Source Catalog (Pasadena: Caltech)

Delfosse, X., et al. 1997, A&A, 327, L25

Delgado-Donate, E. J., Clarke, C. J., & Bate, M. R. 2003, MNRAS, 342, 926

Duchenne, G. 1999, A&A, 341, 547

Duquennoy, A., & Mayor, M. 1991, A&A, 248, 485

Fischer, D. A., & Marcy, G. W. 1992, ApJ, 396, 178

Fukugawa, M. et al. 1996, AJ, 111, 1748

Ghez, A., Neugebauer, G., & Matthews, K. 1993, AJ, 106, 2005 Gizis, J. E., et al.
    2000, MNRAS, 311, 385

Gizis, J.E. et al. 2003, AJ, 125, 3302

Goodwin, S., & Kroupa, P. 2005, A&A, 439, 565

Gullbring, E., et al. et al. 1998, ApJ, 492, 323

Hartigan, P., et al. 1991, ApJ, 382, 617

Hawley, S.L., et al. 2002, AJ, 123, 3409

Hillenbrand, L. & White, R. 2004, ApJ, 604, 741

Hubber, D., & Whitworth, A. 2005, A&A, 437, 113

Koerner, D. et al. 1999, ApJ, 526, L25

Kohler, R., Kunkel, M., Leinert, C., & Zinnecker, H. 2000, A&A, 356, 541

Kraus, A., et al. 2005, ApJ, 633, 452

Kroupa, P. 1995, MNRAS, 277, 1522

Kroupa, P., & Bouvier 2003, MNRAS, 346, 343

Kroupa, P. et al. 2003, MNRAS, 346, 354

Leggett, S., et al. 2000, ApJ, 536, L35

Leggett, S., et al. 2002, ApJ, 564, 452

Leinert, C. et al. 1993, A&A, 278, 129

Luhman, K.L. et al. 2003a, ApJ, 590, 348

Luhman, K. L., et al. 2003b, ApJ, 593, 1093

Luhman, K. L. 2004a, ApJ, 614, 398

Luhman, K. L. 2004b, ApJ, 617, 1216

Luhman, K.L., McLeod, K.K., & Goldenson, N. 2005a, ApJ, 623, 1141

Luhman, K.L., Stauffer, J.R., & Mamajek, E.E. 2005b, ApJ, 628, L69

Luhman, K. L. 2005c, ApJ, 633, L41

Mack, J., et al. 2003, "ACS Data Handbook", Version 2.0, (Baltimore: STScI)

Martin, E.L., et al. 2000, ApJ, 543, 299

Martin, E.L., et al. 2001, ApJ, 561, 195

Martin, E.L., et al. 2003, ApJ, 594, 525

Metchev, S.A., Hillenbrand, L.A. & White, R.J. 2003, ApJ, 582, 1102

Mohanty, S., Jayawardhana, R., Basri, G., 2005, ApJ, 626, 498

Muzerolle, J. et al. 2003, ApJ, 592, 266

Muzerolle, J. et al. 2005, ApJ, 625, 906

Neuhauser, R., Brandner, W., Alves, J., et al. 2002, A&A, 384, 999

Phan-Bao, N., Martín, E. L., Reyl'e, C., Forveille, T., & Lim, J. 2005, A&A, 439, L19

Preibisch, T. et al. 2005, ApJS, 160, 401

Reid, I.N. & Gizis, J.E. 1997, AJ, 113, 2246

Reid, I.N. & Hawley, S.L. 1999, AJ, 117, 343

Reid, I.N. et al. 2001, AJ, 121, 489

Reid, I.N. et al. 2003, AJ, 126, 3007

Reid, I.N. et al. 2004, AJ, 128, 463

Reiners, A., Basri, G., & Mohanty, S. ApJ, 634, 1346

Reipurth, B., & Clarke, C. 2001, AJ, 122, 432

Schlegel, D., Finkbeiner, D., & Davis, M. 1998, ApJ, 500, 525

Siegler, N. et al. 2005, ApJ, 621, 1023

Simon, M. et al. 1995, ApJ, 443, 625

Sirianni, M. et al. 2005, PASP, 117, 1049

Stassun, K. et al. 2006, Nature, 440, 311

Stetson, P.B. 1987, PASP, 99, 191

Strom, K.M. & Strom, S.E. 1994, ApJ, 424, 237

West, A. A., Walkowicz, L. M., & Hawley, S. L. 2005, PASP, 117, 706

White, R. & Basri, G. 2003, ApJ, 582, 1109

White, R.J. & Hillenbrand, L.A. 2004, ApJ, 616, 998

White, R.J. et al. 2009, in preparation

Chapter 4

Unusually Wide Binaries: Are They Wide or Unusual?

Abstract

We present the results of a search for wide binary systems among 783 members of three nearby young associations: Taurus-Auriga, Chamaeleon I, and two subgroups of Upper Scorpius. Near-infrared (JHK) imagery from 2MASS was analyzed to search for wide (1-30″; $\sim$150-4500 AU) companions to known association members, using color-magnitude cuts to reject likely background stars. We identified a total of 131 candidate binary companions with colors consistent with physical association, of which 39 have not been identified previously in the literature. We then pursued an astrometric and spectroscopic campaign to confirm the youth and association of a complete subsample of these candidate wide companions in Taurus and Upper Sco A. Our survey confirmed twelve new binary systems with separations of 3-30″ (3 in Taurus and 9 in Upper Sco) among all of the known members with masses of 2.5-0.012 $M_\odot$, yielding a total sample of 46 systems in these mass and separation range. The total sample and the confirmed subsample both conform to only some expectations from field multiplicity surveys. Higher-mass stars have a higher frequency of wide binary companions, and there is a marked paucity of wide binary systems near the substellar regime. However, the separation distribution appears to be log-flat, rather

than declining as in the field, and the mass ratio distribution is more biased toward similar-mass companions than the IMF or the field G dwarf distribution. The maximum separation also shows no evidence of a limit at <5000 AU until the abrupt cessation of any wide binary formation at system masses of ∼0.3 $M_\odot$. We attribute this result to the post-natal dynamical sculpting that occurs for most field systems; our binary systems will escape to the field intact, but most field stars are formed in denser clusters and do not. In summary, only wide binary systems with masses <0.3 $M_\odot$ appear to be "unusually wide". Finally, we find that the binary frequency in the USco-B subgroup is significantly higher than in the USco-A subgroup and is consistent with the measured values in Taurus and Cham I. This discrepancy, the absence of high-mass stars in USco-B, and its marginally distinct kinematics suggest that it might not be directly associated with the OB associations of Sco-Cen, but instead represents an older analogue of the younger ρ Oph or Lupus associations.

4.1   Introduction

The frequency and properties of multiple star systems are important diagnostics for placing constraints on star formation processes. This motivation has prompted numerous attempts to characterize the properties of nearby binary systems in the field. These surveys (e.g., Duquennoy & Mayor 1991; Fischer & Marcy 1992; Close et al. 2003; Bouy et al. 2003; Burgasser et al. 2003) have found that binary frequencies and properties are very strongly dependent on mass. Solar-mass stars have high binary frequencies (>60%) and maximum separations of up to ∼10^4 AU. By contrast, M dwarfs have moderately high binary frequencies (30-40%) and few binary companions with separations of more than ∼500 AU, while brown dwarfs have low binary frequencies (∼15% for all companions with separations >2-4 AU) and few companions with separations >20 AU.

The mass-dependent decline in the maximum observed binary separation (or binding energy) has been described by Reid et al. (2001) and Burgasser et al.(2003) with an empirical function that is exponential at high masses and quadratic at low masses.

The mechanism that produces the mass dependence is currently unknown. Simulations show that the empirical limit is not a result of dynamical evolution in the field (e.g., Burgasser et al. 2003; Weinberg et al. 1987) since the rates of binary disruption (due to single stellar encounters with small impact parameters) and evolution in the separation distribution (due to many encounters at large impact parameters) are far too low. This suggests that the limit must be set early in stellar lifetimes, either as a result of the binary formation process or during early dynamical evolution in relatively crowded natal environments.

Studies of nearby young stellar associations have identified several candidate systems which might be unusually wide binaries (Chauvin et al. 2004; Caballero et al. 2006; Jayawardhana & Ivanov 2006; Luhman et al. 2006a, 2007; Close et al. 2007; Kraus & Hillenbrand 2007b). However, there are several factors that must be considered when interpreting these discoveries. Most were identified serendipitously and not as part of a survey, so the actual frequency of these candidates is not well constrained. Further, several of these systems do not seem to be unusual in comparison to field systems of similar mass. Finally, many of these systems have not been surveyed at high angular resolution, so they could be hierarchical multiples with higher total masses.

In the first half of this chapter, we describe our program to address these problems by using archival 2MASS data to systematically search for candidate wide binary systems among all of the known members of three nearby young associations (Upper Sco, Taurus-Auriga, and Chamaeleon-I; Kraus & Hillenbrand 2007a, hereafter KH07a). In Section 4.2, we describe the selection of our survey sample, and we describe our data processing techniques in Section 4.3. We summarize the results of our search in Section 4.4.

Our preliminary results broadly agreed with the standard paradigm; there is a significant deficit of wide systems among very low-mass stars and brown dwarfs as compared to their more massive counterparts. However, we also found that most of these wide systems were concentrated in the very sparsest T associations, Taurus and Cham-I. Upper Sco is not significantly more dense than either of these associations,

so it is unclear why it might have such a meager wide binary population. We also found a few candidate systems which appeared to be unusually wide for their mass. However, photometric criteria alone are not sufficient to reject all background stars and identify a handful of genuine systems.

Thus, in the second half of this chapter, we describe our astrometric and spectroscopic follow-up campaign to confirm or reject the youth and association of our new sample of candidate binary companions. In Section 4.5, we describe the compilation of our sample of candidate wide binary systems. In Section 4.6, we describe the observations and analysis conducted for our survey, and in Section 4.7, we evaluate this evidence in order to distinguish association members from field stars. Finally, in Section 4.8, we describe the mass-dependent binary frequency, mass ratio distribution, and separation distribution of these systems, plus we examine the criteria that might define an "unusually wide" binary system.

4.2   Member Sample Selection

In Table 4.1, we describe the young associations from which we have drawn our sample: Taurus-Auriga, Chamaeleon I, and the two proposed subgroups of Upper Scorpius. The sample regions have been selected to include all large stellar populations (>100 known members) which are not heavily embedded, are located at distances of <200 pc, and have ages <30 Myr. These criteria neglect small associations and moving groups which can not contribute significant statistics (TW Hya, MBM 12, Chamaeleon II, η and ϵ Cham, and the Lupus clouds), distant populations for which seeing-limited observations on a small telescope cannot probe sufficiently small separations (IC 348 and the subgroups of Orion), embedded populations like the ρ Oph complex, and old populations in which the wide binary population may have been shaped by dynamical evolution (Praesepe, Pleiades, α Persei).

In Table 4.2, we list the association members which we have adopted as our primary sample in the multiplicity search. The regional membership of our sample has been confirmed via low-resolution spectroscopy to verify signatures of youth, so

contamination of the primary sample should be negligible. As we discuss in Section 4.4.2, the surveys from which we draw our sample are likely to be incomplete due to selection biases; many of the new candidate companions found here would have been identified in previous surveys if they were complete and unbiased. This could potentially cause us to overestimate the wide binary frequency. Wide binaries would only be excluded from our sample if both components were absent from previous membership surveys, so they are less likely to have been omitted from our sample than single members. However, this effect would have been more prevalent among faint low-mass systems (where incompleteness is higher). We are testing for a decline in the binary frequency with mass, and any detection of this trend would be robust against this bias.

Saturation occurs for 2MASS sources brighter than $K \sim 8$, but the images can still be used for sources as bright as $K \sim 6$; we have neglected only the high-mass association members which are brighter than this limit, corresponding to spectral types earlier than G0. These bright stars typically have been studied with adaptive optics (e.g., Kouwenhoven et al. 2005 for the Sco-Cen complex), so analysis of 2MASS data would not contribute significant new results. We also omit all sources which do not have confirmed spectral types since we can not estimate their mass. This criterion should eliminate most of the sources which are embedded in massive envelopes and surrounded by resolved nebulosity. Finally, four of our primary sample members are fainter than our detection limit for binary companions ($K = 14.3$), but we retain them in our sample in case they are binary companions to higher-mass association members which have not yet been identified.

In the following subsections, we briefly describe each association and summarize the construction of our member sample.

Table 4.1. Nearby Young Associations

Name	Distance (pc)	Age (Myr)	Type	Members
Chamaeleon I	170	1-2	T Assoc.	147
Taurus-Auriga	145	1-2	T Assoc.	235
Upper Scorpius A	145	5	OB Assoc.	356
Upper Scorpius B	145	5	OB Assoc.[a]	45

[a]As we discuss in Appendix A, the nature of Upper Sco B is still uncertain.

Table 4.2.   Confirmed Members of Nearby Young Associations

| Name | Region | RA | DEC | K | $J-K$ | $H-K$ | SpT | Mass | χ_3[a] | μ_α,μ_δ | References |
		(Eq=2000)						$(M_\odot)$		(mas yr^{-1})	
ScoPMS005	UScoA	15 54 59.86	-23 47 18.2	7.03	0.54	0.16	G2	1.66	26.57	-28,-38	Walter et al.(1994)
ScoPMS013	UScoA	15 56 29.42	-23 48 19.8	8.75	0.92	0.23	M1.5	0.54	2.00	16,-42	Walter et al.(1994)
ScoPMS014	UScoA	15 56 54.97	-23 29 47.8	10.29	0.93	0.30	M3	0.36	1.67	-8,-28	Walter et al.(1994)

[a]The χ_3 statistic is a measure of how well each object is fit by a single point source; see Section 4.3.2.

Note. — The full table of 783 sample members can be accessed from the website http://www.astro.caltech.edu/~alk/ (in PDF, TeX, or plain-text formats) or from the published article in ApJ.

Table 4.3.   Close Pairs of Confirmed Association Members

Name	Primary			Secondary			Projected Sep($''$)	Position Angle(deg)
	$J-K$	$H-K$	K	$J-K$	$H-K$	K		
2M11103-7722 ISO350	2.00	0.68	10.03	2.06	0.70	10.67	9.51	145.7
ChaHa4 ChaHa10	1.14	0.41	11.02	1.06	0.33	13.24	20.83	128.5
ChaHa10 ChaHa11	1.06	0.33	13.24	1.04	0.37	13.55	19.60	58.9
CHX18N T49	1.34	0.52	7.77	1.60	0.64	8.87	24.38	255.7
CHXR14 N CHXR14 S	0.94	0.23	9.60	0.98	0.23	9.75	28.17	166.6
CHXR20 T22	1.30	0.32	8.88	1.42	0.40	9.39	28.46	349.2
CHXR30 A CHXR30 B	2.71	0.83	9.09	3.92	1.54	9.95	9.93	295.4
CHXR60 Hn18	0.99	0.28	10.58	1.06	0.31	10.80	28.28	220.6
CHXR68 A CHXR68 B	0.92	0.24	8.87	0.98	0.27	10.26	4.39	212.4
ESO-Ha-566 CHSM15991	1.32	0.42	11.03	1.91	0.74	14.14	23.65	93.9
Hn10E C1-25	1.91	0.69	10.05	3.80	1.42	10.00	19.17	231.0
Hn21 W Hn21 E	1.34	0.44	10.65	1.27	0.48	11.49	5.43	69.3
ISO143 ISO138	1.48	0.56	11.10	1.02	0.43	13.04	18.16	223.8
ISO237 T45A	2.31	0.82	8.62	1.33	0.40	9.24	28.32	235.7
T28 ChaHa8	1.91	0.72	8.26	1.27	0.49	11.51	28.87	164.3
T29 ESO-Ha-562	2.67	1.09	6.83	3.33	1.37	8.30	16.37	81.8
T31 T30	1.74	0.68	6.96	2.38	0.97	9.89	16.52	221
T34 ChaHa13	1.17	0.32	10.02	1.12	0.4	10.67	25.41	3.9

Table 4.3 (cont'd)

Name	Primary			Secondary			Projected Sep($''$)	Position Angle(deg)
	$J-K$	$H-K$	K	$J-K$	$H-K$	K		
T47	1.97	0.78	9.18	1.30	0.35	10.75	12.09	161.3
ESO-Ha-568								
T52	1.44	0.62	6.85	1.79	0.73	9.13	11.18	99.2
T53								
DHTau	1.59	0.65	8.18	0.93	0.21	8.39	15.23	126
DITau								
FVTau	2.48	0.88	7.44	1.93	0.62	8.87	12.29	105.7
FVTau/c								
FZTau	2.55	1.05	7.35	1.93	0.62	8.05	17.17	250.5
FYTau								
GGTau A	1.31	0.45	7.36	1.09	0.42	9.97	10.38	185.1
GGTau B								
GHTau	1.32	0.44	7.79	1.19	0.40	6.96	21.77	15.2
V807Tau								
GKTau	1.59	0.64	7.47	1.45	0.53	7.89	13.14	328.4
GITau								
HBC352	0.51	0.14	9.58	0.59	0.14	9.86	8.97	70.8
HBC353								
HBC355	0.62	0.13	10.20	0.73	0.15	11.11	6.31	298.3
HBC354								
HLTau	3.21	1.76	7.41	2.09	0.86	7.29	23.31	91.2
XZTau								
HPTau-G2	0.87	0.26	7.23	1.92	0.84	7.63	21.30	296.9
HPTau								
HPTau-G2	0.87	0.26	7.23	1.24	0.36	8.80	10.09	243.4
HPTau-G3								
2MASSJ04554757+3028077	1.07	0.33	9.98	1.03	0.43	12.16	6.31	115.7
2MASSJ04554801+3028050								
LkHa332-G1	1.64	0.46	7.95	1.56	0.44	8.23	25.88	254.5
LkHa332-G2								
LkHa332-G2	1.64	0.46	7.95	1.87	0.66	7.94	10.51	35.3
V955Tau								
MHO-2	3.73	1.63	7.79	4.70	2.10	7.78	3.93	333.9
MHO-1								
V773TauA	1.28	0.43	6.21	1.52	0.69	11.64	23.38	215.9
2MASSJ04141188+2811535								

Table 4.3 (cont'd)

Name	Primary			Secondary			Projected Sep($''$)	Position Angle(deg)
	$J-K$	$H-K$	K	$J-K$	$H-K$	K		
V928Tau	1.43	0.33	8.11	1.16	0.41	10.38	18.25	228.2
CFHT-Tau-7								
RXJ1524.2-3030A	0.63	0.16	8.68	0.99	0.29	9.60	20.18	87.3
RXJ1524.2-3030B								
RXJ1537.0-3136A	0.52	0.04	7.74	0.90	0.18	7.65	5.37	285.0
RXJ1537.0-3136B								
RXJ1539.4-3446B	1.21	0.43	7.98	1.61	0.60	9.29	6.36	98.1
RXJ1539.4-3446C								
RXJ1540.7-3121A	0.83	0.26	10.53	0.86	0.27	10.66	5.95	75.5
RXJ1540.7-3121B								
RXJ1558.1-2405A	0.79	0.16	8.96	0.89	0.25	11.06	18.15	254.4
RXJ1558.1-2405B								
RXJ1604.3-2130A	1.44	0.60	8.51	1.02	0.27	9.43	16.22	215.9
RXJ1604.3-2130B								
USco-160428.4-190441	1.04	0.27	9.28	1.02	0.31	11.01	9.77	321.3
USco-160428.0-190434								
USco-160707.7-192715	0.95	0.24	9.80	1.00	0.29	11.17	23.45	140.4
USco-160708.7-192733								
USco-160822.4-193004	0.97	0.18	9.06	1.11	0.27	9.47	13.47	71.4
USco-160823.2-193001								
USco-160900.7-190852	1.07	0.32	9.15	1.01	0.38	10.96	18.92	326.5
USco-160900.0-190836								
USco-161010.4-194539	0.97	0.28	10.41	0.96	0.33	11.38	25.59	160.8
USco-161011.0-194603								
ScoPMS008b	0.97	0.32	9.33	1.03	0.38	9.77	25.61	68.6
ScoPMS008a								

4.2.1   Scorpius-Centaurus

The Sco-Cen OB Association consists of three distinct subgroups: Upper Scorpius (USco; 5 Myr and 145 pc), Upper Centaurus-Lupus (UCL; 13 Myr and 160 pc), and Lower Centaurus-Crux (LCC; 10 Myr and 118 pc) (de Geus et al. 1989; de Zeeuw et al. 1999). Sco-Cen has been recognized for nearly a century as a moving group of early-type stars (e.g., Kapteyn 1914; Blaauw 1946; Bertiau 1958; Jones 1971). However, surveys to identify low-mass stellar members have been undertaken only in the past 15 years and have concentrated almost exclusively on USco. Initial surveys (Walter et al. 1994; Kunkel 1999) identified candidate members from surveys for X-ray emission, while subsequent surveys (Preibisch et al. 1998; Ardila et al. 2000; Preibisch et al. 2001; Preibisch et al. 2002; Martin et al. 2004; Slesnick et al. 2006a) used wide-field optical/NIR surveys to select candidate members with colors and magnitudes consistent with the assumed age and distance. Membership was confirmed with low- or intermediate-resolution spectroscopy to confirm indicators of

youth such as lithium absorption, Hα emission, or low surface gravity. Proper-motion member identification is typically not possible for faint Sco-Cen members since their proper motions are not sufficiently distinct from those of background stars; the only major effort has been by Mamajek et al. (2003), who identified candidate G- and K-dwarf members of UCL and LCC based on proper motions, then confirmed their membership with low-resolution spectroscopy.

The sample sizes for UCL and LCC are marginal (∼50 members each) and span a limited range of masses, and the associations' low galactic latitude ($|b| < 20$) results in substantial contamination from reddened background stars, so we have chosen to only consider Upper Sco. We select our sample from the surveys of Walter et al.(1994), Preibisch et al.(1998), Kunkel (1999), Ardila et al.(2000), Preibisch et al.(2001), Preibisch et al.(2002), Martin et al.(2004), and Slesnick et al.(2006a).

Brandner et al.(1996) noted that some of the objects in these surveys form a distinct subgroup in the southwest, near the border with UCL; they named the main population Upper Sco A and the subgroup Upper Sco B (hereafter USco-A and USco-B). A multiplicity survey by Kohler et al.(2000) subsequently found that these two populations might have distinct binary statistics, with a much wider mean separation in USco-B. As we show in Appendix B, the members of USco-B also appear to have distinct kinematics. These results suggest that USco-B should be treated as a distinct population. Based on the population kinematics and the previous dividing lines adopted by Brandner et al. and Kohler et al., we assign all sample members west of 16h and south of -28° to USco-B, and all remaining members to USco-A. It is quite likely that there is some overlap along this border, but the precision of the kinematic data does not allow us to unambiguously determine this or to establish the subgroup membership of individual sources.

We also note that two USco members, ScoPMS008A and ScoPMS008B, are located ∼15″ from an early type USco member, HD 142424 (A8IV/V; de Zeeuw et al. 1999). It is possible that these stars are companions to HD 142424 and not independent primaries; since they fall within our identification range for binary companions in USco-A (<20″), then we do not treat these sources as independent primaries. Kohler

et al.(2000) found (and we verify) that ScoPMS008A is itself a binary system with a separation of $\sim$1.6″, which suggests that this could be at least a quadruple system.

4.2.2 Taurus

The Taurus-Auriga association (Taurus; 1-2 Myr; 145 pc; Bertout et al. 1999; White & Ghez 2001) has been recognized for more than 60 years as the nearest northern site of low-mass star formation and is the home of the archetypical star T Tauri. The low-mass stellar population of Taurus-Auriga has been classified gradually over this time period (e.g., Joy et al. 1945; Herbig et al. 1952; Cohen & Kuhi 1979); unlike Sco-Cen, Taurus is largely devoid of stars more massive than 1-2 $M_\odot$.

A census of known Taurus members was presented in Kenyon & Hartmann (1995) and has been supplemented by additional surveys to identify very-low-mass stellar and substellar members of Taurus-Auriga by Briceno et al.(1993, 1998, 2002), Strom & Strom (1994), Martin et al.(2001), Luhman et al.(2003a, 2004d, 2006), Guieu et al.(2005), and Slesnick et al.(2006b). Members of Taurus-Auriga have also been confirmed in a follow-up survey of continuum (heavily veiled) sources by White & Basri (2003) and a survey for Hyades members by Reid & Hawley (1999). Finally, it was pointed out by White et al.(2006) that the source FV Tau/c2 (Hartigan et al. 1994) was omitted from the compilation of Kenyon & Hartmann. We have constructed our Taurus source list from the Kenyon & Hartmann census, plus all subsequent surveys.

4.2.3 Chamaeleon I

The Chamaeleon I complex (ChamI; 1-2 Myr; $\sim$160-170 pc; Whittet et al. 1997; Wichmann et al. 1998; Bertout et al. 1999) is another nearby site of ongoing star formation. Like Taurus-Auriga, it is composed primarily of low-mass stars and molecular clouds and possesses few high-mass stars. Much of its stellar population was identified by optical and near-infrared surveys during the 1970s and 1980s (e.g Henize & Mendoza 1973; Schwartz 1977; Glass 1979; Baud et al. 1984).

Carpenter et al.(2002) and Luhman (2004b) have compiled censuses of known members and candidate members based on these and other surveys, and Luhman (2004b) confirmed the membership of many candidate members using optical and NIR spectroscopy. An objective prism survey of the entire cloud by Cameron et al. (2004) also confirmed 4 additional candidate members and identified 7 new members. Finally, one candidate substellar member from the survey of Oasa et al. (1999) was spectroscopically confirmed as a ChamI member by Luhman et al. (2004c). We have constructed our ChamI sample from the 151 confirmed ChamI members of Luhman (2004b), Luhman et al.(2004c), and Cameron et al.(2004) with spectral types later than G0.

4.2.4 Spectroscopically Confirmed Stellar Pairs

Spectroscopic surveys of these stellar associations have identified many close ($<30''$) pairs of members. Given the typical low surface density of association members on the sky, these stars could be gravitationally bound binary companions. We list these candidate binary systems in Table 4.3. Many systems have projected separations lower than our survey's outer identification limits (Section 4.4.1); in these cases, we have removed the secondary star in each pair from our statistical sample. Candidate secondaries at wider separations are considered to be independent systems for statistical purposes.

4.3 2MASS Data and Analysis Techniques

4.3.1 The Two-Micron All-Sky Survey

The Two-Micron All-Sky Survey (2MASS; Skrutskie et al. 2006) observed 99.998% of the sky in the J, H, and K_s bands over an interval of 4 years. Each point on the sky was imaged six times and the coadded total integration time was 7.8s, yielding 10σ detection limits of $K = 14.3$, $H = 15.1$, and $J = 15.8$. The saturation levels depend on the seeing and sky background for each image, but are typically $J < 9$, $H < 8.5$,

and $K_s < 8$. The pixel scale of the detector was 2 arcsec pix^{-1}, but acquisition of multiple images allowed for subsampling to increase the effective resolution; the final pixel scale for each processed image is 1 arcsec pix^{-1}, which critically samples stellar point-spread functions (PSFs) given a typical resolution of $3''$ FWHM. The typical astrometric accuracy attained for the brightest unsaturated sources ($K \sim 8$) is ~ 100 mas, and the photometric zero-points are calibrated to <0.02 mag.

The 2MASS Point Source Catalog (PSC; Cutri et al. 2003) and the processed survey images are available from the 2MASS website.[1] We use PSC data to identify all wide ($>5''$) visual companions to our sample members. However, the PSC does not always distinguish multiple point sources in close proximity ($<5''$), instead reporting only the brightest source. This suggests that wide neighbors to our sample members should be identified in the PSC, but most close neighbors are probably absent.

We address this incompleteness by working directly with the processed survey images to identify close ($<5''$) companions via PSF-fitting photometry. From the 2MASS website, we extracted postage-stamp ($60 \times 60''$) and wide-field ($510 \times 1024''$) images for each of the association members described in Section 4.2. The wide-field images were used to create reference PSFs for each science target, while the postage-stamp images have been used to identify close visual companions. The width of the wide-field images ($510''$) corresponds to the width of each 2MASS survey tile; any image with larger width would include data taken at different epochs, and therefore with different seeing conditions. The height was chosen to allow for >10 PSF reference stars brighter than $K \sim 11$ in all fields. The size of the overlap region between adjacent tiles was $60''$ in right ascension and $8.5'$ in declination, so each science target appeared to be $>30''$ away from the edge in at least one tile.

The 2MASS survey images were produced by coadding multiple exposures taken in sequence, each offset by $\sim 85''$ in declination, so drawing PSF reference stars from several arcminutes away could lead to nonuniform images. Only sources $<40''$ north or south of a science target were observed in all six exposures that the science target was observed, and sources $>500''$ north or south do not share any simultaneous

---

[1]http://www.ipac.caltech.edu/2mass/

scans. However, all of the scans which contribute to a wide-field image were observed within ~30 seconds. We do not expect the seeing-based PSF to change on this short timescale, and we have found that the PSF is usually constant over each entire wide-field image (σ_{FWHM}~0.1″).

4.3.2   Data Reduction and Source Identification

We identified candidate companions and measured their fluxes from the postage-stamp image of each sample member using the IRAF[2] package DAOPHOT (Stetson 1987), specifically with the PSF-fitting photometry routine ALLSTAR. The template PSFs for each postage-stamp image were created using the PSTSELECT and PSF tasks. We selected template stars for each source from the corresponding wide-field image; each PSF was based on the eight brightest, unsaturated stars which appeared to be isolated under visual inspection. The appropriate photometric zero-point was extracted from the image headers. We compared PSF-fitting magnitudes for single stars to the corresponding PSC values in order to test our results; there is no systematic offset, and the standard deviation of the random scatter in $m_{PSF} - m_{PSC}$ is ~0.03 magnitudes.

As we have discussed in previous publications (Kraus et al. 2005, 2006), one limitation of ALLSTAR-based PSF photometry is that binaries with very close ($<\theta_{FWHM}$) separations are often not identified, even when their combined PSF deviates significantly from that of a true point source. This limitation can be overcome for known or suspected binaries by manually adding a second point source in approximately the correct location and letting ALLSTAR recenter it to optimize the fit. However, this method requires objective criteria for identifying suspected binaries; subjective selection methods like visual inspection would not allow us to rigorously choose and characterize a statistically complete sample. We have found that ALLSTAR's χ^2 statistic, which reports the goodness-of-fit between a source and the template PSF, is

---

[2]IRAF is distributed by the National Optical Astronomy Observatories, which are operated by the Association of Universities for Research in Astronomy, Inc., under cooperative agreement with the National Science Foundation.

an excellent diagnostic for this purpose. Since there are images in three bandpasses, we use a single diagnostic value, denoted χ_3, which is the sum of the three χ^2 values obtained for each association member when fit with a single point source. We list the value of χ_3 for each association member in Table 4.2.

In Figure 4.1, we plot the values of χ_3 as a function of K-band magnitude for a subset of sample members with no known companions between $0.5''$ and $15''$ (according to the surveys of Leinert et al. 1993; Ghez et al. 1993; Simon et al. 1995; Duchene 1999; Kohler et al. 2000; Kraus et al. 2005, 2006; White et al. 2006). The goodness of fit degrades rapidly for saturated stars ($K < 8$), so our technique does not discriminate betweeen single stars and candidate binaries in this regime. However, since there are few stars brighter than the saturation limit, we decided not to reject them until we were certain we could not identify any binary systems via other methods. The distribution of χ_3 values for unambiguously unsaturated stars ($K > 8.5$) is not normally distributed, but 95% of these stars produce fits with $\chi_3 < 2.5$, so we have selected all sources with $\chi_3 \geq 2.5$ as candidate binary systems.

The mean value of χ_3 for single stars should be ~ 3 since it represents the sum of 3 variables which follow a χ^2 distribution. However, we find that the mean value reported by ALLSTAR for unsaturated single sources is ~ 1.75. This disagreement is caused by an overestimate of the photometric errors in each observation by ALLSTAR. The coadding and subsampling process used in the 2MASS image processing pipeline results in correlated noise between adjacent pixels of the final survey images, so the true uncertainties are lower than those estimated solely by Poisson statistics (Skrutskie et al. 2006).

We identified the candidate binaries in our sample based on this empirically motivated χ_3 selection criterion, and then we attempted to fit each with a pair of point sources separated initially by the PSF FWHM ($3''$) and with position angle corresponding to the angle of maximum elongation of the system PSF. The ALLSTAR routine optimized the components' separation, position angle, and magnitudes to produce the optimal fit; as we further summarize in Section 4.3.3, known binaries were typically fit with consistent positions and flux ratios in all three bandpasses

while contaminants (such as sources with an erroneous template PSF in one filter) did not produce consistent fits in multiple images. We adopt the criterion that any candidate binary with component positions within $1''$ (3σ for astrometry of very close, faint companions; Section 4.3.4) in all three filters is a bona-fide visual binary. We found that saturated stars produced fits for erroneous companions at separations of 1.0-1.5$''$, so we have rejected all candidate companions to saturated targets ($K_{tot} < 8$) with separations of $<2''$. Known binaries with wider separations produced consistent fits even in the saturated regime for systems fainter than $K \sim 6$, so we adopted this as a maximum brightness limit for our sample.

Finally, we compared the location of each candidate companion with the on-line catalog of 2MASS image artifacts. We found that a candidate companion to MHO-Tau-4 was coincident with a persistence artifact flag. Furthermore, a previous high-resolution imaging survey with HST (Kraus et al. 2006) found no optical counterpart to a limit of $z' \sim 24$, so we removed this candidate companion from further consideration and treat MHO-Tau-4 as a single star.

4.3.3   Sensitivity Limits

We determined companion detection limits as a function of distance from the primary stars via a Monte Carlo simulation similar to that of Metchev et al. (2003). We used the IRAF task DAOPHOT/ADDSTAR to add artificial stars at a range of radial separations and magnitudes to the images of FO Tau, MHO-Tau-5, KPNO-Tau-8, and KPNO-Tau-9. These four sources have been shown to be single to the limits of high-resolution imaging (Ghez et al. 1993; Kraus et al. 2006) and span the full range of brightness in this sample. We then attempted to identify the artificial companions via PSF-fitting photometry. Our photometric routines attempt simultaneous source identification in all three filters in order to separate erroneous detections from genuine companions, so we created the same synthetic source in all three filters using colors from the 2 Myr Baraffe isochrones (Baraffe et al. 1998).

In Figure 4.2, we show our survey's 50% detection limits as a function of separation
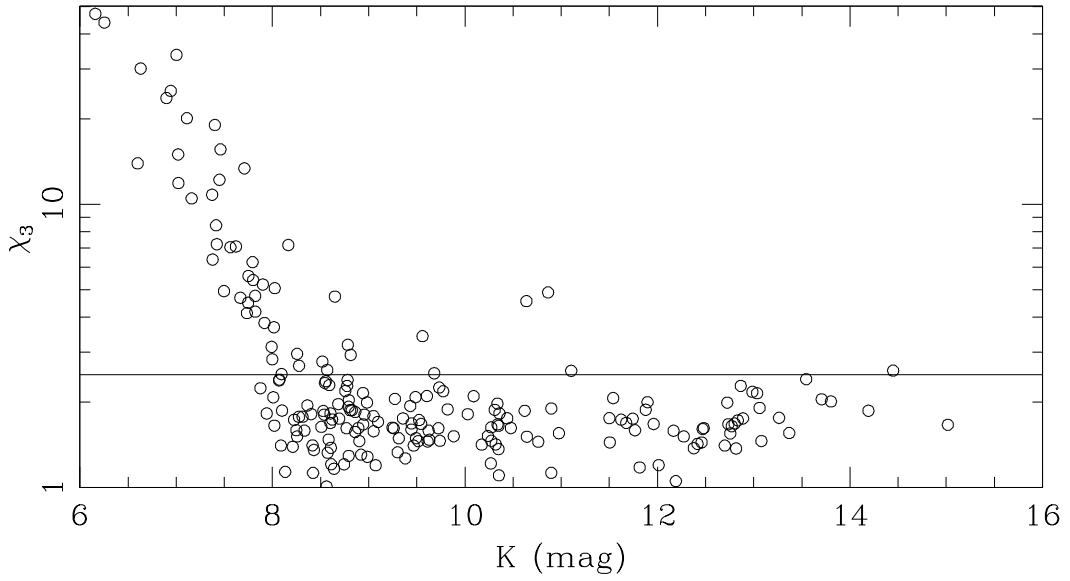
Figure 4.1 A plot of the goodness-of-fit as a function of K-band magnitude for 203 objects with no wide companions (0.5-15″). The sharp increase in χ_3 at $K \sim 8$ is due to the onset of image saturation; the stars in this brightness range are typically late K or early M, so saturation begins simultaneously in all three bands. The solid line at $\chi_3 = 2.5$ denotes the 95% confidence interval for nominally single stars; we have selected all sample members above this limit as candidate close binaries. We found that our fitting algorithm for identifying companions is effective for mildly saturated stars, so we include association members up to $K = 6$.

for identifying candidate companions using the same PSF-fitting algorithm as our actual search program. The minimum separation at which we can detect equal-flux companions is $\sim1''$ for bright, unsaturated sources and $\sim1.6''$ for sources just above our adopted K band magnitude limit ($K = 14.3$). The 10% and 90% detection limits are typically ~0.5 magnitudes below and above the 50% limit. The sensitivity of PSF-fitting photometry falls at separations $>5''$ since objects become cleanly resolved and most companion flux falls outside the fitting radius for the primary. However, the PSC is complete to at least $K = 14.3$ at larger separations, so wider companions will be recovered by our search of the catalog.

We also show the separation and flux ratio for known binary systems which have been detected in K-band surveys (Kohler et al. 2000; White et al. 2006) and whether these systems were unambiguously recovered (via either PSF-fitting photometry or the PSC), identified as candidate systems based on the χ_3 criterion, or not recovered. The limits between detected and nondetected systems are roughly consistent with our empirically determined magnitude limits, but there are few known systems which fall near these limits. There are only two known wide systems among the faintest members of our sample ($K > 11$), so we can not significantly test the detection limits of our search method in this brightness range. However, we identified four additional candidate companions to sources in this brightness range, plus numerous likely background stars, so our survey appears to be sensitive to companions in this regime.

4.3.4   Uncertainties in Binary Properties

Many of our candidate binaries have separations of $<\theta_{FWHM}$, so our measurements could be subject to significant uncertainties. We tested these uncertainties by using a Monte Carlo routine to produce synthetic images for binaries spanning a range of primary brightnesses, flux ratios, and separations. Specifically, we used ADDSTAR to construct simulated JHK images, and then we measured the binary fluxes and separations for each set of simulated images using ALLSTAR. For each combination
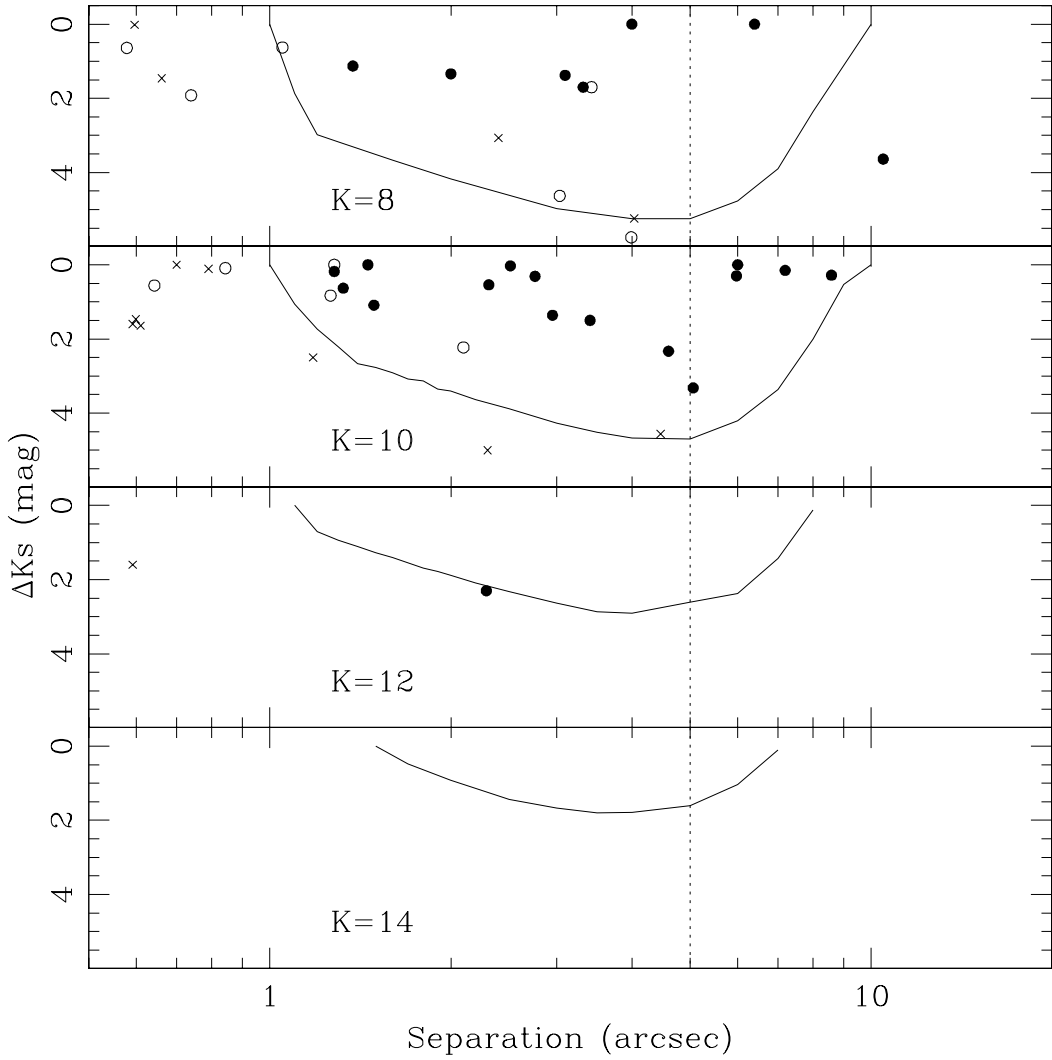
Figure 4.2 Detection frequencies as a function of separation for artificially-introduced companions to four known single objects spanning the survey sample's brightness range: FO Tau ($K = 8.12$), MHO-Tau-5 ($K = 10.06$), KPNO-Tau-8 ($K = 11.99$) and KPNO-Tau-9 ($K = 14.19$). The solid lines denote the 50% detection limit for our PSF-fitting photometry. The symbols represent known binary companions from high-resolution K-band multiplicity surveys in Upper Scorpius (Kohler et al. 2000) and Taurus (White et al. 2006 and references therein). Filled circles denote companions which we recovered, open circles denote companions which passed our χ^2 criterion but did not produce significant fits, and crosses denote companions which were not recovered. The dotted line shows the minimum separation at which the PSC will identify all companions bright enough to be considered in our search ($K < 14.3$).
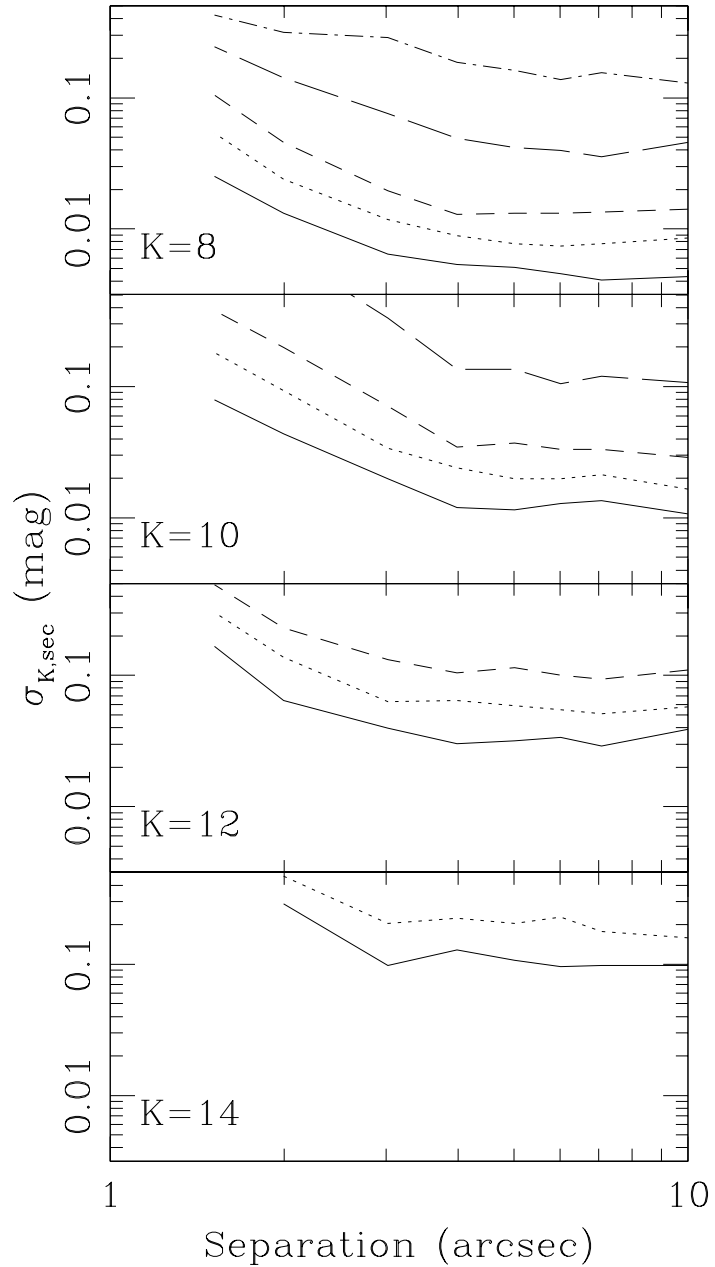
Figure 4.3 The uncertainty in the measured binary companion brightness as a function of separation for simulated binary images spanning the range of primary and secondary brightnesses. The flux ratios shown are $\Delta K =$0, 1, 2, 4, and 6 (solid, dotted, short-dashed, long-dashed, dash-dotted lines, respectively). The photometric uncertainties increase sharply at separations of $<3''$, suggesting that observed photometric colors will not be accurate in this separation range.
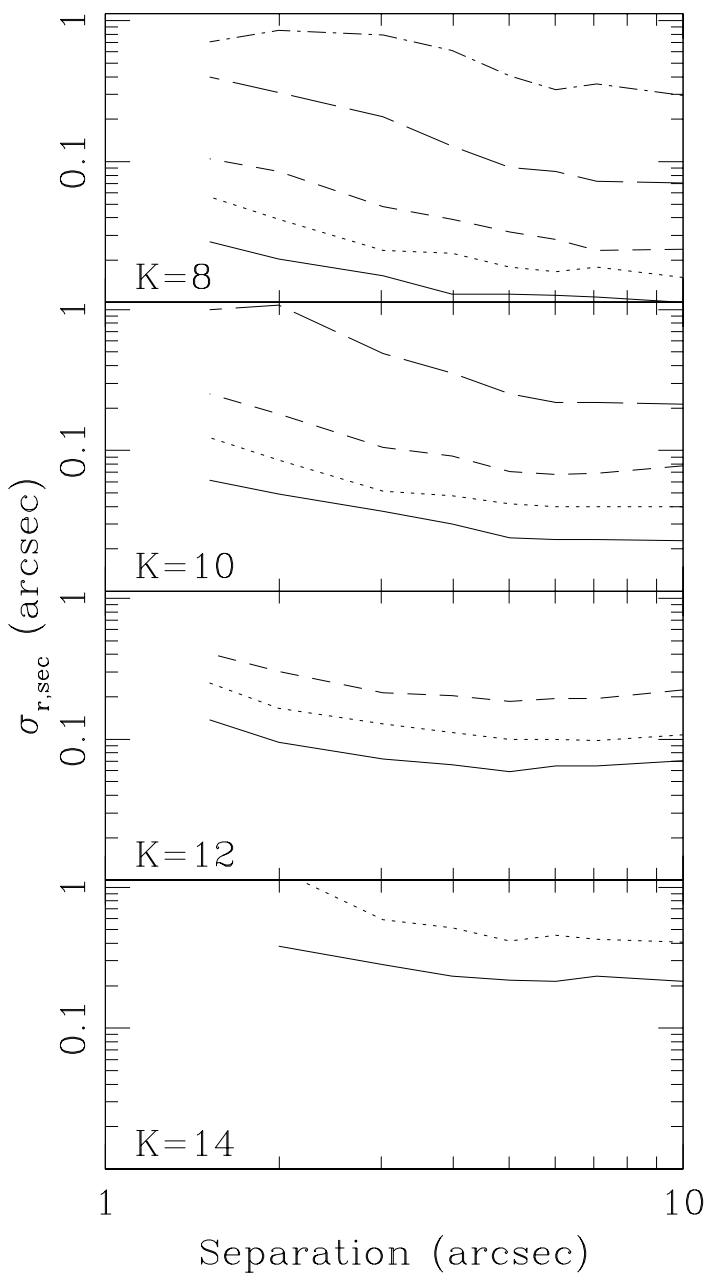
Figure 4.4 As in Figure 3.3, showing uncertainties in binary secondary positions as a function of separation.

of parameters, we produced 100 sets of synthetic images with randomly distributed position angles. The $J - K$ and $H - K$ colors for the secondaries were drawn from the 2 Myr isochrone of Baraffe et al.(1998) in order to determine realistic values for ΔK, ΔH, and ΔJ.

In Figure 4.3, we show the standard deviation in the measured brightness for our simulated binary companions as a function of separation. These simulations predict that photometric uncertainties increase significantly at separations of $<3''$, so measured colors may not be reliable at small separations. As we describe in Section 4.3.5, these colors are necessary at large separations ($>5''$) to distinguish candidate companions from background stars. However, contamination from background sources should be low at small separations ($<3''$) due to their low surface density, so we can neglect these selection criteria with only a minor increase in the number of erroneous binary identifications.

In Figure 4.4, we show a similar plot of the RMS scatter in the measured position of the secondary. The typical standard deviations are $<0.3''$ for all but the faintest companions, so the uncertainties in our measured separations should have similar precision. Given these positional uncertainties, the corresponding uncertainties in position angles range from 1° to 10°, depending on the binary separation. The standard deviations in secondary position for our simulated images are consistent with the scatter between the three filters for each observed binary, so we adopt the results from these simulations as our estimated uncertainties.

We also conducted Monte Carlo tests to determine the probability of mistakenly identifying a true single star as a binary. We constructed a series of simulated images (100 each for four objects spanning our sample's range of brightness), and then tried to fit each object with two point sources. We found that this never produced consistent fits in 3 filters, though faint peaks due to noise were occasionally identified in one of the 3 images. This suggest that the probability of an erroneous binary identification due to statistical errors is low ($< 1\%$). This agrees with our results for known single stars; as we note in Section 4.3.2, 5% of known single stars fall above our χ_3 criterion for identifying candidate binaries. However, none of these yielded fits for multiple

point sources in all 3 filters.

4.3.5   Field Star Contamination

The identification of binary companions based solely on proximity is complicated by contamination from foreground dwarfs, background giants, and reddened early-type background dwarfs. We have conducted follow-up spectroscopic and astrometric observations to confirm association membership, but to provide context to the entire sample and to avoid expensive levels of contamination, we must limit the survey to a total area in which the contamination from background stars is small compared to the number of candidate binary companions. We estimate the surface density of contaminants for each association based on the total number of objects within an annulus of 30-90″ from all of the association members in our sample. Field surveys (e.g., Duquennoy & Mayor 1991; Reid & Gizis 1997) have identified few binaries with projected separations of >500 AU (>30″ at the distance of our sample members), so this method will also address the probability of chance alignment with other association members.

Our estimate of the contamination could be influenced by variations in background source counts due to the large angular extent of these associations or by variations in galactic latitude or extinction. The result would be a systematic overestimation of the association probability for candidate companions at points of high contamination and a corresponding underestimation at points of low contamination. However, any local deviation from the mean contamination rate should not affect the binary statistics for the association as a whole since the ensemble background at 30-90″ will match the ensemble background at <30″. Our subsequent cuts against color, mass ratio, and separation will also help to homogenize the sample by preferentially removing background stars.

Most previous multiplicity surveys were based on observations in a single optical or near-infrared bandpass (e.g., Kohler et al. 2000); in the absence of color information, these surveys can only estimate physical association probabilities for candidate

companions based on the surface density of background stars of similar brightness. Since 2MASS includes images in 3 filters, we can reject most background stars by requiring colors consistent with regional membership (Section 4.4.1). Specifically, we have plotted $(K, J - K)$ and $(K, H - K)$ color-magnitude diagrams for each region and we require prospective binary companions to fall above a smoothed field main sequence (Bessell & Brett 1988; Leggett et al. 2001) for the regional distance in both CMDs. We have chosen to use K as a proxy for luminosity instead of J in order to minimize the effect of extinction for background stars. This choice will cause disk-bearing association members to sit preferentially higher in our color-magnitude diagrams, but this moves them further from our selection cutoff, so our results should be robust.

As a test of these color criteria, we have plotted color-magnitude diagrams for the members of our primary sample. We find that $\sim$97% of the primaries have colors consistent with our definition of association membership, so any incompleteness in the selection of binary companions should be negligible. Most unselected primaries fall just below our color cuts; the only sample members which fall well below the association sequences are GSC 06191-00552 and USco-160803.6-181237. Both of these objects are claimed to be spectroscopically-confirmed members of USco-A, but the spectra are not available in the literature. We have not detected any binary companions to these objects, so their erroneous inclusion in our sample would not significantly change our results. However, it might be prudent to reconsider their membership status with additional spectroscopic observations in the future.

Table 4.4.   Association Star Counts

Sep (″)	Chamaeleon I ($N = 147$)[a]			Taurus-Auriga ($N = 235$)[a]			USco-A ($N = 356$)[a]			USco-B ($N = 45$)[a]		
	Source Count[b]	Color Valid[b]	Bkgd Stars[b]	Source Count	Color Valid	Bkgd Stars	Source Count	Color Valid	Bkgd Stars	Source Count	Color Valid	Bkgd Stars
0-3[c]	7	-	0.9	9	-	0.9	15	-	2.0	8	-	0.3
3-5	5	5	1.0	6	5	0.7	8	4	0.3	1	0	0.1
5-10	8	6	4.8	10	5	3.1	12	5	1.4	6	4	0.4
10-15	19	12	8.0	22	11	5.2	32	8	2.4	3	0	0.6
15-20	20	13	11.2	23	13	7.2	36	6	3.4	4	0	0.8
20-25	34	18	14.4	21	12	9.3	44	6	4.3	5	1	1.1
25-30	39	28	17.6	33	16	11.4	60	5	5.3	9	4	1.3
30-90	766	461	-	733	298	-	1566	138	-	215	34	-

[a]The total sample size for each region, as summarized in Table 4.1.

[b]The number of unassociated contaminants was estimated from the surface density of sources which meet our color selection criteria in the 30-90″ separation range; most of these sources should be foreground stars, background stars, or unbound association members.

[c]We cannot use color criteria at separations of $< 3″$ due to the poor photometric precision (Section 4.3.4), so the surface density of unassociated contaminants is higher.

Table 4.5. Candidate Wide Binary Systems (Full Table)

| Name | Primary | | | Secondary | | | Projected | Position | μ_α,μ_δ[a] | Ident | References |
	$J-K$	$H-K$	K	$J-K$	$H-K$	K	Sep($''$)	Angle(deg)	(mas yr^{-1})	Method	
2M11103-7722	2.00	0.68	10.03	2.21	0.77	13.85	9.30	108.8	-	PSC	-
C7-1	1.78	0.62	10.55	1.67	0.43	13.32	5.73	214.9	0,0	PSC	-
CHSM1715	2.05	0.85	10.9	1.42	0.43	13.94	9.07	30.3	-58,42	PSC	-
CHXR26	2.02	0.46	9.92	2.68	1.07	9.98	1.41	215.2	-	PSF	Luhman (2004b)
CHXR28	1.17	0.32	8.23	1.53	0.39	8.83	1.78	121.6	-	PSF	Brandner et al.(1996)
CHXR9C	1.01	0.24	8.95	1.15	0.54	13.46	4.53	333.0	-	PSF	-
KG102	1.15	0.34	12.01	1.29	0.58	13.05	2.24	223.7	-	PSF	Persi et al. 2005
T3	2.68	1.15	8.87	1.29	0.41	10.35	2.22	290.7	-	PSF	Reipurth & Zinnecker (1993)
T6	1.50	0.65	7.76	1.38	0.50	11.15	4.99	123.0	0,0	PSC	Ghez et al.(1997)
T14A	1.88	0.79	12.45	2.38	1.26	13.56	2.5	52.5	-	PSF	Haisch et al.(2004)
T26	1.60	0.73	6.22	1.13	0.43	7.28	4.16	203.4	-24,6	PSC	Reipurth & Zinnecker (1993)
T33A+B	1.91	0.89	7.22	1.89	1.09	7.76	2.46	286.0	-	PSF	Chelli et al.(1988)
T39	0.97	0.19	8.96	1.03	0.29	9.98	4.17	77.1	0,0	PSC	Reipurth & Zinnecker (1993)
T51	1.05	0.42	8.27	1.75	0.63	10.04	1.98	161.9	-	PSF	Reipurth & Zinnecker (1993)
2MASSJ04080782+2807280	1.06	0.35	11.39	0.77	0.21	9.34	9.43	351.1	0,0	PSC	-
2MASSJ04414489+2301513	1.26	0.57	13.16	0.88	0.24	9.85	12.37	57.3	-2,-18	PSC	-
CIDA-9	1.68	0.6	11.49	1.38	0.56	12.15	2.33	59.3	-	PSF	White et al.(2006)
CoKuTau3	2.22	0.66	8.66	2.48	1.10	9.91	2.07	174.9	-	PSF	Leinert et al.(1993)
CoKuTau3	2.32	0.79	8.41	2.77	0.81	13.38	12.60	349.2	-	PSC	-
DKTau	1.27	0.52	7.78	1.75	0.57	8.38	2.37	119.7	-	PSF	Leinert et al.(1993)
FWTau	0.95	0.29	9.39	1.37	0.38	9.42	12.22	246.7	0,0	PSC	Hartmann et al.(2005)
GGTauB	0.97	0.37	10.29	1.53	0.65	11.39	1.55	130.3	-	PSF	Leinert et al.(1993)
Haro6-37	1.70	0.69	7.76	1.77	0.60	8.58	2.70	37.9	-	PSF	Leinert et al.(1993)
HBC356	0.57	-0.08	10.82	0.83	0.49	10.9	1.17	1.1	-	PSF	White et al.(2006)
HBC427	0.83	0.19	8.13	0.77	0.19	9.02	14.9	154.0	0,0	PSC	-
HNTau	2.36	1.08	8.40	1.13	0.68	11.59	3.10	218.7	-	PSF	Leinert et al.(1993)
HVTau	1.26	0.48	7.94	1.92	0.89	12.29	3.76	43.9	-	PSF	Simon et al.(1995)
ISTau	1.68	0.65	8.64	1.87	0.53	13.46	10.85	57.4	18,-302	PSC	-
ITTau	1.94	0.81	8.07	1.62	0.34	9.81	2.37	223.4	-	PSF	White & Ghez (2001)
J1-4872	1.14	0.30	8.56	1.21	0.48	9.25	3.38	232.9	-	PSF	Reipurth & Zinnecker (1993)
JH112	2.07	0.83	8.17	1.91	0.61	9.20	6.56	34.3	0,0	PSC	White et al.(2006)
JH223	1.22	0.43	9.52	1.17	0.4	12.19	2.06	342.3	-	PSF	White et al.(2006)
LkCa4	0.93	0.20	8.32	1.53	0.42	13.57	8.86	154.6	-310,-134	PSC	-

Table 4.5 (cont'd)

Name	Primary J−K	H−K	K	Secondary J−K	H−K	K	Projected Sep('')	Position Angle(deg)	μ_α,μ_δ[a] (mas yr^{-1})	Ident Method	References
LkCa7	0.89	0.77	8.24	0.54	-2.58	12.04	1.18	25.1	-	PSF	Leinert et al.(1993)
UZTau	1.78	0.76	7.35	1.94	0.53	7.47	2.80	275.8	-10,-20	PSC	White & Ghez (2001)
V410-Xray5a	1.84	0.63	10.15	2.12	0.71	13.82	13.27	47.7	-	PSC	-
V710Tau	0.63	0.45	8.65	0.46	0.29	8.52	3.03	178.5	8,-28	PSC	Leinert et al.(1993)
GSC 06785-00476	0.59	0.14	8.92	0.87	0.28	11.96	6.30	82.6	-	PSC	-
GSC 06204-01067	0.97	0.22	8.75	1.09	0.39	10.56	2.49	89.2	-	PSF	-
GSC 06780-01061	0.89	0.39	9.06	1.04	-0.13	10.36	1.50	270.3	-	PSF	-
GSC 06784-00039	0.64	0.14	7.91	1.11	0.42	13.03	13.53	77.5	-	PSC	-
GSC 06784-00997	0.89	0.17	8.36	0.91	0.31	11.26	4.81	240.4	-16,-32	PSC	-
GSC 06213-00306	0.93	0.24	8.59	1.04	0.33	10.73	3.18	305.5	-	PSF	-
GSC 06793-00868	0.88	0.19	9.25	1.06	0.22	9.59	2.01	156.5	-	PSF	-
GSC 06793-00806	1.31	0.60	8.26	1.10	0.15	9.31	1.89	342.4	-	PSF	Gregorio-Hetem 1992
RXJ1555.8-2512	0.46	0.10	8.29	0.93	0.34	12.53	14.61	298.1	74,316	PSC	-
RXJ1555.8-2512	0.46	0.10	8.29	0.96	0.27	10.00	8.91	318.4	0,0	PSC	-
RXJ1558.8-2512	0.90	0.21	9.65	0.92	0.26	11.53	11.35	130.1	0,0	PSC	-
RXJ1559.2-2606	0.72	0.11	9.41	0.94	0.31	10.65	2.96	328.3	-	PSF	Kohler et al.(1999)
RXJ1600.7-2343	0.95	0.02	10.81	0.92	0.54	10.89	1.41	28.3	-	PSF	Kohler et al.(1999)
RXJ1602.8-2401B	0.80	0.16	8.93	0.92	0.34	11.62	7.22	352.9	-	PSC	-
RXJ1606.6-2108	1.30	0.63	9.43	0.61	-0.19	10.27	1.17	28.2	-	PSF	Kohler et al.(1999)
SCH16151115-24201556	1.06	0.42	13.17	0.96	0.30	12.13	17.96	69.8	0,0	PSC	-
ScoPMS008a	0.93	0.32	10.14	0.98	0.14	10.97	1.58	95.4	-	PSF	Kohler et al.(1999)
ScoPMS016	1.04	0.19	9.59	0.86	0.30	10.00	1.37	45.0	-	PSF	Kohler et al.(1999)
ScoPMS042b	1.06	0.28	9.62	1.05	0.42	11.93	4.58	6.8	-8,-6	PSC	Kohler et al.(1999)
ScoPMS048	0.89	0.23	8.09	0.80	0.13	8.34	3.05	192.1	0,0	PSC	Kohler et al.(1999)
ScoPMS052	0.82	0.17	7.49	1.17	0.36	9.11	19.06	269.5	4,-18	PSC	Martin et al.(1998)[b]
USco80	0.93	0.32	12.08	0.92	0.25	10.19	12.27	15.2	0,0	PSC	-
USco-155532.4-230817	0.65	-0.08	12.94	1.43	0.73	13.19	1.79	207.7	-	PSF	
USco-160202.9-223613	0.86	0.13	11.90	1.22	0.50	12.80	2.30	94.7	-	PSF	Bouy et al.(2006)
USco-160258.5-225649	0.54	-0.13	10.61	2.49	1.20	11.35	1.21	59.1	-	PSF	-
USco-160611.9-193532	0.99	0.33	11.02	1.22	0.54	11.78	10.78	226.5	-8,-18	PSC	-
USco-160700.1-203309	1.17	0.34	9.94	1.03	0.30	9.54	11.65	293.1	-2,-22	PSC	-
USco-160702.1-201938	1.08	0.34	11.86	1.22	0.50	12.11	1.63	242.3	-	PSF	-
USco-160904.0-193359	0.86	0.34	11.37	1.09	0.25	11.74	1.28	328.5	-	PSF	-

Table 4.5 (cont'd)

Name	Primary			Secondary			Projected	Position	μ_α,μ_δ[a]	Ident	References
	$J-K$	$H-K$	K	$J-K$	$H-K$	K	Sep($''$)	Angle(deg)	(mas yr^{-1})	Method	
USco-160908.4-200928	1.00	0.27	9.98	0.96	0.24	10.30	1.93	139.4	-	PSF	-
USco-160936.5-184800	1.26	0.48	10.28	1.24	0.32	12.50	19.97	2.2	24,-2	PSC	-
USco-161031.9-191305	1.03	0.26	8.99	1.22	0.45	12.73	5.71	114.0	-	PSC	-
USco-161039.5-191652	1.04	0.26	10.27	1.05	0.38	12.25	14.95	183.2	-66,-124	PSC	-
GSC 06770-00655	0.58	0.11	9.75	0.83	0.22	10.56	9.01	327.80	0,0	PSC	-
GSC 06770-00655	0.58	0.11	9.75	0.88	0.25	10.01	29.62	325.3	16,-10	PSC	-
RXJ1528.7-3117	0.79	0.31	7.5	0.39	0.31	8.06	2.46	181.8	-	PSF	Kohler et al.(1999)
RXJ1529.4-2850	0.73	0.66	7.71	0.68	0.26	7.87	2.07	168.3	-	PSF	Kohler et al.(1999)
RXJ1530.4-3218	0.51	0.36	7.74	0.78	0.39	7.83	2.07	23.0	-	PSF	Kohler et al.(1999)
RXJ1536.5-3246	0.86	0.22	10.26	0.87	0.25	10.54	2.37	134.9	-	PSF	Kohler et al.(1999)
RXJ1539.4-3446B	1.21	0.43	7.98	2.31	0.77	10.24	27.80	9.9	0,0	PSC	-
RXJ1539.4-3446B	1.21	0.43	7.98	3.06	0.97	13.13	29.37	79.6	-	PSC	-
RXJ1543.8-3306	0.91	0.34	10.24	0.82	0.14	10.64	2.79	185.1	-	PSF	Kohler et al.(1999)
RXJ1545.2-3417	1.11	0.54	7.04	1.23	0.81	8.36	2.60	297.2	-	PSF	Kohler et al.(1999)
RXJ1554.0-2920	0.96	0.14	8.87	0.43	0.25	10.81	1.44	73.8	-	PSF	Kohler et al.(1999)
RXJ1554.0-2920	0.91	0.25	8.74	0.74	0.19	10.61	26.33	257.5	0,0	PSC	-

[a]An entry of 0,0 denotes a source which was detected by the USNO-B survey, but did not show a significant proper motion. An entry of "-" denotes a source which was not detected by the USNO-B survey.

[b]ScoPMS052 B is also known as GSC06209-01312; Martin et al.(1998) identified it as a WTTS.

Table 4.6.   Ultrawide Visual Companions (Full Table)

| Name | Primary | | | Secondary | | | Projected Sep($''$) | Position Angle(deg) | μ_α,μ_δ (mas yr^{-1}) | References |
	$J-K$	$H-K$	K	$J-K$	$H-K$	K				
C1-6	3.92	1.68	8.67	1.93	0.80	14.10	27.58	156.0	-	OTS12 (candidate; Oasa et al. 1999)
C1-6	3.92	1.68	8.67	2.26	0.70	13.75	24.51	123.8	-	OTS14 (candidate; Oasa et al. 1999)
Cam2-19	2.40	0.74	10.25	2.36	0.72	13.45	23.13	107.6	-	-
Cam2-42	2.44	0.73	9.16	2.09	0.50	13.51	27.64	261.7	-	-
Cam2-42	2.44	0.73	9.16	2.11	0.65	14.14	28.18	180.4	-	-
ChaHa11	1.04	0.37	13.55	1.35	0.31	12.50	20.96	22.1	20,-14	-
ChaHa7	1.19	0.48	12.42	2.65	0.85	9.88	14.47	347.4	0,0	[CCE98] 2-26 (candidate; Cambresy et al. 1998)[a]
CHSM10862	1.61	0.67	12.33	0.94	0.15	10.39	14.22	184.6	0,0	-
CHX18N	1.34	0.52	7.77	0.99	0.24	7.46	29.85	154.1	0,0	-
CHXR15	1.02	0.38	10.24	2.73	0.99	13.96	26.27	164.1	-	-
CHXR22E	1.89	0.57	10.00	1.58	0.48	12.48	10.65	301.7	0,0	CHXR22W (background; Luhman 2004b)
CHXR26	2.25	0.70	9.35	2.78	0.87	10.86	24.20	3.9	0,0	[CCE98] 2-27 (candidate; Cambresy et al. 1998)
CHXR28	1.52	0.36	7.69	1.59	0.45	13.6	19.82	78.7	0,0	-
CHXR30A	2.71	0.83	9.09	1.85	0.57	12.01	25.72	56.5	2,12	-
CHXR35	0.98	0.35	10.87	1.28	0.51	13.4	11.23	321.5	0,0	-
CHXR40	1.11	0.27	8.96	0.58	0.18	7.85	28.99	129.3	-26,10	CHX15A (candidate; Luhman 2004b)
CHXR47	1.46	0.41	8.28	1.34	0.37	13.35	13.62	251.9	0,0	-
CHXR54	0.91	0.22	9.5	1.81	0.69	13.73	27.26	316.7	36,-12	-
CHXR74	1.23	0.30	10.21	1.46	0.59	14.12	11.27	128.2	0,0	-
CHXR76	1.17	0.32	10.95	2.65	0.85	9.88	27.86	169.4	0,0	[CCE98] 2-26 (candidate; Cambresy et al. 1998)[a]
CHXR78C	1.09	0.33	11.22	1.26	0.33	8.29	20.86	19.1	0,0	CHXR78NE (background; Luhman 2004b)
CHXR79	2.59	1.05	9.07	1.96	0.59	13.05	17.72	289.8	0,0	-
ESO-Ha-560	1.21	0.37	11.03	1.89	0.61	13.32	23.06	182	0,0	-
ESO-Ha-569	1.38	0.48	14.58	2.19	0.85	14.16	23.93	170.9	-	-
Hn11	2.33	0.82	9.44	2.18	0.76	14.04	25.52	167.5	-	OTS36 (candidate; Oasa et al. 1999)
Hn11	2.33	0.82	9.44	2.88	1.11	13.77	18.08	356.4	-	OTS32 (candidate; Luhman 2004b)
Hn12W	0.95	0.33	10.78	1.64	0.58	13.48	29.78	296.6	0,0	-
Hn5	1.44	0.60	10.13	0.78	0.24	9.35	23.68	172.1	0,0	-
Hn5	1.44	0.60	10.13	1.39	0.39	13.14	17.74	51.3	-26,10	-
ISO165	1.62	0.62	11.44	1.33	0.57	12.96	14.46	230.6	-	ChaI737 (candidate; Lopez-Marti et al. 2004)
ISO237	2.31	0.82	8.62	2.00	0.71	13.36	23.96	342.5	-	OTS42 (background;Luhman 2004b)
ISO256	2.93	1.17	11.34	2.03	0.74	14.06	28.69	244.8	-	-
KG102	1.26	0.43	11.80	1.16	0.40	13.49	18.82	312.3	0,0	KG102-Anon1 (candidate; Persi et al. 2005)

Table 4.6 (cont'd)

Name	Primary			Secondary			Projected Sep($''$)	Position Angle(deg)	μ_α,μ_δ (mas yr^{-1})	References
	$J-K$	$H-K$	K	$J-K$	$H-K$	K				
OTS44	1.75	0.77	14.67	2.33	0.70	13.27	27.75	17	0,0	OTS46 (candidate; Oasa et al. 1999)
T11	0.91	0.25	8.20	2.36	0.74	12.42	21.65	152.3	0,0	-
T11	0.91	0.25	8.20	2.51	0.73	14.21	28.31	57	-	-
T21	1.18	0.41	6.42	1.94	0.67	13.6	21.90	246.6	-	NIR9 (candidate; Persi et al. 2001)
T27	1.14	0.39	9.52	1.02	0.30	12.61	24.70	315.4	0,0	-
T42	3.01	1.34	6.46	3.47	1.20	11.97	27.84	314.6	-	Cam2-44 (background; Luhman 2004b)
T43	2.04	0.75	9.25	1.45	0.39	13.59	22.88	254.4	-30,40	-
T46	1.46	0.51	8.45	1.09	0.32	12.89	27.88	136.5	0,0	-
T51	1.28	0.52	8.00	0.94	0.15	8.57	11.40	65.7	-	CHX20A (background; Luhman 2004b)
2MASSJ04161885+2752155	1.19	0.43	11.35	1.12	0.28	11.95	28.04	218.2	-10,6	-
2MASSJ04213460+2701388	1.46	0.53	10.44	1.62	0.53	13.14	17.18	265.7	0,0	-
CFHT-Tau-4	1.84	0.68	10.33	2.41	0.71	13.89	24.40	72.9	-	-
CFHT-Tau-7	1.16	0.41	10.38	0.81	0.25	11.20	21.76	207.2	0,0	JH90 (candidate; Jones & Herbig 1979)
CFHT-Tau-21	2.57	1.03	9.01	1.44	0.45	11.07	23.31	152.1	0,0	-
DGTau	1.70	0.73	6.99	2.27	0.69	13.7	16.43	234.3	-	-
DOTau	2.17	0.94	7.3	3.01	1.05	10.58	28.75	8.4	-	-
FMTau	1.57	0.63	8.76	2.76	0.81	13.74	26.21	91.7	-	-
FOTau	1.53	0.45	8.12	1.62	0.48	14.10	26.19	250.8	-12,22	-
FSTau	2.53	1.07	8.18	3.33	1.60	11.75	19.88	275.8	64,22	Haro 6-5 B[b]
GMAur	1.06	0.32	8.28	0.73	0.15	8.56	28.31	202.2	0,0	-
I04158+2805	2.60	1.17	11.18	1.27	0.39	12.16	25.34	28.9	0,0	-
I04216+2603	1.74	0.70	9.05	1.24	0.39	12.71	27.96	337.0	34,-16	-
I04385+2550	2.65	0.92	9.20	1.79	0.51	12.23	18.94	343.3	2,4	-
IPTau	1.43	0.54	8.35	1.16	0.38	13.43	15.75	55.7	228,-164	NLTT 13195 (foreground; Salim & Gould 2003)
ISTau	1.68	0.65	8.64	1.75	0.46	14.28	28.73	261.1	-4,12	-
LkCa15	1.26	0.44	8.16	0.96	0.20	7.02	27.62	4.6	6,4	-
MHO-2	3.73	1.63	7.79	3.28	1.11	12.11	26.32	269.9	-	-
V410-Anon20	4.47	1.48	11.93	4.45	1.44	12.55	22.71	115.3	-	V410-Anon21 (background; Luhman 2000)
V410-Xray1	1.94	0.65	9.08	1.45	0.51	11.74	27.95	137.4	0,0	-
V410-Xray2	4.56	1.49	9.22	4.04	1.55	13.69	17.72	105.6	-	-
V410-Xray6	1.40	0.47	9.13	2.61	0.81	13.35	26.49	34.4	-	-
V710Tau	0.63	0.45	8.65	2.22	0.89	10.04	27.97	105.7	10,-20	-
DENIS-P-J162041.5-242549.0	1.49	0.52	12.9	1.32	0.35	11.62	26.73	164.5	4,12	-

121

4.4   2MASS Results

4.4.1   Candidate Binary Companions

We identified a total of 451 well-resolved visual companions brighter than $K = 14.3$ within $30''$ of our sample members in the 2MASS PSC (Section 4.3.1), as well as 48 close ($<5''$) candidate companions based on our PSF-fitting photometry of 2MASS image data (Section 4.3.2). We have chosen $30''$ ($\sim$5000 AU) as an absolute upper limit for for identifying candidate companions since it corresponds to the maximum separation seen for field binaries at the distances of these association members. We also found 3280 visual companions within 30-90$''$ of our sample members. Since the ratio of sources at 0-30$''$ and 30-90$''$ is roughly equal to the ratio of areas (1/8), we expect that most of the sources within $30''$ of our sample stars are foreground or background stars having colors inconsistent with association membership.

In Figure 4.5, we present $(K, J-K)$ and $(K, H-K)$ color-magnitude diagrams for the four regions showing all confirmed association members in our sample and all companions in two separation ranges (5-15$''$ and 30-90$''$) corresponding to likely companions and likely background stars. We summarize the number of objects which pass or fail the color selection criteria (Section 4.3.5) as a function of separation in Table 4.4. We also estimate the number of contaminants which are expected to pass both selection criteria in each separation range, assuming that the source density at 30-90$''$ represents the contaminant source density.

We showed in Section 4.3.4 that the uncertainties in our PSF-fitting photometry become significant at small separations, so we cannot use color criteria to identify candidate companions inside $\sim$3$''$. However, given the low surface density of background sources and the faintness of most nonmembers, we expect only a small level of contamination in this separation range. Each of the 39 candidate companions at separations $<3''$ has a sufficiently high probability of physical association ($>$80%) to merit inclusion in our sample without using color cuts.

We have defined the maximum separation at which we identify candidate binary companions by requiring that the number of sources which pass our color selection

Table 4.6 (cont'd)

Name	Primary			Secondary			Projected Sep($''$)	Position Angle(deg)	μ_α,μ_δ (mas yr^{-1})	References
	$J-K$	$H-K$	K	$J-K$	$H-K$	K				
SCH16075850-20394890	1.01	0.37	12.59	3.25	1.50	7.81	21.52	200.7	-4,-26	The (1964)[d]
SCH16075850-20394890	1.01	0.37	12.59	1.90	0.92	13.98	22.94	285.5	0,0	-
SCH16182501-23381068	1.28	0.44	12.45	1.31	0.34	12.25	24.73	229.1	0,0	-
SCH16213591-23550341	1.22	0.46	12.73	1.42	0.38	12.54	25.65	165.3	0,0	-
USco-160245.4-193037	0.99	0.31	11.14	1.14	0.58	13.88	28.19	72.9	40,-26	-
USco-160428.4-190441	1.04	0.27	9.28	0.78	0.19	9.79	24.15	134.3	-2,4	Field; Preibisch et al.(1998)[c]

[a]The source [CCE98] 2-26 is an ultrawide neighbor of both ChaHa7 and CHXR76; its physical association, if any, is uncertain.

[b]Haro 6-5 B is a known member of Taurus (Mundt et al. 1984), but was not included as part of our statistical sample because its spectral type is uncertain.

[c]USco-160428.4-190441 B is also known as GSC06208-00611; Preibisch et al.(1998) identified it as a field star.

[d]SCH16075850-20394890 B is also known as T64-2; The (1964) identified it as a strong Hα emitter.
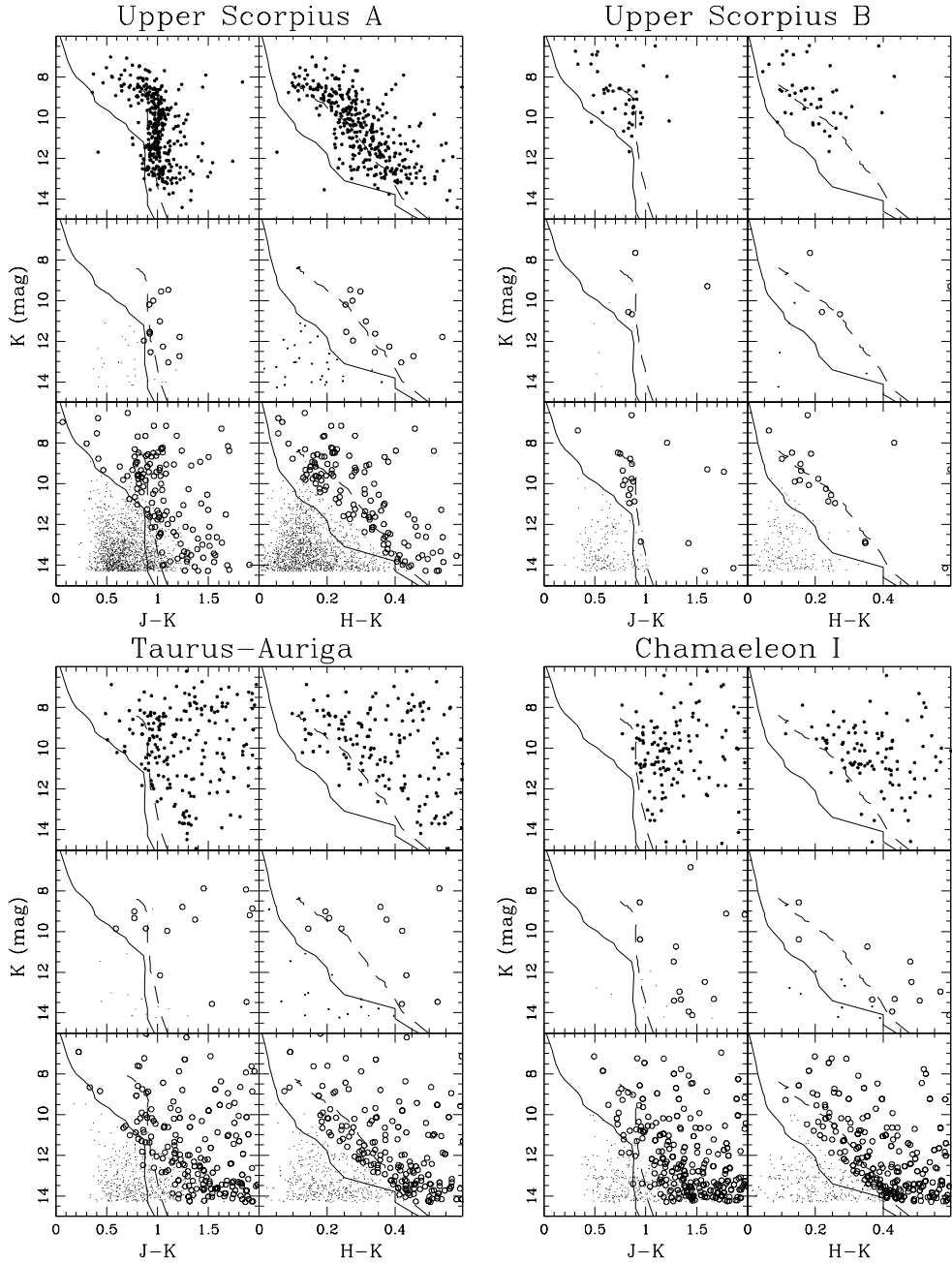
Figure 4.5 $K, J - K$ and $K, H - K$ color-magnitude diagrams for the four regions in our survey. The top panels show the confirmed association members in our survey, the middle panels show all objects within 5-15$''$ of known association members, and the bottom panels show all objects within the background annuli (30-90$''$). The solid line shows the main sequence at the association distance and the dashed line shows the isochrone for the adopted association age (Table 4.2). In the top panels, association members are shown with filled circles. In all other panels, sources which lie above a smoothed main sequence in both CMDs are shown with open circles and other sources are shown with small dots.

requirement in each separation bin be >2 times the number of expected background companions. The corresponding probability that any individual source inside that separation limit is a background star will be <50%. Based on the expected contamination rates and visual companion counts in Table 4.4, these separations are $10''$ for ChamI, $15''$ for Taurus, $20''$ for USco-A, and $30''$ for USco-B. The separation limit is lower for regions with higher extinction since a higher fraction of background stars are reddened into our selection range. We adopt these separation limits as our criteria for identifying candidate binary companions. We note that sources at higher separations still have a nonnegligible probability of association, but the probability that any individual source is a binary companion will be low.

Using the color and separation cuts described above, we have identified (of 451 sources identified in the PSC and 48 sources identified with PSF-fitting photometry) a total of 18 candidate binary companions in ChamI, 32 in Taurus, 40 in USco-A, and 17 in USco-B. Of these candidates, 4, 7, 23, and 5, respectively, have not been previously reported in the literature. We summarize the binary properties of these candidate systems in Table 4.5. Some of the very wide and very faint companions are likely to be unassociated foreground or background stars, so we will consider a restricted range of separations and mass ratios in our subsequent statistical analysis. In Table 4.6, we list the other visual companions with separations $<30''$ (but wider than the association's companion identification limit) which have colors consistent with association membership and separations greater than the limits given above. Many of these sources are expected to be background stars, but additional information (such as optical photometry or kinematic data) could be used in the future to remove additional contaminants and more securely identify any ultrawide binary companions.

4.4.2 Previous Observations

Many of our candidate companions have been identified previously in the literature, but as we note in Tables 4.5, 4.6, and 4.9, several of our candidates have also been rejected as association members based on the absence of spectroscopic signatures of

youth. Some of the candidates we list have probably been considered and rejected in previous work, but most surveys do not publish their catalogue of confirmed field stars, so we cannot assess this number.

We also find that five members of our sample (USco-160700.1-203309, SCH16151115-24201556, and USco80 in USco-A; 2MASSJ04080782+2807280 and 2MASSJ04414489 +2301513 in Taurus) have candidate companions which are significantly brighter, and thus are likely to be the system primary (making the known association member a binary secondary). This result is not surprising for the three Upper Sco members. Upper Sco is thought to contain several thousand low-mass members, and photometric surveys have identified many more candidates than could be confirmed via spectroscopy, so there are many more association members awaiting discovery. The two Taurus members are located on the edges of the association and were discovered by the only survey which considered these areas (Luhman 2006). Our newly-identified candidate companions are both brighter than the upper brightness limit for this survey ($H = 10.75$), so there were no previous opportunities for them to have been discovered.

Finally, we find that 5 candidate companions identified in previous surveys have 2MASS colors inconsistent with association membership: UX Tau B, V819 Tau B, HBC355 (HBC354 B), RXJ1524.2-3030B B, and RXJ1559.8-2556 B. Since $\sim$3% of the spectroscopically confirmed association members in our primary star sample did not meet both color cuts, we expect (adopting the same percentage for the secondaries) that only $\sim$1-2 bona fide binary companions would not be selected. However, close pairs of stars have larger photometric errors, which increases the probability that some companions might fall outside our selection cuts. Of these five companions, three fall just below the color cuts (UX Tau B, HBC 355, and RXJ1524.2-3030B B) in our CMDs and the other two fall significantly below the color cuts, so we suggest that the first three are erroneous rejections, and therefore we keep these objects, while we consider the other two to be valid rejections.[3]

---

[3]V819 Tau B has also been classified as a background star by Woitas et al.(2001) due to its position on a (J,J-K) CMD and by Koenig et al.(2001) due to an absence of x-ray emission. UX Tau B and HBC355 are spectroscopically confirmed cluster members, and no membership assessments

Table 4.7. Inferred Binary Properties (Full Table)

Name	Primary		Secondary		Projected	Mass
	SpT	Mass	SpT	Mass	Separation(AU)	Ratio(q)
2M11103	M4	0.27	(M8.5)	(0.02)	1535	0.08
2M11103(/ISO250)	M4	0.27	M4.75(M5.5)	0.20(0.15)	1569	0.56
C7-1	M5	0.18	(M8)	(0.03)	945	0.18
CHSM1715	M4.25	0.25	(M7)	(0.05)	1497	0.18
CHXR9C	M2.25	0.47	(M9)	(0.02)	747	0.05
CHXR26	M3.5	0.33	(M5)	(0.19)	233	0.57
CHXR28	K6	0.77	(M3)	(0.4)	294	0.52
CHXR30 A	K8	0.68	M1.25(M5.5)	0.56(0.14)	1638	0.2
CHXR68 A	K8	0.68	M2.25(M4.5)	0.54(0.22)	724	0.32
Hn21 W	M4	0.27	M5.75(M5.5)	0.12(0.14)	896	0.52
KG102	M5.5	0.14	(M7)	(0.06)	370	0.41
T3	M0.5	0.6	(M1)	(0.56)	366	0.93
T6	K0	1.69	(M5)	(0.17)	823	0.1
T14A	K7	0.72	(M4.5)	(0.22)	413	0.3
T26	G2	2.34	(K0)	(1.66)	686	0.71
T33A+B	G7	2.14	(K0)	(1.63)	406	0.76
T39	M2.25	0.5	(M4.5)	(0.22)	688	0.43
T51	K3.5	0.93	(M5)	(0.16)	327	0.17
2MASSJ04080782+2807280	M3.75	0.3	(K1)	(1.47)	1367	4.9
2MASSJ04414489+2301513	M8.25	0.027	(M3.5)	(0.3)	1794	11
2MASSJ04554757+3028077	M4.75	0.20	M5.6(M7.5)	0.13(0.04)	915	0.22
CIDA-9	M0	0.64	(M2.5)	(0.47)	338	0.73
CoKuTau3	M1	0.57	(M5)	(0.17)	300	0.29
DKTau	K7	0.72	(M3.5)	(0.32)	344	0.45
FVTau	K5	0.82	M3(M2.5)	0.40(0.46)	1782	0.56
FWTau	M5.5	0.14	(M6)	(0.09)	1772	0.65
GGTau A(/B)	K7	0.72	M5(M6)	0.18(0.1)	1505	0.14
GGTau Bab	M5	0.18	(M7)	(0.05)	225	0.29
GKTau	K7	0.72	K6(M0)	0.77(0.62)	1905	0.86
Haro6-37	K6	0.77	(M2.5)	(0.42)	392	0.55
HBC352	G0	2.49	G5(G8)	2.26(2.04)	1301	0.82
HBC355	K2	1.2	K3(K7)	0.94(0.67)	915	0.56
HBC356	K2	1.2	(K3)	(0.96)	170	0.8
HBC427	K7	0.72	(M3)	(0.39)	2161	0.54
HNTau	K5	0.82	(M4.5)	(0.2)	450	0.24
HPTau-G2	G0	2.49	K7(K7)	0.72(0.75)	1463	0.3

are available for the other two sources.

Table 4.7 (cont'd)

Name	Primary		Secondary		Projected	Mass
	SpT	Mass	SpT	Mass	Separation(AU)	Ratio(q)
HVTau	M1	0.57	(M8.5)	(0.02)	545	0.04
ISTau	K7	0.72	(M8.5)	(0.02)	1573	0.03
ITTau	K0	1.69	(K7)	(0.73)	344	0.43
J1-4872	K7	0.72	(M3)	(0.41)	490	0.57
JH112	K6	0.77	(M3)	(0.42)	951	0.55
JH223	M2	0.5	(M6.5)	(0.07)	299	0.13
LkCa4	K7	0.72	(M9)	(0.01)	1285	0.02
LkCa7	K7	0.72	(M7)	(0.05)	171	0.07
LkHa332-G2/V955 Tau	K7	0.72	K7(M0)	0.72(0.64)	1524	0.89
MHO-2	M2.5	0.45	M2.5(M4.5)	0.45(0.21)	570	0.47
UZTau	M1	0.57	(M2.5)	(0.46)	406	0.81
V410-Xray5a	M5.5	0.14	(M9)	(0.01)	1924	0.1
V710Tau	M1	0.57	(M2)	(0.49)	439	0.86
GSC 06785-00476	G7	1.56	(M8)	(0.3)	914	0.19
GSC 06204-01067	M2	0.49	(M5.5)	(0.11)	361	0.23
GSC 06780-01061	M3	0.36	(M5)	(0.12)	218	0.33
GSC 06784-00039	G7	1.56	(M7.5)	(0.05)	1962	0.03
GSC 06784-00997	M1	0.6	(M6)	(0.07)	697	0.11
GSC 06213-00306	K5	0.87	(M4.5)	(0.17)	461	0.2
GSC 06793-00868	M1	0.6	(M3)	(0.39)	291	0.65
GSC 06793-00806	M1	0.6	(M3.5)	(0.31)	274	0.51
RXJ1555.8-2512	G3	1.65	(M0)	(0.73)	1292	0.44
RXJ1555.8-2512	G3	1.65	(M5.5)	(0.1)	2118	0.06
RXJ1558.1-2405	K4	0.95	M5(M4)	0.13(0.22)	2632	0.23
RXJ1558.8-2512	M1	0.6	(M5)	(0.14)	1646	0.23
RXJ1559.2-2606	K2	1.12	(M2)	(0.48)	429	0.43
RXJ1600.7-2343	M2	0.49	(M2)	(0.48)	204	0.97
RXJ1602.8-2401B	K4	0.95	(M5)	(0.13)	1047	0.14
RXJ1604.3-2130	K2	1.12	M2(K5)	0.49(0.9)	2352	0.8
RXJ1606.6-2108	M1	0.6	(M1.5)	(0.54)	170	0.9
SCH16151115-24201556	M6	0.074	(M4.5)	(0.17)	2604	2.3
ScoPMS008a	M4	0.24	(M9)	(0.01)	229	0.05
ScoPMS016	M0.5	0.64	(M1.5)	(0.52)	199	0.82
ScoPMS042b	M3	0.36	(M7)	(0.06)	664	0.17
ScoPMS048	K0	1.35	(K1)	(1.27)	442	0.94
ScoPMS052	K0	1.35	(M2.5)	(0.45)	2764	0.33

Table 4.7 (cont'd)

| Name | Primary | | Secondary | | Projected | Mass |
	SpT	Mass	SpT	Mass	Separation(AU)	Ratio(q)
USco80	M4	0.24	(K5)	(0.89)	1779	3.7
USco-155532.4-230817	M1	0.6	(M3.5)	(0.28)	260	0.46
USco-160202.9-223613	M0	0.68	(M4)	(0.25)	334	0.37
USco-160258.5-225649	M2	0.49	(M7)	(0.06)	175	0.13
USco-160428.4-190441	M3	0.36	M4(M5.5)	0.24(0.1)	1417	0.27
USco-160611.9-193532	M5	0.13	(M6)	(0.07)	1563	0.5
USco-160700.1-203309	M2	0.49	(M6)	(0.78)	1689	1.6
USco-160702.1-201938	M5	0.13	(M5.5)	(0.1)	236	0.77
USco-160822.4-193004	M1	0.6	K9(M3)	0.71(0.38)	1953	0.63
USco-160900.7-190852	K9	0.71	M5(M4.5)	0.13(0.18)	2743	0.25
USco-160904.0-193359	M4	0.24	(M5)	(0.15)	186	0.63
USco-160908.4-200928	M4	0.24	(M4.5)	(0.19)	280	0.8
USco-160936.5-184800	M3	0.36	(M6)	(0.07)	2896	0.19
USco-161031.9-191305	K7	0.77	(M7.5)	(0.04)	828	0.05
USco-161039.5-191652	M2	0.49	(M5.5)	(0.11)	2168	0.22
GSC06770-00655	K5	0.87	(M2.5)	(0.43)	1306	0.49
GSC06770-00655	K5	0.87	(M0)	(0.68)	4295	0.78
RXJ1524.2-3030A	K0	1.35	M1(K7)	0.60(0.76)	2926	0.56
RXJ1529.4-2850	G8	1.52	(G9)	(1.44)	357	0.95
RXJ1529.4-2850	G8	1.52	(G8)	(1.47)	300	0.97
RXJ1530.4-3218	G7	1.56	(G8)	(1.47)	300	0.94
RXJ1536.5-3246	M3	0.36	(M3.5)	(0.3)	344	0.82
RXJ1537.0-3136	G7	1.56	K7(G8)	0.77(1.48)	779	0.95
RXJ1539.4-3446B	K7	0.77	(M7)	(0.06)	4031	0.08
RXJ1539.4-3446B	K7	0.77	(>M9)	(<0.01)	4259	<0.02
RXJ1539.4-3446B(/C)	K7	0.77	M2(M4)	0.49(0.22)	922	0.29
RXJ1540.7-3121	M4	0.24	M5(M4.5)	0.13(0.21)	863	0.89
RXJ1543.8-3306	M3	0.36	(M3.5)	(0.29)	405	0.8
RXJ1545.2-3417	K0	1.35	(M0)	(0.7)	377	0.52
RXJ1554.0-2920	M0	0.68	(M4)	(0.23)	209	0.34
RXJ1554.0-2920	M0	0.68	(M4.5)	(0.18)	3818	0.26

Note. — Values in parentheses are estimated from the system flux ratio ΔJ and the spectroscopically determined properties of the primary. Estimated statistical uncertainties are $\sim$10% for mass ratios, $\sim$20% for secondary masses, $\sim$2-3 subclasses for spectral types, and $\sim$10% for projected separations.

4.4.3 Inferred Stellar Properties

In Table 4.2, we list the inferred spectral types and masses for all of the association and cluster members in our sample. Spectral types are taken from the primary reference and were typically determined via low- or intermediate-resolution spectroscopy. We assume that the spectroscopically determined spectral type and mass for previously-unresolved binary systems corresponds to the primary mass and spectral type. Equal-mass binary components should have similar spectral types and the flux from inequal-mass systems should be dominated by the primary; in either case, spectroscopic observations of the unresolved system should have been affected only marginally by

the flux from the secondary.

We estimated the masses of sample members by combining mass-temperature and temperature-SpT relations from the literature. No single set of relations spans the entire spectral type range of our sample, so we have chosen the M dwarf temperature scale of Luhman et al.(2003b), the early-type ($\leq$M0) temperature scale of Schmidt-Kaler (1982), the high-mass stellar models of D'Antona & Mazzitelli (1997; DM97), and the low-mass stellar models of Baraffe et al.(1998; NextGen). We apply the DM97 mass-temperature models for masses of >1 $M_\odot$ and the NextGen models for masses of <0.5 $M_\odot$; in the 0.5-1.0 $M_\odot$ regime, we have adopted an average sequence. For each association, we adopt the models corresponding to the mean age listed in Table 4.1; this will introduce some uncertainty given the unknown age spread for each association. Large systematic errors may be present in these and all pre-main sequence models (e.g., Baraffe et al. 2002; Hillenbrand & White 2004; Close et al. 2005; Reiners et al. 2005), so they are best used for relative comparison only.

Much of the uncertainty in theoretical mass-temperature relations can be assessed in terms of a zero-point shift in the mass; preliminary observational calibrations by the above authors suggest that theoretical models overestimate masses by 10-20% over most of our sample mass range. This suggests that theoretical predictions of relative properties (e.g., mass ratios, $q = m_s/m_p$) might be more accurate than absolute properties (e.g., individual component masses) since the systematic mass overestimates will cancel. Relative quantities are also largely independent of age and extinction, which are expected to be similar for binary components. We have combined our adopted mass-luminosity-SpT relations with the near-infrared colors of Bessell & Brett (1988) and the K-band bolometric corrections of Leggett et al.(1998, 2000, 2002) and Masana et al.(2006) to predict values for q as a function of primary brightness m and flux ratio Δm in all three 2MASS filters. Some of our sample members could possess K-band excesses due to hot inner disks, so we have adopted the q values predicted by the J-band fluxes; this will not eliminate the effect, but should minimize it. We have also combined our derived q values with the estimated primary masses to predict secondary masses, and we use our mass-SpT relations to

predict the corresponding secondary spectral types.

We list the derived values for each binary system in Table 4.7. Some wide binaries have independent SpT determinations for both components, so we report derived quantities with parentheses and measured quantities without. The typical uncertainties in q are $\sim$10% and represent the uncertainties in the photometry and the assigned spectral types, though some systematic effects (e.g., unresolved multiplicity or different levels of extinction) could produce far larger values. This can be seen in the discrepancies for some systems (e.g., GG Tau AB, MHO-2/1) which are known to be hierarchical multiple systems. We can not quantify the unknown uncertainties in the theoretical models, but they should be considered when interpreting these results. The typical uncertainty in physical separation is $\sim$10% and reflects the uncertainty in angular separation and the unknown depth of each system in its association; we assume each association has a total depth equal to its extent on the sky ($\sim$40 pc for Taurus and Upper Sco, $\sim$20 pc for ChamI). The uncertainty in the mean association distance ($\sim$5 pc) introduces a systematic uncertainty of $\pm$3%, but this is generally negligible.

4.4.4 Binary Statistics

Multiplicity surveys typically consider the frequency of binary systems for restricted ranges of parameter space (observed separations and mass ratios) corresponding to the survey completeness limits. For our analysis, we select a range of projected separations (330-1650 AU, set by the inner and outer detection limits of ChamI since those limits are most restrictive) and flux ratios ($\Delta K < 2$, corresponding to $q >$0.25) that should be complete for all but the lowest-mass brown dwarfs in our sample. The inner separation limit and mass ratio limit are set by the resolution limit for low-mass sample members ($K \sim$12.3) in ChamI, while the outer separation limit is set by the background contamination in ChamI, where our mass ratio cut allows us to choose a 90% pure sample for separations $<10''$.

In Figure 4.6, we present plots of the wide binary frequency as a function of pri-

mary mass for each region in our sample. The binary fractions plotted correspond to our designated completeness regime: mass ratios $q > 0.25$ and projected separations of 330-1650 AU. In the bottom panel, we show the field binary frequency in the same range of mass ratios and projected separations for solar-type stars (Duquennoy & Mayor 1991), early-mid M dwarfs (M0-M6; Reid & Gizis 1997), and brown dwarfs (Bouy et al. 2003; Burgasser et al. 2003). We also show the corresponding frequencies for early-type stars in USco-A and USco-B (Kouwenhoven et al. 2005). The bin sizes were chosen to evenly sample the mass range of our survey (0.025-2.50 $M_\odot$ for which the primary targets were brighter than our brightness cutoff ($K = 14.3$). For each region in our survey, we also show the expected frequency for foreground and background sources which pass our color selection criteria and have $\Delta K < 2$, assuming a background source count function N(K) matching that shown in Figure 4.2; in all cases, the expected contamination rate is negligible. USco-A, ChamI, and Taurus all show a decline in the binary frequency with mass, consistent with the results shown for field multiplicity surveys. USco-B does not show a decline, but the uncertainties are not small enough to strongly constrain the slope of any mass dependence.

This binary search may not be complete for objects in the lowest-mass bin where some binary companions could have been fainter than the survey detection limits ($K > 14.3$), so the true upper limits may be marginally higher. However, it has been observationally determined that most very low mass binaries in the field have mass ratios near unity ($q > 0.7$) and much smaller separations (<20 AU), so we are unlikely to have missed any wider or lower-mass ratio companions (Close et al. 2003; Burgasser et al. 2003; Bouy et al. 2003).

Another interesting distribution to consider would be the mass ratio distribution for wide binaries as a function of mass and environment. Unfortunately, extending our binary results along another axis of parameter space exceeds the statistical limits of our sample, leaving most bins with only 0-1 detections. The best solution for this is to combine all regions into a single population. In Figure 4.7, we plot the mass ratio distribution in our survey separation range (330-1650 AU) for the three highest-mass bins. We also show the best-fit distribution for solar-type stars in the

field (Duquennoy & Mayor 1991).

This result should be treated with caution since it represents an admixture of formation environments which likely does not match the composition of the field. As we show in Figure 4.6, the binary frequency appears to be fundamentally different in the dark cloud complexes (Taurus and Chamaeleon) than in USco-A. This distinction suggests that binary formation processes can vary significantly between different environments, and therefore that analysis of other binary properties should take the environment into account when possible.

4.5 Follow-up Sample

For our follow-up study, we do not include any of the candidates in Cham-I or the southern subgroup of Upper Sco (USco-B) since our observations were all conducted from northern sites. We consider every candidate in the other two associations with a separation of $>3''$ (out to a limit of $30''$) and a flux ratio of $\Delta K < 3$ (corresponding to mass ratios $q > 0.1$). We also considered all 14 candidates in Taurus with larger flux ratios, yielding a complete sample down to the 10σ flux limit of 2MASS ($K = 14.3$); we were not able to gather sufficient information to consider 2 of the 3 candidates with large flux ratios in Upper Sco.

We list all of the previously-unconfirmed candidate companions in our sample in Table 4.8. Some of the sources in our sample have been identified previously in the literature as either field stars or association members based on a wide variety of characteristics: proper motions, the presence of a disk, low surface gravity, or the presence of lithium. We summarize these identifications in Tables 4.9 and 4.10, respectively. Table 4.10 also includes all of the systems we identified in a similar compilation in KH07a.

Finally, in Tables 4.8-4.10 we have compiled updated spectral types for all members of our sample. Our original survey used the spectral types assigned in the discovery survey or in compilation papers (e.g., Kenyon & Hartmann 1995), but a significant number of system components have had more precise spectral type estimates
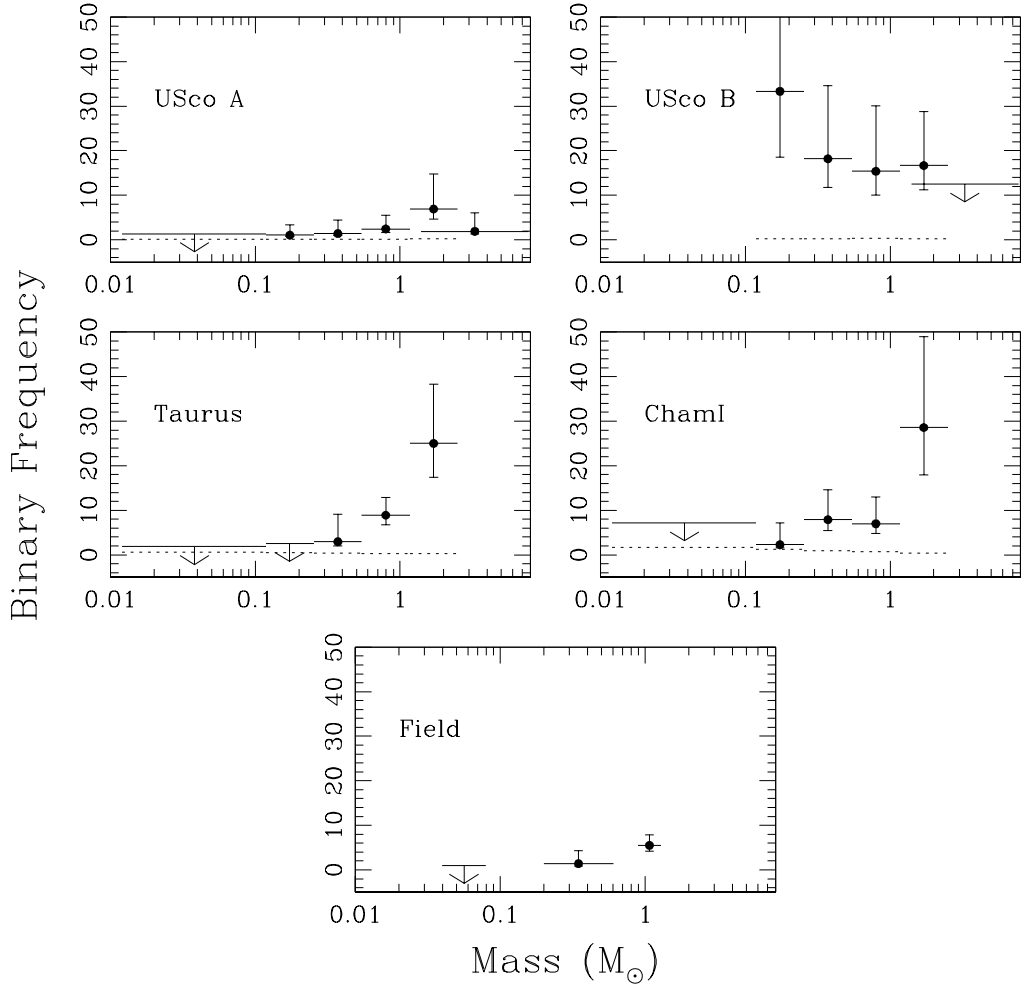
Figure 4.6 The wide (330-1650 AU) binary frequency as a function of mass for each region and as determined from field multiplicity surveys. The higher-mass histogram bins are equally sized in *logM*, but the three lowest-mass bins have been combined to illustrate the absence of any companions. The error bars are calculated assuming binomial statistics. The highest-mass datapoints for USco-A and USco-B denote the results of Kouwenhoven et al.(2005). The dashed lines show the expected frequency for each bin solely from foreground and background sources and unbound association members; they are not distinguishable from zero in most bins. Most upper limits for the lowest-mass bins are also very close to zero.
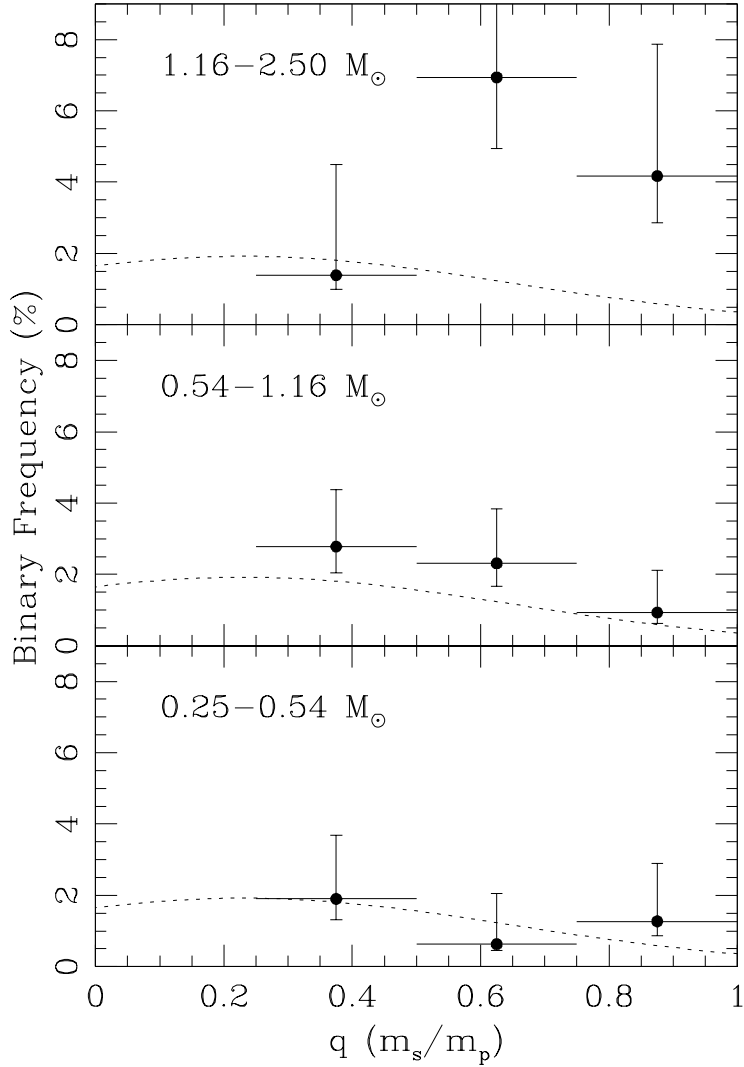
Figure 4.7 The mass ratio distribution for wide binaries in the three highest-mass bins of our survey, calculated as a frequency among all sample members. The mass ratio distribution function found by Duquennoy & Mayor (1991) for field solar-type stars is denoted with a dashed line. These results represent the sum over all associations in our sample; the binary frequency varies between environments (Figure 4.6) and our sample represents a different admixture of formation environments than the field sample, so the sample and field frequencies should be compared with caution.

Table 4.8. Candidate Wide Companions in Taurus and Upper Sco

Known Member	Candidate Companion	Sep ('')	PA (deg)	ΔK (mag)	SpT_{known}	Ref
Taurus						
2M04414489+2301513	2M04414565+2301580	12.37	57.3	-3.31	M8.25	1
2M04080782+2807280	2M04080771+2807373	9.43	351.1	-1.96	M3.75	1
LkCa 15	2M04391795+2221310	27.62	4.6	-1.14	K5	4
FW Tau	2M04292887+2616483	12.22	246.7	0.03	M5.5+(M5.5)	3
GM Aur	2M04551015+3021333	28.31	202.2	0.28	K7	4
2M04161885+2752155	2M04161754+2751534	28.04	218.2	0.60	M6.25	1
CFHT-Tau-7	2M04321713+2421556	21.76	207.2	0.82	M5.75	1
HBC 427	2M04560252+3020503	14.90	154.0	0.89	K5+?	5
I04158+2805	2M04185906+2812456	25.34	28.9	0.98	M5.25	1
JH 112	2M04324938+2253082	6.56	34.3	1.03	K7	7
V710 Tau AB	2M04315968+1821305	27.97	105.7	1.39	M0.5+M2	9, 24
CFHT-Tau-21	2M04221757+2654364	23.31	152.1	2.06	M2	1
V410 X-ray1	2M04175109+2829157	27.95	137.4	2.66	M4	8
2M04213460+2701388	2M04213331+2701375	17.18	265.7	2.70	M5.5	2
I04385+2550	2M04413842+2556448	18.94	343.3	3.03	M0.5	6
DO Tau	2M04382889+2611178	28.75	8.4	3.28	M0	7
CFHT 4	2M04394921+2601479	24.40	72.9	3.56	M7	19
I04216+2603	2M04244376+2610398	27.96	337.0	3.66	M0	7
V410 X-ray 5a	2M04190271+2822421	13.27	47.7	3.67	M5.5	22
V410 X-ray 6	2M04190223+2820039	26.49	34.4	4.22	M5.5	22
MHO-Tau-2	2M04142440+2805596	26.32	269.9	4.32	M2.5+M2.5	21
V410 X-ray 2	2M04183574+2830254	17.72	105.6	4.47	M0	23
IS Tau	2M04333746+2609550	10.85	57.4	4.82	M0+M3.5	20
CoKu Tau/3	2M04354076+2411211	12.60	349.2	4.97	M1	7
FM Tau	2M04141556+2812484	26.21	91.7	4.98	M0	7
LkCa 4	2M04162839+2807278	8.86	154.6	5.25	K7	7
IS Tau	2M04333467+2609447	28.73	261.1	5.64	M0+M3.5	20
FO Tau	2M04144741+2812219	26.19	250.8	5.98	M3.5+M3.5	20
DG Tau	2M04270370+2606067	16.43	234.3	6.71	K2	6
Upper Sco						
SCH160758.50-203948.90	2M16075796-2040087	21.52	200.7	-4.78	M6	14
USco80	2M15583621-2348018	12.27	15.2	-1.89	M4	18
DENIS162041.5-242549.0	2M16204196-2426149	26.73	164.5	-1.28	M7.5	10
SCH161511.15-242015.56	2M16151239-2420091	17.96	69.8	-1.04	M6	14
UScoJ160700.1-203309	2M16065937-2033047	11.65	293.1	-0.40	M2	17
SCH161825.01-233810.68	2M16182365-2338268	24.73	229.1	-0.20	M5	14
SCH162135.91-235503.41	2M16213638-2355283	25.65	165.3	-0.19	M6	14
ScoPMS048	ScoPMS 048 B	3.05	192.1	0.25	K2+M4	16
SCH160758.50-203948.90	2M16075693-2039424	22.94	285.5	1.39	M6	14
RXJ 1555.8-2512	2M15554839-2512174	8.91	318.4	1.71	G3	13
RXJ 1558.8-2512	2M15585415-2512407	11.35	130.1	1.88	M1	13
GSC 06213-00306	GSC 06213-00306 B	3.18	305.5	2.14	G9+G9	11
UScoJ160936.5-184800	2M16093658-1847409	19.97	2.2	2.22	M3	17
ScoPMS042b	2M16102177-1904021	4.58	6.8	2.31	M3	15
RXJ 1602.8-2401B	2M16025116-2401502	7.22	352.9	2.69	K4	13
UScoJ160245.4-193037	2M16024735-1930294	28.19	72.9	2.74	M5	17
GSC 06784-00997	2M16101888-2502325	4.81	240.4	2.90	M1	12
GSC 06785-00476	2M15410726-2656254	6.30	82.6	3.04	G7	12
UScoJ161031.9-191305	2M16103232-1913085	5.71	114.0	3.74	K7	17
RXJ 1555.8-2512	2M15554788-2512172	14.61	298.1	4.24	G3	13

published since their discovery. Unless otherwise noted, the masses were estimated using the methods described in Section 4.3.4. In hierarchical multiple systems where components are themselves known to be multiple from previous AO, speckle, or RV surveys, we have noted the known or estimated spectral type of each, and report the corresponding known or estimated system mass. We also have updated the spectral types and multiplicity (and therefore the masses) for all sample members that do not have wide companions, so the analysis in Section 4.5 is performed with a uniform sample.

Table 4.8 (cont'd)

Known Member	Candidate Companion	Sep ($''$)	PA (deg)	ΔK (mag)	SpT_{known}	Ref
GSC 06784-00039	2M16084438-2602139	13.53	77.5	5.12	G7	12

Note. — The astrometry and photometry for each candidate system have been adopted from our re-reduction of the 2MASS atlas images (KH07a). References: (1) Luhman (2006a), (2) Luhman (2004), (3) White & Ghez (2001), (4) Simon et al.(2000), (5) Steffen et al.(2001), (6) White & Hillenbrand (2004), (7) Kenyon & Hartmann (1995), (8) Strom & Strom (1994), (9) Hartigan et al.(1994), (10) Martín et al.(2004), (11) Guenther et al.(2007), (12) Preibisch et al.(1998), (13) Kunkel (1999), (14) Slesnick et al.(2006a), (15) Walter et al.(1994), (16) Prato et al.(2002a), (17) Preibisch et al.(2002), (18) Ardila et al. (2000), (19) Martín et al.(2001), (20) Hartigan & Kenyon (2003), (21) Briceno et al.(1998), (22) Luhman (1999), (23) Luhman & Rieke (1998), (24) Leinert et al.(1993)

Table 4.9.   Previously Confirmed Field Stars

Known Member	Field Star	Sep ($''$)	PA (deg)	ΔK (mag)	Evidence	Ref
IP Tau	NLTT 13195	15.75	55.7	5.08	Proper Motion	Salim & Gould (2003)
V410 Anon 20	V410 Anon 21	22.71	115.3	0.62	Early SpT	Luhman (2000)
USco160428.4-190441	GSC06208-00611	24.15	134.3	0.51	Lithium	Preibisch et al.(1998)
USco161039.5-191652	SIPS1610-1917	14.95	183.2	1.98	Proper Motion	Deacon & Hambly (2007)[a]

Note. — The astrometry and photometry for each pair of stars have been adopted from our re-reduction of the 2MASS atlas images (KH07a).

[a]Deacon & Hambly (2007) identified SIPS1610-1917 as USco161039.5-191652, but inspection of the original photographic plates shows that SIPS1610-1917 is the candidate companion that we identified in KH07a (2M16103950-1917073). Its high proper motion demonstrates that it is a field star, not a bound companion.

4.6   Follow-up Observations and Analysis

4.6.1   Optical Spectroscopy

We obtained intermediate-resolution optical spectra for 14 Taurus candidates and 8 Upper Sco candidates that were wide enough to be easily resolved and optically bright enough to be observed with short ($\leq$10 min) exposures. These spectra were measured with the Double Spectrograph (Oke & Gunn 1982) on the Hale 5m telescope at Palomar Observatory in December 2006 and May 2007. The spectra presented here were obtained with the red channel using a 316 l/mm grating and a 2.0$''$ slit, yielding a spectral resolution of $R \sim$1250 over a wavelength range of 6400-8800 angstroms. Wavelength calibration was achieved by observing a standard lamp after each science target, and flux normalization was achieved by periodic observation of spectrophotometric standard stars from the compilation by Massey et al.(1988). We summarize all of the observations in Table 4.11.

Table 4.10. Previously Confirmed Companions

Primary	Secondary	Sep ('')	PA (deg)	ΔK (mag)	SpT_{prim}	SpT_{sec}	Refs
				Taurus			
2M04554757+3028077	2M04554801+3028050	6.31	115.7	2.18	M4.75	M5.5	1
DH Tau	DI Tau	15.23	126.0	0.21	M0+M7.5	M0+?	2, 3, 4
FS Tau	Haro 6-5B	19.88	275.8	3.57	M0+M3.5	K5	5, 6
FV Tau	FV Tau/c	12.29	105.7	1.43	K5+cont	M2.5+M3.5	2, 3, 5
FZ Tau	FY Tau	17.17	250.5	0.70	K7	M0	2
GG Tau Aab	GG Tau Bab	10.38	185.1	2.61	K7+M0.5	M5.5+M7.5	7
GK Tau	GI Tau	13.14	328.4	0.42	K7+cont	K5	2, 8
HBC 352	HBC 353	8.97	70.8	0.28	G5	K3	2
HBC 355	HBC 354	6.31	298.3	0.91	K2	K2	2
HN Tau A	HN Tau B	3.10	18.7	3.19	K5	M4.5	8, 9
HP Tau-G2	HP Tau	21.30	296.9	0.40	G0	K3	2, 10
HP Tau-G2	HP Tau-G3	10.09	243.4	1.57	G0	K7+?	2, 10
HV Tau AB	HV Tau C	3.76	43.9	4.35	M2+?	K6	6, 11
J1-4872 Aab	J1-4872 Bab	3.38	232.9	0.69	M0+M0	M1+M1	8
LkHa332-G1	LkHa332-G2	25.88	254.5	0.28	M1+?	M0.5+M2.5	2, 5, 12
MHO-Tau-1	MHO-Tau-2	3.93	153.9	0.01	M2.5	M2.5	13
UX Tau AC	UX Tau Bab	5.856	269.7	2.22	K2+M3	M2+?	8
UZ Tau Aab	UZ Tau Bab	3.56	273.5	0.24	M1+?	M2+M3	2, 5, 14, 15
V710 Tau A	V710 Tau B	3.03	178.5	-0.13	M0.5	M2	9
V773 Tau	2M04141188+2811535	23.38	215.9	5.43	K2+K5+M0.5+?	M6.25	1, 15
V807 Tau	GH Tau	21.77	195.2	0.83	K5+M2+?	M2+M2	5, 25
V928 Tau	CFHT-Tau-7	18.25	228.2	2.27	M0.5+?	M5.75	2, 16, 17
V955 Tau	LkHa332-G2	10.51	35.3	0.01	K7+M2.5	M0.5+M2.5	2, 5, 12
XZ Tau	HL Tau	23.31	271.2	0.12	M2+M3.5	K5	2, 5
				Upper Sco			
RXJ1558.1-2405A	RXJ1558.1-2405B	18.15	254.4	2.10	K4+?	M5+?	18, 19
RXJ1604.3-2130A	RXJ1604.3-2130B	16.22	215.9	0.92	K2	M2+?	18, 19
ScoPMS 052	RXJ1612.6-1859	19.06	269.5	1.62	K0+M2	M1	20, 21
UScoJ160428.4-190441	UScoJ160428.0-19434	9.77	321.3	1.73	M3+?	M4	22, 23
UScoJ160611.9-193532 A	UScoJ160611.9-193532 B	10.78	226.5	0.76	M5+M5	M5	22, 24
UScoJ160707.7-192715	UScoJ160708.7-192733	23.45	140.4	1.37	M2+?	M4	22
UScoJ160822.4-193004	UScoJ160823.2-193001	13.47	71.4	0.41	M1	M0	22
UScoJ160900.7-190852	UScoJ160900.0-190836	18.92	326.5	1.81	M0	M5	22
UScoJ161010.4-194539	UScoJ161011.0-194603	25.59	160.8	0.97	M3	M5	22

Note. — The astrometry and photometry for each candidate system have been adopted from our re-reduction of the 2MASS atlas images (KH07a). References: (1) Luhman (2004), (2) Kenyon & Hartmann (1995), (3) Ghez et al.(1993), (4) Itoh et al.(2005), (5) Hartigan & Kenyon (2003), (6) White & Hillenbrand (2004), (7) White et al.(1999), (8) Duchene et al.(1999), (9) Hartigan et al.(1994), (10) Simon et al. (1995), (11) Stapelfeldt et al.(2003), (12) White & Ghez (2001), (13) Briceno et al.(1998), (14) Prato et al.(2002b), (15) Correia et al. (2006), (15) Boden et al.(2007), (16) Simon et al.(1996), (17) Luhman (2006), (18) Kunkel (1999), (19) Köhler et al.(2000), (20) Walter et al. (1994), (21) Prato (2007), (22) Preibisch et al.(2002), (23) Kraus et al.(2008), (24) Kraus & Hillenbrand (2007b), (25) Schaefer et al. (2006).

Table 4.11.   Spectroscopic Observations

Candidate Companion	Instrument	t_{int} (sec)
2M04080771+2807373	DBSP	300
2M04161754+2751534	DBSP	300
2M04213331+2701375	DBSP	600
2M04414565+2301580	DBSP	300
2M04394921+2601479	NIRSPEC	300
2M04221757+2654364	DBSP	300
2M04321713+2421556	DBSP	300
2M04354076+2411211	NIRSPEC	300
2M04382889+2611178	NIRSPEC	300
2M04141556+2812484	NIRSPEC	300
2M04292887+2616483	DBSP	300
2M04551015+3021333	DBSP	30
2M04560252+3020503	DBSP	240
2M04185906+2812456	DBSP	300
2M04244376+2610398	NIRSPEC	300
2M04333746+2609550	NIRSPEC	300
2M04324938+2253082	DBSP	600
2M04391795+2221310	DBSP	60
2M04162839+2807278	NIRSPEC	300
2M04142440+2805596	NIRSPEC	300
2M04190271+2822421	NIRSPEC	300
2M04175109+2829157	DBSP	300
2M04183574+2830254	NIRSPEC	300
2M04315968+1821305	DBSP	600
2M04190223+2820039	NIRSPEC	300
2M16204196-2426149	DBSP	300
2M15554839-2512174	DBSP	300
2M16075796-2040087	DBSP	60
2M16151239-2420091	DBSP	300
2M16182365-2338268	DBSP	300
2M16213638-2355283	DBSP	300
2M15583621-2348018	DBSP	180
2M16065937-2033047	DBSP	60

The spectra were processed using standard IRAF tasks; we used the IRAF task SPLOT to measure equivalent widths of spectral lines. Several of the fainter candidates have very noisy spectra because we recognized from short preliminary exposures that they were heavily reddened background stars and not late-type association members; given their brightness and color, these candidates would possess deep TiO bands if they were members.

4.6.2   Near-Infrared Spectroscopy

We obtained intermediate-resolution near-infrared spectra for 11 of our Taurus candidates that were too faint and red for optical spectroscopy. These spectra were

obtained using NIRSPEC on the Keck-II 10m telescope on JD 2454398 with the NIRSPEC-7 (K) filter using the low-resolution grating and a $0.76''$ slit. The corresponding spectral resolution is $R \sim 1500$ spanning 1.95-2.37 μm, though variations in the deep telluric absorption features shortward of 2.05 μm limit the useful range to $\lambda > 2.05$ μm. Wavelength calibration was achieved with respect to standard Ne lamps, and telluric correction was achieved by observing a bright F star, HD 26784.

All spectra were obtained in an ABBA nod pattern to allow for sky subtraction. As for the optical spectra above, the infrared spectra were processed using standard IRAF tasks, and we used the IRAF task SPLOT to measure equivalent widths of spectral lines. We summarize the observations in Table 4.11.

4.6.3 Imaging

We obtained high-precision astrometric measurements for a subset of our candidate companion sample in the course of several adaptive optics observing runs at the Keck-2 10m telescope and the Palomar Hale 200" telescope. All observations were obtained using the facility adaptive optics imagers, NIRC2 and PHARO. Most of our targets were observed using natural guide star adaptive optics (NGSAO), but several faint targets were observed at Keck with laser guide star adaptive optics (LGSAO; Wizinowich et al. 2006). We also observed a small number of targets with seeing-limited imaging during periods of moderate cloud cover that prevented the use of adaptive optics. We summarize all of these observations in Table 4.12.

For faint targets, images were obtained using the K' filter at Keck or the K_s filter at Palomar. For brighter targets, we used the $Br\gamma$ filter, which attenuates flux by a factor of ~ 10 relative to broadband K filters. All of our NIRC2 observations were obtained in the 10 mas pix^{-1} or 40 mas pix^{-1} modes, depending on whether the binary could fit in the narrow-frame FOV ($10.18''$) or required the wide-frame FOV ($40.64''$). All PHARO observations were obtained with the 25 mas pix^{-1} mode ($FOV = 25.6''$). All Palomar image sets were obtained in a five-point box dither pattern. At Keck, all NGSAO observations and early LGSAO observations were obtained in a three-point

box dither pattern (designed to avoid the bottom-left quadrant, which suffers from high read noise); later LGSAO observations were obtained in a diagonal two-point dither pattern because experience showed that dithers degrade the AO correction until several exposures have been taken with the Low-Bandwidth Wavefront Sensor, imposing a significant overhead.

Most of the targets are relatively bright and require very short integration times to avoid nonlinearity, so most exposures were taken in correlated double-sampling mode, for which the array read noise is 38 electrons read^{-1}. Where possible, we observed targets in multiple correlated double-sampling mode, where multiple reads are taken at the beginning and ending of each exposure; this choice reduces the read noise by approximately the square root of the number of reads. In most cases, the read noise is negligible compared to the signal from the science targets. The read noise is negligible (<10 electrons read $^{-1}$) in all PHARO exposures.

The data were flat-fielded and dark- and bias-subtracted using standard IRAF procedures. The NIRC2 images were distortion-corrected using new high-order distortion solutions (Cameron 2008) that deliver a significant performance increase as compared to the solutions presented in the NIRC2 pre-ship manual;[4] the typical absolute residuals are $\sim$4 mas in wide camera mode and $\sim$0.6 mas in narrow camera mode. The PHARO images were distortion-corrected using the solution derived by Metchev (2005). We adopted the NIRC2 narrow-field plate scale (9.963 $\pm$0.003 mas pix^{-1}) and y-axis PA (in degrees east of north; +0.13 $\pm$0.01^o) reported by Ghez et al.(2008). As we will report in a future publication (Kraus, Ireland, et al., in prep), we then used observations of the M5 core (e.g., Cameron et al. 2009) to extrapolate corresponding values for the NIRC2 wide-field camera (39.83 $\pm$0.04 mas pix^{-1} and +0.34$\pm$0.02^o) and the PHARO narrow-field camera (25.19$\pm$0.04 mas pix^{-1} and +2.15$\pm$0.10^o, assuming the Cassegrain ring is set at +335°). The rotation for PHARO might change over time and this value has only been confirmed for 2007, so new calibrations will be needed for any other epochs. The values for PHARO also differ from those adopted in Kraus et al.(2008), where we used old values of the plate scale and rotation, so we

---

[4]http://www2.keck.hawaii.edu/realpublic/inst/nirc2/

have recalibrated the previous results to match the updated values.

We measured photometry and astrometry for our sources using the IRAF package DAOPHOT (Stetson 1987). For systems with small or moderate separations, we used the PSF-fitting ALLSTAR routine. For systems with wider separations, where anisoplanatism produced significantly different PSFs, we used the PHOT package. We analyzed each frame separately in order to estimate the uncertainty in individual measurements and to allow for the potential rejection of frames with inferior AO correction; our final results represent the mean value for all observations in a filter. For observations where the primary star was single or the secondary was close to on-axis ($\rho < 5''$), we used that source to produce individual template PSFs for each image. In the few cases where a source was itself a close binary, we measured photometry and astrometry for each close component using the PSF reconstruction technique that we described in Kraus & Hillenbrand (2007b), then combined the values to find the photocenter.

We calibrated our photometry using the known 2MASS K_s magnitudes for each of our science targets; in cases where the binary system was not resolved in the 2MASS PSC, we invoked the estimated K_s magnitudes for each component from our discovery survey (KH07a). Our broadband photometry was obtained using both K' and K_s filters, but previous comparisons have shown that the filter zero points differ by <0.01 mag for objects with typical stellar colors (Carpenter 2001; Kim et al. 2005). The midpoint of the narrow $Br\gamma$ filter is very close to the midpoint of typical K filters (2.166μ), so its calibration uncertainty should be similar. The calibration process could introduce larger systematic uncertainties ($\sim$0.1 mag) if any of the sources are variable, as many pre-main sequence stars tend to be, but these cases should be easily identified if the calibrated flux ratios for candidate binary components do not agree with previous measurements.

Finally, we note that one target (the candidate companion to USco80) was resolved to be a close equal-flux pair. Our analysis for the system reflects this discovery, and we will describe this observation in more detail in a future publication that summarizes our ongoing survey of the multiplicity of very low-mass stars and brown dwarfs.

Table 4.12.   Imaging Observations

Candidate Companion	Telescope/ Mode	T_{int} (sec)	Scale (mas)	Epoch(JD- 2450000)
2M04080771+2807373	Keck/NGS	40	40	54069
GSC 06213-00306 B	Keck/NGS	120	10	54187
2M16101888-2502325	Keck/NGS	160	10	54188
2M15410726-2656254	Pal/NGS	50	25	54198
2M15554839-2512174	Pal/NGS	297	25	54198
2M16151239-2420091	Keck/LGS	20	40	54188
2M16182365-2338268	Pal/Seeing	1427	25	54199
2M16213638-2355283	Pal/Seeing	1308	25	54199
2M15583621-2348018	Keck/LGS	120	40	54188

4.6.4   Archival Astrometry

We retrieved relative astrometry for our wide companion sample from several all-sky imaging surveys: the Two-Micron All-Sky Survey (2MASS; Skrutskie et al. 2006), the Deep Near Infrared Survey (DENIS; Epchtein et al. 1999), and the United States Naval Observatory B1.0 survey (USNOB; Monet et al. 2003). The DENIS and 2MASS source catalogues are based on wide-field imaging surveys conducted in the optical/NIR (IJK and JHK, respectively) using infrared array detectors, while US-NOB is based on a digitization of photographic plates from the Palomar Observatory Sky Surveys.

In our discovery survey (KH07a), we presented 2MASS astrometry for each filter that was measured directly from the processed atlas images, so we have adopted those values. We extracted DENIS astrometry from the source catalog, which contains the average value for all three filters. The USNOB source catalog reports processed astrometry as well as individual astrometric measurements for each epoch; we have chosen to work with the individual measurements since it is unclear how the US-NOB astrometric pipeline weighted individual measurements or rejected potentially erroneous measurements.

Both 2MASS and DENIS quote astrometric uncertainties of 70-100 mas for individual sources spanning the brightness range of our sample, while USNOB reports uncertainties of ∼200-300 mas in each epoch. However, the quoted uncertainties include significant systematic terms resulting from the transformation to an all-sky reference frame. We have conducted tests with our known binary systems with existing high-

precision measurements (Table 4.10) which suggest that narrow-angle astrometry on angular scales of $<1'$ is accurate to $\sim$70 mas for 2MASS/DENIS and 100-200 mas for USNOB, depending on brightness, so we adopt these lower values as the astrometric uncertainties for all measurements.

We also collated all of the astrometric observations reported in the literature for our wide companion sample. Most of these measurements were obtained using high-resolution imaging techniques: lunar occultation interferometry, speckle interferometry, and adaptive optics imaging. However, some were also obtained with seeing-limited imaging. In each case, we adopt the uncertainties reported in the literature, but it is unclear in many cases whether all possible sources of systematic error (such as geometric distortion or unresolved multiplicity) have been assessed.

4.6.5 Stellar and Companion Properties

Stellar properties can be difficult to estimate from observed properties, particularly for young stars, since pre-main-sequence stellar evolutionary models are not well-calibrated. The masses of a given sample could be systematically uncertain by as much as 20% (e.g., Hillenbrand & White 2004), and individual masses could be uncertain by factors of 50% or more due to unresolved multiplicity or the intrinsic variability that accreting young stars often display. These caveats suggest that any prescription for determining stellar properties should be treated with caution.

We estimated the properties of our sample members using the methods described in our original discovery survey (KH07a). This procedure calculates component masses by combining the 2- or 5-Myr isochrones of Baraffe et al.(1998) and the M dwarf temperature scale of Luhman et al. (2003) to convert observed spectral types to masses. Relative properties (mass ratios q) are calculated by combining the Baraffe isochrones and Luhman temperature scale with the empirical NIR colors of Bessell & Brett (1998) and the K-band bolometric corrections of Leggett et al.(1998) to estimate q from the observed flux ratio ΔK. The observed flux ratio is not sensitive to the distance or extinction for a system (unless differential extinction is present),

so the relative system properties should not be affected by these potential sources of error. We also used these techniques to estimate masses for all single stars and confirmed binary pairs in our sample.

For all binary systems without spatially resolved spectra, we have adopted the previously-measured (unresolved) spectral type for the brightest component and inferred its properties from that spectral type. This assumption should be robust since equal-flux binary components will have similar spectral types and significantly fainter components would not have contributed significant flux to the original discovery spectrum. The properties of all fainter binary components were then inferred using the methods described in the previous paragraph. When we compute mass-dependent properties (mass ratios and total system masses) for our samples, we sum the masses of all sub-components of our wide "primary" and "secondary."

Projected spatial separations are calculated assuming the mean distance for each association, $\sim$145 pc (de Zeeuw et al. 1999; Torres et al. 2007). If the total radial depth of each association is equal to its angular extent ($\sim$15° or $\sim$40 pc), then the unknown depth of each system within its association implies an uncertainty in the projected spatial separation of $\pm$15%. The systematic uncertainty due to the uncertainty in the mean distance of each association is negligible in comparison ($<$5%).

4.7 Results

4.7.1 Optical Spectroscopy

The spectra show that our candidate companions can be divided into three groups: background dwarfs, background GK giants, and young association members. We plot the corresponding spectra in Figures 4.8-4.10, respectively, and we summarize our spectral classifications in Table 4.15.
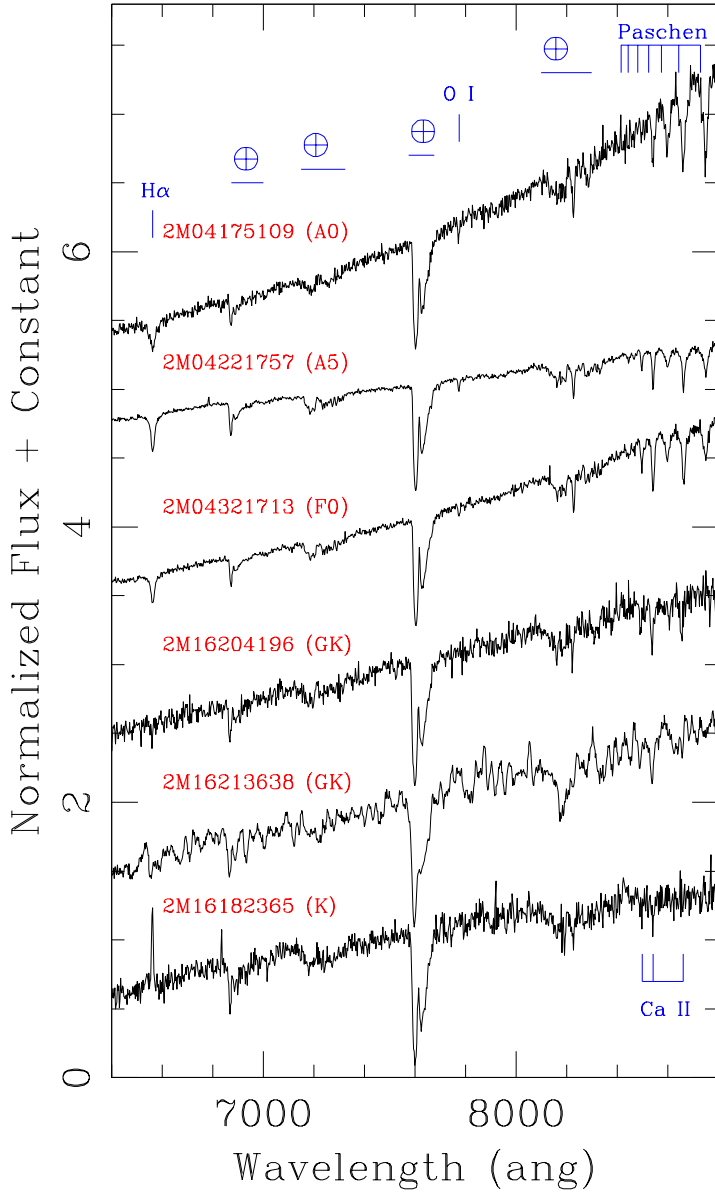
Figure 4.8 Six field dwarfs that are located behind Taurus or Upper Sco. The top three spectra show clear absorption from the Paschen-14 and -12 lines, indicating that the sources are background A-F stars. The next two spectra show absorption from the Ca II infrared triplet, but no absorption features from the Paschen series or from TiO bands, indicating that the sources are G-K stars. Finally, the bottom star shows $H\alpha$ emission that might indicate accretion (and youth), but it could also indicate the presence of an active M dwarf companion. In all cases, the stars are too faint for their spectral type to be members, indicating that they are located behind the associations. Finally, we note that the spectrum for 2M16213638-2355283 was smoothed with a five-pixel average to emphasize the absence of broad TiO absorption bands, so most apparently narrower features (i.e., the apparent absorption feature at 8200A) are noise artifacts. All relevant spectral features and atmospheric absorption bands have been labeled.

4.7.1.1   Background Dwarfs

Early-type A and F dwarfs are easily identified by the presence of the Paschen series at >8400 angstroms, and specifically by the Paschen-12 and -14 lines at 8595 and 8748 angstroms. The Paschen sequence fades and the CaII infrared triplet grows between late A and late F, so the relative depths of Paschen-14 and the CaII triplet provide an excellent diagnostic for temperature in this range. We identified three sources with these key features, and we determined approximate spectral types for each source by comparing our spectra to the standard stars of Torres-Dodgen & Weaver (1993) and Allen & Strom (1995).

All three of the A-F stars that we observed are faint ($K \sim$11-12) and reddened to varying degrees ($J - K \sim 0.8$ for 2M04321713+2421556 and $J - K \sim 1.4$ for the other two stars). Assuming their dereddened colors are $J - K \sim 0.0$, these colors suggest extinctions of $A_K \sim 0.5$ and $A_K \sim 1.0$, respectively, according the reddening law of Schlegel et al. (1997). The corresponding dereddened apparent magnitudes are far too faint ($K > 10$) to denote association members, suggesting that these stars are located beyond the association at a distance of $\sim$1 kpc.

We also identified two additional candidates, 2M16204196-2426149 and 2M16213638-2355238, that also appear to be reddened dwarfs. The Ca II infrared triplet is clearly detected for the former, but there is no convincing evidence of the Paschen series or TiO absorption bands, suggesting that it has a spectral type between early G and mid K. As we will describe in the next subsection, background giants possess a significant CN band at 7900A that this star appears to lack, suggesting that it is a dwarf. The spectral type of 2M16213638-2355238 is more difficult to assess due to the higher noise, but the absence of the TiO absorption bands suggests a spectral type of <M0.

Like the A-F stars, these candidate companions are faint and reddened ($K = 11.5$ to 12.5, $J - K \sim 1.4$, $H - K \sim 0.35$). If they have the dereddened colors of a G-K star ($J - K \sim 0.5$, $H - K \sim 0.1$; Bessell & Brett 1988), then these colors suggest an extinction of $A_K \sim$0.6 and corresponding dereddened apparent magnitudes of $K \sim$11 to 12. This flux is far too faint to identify either source as a G-K type Upper Sco

member, but is approximately consistent with a dwarf at a distance of $\sim$200-500 pc. This interpretation would normally be suspect for an object located behind Upper Sco since most of the interstellar material in the region has been dispersed, but both of these objects are located close to the edge of Ophiuchus, so the presence of interstellar material is not surprising. For example, Bouy et al.(2007) noted that extinction is locally higher along the line of sight to DENIS162041.5-242549.0 ($A_V = 3.3$ or $A_K \sim 0.3$).

Finally, 2M16182365-2338268 appears to be a K dwarf in the background of the association; the absence of TiO absorption at 6700 angstroms and the CaII infrared triplet at 8500 angstroms suggest that the spectral type is not >K7 or <K0, and the shape of the continuum indicates moderate reddening that would not occur if it were in the foreground. As in the previous cases, it is faint and red ($K = 12.25$, $J-K = 1.31$, $H-K = 0.34$). If its intrinsic colors are $J-K = 0.6$ and $H-K = 0.12$, then the apparent colors suggest an extinction of $A_V \sim$4 and a dereddened apparent magnitude of $K \sim 11.8$. This flux places the candidate well below the association sequence, but is consistent with a K5V star at a distance of $\sim$300 pc.

The presence of moderate $H\alpha$ emission makes this identification somewhat arguable since $H\alpha$ emission is a key indicator of accretion (and youth). However, it could also indicate the presence of an (unresolved) active M dwarf companion, so it is not conclusive by itself. As we will describe in Section 4.7.3, this candidate's relative proper motion is also inconsistent with comovement, which supports the spectroscopic identification of this candidate as a nonmember.

4.7.1.2 Background Giants

Background giants can also be easily identified, most readily by the presence of a broad CN absorption band at 7900 angstroms. It has long been known (e.g., White & Wing 1978; MacConnell et al. 1992; Torres-Dodgen & Weaver 1993) that this CN band is extremely sensitive to luminosity class: very deep for supergiants, shallow for giants, and completely absent for dwarfs. This result suggests that any source with detectable CN absorption is a luminous, distant background giant rather than
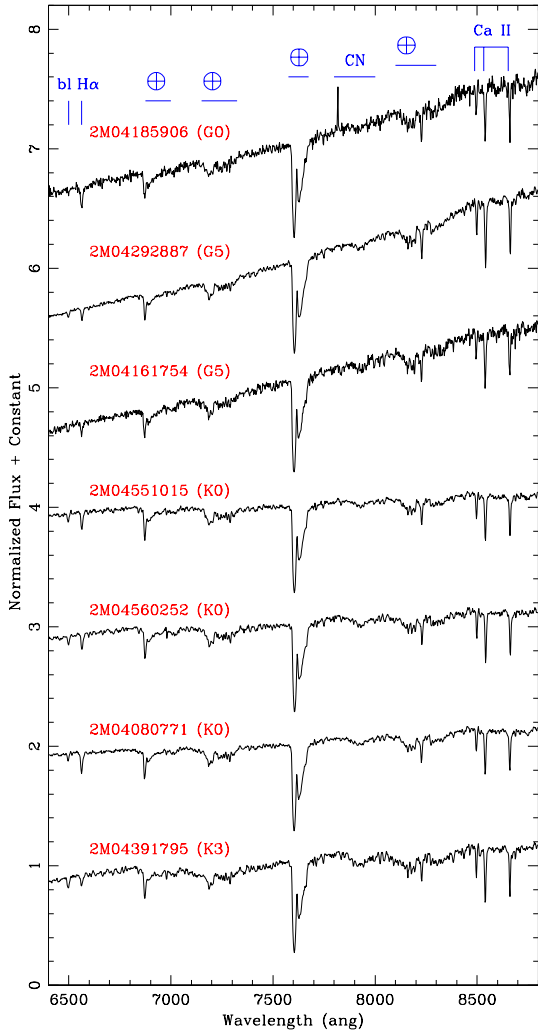
Figure 4.9 Eight field giants that are located behind Taurus or Upper Sco. All spectra show absorption from the CN band at 7900 angstroms and deep, narrow absorption lines in the CaII infrared triplet, indicating that the sources are giants. Given their brightness, all are located behind the associations, consistent with the significant reddening seen for several of them. The approximate spectral type has been estimated based on the ratio of line strengths for Hα and the blend of several metal lines at 6497 Å (denoted bl). All relevant spectral features and atmospheric absorption bands have been labeled.

an association member. The depth of the CN band has been characterized via the narrowband photometric system first described by Wing (1971), but that system is calibrated using fluxes beyond the red limit of our spectra, so we could not implement it without significant modification. Our only goal is to identify background giants and remove them from further consideration, so we opted simply to identify the presence of CN absorption by visual inspection. The deep, narrow absorption lines in the CaII infrared triplet also support our identifications.

There are few spectral type indicators in this wavelength range for G-K stars, and most are poorly calibrated, but we have used them to assess approximate spectral types with respect to the standard stars of Torres-Dodgen & Weaver (1993) and Allen & Strom (1995). We can rule out spectral types of $\geq$K4 for all of these stars since TiO absorption appears and grows with decreasing temperature. The relative depths of Hα and the metal blend at 6497 angstroms gradually change across the G and K spectral types, with the blend appearing at $\sim$G0 and equaling the depth of Hα at K3, so we used their relative depths to assess stars as spectral type G0, G5, K0, or K3. Residual absorption in the Paschen-14 line can also persist as late as $\sim$G5, which also helped us to distinguish between G giants and K giants.

4.7.1.3   Young Stars

Stellar youth is most commonly inferred from three major classes of spectroscopic features: accretion signatures like Hα, HeI, and CaII emission, low-gravity diagnostics like shallow absorption from the Na-8189 doublet, or lithium absorption at 6708A. The spectral resolution of our observations ($R \sim$1200) can detect lithium only at very high S/N. Surface gravity can be assessed for stars later than M1 by the depth of the Na-8189 doublet, but all of the standard gravity indicators for G-K stars have wavelengths shorter than the blue limit of our spectra, so for G-K stars, our only option is to search for accretion signatures. We identified one G-K star based on its accretion and 7 M stars based on their surface gravity.

The optical classification of M stars is very straightforward due to their numerous and distinct molecular bands. Across the wavelength range of our spectra, early
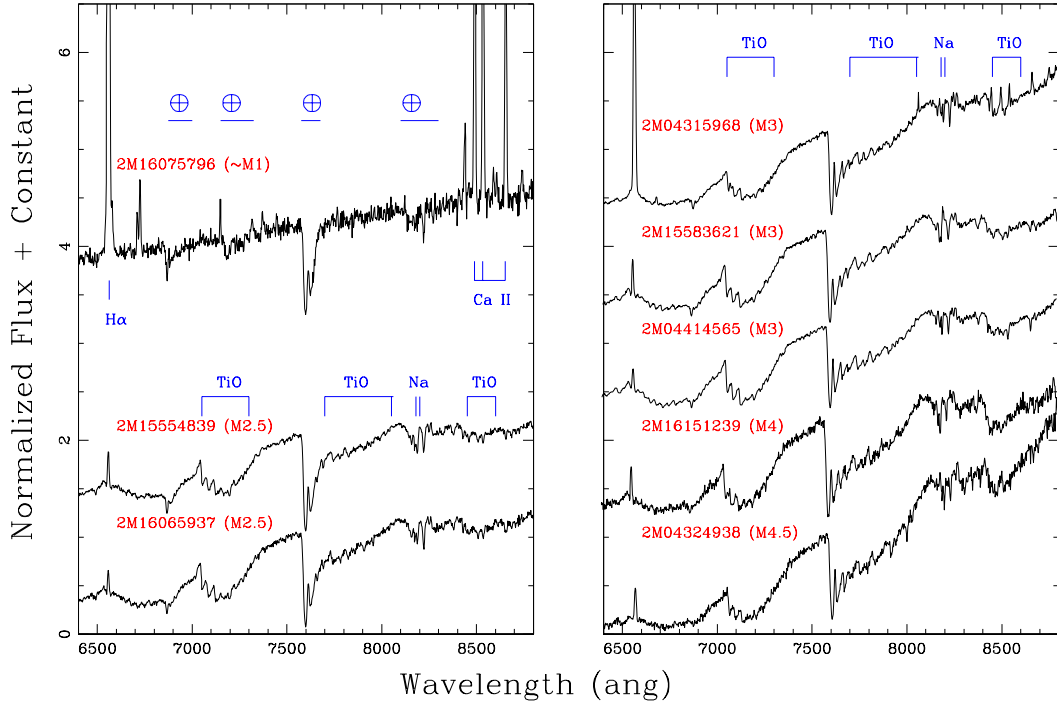
Figure 4.10 Spectra for eight new association members. One star in Upper Sco (2M16075796; top left) shows extremely strong emission at Hα and Ca II, consistent with strong accretion. The other seven stars are M dwarfs with low surface gravity (as measured from the Na-8189 doublet), which indicates that these stars have not yet contracted to the zero-age main sequence. All strong spectral features and atmospheric absorption bands have been labeled. We find that 2M16075796 also has numerous emission lines which are usually associated with accretion-driven jets: [N II] 6584, [S II] 6717/6731, [Fe II] 7155, [Ca II] 7323, [Ni II] 7378, OI 8446, and the Paschen series.

M stars are most distinctly classified by the depth of the TiO bandhead at 7050 angstroms, while mid-M stars are more distinctively classified by the depth of the TiO bandhead at 8500 angstroms. We have assessed all spectral types using the spectral indices TiO_{7140} and TiO_{8465} (Slesnick et al. 2006a), supported by a visual inspection of each spectrum. We adopted our spectral standards from a list originally observed by Slesnick et al.(2006a, 2006b) using DBSP with identical instrument settings. We assessed the surface gravity using the Na_{8189} index developed by Slesnick et al.(2006a), confirming that each source was young by comparing its TiO_{7140} and Na_{8189} indices to the dwarf, young star, and giant results that they reported for their survey. As we show in Figure 4.10, qualitative inspection of the Na-8189 doublet for all seven M stars in our sample indicated that it was shallower than the field, but roughly similar to known members of Taurus or Upper Sco.

The other young star in our optical spectroscopy sample, 2M16075796-204087, is easily identified by the obvious presence of accretion signatures; as we demonstrate in Figure 4.10, it shows tremendous Hα emission ($EW = -357$ angstroms) and significant emission from HeI (-15.34 angstroms) and the CaII infrared triplet (-30.0, -31.8, and -25.4 angstroms at 8500, 8542, and 8664 angstroms). The absence of absorption features makes it impossible to place an early limit on the star's spectral type. Its J band magnitude ($J = 11.06$), which should be least affected by optical veiling or NIR disk emission, is roughly consistent with other M0-M2 members, so we have assigned a preliminary spectral type of M1.

4.7.2   Near-Infrared Spectroscopy

K-band spectra include several key features that are useful for stellar classification (e.g., Slesnick et al. 2004). The Brγ absorption line at 2.166 μm is ubiquitous for all stars with spectral types earlier than K, but disappears entirely by mid-K. Conversely, the CO absorption bandheads at $\geq$2.3 μm are present (with similar depths) for all late-type stars, but they start to weaken at mid-K and disappear entirely for stars earlier than late-G. Both Brγ and the CO bandheads can also appear in emission for
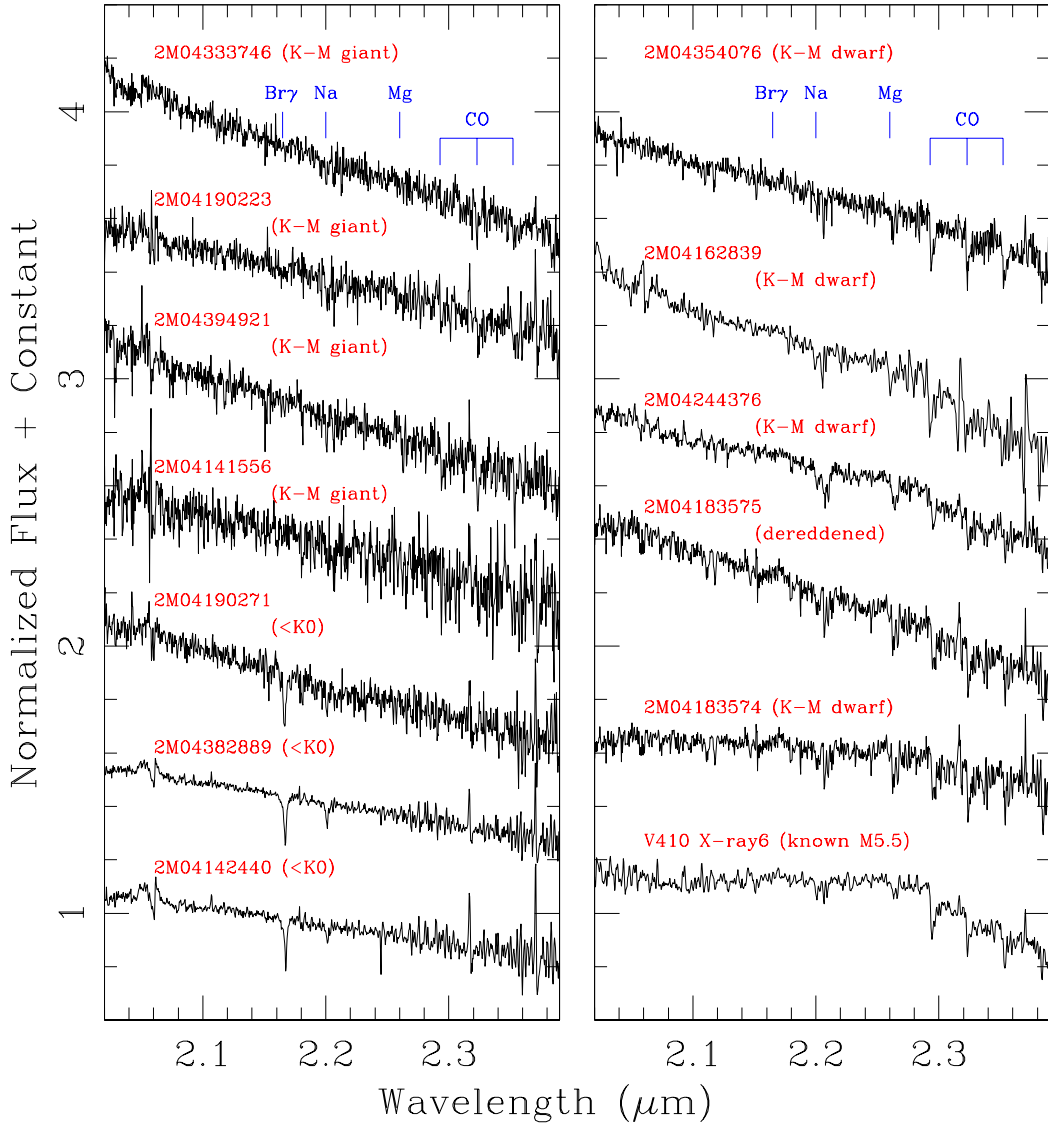
Figure 4.11 K-band spectra for 11 candidate companions and one known Taurus member (V410 X-ray6; M5.5). The three companions in the bottom left all possess significant Brγ absorption, which indicates that the sources are background early-type stars. The rest of the candidates appear to be field K-M stars, divided between dwarfs and giants. All relevant spectral features have been labeled.

young stars. A broad steam absorption band at <2 μm is also a key indicator for identifying M stars with low S/N spectra since it grows with decreasing temperature, though its depth is gravity sensitive; at a given spectral type, it is deeper for dwarfs than for giants. The depths of the Na and Mg doublets (at 2.2 and 2.26 μm) are also useful for distinguishing the luminosity classes of stars because they increase with surface gravity, though the identification requires good S/N. Finally, our efforts are aided significantly by the faintness of our targets; any candidates with spectral types earlier than mid-M must fall significantly below the association sequence on an HR diagram.

We plot all of our K-band spectra in Figure 4.11, including a spectrum of the known member V410 X-ray 6 (M5.5) to demonstrate the expected morphology for young low-mass stars or brown dwarfs. Three of our candidate companions show clear Brγ absorption, indicating that the sources are background stars with early spectral types ($<$K0). The other 8 targets all show some degree of absorption in the CO bandheads, indicating spectral types of K-M. However, seven of these targets clearly show no evidence of steam absorption, indicating that the sources are either background K-M giants or dwarfs with spectral types $<$M1. In either case, all sources are too faint for their dereddened magnitudes to fall along the Taurus sequence, so we have divided them into giants or dwarfs based on the strength of their Na and Mg doublets. These classifications are preliminary due to the low S/N of many spectra, but they are sufficient to rule out the possibility of membership.

The eighth K-M star (2M04183574+2830254, the neighbor of V410 X-ray 2) is significantly reddened, which complicates its classification. Its NIR colors ($J-K=4$, $H-K=1.5$) suggest a visual extinction of $A_V \sim 20$ (matching the value for V410 X-ray 2 itself, based on its 2MASS colors), so we removed this effect with the IRAF task deredden. As we show in Figure 4.11, the dereddened spectrum possesses significant Na and Mg absorption, but no steam absorption, suggesting that it is a field dwarf with spectral type $<$M1 and that it is located behind the material that obscures V410 X-ray 2.

4.7.3   Astrometry

The other standard method for confirming candidate binary companions is to test for common proper motion. This test is less useful for young stars because other (gravitationally unbound) association members are also comoving to within the limits of our observational uncertainties. However, proper motion analysis can still be used to eliminate foreground and background stars that coincidentally fall along the association color-magnitude sequence but possess distinct kinematics.

In Table 4.13, we list the relative astrometric measurements for each candidate binary pair that we obtained from the literature and from our observations. We computed relative proper motions by using a weighted least squares fit to determine the relative motion in each dimension, rejecting the worst-fitting measurement if it differed from the fit by more than 3σ (where σ is the observational error, not the dispersion in the fit). A cutoff of 3σ in a bivariate normal distribution corresponds to a confidence level of $\sim$99%, so we do not expect many valid measurements to be flagged. We did not reject multiple measurements that differ by $>3\sigma$ because the high scatter could indicate an astrophysical source for the poor astrometric fit (such as further unresolved multiplicity).

In Table 4.14, we list the proper motions that we derived for each candidate companion. In Figure 4.12, we plot the relative proper motion of each candidate companion with respect to its corresponding known association member. For each association, there are two major concentrations: one group centered on the origin, corresponding to comoving young association members, and one group centered on the inverse proper motion for that association, corresponding to nonmoving background stars. There are also several objects which fall outside both concentrations, which could correspond to either independently moving field dwarfs or objects with erroneous astrometry. We also specifically mark those objects which were spectroscopically confirmed to be members or nonmembers; all 5 spectroscopic members and only 1 of 9 confirmed nonmembers fall in the cluster of sources centered on the origin ($\Delta\mu$<12 mas yr^{-1}).

We find that 7 of the 15 candidates without spectra fall inside this limit, which suggests that no more than $\sim$1 of them is also comoving by chance. We therefore treat all candidates which are comoving to $<$12 mas yr^{-1} as likely companions and all other candidates as likely contaminants. We have opted not to use more rigorous selection criteria (based on our formal uncertainties) because the distribution of likely members seems too large for our uncertainties to be accurate, even among our spectroscopically confirmed subsample alone. Given the many astrophysical and observational sources of systematic uncertainty that can influence high-precision astrometry, all of our proper motion uncertainties are probably underestimated by a factor of $\sim$2 (the multiplier needed to bring our uncertainties in line with the observed scatter).

We list all of our membership assessments in Table 4.15, denoting likely companions and likely contaminants with "Y?" and "N?", respectively. Spectroscopic membership analysis should generally supercede these determinations, and given the value of directly determining a companion's stellar properties, follow-up observations for all of these likely companions should be a high priority. However, the existing data should suffice for studying the bulk properties of our sample.

Table 4.13.   Astrometric Data

Known Member	Candidate Companion	Epoch (JD-2450000)	Sep (mas)	PA (deg)	Ref
		New			
2M040807.82+280728.0	2M040807.71+280737.3	54069	9508±15	351.15±0.02	Keck-NGS
DG Tau	2M042703.70+260606.7	54434	16322±29	235.35±0.11	Palomar-NGS
GSC 06213-00306	GSC 06213-00306 B	54187	3213±2	306.3±0.02	Keck-NGS
GSC 06784-00997	2M161018.88-250232.5	54188	4896±2	241.24±0.02	Keck-NGS
GSC 06785-00476	2M154107.26-265625.4	54198	6270±10	82.65±0.1	Palomar-NGS
RXJ 1555.8-2512-n	2M155548.39-251217.4	54198	8877±14	319.73±0.1	Palomar-NGS
RXJ 1555.8-2512-f	2M155547.88-251217.2	54198	14524±23	299.27±0.1	Palomar-NGS
SCH161511.15-242015.56	2M161512.39-242009.1	54188	17885±22	70.24±0.07	Keck-LGS
SCH161825.01-233810.68	2M161823.65-233826.8	54199	24510±50	229.87±0.12	Palomar-Seeing
USco80	2M155836.21-234801.8	54188	12274±23	15.59±0.04	Keck-LGS
		Archival			
2M04080782+2807280	2M04080771+2807373	50781	9432±70	351.0±0.4	2MASS H
2M04080782+2807280	2M04080771+2807373	50781	9420±70	350.7±0.4	2MASS J
2M04080782+2807280	2M04080771+2807373	50781	9416±70	351.7±0.4	2MASS K
2M04080782+2807280	2M04080771+2807373	35403	7850±200	353.2±1.5	USNOB B1
2M04080782+2807280	2M04080771+2807373	48896	8620±200	351.0±1.3	USNOB B2
2M04161885+2752155	2M04161754+2751534	50782	28063±70	218.3±0.1	2MASS H
2M04161885+2752155	2M04161754+2751534	50782	28033±70	218.3±0.1	2MASS J
2M04161885+2752155	2M04161754+2751534	48896	27760±200	217.5±0.4	USNOB B2
2M04161885+2752155	2M04161754+2751534	50337	27970±200	218.7±0.4	USNOB I2
2M04161885+2752155	2M04161754+2751534	35403	28630±200	215.9±0.4	USNOB R1
2M04161885+2752155	2M04161754+2751534	47827	28000±200	218.3±0.4	USNOB R2

Note. — The full version of this table will be available in the online version of ApJ.

Table 4.14.   Companion Kinematics

Known Member	Candidate Companion	Relative Motion μ_α	μ_δ	σ_μ (mas yr^{-1})
2M040807.82+280728.0	2M040807.71+280737.3	-7	24	3
2M041618.85+275215.5	2M041617.54+275153.4	-15	27	5
2M042134.60+270138.8	2M042133.31+270137.5	6	17	4
CFHT-Tau-21	2M042217.57+265436.4	-11	5	3
CFHT-Tau-7	JH90	-4	20	4
DG Tau	2M042703.70+260606.7	2	22	5
FO Tau	2M043828.89+261117.8	-44	98	5
FW Tau	2M042928.87+261648.3	-2	28	3
GM Aur	2M045510.15+302133.3	-2	25	3
HBC 427	2M045602.52+302050.3	58	-83	5
I04385+2550	2M044138.42+255644.8	8	23	4
IS Tau	2M043334.67+260944.7	-10	33	4
V710 Tau AB	2M043159.68+182130.5	-1	8	3
GSC 06213-00306	GSC 06213-00306 B	0	8	5
GSC 06784-00997	2M161018.88-250232.5	-4	10	5
GSC 06785-00476	2M154107.26-265625.4	0	-12	4
RXJ 1555.8-2512	2M155547.88-251217.2	16	19	5
RXJ 1555.8-2512	2M155548.39-251217.4	6	11	5
RXJ 1558.8-2512	2M155854.15-251240.7	10	19	3
RXJ 1602.8-2401B	2M160251.16-240150.2	11	3	5
SCH160758.50-203948.90	2M160756.93-203942.4	19	21	4
SCH161511.15-242015.56	2M161512.39-242009.1	-4	-2	4
SCH161825.01-233810.68	2M161823.65-233826.8	-6	43	5
ScoPMS042b	2M161021.77-190402.1	2.7	0.5	1
ScoPMS048	ScoPMS 048 B	-2	3.9	0.8
UScoJ160245.4-193037	2M160247.35-193029.4	55	-2	4
UScoJ160700.1-203309	2M160659.37-203304.7	-5	3	3
UScoJ160936.5-184800	2M160936.58-184740.9	29	13	3
UScoJ161031.9-191305	2M161032.32-191308.5	-9	-5	5
USco80	2M155836.21-234801.8	1	0	3
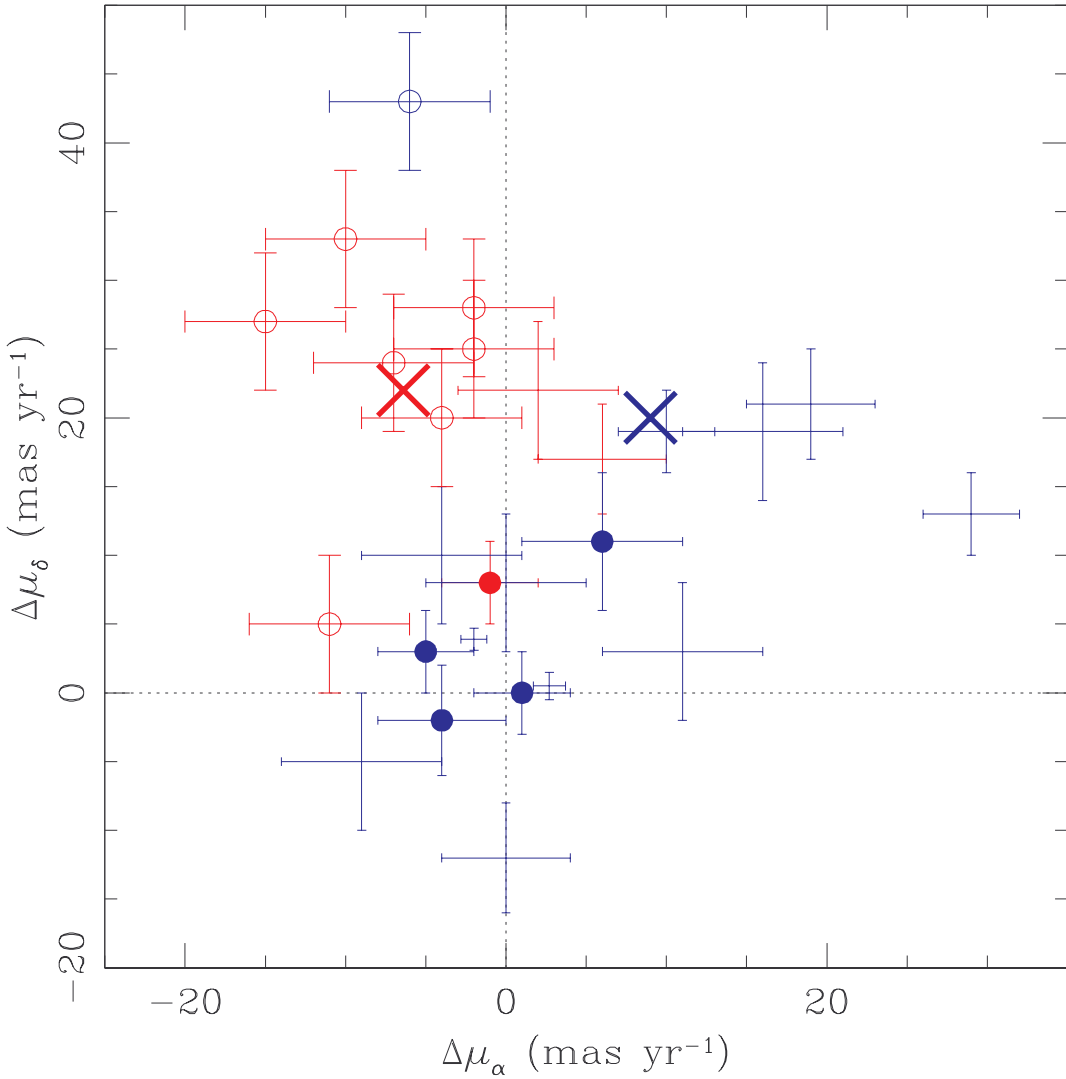
Figure 4.12 Relative proper motions of each candidate companion with respect to the known association member. Red=Taurus, Blue=USco. The crosses shown the expected motion (in each association) for a wide neighbor which is actually a nonmoving background stars; each set of association members shows a concentration around this reflex motion (denoting nonmoving background stars) and a concentration around the origin (denoting comoving association members). We denote spectroscopically-confirmed members with filled circles and nonmembers with open circles, leaving only error bars for candidates without spectroscopy; we find general agreement between the two methods, with only one spectroscopic nonmember in the overall distribution of members. This suggests that astrometric confirmation is generally sufficient for our purpose, though follow-up spectroscopy is very valuable for determining stellar properties.

Table 4.15.   Status Determinations

Known Member	Candidate Companion	Spectroscopic Determination	Astrometric Determination	Final Determination	Spectral Class	EW(Hα)
$\Delta K <3$						
2M04080771+2807373	2M040807.82+280728.0	N	N?	N	K0 III	2.1
2M04161754+2751534	2M041618.85+275215.5	N	N?	N	G5 III	1.6
2M04213331+2701375	2M042134.60+270138.8	..	N?	N	..	..
2M04414565+2301580	2M044144.89+230151.3	Y	.	Y	M3	-5.7
2M04221757+2654364	CFHT-Tau-21	N	Y?	N	A5	4.8
2M04321713+2421556	CFHT-Tau-7	N	N?	N	F5	5.5
2M04292887+2616483	FW Tau	N	N?	N	G5 III	1.5
2M04551015+3021333	GM Aur	N	N?	N	K0 III	1.8
2M04560252+3020503	HBC 427	N	N?	N	K0 III	1.7
2M04185906+2812456	I04158+2805	N	..	N	G0 III	3
2M04413842+2556448	I04385+2550	..	N?	N	..	..
2M04324938+2253082	JH 112	Y	..	Y	M4.5	-22
2M04391795+2221310	LkCa 15	N	..	N	K3 III	1.3
2M04175109+2829157	V410 X-ray1	N	..	N	A0	9.8
2M04315968+1821305	V710 Tau AB	Y	Y?	Y	M3	-120
2M16204196-2426149	DENIS162041.5-242549.0	N	..	N	G-K V	1.6
GSC 06213-00306 B	GSC 06213-00306	..	Y?	Y	..	..
2M16101888-2502325	GSC 06784-00997	..	Y?	Y	..	..
2M15410726-2656254	GSC 06785-00476	..	Y?	Y	..	..
2M15554839-2512174	RXJ 1555.8-2512	Y	Y?	Y	M2.5	-6.6
2M15585415-2512407	RXJ 1558.8-2512	..	N?	N	..	..
2M16025116-2401502	RXJ 1602.8-2401B	..	Y?	Y	..	..
2M16075693-2039424	SCH160758.50-203948.90	..	N?	N	..	..
2M16075796-2040087	SCH160758.50-203948.90	Y	..	Y	~M1	..
2M16151239-2420091	SCH161511.15-242015.56	Y	Y?	Y	M4	-14.8
2M16182365-2338268	SCH161825.01-233810.68	N?	N?	N	K V	-6.9
2M16213638-2355283	SCH162135.91-235503.41	N	..	N	G-K V	..
2M16102177-1904021	ScoPMS042b	..	Y?	Y	..	..
ScoPMS 048 B	ScoPMS048	..	Y?	Y	..	..
2M16024735-1930294	UScoJ160245.4-193037	..	N?	N	..	..
2M16065937-2033047	UScoJ160700.1-203309	Y	Y?	Y	M2.5	-5.9
2M16093658-1847409	UScoJ160936.5-184800	..	N?	N	..	..
2M15583621-2348018	USco80	Y	Y?	Y	M3	-9.9
$\Delta K >3$						
2M04394921+2601479	CFHT 4	N	..	N	K-M III	..
2M04354076+2411211	CoKu Tau/3	N	..	N	K-M V	..
2M04270370+2606067	DG Tau	..	N?	N	..	..
2M04382889+2611178	DO Tau	N	..	N	<K	..
2M04141556+2812484	FM Tau	N	..	N	K-M V	..
2M04144741+2812219	FO Tau	..	N?	N	..	..
2M04244376+2610398	I04216+2603	N	..	N	K-M V	..
2M04333746+2609550	IS Tau	N	..	N	K-M III	..
2M04333467+2609447	IS Tau	..	N?	N	..	..
2M04162839+2807278	LkCa 4	N	..	N	K-M III	..
2M04142440+2805596	MHO-Tau-2	N	..	N	<K	..
2M04183574+2830254	V410 X-ray 2	N	..	N	K-M V	..
2M04190271+2822421	V410 X-ray 5a	N	..	N	<K	..
2M04190223+2820039	X410 X-ray 6	N	..	N	K-M III	..
2M16084438-2602139	GSC 06784-00039	..	..	..	..	..
2M15554788-2512172	RXJ 1555.8-2512	..	N?	N	..	..

Table 4.15 (cont'd)

Known Member	Candidate Companion	Spectroscopic Determination	Astrometric Determination	Final Determination	Spectral Class	EW(Hα)
2M16103232-1913085	UScoJ161031.9-191305	..	Y?	Y	..	..

4.7.4 Association Members and Background Stars

In Table 4.15, we summarize our spectroscopic and astrometric membership assessments for each candidate young stars in our sample, along with the final membership assessments that we will use in our subsequent statistical arguments. We found that 11 of the 18 USco candidates and 3 of the 15 Taurus candidates with separations of 3-30″ and flux ratios ΔK <3 are comoving young stars, while most of the candidates that we considered with more extreme flux ratios are not associated. We were not able to test the association of one USco candidates with a larger flux ratio, and even though another appears comoving, its faintness and the high density of stars in the direction of Upper Sco (and thus the bulge) suggests that cutting our statistical analysis at ΔK <3 would be prudent.

The total number of confirmed background stars (28 in Taurus and 8-9 in Upper Sco) is consistent within <2σ with the number that we projected in our original survey (36±6 and 16±4). In Table 4.16, we list the stellar properties for each pair of newly-confirmed young stars, plus all of the pairs listed in Table 4.17; we derived these properties using the methods described in Section 4.6.4. The mass ratios for hierarchical triple systems were computed by summing all sub-components within each member of the wide pair.

4.8 The Properties of Wide Binary Systems

In the following subsections, we explore the implications of our survey of wide (3-30″) multiplicity. In Section 4.8.1, we examine the mass-dependent frequency of wide binary systems for each association and discuss the differences between Taurus and Upper Sco. In Sections 4.8.2 and 4.8.3, we examine the mass ratio distributions

Table 4.16.   Binary Properties

Primary	Secondary	M_{prim} $(M_\odot)$	M_{sec} $(M_\odot)$	q^{a} (M_s/M_p)	r (AU)
Known					
2M04554757+3028077	2M04554801+3028050	0.20	0.14	0.70	915
DH Tau	DI Tau	0.64+0.044	0.64+(0.08)	1.06	2208
FS Tau	Haro 6-5B	0.64+0.33	0.82	0.85	2883
FV Tau	FV Tau/c	0.82+(0.62)	0.45+0.33	0.54	1782
FZ Tau	FY Tau	0.72	0.64	0.89	2490
GG Tau Aab	GG Tau Bab	0.72+0.60	0.14+0.044	0.14	1505
GK Tau	GI Tau	0.72+(0.027)	0.82	1.09	1905
HBC 352	HBC 353	2.26	0.94	0.42	1301
HBC 355	HBC 354	1.2	1.2	1.00	915
HN Tau A	HN Tau B	0.82	0.22	0.27	450
HP Tau-G2	HP Tau	2.49	0.94	0.38	3089
HP Tau-G2	HP Tau-G3	2.49	0.72+(0.10)	0.33	1463
HV Tau AB	HV Tau C	0.50+(0.31)	0.77	0.95	545
J1-4872 Aab	J1-4872 Bab	0.64+0.64	0.57+0.57	0.89	490
LkHa332-G1	LkHa332-G2	0.57+(0.57)	0.60+0.45	0.92	3753
MHO-Tau-1	MHO-Tau-2	0.45	0.45	1.00	570
UX Tau AC	UX Tau Bab	1.20+0.40	0.50+(0.40)	0.56	849
UZ Tau Aab	UZ Tau Bab	0.57+(0.16)	0.50+0.40	1.23	516
V710 Tau A	V710 Tau B	0.60	0.50	0.83	439
V773 Tau	2MASSJ041411.88+281153.5	1.20+0.94+0.60+(0.58)	0.09	0.027	3390
V807 Tau	GH Tau	0.82+0.50+(0.50)	0.50+0.50	0.55	3157
V928 Tau	CFHT-Tau-7	0.60+(0.60)	0.12	0.10	2646
V955 Tau	LkHa332-G2	0.74+0.45	0.60+0.45	0.88	1524
XZ Tau	HL Tau	0.50+0.33	0.82	0.99	3380
RXJ1558.1-2405A	RXJ1558.1-2405B	0.95+(0.14)	0.13+(0.03)	0.15	2632
RXJ1604.3-2130A	RXJ1604.3-2130B	1.12	0.49+(0.36)	0.76	2352
ScoPMS 052	RXJ1612.6-1859	1.35+0.49	0.60	0.33	2764
UScoJ160428.4-190441	UScoJ160428.0-19434	0.36+(0.36)	0.24	0.33	1417
UScoJ160611.9-193532 A	UScoJ160611.9-193532 B	0.13+0.13	0.13	0.50	1563
UScoJ160707.7-192715	UScoJ160708.7-192733	0.49+(0.08)	0.24	0.42	3400
UScoJ160822.4-193004	UScoJ160823.2-193001	0.60	0.68	1.13	1953
UScoJ160900.7-190852	UScoJ160900.0-190836	0.68	0.13	0.19	2743
UScoJ161010.4-194539	UScoJ161011.0-194603	0.36	0.13	0.36	3711
New					
2M04414565+2301580 A[b]	2M04414565+2301580 B	0.40	0.027	0.07	1794
JH112 A	JH112 B	0.72	0.22	0.31	951
V710 Tau AB	V710 Tau C	0.60+0.50	0.40	0.36	4056
GSC06213-00306 A	GSC06213-00306 B	1.43+1.43	(0.61)	0.21	461
GSC 06785-00476 A	GSC 06785-00476 B	1.51	(0.20)	0.13	914
GSC 06784-00997 A	GSC 06784-00997 B	0.60	(0.05)	0.09	697
RXJ1555.8-2512 A	RXJ1555.8-2512 B	1.65	0.43	0.26	1292
RXJ1602.8-2401B	RXJ1602.8-2401B	0.95	(0.11)	0.12	1047
2M16075796-2040087 A[b]	2M16075796-2040087 B	0.7	0.074	0.10	3120
2M16151239-2420091 A[b]	2M16151239-2420091 B	0.24	0.074	0.31	2604
ScoPMS042b A	ScoPMS042b B	0.36	(0.05)	0.14	664
ScoPMS048 A	ScoPMS048 B	1.12+0.24	(1.06)	0.78	442
2M16065937-2033047 A[b]	2M16065937-2033047 B	0.49	0.43	0.88	1689
UScoJ161031.9-191305 A	UScoJ161031.9-191305 B	0.77	(0.033)	0.043	828
USco80 Aab[b]	USco80 B	0.36+(0.36)	0.24	0.33	1779

Note. — Masses for all members with known spectral types were estimated using the mass-SpT relations described in Section 4.6.5, while masses in parentheses (for sources without spectral types) were estimated using the estimated mass of the system primary and the measured flux ratio. The references for these flux ratios are listed in Tables 4.8 and 4.10. Our model-dependent masses are uncertain to ∼20%, and the mass ratios and projected separations have typical uncertainties of ∼10%. Finally, some hierarchical multiple systems have mass ratios $q >1$, where the combined mass for all components of B is higher than that of A. We preserve the existing naming scheme for continuity, but will invert this mass ratio during our analysis (Section 4.8) to reflect that B is the most massive component.

[a]For hierarchical multiple systems, we computed the mass ratio by summing the individual stellar masses in all sub-components of the wide "primary" and "secondary."

[b]Several newly-identified companions appear to be more massive than the known member, suggesting that the known member is the binary secondary. In cases where the known member had a generic name (i.e., USco80), we have appropriated that name for the new member to avoid name proliferation in the literature. For systems with coordinate-based names, we have used the 2MASS name of the new member to avoid confusion over coordinates.
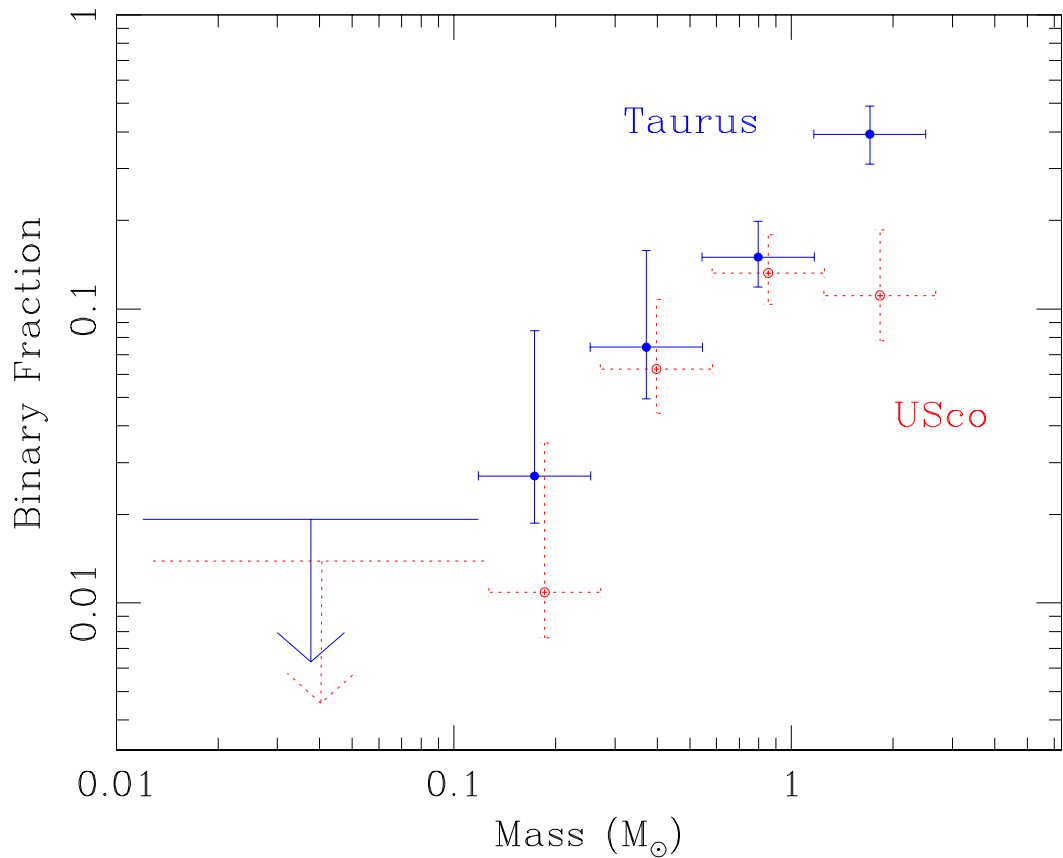
Figure 4.13 Wide binary frequency as a function of primary mass. The overall binary frequency declines with mass, reaching upper limits of ∼1-2% for the substellar regime (M <0.1 $M_\odot$). The binary frequency for high-mass stars (1.15-2.50 $M_\odot$) is significantly higher in Taurus than in Upper Sco, but otherwise, the binary frequencies are not significantly different.
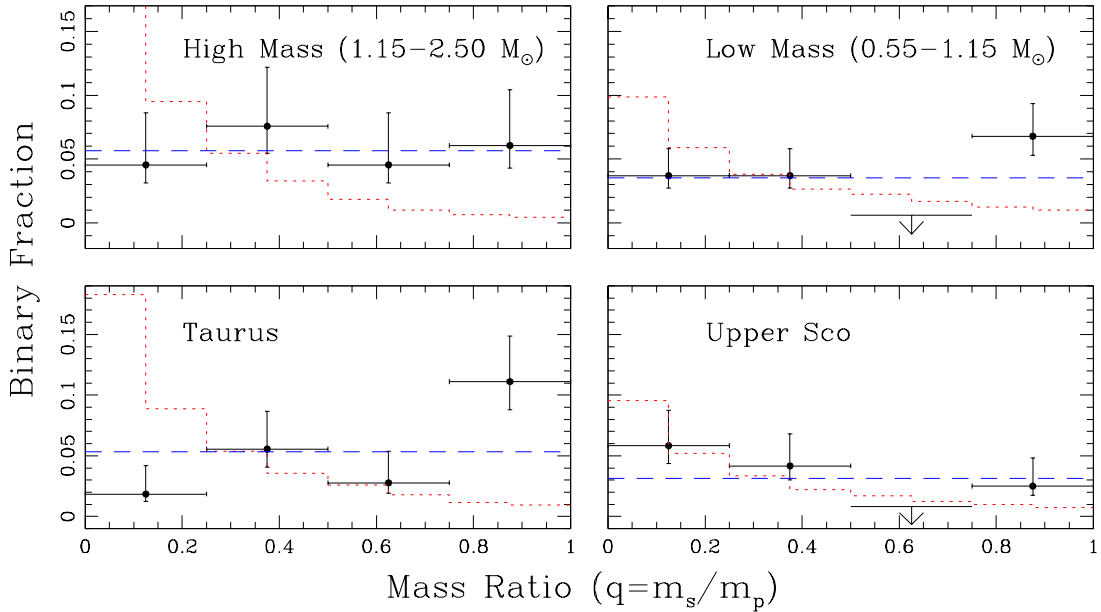
Figure 4.14 Top: Mass ratio distribution for high-mass stars (1.15-2.50 $M_\odot$) and intermediate-mass stars (0.55-1.15 $M_\odot$). Bottom: Mass ratio distribution for Taurus and Upper Sco when the two mass ranges are combined (0.55-2.50 $M_\odot$). The lowest bin is incomplete at $q<0.02$-0.04, but this should not affect our results because companions with such extreme mass ratios do not seem to form often (e.g., Kraus et al. 2008). In each case, we also plot the expected distribution if the companions were drawn randomly from an IMF (red dotted line) or from a constant distribution (blue dashed line) with the same frequency. The IMF does not produce a satisfactory fit for most cases, but a constant distribution does. Finally, we also note that the shape of the IMF distribution varies between subsamples, depending on the masses of the primary stars that make up those subsamples. The first IMF bin for the high-mass subsample is 24%; we truncated the plot at 17% in order to improve resolution for the other bins and the intermediate-mass subsample.
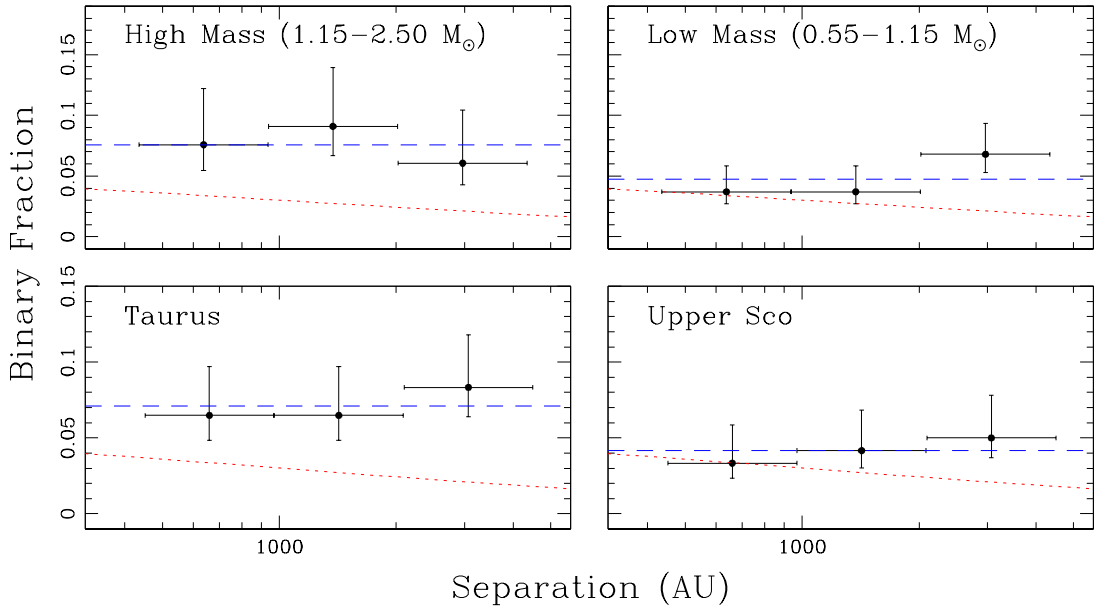
Figure 4.15 Separation distributions for the same four subsamples plotted in Figure 4.14. We also plot the log-normal separation distribution found by DM91 for field solar-mass stars, normalized to the DM91 binary frequency (red dotted line), and a log-constant distribution normalized to the same binary frequency as that subsample (blue dashed line). The DM91 distribution underpredicts the overall binary frequency for high-mass stars and Taurus, and even the expected trend (declining frequency with increasing separation) does not match with the data. The log-constant distribution produces a better fit in all cases. Even if we renormalize the DM91 function to our binary frequency, it still does not fit our intermediate-mass or Upper Sco subsamples.
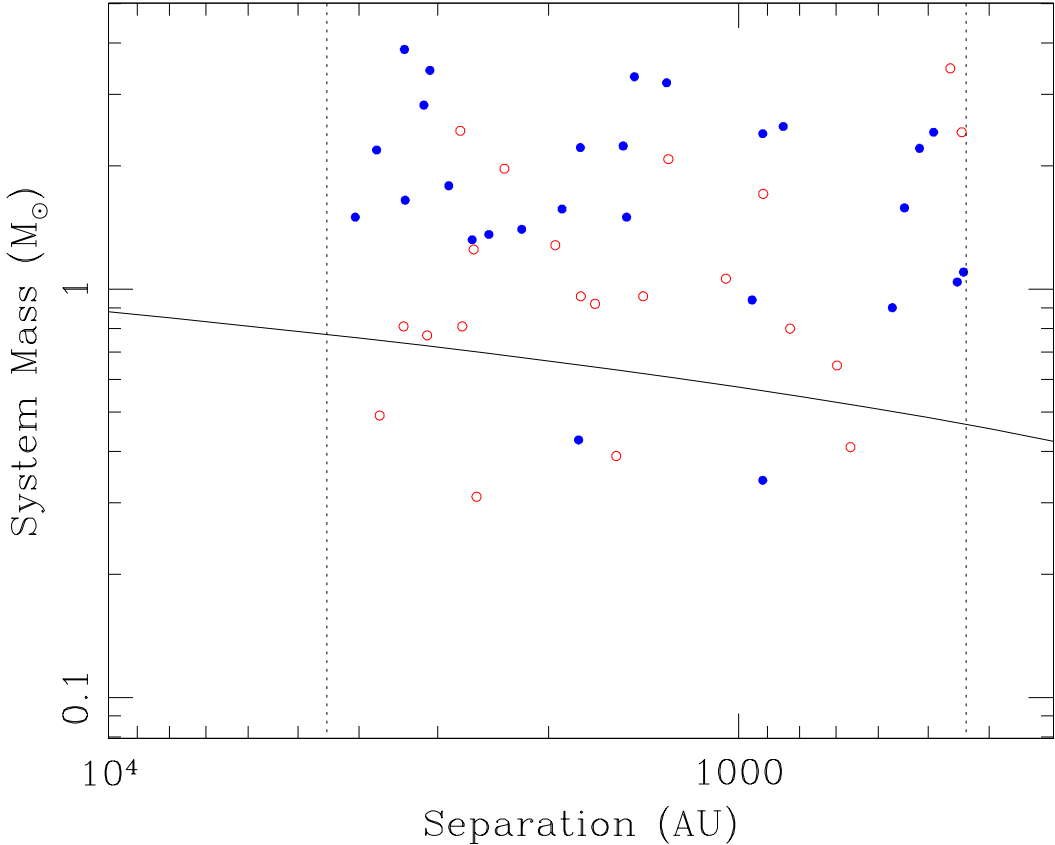
Figure 4.16 Total system mass as a function of separation for all of our wide binary systems in Taurus (blue filled circles) and Upper Sco (red open circles). We also show the empirical "maximum separation limit" observed in the field by Reid et al.(2001) and Burgasser et al.(2003) (solid line) and the separation limits of our survey (dotted lines). Six pairs with masses of >0.3-0.4 $M_{\odot}$ exceed the emperical mass-separation limit, suggesting that it might not be a primordial feature for these higher-mass systems. However, we found no wide binary systems with total masses of <0.3 $M_{\odot}$, suggesting that there is a genuine primordial paucity of wide low-mass systems.

and separation distributions for each association and in two different mass ranges, then compare them to functional forms that might be expected. Finally, in Section 4.8.4, we examine the separation as a function of mass for our new binary systems and compare our sample to the empirical upper limit that has been suggested based on field multiplicity surveys. This discussion is limited to only the spectroscopically and astrometrically confirmed sample since field contamination was significant for the unconfirmed sample. However, the confirmed sample does not include Cha-I or USco-B, so we direct the reader toward our earlier discussion of the unconfirmed sample in Kraus & Hillenbrand (2007).

As we described in our preliminary survey (Section 4.3.3 and Figure 4.2) and in Section 4.6.4, our census of this separation range is complete for all candidate companions brighter than $K = 14.3$ (~ 15 M_{Jup} in Taurus or ~ 20 M_{Jup} in Upper Sco), except for two candidate companions in Upper Sco with $\Delta K > 3.75$ ($q < 0.05$, if they are associated) that we were not able to observe. Our survey also could not reach fainter than $\Delta K \sim 5.5$ at separations of 3-5″ so it is possible that some close candidate companions with extreme mass ratios might have been missed around the highest-mass stars. However, there is only one such companion at separations $>5″$ in Taurus (2M04141188+2811535), which suggests that the probability is low. We note that there is one triple system (the nonhierarchical HP Tau-G2, HP Tau, and HP Tau-G3) where all three components fall in this separation range; we will treat HP Tau and HP Tau-G3 as independent companions to HP Tau-G2 for statistical purposes. There is also a probable triple system (the possibly hierarchical V955 Tau, LkHa332-G1, and LkHa332-G2) where LkHa332-G2 is $\sim 11″$ away from V955 Tau and $\sim 26″$ away from LkHa332-G1, but V955 Tau and LkHa332-G1 are $>30″$ apart. Since all three of these objects have very similar masses (1.05-1.20 $M_\odot$, all being close binary pairs) and it is not clear if the system is truly hierarchical, we will consider this triplet as a closer 11″pair and a wider 26″pair. Finally, for all hierarchical systems, we have treated each component of the wide pair as a single object with the summed mass of all sub-components.

4.8.1 The Mass Dependence of the Wide Binary Frequency

Field surveys have shown that the binary frequency and binary separation distribution both decline with decreasing mass, implying that the wide ($\sim$500-5000 AU) binary frequency should strongly decline over the mass range of our sample. Our preliminary survey paper (KH07a) also found this trend at young ages, suggesting that it is a primordial effect. However, we also found the wide binary frequency for a given mass to be higher in the lowest-density regions, like Taurus and Chamaeleon-I, than in moderately denser regions like Upper Sco.

In Figure 4.13, we plot the mass-dependent binary frequency for four sets of masses in the stellar regime, plus all sources near and below the substellar boundary. The complete sample comprises all of the stars that we considered in our original survey (KH07a), with all confirmed binary systems drawn from Table 4.15 of this work. In both associations, the binary frequency clearly declines over the full mass range; we found frequencies of >10% for stars more massive than $\sim$1 $M_\odot$, declining to upper limits of <1-2% in the substellar regime. This decline appears to be relatively smooth and monotonic in Taurus, but it is unclear whether Upper Sco features a shallower version of the decline or a more abrupt shift from a high value to a low value at $\sim$0.5 $M_\odot$.

The binary frequency is similar across most of the mass range for these two associations. This result differs from our initial statistical sample, but adding additional systems with larger separations or mass ratios drove the two distributions closer together in our updated analysis. However, we have again found a significantly higher binary frequency among the highest-mass stars in Taurus as compared to their counterparts in Upper Sco; this result was the only highly significant difference in our initial analysis, and our updated results find it to be a 4σ effect.

This regional difference among the highest-mass stars is difficult to explain in terms of binary destruction processes. Dynamical disruption (perhaps due to a more crowded natal environment) should preferentially destroy low-mass binaries before high-mass binaries. The similarity between the two environments in the lower-mass

regime seems to rule disruption out. However, it is also possible that the highest-mass stars only form in the densest parts of their natal environment, where binary disruption is significantly enhanced as compared to the sparse outer reaches of a collapsing molecular cloud. High-mass stars are significantly less common than their lower-mass counterparts, so even if these dense central areas also caused the disruption of lower-mass binaries, it might not be strongly reflected in the overall binary population (which could be dominated by a majority of systems that form outside the densest concentrations).

4.8.2   The Mass Ratio Distribution of Wide Binaries

Field surveys have also suggested that the mass ratio distribution varies significantly with primary mass. DM91 found that G dwarfs tend to have lower mass companions (with a modal mass ratio of $q \sim 0.3$), while surveys of M dwarfs by FM92 and RG97 found a flat distribution and several recent surveys of brown dwarfs (e.g. Close et al. 2003; Burgasser et al. 2003; Bouy et al. 2003) found that their mass ratios are sharply peaked toward unity. By contrast, surveys of young associations have found that flat mass ratio distributions seem to dominate across a range of system masses, from ~ 2 $M_\odot$ to at least as low as 0.5 $M_\odot$ (e.g., Kraus et al. 2008 for Upper Sco), though a distribution biased toward unity seems to be universal among the lowest-mass stars and brown dwarfs (Kraus et al. 2006; Ahmic et al. 2007).

In Figure 4.14, we plot the mass ratio distribution for four subsets of our sample. In the top panels, we show the distribution spanning both associations for the highest-mass bin (1.15-2.50 $M_\odot$) as compared to the intermediate-mass bin (0.55-1.15 $M_\odot$), while in the bottom panels, we show the distribution for both mass bins as determined individually in Taurus and Upper Sco. We also show two possible mass ratio distributions: a flat distribution and a distribution where companions are randomly drawn from the IMF. We adopted our IMF from the spectroscopic membership surveys of Upper Sco by Preibisch et al.(1998, 2002) and Slesnick et al.(2006a); this function is defined as a broken power law (Scalo 1998; Kroupa 2002): $\Psi(M) = dN/dM \propto M^{-\alpha}$,

where $\alpha = -2.8$ for $0.6 < M < 2.5$ $M_\odot$, $\alpha = -0.9$ for $0.15 < M < 0.6$ $M_\odot$, and $\alpha = -0.6$ for $0.02 < M < 0.15$ $M_\odot$. This broken power law mass function is rougly equivalent to the continuous log-normal mass function that has also been suggested (Miller & Scalo 1979; Chabrier 2001). Several other possible mass ratio distributions have been suggested, including a truncated Gaussian (DM91) and a log-normal distribution (Kraus et al. 2008), but the first has been largely discounted by now and the latter does not differ significantly from a flat distribution given our sample size. The wider array of possible mass ratio distributions has been summarized and weighed by Kouwenhoven et al.(2009), but our sample size does not allow most of the fine distinctions found in that paper.

We have found that drawing companions from the IMF produces a very poor fit in most cases; a one-sample Kolmogorov-Smirnov test find that $D = 0.53$ for the high-mass subset (1.15-2.50 $M_\odot$), $D = 0.40$ for the intermediate-mass subset (0.55-1.15 $M_\odot$), $D = 0.57$ for the Taurus subset, and $D = 0.20$ for the Upper Sco subset. The first three results all imply disagreement at $P > 99\%$, but the Upper Sco subset (which is smallest, $N = 15$) is not inconsistent ($P < 80\%$). The flat distribution yields $D = 0.17$, $D = 0.24$, $D = 0.33$, and $D = 0.40$, respectively, or confidence values of $P < 80\%$, $P \sim 90\%$, $P \sim 99\%$, and $P \sim 99\%$. The goodness of fit for the Upper Sco subsample is significantly worse than for the IMF-derived distribution, but the others all have better goodness of fit (though the low-mass and Taurus results still indicate disagreement).

Our results for Taurus and for both mass ranges are similiar to those that we reported for close binaries in Upper Sco (Kraus et al. 2008), with similar-mass companions typically over-represented compared to the IMF. Our results for wide binaries in Upper Sco show little evidence of this trend, but the sample is also smaller than for Taurus. We also note that among the low-mass subsample, Taurus binaries have predominantly similar masses (9/12 with $q > 0.75$) while Upper Sco binaries tend to have low-mass secondaries (6/11 with $q < 0.25$). Dividing the sample this finely reduces the significance of our results even further, especially since most of the solar-type stars in Upper Sco remain unidentified and the current census could be subject to some un-

known bias, but this difference in the mass ratio distributions presents an intriguing hint of an environmental effect. As a whole, though, our results argue against a mechanism that forms binaries via random pairing, including their formation in entirely separate cloud cores. Our results also suggest that the masses of binary companions could be selected via a similar process across a wide range of mass, given that the mass ratio distribution is mostly similar at separations spanning 5 to 5000 AU.

Finally, we note that this distribution could be replicated by forming wide binaries out of small-N clusters, since dynamical interactions could force out the lower-mass members and leave the two highest-mass members as a bound pair. However, other features of pre-main sequence stars place strict limits on the amount of dynamical sculpting in these early groups. Most young stars in this mass range have disks at ages of 1-2 Myr, including many wide binary components (e.g., Furlan et al. 2006; Scholz et al. 2006), which suggests that they have not been involved in any energetic interactions. Also, many lower-mass stars ($M \sim 0.4$-0.7 $M_\odot$) are found in binaries with separations of 10-500 AU (e.g., Kraus et al. 2008), and few such binaries would survive in a dynamically active environment. These observations seem to suggest that a dynamical solution can not simultaneously satisfy all of the data.

4.8.3   The Separation Distribution of Wide Binaries

Finally, the binary parameter that varies most distinctly among field systems is the separation distribution. DM91 found that G dwarfs have a mean separation of ~ 30 AU and some systems are as wide as $\sim 10^4$ AU, while the recent substellar surveys have found a mean separation of ~ 4 AU and very few systems wider than 20 AU, and the M dwarf surveys of FM92 and RG97 seem to suggest intermediate properties. Our results for smaller separations in Upper Sco (Kraus et al. 2008) are not strongly indicative because that survey spanned the peak of the DM91 distribution (where it is approximately flat in log-separation), but it appears that there is no significant difference in the separation distribution between 0.5 and 2 $M_\odot$ across a range of 5-500 AU. In Figure 4.15, we plot the separation distribution of our sample of wide binary

systems, spanning separations of 500-5000 AU, as well as the separation distribution suggested by DM91 (a log-normal function) and a log-constant distribution. As for Figure 4.14, we compare our high-mass and intermediate-mass samples (top) and our Taurus and Upper Sco samples (bottom).

In all cases, it appears that the companion frequency increases or is flat with increasing separation. When we test the log-constant distribution with a one-sample Kolmogorov-Smirnov test, we typically find good agreement ($D_H = 0.16$, $D_L = 0.22$, $D_T = 0.14$, and $D_U = 0.15$). In all cases, the confidence level is $<85\%$. This is not unexpected; our results for two-point correlation functions indicate that the separation distribution function is approximately log-flat out to even larger separations ($\sim$20,000 AU; Kraus & Hillenbrand 2008). Kouwenhoven et al. (2007) also reported that the log-flat separation distribution produces a satisfactory fit for higher-mass binaries in Sco-Cen.

When we test the DM91 separation distribution with a one-sample Kolmogorov-Smirnov test, we find results that are less consistent, but not necessarily inconsistent: $D_H = 0.25$, $D_L = 0.30$, $D_T = 0.22$, and $D_U = 0.23$. The high-mass, Taurus, and Upper Sco subsamples are not inconsistent ($P <85\%$), but the low-mass sample disagrees at $P \sim$97%. However, given our results for two-point correlation functions that support the log-flat distribution conclusively at larger separations, we find it preferable to the log-normal distribution. We also note that the DM91 distribution is independently normalized by the DM91 binary frequency, and K-S tests ignore the binary frequencies by implicitly renormalizing them to the same value. It is illustrative to preserve this normalization by using a χ^2 test. We found fit parameters of $\chi^2_H = 15.7$ for the high-mass subset, $\chi^2_L = 11.0$ for the low-mass subset, $\chi^2_T = 19.2$ for the Taurus subset, and $\chi^2_U = 6.4$ for the Upper Sco subset. The high-mass and Taurus subsets disagree at very high confidence ($>$99.9%, while the low-mass subset disagrees at $P \sim$99% and the Upper Sco subset disagrees at $P \sim$90%. We therefore confirm the well-known result that the DM91 binary frequency is less than the binary frequency for these young stellar populations, indicating that binary companions are over-abundant with respect to the field (e.g., Ghez et al. 1994; Kouwenhoven et al.

2007).

The presence of a log-flat primordial separation distribution suggests that the field separation distribution may be a result of post-natal dynamical evolution. The stars in these associations should escape to the field with no further sculpting, and the dynamical simulations of Weinberg et al. (1987) suggest that the field stellar density is too low to affect binaries closer than $\sim 10^4$ AU. However, it has been suggested that many (or perhaps even most) stars are born in much denser clusters (Lada & Lada 2003), though there are also arguments to the contrary (Adams & Myers 2001). If this model is true, then the majority of stars could linger in a relatively high-density environment for >1 Gyr. Observations suggest that the cluster environment is typically dense enough to remove most of the binaries with separations of >100 AU (e.g., Praesepe, Patience et al. 2002; Coma Ber, Kraus et al., in prep).

Therefore, the field population almost certainly represents a mix of binary populations, a suggestion discussed by Kroupa (1998) and Kroupa et al.(1999). Those stars which are born in T associations and OB associations enter the field almost immediately, with their wide binary population nearly intact. In contrast, stars that form in clusters are stripped of their outer binary companions, with the degree of stripping depending on the density of the cluster environment, the density evolution over time, and the elapsed time until a typical star is tidally removed and joins the field (Kroupa et al. 2001; Kroupa & Bouvier 2003). A survey of wide binary systems in young clusters like the ONC or IC348 should directly reveal this sculpting process, but the crowded environment makes it difficult to distinguish bound binary systems from chance alignments (e.g., Simon 1997; Köhler et al. 2006).

We must add a caveat that the primordial multiplicity of dense clusters is still not well-constrained for wide separations, especially at >500 AU where it is impossible to distinguish bound companions from chance alignments. The absence of wide binary systems in open clusters does not necessarily indicate that they form and are disrupted; a primordial deficiency of wide binary systems could also explain the data. Studies of the ONC by Köhler et al.(2006) and Reipurth et al.(2007) find that the binary frequency at smaller separations ($\sim$60–600 AU) is a factor of >2 lower than in

Taurus-Auriga and Sco-Cen, though low number statistics forced their measurements to span a wide range of primary masses that might not be equally represented in the surveys of closer associations. Köhler et al. further suggest that there is little evidence of a density dependence between the core and halo of the ONC, arguing against a dynamical origin of the lower binary frequency. However, the larger sample studied by Reipurth et al. shows a steep decrease in the separation distribution at $\sim$225 AU that is most pronounced in the cluster core, indicating a possible signature of dynamical disruption for wider binary systems. In addition, both of these results depend on the membership census of the ONC (e.g., Jones & Walker 1988; Hillenbrand 1997), which is still uncertain for many candidates.

The most compelling argument for an environmental difference in the primordial binary properties was set forth by Durisen & Sterzik (1994) and Sterzik et al.(2003), who predicted that regions with a higher gas temperature should have a binary separation distribution that is biased to smaller values. One source of this heating could be nearby high-mass stars, which would naturally predict the absence of high-mass binary systems in dense clusters with numerous OB stars. However, feedback from these high-mass stars should dispel the natal gas and shut down star formation, so delicate timing would be required in order for this effect to play a significant role. An indirect test of the primordial binary properties was attempted by Kroupa et al.(1999) by using N-body simulations to evolve several candidate proto-ONC clusters forward to the present day. They concluded that in order to fit the current dynamical state, a binary frequency lower than in Taurus-Auriga was required. However, they only tested six model populations, so their simulation results could include significant degeneracy between choices of parameters. There have also been numerous observational advances in the past decade, and the simulated results of Kroupa et al. should be confronted with these new findings.

Finally, if the separation distribution is truly log-flat for Taurus and Upper Sco, then there is at most a moderate decrement with respect to the binary separation distribution at smaller separations. Our previous high-resolution imaging survey of Upper Sco (Kraus et al. 2008) found that for separations of 5-500 AU and primary

masses of 0.5-2.0 $M_\odot$, the binary frequency is $19^{+3}_{-2}\%$ per decade of separation. In our wide binary sample spanning 500-5000 AU, the corresponding frequencies are $23^{+6}_{-4}\%$ for the high-mass subsample, $14^{+3}_{-2}\%$ for the low-mass subsample, $21^{+4}_{-3}\%$ for the Taurus subsample, and $13^{+4}_{-3}\%$ for the Upper Sco subsample. A comprehensive multiplicity survey of Taurus will be required to place these statistics in context, but we find it intriguing that the binary frequency is so similar across three decades of separation (or 9 decades of mean density in the original cloud core). Either a single binary formation process operates across the full range of length scales, or several binary formation processes all yield similar frequencies.

4.8.4   Unusually Wide Binary Systems

As we described above, the separation distribution in the field seems to be strongly mass-dependent. Field surveys also suggest an empirical relation between the total mass of a system and its maximum possible separation, where the relation is logarithmic in the solar-mass regime ($\log a_{max} = 3.3 M_{tot} + 1.1$ if $M_{tot} > 0.3$ $M_\odot$; Reid et al. 2001) and quadratic in the low-mass regime ($a_{max} = 1400 M_{tot}^2$ if $M_{tot} < 0.3$ $M_\odot$; Burgasser et al. 2003). This relation also provides a good working definition for what might be considered an "unusually wide" binary system; many such systems have been reported in nearby star-forming regions, but the absence of a rigorous definition has led to much confusion regarding their true uniqueness.

Our results suggest that the binary frequency is strongly mass-dependent for young stars, but the form of the separation distribution may not change significantly. If the field a_{max}-M_{tot} relation is genuinely primordial, then our separation-limited (500-5000 AU) sample should include no binary systems with masses of $M_{tot} < 0.5$ $M_\odot$ and a limited range of separations for $0.5 < M_{tot} < 0.8$ $M_\odot$. However, if the field star population (which mostly forms in clusters) is sculpted by post-natal dynamical interactions in those clusters, then these limits might not be present in our sample.

In Figure 4.16, we plot the projected separation and total mass of each of the systems in our survey, plus the empirical a_{max}-M_{tot} relation observed in the field. As

we noted in the previous section, there is a genuine paucity of wide systems among the lowest-mass members, so any additional systems discovered with $M_{tot} < 0.3\ M_\odot$ should be considered genuinely "unusual". However, we see six intermediate-mass systems that seem to exceed this limit, and no evidence of an outer envelope. Our sample includes six systems that all have a total mass of $\sim$0.3-0.4 $M_\odot$, and even they seem to span the full separation range of our survey. Some of these systems could be chance alignments of two low-mass stars, but this number must be small because there are none among the least-massive third of our sample ($M < 0.3\ M_\odot$). Based on our analysis of the associations' two-point correlation functions (Kraus & Hillenbrand 2008), we expect <2 chance alignments in Upper Sco and <1 chance alignments in Taurus for all unassociated pairs of members with $M < 0.4\ M_\odot$, whereas we actually observe 4 and 2, respectively. We would also expect chance alignments to be concentrated at the largest separations, not distributed evenly in logarithmic separation, and to include more pairs with a total mass $<0.3\ M_\odot$.

Our survey shows that in a dynamically unevolved population like Taurus or Upper Sco, $6^{+3}_{-2}\%$ (Taurus 2/31, USco 4/65) of all single stars or binary systems with a total mass of $0.25 < M < 0.50\ M_\odot$ have a companion with a projected separation of 500–5000 AU. As a result, at least this many systems exceed the field M_{tot}-a_{max} limit. By contrast, $<0.4\%$ (Taurus 0/89, USco 0/167) of all binary systems or single stars with a total mass of $<0.25\ M_{sun}$ have such a wide companion. The first result implies that the field M_{tot}-a_{max} relation is another consequence of dynamical sculpting for the majority of field stars that form in dense clusters. Systems with lower binding energy are more prone to disruption in a dense environment, so high-mass systems can maintain wider binary components than their lower-mass counterparts. However, dynamical sculpting can not explain the sharp paucity of primordial wide systems below $M_{tot} \sim 0.3\ M_\odot$, or that wide systems seem to decline rapidly in frequency below $M_{tot} \sim 0.7$-0.8 $M_\odot$. This result could indicate a critical mass limit for large-scale fragmentation of a collapsing cloud core.

4.9 Summary

In this chapter, we have presented an astrometric and spectroscopic follow-up campaign to confirm the youth and association of a complete sample of wide binary companions to intermediate- and low-mass stars ($2.5 > M_{prim} > 0.02$ $M_{\odot}$. Our survey found twelve new wide binary companions with separations of 3-30″ (3 in Taurus and 9 in Upper Sco), raising the total number of such systems to 46. Our survey should be complete for all companions with masses $M_{sec} > 15$-20 M_{Jup} and mass ratios $q > 0.02$-0.04.

In some respects, this wide binary population conforms to expectations from field multiplicity surveys; higher-mass stars have a higher frequency of wide binary companions, and there is a marked paucity of wide binary systems near and below the substellar regime. However, this wide binary population also deviates significantly from other established properties of field binary systems. The separation distribution appears to be nearly log-flat across a very wide range of separations (5-5000 AU), and the mass ratio distribution seems more biased toward similar-mass companions than would be expected for an IMF-shaped distribution or from the field G-dwarf distribution. Finally, the maximum binary separation also shows markedly different behavior, with no evidence of a mass-dependent separation limit for system masses > 0.3 $M_{\odot}$ and abrupt cessation of any wide binary formation (for separations > 500 AU) below this limit.

We attribute these differences to the post-natal dynamical sculpting that occurs for most field systems. All of the systems in our sample, which come from unbound low-density associations, will escape to the field without further dynamical evolution. However, most stars seem to form in denser clusters; even if a wide binary population forms for these stars, it will most likely be stripped before the stars can escape into the field. This explanation suggests that the properties of wide binary systems in the field are not representative of their formation process.

Finally, we note that wide ($\sim$500-5000 AU) binary systems with total masses of < 0.3 $M_{\odot}$ appear to be very rare at all ages, suggesting that any system in this range

of parameter space is indeed "unusually wide". However, additional follow-up is required to determine the true total mass of a system, as there are many hierarchical multiple systems (e.g., USco80 and UScoJ160611.9-193533) that could masquerade as "unusually wide low-mass binaries" until AO and radial velocity surveys discover their higher-order multiplicity.

Acknowledgements

Bibliography

Abt, H. & Levy, S. 1976, ApJS, 30, 273

Adams, F. & Myers, P. 2001, ApJ, 553, 744

Ageorges, N. et al. 1997, A&A, 326, 632

Ahmic, M., Jayawardhana, R., Brandeker, A., Scholz, A., van Kerkwijk, M., Delgado-Donate, E., & Froebrich, D. 2007, ApJ, 671, 2074

Allen, L. & Strom, S. 1995, AJ, 109, 1379

Ardila, D., Martín, E., & Basri, G. 2000, AJ, 120, 479

Baraffe, I., Chabrier, G., Allard, F. & Hauschildt, P.H. 1998, A&A, 337, 403

Baraffe, I., Chabrier, G., Allard, F. & Hauschildt, P.H. 2002, A&A, 382, 563

Bate, M., Clarke, C., & McCaughrean, M. 1998, MNRAS, 297, 1163

Bate, M. & Bonnell, I. 2005, MNRAS, 356, 1201

Baud et al. 1984, ApJ, 278, 53

Bertiau, F. 1958, ApJ, 128, 533

Bertout et al. 1999, A&A, 352, 574

Bessell, M. & Brett, J. 1988,PASP, 100, 1134

Blaauw, A. 1946, Publ. Kapteyn Astron. Lab., 52, 1

Boden, A. et al. 2007, ApJ, 670, 1214

Bonnarel, F. et al. 2000, A&AS,143, 33

Bouy, H., Brandner, W., Martín, E., Delfosse, X., Allard, F., & Basri, G. 2003, AJ, 126, 1526

Bouy, H. et al. 2006a, A&A, 637, 1056

Bouy, H. et al. 2006b, A&A, 451, 177

Bouy, H., Huelamo, N., Martín, E., Barrado y Navascues, D., Sterzik, M., & Pantin, E. 2007, A&A, 463, 641

Brandner, W. et al. 1996, A&A, 307, 121

Briceno, C. et al. 1993, PASP, 105, 686

Briceno, C., Hartmann, L., Stauffer, J., & Martín, E. 1998, AJ, 115, 2074

Briceno, C. et al. 2002, ApJ, 580, 317

Burgasser, A., Kickpatrick, J.D., Reid, I.N., Brown, M., Miskey, C., & Gizis, J. 2003, ApJ, 125, 850

Caballero, J., Martín, E., Dobbie, P., & Barrado y Navascues, D. 2006, A&A, 460, 635

Cambresy, L. et al. 1998, A&A, 338, 977

Cameron, P.B., Britton, M., & Kulkarni, S. 2009, AJ, 137, 83

Cameron, P.B. (PhD thesis, California Institute of Technology, 2008)

Carpenter, J. 2001, AJ, 121, 2851

Carpenter, J. et al. 2002, AJ, 124, 1001

Chabrier, G. et al. 2000, ApJ, 542, 464

Chabrier, G. 2001, ApJ, 554, 1274

Chauvin, G., Lagrange, A., Dumas, C., Zuckerman, B., Mouillet, D., Song, I., Beuzit, J., & Lowrance, P. 2004, A&A, 425, 29

Chelli, A. et al. 1988, A&A, 207, 46

Close, L., Siegler, N., Freed, M., & Biller, B. 2003, ApJ, 587, 407

Close, L. et al. 2005, Nature, 435, 287

Close, L. et al. 2007, ApJ, 660, 1492

Cohen, M. & Kuhi, L. 1979, ApJS, 41, 743

Comeron, F. et al. 2004, A&A, 417, 583

Correia, S., Zinnecker, H., Ratzka, Th., & Sterzik, M. 2006, A&A, 459, 909

Cutri, R. et al. 2003, "2MASS All Sky Catalog of Point Sources"

D'Antona, F. & Mazzitelli, I. 1997, MmSAI, 68, 807

de Geus, E. et al. 1989, A&A, 216, 44

de Zeeuw, P., Hoogerwerf, R., de Bruijne, J., Brown, A., & Blaauw, A. 1999, AJ, 117, 354

Deacon, N. & Hambly, N. 2007, A&A, 468, 163

Delgado-Donate, E. et al. 2003, MNRAS, 347, 759

Duchene, G. 1999, A&A, 341, 547

Duchene, G., Monin, J.-L., Bouvier, J., & Menard, F. 1999, A&A, 351, 954

Duquennoy, A. & Mayor, M. 1991, A&A, 248, 485

Durisen, R. & Sterzik, M. 1994, A&A, 286, 84

Elmegreen, B. 2008, ApJ, 672, 1006

Epchtein, N. et al. 1999, A&A, 349, 236

Fischer, D. & Marcy, G. 1992, ApJ, 396, 178

Frink, S., Roser, S, Neuhauser, R., & Sterzik, M. 1997, A&A, 325, 613

Furlan, E. et al. 2006, ApJS, 165, 568

Ghez, A., Neugebauer, G., & Matthews, K. 1993, AJ, 106, 2005

Ghez, A. et al. 1997, ApJ, 481, 378

Ghez, A. et al. 2008, ApJ, 689, 1044

Glass, I. 1979, MNRAS, 187, 305

Gomez, M., Hartmann, L., Kenyon, S., & Hewett, R. 1993, AJ, 105, 1927

Goodwin, S. & Kroupa, P. 2005, A&A, 439, 565

Gregorio-Hetem, J. et al. 1992, AJ, 103, 549

Guenther, E., Esposito, M., Mundt, R., Covino, E., Alcala, J., Cusano, F., & Stecklum, B. 2007, A&A, 467, 1147

Guieu, S. et al. 2005, A&A, 446, 485

Haisch, K. et al. 2004, AJ, 127, 1747

Hambly, N. et al. 2001, MNRAS, 326, 1279

Hartigan, P., Strom, K., & Strom, S. 1994, ApJ, 427, 961

Hartigan, P. & Kenyon, S. 2003, ApJ, 583, 334

Hartmann, L. et al. 2005, ApJ, 629, 881

Henize, K. & Mendoza, E. 1973, ApJ, 180, 115

Herbig, G. 1952, JRASC, 46, 222

Hewett, P. 1982, MNRAS, 201, 867

Hillenbrand, L. 1997, AJ, 113, 1733

Hillenbrand, L. & White, R. 2004, ApJ, 604, 741

Itoh, Y. et al. 2005, ApJ, 620, 984

Jayawardhana, R. & Ivanov, V. 2006, Science, 313, 1279

Jones, D. 1971, MNRAS, 152, 231

Jones, B. & Herbig, G. 1979, AJ, 84, 1872

Jones, B. & Walker, M. 1988, AJ, 95, 1755

Joy, A. 1945, ApJ, 102, 168

Kapteyn, J. 1914, ApJ, 40, 43

Kenyon, S. & Hartmann, L. 1995, ApJS, 101, 117

Kim, S., Figer, D., Lee, M., & Oh, S. 2005, PASP, 117, 445

Kiminki, D. et al. 2007, ApJ, 664, 1102

Koenig, B. et al. 2001, A&A, 369, 971

Köhler, R. et al. 2000, A&A, 356, 541

Köhler, R., Petr-Gotzens, M., McCaughrean, M., Bouvier, J., Duchêne, G., Quirren-
    bach, A., & Zinnecker, H. 2006, A&A, 458, 461

Kouwenhoven, M. et al. 2005, A&A, 430, 117

Kouwenhoven, M.B.N., Brown, A.G.A., & Kaper, L. 2007, A&A, 464, 581

Kouwenhoven, M.B.N., Brown, A.G.A., Goodwin, S.P., Portegies Zwart, S.F., &
    Kaper, L. 2009, A&A, 493, 979

Kraus, A. et al. 2005, ApJ, 633, 452

Kraus, A. et al. 2006, ApJ, 649, 306

Kraus, A. & Hillenbrand, A. 2007, ApJ, 662, 413 (KH07a)

Kraus, A. & Hillenbrand, A. 2007, ApJ, 664, 1167

Kraus, A., Ireland, M., Martinache, F., & Lloyd, J. 2008, ApJ, in press

Kroupa, P. 1998, MNRAS, 298, 231

Kroupa, P., Petr, M., & McCaughrean, M. 1999, New Astronomy, 4, 495

Kroupa, P., Aarseth, S., & Hurley, J. 2001, MNRAS, 321, 699

Kroupa, P. 2002, Science, 295, 82

Kroupa, P. & Bouvier, J. 2003, /mnras, 346, 343

Kroupa, P. et al. 2003, MNRAS, 346, 354

Kunkel, M. (PhD thesis, University of Wurzburg, 1999)

Lada, J. & Lada, E. 2003, ARA&A, 41, 57

Larson, R. 1995, MNRAS, 272, 213

Leggett, S. et al. 1998, ApJ, 509, 836

Leggett, S. et al. 2000, ApJ, 535, 965

Leggett, S. et al. 2001, ApJ, 548, 908

Leggett, S. et al. 2002, ApJ, 564, 452

Leinert, Ch. et al. 1993, A&A, 278, 129

Lopez-Marti, B. et al. 2004, A&A, 416, 555

Luhman, K. & Rieke, G. 1998, ApJ, 497, 354

Luhman, K. 1999, ApJ, 525, 466

Luhman, K. 2000, ApJ, 544, 1044

Luhman, K., Stauffer, J., Muench, Al, Rieke, G., Lada, E., Bouvier, J., & Lada, C. 2003, ApJ, 593, 1093

Luhman, K. et al. 2003a, ApJ, 590, 348

Luhman, K. et al. 2003b, ApJ, 593, 1093

Luhman, K. 2004, ApJ, 617, 1216

Luhman, K. 2004a, ApJ, 602, 816

Luhman, K. 2004b, ApJ, 614, 398

Luhman, K. et al. 2004c, ApJ, 617, 565

Luhman, K. 2004d, ApJ, 617, 1216

Luhman, K. et al. 2005, ApJ, 623, 1141

Luhman, K. 2006, ApJ, 645, 676

Luhman, K. et al. 2006a, ApJ, 649, 894

Luhman, K., Whitney, B., Meade, M., Babler, B., Indebetouw, R., Bracker, S., & Churchwell, E. 2006b, ApJ, 647, 1180

Luhman, K. 2006, ApJ, 645, 676

Luhman, K., Allers, K., Jaffe, D., Cushing, M., Williams, K., Slesnick, C., & Vacca, W. 2007, ApJ, 659, 1629

MacConnell, D., Wing, R., & Costa, E. 1992, AJ, 104, 821

Mamajek, E. et al. 2003, AJ, 124, 1670

Martín, E. et al. 1998, MNRAS, 300, 733

Martín, E. et al. 2000, ApJ, 543, 299

Martín, E., Dougados, C., Magnier, E., Menard, F., Magazzu, A., Cuillandre, J., & Delfosse, X. 2001, ApJ, 561, 195

Martín, E. et al. 2003, ApJ, 594, 525

Martín, E., Delfosse, X., & Guieu, S. 2004, AJ, 127, 449

Masana, E. et al. 2006, A&A, 450, 735

Massarotti, A., Latham, D., Torres, G., Brown, R., & Oppenheimer, B. 2005,AJ, 129, 2294

Massey, P., Strobel, K., Barnes, J., & Anderson, E. 1988, ApJ, 328, 315

Metchev, S. (PhD thesis, California Institute of Technology, 2005)

Miller, G. & Scalo, J. 1979, ApJS, 41, 513

Mohanty, S. et al. 2005, ApJ, 626, 498

Monet, D. et al. 2003, AJ, 125, 984

Oasa, Y. et al. 1999, ApJ, 526, 336

Oke, B. & Gunn, J. 1982, PASP, 94, 586

Padgett, D. et al. 2006, BAAS, 209, 3016

Palla, F. & Stahler, S. 1999, ApJ, 525, 772

Patience, J. et al. 2002, AJ, 123, 1570

Peebles, J. 1980, The Large Scale Structure of the Universe (Princeton: Princeton Univ. Press)

Persi, P. et al. 2001, A&A, 376, 907

Persi, P. et al. 2005, A&A, 431, 539

Prato, L., Simon, M., Mazeh, T., McLean, I., Norman, D., & Zucker, S. 2002a, ApJ, 569, 863

Prato, L., Simon, M., Mazeh, T., Zucker, S., & McLean, I. 2002b, ApJ, 579, 99

Prato, L. 2007, ApJ, 657, 338

Preibisch, T., Guenther, E., Zinnecker, H., Sterzik, M., Frink, S., & Roeser, S. 1998, A&A, 333, 619

Preibisch, T. et al. 2001, AJ, 121, 1040

Preibisch, T. et al. 2002, AJ, 124, 404

Reid, I.N. & Gizis, J. 1997, AJ, 113, 2246

Reid, I.N. & Hawley, S. 1999, AJ, 117, 343

Reid, I., Gizis, J., Kirkpatrick, J., & Koerner, D. 2001, AJ, 121, 489

Reiners, A. et al. 2005, ApJ, 634, 1346

Reipurth, B. & Zinnecker, H. 1993, A&A, 278, 81

Reipurth, B., Guimarães, M., Connelley, M., & Bally, J. 2007, AJ, 134, 2272

Salim, S. & Gould, A. 2003, ApJ, 582, 1011

Sartori, M. et al. 2003, A&A, 404, 913

Schmidt-Kaler, Th., "Physical Parameters of the Stars", Landolt-Bornstein Numerical Data and Functional Relationships in Science and Technology, New Series, Group VI, Volume 2b, Springer-Verlag, Berlin, 1982

Scalo, J. 1998, in APS Conf. Ser. 142, The Stellar Initial Mass Function, ed. G. Gilmore & D. Howell (San Francisco:ASP), 201

Scholz, A., Jayawardhana, R., & Wood, K. 2006, ApJ, 645, 1498

Schwartz, R. et al. 1977, ApJS, 35, 161

Siegler, N. et al. 2003, ApJ, 598, 1265

Siegler, N. et al. 2005, ApJ, 621, 1023

Simon, M. et al. 1995, ApJ, 443, 625

Simon, M., Holfeltz, S., Taff, L. 1996, ApJ, 469, 890

Simon, M. 1997, ApJ, 482, 81

Simon, M., Dutrey, A., & Guilloteau, S. 2000, ApJ, 545, 1034

Skrutskie, M. et al. 2006, AJ, 131, 1163

Slesnick, C., Hillenbrand, L., & Carpenter, J. 2004, ApJ, 610, 1045

Slesnick, C., Carpenter, J., & Hillenbrand, L. 2006a, AJ, 131, 3016

Slesnick, C., Carpenter, J., Hillenbrand, L., & Mamajek, E. 2006b, AJ, 132, 2665

Stapelfeldt, K., Menard, F., Watson, A., Krist, J., dougados, C., Padgett, D., &
    Brandner, W. 2003, ApJ, 589, 410

Steffen, A. et al. 2001, AJ, 122, 997

Sterzik, M. & Durisen, R. 1998, A&A, 339, 95

Sterzik, M., Durisen, R., & Zinnecker, H. 2003, A&A, 411, 91

Stetson, P. 1987, PASP, 99, 191

Strom, K. & Strom, S. 1994, ApJ, 424, 237

Tamura, M. et al. 1996, AJ, 112, 2076

The, P-S. 1964, PASP, 76, 293

Torres-Dodgen, A. & Weaver, W.B. 1993, PASP, 105, 693

Torres, R., Loinard, L., Mioduszewski, A., & Rodriguez, L. 2007, ApJ, 671, 1813

Walter, F., Vrba, F., Mathieu, R., Brown, A., & Myers, P. 1994, AJ, 107, 692

Weinberg, M., Shapiro, S., & Wasserman, I. 1987, ApJ, 312, 367

White, N. & Wing, R. 1978, ApJ, 222, 209

White, R., Ghez, A., Reid, I.N., & Schultz, G. 1999, ApJ, 520, 811

White, R. & Ghez, A. 2001, ApJ, 556, 265

White, R. & Basri, G. 2003, ApJ, 582, 1109

White, R. & Hillenbrand, L. 2004, ApJ, 616, 998

Whittet, D. et al. 1997, A&A, 327, 1194

Wichmann, R. et al. 1998, MNRAS, 301, 39

Wing, R. 1971, Late-Type Stars, Ed. G. W. Lockwood & H. M. Dyck. Kitt Peak National Observatory, 554, 145

Wizinowich, P. et al. 2006, PASP, 118, 297

Woitas, J. et al. 2001, A&A, 376, 982

Zuckerman, B., Song, I., & Bessell, M. 2004, ApJ, 613, 65

Chapter 5

Mapping the Shores of the Brown Dwarf Desert in Upper Scorpius

Abstract

We present the results of a survey for stellar and substellar companions to 82 young stars in the nearby OB association Upper Scorpius. This survey used nonredundant aperture-mask interferometry to achieve typical contrast limits of $\Delta K \sim$5-6 at the diffraction limit, revealing 12 new binary companions that lay below the detection limits of traditional high-resolution imaging; we also summarize a complementary snapshot imaging survey that discovered 7 directly resolved companions. The overall frequency of binary companions ($\sim$35$^{+5}_{-4}$% at separations of 6-435 AU) appears to be equivalent to field stars of similar mass, but companions could be more common among lower-mass stars than for the field. The companion mass function has statistically significant differences compared to several suggested mass functions for the field, and we suggest an alternate log-normal parameterization of the mass-function. Our survey limits encompass the entire brown dwarf mass range, but we only detected a single companion that might be a brown dwarf; this deficit resembles the so-called "brown dwarf desert" that has been observed by radial-velocity planet searches. Finally, our survey's deep detection limits extend into the top of the planetary mass function, reaching 8-12 M_{Jup} for half of our sample. We have not identified any plan-

---

etary companions at high confidence ($\geq 99.5\%$), but we have identified four candidate companions at lower confidence ($\geq 97.5\%$) that merit additional followup to confirm or disprove their existence.

5.1 Introduction

The detection and characterization of low-mass companions has become one of the highest priorities of the astronomical community. Radial velocity surveys have discovered over 200 extrasolar planetary companions over the past decade, and both RV surveys and coronagraphic imaging surveys have discovered an abundance of stellar-mass companions (e.g., Marcy & Butler 2000; McCarthy & Zuckerman 2004; Metchev 2005; Johnson et al. 2006; Naef et al. 2007). However, very few brown dwarf companions have been identified, an unexpected result given that the observational signatures of more massive companions are far larger than those of planetary-mass companions and that free-floating brown dwarfs are very common (Kirkpatrick et al. 2000; Luhman et al. 2003; Chiu et al. 2006; Slesnick et al. 2006a, 2006b). This dearth of companions between the stellar and planetary mass regimes is popularly known as the "brown dwarf desert". The existence and extent of the brown dwarf desert can provide key constraints on star and planet formation since it represents the extreme mass limit of both processes.

If the stellar-mass binary companions of solar-mass stars are drawn from the Initial Mass Function (IMF; e.g., Kroupa 1995) or formed via some other process that preferentially forms low-mass companions (e.g., Duquennoy & Mayor 1991, hereafter DM91), then brown dwarf companions should be common unless another process inhibits their formation or dynamically strips them. However, if stellar companions are formed via the fragmentation of a protostellar core, then there are no a priori expectations that brown dwarfs should form. Indeed, even if fragmentation can form an extremely inequal-mass pair, the long collapse timescale for low-mass objects might lead to their preferential photoevaporation by the higher-mass, more luminous companion.

It is also unclear whether brown dwarfs could form via planetary formation processes. Radial velocity surveys suggest that the giant planetary mass function is well-fit by a power law, $dN/dm \propto M^{-1.05}$, for masses of ∼1-10 M_{Jup} (Marcy et al. 2005). If this power law extends to higher masses, there should be as many "planetary" companions with masses of 10-25 M_{Jup} as with masses of 4-10 M_{Jup} or 1.6-4.0 M_{Jup}. An absence of these companions suggests either that the function is not a power law or that the power law is truncated by some limit. For example, submillimeter disk surveys suggest that protoplanetary disks have a mean mass of ∼5 M_{Jup} by the age of 1-2 Myr (Andrews & Williams 2005), with a small fraction (∼5%) having masses of ∼30-100 M_{Jup}. Unless massive planets are formed very early or efficiently accrete the entire disk mass, this could impose an upper cutoff on the distribution of planetary masses.

The brown dwarf desert has been studied mostly at very small or very large separations. The radial velocity exoplanet surveys that have proven so successful over the past decade should have detected any brown dwarfs within their outer separation limit (∼3-5 AU), and they have set very low upper limits on the frequency of close brown dwarf companions to solar mass stars (<1%; Marcy & Butler 2000; Grether & Lineweaver 2006). Similarly, high-resolution coronagraphic imaging surveys have demonstrated sufficient sensitivity to identify brown dwarf companions at typical separation limits of >50 AU (e.g., Gizis et al. 2001; Neuhäuser et al. 2003; McCarthy & Zuckerman 2004; Neuhäuser & Guenther 2004; Metchev 2005). They have measured frequencies which are low, but somewhat inconsistent (and perhaps not anomalously low; 1±1% by McCarthy & Zuckerman, compared to $6.8^{+8.3}_{-4.9}$% by Metchev and 18±14% by Gizis et al.). A survey for wide companions to high-mass (2-8 $M_\odot$) stars in Upper Sco by Kouwenhoven et al. (2007) found a relatively low frequency for brown dwarf companions, 0.5±0.5% at separations of 130-520 AU. Finally, there have been an intriguing sample of candidate planetary-mass companions identified at large separations (e.g., Chauvin et al. 2004; Neuhäuser et al. 2005), but both their mass and formation mechanism are still uncertain and their frequency is still unconstrained (e.g., Masciadri et al. 2005; Kraus et al. 2006; Biller et al. 2007;

Ahmic et al. 2007).

However, these surveys do not study the actual separation range where most giant planets and binary companions are expected to form. Most giant planets at small orbital radii (≤ 5 AU) are thought to have migrated inward, so their mass distribution may not match that of their more distant counterparts. The binary formation process may also be different for small separations (≤ 10 AU), with H_2 dissociation softening the equation of state and leading to enhanced fragmentation over that expected for larger length scales (Whitworth & Stamatellos 2006). Similarly, giant planets are not expected to form at very large radii (≥ 30 AU) since the formation timescale is too long, and the frequency of wide binary companions may differ significantly from those of closer binaries (e.g., Kraus & Hillenbrand 2007a) since the fragmentation occurs on a length scale that is several orders of magnitude larger.

Ideally, the desert should be studied at the separation range where giant planets and most binaries are thought to form ($\sim$5-30 AU; Lissauer & Stephenson 2007; DM91), but this has been impossible using existing techniques. For example, theoretical models (Chabrier et al. 2000) suggest that a 50 M_{Jup} brown dwarf located 15 AU (1-2$''$) from a nearby field star will have a contrast ratio of $\Delta K \sim$10-15 magnitudes at a separation of only $\sim 1''$. The contrast problem could have been addressed by observing young stars since their substellar companions would be intrinsically more luminous ($\Delta K <$5 mag), but most young stars are further away, so the separations are even smaller (0.1-0.2$''$; $\sim \lambda/D$). Sensitivities near the diffraction limit have traditionally been far too shallow to detect such companions. However, new advances in high-resolution imaging techniques are now opening up this critical regime; our survey will use one such technique, non-redundant aperture mask interferometry.

The technique of non-redundant aperture masking has been well-established as a means of achieving the full diffraction limit of a single telescope (e.g., Nakajima et al. 1989; Tuthill et al. 2000). The reason for the technique's success over direct imaging is that the calibration is independent of structure of the wavefront over scales larger than a single sub-aperture, but it still preserves the angular resolution of the full aperture. This technique, when applied to seeing-limited observations, requires

observations to be taken in a speckle mode with sub-apertures of diameter smaller than the atmospheric coherence length, limiting the technique to objects brighter than about $m_H = 5$. The use of adaptive optics allows for longer integration times and larger sub-apertures, extending the technique to much fainter targets.

Published detections have been able to recover astrometrically discovered binary systems with contrast ratios of 3:1 at 0.6 λ/D and 100:1 at λ/D (Pravdo et al. 2006; Lloyd et al. 2006; Ireland et al. 2008) using total observation times of $\sim$10 minutes. The inner limit of companion detectability at high contrast is $\lambda/2B_L$, where B_L is the longest baseline in the mask (typically 80-95% of the aperture diameter). equal to the contrast ratio of the binary Typical closure phase errors are such that aperture masking can unveil high contrast companions at separations $\sim$5 times closer than direct imaging in both H and K bands.

In this paper, we describe an aperture-mask interferometry and direct imaging survey to detect stellar and substellar companions to young stars in the nearby OB association Upper Scorpius. This survey directly studies the age and separation range corresponding to the peak of planet formation, offering the first glimpse of the brown dwarf desert in this critical range of parameter space. In Section 5.2, we describe our survey sample, and in Section 5.3, we describe the observations and data analysis techniques. In Section 5.4, we summarize the results of our survey. In Section 5.5, we combine these results with previous binary surveys to place constraints on the stellar binary frequency, mass function, and separation distribution, and in Section 5.6, we consider constraints on the corresponding parameters for the planetary population. Finally, in Section 5.7, we discuss the implications of our survey for the extent and aridity of the brown dwarf desert.

5.2   Survey Sample

Upper Sco is an ideal target for large-scale surveys to detect brown dwarf or planetary companions. It is young enough ($\sim$5 Myr) that substellar companions are much more luminous than those of typical field stars, and this age is thought to be the peak epoch

of giant planet formation (Lissauer & Stephenson 2007, and references therein). Its relative proximity (∼145 pc; de Zeeuw et al. 1999) also means that the resolution limit of large telescopes (∼40-100 mas; 6-15 AU) corresponds to the giant planet separation regime of our own solar system. Finally, the association has been very intensely studied, with several hundred members identified in the past decade, so it provides a much larger sample of well-characterized members than nearby moving groups.

We compiled a preliminary list of 356 targets from the known members of Upper Sco as compiled in Kraus & Hillenbrand (2007a); this census included all spectroscopically confirmed members with spectral type G0 or later from the recent surveys by Walter et al. (1994), Preibisch et al.(1998, 2001, 2002), Kunkel (1999), Ardila et al.(2000), Martin et al.(2004), and Slesnick et al.(2006a). We also added two stars that were not included in that census: RXJ1550.9-2534 (which was originally classified as F9 by the HD catalogue but was reclassified as G1 by the Michigan Spectral Survey; Houk & Smith-Moore 1988) and V1149 Sco (which was not included in any large membership surveys since it was identified as a young star before they were conducted; Stephenson 1987).

All of our observations have been conducted from northern sites, so we removed 25 of the 26 stars south of $\delta = -25^o$ from further consideration. The only exception was RXJ1550.9-2534, which we retained in order to make a complete group of four science targets of similar brightness and airmass. As we describe below, preliminary imaging showed that it was an obvious binary that is not suitable for masking observations anyway, but we retain it in our sample for statistical purposes. We also rejected 230 of the remaining low-mass association members which were optically fainter than the useful limit of the AO system ($R \geq 14$). Finally, we removed the 23 known binaries with separations of $<3''$. In close systems, the stellar companion would have dominated the signal in our observations, complicating any search for fainter companions. Wider binaries (with separations near the seeing limit) were rejected because they are generally not corrected well by the AO system, though we still observed several of them with direct imaging in order to test whether this would

actually occur. A total of seven targets were not discovered to be binaries until we arrived at the telescope and obtained quick direct imaging observations; these targets were also removed from the aperture mask sample. We mistakenly removed one more target, USco-160643.8-190805, that we initially thought was a binary based on direct imaging. Subsequent analysis showed that it was flagged as a binary erroneously; we will not consider it in our statistical sample because we only have imaging data and not masking data.

These cuts left a total of 72 Upper Sco members in our aperture mask sample, plus 11 members (10 known or new binary systems and 1 erroneous omission) that we only observed with direct imaging. We list all of these targets in Table 5.1, where we also include each target's spectral type (adopted from the discovery survey), mass (as determined in Section 5.3.3), and R and K magnitudes, plus the target group that it was observed with (as described in Section 5.3.1). In Table 5.2, we list the 19 known binary systems that would have passed our selection criteria. We did not observe any of these systems, but we will include them in our sample for determining stellar binary statistics since they have known binary companions. Our upper limits on the existence of planetary-mass companions will not include any known or newly-discovered binary systems.

Table 5.1.   Upper Sco Sample

| Name | RA | DEC | SpT | Mass | R | K | Group |
	(J2000)			$(M_\odot)$	(mag)	(mag)	
RXJ1550.0-2312	15 50 04.99	-23 11 53.7	M2	0.49	13.1	8.93	14
RXJ1550.9-2534	15 50 56.42	-25 34 19.0	G1	1.75	9.4	7.91	...
RXJ1551.1-2402	15 51 06.61	-24 02 19.0	M2	0.49	13.5	9.73	17
RXJ1557.8-2305	15 57 50.03	-23 05 09.4	M0	0.68	12.7	9.27	12
RXJ1558.1-2405	15 58 08.15	-24 05 53.0	K4	0.95	11.4	8.96	8
RXJ1558.2-2328	15 58 12.71	-23 28 36.4	G2	1.66	9.9	8.02	1
RXJ1600.2-2417	16 00 13.30	-24 18 10.6	M0	0.68	13.1	9.51	14
RXJ1600.6-2159	16 00 40.57	-22 00 32.2	G9	1.43	10.2	8.44	3
RXJ1600.7-2127	16 00 42.77	-21 27 38.0	K7	0.77	11.7	8.92	10
RXJ1601.1-2113	16 01 08.01	-21 13 18.5	M0	0.68	12.0	8.80	9
RXJ1601.9-2008	16 01 58.23	-20 08 12.2	G5	1.62	9.9	7.67	2
RXJ1602.0-2221	16 02 00.39	-22 21 23.7	M1	0.60	12.8	8.84	12
RXJ1602.8-2401B	16 02 51.24	-24 01 57.4	K4	0.95	11.1	8.93	4
RXJ1602.8-2401A	16 02 52.43	-24 02 22.7	K0	1.35	10.4	7.65	1
RXJ1603.6-2245	16 03 35.50	-22 45 56.1	G9	1.43	10.6	8.36	3
RXJ1603.9-2031A	16 03 57.68	-20 31 05.5	K5	0.87	12.0	8.37	10
RXJ1604.3-2130	16 04 21.66	-21 30 28.4	K2	1.12	11.8	8.51	11
RXJ1605.6-2152	16 05 39.36	-21 52 33.8	M1	0.60	13.6	9.47	17
RXJ1606.2-2036	16 06 12.54	-20 36 47.3	K5	0.87	12.5	8.90	12
RXJ1607.0-2043	16 07 03.73	-20 43 07.4	M1	0.60	13.6	9.53	17
RXJ1607.0-2036	16 07 03.56	-20 36 26.5	M0	0.68	11.3	8.10	...
USco-155655.5-225839	15 56 55.46	-22 58 40.4	M0	0.68	13.2	9.43	14,15
USco-160142.6-222923	16 01 42.55	-22 29 23.9	M0	0.68	13.8	10.22	19
USco-160341.8-200557	16 03 41.87	-20 05 57.8	M2	0.49	13.7	9.49	18
USco-160343.3-201531	16 03 43.35	-20 15 31.5	M2	0.49	13.7	9.72	18
Usco-160428.4-190441	16 04 28.39	-19 04 41.4	M3	0.36	13.6	9.28	...
USco-160517.9-202420	16 05 17.92	-20 24 19.5	M3	0.36	13.3	9.14	15
USco-160643.8-190805	16 06 43.86	-19 08 05.6	K6	0.82	12.8	9.20	...
USco-160707.7-192715	16 07 07.67	-19 27 16.1	M2	0.49	13.8	9.80	19
USco-160801.4-202741	16 08 01.42	-20 27 41.7	K8	0.68	13.0	9.29	16
USco-160822.4-193004	16 08 22.34	-19 30 05.2	M1	0.60	12.9	9.06	12
USco-160823.2-193001	16 08 23.25	-19 30 00.9	K9	0.68	13.2	9.47	15
USco-160823.8-193551	16 08 23.88	-19 35 51.8	M1	0.60	13.3	9.25	...
USco-160825.1-201224	16 08 25.11	-20 12 24.6	M1	0.60	13.9	9.87	20
USco-160900.7-190852	16 09 00.76	-19 08 52.6	K9	0.68	13.1	9.15	15
USco-160908.4-200928	16 09 08.45	-20 09 27.8	M4	0.24	13.8	9.52	...

Table 5.1 (cont'd)

Name	RA	DEC	SpT	Mass ($M_\odot$)	R (mag)	K (mag)	Group
	(J2000)						
USco-160916.8-183522	16 09 16.85	-18 35 22.6	M2	0.49	14.0	9.67	20
USco-160946.4-193735	16 09 46.44	-19 37 36.1	M1	0.60	13.8	9.63	19
USco-160954.4-190654	16 09 54.41	-19 06 55.1	M1	0.60	13.7	9.60	18
USco-161031.9-191305	16 10 31.96	-19 13 06.2	K7	0.77	13.0	8.99	12
USco-161115.3-175721	16 11 15.34	-17 57 21.4	M1	0.6	13.2	9.20	15
USco-161347.5-183459	16 13 47.51	-18 35 00.4	M2	0.49	14.1	9.91	20
USco-161358.1-184828	16 13 58.15	-18 48 29.0	M2	0.49	14.0	9.88	20
GSC 06764-01305	15 35 57.80	-23 24 04.6	K3	0.99	12.0	9.43	11
GSC 06195-00768	15 57 02.34	-19 50 42.0	K7	0.77	11.1	8.37	...
GSC 06191-00019	15 59 02.09	-18 44 14.3	K6	0.82	11.1	8.11	...
GSC 06191-00552	15 58 47.70	-17 57 59.0	K3	0.99	11.5	8.33	5
GSC 06204-00812	16 03 02.69	-18 06 05.0	K4	0.95	11.3	8.73	5
GSC 06204-01067	16 03 23.68	-17 51 42.3	M2	0.49	12.4	8.61	...
GSC 06208-00834	16 06 31.70	-20 36 23.3	K6	0.82	12.4	8.73	10
GSC 06209-00735	16 08 14.74	-19 08 32.8	K2	1.12	11.0	8.43	5
GSC 06205-00954	16 08 31.38	-18 02 41.4	M0	0.68	12.2	8.91	9
GSC 06209-01501	16 08 56.73	-20 33 46.0	K5	0.87	11.9	8.62	9
GSC 06213-01358	16 09 30.30	-21 04 58.9	M0	0.68	12.1	8.92	9
GSC 06213-00194	16 09 40.99	-22 17 59.4	M0	0.68	11.6	8.44	7
GSC 06213-00306	16 10 42.03	-21 01 32.0	K5	0.87	11.9	8.56	6
GSC 06793-00868	16 11 56.33	-23 04 05.1	M1	0.6	12.2	8.82	...
GSC 06793-00797	16 13 02.72	-22 57 44.6	K4	0.95	11.7	8.46	8
GSC 06213-00306	16 13 18.59	-22 12 48.9	G9	1.43	9.8	7.43	1,2
GSC 06793-00994	16 14 02.12	-23 01 02.2	G4	1.63	10.9	8.61	4
GSC 06793-00806	16 15 34.57	-22 42 42.1	M1	0.60	11.2	7.91	7
GSC 06793-01406	16 16 17.95	-23 39 47.7	G7	1.56	9.9	8.10	2
GSC 06214-02384	16 19 33.96	-22 28 29.4	K0	1.35	10.5	8.51	3
GSC 06794-00480	16 20 45.96	-23 48 20.9	K3	0.99	11.9	8.93	8
GSC 06214-00210	16 21 54.67	-20 43 09.1	M1	0.60	11.6	9.15	8
GSC 06794-00537	16 23 07.83	-23 00 59.7	K2	1.12	11.0	8.18	4
GSC 06794-00156	16 24 51.36	-22 39 32.5	G6	1.59	9.3	7.08	1
GSC 06794-00337	16 27 39.56	-22 45 23.0	K1	1.25	10.9	8.08	6
GSC 06228-01359	16 35 48.36	-21 48 39.7	M0	0.68	12.4	8.48	10
ScoPMS015	15 57 19.99	-23 38 50.0	M0	0.68	12.4	8.88	...
ScoPMS017	15 57 34.31	-23 21 12.3	M1	0.60	12.9	8.99	14
ScoPMS019	15 59 59.95	-22 20 36.8	M1	0.60	12.3	8.63	11

Table 5.1 (cont'd)

Name	RA	DEC	SpT	Mass	R	K	Group
	(J2000)			$(M_\odot)$	(mag)	(mag)	
ScoPMS021	16 01 25.64	-22 40 40.3	K1	1.25	13.6	8.52	16
ScoPMS022	16 02 08.45	-22 54 58.9	M1	0.60	13.4	9.55	17
ScoPMS027	16 04 47.76	-19 30 23.1	K2	1.12	11.0	8.04	5
ScoPMS028	16 05 27.27	-19 38 46.6	M1	0.60	13.3	9.55	16
ScoPMS042b	16 10 21.74	-19 04 06.7	M3	0.36	13.8	9.62	19
ScoPMS044	16 11 08.91	-19 04 46.9	K2	1.12	11.3	7.69	7
ScoPMS045	16 11 20.58	-18 20 54.9	K5	0.87	11.4	8.56	6
ScoPMS048	16 11 59.28	-19 06 53.3	K0	1.35	11.1	8.09	7
ScoPMS060	16 17 31.39	-23 03 36.0	G0	1.71	9.7	7.97	2
ScoPMS214	16 29 48.70	-21 52 11.9	K0	1.35	10.5	7.76	4
V1149 Sco	15 58 36.90	-22 57 15.0	G7	1.56	10.2	7.05	3

Note. — Typical uncertainties are $\sim$1 subclass for spectral types, $\sim$0.2 mag for R magnitudes (taken from NOMAD; Zacharias et al. 2004), and $\sim$0.02 mag for K magnitudes (taken from 2MASS; Skrutskie et al. 2006). The uncertainties in mass are dominated by systematic errors, including a global zero-point uncertainty of $\sim$20% and individual uncertainties of as much as $\sim$100% due to the possibility of further unresolved multiplicity.

5.3 Observations and Data Analysis

5.3.1 Observations

We observed our target sample in April-July 2007 with the Keck-II 10m and Palomar Hale 200" telescopes. All observations were obtained using the facility adaptive optics imagers, NIRC2 and PHARO. Both instruments have aperture masks permanently installed at or near the pupil plane in filter or pupil-stop wheels. The seeing quality was well above average for most of the Keck observations, yielding superb AO correction for bright targets and acceptable strehl ratios ($\sim$15-20%) even for targets as faint as $R \sim$14. The Palomar observations were obtained under approximately median conditions ($\sim$1″ seeing).

All observations conducted at Keck were obtained with a K' filter, while those conducted at Palomar were obtained with a methane short filter, which is in H-band (central wavelength 1.57 μm, bandpass 0.1 μm). This filter was used instead of full H-band because of calibration errors related to dispersion that had been found in previous data sets. This strategy allowed us to achieve similar resolution limits at both telescopes, despite the smaller aperture size at Palomar. Our Palomar observations

Table 5.2.   Known Binary Systems

Primary	RA	DEC	SpT$_{prim}$	M_{prim}	R	K	ΔK	Sep	PA	Ref
	(J2000)			($M_\odot$)	(mag)	(mag)	(mag)	(mas)	(deg)	
GSC 06780-01061	16 06 54.36	-24 16 10.8	M3	0.36	12.2	8.86	1.3	1500	270.0	Kraus & Hillenbrand (2007a)
GSC 06793-00569	16 13 29.29	-23 11 07.5	K1	1.25	11.1	8.49	2.7	1430	91.4	Metchev (2005)
GSC 06793-00819	16 14 11.08	-23 05 36.2	K0	1.35	10.0	7.46	0.21	222	304.8	Metchev (2005)
RXJ1600.5-2027	16 00 31.35	-20 27 05.0	M1	0.60	12.8	8.83	0.43	189	171.7	Köhler et al.(2000)
RXJ1601.7-2049	16 01 47.43	-20 49 45.8	M0	0.68	12.4	8.61	0.58	205	324.7	Köhler et al.(2000)
RXJ1601.8-2445	16 01 51.49	-24 45 24.9	K7	0.77	11.4	8.49	1.00	76	289.6	Köhler et al.(2000)
RXJ1602.9-2022	16 02 53.96	-20 22 48.1	K7	0.77	11.7	8.19	0.18	310	5.3	Köhler et al.(2000)
RXJ1603.9-2031B	16 03 54.96	-20 31 38.4	M0	0.68	12.5	8.62	0.53	121	140.9	Köhler et al.(2000)
RXJ1606.6-2108	16 06 37.41	-21 08 40.5	M1	0.60	13.2	9.11	0.09	1279	33.9	Köhler et al.(2000)
RXJ1607.0-1911	16 07 03.94	-19 11 33.9	M1	0.60	13.4	9.22	1.47	599	87.6	Köhler et al.(2000)
ScoPMS005	15 54 59.86	-23 47 18.2	G2	1.66	8.6	7.03	1.99	766	232.0	Köhler et al.(2000)
ScoPMS013	15 56 29.42	-23 48 19.8	M1.5	0.54	11.6	8.75	0.62	92	169.8	Köhler et al.(2000)
ScoPMS016	15 57 25.76	-23 54 22.0	M0.5	0.64	13.1	9.09	0.63	1324	226.0	Köhler et al.(2000)
ScoPMS020	16 01 05.19	-22 27 31.2	M3	0.36	12.9	8.75	0.60	193	313.7	Köhler et al.(2000)
ScoPMS023	16 02 10.45	-22 41 28.0	K5	0.87	10.2	8.06	0.65	300	345.6	Köhler et al.(2000)
ScoPMS029	16 05 42.67	-20 04 15.0	M2	0.49	13.4	9.16	0.56	643	352.6	Köhler et al.(2000)
ScoPMS031	16 06 21.96	-19 28 44.6	M0.5	0.64	12.8	8.62	0.64	578	148.2	Köhler et al.(2000)
ScoPMS042a	16 10 28.58	-19 04 47.0	M1	0.60	13.0	8.71	0.42	299	84.1	Köhler et al.(2000)
ScoPMS052	16 12 40.51	-18 59 28.3	K0	1.35	10.4	7.49	1.10	144	162.2	Metchev (2005)

Note. — Typical uncertainties are ∼1 subclass for spectral types, ∼0.2 mag for R magnitudes (taken from NOMAD; Zacharias et al. 2004), and ∼0.02 mag for K magnitudes (taken from 2MASS; Skrutskie et al. 2006). The uncertainties in masses are dominated by systematic errors, including a global zero-point uncertainty of ∼20% and individual uncertainties of as much as ∼100% due to the possibility of further unresolved multiplicity. Typical uncertainties in binary properties are ∼0.1 mag in ΔK, ∼10 mas in separation, and ∼1 deg in PA.

suffered a modest loss of sensitivity since the strehl is lower in H than in K', but the typical sensitivity limit in H still allows us to detect a ~ 30 M_{Jup} companion at 40 mas for half of our sample members. Observing in K would have yielded limits of $\Delta K \leq 1$ magnitude deeper (equivalent to $\Delta H \leq 1.5$ since low-mass companions are redder in $H - K$), and we decided this was not as important since the corresponding detection limits ($\geq$15-20 M_{Jup}) could not have reached the planetary mass range.

Observations at Keck used a 9 hole mask, with the longest baseline 8.27 m and the shortest baseline 1.67 m. We used a multiple-correlated double sampling readout in a 512x512 subarray of the ALADDIN detector, with 16 endpoint reads and a 10 s exposure per frame. Observations at Palomar with PHARO also used a 9 hole mask, with the longest baseline 3.94 m and the shortest baseline 0.71 m. To maximize the number of reads, we used either a 256x256 or 150x150 sub-array mode in one quadrant of the HAWAII detector, with a total of 16 or 28 reads respectively per array reset. Every read was saved to disk, so that in post-processing each file could be split into sub-frames. Splitting the data into more sub-frames minimizes sensitivity to changing seeing or AO instabilities, and using less sub-frames minimizes sensitivity to readout noise. We found that for the typical magnitudes of our targets, signal-to-noise was optimized by using read pairs separated by one read: giving 862 ms exposure times for the 256x256 sub-array mode, and 430 ms exposure times for the 150x150 sub-array mode.

A key requirement for obtaining good contrast limits is the contemporaneous observation of calibrator sources, ideally single stars which are nearby on the sky and similar in both optical and near-infrared brightness. A typical observing mode for isolated field stars is to obtain several sets of observations for a science target, interspersing visits to calibrator stars between each science observation. As a result, observations for a single science target might require as many as six target acquisitions (three calibrators, plus three visits to the source). However, all of our science targets are located in close proximity on the sky ($<10^o$) and they span a continuous range of brightness, so we were able to use the same calibrator star for multiple science targets and to intercalibrate between science targets. To this end, we divided our

sample into 20 groups of $\sim$4 similar-brightness stars each, then observed each group contemporaneously. Specifically, we visited each group member three times, plus we obtained one visit for each of two independent field calibrators. This allowed us to typically observe four science targets with a total of 14 acquisitions, for an average of 3.5 acquisitions per target. The average total time per acquisition was $\sim$4 minutes, so our strategy required $\sim$15 minutes per target.

We summarize the composition of our target groups and list the independent calibrators in Table 5.3. We also include the observation date and the mean R and K magnitudes for each group. Some of our groups are bigger or smaller because our acquisition images showed that several intended targets were resolved binaries (Section 5.3.3). When this occurred, we removed the binary system from our sample; in the case of Groups 12-15, we found a large number of binaries, so we rearranged the group composition at the telescope and eliminated Group 13.

Finally, a large fraction of our sample has been observed previously with high-resolution imaging (Brandner et al. 1996; Metchev 2005; Bouy et al. 2006), so we knew a priori whether these stars had known companions. However, many of our targets have been observed only with speckle imaging (Köhler et al. 2000) or have not been observed with any high-resolution techniques. For these sources, we decided to obtain quick observations in direct-imaging mode in order to screen out obvious binaries. This also allowed us to test for companions at separations outside the nominal limit of aperture-mask interferometry (240 mas at Palomar and 320 mas at Keck).

In Table 5.4, we list all of the sources that were observed with direct imaging and summarize the observations. We observed all of these sources with NIRC2 or PHARO using the smallest pixel scale available (10 or 25 mas pix^{-1}, respectively) and a two-point diagonal dither pattern. Faint stars were observed with a K' or K_s filter, while bright stars that would have saturated the detector were observed with a $Br\gamma$ filter, which attenuates flux by a factor of $\sim$10 relative to broadband K filters.

Table 5.3.　Aperture Mask Observations

Group	Science Targets	Calibrator Stars	Telescope	R (mag)	K (mag)	Epoch (JD-2450000)
1	GSC 06213-00306, GSC 06794-00156 RXJ1558.2-2328, RXJ1602.8-2401A	2M1618-2245, 2M1613-2218	Keck	9.3-10.4	7.08-8.02	4257
2	GSC 06213-00306, GSC 06793-01406 RXJ1601.9-2008, ScoPMS060	2M1602-1945, 2M1617-2320	Palomar	9.7-9.9	7.43-8.10	4251
3	GSC 06214-02384, RXJ1600.6-2159 RXJ1603.6-2245, V1149 Sco	2M1559-2303, 2M1620-2231	Palomar	10.2-10.6	7.05-8.36	4252
4	GSC 06793-00994, GSC 06794-00537 RXJ1602.8-2401B, ScoPMS214	2M1613-2311, 2M1630-2118	Palomar	10.5-11.1	7.76-8.93	4312
5	GSC 061901-00552, GSC 06204-00812 GSC 06209-00735, ScoPMS027	2M1558-1747, 2M1606-1924	Palomar	11.0-11.5	8.04-8.73	4250
6	GSC 06213-00306, GSC 06794-00337 ScoPMS045	2M1610-1818, 2M1629-2245	Palomar	10.9-11.9	8.08-8.56	4251
7	GSC 06213-00194, GSC 06793-00806 ScoPMS044, ScoPMS048 A	2M1609-2216, 2M1611-1906	Palomar	11.1-11.6	7.69-8.44	4252
8	GSC 06793-00797, GSC 06794-00480 GSC 06214-00210, RXJ1558.1-2405	2M1622-2036, 2M1558-2412	Palomar	11.4-11.9	8.46-9.15	4252
9	GSC 06205-00954, GSC 06209-01501 GSC 06213-01358, RXJ1601.1-2113	2M1601-2123, 2M1608-2022	Palomar	11.9-12.2	8.62-8.92	4250
10	GSC 06208-00834, GSC 06228-01359 RXJ1600.7-2127, RXJ1603.9-2031A	2M1602-2133, 2M1635-2204	Palomar	11.7-12.4	8.37-8.92	4250
11	GSC 06764-01305, GSC 06793-00868 RXJ1604.3-2130, ScoPMS019	2M1613-2303, 2M1535-2330	Keck	11.8-12.3	8.51-9.43	4257
12	RXJ1557.8-2305, RXJ1602.0-2221 RXJ1606.2-2036, USco-160822.4-193004 USco-161031.9-191305	2M1608-1916	Keck	12.4-13.0	8.61-9.27	4257
14	RXJ1550.0-2312, RXJ1600.2-2417 ScoPMS017, USco-155655.5-225839	2M1600-2421, 2M1543-1929	Keck	12.8-13.0	8.99-9.29	4256
15	USco-155655.5-225839, USco-160517.9-202420 USco-160823.2-193001, USco-160900.7-190852 USco-161115.3-175721	2M1557-2251, 2M1611-1802	Keck	13.1-13.3	9.14-9.47	4257
16	ScoPMS021, ScoPMS028 USco-160801.4-202741, USco-160823.8-193551	2M1606-1949, 2M1607-2027 2M1601-2227	Keck	13.3-13.6	8.52-9.55	4257
17	RXJ1551.1-2402, RXJ1605.6-2152	2M1550-2412, 2M1607-2050	Keck	13.4-13.6	9.47-9.73	4256

Table 5.3 (cont'd)

Group	Science Targets	Calibrator Stars	Telescope	R (mag)	K (mag)	Epoch (JD-2450000)
	RXJ1607.0-2043, ScoPMS022					
18	USco-160341.8-200557, USco-160343.3-201531	2M1610-1904, 2M1614-1846	Keck	13.7-13.8	9.49-9.72	4256
	USco-160908.4-200928, USco-160954.4-190654					
19	ScoPMS042b, USco-160142.6-222923	2M1602-2229, 2M1607-1929	Keck	13.8-13.8	9.62-10.22	4256
	USco-160707.7-192715, USco-160946.4-193735					
20	USco-160825.1-201224, USco-160916.8-183522	2M1614-1846, 2M1608-2008	Keck	13.9-14.1	9.67-9.91	4256
	USco-161347.5-183459, USco-161358.1-184828					

Table 5.4.   Direct Imaging Observations

Name	Telescope	T_{int} (s)	Filter	Epoch (JD-2450000)
GSC 06191-00019	Pal	56.64	Ks	4251
GSC 06195-00768	Pal	18.41	Ks	4199
GSC 06204-01067	Pal	56.64	Ks	4252
GSC 06205-00954	Pal	56.64	Ks	4250
GSC 06208-00834	Pal	56.64	Ks	4250
GSC 06209-01501	Pal	56.64	Ks	4250
GSC 06213-00194	Pal	56.64	Ks	4251
GSC 06213-00306	Pal	56.64	Ks	4251
GSC 06213-01358	Pal	56.64	Ks	4250
GSC 06214-00210	Pal	56.64	Ks	4251
GSC 06214-02384	Pal	56.64	Ks	4251
GSC 06764-01305	Pal	56.64	Ks	4252
GSC 06793-00797	Pal	56.64	Ks	4251
GSC 06793-00806	Pal	56.64	Ks	4251
GSC 06793-00868	Pal	56.64	Ks	4252
GSC 06793-00994	Pal	56.64	Ks	4251
GSC 06794-00156	Pal	56.64	Ks	4251
GSC 06794-00480	Pal	56.64	Ks	4251
GSC 06794-00537	Pal	56.64	Ks	4251
RXJ1550.0-2312	Keck	32	Brg	4256
RXJ1550.0-2312	Keck	32	Brg	4257
RXJ1550.9-2534	Keck	32	Brg	4257
RXJ1551.1-2402	Keck	32	Brg	4256
RXJ1557.8-2305	Keck	32	Brg	4257
RXJ1558.1-2405	Pal	56.64	Ks	4252
RXJ1558.2-2328	Pal	56.64	Ks	4251
RXJ1600.7-2127	Pal	56.64	Ks	4250
RXJ1601.1-2113	Pal	56.64	Ks	4250
RXJ1601.9-2008	Pal	56.64	Ks	4251
RXJ1602.0-2221	Keck	32	Brg	4257
RXJ1602.8-2401A	Keck	16	Brg	4257
RXJ1602.8-2401B	Pal	56.64	Ks	4251
RXJ1603.6-2245	Pal	56.64	Ks	4251
RXJ1603.9-2031A	Pal	56.64	Ks	4250
RXJ1604.3-2130	Pal	56.64	Ks	4252
RXJ1606.2-2036	Pal	56.64	Ks	4252

Table 5.4 (cont'd)

Name	Telescope	T_{int} (s)	Filter	Epoch (JD-2450000)
RXJ1607.0-2036	Pal	56.64	Ks	4251
ScoPMS015	Pal	56.64	Ks	4250
ScoPMS017	Keck	32	Brg	4256
ScoPMS019	Pal	56.64	Ks	4252
ScoPMS022	Keck	32	Brg	4256
ScoPMS027	Pal	28.32	Ks	4250
ScoPMS028	Keck	32	Brg	4257
ScoPMS042b	Keck	44	Brg	4256
ScoPMS044	Pal	56.64	Ks	4251
ScoPMS045	Pal	56.64	Ks	4251
ScoPMS048	Pal	56.64	Ks	4251
USco-160341.8-200557	Keck	32	Brg	4256
Usco-160428.4-190441	Keck	32	Brg	4257
USco-160517.9-202420	Keck	32	Brg	4257
USco-160643.8-190805	Pal	56.64	Ks	4252
USco-160707.7-192715	Keck	36	Brg	4256
USco-160801.4-202741	Pal	56.64	Ks	4252
Usco-160823.2-193001	Keck	32	Brg	4257
USco-160823.8-193551	Keck	32	Brg	4257
USco-160825.1-201224	Keck	32	Brg	4256
USco-160900.7-190852	Pal	56.64	Ks	4252
USco-160908.4-200928	Keck	32	Brg	4256
USco-160916.8-183522	Keck	32	Brg	4256
USco-160954.4-190654	Keck	32	Brg	4256
USco-161031.9-191305	Pal	56.64	Ks	4252
USco-161115.3-175721	Keck	32	Brg	4257
USco-161347.5-183459	Keck	32	Brg	4256

5.3.2 Aperture Mask Analysis and Detection Limits

The aperture-masking analysis pipeline is similar to that used for several previous papers containing Palomar masking data (Pravdo et al. 2006; Lloyd et al. 2006; Martinache et al 2007). After subtracting the bias (dark) level, flat-fielding and removing bad pixels, the data are windowed by a super-Gaussian (a function of the form $\exp(-kx^4)$). This window both limits sensitivity to readout noise and acts as a spatial-filter. Each frame is then Fourier-transformed, and the complex visibility extracted for each baseline. Complex visibilities cannot be directly used for high-fidelity measurements because of their sensitivity to variable optical aberrations and non common path errors. Instead, we use the averaged squared visibility and the complex triple product (Lohmann et al., 1983). For each visit to each star, we extract squared-visibility, closure-phase, and the uncertainties on these quantities based on the scatter within one visit. Finally, the calibration process consists of estimating
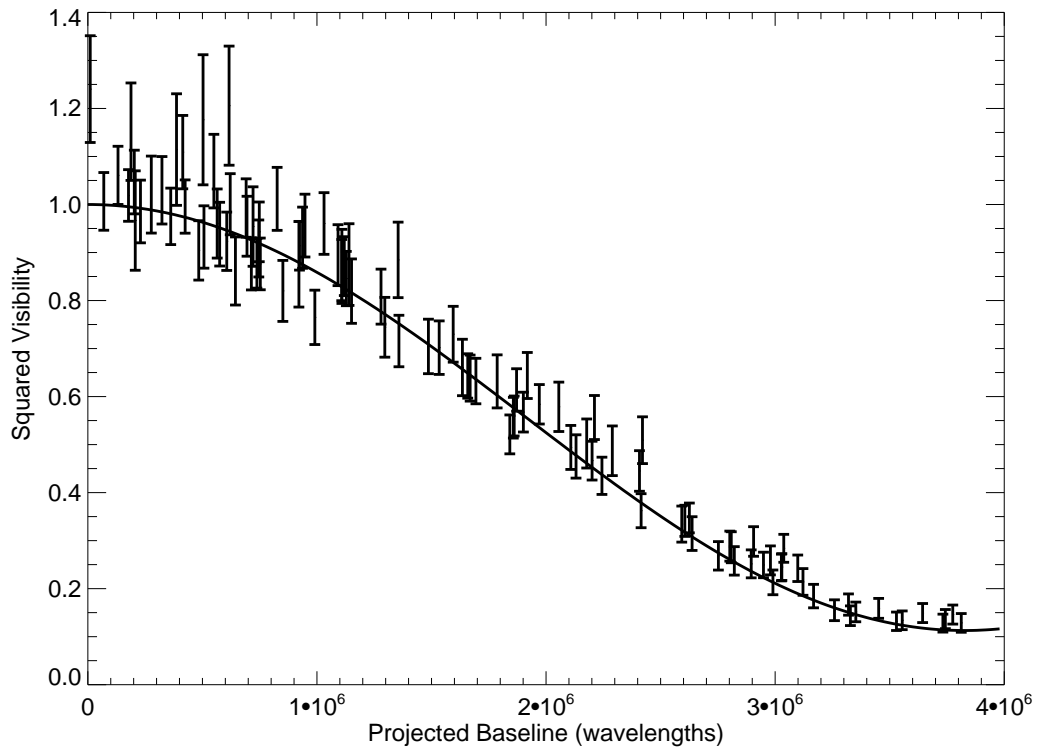
Figure 5.1 The squared visibilities as a function of projected baseline for the 27 mas binary RXJ1550.0-2312. Despite a separation of only 0.6 λ/D, the binary system is clearly detected; the solid line denotes our best-fit value for the system parameters (Table 5.5).
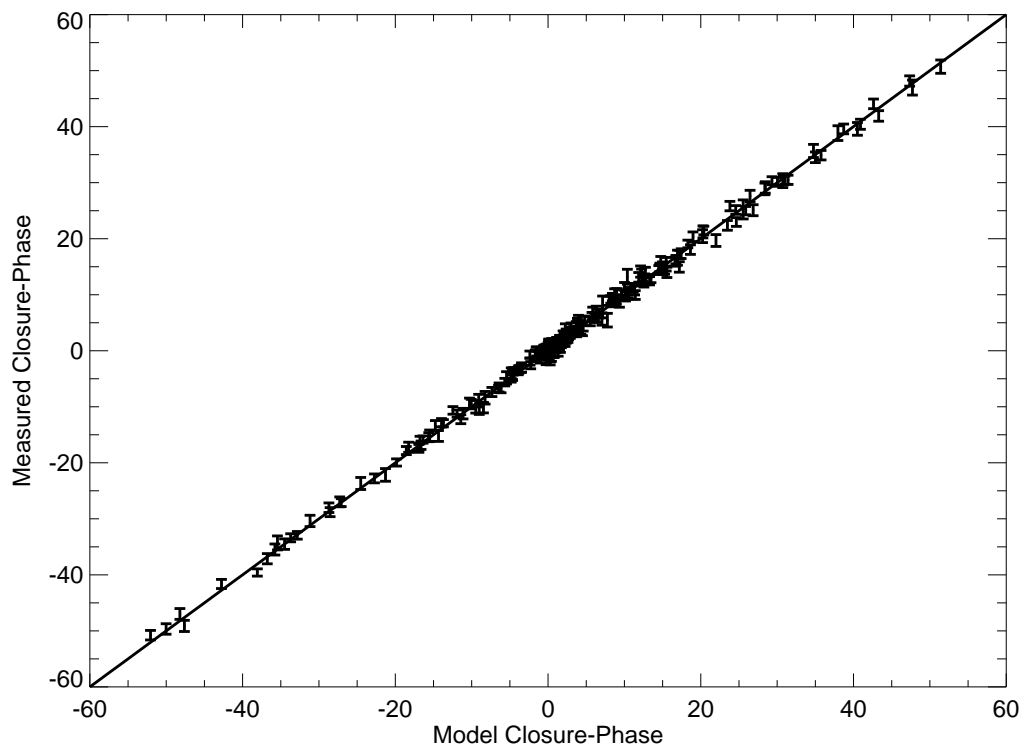
Figure 5.2 The measured close phases as a function of modeled closure phases for RXJ1550.0-2312, assuming that it has the best-fit parameters that we list in Table 5.5 (a 27 mas binary with a flux ratio of 2:1).

the instrumental squared-visibilities and closure-phases. The target star's squared visibilities are divided by the instrumental squared-visibilities and the instrumental closure-phase is subtracted from the measured closure-phase.

Figures 5.1 and 5.2 show a fit to data for the 27 mas separation binary RXJ1550.0-2312. Squared visibility is plotted against baseline projected along the axis of the binary. As closure-phase is a multi-dimensional quantity, we chose to simply plot the measured closure-phases versus the model closure-phases. Despite this binary being at a separation of only $0.6\lambda/D$, it is clear that it is an extremely-high signal-to-noise detection. Note that only closure-phase was used in the fit: calibration errors are evident in the squared visibility data with the few points that have squared visibility greater than 1.0.

The error analysis procedure used to calculate the covariance matrix of closure-phase for each target is given in detail in Appendix A of the published version of this paper. For all targets, an attempt at fitting a binary solution was made, by first searching exhaustively in a grid in position angle and separation at high-contrast and then by a gradient descent search to find the χ^2 minimum. Errors in binary parameters were calculated from the curvature of the χ^2 surface at the χ^2 minimum (i.e., the same method as most least-squares algorithms). Detections were retained if their contrast was greater than a 99.9% confidence threshold.

In order to calculate a detection threshold, we simulated 10000 data sets with the identical (u, v)-sampling and error properties of each target. For each of these simulated data sets, we calculated the best fit contrast ratio for every value of separation and position angle in a large grid, and then tabulated the maximum contrast ratio (i.e., brightest fitted companion) within a series of annuli. Our 99.9% upper limits to companion brightness within each annulus was taken to be the contrast ratio where 99.9% of the simulations had no fitted companion brighter than this limit anywhere within the annulus. Details of the simulation and fitting algorithms can be found in the Appendix A of the published version of this paper.

5.3.3 Imaging Analysis and Detection Limits

The imaging data were flat-fielded and dark- and bias-subtracted using standard IRAF procedures. We measured PSF-fitting photometry and astrometry for our sources using the IRAF package DAOPHOT (Stetson 1987), and specifically with the ALLSTAR routine. Where possible, we analyzed each frame separately in order to estimate the uncertainty in individual measurements and to allow for the potential rejection of frames with inferior AO correction; our final results represent the mean value for all observations in a filter. If the companion could not be easily distinguished in a single filter, we measured photometry from the coadded sum of all images at each dither position.

In all cases, we used the science target (or the primary star of a binary) to produce an analytic PSF composed of a Gaussian core with Lorentzian wings. If the science target was a close binary, we reconstructed the PSF using the algorithm described in Kraus & Hillenbrand (2007b), which iteratively fits a template PSF to the primary and then subtracts the secondary to fit an improved estimate of the primary. Three sources appeared to be marginally detected in our observations; we retained these sources in our aperture mask sample and later confirmed their multiplicity (Section 5.4), so we processed their images with our PSF reconstruction routine and report the results. Finally, we calibrated our photometry using the known 2MASS K_s magnitudes for each of our science targets; these absolute magnitudes are uncertain by $\sim$0.1-0.2 magnitudes due to the intrinsic variability of young stars (resulting from accretion or rotation).

At small separations ($\leq 5\lambda/D$), our imaging data for apparently single stars will be superceded by our aperture mask data, so the detection limits are not important. At larger separations ($\geq 5\lambda/D$), where spurious sources corresponding to AO speckles dominate, we adopted the detection limits suggested by Metchev (2005) for similar observations: $\Delta K = 4$ at 250-500 mas, $\Delta K = 5$ at 500-1000 mas, and the sky background limit ($K \sim$16.5-17.5) at separations of $\geq 1''$. We tested these limits for a set of the apparently single stars in our sample by subtracting an analytic PSF from

the science target, then compiling the statistics for all apparently spurious detections. In all cases, the AO speckles fall at least a magnitude below our adopted limits.

Finally, the NIRC2 images were distortion-corrected using new high-order distortion solutions (P.B. Cameron, priv. comm.) that deliver a significant performance increase as compared to the solutions presented in the NIRC2 pre-ship manual[1]; the typical absolute residuals for bright, well-resolved stars are ≤1 mas in narrow camera mode. The PHARO images were distortion-corrected using the solution derived by Metchev (2005), with fractional uncertainties in relative astrometry of ∼0.15%. These uncertainties limit our astrometry for most close, well-resolved binary systems. The uncertainty for wider (≥2-3″) pairs seems to be driven by variation due to differential tilt jitter, while the uncertainty for close blended pairs is driven by our ability to accurately model the single-star PSF.

5.3.4 Stellar and Companion Properties

Stellar properties can be difficult to estimate, particularly for young stars, since pre-main-sequence stellar evolutionary models are not well-calibrated. The mass of a given sample could be systematically uncertain by as much as 20% (e.g., Hillenbrand & White 2004), and individual masses could be uncertain by factors of 2 or more due to unresolved multiplicity or the intrinsic variability that young stars often display (from accretion or rotational modulation of star spots). This suggests that any prescription for determining stellar properties should be treated with caution.

We estimated the properties of all of our sample members using the methods described in Kraus & Hillenbrand (2007a). This procedure combines the 5 Myr isochrone of Baraffe et al.(1998) and the temperature scales of Schmidt-Kaler (1982) and Luhman et al.(2003) to directly convert observed spectral types to masses. Relative properties (mass ratios q) for all binaries in our sample were calculated by combining these isochrones and temperature scales with the empirical NIR colors of Bessell & Brett (1998) and the K-band bolometric corrections of Leggett et al.(1998) to esti-

---

[1]http://www2.keck.hawaii.edu/realpublic/inst/nirc2/

mate q from the observed flux ratio ΔK. We also used these techniques to estimate masses for all of our sample members, which we list in Tables 5.1 and 5.2.

For all binary systems, we have adopted the previously-measured (unresolved) spectral type for the brightest component and inferred its properties from that spectral type. This should be a robust assumption since equal-flux binary components will have similar spectral types and significantly fainter components would not have contributed significant flux to the original discovery spectrum. Projected spatial separations are calculated assuming the mean distance of Upper Sco, 145±2 pc (de Zeeuw et al.(1999). If the total radial depth of Upper Sco is equal to its angular extent (±8° or ±20 pc), then the unknown depth of each system within Upper Sco implies an uncertainty in the projected spatial separation of ±14%. The systematic uncertainty due to the uncertainty in the mean distance of Upper Sco is negligible in comparison (≤2%).

Finally, the sensitivity limits for some of our sample members extend to the bottom of the brown dwarf mass range and could potentially encompass the top of the planetary mass range. However, mass estimates for young giant planets are completely uncalibrated and there are ongoing debates regarding their peak and typical luminosities. The models of Baraffe et al.(2003) imply that a survey sensitive to $K \sim 16$ could detect 7-10 M_{Jup} planets at the distance and age of Upper Sco. However, more detailed models of planet formation by Marley et al.(2007) suggest that the typical luminosity of a young planet could be 1-2 orders of magnitude lower than previously predicted. These models differ primarily in their treatment of the initial conditions; recent models suggest that accretion shocks could dispel much of the initial energy, leading to lower internal entropy and correspondingly lower initial temperatures than the earlier models predicted. We can not currently resolve this controversy, so we only note that our limits on the presence of massive planets should be considered with caution.
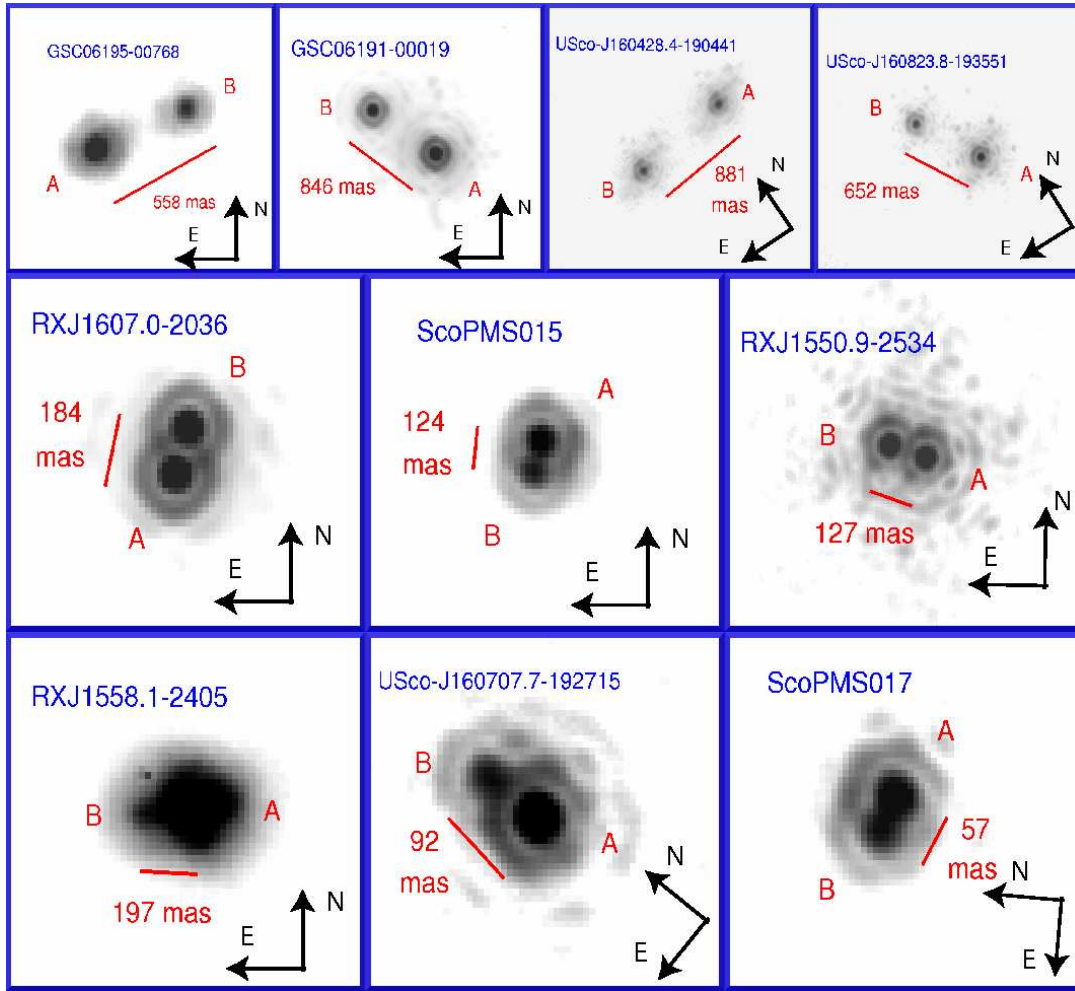
Figure 5.3 Ten new systems that we observed with direct imaging. The top row shows relatively wide (0.5-1.0″) pairs, the middle row shows close, equal-flux pairs that are still easily distinguished, and the bottom row shows three very close or unequal-flux systems that could be difficult to identify with direct imaging alone, but were easily identified with aperture masking.
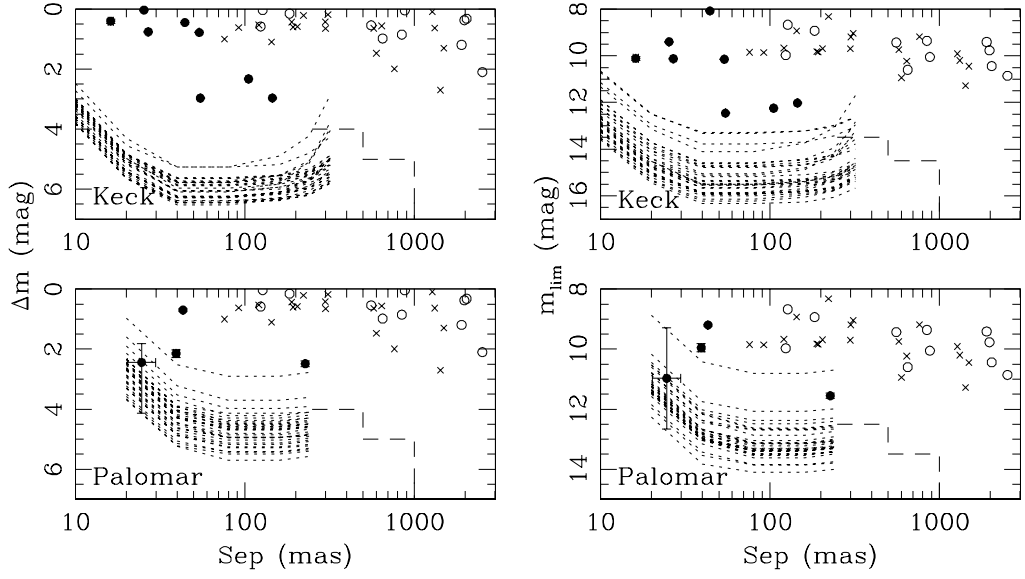
Figure 5.4 Contrast ratio (left) and secondary brightness (right) as a function of separation for our new systems identified via masking (filled circles) and imaging (open circles), plus all known binary systems (crosses). We also show the corresponding aperture-masking detection limits for all apparently single stars in our survey (short-dashed lines) and our adopted sensitivity limits for our imaging data (long-dashed line).
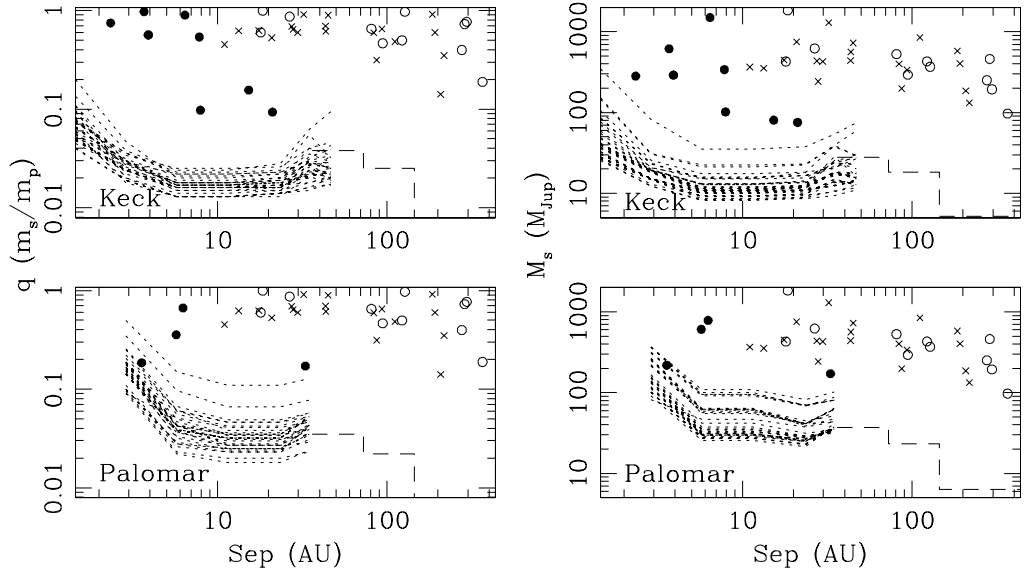
Figure 5.5 As in Figure 5.4, but showing mass ratio (left) and secondary mass (right) as a function of separation.

5.4　New Companions in Upper Sco

Our aperture mask survey is sensitive to companions with separations between $\sim\lambda/4D$ and $\sim6\lambda/D$ (at Keck) or $\sim4\lambda/D$ (at Palomar), corresponding to separation ranges of $\sim$10-320 mas and $\sim$20-240 mas, respectively. In this separation range, we identified 12 members of Upper Sco which possess a candidate companion at a confidence level of $\geq$99.5% (99.9% per annulus); the other 60 masking sample members appear to be single to within the detection limits we derived in Section 5.3.2. In Table 5.5, we list all of our newly-identified candidate companions and report their flux ratios, separations, and position angles. In Table 5.6, we summarize our derived upper limits as a function of separation for the 60 remaining members of our sample. The detection limits decline rapidly between $\sim\lambda/4D$ and $\sim2\lambda/3D$, but they are relatively flat at larger separations, extending to contrast ratios of $\sim$5.0-6.5 magnitudes at Keck and $\sim$4.5-5.5 magnitudes at Palomar.

The system RXJ1550.0-2312 was observed on separate nights with separate calibrator sets at Keck in order to confirm the accuracy and repeatablity of our measurements. The separations and contrast ratios measured at each epoch agree to within <1 σ, suggesting that our results are repeatable and our assessed uncertainties are valid. We also we note that three of our calibrators appear to have companions. We did not use these observations in our final data calibration, and we report their astrometry in Table 5.4 for completeness. Finally, we note that the system GSC 06209-00735 has been previously identified as an SB1 by Guenther et al.(2007). The orbital period that they derived (2045$\pm$16 d) is consistent with the projected separation (25$\pm$5 mas; 3.6$\pm$0.7 AU) of our newly-imaged companion, so these detections appear to denote the same companion. Two more astrometric detections should allow us to resolve the orbital parameters which were not determined in the RV orbit ($K2$, i, and Ω) and directly measure the masses of both stars.

In Table 5.7, we summarize the observed properties of 7 newly-detected binary systems discovered in our snapshot imaging program, three systems which were discovered in our aperture mask survey and subsequently recovered in our imaging data,

and 9 known binary systems for which we report updated properties. In Figure 5.3, we show the corresponding discovery images for our newly-discovered binaries. We do not report any new candidate companions discovered outside a radius of $2''$ or with $K \geq 15$ because of the significant probability that any such companions are background stars. We have previously estimated the density of background stars brighter than $K \sim 15$ to be ~ 1 arcmin^{-2} (Kraus & Hillenbrand 2007a), so the expected number of such contaminants inside $\sim 3''$ is only ~ 1. However, there are many background bulge giants with apparent brightness $K \sim 16$-17 that could be mistaken for faint wide companions, so an extension of these limits will require second-epoch observations to confirm common proper motion. Finally, we note that 4 of these sources fell near or inside the detection limits of the speckle interferometry survey of Köhler et al.(2000); their nondetection is most likely explained by an unfavorable orbital phase in 1994-1995 and 14 years of orbital motion.

In Table 5.8, we list the inferred stellar and binary properties for each of our newly-identified binary systems and the binary systems that we collated from the literature. In Figures 5.4 and 5.5, we plot the contrast ratio and mass ratio versus the separation of all of our newly-detected companions, plus the corresponding detection limits for apparently single stars. The vast majority of our newly-identified candidate companions sit well above our survey's detection limits, suggesting that they are all valid detections. Their typical flux ratios ($\Delta K \leq 3$) indicate that they have stellar masses. Both panels of Figure 5.3 show an obvious dearth of companions with flux ratios $\Delta K \geq 3$, corresponding roughly to the substellar mass range. Our survey should have clearly detected any source in this range of parameter space, as has been proven for orbital monitoring of field binaries like GJ 802 (Lloyd et al. 2006; Ireland et al. 2008), so this deficit seems to represent a genuine absence of companions.

Finally, we did not detect any candidate companions near the typical detection limits of our survey, which correspond to 99.9% confidence limits in any single separation bin or $\sim 99.5\%$ across all separation bins. We would expect an average of 0.3 false detections for the 60 targets listed in Table 5.6, so our nondetection is consistent with the statistical estimate. We did detect four candidate companions with

Table 5.5. Companions Identified with the Aperture Mask

Primary	Telescope	Δm (mag)	Sep (mas)	PA (deg)
GSC 06209-00735[a]	Palomar	2.44±1.16	24.6±5.2	42.5±3.6
GSC 06764-01305	Keck	2.97±0.01	54.68±0.16	173.76±0.19
GSC 06794-00156	Keck	0.45±0.01	44.30±0.07	230.74±0.08
RXJ1550.0-2312	Keck	0.76±0.01	26.95±0.05	222.13±0.13
RXJ1550.0-2312	Keck	0.76±0.01	26.93±0.04	222.07±0.11
RXJ1558.1-2405	Palomar	2.48±0.09	227.67±1.99	99.23±0.47
RXJ1601.9-2008	Palomar	2.14±0.13	39.31±1.57	217.67±0.59
ScoPMS017	Keck	0.78±0.01	53.86±0.19	68.93±0.20
ScoPMS019	Keck	0.03±0.01	25.40±0.12	113.55±0.62
ScoPMS027	Palomar	0.70±0.03	43.18±0.12	68.63±0.29
USco-160517.9-202420	Keck	0.40±0.07	16.15±0.59	251.12±1.11
USco-160707.7-192715	Keck	2.33±0.01	105.25±0.21	0.90±0.09
USco-161031.9-191305	Keck	2.96±0.02	145.55±0.43	81.63±0.14
Calibrators				
2M1535-2330	Keck	1.35±0.01	92.35±0.17	311.46±0.09
2M1601-2227	Keck	0.64±0.09	249.76±0.5	328.73±0.14
2M1613-2218	Keck	3.97±0.07	93.33±1.04	11.9±0.6

[a]The contrast ratio and separation are highly degenerate at separations this small, but at the least favorable separation, the secondary flux still represents a $>7\ \sigma$ detection.

lower confidence levels (99.5-99.9% in their separation bin, corresponding to overall confidence levels of ∼97.5%-99.5%). We would only expect to observe ∼1.5 false detections with this range of confidence levels, so 4 represents a marginally significant excess. A discussion off this is given in Section 5.6.3.

Table 5.6. Upper Limits for Undetected Companions

Primary	Telescope	Δm[a]						$q\ (m_s/m_p)$[a]					
		10-20	20-40	40-80	80-160	160-240	240-320	10-20	20-40	40-80	80-160	160-240	240-320
GSC 06191-00552[b]	Palomar	...	3.12	4.71	5.03	4.97	...	...	0.110	0.028	0.025	0.034	...
GSC 06204-00812	Palomar	...	3.23	4.81	5.13	5.03	...	...	0.100	0.029	0.025	0.041	...
GSC 06205-00954	Palomar	...	2.46	4.02	4.50	4.42	...	...	0.157	0.042	0.035	0.050	...
GSC 06208-00834	Palomar	...	2.71	4.30	4.81	4.66	...	...	0.161	0.036	0.030	0.043	...
GSC 06209-01501	Palomar	...	2.62	4.19	4.53	4.49	...	...	0.166	0.039	0.032	0.034	...
GSC 06213-00194	Palomar	...	2.34	3.93	4.43	4.30	...	...	0.185	0.043	0.036	0.048	...
GSC 06213-00306	Palomar	...	2.32	3.89	4.13	4.10	...	...	0.089	0.051	0.041	0.047	...
GSC 06213-00306	Keck	3.23	5.06	5.89	5.80	5.54	5.20	0.098	0.020	0.014	0.015	0.026	0.019
GSC 06213-00306	Palomar	...	3.69	5.24	5.71	5.57	...	...	0.092	0.022	0.018	0.024	...
GSC 06213-01358	Palomar	...	2.66	4.25	4.70	4.58	...	...	0.143	0.038	0.032	0.052	...
GSC 06214-00210	Palomar	...	1.90	3.52	3.98	3.91	...	...	0.250	0.060	0.046	0.053	...
GSC 06214-02384	Palomar	...	2.88	4.45	4.86	4.76	...	...	0.182	0.043	0.028	0.044	...
GSC 06228-01359	Palomar	...	2.70	4.29	4.65	4.57	...	...	0.143	0.038	0.032	0.052	...
GSC 06793-00797	Keck	3.57	5.40	6.25	6.10	5.75	4.94	0.056	0.019	0.013	0.014	0.024	0.023
GSC 06793-00797	Palomar	...	2.14	3.71	4.21	4.10	...	...	0.222	0.062	0.038	0.047	...
GSC 06793-00806	Palomar	...	0.97	2.52	2.90	2.78	...	...	0.499	0.150	0.109	0.128	...
GSC 06793-00994	Palomar	...	3.65	5.23	5.49	5.40	...	...	0.153	0.032	0.024	0.036	...
GSC 06793-01406	Palomar	...	3.06	4.61	4.95	4.82	...	...	0.187	0.056	0.042	0.053	...
GSC 06794-00337	Palomar	...	2.70	4.29	4.60	4.51	...	...	0.190	0.047	0.034	0.039	...
GSC 06794-00480	Palomar	...	1.59	3.23	3.70	3.60	...	...	0.349	0.097	0.066	0.077	...
GSC 06794-00537	Palomar	...	3.31	4.87	5.18	5.08	...	...	0.100	0.026	0.023	0.031	...
RXJ1551.1-2402	Keck	3.07	4.88	5.76	5.63	5.45	5.04	0.073	0.036	0.022	0.023	0.035	0.029
RXJ1557.8-2305	Keck	2.98	4.81	5.78	5.55	5.13	3.96	0.084	0.028	0.018	0.020	0.033	0.039
RXJ1558.2-2328	Keck	3.12	4.93	5.77	5.67	5.42	5.02	0.200	0.047	0.02	0.022	0.031	0.043
RXJ1600.2-2417	Keck	2.72	4.55	5.27	5.18	4.80	4.26	0.109	0.029	0.022	0.023	0.030	0.034
RXJ1600.6-2159	Palomar	...	2.93	4.52	4.95	4.86	...	...	0.177	0.043	0.027	0.042	...
RXJ1600.7-2127	Palomar	...	2.44	4.05	4.47	4.38	...	...	0.187	0.043	0.034	0.040	...
RXJ1601.1-2113	Palomar	...	2.64	4.23	4.68	4.62	...	...	0.143	0.039	0.032	0.053	...
RXJ1602.0-2221	Keck	2.48	4.30	5.26	4.90	4.23	2.86	0.136	0.038	0.024	0.028	0.062	0.094
RXJ1602.8-2401A	Keck	3.06	4.87	5.64	5.57	5.39	4.99	0.108	0.022	0.016	0.016	0.027	0.021
RXJ1602.8-2401B	Palomar	...	2.52	4.08	4.58	4.50	...	...	0.167	0.042	0.031	0.035	...
RXJ1603.6-2245	Palomar	...	3.10	4.65	4.94	4.90	...	...	0.143	0.037	0.027	0.029	...
RXJ1603.9-2031A[b]	Palomar	...	2.86	4.45	4.94	4.86	...	...	0.143	0.033	0.027	0.039	...

Table 5.6 (cont'd)

Primary	Telescope	Δm[a] 10-20	20-40	40-80	80-160	160-240	240-320	$q\ (m_s/m_p)$[a] 10-20	20-40	40-80	80-160	160-240	240-320
RXJ1604.3-2130	Keck	3.57	5.43	6.23	6.15	5.79	5.50	0.060	0.018	0.013	0.013	0.021	0.017
RXJ1605.6-2152[b]	Keck	3.20	5.05	6.09	5.93	5.66	5.24	0.064	0.030	0.017	0.018	0.029	0.025
RXJ1606.2-2036	Keck	2.99	4.83	5.72	5.54	5.05	4.05	0.094	0.025	0.017	0.018	0.022	0.034
RXJ1607.0-2043	Keck	3.15	4.99	5.85	5.78	5.56	5.16	0.066	0.030	0.019	0.020	0.028	0.025
ScoPMS021	Keck	3.37	5.19	6.06	5.94	5.75	5.05	0.081	0.020	0.013	0.014	0.016	0.020
ScoPMS022	Keck	3.14	4.97	5.96	5.84	5.63	5.21	0.066	0.030	0.018	0.019	0.029	0.025
ScoPMS028	Keck	3.02	4.85	5.64	5.54	5.40	4.86	0.078	0.031	0.021	0.022	0.027	0.029
ScoPMS042b	Keck	3.22	5.07	5.85	5.72	5.48	4.99	0.075	0.034	0.025	0.026	0.040	0.034
ScoPMS044	Palomar	...	2.48	4.05	4.38	4.29	...	...	0.182	0.05	0.035	0.053	...
ScoPMS045[b]	Palomar	...	3.28	4.86	5.28	5.23	...	...	0.100	0.028	0.023	0.043	...
ScoPMS048	Palomar	...	2.34	3.93	4.29	4.20	...	...	0.258	0.067	0.049	0.057	...
ScoPMS060	Palomar	...	3.31	4.89	5.26	5.17	...	...	0.206	0.061	0.046	0.057	...
ScoPMS214	Palomar	...	3.58	5.14	5.41	5.30	...	...	0.096	0.023	0.020	0.023	...
USco-155655.5-225839	Keck	3.48	5.31	6.23	6.15	5.95	5.60	0.050	0.025	0.015	0.015	0.018	0.020
USco-160142.6-222923	Keck	3.18	5.00	5.79	5.68	5.52	5.00	0.067	0.027	0.018	0.019	0.023	0.025
USco-160341.8-200557	Keck	3.66	5.50	6.39	6.28	5.88	5.38	0.053	0.028	0.017	0.017	0.027	0.026
USco-160343.3-201531	Keck	3.82	5.65	6.52	6.34	6.05	5.66	0.049	0.024	0.016	0.017	0.021	0.023
USco-160801.4-202741	Keck	3.31	5.13	6.06	6.00	5.71	5.32	0.057	0.026	0.016	0.016	0.024	0.022
USco-160822.4-193004	Keck	3.30	5.13	6.05	5.82	5.08	3.76	0.060	0.029	0.017	0.019	0.040	0.046
USco-160823.2-193001	Keck	3.79	5.64	6.46	6.35	6.20	5.77	0.041	0.019	0.013	0.014	0.016	0.017
USco-160825.1-201224	Keck	3.64	5.46	6.28	6.09	5.91	5.43	0.048	0.024	0.016	0.017	0.021	0.023
USco-160900.7-190852	Keck	3.81	5.63	6.38	6.33	6.14	5.72	0.040	0.019	0.013	0.014	0.015	0.018
USco-160916.8-183522	Keck	3.57	5.40	6.25	6.14	5.97	5.44	0.055	0.029	0.018	0.018	0.020	0.025
USco-160946.4-193735	Keck	3.59	5.42	6.28	6.18	5.98	5.56	0.049	0.024	0.016	0.016	0.022	0.022
USco-160954.4-190654	Keck	3.59	5.42	6.26	6.09	5.68	4.96	0.049	0.024	0.016	0.017	0.030	0.028
USco-161115.3-175721	Keck	3.80	5.63	6.45	6.31	6.15	5.72	0.045	0.024	0.015	0.016	0.023	0.020
USco-161347.5-183459	Keck	2.99	4.83	5.61	5.53	5.33	4.88	0.077	0.036	0.023	0.024	0.055	0.032
USco-161358.1-184828	Keck	3.72	5.56	6.45	6.38	6.19	5.80	0.051	0.024	0.016	0.017	0.018	0.021
V1149 Sco	Palomar	...	3.49	5.06	5.43	5.35	...	...	0.154	0.038	0.025	0.035	...

[a]The range of each separation bin is reported in units of mas, and the corresponding detection limits are reported in terms of δm or q.

[b]We detected candidate companions at lower confidence (97.5-99.5%) for these four sources; we plan to obtain additional observations to confirm or disprove them.

Table 5.7.   Companions Identified with Direct Imaging

Name	Telescope	Δm (mag)	Sep (mas)	PA (deg)
New				
GSC 06191-00019	Palomar	0.85±0.01	845.8±1	58.0±0.1
GSC 06195-00768	Palomar	0.54±0.01	558±1	292.1±0.3
RXJ1550.9-2534	Keck	0.03±0.01	127.5±1	72.70±0.06
RXJ1558.1-2405[a]	Palomar	1.86±0.03	197±2	98.8±0.3
RXJ1607.0-2036	Palomar	0.15±0.03	183.8±1	344.2±0.3
ScoPMS015	Palomar	0.58±0.02	124.1±1	166.5±0.4
ScoPMS017[a]	Keck	0.65±0.01	57.1±1	68.34±0.11
USco-160428.4-190441	Keck	0.04±0.01	881.1±1	128.13±0.10
USco-160707.7-192715[a]	Keck	1.59±0.01	91.8±1	2.1±0.3
USco-160823.8-193551	Keck	0.98±0.01	651.5±1	64.61±0.11
Known				
GSC 06204-01067	Palomar	2.10±0.01	2528±4	93.04±0.02
GSC 06213-00306	Palomar	2.37±0.01	3186±5	305.11±0.01
GSC 06793-00806	Palomar	1.19±0.01	1907±3	338.81±0.03
GSC 06793-00868	Palomar	0.37±0.01	1981±4	155.29±0.06
RXJ1602.8-2401B	Palomar	2.91±0.02	7198±13	352.22±0.04
ScoPMS048	Palomar	1.76±0.01	3394±5	191.22±0.01
ScoPMS042b	Keck	2.48±0.03	4606±2	6.71±0.03
USco-160908.4-200928	Keck	0.32±0.01	2042±1	139.36±0.07
USco-161031.9-191305	Palomar	3.83±0.02	5775±9	112.66±0.02

[a]Uncertainties are difficult to estimate due to to significant blending of the PSFs. The values and uncertainties from the aperture-masking detection in Table 5.5 should be used for this system.

Table 5.8.   Companion Properties

Name	Sep (AU)	q (m_s/m_p)	M_{prim} $(M_\odot)$	M_{sec} $(M_\odot)$	Source
GSC 06191-00019	122.6	0.50	0.82	0.41	Palomar-Imaging
GSC 06195-00768	80.9	0.65	0.77	0.50	Palomar-Imaging
GSC 06204-01067	366.6	0.19	0.49	0.09	Palomar-Imaging
GSC 06209-00735	3.6	0.18	1.12	0.21	Palomar-Masking
GSC 06213-00306	462.0	0.15	0.87	0.13	Palomar-Imaging
GSC 06214-00210	318.6	0.02	0.60	0.011	Palomar-Imaging
GSC 06764-01305	7.9	0.10	0.99	0.10	Keck-Masking
GSC 06780-01061	217.5	0.35	0.36	0.13	Kraus & Hillenbrand (2007a)
GSC 06793-00569	207.4	0.14	1.25	0.18	Metchev (2005)
GSC 06793-00806	276.5	0.40	0.60	0.24	Palomar-Imaging
GSC 06793-00819	32.2	0.91	1.35	1.23	Metchev (2005)
GSC 06793-00868	287.3	0.73	0.60	0.44	Palomar-Imaging
GSC 06794-00156	6.4	0.90	1.59	1.43	Keck-Masking
RXJ1550.0-2312	3.9	0.56	0.49	0.28	Keck-Masking (1)
RXJ1550.0-2312	3.9	0.56	0.49	0.28	Keck-Masking (2)
RXJ1550.9-2534	18.5	1.00	1.75	1.74	Keck-Imaging
RXJ1558.1-2405	33.0	0.17	0.95	0.16	Palomar-Masking
RXJ1558.1-2405	28.6	0.25	0.95	0.23	Palomar-Imaging
RXJ1600.5-2027	27.4	0.69	0.60	0.41	Köhler et al.(2000)
RXJ1601.7-2049	29.7	0.60	0.68	0.41	Köhler et al.(2000)
RXJ1601.8-2445	11.0	0.45	0.77	0.35	Köhler et al.(2000)
RXJ1601.9-2008	5.7	0.36	1.62	0.58	Palomar-Masking
RXJ1602.8-2401B	1043.7	0.10	0.95	0.10	Palomar-Imaging
RXJ1602.9-2022	45.0	0.90	0.77	0.69	Köhler et al.(2000)
RXJ1603.9-2031B	17.6	0.63	0.68	0.43	Köhler et al.(2000)
RXJ1606.6-2108	185.5	0.91	0.60	0.55	Köhler et al.(2000)
RXJ1607.0-1911	86.9	0.31	0.60	0.19	Köhler et al.(2000)
RXJ1607.0-2036	26.7	0.87	0.68	0.59	Palomar-Imaging
ScoPMS005	111.1	0.48	1.66	0.80	Köhler et al.(2000)
ScoPMS013	13.3	0.62	0.54	0.34	Köhler et al.(2000)
ScoPMS015	18.0	0.60	0.68	0.41	Palomar-Imaging
ScoPMS016	192.0	0.60	0.64	0.38	Köhler et al.(2000)
ScoPMS017	7.8	0.54	0.60	0.32	Keck-Masking
ScoPMS017	8.3	0.59	0.60	0.35	Keck-Imaging
ScoPMS019	3.7	0.97	0.60	0.58	Keck-Masking
ScoPMS020	28.0	0.64	0.36	0.23	Köhler et al.(2000)

Table 5.8 (cont'd)

Name	Sep (AU)	q (m_s/m_p)	M_{prim} ($M_\odot$)	M_{sec} ($M_\odot$)	Source
ScoPMS023	43.5	0.61	0.87	0.53	Köhler et al.(2000)
ScoPMS027	6.3	0.66	1.12	0.74	Palomar-Masking
ScoPMS029	93.2	0.65	0.49	0.32	Köhler et al.(2000)
ScoPMS031	83.8	0.59	0.64	0.38	Köhler et al.(2000)
ScoPMS042a	43.4	0.70	0.60	0.42	Köhler et al.(2000)
ScoPMS048	492.1	0.30	1.35	0.40	Palomar-Imaging
ScoPMS052	20.9	0.53	1.35	0.71	Metchev (2005)
Usco-160428.4-190441	127.8	0.97	0.36	0.35	Keck-Imaging
USco-160517.9-202420	2.3	0.75	0.36	0.27	Keck-Masking
USco-160707.7-192715	15.3	0.16	0.49	0.08	Keck-Masking
USco-160707.7-192715	13.3	0.28	0.49	0.14	Keck-Imaging
USco-160823.8-193551	94.5	0.46	0.60	0.28	Keck-Imaging
USco-160908.4-200928	296.1	0.77	0.24	0.18	Keck-Imaging
USco-161031.9-191305	21.1	0.09	0.77	0.07	Keck-Masking
USco-161031.9-191305	837.4	0.04	0.77	0.03	Palomar-Imaging

Note. — Typical uncertainties in separations are ∼15% and result from the unknown depth of each system within the association. The uncertainties in masses are dominated by systematic errors, including a global zero-point uncertainty of ∼20% and individual uncertainties of as much as ∼100% due to the possibility of further unresolved multiplicity. The mass ratio estimates should be more precise (∼5-10%) since many systematics (distance, age, extinction, and zero-point shifts) are cancelled, but they are still vulnerable to large systematic errors due to unresolved multiplicity.

5.5 The Stellar Sea

The properties of multiple star systems are important diagnostics for placing constraints on star formation processes. A comprehensive theory of star formation should be able to reproduce the observed separation distribution, mass ratio distribution, and total fraction of binary systems, as well as any mass or environmental dependences of these properties. The mass ratio distribution also plays a critical role in defining the brown dwarf desert since the bottom tail of the distribution represents the upper bound of the desert.

Most recent efforts to model binary formation have typically assumed that stellar and prestellar interactions play a key role in establishing binary properties. The most popular type of model assumes that a cluster of 5-10 protostellar embryos form from a single turbulently fragmenting cloud core (e.g., Kroupa 1995; Sterzik & Durisen 1998; Kroupa & Bouvier 2003; Kroupa et al. 2003; Delgado-Donate et al. 2003; Hubber & Whitworth 2005); these embryos would then undergo mass accretion and dynamical
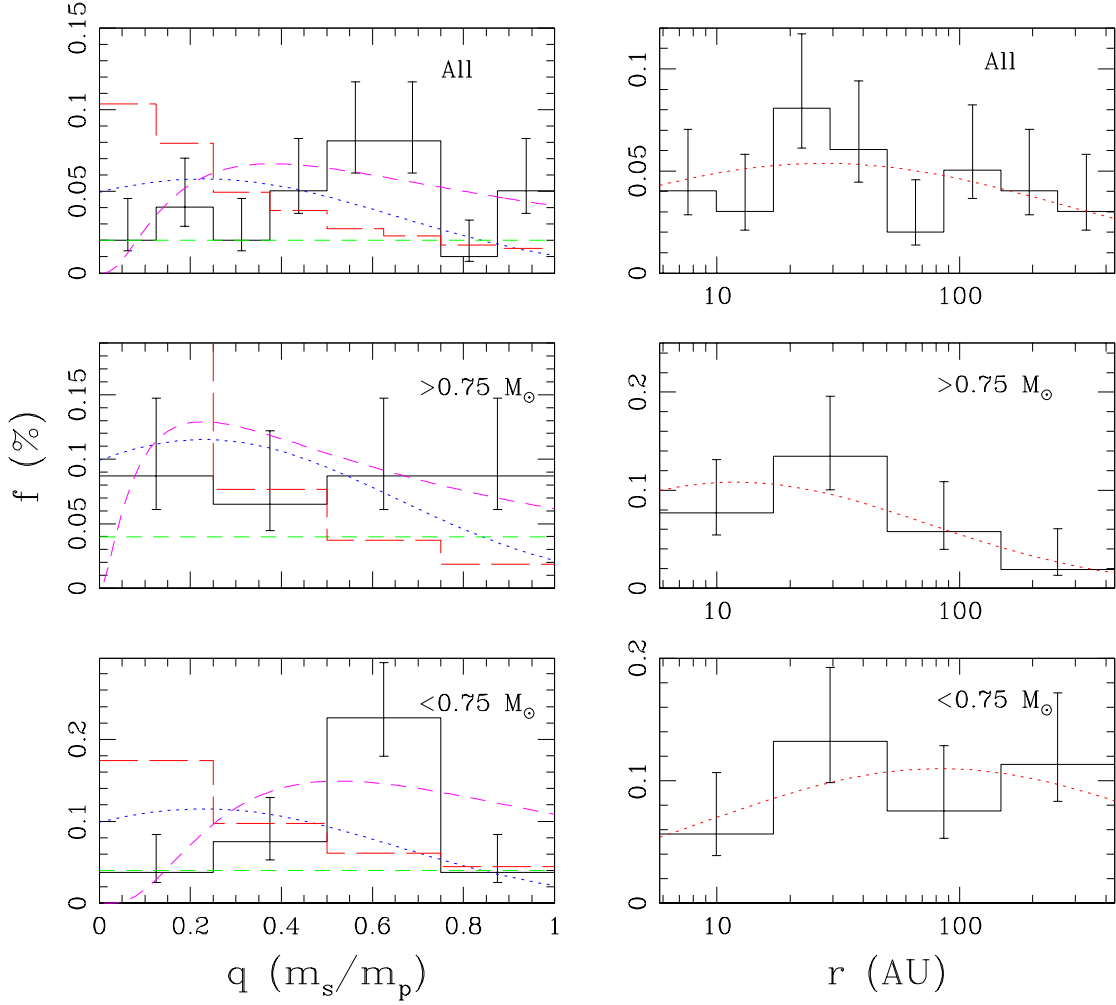
Figure 5.6 The mass ratio distributions (left) and separation distributions (right) for all stars in our sample (top), the more massive half (FGK stars; $M > 0.75\ M_\odot$; middle), and the less massive half (M stars; $M < 0.75\ M_\odot$; bottom). On the left, we overplot several suggested mass functions: a truncated Gaussian distribution (blue dotted), a constant distribution (green dashed), a distribution of companions drawn from the IMF (red long-dashed), and the best-fit log-normal distribution (magenta dashed). On the right, we overplot the best-fit lognormal distribution (red dashed) for each subsample.

evolution to form single stars and stable multiple systems. However, other stellar properties place strong limits on the rate of early dynamical evolution. Close stellar encounters would tend to dissipate or truncate disks, with smaller stars having fewer and shorter-lived disks, but there is no evidence for this trend (e.g., White & Basri 2003; Luhman 2004; Scholz et al. 2006). Dynamical encounters might also eject lower-mass stars and brown dwarfs, but no such ejected population is seen (Luhman 2006), though some models suggest that strong ejections might be rare (Bate & Bonnell 2005). Finally, any dynamically active environment would truncate the stellar binary separation distribution for all stars in the association. The absence of low-mass wide binaries has often been interpreted as a sign of this process, but this absence is seen even in environments where the wide binary frequency is very high for solar-mass stars (Kraus & Hillenbrand 2007a), so it may have another explanation.

Modeling efforts that concentrate on other binary formation processes have not advanced sufficiently to make any rigorous prediction. These processes, which are summarized by Goodwin & Kroupa (2007), include fragmentation of massive circumstellar discs, the role of magnetic support in prestellar cores, and fission of quasi-static rotating cores. All of these processes are more significant for isolated cores than for the dynamically-active turbulent fragmentation scenario discussed above, so the limits on dynamical activity of young stars suggest that they should be considered in more detail in the future.

Given the absence of theoretical predictions, we are left only with empirical comparisons to other samples. Previous field multiplicity surveys (DM91; Fischer & Marcy 1992, hereafter FM92; Reid & Gizis 1997, hereafter RG97) have suggested a range of possible results for the separation distribution, mass ratio distribution, and total frequency of binary systems. We will compare our results to these surveys and to the expected result if binary companions are drawn from an IMF. None of these explanations produce an acceptable fit for our mass ratio distribution, so the next step is to test other analytic distributions. Our number statistics do not support strong constraints on this analysis yet, so we will limit our analysis to a single functional form (the log-normal distribution) until we conclude the second half of our survey,

Table 5.9. Binary Mass Ratio Distributions

Distribution	Masses	χ^2	P	D_{KS}	P
Gaussian	All	21.2	0.007	0.35	0.00025
	High	5.1	0.28	0.34	0.047
	Low	13.6	0.009	0.41	0.0016
Constant (16%)	All	31.9	0.0001	...	...
	High	11.5	0.021	...	...
	Low	18.3	0.0011	...	...
Constant (35%)	All	11.4	0.18	0.19	0.14
	High	0.17	0.997	0.18	0.67
	Low	11.1	0.025	0.24	0.17
IMF	All	37.0	0.000005	0.46	0.0000004
	High	14.0	0.003	0.52	0.0003
	Low	21.3	0.00009	0.44	0.0005
Log-normal	All	9.7	0.14	0.15	0.41
	High	1.5	0.47	0.21	0.49
	Low	7.6	0.022	0.22	0.23

an examination of young stars in Taurus.

Finally, we note that two of the systems among our sample (USco-160428.4-190441 and USco-160825.1-201224) would have fallen below the optical flux limit of our sample ($R \leq 14$, imposed by the AO system) if the primaries were single. Including these systems in our statistical analysis would bias our results toward higher binary frequencies, so we have omitted them from our subsequent analysis. There is also an opposing effect due to the inclusion of unresolved binary pairs (which we identify as single stars) that would be omitted by the same criterion if we knew they were binaries. We obviously can not identify these systems, so we only note that the effect should be small. If the binary frequency at small separations is $\sim$10-20% and the mass ratio distribution is similar to the distribution we observe, then no more than 1-2 unresolved systems should be included as "single stars". This systematic bias should not be significant compared to the statistical uncertainties in our results. We also note that our entire analysis must implicitly adopt the assumption that the mass ratio distribution and separation distribution are uncorrelated over the survey's separation range. This assumption has not been rigorously tested, but a simultaneous investigation of both parameters would require a far larger sample.

5.5.1   The Mass Ratio Distribution

Observations of field stars have suggested that the mass ratio distribution is strongly dependent on mass. DM91 showed that F and G stars have mass ratio distributions biased toward inequal masses, roughly consistent with a truncated Gaussian distribution (albeit with few constraints for $q < 0.1$). By contrast, FM92 and RG97 found a distribution for early M dwarfs that is roughly flat, and numerous surveys have shown that the distribution for late-M dwarfs and brown dwarfs is biased toward equal masses ($q \geq 0.7$; Close et al. 2003; Bouy et al. 2003; Burgasser et al. 2003). However, these surveys have all studied old field populations. Simulations show that dynamical evolution is typically not significant once a star enters the field (e.g., Weinberg et al. 1987), but a large fraction of stars are thought to be drawn from dense cluster environments (like the Orion Nebula Cluster or the Pleiades), so their properties could have been shaped by significant dynamical evolution in their natal environment. This suggests that primordial binary properties could differ significantly from those of their older brethren.

In the left side of Figure 5.6, we plot histograms of the mass ratio distribution for our entire sample of 99 stars, only the higher-mass stars (46 FGK dwarfs, representing masses ≥ 0.7 $M_\odot$), and only the lower-mass stars (55 M dwarfs, representing masses ≤ 0.7 $M_\odot$). The mass ratio distributions are plotted for projected separations of 0.04-3.0″ (6-435 AU), where the inner bound is defined by the inner limit for our survey to be sensitive to $q \sim 0.04$ and the outer bound is defined by the field star contamination rate predicted for Upper Sco binaries by Kraus & Hillenbrand (2007a). All of the number statistics are only moderately significant, but they still suffice for placing limits on the range of functional forms for the primordial mass ratio distribution.

In all three cases, our survey's mass ratio distribution is not strongly inconsistent with a constant distribution, so our ability to test more complex functional forms is limited. However, our data will suffice to test previously-suggested functions. To this end, we have compared our results to three distributions: a Gaussian distribution like that suggested by DM91, a constant distribution like that suggested by FM92,

and a distribution which was assembled by assuming stars are randomly drawn from the IMF of Upper Sco. None of these functions feature a low-mass cutoff that could explain the brown dwarf desert, so we have also conducted preliminary tests of a new functional form: the log-normal distribution. Our constraints on this distribution are not very stringent, but they allow some preliminary conclusions. We will summarize the results for each of these tests in the following subsections, and we report the goodness of fit statistics (as measured with χ^2 and Kolmogorov-Smirnov tests) in Table 5.9. The Kolmogorov-Smirnov test is more sensitive in cases where the bin size is a significant fraction of the total range of parameter space or when the trial distribution function changes rapidly accross a bin, so all of our conclusions are based on its results.

5.5.1.1   The Gaussian Distribution

DM91 found that the mass ratio distribution for field F and G dwarfs could be well-fit by a Gaussian distribution centered at low q values ($\mu = 0.23$, $\sigma = 0.42$). Their survey was not sensitive to substellar companions ($q < 0.1$), but if this functional form is valid, it suggests that substellar companions should be very common ($f \sim 10\%$, with 4% falling in our survey's separation range). However, there are no physical motivations for assuming that an arbitrarily chosen segment of a Gaussian function (-0.5σ to +2.0σ) should predict the mass ratio distribution, so any similarity may be a coincidence. In the three left-hand panels of of Figure 5.6, we plot the q distribution suggested by DM91 with a blue dotted line. This distribution was originally defined for all separations, but DM91 found that only 40% of their systems fell within our survey's separation range, so we have scaled their function by this amount. This ensures that the overall binary frequency and the shape of the distribution are directly comparable.

Visual inspection shows that our full sample's q distribution is more biased toward equal-mass companions than that of DM91, an observations that is supported by goodness-of-fit tests. This level of disagreement could be a result of our wider mass range than DM91's sample since lower-mass binary systems are thought to have mass

ratios that are not as biased toward low masses. The relative levels of agreement for our high-mass and low-mass subsamples support this assessment; the high-mass subsample is only somewhat inconsistent with the DM91 distribution, while the low-mass subsample is very significantly inconsistent.

5.5.1.2 The Constant Distribution

A field binary survey by FM92 found that the mass ratio distribution for field early M dwarfs seemed to be better fit by a flat distribution of mass ratios for $q \geq 0.4$. RG97 found that this flat distribution extends to much lower mass ratio distributions for M dwarfs, though they also suggested the existence of a possible peak near unity ($q \geq 0.8$). As with the Gaussian distribution, a flat distribution would suggest that substellar companions are not uncommon relative to stars, but these survey were not sensitive enough to actually detect most brown dwarf secondaries. Their total binary fractions ($20^{+7}_{-5}\%$ for $q > 0.4$ or $16^{+7}_{-4}\%$ for all q, respectively, in this separation range) are marginally inconsistent, but the RG97 sample (which is more rigorously volume-limited) contains 17 of the 37 binary systems considered by FM92, so we will adopt their value. In the three left-hand panels of Figure 5.6, we plot the flat q distribution suggested by RG97 with a green dashed line.

Visual inspection suggests that a constant distribution might be more appropriate for our sample's q distribution than the DM91 Gaussian distribution. However, the flat distribution of RG97 appears to fall systematically too low for the full sample and both subsamples, yielding high χ^2 values. If we renormalize the flat distribution to match our overall binary frequency ($36^{+5}_{-4}\%$), we find much better agreement. The corresponding Kolmogorov-Smirnov tests, which only measure the cumulative density function and implicity include our renormalization, also find that a constant distribution is consistent or perhaps marginally inconsistent. We also note that we found no clear evidence of an excess of equal-mass binaries; the 2σ upper limit in the highest-mass bin of our entire sample ($q > 0.875$) is $f < 11.4\%$.

5.5.1.3   A Distribution Drawn from the IMF

Some theories also suggest that binary companions could be drawn randomly from the IMF. This idea used to be popular since it could be naturally explained as a result of random pairing and because previous results were moderately consistent, but it has fallen out of favor as the role of dynamical interactions has been increasingly constrained. However, an IMF could still be valid for wide binaries (which may form during the turbulent fragmentation of a large cloud core) and it is not clear where this regime ends and where the binary fragmentation of a collapsing protostar begins. This suggests that it would be prudent to test the validity of an IMF-based q distribution. We adopted our IMF (hereafter the companion mass function, or CMF) from the spectroscopic membership surveys of Preibisch et al. (1998, 2002), and Slesnick et al.(2006a, 2007); this IMF can be described by a broken power law, $\Psi(M) = dN/dM \propto M^{-\alpha}$, where $\alpha = -2.8$ for $0.6 < M < 2.0$ $M_\odot$, $\alpha = -0.9$ for $0.15 < M < 0.6$ $M_\odot$, and $\alpha = -0.6$ for $0.02 < M < 0.15$ $M_\odot$.

We derived the expected q distribution for our sample by assuming that every binary primary had a companion randomly drawn from the lower-mass regime of the CMF. Most implementations of this process use Monte Carlo simulations to draw a suitable population from the CMF, but our CMF is defined as a simple analytic function, so we chose to directly convert it into a q distribution: $dN/dq = (dN/dM_{sec})(dM_{sec}/dq) \propto \Psi(qM_{prim})/M_{prim}$, where the full distribution $f(q)$ is the normalized sum of all functions dN/dq as defined for each binary primary. In the three left-hand panels of Figure 5.6, we plot our IMF-based q distribution with a red long-dashed line. Unlike the previous two distributions, our IMF-based distribution is fundamentally different for our entire sample and for each subsample since they represent different sets of primary masses.

The bottom-heavy nature of the IMF suggests that of all sources with masses ≤ 1 $M_\odot$, approximately 1/4 should be substellar and many of the rest should fall at the very bottom of the stellar mass range. This distribution disagrees very significantly with our results, and all statistical tests conclusively rule out the possibility that the

companions in our sample might have been randomly drawn from the IMF.

5.5.1.4   A Parameterized Log-Normal Distribution

As well as simply testing fixed distributions, we can use Bayesian analysis to draw conclusions about the most likely models from a class of distributions. We chose distributions that are log-normal in q (base-10), with a mean at $q = 1$. We chose this distribution because it is based on the following ad-hoc model: beginning with two equal-mass cores, we accrete matter stochastically onto the two cores such that the mean accretion rate onto each core is proportional to the core mass. Applying the central limit theorem to the logarithm of the core mass ratio, we arrive at a log-normal distribution in q. This distribution also has the important property that the functional form is the same in $1/q$ as in q, meaning that it does not matter whether the "primary" or "secondary" star is used as the reference for calculating q. Amongst differentiable q distributions, only distributions that have an asymptotic power-law slope of -1 at $q = 1$ can be written so that they have this property. This distribution has a corresponding probability density function:

$$f(q) = \exp(-\log(q)^2/2\sigma^2)/q. \tag{5.1}$$

The likelihood function is then given by:

$$L(\{q_i\}|\sigma) = \Pi_i \frac{\exp(-\log(q_i)^2/2\sigma^2)/q_i}{\int_{0.04}^{1.0} \exp(-\log(x)^2/2\sigma^2)/x\,dx}. \tag{5.2}$$

The normalization in this equation explicitly includes our lower limit for q. Using a uniform prior on σ, we find that the best fit value of σ is $0.428^{+0.059}_{-0.049}$. This is our best fit distribution of all tested distributions, and predicts that only 1.2% of all companions are brown dwarfs in our separation range (meaning $q < 0.08$ here). It reproduces the peak in the companion distribution at $q \sim 0.4$ similar to that seen by DM91, but without the lack of near equal-mass companions predicted by their preferred distribution.

The low-mass subsample has a best fit value of σ of $0.347^{+0.063}_{-0.049}$, and the high-

mass subsample has a best fit σ of $0.528^{+0.148}_{-0.092}$. These values of σ are significantly different at the 96% level. This demonstrates that the lower mass subsample prefers more equal-mass companions to the higher mass subsample, consistent with results for low-mass binaries in the field. We have plotted all three best-fitting log-normal distributions in the right-hand panels of Figure 5.6 (magenta dashed line).

5.5.2   The Binary Separation Distribution

Field surveys have also suggested that the separation distribution depends strongly on mass; the shape seems to be log-normal for a wide range of masses, but the mean and maximum separations decline with decreasing mass. DM91 found that the separation distribution for solar-mass stars has a mean separation of $\sim$30 AU and some binaries as wide as 10^4 AU. FM92 and RG97 found that early M binaries have a mean separation which is marginally consistent (4-30 AU), but few have separations $\geq 10^3$ AU. Finally, recent surveys have shown that late M dwarfs and brown dwarfs have very small mean and maximum separations (4 and 20 AU, respectively; Close et al. 2003; Bouy et al. 2003; Burgasser et al. 2003). As we described above, many field stars formed in denser environments, so there has probably been some dynamical evolution that disrupted wide binaries. However, surveys of older clusters (e.g., Patience et al. 2002) suggest that the old binary population is only severely depleted by intra-cluster dynamical interactions at separations of $\geq$100-200 AU. This suggests that only the outer edge of our sample's separation distribution should differ significantly from the field.

Interpretation of the companion separation distribution is usually complicated by observational realities. The most meaningful quantity to consider is the distribution of semimajor axes, but the semimajor axis can only be determined as part of an orbital solution. Some authors convert the projected separation for each star into an estimated semimajor axis using a single corrective factor (typically $a = 1.26r$), but this choice is only valid on a statistical level and carries implicit assumptions about the eccentricity distribution that are extrapolated from much shorter-period binaries.

Therefore, we choose to report the observed projected separation distribution only. In the right side of Figure 5.6, we plot histograms of the separation distributions for our entire sample, only the higher-mass FGK stars, and only the lower-mass M dwarfs. This distribution spans separations of 6-435 AU, the range where our survey is sensitive to most brown dwarf companions.

We find that the separation distribution for our sample is consistent with a distribution constant with $\log(r)$, with r the apparent separation on the sky. A one-sided Kolmogorov-Smirnoff test over the separation range 6-435 AU gives $D = 0.13$, with $p = 0.57$. In order to examine what our separation distribution is not consistent with, we have also attempted to fit log-normal distributions over the separation range 6-435 AU, where the likelihood of a particular value of the mean μ and standard deviation σ is given by:

$$L(\{r_i\}|\mu,\sigma) = \Pi_i \frac{\exp(-(\mu - \log(r_i))^2/2\sigma^2)}{\int_{\log(r_{\min})}^{\log(r_{\max})} \exp(-(\mu - x)^2/2\sigma^2)dx}. \tag{5.3}$$

As in the previous subsection, the normalization on the denominator is an explicit integral rather than the standard normalization for a Gaussian because of our artificial truncation of the distribution at 6 and 435 AU. We take the prior distribution of μ to be uniform between 0 and 3 (i.e., median separations between 1 and 1000 AU), and the prior distribution of σ to be uniform between 0 and 2. The most likely values of μ and σ are then 1.44 and 1.01 for the entire sample, 1.08 and 0.79 for the high-mass sample, and 1.92 and 0.97 for the low-mass sample. However, integrating over all μ, the most likely value of σ is our upper limit of 2, demonstrating that the data are consistent with an approximately flat distribution. The most important point to come out of this analysis is that the 90% confidence lower limit on σ is 0.94, suggesting that we have detected at most two thirds of the companions in our sample, with the remaining companions being at smaller or greater separations.

The separation distributions for the high and low-mass samples follows the opposite trend to that suggested in the literature. Our low-mass sample has a median separation of 81 AU, while our high-mass sample has a median separation of 21 AU.

This difference is not statistically significant since both distributions are consistent with a constant distribution, and a 2-sided Kolmogorov-Smirnoff test gives a difference statistic $D = 0.30$, with $p = 0.36$. It is interesting, however, that we do not see the trend toward smaller separations with lower masses as seen in field dwarfs (e.g., Allen (2007), who finds $\mu = 0.86$ and $\sigma = 0.28$ for ultracool field dwarfs). We hope to repeat this analysis with more conclusive results after we complete our survey sample.

5.5.3 The Total Binary Fraction

The total binary fraction, representing the integrated separation and mass ratio distributions, provides a useful comparison for different populations. It does not provide any additional information about the binary formation process that is not implicitly included in its component distributions, but it is very useful in other contexts like correcting the IMF for undetected multiplicity or relating the IMF to the prestellar core mass function. Previous surveys suggest that the binary fraction is close to unity for early-type stars, declining to $\sim$60% for solar-mass stars, and $\sim$30% for early M stars; in all cases, $\sim$40-50% of binaries fall within the same separation range as our survey (6-435 AU).

We found binary fractions of 35^{+5}_{-4}% for our entire sample, 33^{+7}_{-5} for our high-mass (FGK) subsample, and 38^{+7}_{-6}% for our low-mass (early M) subsample. The first two results are roughly consistent with those observed in the field, but the second result is significantly higher than the value observed in the field. A survey of wide multiplicity has found that there are only four binaries with separations of 3-30″ among our sample members (Kraus & Hillenbrand 2007a; Kraus & Hillenbrand 2009), but there are likely to be a significant number at smaller separations; we discovered some of these binaries inside the nominal completeness limit of our survey, and future RV surveys are likely to uncover many more. If the binary fraction at separations $\leq$6 AU is as high in Upper Sco as in the field, then the binary fraction for early M dwarfs in Upper Sco could be as high as is observed for field F-G dwarfs ($\geq$60%).

5.6 The Farthest Shore?

In the past 15 years, the search for extrasolar planets has become one of the major goals of the astronomical community. Radial velocity searches have discovered hundreds of planets and allowed us to probe the dynamics of planetary systems (e.g., Marcy et al. 2005), and more recently, transit searches have uncovered dozens of additional planets and allowed us to study their fundamental properties (masses and radii; O'Donovan et al. 2007; Torres 2007). However, the direct observation of extrasolar planetary systems has proven to be an elusive goal. Advances in high-resolution imaging (mostly aimed at speckle suppression) are allowing for increasingly strict upper limits on their existence, but no planetary companions at separations comparable to our own solar system have been directly imaged yet. An intriguing sample of candidate planetary-mass companions have been identified at much wider separations (e.g., Chauvin et al. 2004; Neuhäuser et al. 2005), but their mass and formation mechanism are still uncertain.

The difficulty of directly detecting extrasolar planets with existing methods suggests that a change of strategy is in order. Previous surveys have typically used spectral or rotational differential imaging (Masciadri et al. 2005; Biller et al. 2007; Lafreniere et al. 2007) to cancel AO speckles, though some surveys have also used direct imaging (typically in the mid-infrared; Kasper et al. 2007) and simply accepted the inherent limits from speckle noise. All of these surveys produce their deepest limits at wide separations ($\geq 0.5''$), so they can only probe the regime of likely planet formation (5-30 AU) for relatively nearby stars ($d \leq 30$ pc); even for these stars, existing surveys can not probe deep enough to identify old ($\tau \geq 1$ Gyr) planets, so they must study intermediate-age ($\tau \sim 10$-200 Myr) members of nearby moving groups. By contrast, our survey achieves its deepest limits at much smaller angular separations, so we can probe deeper into the planetary separation regime of nearby moving group members (Ireland & Kraus, in prep) and finally systematically survey the nearest very young associations like Upper Sco.

However, we must include a cautionary note: the fact that we found no high-

confidence planetary detections could allow us to place upper limits on the existence of massive Jupiter analogues, but as we have previously described, it could also show that current models severely overestimate the luminosity of young planets. The core-accretion models which predicted this underluminosity have difficulty producing 10 M_{Jup} planets, so it is possible that massive planets are formed via disk fragmentation (which may not suffer this underluminosity). However, all of our subsequent results should be taken with some skepticism. We list all of our detection limits in Table 5.6, so if the models are updated in the future, it should be trivial to re-analyze our results and produce new limits.

5.6.1 Modeling the Population of Young Planets

We expect that the planetary population over our range of interest will be described by three parameters: the total frequency f, a power-law mass distribution $dN/dM \propto M^{\alpha}$, and a power-law semimajor axis distribution $dN/da \propto a^{\beta}$. We can place constraints on these parameters by simulating a population of planetary systems for each set of parameters, then convolving this population with our detection limits to determine the level of consistency with our nondetection. Our survey's detection limits can not be directly translated into limits on the planetary population since planets could be obscured by projection effects, so for each simulated planet, we also invoke a random inclination angle, a random true anomaly, and an eccentricity drawn from the approximately Gaussian distribution observed for radial velocity planets (Juric & Tremaine 2007). We note that Juric & Tremaine chose to fit their eccentricity distribution with a Schwartzschild function, but given the uncertainties in the observational statistics, it is not possible to determine whether a Schwartzschild or Gaussian function is more appropriate. We have adopted the more computationally convenient form.

Our specific implementation uses a mass drawn from between 1 and 30 M_{Jup}, a semimajor axis drawn from between 3 and 36 AU, and an eccentricity drawn from a Gaussian distribution between 0.0 and 0.8 with mean $\mu_e = 0.3$ and standard deviation $\sigma_e = 0.3$. We do not directly model the planetary frequency f in our Monte Carlo

routine because it can be added analytically. We adopted the upper mass limit (30 M_{Jup}) to match the most massive T Tauri disks at ages of 1-2 Myr (only $\sim$1% of which significantly exceed this mass; Andrews & Williams 2005). After conducting our simulations for a range of values of f, α, and β, we compiled a three-dimensional probability density function $P(f, \alpha, \beta)$ which corresponds to the probability that we would have detected a planet, then extracted three-dimensional confidence surfaces which correspond to the 50%, 90%, 95%, and 99% probabilities that our observations actually would have found no planets.

5.6.2 Limits on the Population of Young Planets

It is difficult to present a set of three-dimensional confidence surfaces in a two-dimensional medium, so we have chosen to present a selection of two-dimensional slices where we fix one parameter to its current best-estimated value. The statistics of radial velocity surveys have finally become significant enough to suggest possible values of our distribution parameters, so we have adopted these canonical values ($f = 5\%$, $\alpha = -1.05$, $\beta = -1.0$; Marcy et al. 2005) to produce our three confidence plots. The canonical distribution values are derived from radial velocity surveys; they have found the power-law exponents α and β for their sample of (short-period) planets, and they extrapolate that $\sim$5% of their sample members have long-term linear RV trends suggestive of massive long-period planets. The power law exponents may not be valid since many gas giants at small separations are thought to have migrated there, but these values represent the best constraint available.

   In the three panels of Figure 5.7, we present the joint confidence intervals for each pair of values if we fix the third value to the canonical estimate. These results suggest that the canonical planetary distribution can only be ruled out at the $\sim$50% level. This is not a statistically significant level, but it is much better than any previous imaging survey could have achieved. We also find that a much higher planetary frequency is significantly ruled out for most values of α and β; the only values which are consistent require either the mass function or the separation distribution to be very
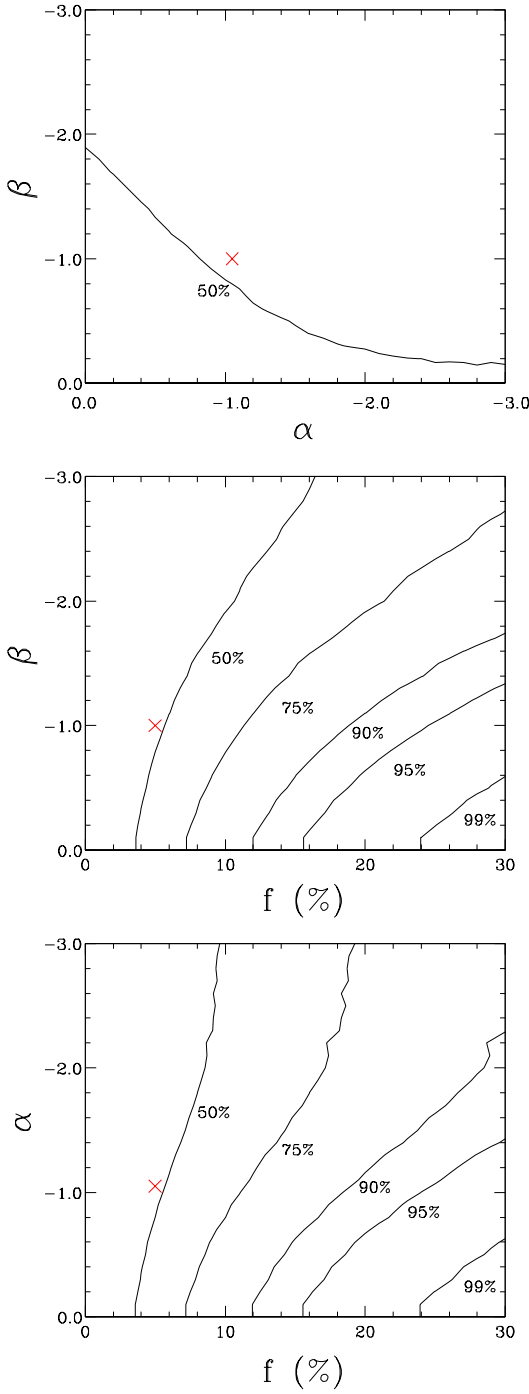
Figure 5.7 Our survey's joint limits on the total giant planet frequency f, the mass function power law α, and the semi-major axis distribution power law β, assuming we fix each parameter at the canonical value suggested by RV surveys (e.g., Marcy et al. 2005): $f = 5\%$ (top), $\alpha = -1.05$ (middle), and $\beta = -1.0$ (bottom). In each case, we also denote the confidence level corresponding to all three canonical values with red crosses.

steep, placing most planets in a regime that our survey can not search. Otherwise, we can not rule out significant regions of parameter space. In particular, if the canonical planetary frequency (f =5%) is accurate, then we can not place any constraints beyond the 70% level on values of α or β. This is a straightforward result of our sample size; with 60 targets, a frequency of 5% suggests that only 3 wide planets exist in our sample. Only unrealistically top-heavy mass or separation distributions would place a significant number of planets in our survey's detection limits.

Finally, we can determine a direct constraint on the total frequency of wide high-mass planets by adopting the canonical values for both α and β, reducing the confidence surface to a confidence interval. If we assume that $\alpha= -1.05$ and $\beta= -1.0$, then there is a 90% probability that $f < 19\%$ and a 95% probability that $f < 24\%$. We can not place similar limits on α and β because these confidence limits correspond to a total of 2.3 and 3.0 expected detections, respectively; if the total planetary frequency is only $f = 5\%$, then only extremely top-heavy power laws would allow for that many expected detections among our 60 targets.

5.6.3   An Ocean in the Distance?

Our survey did not identify any faint companions at a confidence level of $\geq 99.5\%$, but it did identify four faint candidate companions at confidence levels of 97.5% to 99.5%. Based on our total sample size (60 targets), the expected number of spurious detections with a confidence level >97.5% is only ∼1.5; according to Poisson statistics, the probability of identifying 4 or more of these spurious detections is only 7%, so this seems to represent a marginally significant excess. We will try to obtain followup observations for each marginal detection in the upcoming observing season; given their faintness, any genuine companion in this group could represent the first directly-imaged massive Jupiter analogue.

5.7 How Arid is the Brown Dwarf Desert?

Many multiplicity surveys suggest that the binary companion mass function declines as it enters the brown dwarf mass range, and all results from RV surveys suggest the same for the planetary mass function. In light of these results, it is not surprising that brown dwarf companions are uncommon. The interesting question is whether they are more uncommon than predicted by the tails of both mass functions; if so, then this deficit genuinely represents a brown dwarf "desert".

Our results suggest that the stellar mass ratio distribution is constant or at least not biased heavily toward low-mass companions. Given our observed total binary fraction ($35^{+5}_{-4}\%$), a constant mass ratio distribution predicts that $\sim 3.5\%$ of all stars should have a substellar or nearly-substellar companion with $q \leq 0.1$ at separations of 6-435 AU. We have found two such companions ($1.8^{+2.3}_{-0.6}\%$), a result which is entirely consistent with that claim. However, both companions fall at the upper end of this range ($q = 0.10$ and $q = 0.09$), and only one is possibly substellar ($M_{sec} \sim 0.07$ $M_{\odot}$); given the uncertainties inherent to our estimates of stellar properties, it is not inconceivable that both companions could fall in the range $q > 0.1$. This would be consistent with estimates for wide companions to much higher-mass Upper Sco members; Kouwenhoven et al.(2007) found that only $0.5 \pm 0.5\%$ of the B and A stars in Upper Sco have substellar companions with separations of 130-520 AU.

Our estimate of the contribution from planetary formation processes is much more uncertain. If the planetary distribution is truly defined by the canonical values given in the literature ($f = 5\%$, $\alpha = -1.05$, and $\beta = -1.0$) and the models describing luminosities of young planets are correct, then our survey would have had a 50% chance of detecting one "planetary" companion of any mass <30 M_{Jup}. This probability would have been higher if the planetary mass function extends beyond 30 M_{Jup} with no cutoff, but even a cutoff at 100 M_{Jup} would imply that our null detection is significant at only $\sim 75\%$. As a result, we can not state with any confidence that the canonical values are incorrect or that there is any sort of high-mass cutoff in the planetary mass function.

5.8 Summary

We present the results of a survey for stellar and substellar companions to 82 young stars in the nearby OB association Upper Scorpius. This survey used nonredundant aperture-mask interferometry to achieve typical contrast limits of $\Delta K \sim$5-6 at the diffraction limit, revealing 12 new companions that lay below the detection limits of traditional high-resolution imaging; we also summarize a complementary snapshot imaging survey that discovered 7 directly resolved companions. The overall frequency of binary companions ($\sim$33$^{+5}_{-4}$% at separations of 6-435 AU, including companions reported in the literature) appears to be similar to field stars of similar mass, but the companion mass function appears to be more biased toward equal-mass companions than the equivalent mass function in the field. This result could indicate an environmental or dynamical effect, but our number statistics are not yet sufficient to place strong constraints on its nature.

Our survey limits encompass the entire brown dwarf mass range and we detected two companions with $q \leq$0.1, a number which is consistent with a flat mass ratio distribution. However, both of these companions have mass ratios near 0.1 and only one has a mass which might fall below the substellar boundary, so we hesitate to rule out the existence of any deficit that might denote a brown dwarf "desert". Our survey's deep detection limits also extend into the top of the planetary mass function; we have not identified any planetary companions at high confidence ($\geq$99.5%), but we have identified four candidate companions at lower confidence ($\geq$97.5%) that merit additional followup to confirm or disprove their existence. The lack of planets within the brown dwarf mass range also is not a significant proof of the existence of a desert.

Finally, we note that our survey results are extremely encouraging with respect to the potential for future discoveries. We are currently extending our survey efforts to the Taurus-Auriga star forming region and to several nearby moving groups, and this expansion of our sample should make any conclusions much more robust. Our ability to precisely measure astrometry for close ($\sim$2-3 AU) binary systems could also allow us to measure dynamical masses for many young stars on a timescale of $\leq$5 yr. Finally,

achieving similar detection limits for planetary-mass companions in Taurus-Auriga and the nearby moving groups will significantly enhance our limits on the properties of young planets; a similar null detection for our full sample would significantly rule out the canonical values for the planetary distribution function, confirming either that these values are wrong or that evolutionary models significantly overestimate the luminosity (and detectability) of young planets.

Acknowledgements

Bibliography

Ahmic, M., Jayawardhana, R., Brandeker, A., Scholz, A., van Kerkwijk, M., Delgado-Donate, E., & Froebrich, D. 2007, ApJ, 671, 2074

Allen, P. 2007, ApJ, 668, 492

Andrews, S. & Williams, J. 2005, ApJ, 631, 1134

Ardila, D. et al. 2000, AJ, 120, 479

Baraffe, I., Chabrier, G., Allard, F., & Hauschildt, P. 1998, A&A, 337, 403

Baraffe, I., Chabrier, G., Barman, T., Allard, F., & Hauschildt, P. 2003, A&A, 402, 701

Bate, M. & Bonnell, I. 2005, MNRAS, 356, 1201

Bessell, M. & Brett, J. 1988, PASP, 100, 1134

Biller, B. et al. 2007, ApJS, 173, 143

Bouy, H. et al. 2003, AJ, 126, 1526

Bouy, H. et al. 2006, A&A, 451, 177

Brandner, W. et al. 1996, A&A, 307, 121

Burgasser, A. et al. 2003, ApJ, 125, 850

Chabrier, G. et al. 2000, ApJ, 542, 464

Chauvin, G., Lagrange, A., Dumas, C., Zuckerman, B., Mouillet, D., Song, I., Beuzit, J., & Lowrance, P. 2004, A&A, 425, 29

Chiu, K., Fan, X., Leggett, S. K., Golimowski, D. A., Zheng, W., Geballe, T. R., Schneider, D. P., & Brinkmann, J. 2006, AJ, 131, 2722

Close, L. et al. 2003, ApJ, 587, 407

de Zeeuw, P., Hoogerwerf, R., de Bruijne, J., Brown, A., & Blaauw, A. 1999, AJ, 117, 354

Delgado-Donate, E. et al. 2003, MNRAS, 347, 759

Duquennoy, A. & Mayor, M. 1991, A&A, 248, 485

Fischer, D. & Marcy, G. 1992, ApJ, 396, 178

Gizis, J., Kirkpatrick, J.D., Burgasser, A., Reid, I.N., Monet, D., Liebert, J., & Wilson, J. 2001, ApJ, 551, L163

Goodwin, S. & Kroupa, P. 2007, in Protostars and Planets V, ed. B. Reipurth, D. Jewitt, & K. Keil (Tucson: Univ. Arizona Press), 133

Grether, D. & Lineweaver, C. 2006, ApJ, 640, 1051

Guenther, E., Esposito, M., Mundt, R., Covino, E., Alcalá, J., Cusano, F., & Stecklum, B. 2007, A&A, 467, 1147

Hillenbrand, L. & White, R. 2004, ApJ, 604, 741

Houk, N. & Smith-Moore, M. 1988, Michigan Spectral Survey (Ann Arbor: Dept. Astron. Univ. Mich.),4

Hubber, D. & Whitworth, A. 2005, A&A, 437, 113

Johnson, J. et al. 2006, ApJ, 647, 600

Juric, M. & Tremaine, S. 2007, submitted to ApJ (astro-ph/0703160)

Kasper, M., Apai, D., Janson, M., & Brandner, W. 2007, A&A, 472, 321

Kirkpatrick, J. D., Reid, I. N., Liebert, J., Gizis, J. E., Burgasser, A. J., Monet, D. G., Dahn, C. C., Nelson, B., & Williams, R. J. 2000, AJ, 120, 447

Köhler, R. et al. 2000, A&A, 356, 541

Kouwenhoven, M.B.N., Brown, A.G.A., & Kaper, L. 2007, A&A, 464, 581

Kraus, A., White, R., & Hillenbrand, L. 2006, ApJ, 649, 306

Kraus, A. & Hillenbrand, L. 2007, ApJ, 662, 413

Kraus, A. & Hillenbrand, L. 2007, ApJ, 664, 1167

Kroupa, P. 1995, MNRAS, 277, 1491

Kroupa, P. & Bouvier, J. 2003, MNRAS, 346, 369

Kroupa, P. et al. 2003, MNRAS, 346, 354

Kunkel, M. (PhD thesis, University of Wurzburg, 1999)

Ireland, M., Kraus, A., Martinache, F., Lloyd, J., & Tuthill, P. 2008, ApJ, 678, 463

Lafreniere, D. et al. 2007, ApJ, 670, 1367

Leggett, S., Allard, F., & Hauschildt, P. 1998, ApJ, 509, 836

Lissauer, J. & Stevenson, D. 2007, in Protostars and Planets V, ed. B. Reipurth, D. JEwitt, & K. Keil (Tucson: Univ. Arizona Press), 591

Lloyd, J., Martinache, F., Ireland, M., Monnier, J., Pravdo, S., Shaklan, S., & Tuthill, P. 2006, ApJL, 650, 131

Lohmann, A. W., Weigelt, G., & Wirnitzer, B. 1983, Appl. Opt., 22, 4028

Luhman, K. et al. 2003, ApJ, 593, 1093

Luhman, K. 2004, ApJ, 602, 816

Luhman, K. 2006, ApJ, 645, 676

McCarthy, C., & Zuckerman, B. 2004, AJ, 127, 2871

Marcy, G. & Butler, R. 2000, PASP, 112, 137

Marcy, G., Butler, R., Fischer, D., Vogt, S., Wright, J., Tinney, C., & Jones, H. 2005, Prog. Theor. Phys. Suppl., 158, 24

Marley, M., Fortney, J., Hubickyj, O., Bodenheimer, P., & Lissauer, J. 2007, ApJ, 655, 541

Martin, E. et al. 2004, AJ, 127, 449

Martinache, F., Lloyd, J., Ireland, M., Yamada, R., & Tuthill, P. 2007, ApJ, 661, 496

Masciadri, E., Mundt, R., Henning, Th., Alvarez, C., & Barrado y Navascues, D. 2005, ApJ, 625, 1004

Metchev, S. (PhD thesis, California Institute of Technology, 2005)

Naef, D. et al. 2007, A&A, 470, 721

Nakajima, T. et al. 1989, AJ, 97, 1510

Neuhäuser, R., Guenther, E., Alves, J., Huélamo, N., Ott, Th., & Eckart, A. 2003, AN, 324, 535

Neuhäuser, R. & Guenther, E. 2004, A&A, 420, 647

Neuhäuser, R., Guenther, E., Wuchterl, G., Mugrauer, M., Bedalov, A., & Hauschildt, P. 2005, A&A, 435, 13

O'Donovan, F. et al. 2007, ApJ, 663, 37

Patience, J. et al. 2002, AJ, 123, 1570

Pravdo, S. et al. 2006, ApJ, 649, 389

Preibisch, T. et al. 1998, A&A, 333, 619

Preibisch, T., Guenther, E., & Zinnecker, H. 2001, AJ, 121, 1040

Preibisch, T., Brown, A., Bridges, T., Guenther, E., & Zinnecker, H. 2002, AJ, 124, 404

Reid, I. & Gizis, J. 1997, AJ, 113, 2246

Schmidt-Kaler, Th., "Physical Parameters of the Stars", Landolt-Bornstein Numerical Data and Functional Relationships in Science and Technology, New Series, Group VI, Volume 2b, Springer-Verlag, Berlin, 1982

Scholz, A., Jayawardhana, R., & Wood, K. 2006, ApJ, 645, 1498

Skrutskie, M. et al. 2006, AJ, 131, 1163

Slesnick, C., Carpenter, J., & Hillenbrand, L.2006a, AJ, 131, 3016

Slesnick, C., Carpenter, J., Hillenbrand, L., & Mamajek, E. 2006b, AJ, 132, 2665

Slesnick, C. (PhD thesis, California Institute of Technology, 2007)

Stephenson, C.B. 1987, ApJ, 300, 779

Sterzik, M. & Durisen, R. 1998, A&A, 339, 95

Stetson, P. 1987, PASP, 99, 191

Torres, G. 2007, ApJL, 671, L65

Tuthill, P. et al. 2000, PASP, 112, 555

Walter, F. et al. 1994, AJ, 107, 692

Weinberg, M., Shapiro, S., & Wasserman, I. 1987, ApJ, 312, 367

White, R. & Basri, G. 2003, ApJ, 582, 1109

Whitworth, A. & Stamatellos, D. 2006, A&A, 458, 817

Zacharias, N., Urban, S.,Zacharias, M., Wycoff, G., Hall, D., Monet, D., & Rafferty, T. 2004, AJ, 127, 3043

Chapter 6

A Keck LGSAO Survey of Multiple Star Formation at the Bottom of the IMF

Abstract

We present the results of a large-scale survey of multiplicity at the bottom of the IMF in several nearby young associations. We confirm the overall trend observed in the field for lower-mass binary systems to be less frequent and more compact, including a null detection for any substellar binary systems with separations wider than $\sim$7 AU. We demonstrate that the binary frequency and binary separations decline between masses of 0.5 $M_\odot$ and 0.03 $M_\odot$, though we can not distinguish the form of this decline due to a degeneracy between the total binary frequency and the mean binary separation. We also show that the mass ratio distribution becomes progressively more concentrated at $q \sim$1 for declining masses, though a small number of systems appear to have unusually wide separations and low mass ratios for their mass. Finally, we report a null detection for planetary-mass companions in our survey, or in any previous survey that was sensitive to such low masses. Depending on the functional form of the companion mass distribution, our null result suggests an upper limit on the companion frequency of $\sim$1% at a 50% confidence level or $\sim$2-3% at a 90% confidence level.

6.1 Introduction

The frequency and properties of multiple star systems offer powerful constraints on star formation and early cluster evolution. The semimajor axis of a binary system should correspond to the characteristic size of its progenitor core at the time of fragmentation, so the binary separation distribution constrains the range of sizes and the size evolution for cores. The overall binary frequency and the mass ratio distribution also constrain the detailed physics of binary fragmentation, and each binary system's mass ratio will depend on the post-fragmentation accretion history. A successful model for star formation should be able to match the observed frequency and properties of the binary star population, as well as any mass-dependent changes in these parameters.

The past two decades have seen numerous studies of nearby field binary systems in order to constrain their frequency and properties. These surveys (e.g., Duquennoy & Mayor 1991; Fischer & Marcy 1992; Close et al. 2003; Bouy et al. 2003; Burgasser et al. 2003) have found that binary frequencies and properties are very strongly dependent on mass. Solar-mass stars have high binary frequencies ($>$60%) and maximum separations of up to $\sim$10^4 AU. By contrast, M dwarfs have moderately high binary frequencies (30-40%) and few binary companions with separations of more than $\sim$1000 AU, while brown dwarfs have low binary frequencies ($\sim$15% for all companions with separations $>$2-4 AU) and few companions with separations $>$10 AU.

However, field multiplicity results face unavoidable ambiguity near and below the substellar regime. Field surveys do not strongly constrain the mass dependence of substellar binary properties due to the degeneracy between brown dwarf masses and ages, and mass ratios are similarly difficult to estimate. Also, the field represents a composite population drawn from all star-formation regions, so field surveys cannot probe the dependence of binary properties on initial conditions (the stellar density or total mass) and evolutionary history (the degree of dynamical evolution each system undergoes before leaving its natal environment). For example, the separation distri-

bution for binary systems is truncated at separations of $\sim$100 AU in open clusters like Praesepe (e.g., Patience et al. 2002), whereas unbound young associations have binary systems as wide as 10^4 AU (Kraus & Hillenbrand 2008, 2009).

These complications have motivated a large number of multiplicity surveys in nearby star-forming regions and young clusters. Several survey programs have found that the solar-mass stars in loosely-bound young associations have extremely high binary frequencies (Ghez et al. 1993; Leinert et al. 1993; Simon et al. 1995; Köhler et al. 2000; Kraus et al. 2008). The binary frequency in young open clusters appears to be significantly lower (e.g., Köhler et al. 2006), which could be interpreted either as early dynamical evolution or a signature of the different primordial environment. Surveys of very low-mass stars and brown dwarfs have concentrated mainly on nearby unbound associations (e.g., Kraus et al. 2005, 2006; Konopacky et al. 2007; Ahmic et al. 2007), but produced results that largely match the field: low-mass binary systems are rare and tend to have small separations and similar component masses.

The aforementioned surveys of low-mass multiplicity in young associations used very modest sample sizes since high-resolution imaging techniques were observationally expensive. As a result, their tentative conclusions raised as many questions as they answered. The handful of binary systems they discovered tended to fall in the upper end of the surveys' mass ranges, with very few binary companions to genuinely substellar companions. This suggested that the binary frequency might decline with mass through this range, an observation that is difficult to test among low-mass field binaries. These surveys also found a handful of apparently planetary-mass companions, including the prototypical example 2MASS1207 B (Chauvin et al. 2004) and the more recently discovered CHXR73 B (Luhman et al. 2006). These objects' properties are highly inconsistent with the expectations of binary formation and planet formation, so it is unclear how they might have formed.

The limited sample sizes and heterogeneous nature of previous surveys have prohibited any detailed analysis of the mass dependence of multiple star formation, especially in the low-mass regime ($M <$0.15 $M_\odot$) where mass-dependent effects seem to be most significant. To address this shortcoming, we present a large-scale survey

of multiplicity at the bottom of the IMF in several nearby young assocations. In Section 6.2, we list our survey's sample and describe our survey's observations, and in Section 6.3, we explain the analysis techniques used in our program. In Section 6.4, we describe the results of our observations. We then use our results and other results from the literature in Section 6.5 to constrain the mass-dependent properties of low-mass multiple star formation. Finally, in Section 6.6, we present similar analysis constraining the frequency and properties of planetary-mass companions like 2M1207 B and CHXR73 B.

6.2 Sample and Observations

6.2.1 Sample Selection

Nearby star-forming regions have been the target of numerous wide-field photometric imaging surveys to detect new low-mass members (e.g., Luhman 2004, 2006; Slesnick et al. 2006a, 2006b, 2008). These surveys identified candidate members based on their location on an optical or near-infrared color-magnitude diagram, and membership was then confirmed spectroscopically via the detection of lithium absorption, excess $H\alpha$ emission, or low surface gravity, all of which are indicators of youth. We chose to concentrate on Taurus-Auriga and Upper Scorpius because they are the nearest young associations that are accessible from the northern hemisphere. In our analysis, we also use results from the literature on the Cha-I association, which is similar to Taurus in age and environment.

Our initial observational sample included all late-type members of each association (SpT$\geq$M4) that had been identified by 2006 and that had not been observed at high angular resolution. However, as we describe in Section 6.3, we lost a significant fraction of our observing time to poor weather and instrument problems. This left our Taurus sample significantly incomplete for members discovered in 2006, plus we were unable to observe three members that had been identified earlier (J1-4423, V410 X-ray 6, and 2M04163049). The effect in Upper Sco was even more severe, limiting

our sample to only the latest-type members (SpT≥M6.5). We were also unable to observe 10 Taurus members that had no suitable tip-tilt stars available. This omission introduces a bias against the most reddened members of Taurus since the most heavily extincted stars were least likely to have an optically bright star nearby that could serve as a tip-tilt reference. The density of field stars is very high in Upper Sco, plus the association is almost completely cleared of its primordial molecular material, so we were always able to find a suitable tip-tilt star.

We have supplemented this observational sample with the results of numerous previous multiplicity surveys. Taurus has been a very popular target for multiplicity surveys, and association members in our spectral type range have been observed with speckle interferometry (Ghez et al. 1993; Konopacky et al. 2007; White et al., in prep), lunar occultations (Simon et al. 1995), HST imaging (Padgett et al. 1999; White & Ghez 2001; Kraus et al. 2006), AO imaging (Correia et al. 2006), and aperture-masking interferometry (Kraus et al., in prep). Upper Scorpius has been the subject of several surveys as well, and members have been observed with speckle interferometry (Köhler et al. 2000), HST imaging (Kraus et al. 2005), and AO imaging (Bouy et al. 2006). In most cases (and almost certainly in aggregate), the sample members were selected seemingly at random. As a result, we adopt the combined set as a statistically randomized sample.

Finally, we also observed a small number of other targets that fall outside these selection parameters, but were considered interesting for other reasons. In both associations, we observed a number of candidate wide binary systems that seemed to have unusually low binding energies. We already fully described one of these observations (for UScoJ1606-1935; Kraus & Hillenbrand 2007b), and we reported the astrometric measurements for the rest in our paper on wide binary formation (Kraus & Hillenbrand 2009). In this chapter, we report on the search for higher-order multiplicity. We also observed several candidate Taurus members discovered by Slesnick et al.(2006b) that are not part of the young Taurus population, but might represent an older, more widely distributed population of young stars and brown dwarfs. Finally, we observed the known binary V928 Tau because it served as the tip-tilt reference for CFHT-Tau-7

and we typically imaged tip-tilt references for a data quality check. However, we do not report any results for CFHT-Tau-7 because the observing conditions at the time were too marginal for adaptive optics to yield any meaningful correction.

In Table 6.1, we list the young association members that we observed in our study. The K magnitude for each target was taken from 2MASS (Skrutskie et al. 2006), while the R magnitude and distance to each star's tip-tilt reference are from the USNO-B1.0 catalog (Monet et al. 2003). We also list references for the handful of objects which have also been observed in other high-resolution imaging surveys; in several cases, the limits derived by Konopacky et al.(2007) at small separations superceded ours, so we adopted those limits where appropriate.

Table 6.1. Observed Sample

Name	RA	DEC	SpT	Mass	K	R_{TT}	d_{TT}	Refs
	(J2000)			($M_\odot$)	(mag)	(mag)	(arcsec)	
Taurus								
SCHJ0359099+2009363	3 59 09.85	+20 09 36.3	M4.75	0.2	12.53	15.2	47.4	
2MASSJ04080782+2806280	4 08 07.82	+28 07 28.0	M3.75	0.3	11.39	12	9.1	
2MASSJ04141188+2811535	4 14 11.88	+28 11 53.5	M6.25	0.09	11.64	10	23.3	
2MASSJ04152409+2910434	4 15 24.09	+29 10 43.4	M7	0.058	12.36	13.4	45.8	
2MASSJ04161885+2752155	4 16 18.85	+27 52 15.5	M6.25	0.09	11.35	16.1	28.1	
SCHJ0416272+2053093	4 16 27.20	+20 53 09.3	M5	0.18	11.11	14.7	21.7	
2MASSJ04163911+2858491	4 16 39.11	+28 58 49.1	M5.5	0.14	11.28	17.6	19.1	
KPNO-Tau-10	4 17 49.55	+28 13 31.9	M5	0.18	10.79	16	0	
V410 X-ray 3	4 18 07.96	+28 26 03.7	M6.5	0.08	10.45	16.8	0	1
KPNO-Tau-11	4 18 30.31	+27 43 20.8	M5.5	0.14	11.01	16.3	0	
2MASSJ04202555+2700355	4 20 25.55	+27 00 35.5	M5.25	0.16	11.51	16.5	24.5	
2MASSJ04213460+2701388	4 21 34.60	+27 01 38.8	M5.5	0.14	10.44	17.5	0	2
CFHT-Tau-10	4 21 46.31	+26 59 29.6	M5.75	0.12	12.13	18.9	12.2	
2MASSJ04215450+2652315	4 21 54.50	+26 52 31.5	M8.5	0.022	13.9	15.3	43.7	
CFHT-Tau-14	4 22 16.44	+25 49 11.8	M7.75	0.038	11.94	11.7	48.9	
2MASSJ04230607+2801194	4 23 06.07	+28 01 19.4	M6.25	0.09	11.2	13.6	49.1	
CFHT-Tau-9	4 24 26.46	+26 49 50.4	M5.75	0.12	11.76	14.2	47.1	
SCHJ0427074+2215039	4 27 07.40	+22 15 03.9	M6.75	0.07	11.29	14.1	46.9	
2MASSJ04284263+2714039 A	4 28 42.63	+27 14 03.9	M5.25	0.16	10.46	16.7	0	2
2MASSJ04290068+2755033	4 29 00.68	+27 55 03.3	M8.25	0.027	12.85	15.9	27.5	
CFHT-Tau-20	4 29 59.51	+24 33 07.9	M5	0.18	9.81	17.5	0	2
CFHT-Tau-16	4 30 23.65	+23 59 13.0	M8.25	0.027	13.7	14.7	31.2	
2MASSJ04311907+2335047	4 31 19.07	+23 35 04.7	M7.75	0.038	12.2	18.6	35.8	
CFHT-Tau-13	4 31 26.69	+27 03 18.8	M7.5	0.051	13.45	16.1	34	
2MASSJ04320329+2528078	4 32 03.29	+25 28 07.8	M6.25	0.09	10.72	15.1	29.1	
V928 Tau	4 32 18.86	+24 22 27.1	M0.5	0.6	7.61	12.4	0	
2MASSJ04322329+2403013	4 32 23.29	+24 03 01.3	M7.75	0.038	11.33	16.2	12	
MHO-Tau-Tau-8	4 33 01.98	+24 21 00.0	M6	0.1	9.73	16.7	0	1
2MASSJ04334291+2526470	4 33 42.91	+25 26 47.0	M8.75	0.018	13.33	16.1	27.9	
2MASSJ04335245+2612548	4 33 52.45	+26 12 54.8	M8.5	0.022	13.99	12.9	44.2	
SCHJ0434454+2308035	4 34 45.40	+23 08 03.5	M5.25	0.16	11.7	13.1	33.6	
2MASSJ04380084+2558572	4 38 00.84	+25 58 57.2	M7.25	0.051	10.1	17.1	53.3	2
SCHJ0438586+2336352	4 38 58.60	+23 36 35.2	M4.25	0.25	11.03	16.3	0	
SCHJ0438587+2323596	4 38 58.70	+23 23 59.6	M6.5	0.08	11.6	17.4	0	
SCHJ0439016+2336030	4 39 01.60	+23 36 03.0	M6	0.1	10.19	14.9	0	

Table 6.1 (cont'd)

Name	RA	DEC	SpT	Mass ($M_\odot$)	K (mag)	R_{TT} (mag)	d_{TT} (arcsec)	Refs
	(J2000)							
SCHJ0439064+2334180	4 39 06.40	+23 34 18.0	M7.5	0.044	11.19	17.3	0	
2MASSJ04400067+2358211	4 40 00.67	+23 58 21.1	M6.25	0.09	11.48	11.6	14.6	
2MASSJ04403979+2519061 A	4 40 39.79	+25 19 06.1	M5.25	0.16	10.24	18.2	0	2
2MASSJ04414489+2301513	4 41 44.89	+23 01 51.3	M8.25	0.027	13.16	14.2	12.5	
2MASSJ04442713+2512164	4 44 27.13	+25 12 16.4	M7.25	0.051	10.76	16.7	0	2
2MASSJ04552333+3027366	4 55 23.33	+30 27 36.6	M6.25	0.09	11.97	16.1	47.8	
2MASSJ04554046+3039057	4 55 40.46	+30 39 05.7	M5.25	0.16	11.77	17.1	0	
2MASSJ04554757+3028077	4 55 47.57	+30 28 07.7	M4.75	0.2	9.98	14.9	0	
2MASSJ03443801+3028050	4 55 48.01	+30 28 05.0	M5.6	0.13	12.16	14.9	5.7	
2MASSJ04554970+3019400	4 55 49.70	+30 19 40.0	M6	0.1	11.86	16.1	7.1	
2MASSJ04555289+3006523	4 55 52.89	+30 06 52.3	M5.25	0.16	10.73	14.6	30	
2MASSJ04555637+3049375	4 55 56.37	+30 49 37.5	M5	0.18	11.09	14.6	27.1	
2MASSJ04574903+3015195	4 57 49.03	+30 15 19.5	M9.25	0.013	14.48	15.7	32.8	
SCHJ0506466+2104298	5 06 46.60	+21 04 29.8	M5.25	0.16	11.11	16.4	0	
SCHJ0516021+2214530	5 16 02.11	+22 14 53.0	M5	0.18	10.75	14.2	18.2	
SCHJ0523500+2435237	5 23 49.97	+24 35 23.8	M6	0.1	12.77	12.9	45.9	
SCHJ0536190+2242428	5 36 19.00	+22 42 42.9	M4.75	0.2	11.27	15.4	0	
SCHJ0537385+2428518	5 37 38.51	+24 28 51.8	M5.25	0.16	10.78	15.8	0	
Upper Sco								
SCHJ15582566-18260865	15 58 25.66	-18 26 08.7	M6	0.074	11.79	11.4	33.6	
USco 80 A	15 58 35.98	-23 48 13.7	M3	0.36	10.19	14.7	0	
USco 80 B	15 58 35.98	-23 48 13.7	M4	0.24	12.08	14.7	13	
SCH15594802-22271650	15 59 48.02	-22 27 16.3	M7.5	0.044	13.16	12.3	50	
USco 109	16 01 19.16	-23 06 39.4	M6	0.074	12.67	12.2	42.1	3
USco 66	16 01 49.56	-23 51 08.2	M6	0.074	11.93	14.5	25.1	3
USco 55	16 02 45.75	-23 04 50.9	M5.5	0.1	11.5	16.9	0.3	3
SCH16044303-23182620	16 04 43.04	-23 18 25.9	M6.5	0.066	12.86	16.7	29	
USco-160702.1-201938 A	16 07 02.12	-20 19 38.8	M5	0.13	12.02	16.5	0.1	
USco-160702.1-201938 B	16 07 02.12	-20 19 38.8	..	..	12.3	16.5	0.1	
USco-160904.0-193359 A	16 09 04.05	-19 34 00.1	M4	0.24	11.46	13.7	37.5	
USco-160904.0-193359 B	16 09 04.05	-19 34 00.1	..	..	11.83	13.7	37.5	
SCHJ16090451-22245259	16 09 04.51	-22 24 52.6	M7	0.058	11.99	14.1	40.8	
USco-160908.4-200928 A	16 09 08.45	-20 09 27.8	M4	0.24	10.12	13.8	0.3	
USco-160908.4-200928 B	16 09 08.45	-20 09 27.8	..	..	10.44	13.8	0.3	
SCH16095991-21554293	16 09 59.91	-21 55 42.5	M6.5	0.066	13.31	16.2	18.2	
SCHJ16095307-19481704	16 09 63.07	-19 48 17.0	M6	0.074	11.76	13.9	28.4	

Table 6.1 (cont'd)

Name	RA	DEC	SpT	Mass ($M_\odot$)	K (mag)	R_{TT} (mag)	d_{TT} (arcsec)	Refs
	(J2000)							
DENIS-P-J161006.0-212744.6	16 10 06.08	-21 27 44.0	M8.5	0.026	13.77	15.3	20	
DENIS-P-J161103.6-242642.9	16 11 03.61	-24 26 42.9	M9	0.018	13.7	15.9	33	
SCH16111711-22171749	16 11 17.12	-22 17 17.4	M7.5	0.044	13.25	15.8	37.8	
SCH16121188-20472698	16 12 11.86	-20 47 26.7	M6.5	0.066	12.61	12.9	38.2	
SCH16131212-23050329	16 13 12.12	-23 05 03.2	M6.5	0.066	13.01	14.9	30.3	
DENIS-P-J161452.6-201713.2	16 14 52.59	-20 17 13.3	M9	0.018	14.06	16.8	16.3	
SCH16151115-24201556	16 15 11.16	-24 20 15.3	M6	0.074	13.17	12.5	49.7	
SCH16183141-24195229	16 18 31.41	-24 19 52.2	M6.5	0.066	12.98	14	41.5	
DENIS-P-J161916.5-234722.9	16 19 16.46	-23 47 23.5	M8	0.031	13.6	12.5	38	
SCH16235158-23172740	16 23 51.56	-23 17 27.0	M8	0.031	12.42	17.3	14.8	
SCH16252862-16585055	16 25 28.60	-16 58 50.9	M8	0.031	12.63	14.4	35	
SCH16253671-22242887	16 25 36.72	-22 24 28.5	M7	0.058	12.46	14.7	42.1	

Note. — References: 1) Kraus et al.(2006) 2) Konopacky et al.(2007) 3) Kraus et al.(2005)

6.2.2   Observations

Most of the observations that we summarize were obtained in 5 observing runs, to-
taling 10 nights, between December 2005 and January 2008. However, some followup
observations were obtained by P. Cameron and N. Law during observing runs in July
2006, December 2006, and and August 2008. Most of our observations were obtained
using laser guide star adaptive optics (LGSAO; Wizinowich et al. 2006) on the Keck-II
telescope with NIRC2 (K. Matthews, in prep), a high spatial resolution near-infrared
camera. During some periods of moderate cloud cover that were not suitable for
laser operation, we also used natural guide star adaptive optics (NGSAO) to observe
sample members with very close and bright tip-tilt stars. In the worst conditions, we
also observed some higher-mass stars that did not fall in our sample; most of these
observations have been described in our previous papers (Kraus et al. 2008; Kraus &
Hillenbrand 2009), so we report the rest here for completeness.

The weather conditions were highly variable over the course of our campaign, with
only five nights of unimpacted laser operation. We lost most or all of five nights: one
night in December 2005 due to a laser malfunction, plus four nights (one each in
November 2006, March 2007, December 2007, and January 2008) to poor weather.
Several of the remaining nights were also impacted by poor seeing. Despite numerous
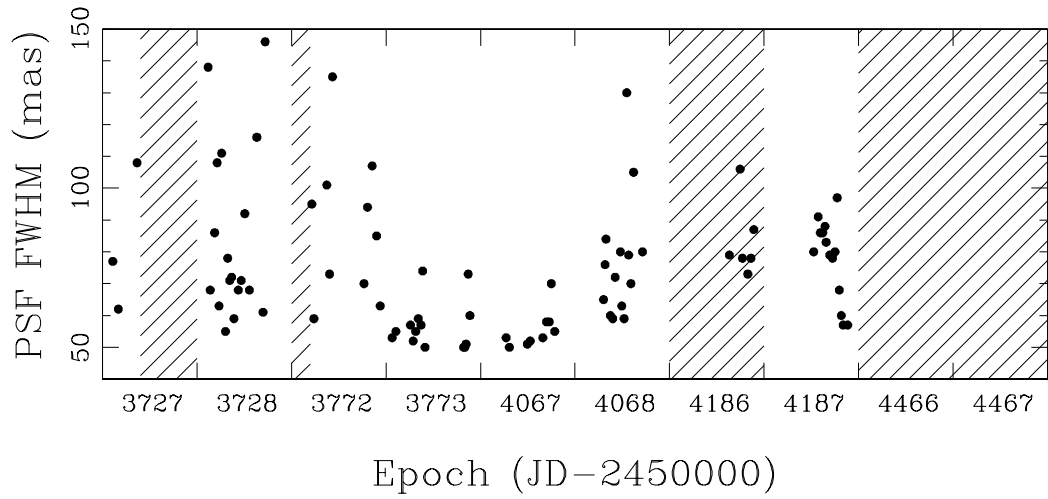
Figure 6.1 PSF FWHM for the best exposure on each of our sample members, plotted against the time within each night that the target was observed. Shaded regions show nights that were heavily impacted or lost due to instrument malfunctions or clouds. A significant fraction of our targets had bright, on-axis tip-tilt stars, so nights where few or no targets were diffraction-limited (FWHM~50 mas) generally had bottom-quartile seeing. Other significant gaps generally indicate observations of Praesepe during the gap between Taurus and Upper Sco or AO-assisted spectroscopy of interesting candidate companions; those results will be presented in future publications.

difficulties, we report 87 observations of young association members with LGSAO and 5 additional observations with NGSAO, encompassing 78 different targets. In Table 6.2, we summarize the observations for each target, including those targets that were observed in multiple epochs to obtain followup astrometry or because superior seeing allowed (or seemed it would allow) for a better AO correction at later times. In Figure 6.1, we show the FWHM of the AO-corrected PSF as a function of time during our observing campaigns; a significant fraction of the targets used bright on-axis tip-tilt stars that should have achieved diffraction-limited performance (strehl$\sim$30%), but we only achieved this performance on two nights.

All of the images presented here were produced with the narrow camera, which has a field of view of $10.2''$ and a pixel size of 9.963 mas pix^{-1} (Ghez et al. 2008). All targets were observed with the K_p filter; some targets were also observed with H and J if we identified a likely companion at the telescope, but the analysis of that data is still ongoing, so we do not present it here. During early observing runs, we used a three-point dither pattern that was designed to avoid the bottom-left quadrant, which suffers from high read noise. After February 2006, we obtained all of our observations in a diagonal two-point dither pattern because experience showed that dithers degrade the AO correction until several exposures have been taken with the low-bandwidth wavefront sensor. The delay before returning to optimal correction represented a significant overhead that we sought to minimize.

Many of the targets are relatively bright in the NIR and require very short integration times to avoid saturation or nonlinearity, so a large fraction of our observations were taken in correlated double-sampling (CDS) mode, for which the array read noise is 38 electrons read^{-1}. Where possible, we observed targets in multiple correlated double-sampling (MCDS) mode, where multiple reads are taken at the beginning and ending of each exposure; this choice reduces the read noise by approximately the square root of the number of reads. This is doubly significant because the read noise per coadd and the total number of coadds per exposure are both reduced. In all cases, the read noise is negligible compared to PSF variations from the primary at separations of $<1''$. However, the read noise always dominated over the sky background

in determining our faint-source detection limits at large separations from the science target. In all cases, the images were flat-fielded and dark- and bias-subtracted using standard IRAF procedures.

In Figures 6.2 and 6.3, we demonstrate the wide range of data quality in our survey. KPNO-Tau-10 and V410 X-ray 3 were observed on the same night in February 2006, albeit several hours apart. The observations of V410 X-ray 3 demonstrate the power of LGSAO observations; this system was identified as a candidate binary in our HST survey based on a marginal elongation of its PSF in i' and z' images, but we were not able to obtain precise photometry or astrometry since the apparent separation was only $\sim$0.5 λ/D. The system is almost resolved in our K' images and clearly resolved in H and J, indicating that V410 X-ray 3 is indeed a genuine binary system. By contrast, the observations of KPNO-Tau-10 show rapid variations in the core PSF shape; if our observation sequence had only included the first four images, we would not have known that we were seeing unstable AO correction and not a genuine binary system.

Table 6.2.   Observations

Target	Epoch (JD-2450000)	Mode	t_{int} (s)	PSF FWHM (mas)	PSF Elongation (%)
SCHJ0359099+2009363	3728	L	250	76	9
V410 X-ray 3	3728	L	150	75	31
2MASSJ04213460+2701388	3728	L	150	56	26
2MASSJ04141188+2811535	3728	N	150	87	11
MHO-Tau-Tau-8	3729	L	150	122	20
2MASSJ04554757+3028077	3729	L	150	63	15
CFHT-Tau-16	3729	L	150	94	32
CFHT-Tau-13	3729	L	150	88	27
CFHT-Tau-20	3729	L	150	59	8
CFHT-Tau-10	3729	L	300	94	90
SCHJ0439016+2336030	3729	L	150	55	6
SCHJ0438586+2336352	3729	L	150	72	10
SCHJ0438587+2323596	3729	L	150	64	13
SCHJ0439064+2334180	3729	L	150	71	13
2MASSJ04141188+2811535	3729	L	150	59	20
2MASSJ04574903+3015195	3729	L	150	68	5
2MASSJ04202555+2700355	3729	L	150	65	24
2MASSJ04311907+2335047	3729	L	150	82	7
2MASSJ04284263+2714039	3729	L	150	64+63	18+18
2MASSJ04380084+2558572	3729	L	150	93	61
2MASSJ04552333+3027366	3729	L	150	118	32
SCHJ0536190+2242428	3729	L	150	57	22
SCHJ0427074+2215039	3773	L	150	76	14
2MASSJ04284263+2714039	3773	L	150	53+53	17+15
CFHT-Tau-9	3773	L	150	83	44
2MASSJ04555289+3006523	3773	L	150	71	25
SCHJ0516021+2214530	3773	L	150	114	50
USco 55	3773	L	150	65	85
USco-160702.1-201938 A	3773	L	150	80+100	25+60
USco-160904.0-193359 A	3773	L	150	90+88	30+15
USco 66	3773	L	150	93	200
SCH16252862-16585055	3773	L	150	60	23
CFHT-Tau-14	3774	L	150	55	20
V410 X-ray 3	3774	L	175	52	37
2MASSJ04141188+2811535	3774	L	150	53	25
KPNO-Tau-11	3774	L	150	51	5

Table 6.2 (cont'd)

Target	Epoch (JD-2450000)	Mode	t_{int} (s)	PSF FWHM (mas)	PSF Elongation (%)
KPNO-Tau-10	3774	L	150	57	7
2MASSJ04554757+3028077	3774	L	150	54	7
MHO-Tau-Tau-8	3774	L	150	53	16
SCHJ0523500+2435237	3774	L	150	66	35
SCHJ0537385+2428518	3774	L	150	50	6
USco-160908.4-200928 A	3774	L	100	51+51	6+5
USco109	3774	L	100	64	19
SCH16121188-20472698	3774	L	175	58	13
SCH16121188-20472698	3919	L	850	57	9
MHO-Tau-Tau-8	4069	L	120	50	20
2MASSJ04311907+2335047	4069	L	330	56	15
2MASSJ04335245+2612548	4069	L	120	50	3
SCHJ0434454+2308035	4069	L	150	50	8
2MASSJ04152409+2910434	4069	L	120	51	8
2MASSJ04320329+2528078	4069	L	120	55	12
2MASSJ04555637+3049375	4069	L	150	57	3
2MASSJ04554970+3019400	4069	L	120	69	139
SCHJ0506466+2104298	4069	L	120	52	5
2MASSJ04400067+2358211	4070	N	120	59	10
2MASSJ04230607+2801194	4070	L	120	69	20
2MASSJ04215450+2652315	4070	L	120	71	35
SCHJ0416272+2053093	4070	L	120	56	9
2MASSJ04290068+2755033	4070	L	120	55	8
2MASSJ04215450+2652315	4070	L	120	64	15
2MASSJ04080782+2806280	4070	N	60	70	80
2MASSJ04322329+2403013	4070	L	150	61	4
2MASSJ04554046+3039057	4070	L	120	56	4
2MASSJ04163911+2858491	4070	L	120	106	60
2MASSJ04161885+2752155	4070	L	120	78	0
2MASSJ04403979+2519061	4070	L	120	62	85
2MASSJ04334291+2526470	4070	N	120	89	23
V928 Tau	4070	N	30	63	71
2MASSJ04163911+2858491	4091	L	150	61	4
2MASSJ04442713+2512164	4091	L	90	59	5
CFHT-Tau-14	4091	L	120	80	8
SCH16131212-23050329	4187	L	150	73	28

Table 6.2 (cont'd)

Target	Epoch (JD-2450000)	Mode	t_{int} (s)	PSF FWHM (mas)	PSF Elongation (%)
SCH15594802-22271650	4187	L	150	97	11
SCH16121188-20472698	4187	L	390	74	11
DENIS-P-J161006.0-212744.6	4187	L	150	66	17
SCH16253671-22242887	4187	L	180	71	17
DENIS-P-J161916.5-234722.9	4187	L	150	76	22
SCHJ15582566-18260865	4188	L	240	68	225
SCH16095991-21554293	4188	L	210	87	10
SCHJ16090451-22245259	4188	L	150	72	29
DENIS-P-J161916.5-234722.9	4188	L	150	79	17.4
SCH16183141-24195229	4188	L	150	80	17.7
SCH16044303-23182620	4188	L	270	80	4
SCH16111711-22171749	4188	L	150	78	7
DENIS-P-J161103.6-242642.9	4188	L	150	73	16.5
DENIS-P-J161452.6-201713.2	4188	L	150	75	3
SCH16235158-23172740	4188	L	210	91	4
SCH16151115-24201556 B	4188	L	150	62	8
USco 80 A	4188	L	120	58	68
USco 80 B	4188	L	90	55	5
SCHJ16095307-19481704	4188	L	150	52	3
2MASSJ04334291+2526470	4689	L	90	54	38

6.3   Analysis Methods

6.3.1   Source Identification and Detection Limits

Source identification in AO imagery is a complicated endeavor. In NGSAO mode, the gross shape of the PSF depends on the target's optical brightness and the seeing, while the fine structure is determined by speckle patterns that continuously change on timescales ranging from seconds to hours. The LGSAO PSF is further complicated by variations in laser return strength, tip-tilt anisoplanatism with respect to off-axis guide stars, and heightened sensitivity to telescope effects like wind shake. Finally, observations in poor weather are further complicated by rapid PSF quality variation due to changing atmospheric conditions. The source detection process can be divided into two regimes: a wide regime where the PSF core is negligible and speckle confusion dominates ($\rho>2$ times the core FWHM), and a close regime where shape and width variations in the PSF core dominate and speckle confusion is negligible. We have adopted a different method in each separation regime.
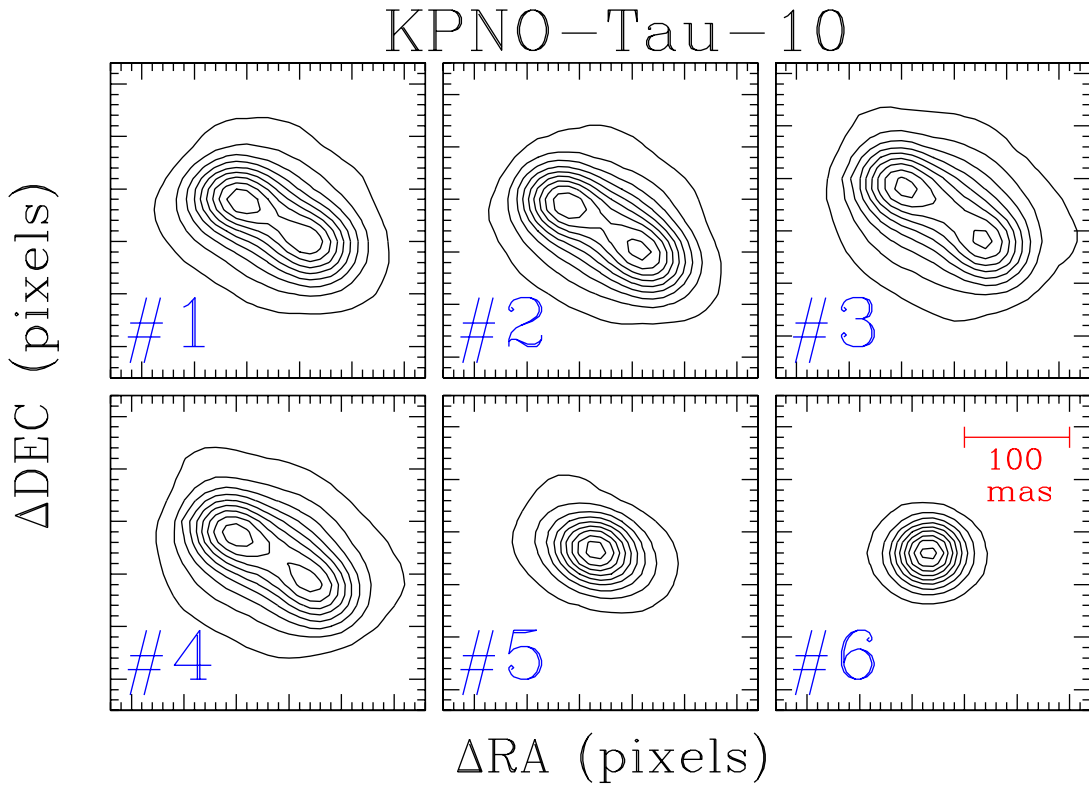
Figure 6.2 KPNO-Tau-10, an apparently single star that we observed as part of our survey. The scale of each contour plot is in detector pixels to illustrate sampling; the pixel scale is 10 mas pix^{-1} and the total FOV of each panel is 300 mas. The six panels show sequential exposures from our observations of Feb 6, 2006; the first four panels show what appears to be a binary system, whereas the fifth panel shows an elongated PSF and the last panel shows an unresolved single star. Poorly-corrected modes periodically appear in low-strehl data, perhaps due to problems with tip-tilt offloading, so any measurements taken under such conditions must be treated with some skepticism.
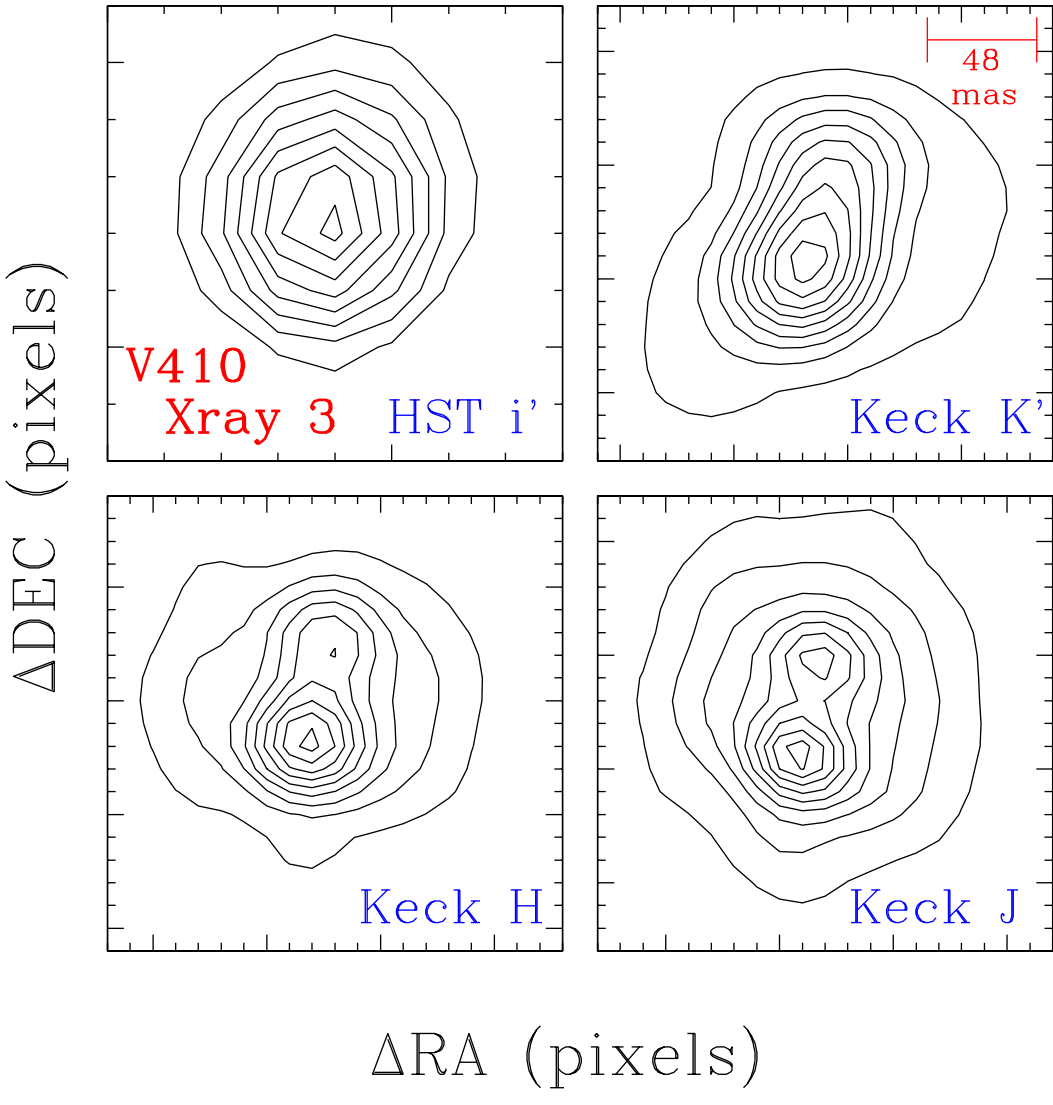
Figure 6.3 V410 X-ray 3, one of the very close binaries that we discovered in our HST-based survey. The scale of each contour plot is in detector pixels to illustrate sampling, so we show the best-fit separation of the binary system for scale in the upper right panel. The HST discovery image (top left) showed a very slight elongation with respect to the rest of our sample, indicating that it was probably a binary system. However, the best-fit separation was $\sim 1/2 \; \Lambda/D$, so the separation and flux ratio were very degenerate. By contrast, the binary is clearly discernible in K' images and is directly resolved in H and J. This resolution can only be attained in the best observing conditions (top $<10\%$), but under those conditions, Keck LGSAO clearly outclasses HST.

6.3.1.1 The Wide, Speckle-Dominated Regime

As was summarized by Metchev & Hillenbrand (2009), there are four common methods used to subtract the primary star's flux and identify companions in AO imagery: subtracting a median PSF representing all similar observations, subtracting a 180° rotated version of the same image, high-pass filtering by subtracting a Gaussian-smoothed version of the same image, or subtracting the azimuthally-averaged profile. We conducted experiments with these techniques, but we found that the speckle mitigation strategies that are vital for high-strehl NGSAO data are actually only marginally useful for low-strehl LGSAO data. Most of the flux that would be found in discrete speckles in high-strehl data is instead averaged into the seeing-limited halo, rendering the PSF less azimuthally variable at a given separation. The brightest speckles remain distinguishable, but at far lower contrast with respect to the surrounding median flux. Since the noise floor is brighter and the noise ceiling is fainter, there is less to be gained from reaching from exceeding the noise ceiling.

The sparsity and relatively low contrast of speckles in LGSAO data suggest that a different strategy is optimal for our data. Speckle mitigation and subtraction of the primary star's flux are observationally expensive, so the preferred strategy should be to characterize the mean and standard deviation of the brightness distribution of the PSF as a function of separation, then set the source detection limit above the expected ceiling for speckle brightness. We characterized the brightness distribution of each target's PSF by measuring the flux through photometric apertures placed at a range of separations and PAs, then measuring the mean and standard deviation for all apertures in a given bin of separation. The apertures were placed on a rectangular grid with spacing of 25 mas in order to ensure that the small number of speckles were detected, and the aperture sizes were matched to the FWHM of the PSF core for the primary. We measured this aperture photometry using the IRAF task phot, which is distributed as part of the DAOPHOT package (Stetson 1987).

In Figure 6.4, we show the contrast as a function of separation for three stars that span our survey's data quality, as well as the 5σ envelope for each source. We
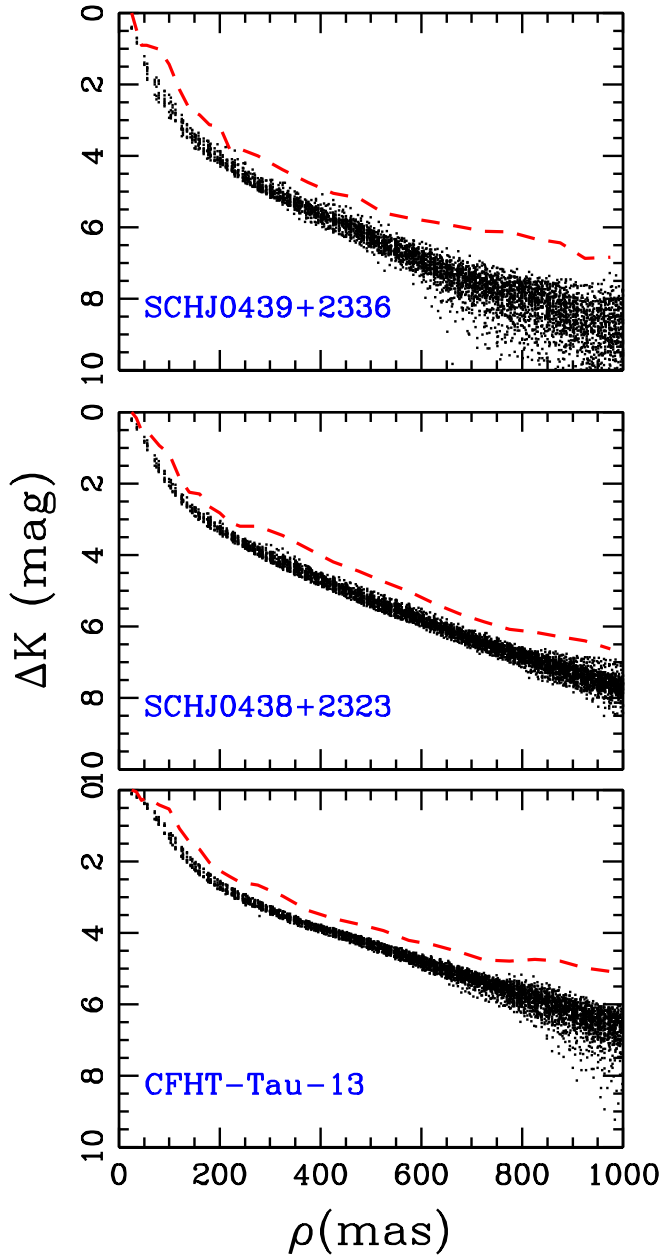
Figure 6.4 Contrast limits at wide separations (>100 mas) for three representative stars in our sample: SCHJ0439+2336 (top), SCHJ0436+2323 (middle), and CFHT-Tau-13 (bottom). The small black points show the flux as a function of separation for apertures placed at a range of separations and PAs from the primary, while the red dashed line shows the +5 sigma envelope above these points. A handful of candidate sources fall above this significance level, but all can be identified as speckles, so we have defined this envelope for each target and use it as our survey's detection limit.

found that there was typically 1 detection at 4–5σ per 2 stars, one detection at 5–6σ per 10 stars, and no detections among any of our targets at 6–10σ. This indicates that a 6σ clip should be completely safe, while a 5σ clip can be adopted if the few remaining speckles can be confidently identified as such. We found that all of the 5-6σ candidate detections fell on the PSF's diffraction spikes, were sufficiently short-lived as to not appear in all observations of a target, or were sufficiently long-lived as to appear in observations of multiple sequential targets. We therefore suggest that all such 5-6σ candidate detections are spurious, and adopt a 5σ clip as our survey's detection limits. All candidate detections that sit well above the 5σ limit appear to be genuine astronomical sources, though not necessarily comoving companions; we will revisit this distinction in Section 6.5.2.

6.3.1.2   The Close, Core-Dominated Regime

For separations near the PSF FWHM, the detection limits are driven by time- and spatially-dependent variations of the shape of the PSF core. LGSAO observations seem to be more susceptible to all of the weather effects that can degrade NGSAO observations, so distinguishing genuine companions from PSF artifacts is a significant challenge. The primary effect we se is for wind shake to cause PSF elongation in the direction of the zenith, perhaps because the tip-tilt sensor and low-bandwidth wavefront sensor operate at a lower rate and can not fully sample high-frequency oscillations of the telescope. Tip-tilt anisoplanatism is also significant for observations with off-axis tip-tilt guide stars, an effect that seems to become worse in poor seeing because the isokinetic angle becomes smaller. This causes elongation along the position angle to the tip-tilt star. Finally, significant variations in the AO correction cause the PSF FWHM itself to vary by a factor of $\sim$3 across our sample; a few of the lowest-quality observations have a PSF FWHM approaching 150 mas.

We have characterized these effects by fitting each science target's PSF core with a bivariate Gaussian distribution. This fit directly yields the degree of elongation (the ratio of the major axis a and minor axis b) and its direction (the PA of the major axis). For each our targets, we report the minor axis FWHM (i.e., the resolution
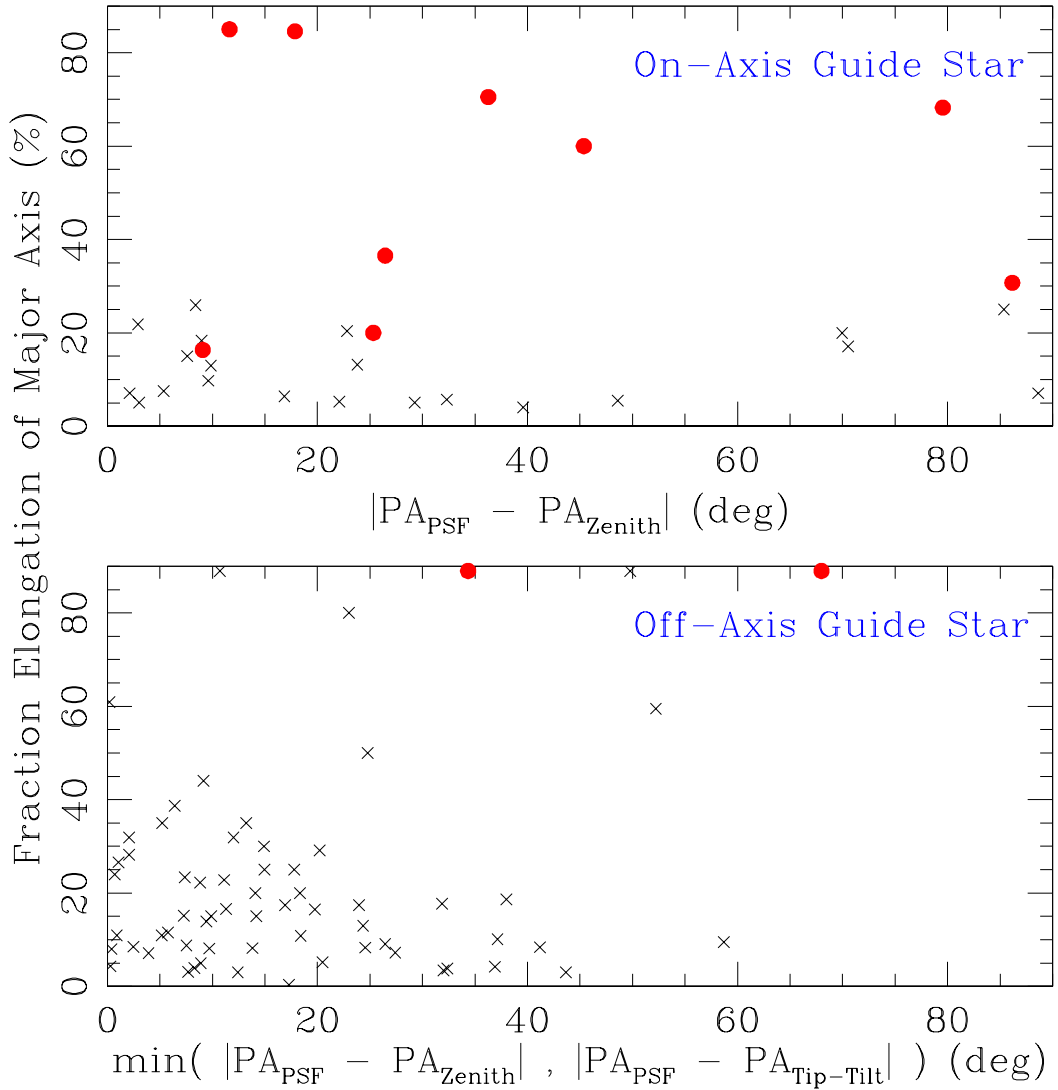
Figure 6.5 Top: Fractional PSF elongation as a function of its alignment with the direction to zenith for independently-confirmed binary systems (red circles) and all other targets (black crosses) that served as their own tip-tilt guide star. Most non-binary sources appear to be roughly aligned with zenith, a trend which indicates that wind-induced telescope shake is common among our observations. All sources which are not known binary systems appear to have PSF elongations of <30%, which seems to be the ceiling for weather-induced effects. Bottom: A similar figure for targets which had off-axis tip-tilt guide stars, where we plot the elongation of the target PSF with respect to the closer of the angle to zenith or the angle to the tip-tilt. Tip-tilt anisoplanatism also seems to induce PSF elongation, but with the exception of firmly-detected binary systems and targets with very poor data quality, the ceiling for observational effects is <40%.

prior to elongation effects) and the fractional elongation in Table 6.2. If windshake and tip-tilt anisoplanatism are the dominant sources of PSF asymmetry, then most sources should have a PA that is preferentially aligned with either the tip-tilt angle or the zenith angle. A set of selection criteria based on these quantities also lends itself to rigorous characterization of the detection limits, as artificial star tests can be used to determine whether a system with given separation and contrast (and perhaps PA) would be detected.

In Figure 6.5 (top), we plot the PSF elongation (the fractional extension of the major axis with respect to the minor axis) and the relative angle between the PSF and the zenith angle ($|\theta_{PSF}\text{-}\theta_{zen}|$) for all science targets which served as their own tip-tilt references. Of the 21 sources which are not independently-confirmed binary systems, 9 are aligned to within $<10^o$ of the zenith angle and 7 of the remaining 12 are aligned to within $10\text{--}45^o$. This strong trend indicates that wind-induced elongation was significant across the majority of our sample, even on those nights with moderate winds. Also, all of the targets that are not independently-confirmed binary systems have elongations of $<30\%$, which seems to be the ceiling for erroneous PSF elongation.

In Figure 6.5 (bottom), we consider the rest of our sample in plotting the PSF elongation versus the minimum of the relative angle either between PSF and zenith ($|\theta_{PSF}\text{-}\theta_{zen}|$) or between PSF and tip-tilt ($|\theta_{PSF}\text{-}\theta_{TT}|$). These targets also show a pronounced tendency to align with either the zenith or tip-tilt, though the result is more complicated because many targets have a net elongation intermediate between the two directions. There are fewer confirmed binary systems for comparison, but most of the targets fall below elongations of 40%, suggesting that this is the ceiling for combined wind and tip-tilt effects. Many of the targets with elongation $>40\%$ fall among our poorest sample and have significantly different elongation angles and magnitudes in each exposure, while all of the remainder present consistent and apparently double-peaked PSFs.

In light of these trends, we have adopted two criteria for identifying a source as a candidate binary system. First, it must have a PSF elongation of $>40\%$, which appears to be the ceiling for any weather-based effect in all but the worst data.

Second, similar PSF elongation must not be seen for other sources in the science target FOV, in our preliminary image of the tip-tilt guide star, or in observations of the previous or subsequent science target. Finally, the astrometry and photometry for a fit of 2 point sources must be consistent across all exposures; the poor data with elongations >40% tends to vary its PSF shape on extremely short timescales, yielding extremely inconsistent fits across the full dataset. We have inferred the source detection limit for each of our targets by measuring its minor-axis FWHM, then using artificial star tests to determine what ranges of companion separation and companion bright would have elongated a circular PSF with that FWHM to >40%.

Finally, there are also some cases where companions can be confidently studied below our survey's detection limit, such as if the companions were previously identified in another survey (i.e., V410 X-ray 3) or if a third bright star can be used as an independent PSF calibrator (P02-083). We have used PSF-fitting techniques (Section 6.3.2.3) to recover the photometry and astrometry for these close binary pairs, though we generally cannot include them in our statistics if their detection relied on a special feature of the system like high-order multiplicity. We also note that we were unable to recover accurate astrometry and photometry for MHO-Tau-8, which suggests that its orbital motion might have carried it inward from its last-known projected separation ($\sim$40 mas; Kraus et al. 2006; White et al., in prep).

6.3.2   Photometry and Astrometry

We measured relative photometry and astrometry for candidate companions using the IRAF package DAOPHOT (Stetson 1987). For source pairs with small separations, where the two PSF cores were not unambiguously resolved, we used the PSF-fitting ALLSTAR routine. For pairs with wider separations, we used the aperture photometry package PHOT. We analyzed each frame separately in order to estimate the uncertainty from the scatter between all frames; this also allowed us to reject some frames with subpar AO correction. Our final results represent the mean and standard deviation for all observations.

For the close binaries that we analyzed with ALLSTAR, we reconstructed the single-star PSF out of the merged binary PSF using the algorithm described in Kraus & Hillenbrand (2007b), which iteratively fits a template PSF to the primary and then subtracts the secondary to fit an improved estimate of the primary. For one triple system, UScoJ1607-2019), we chose to instead use the single primary as a PSF template for fitting the close pair constituting the secondary. This choice allowed us to distinguish the close pair despite a separation ($\sim$50 mas) that was significantly lower than the PSF FWHM ($\sim$80 mas).

Our relative astrometric measurements were distortion-corrected using new high-order distortion solutions (P.B. Cameron, priv. comm.) that deliver a significant performance increase as compared to the solutions presented in the NIRC2 pre-ship manual.[1] This distortion solution was derived from observations of a pinhole mask in the NIRC2 filter wheel, so it does not include any distortions introduced upstream of this point. The remaining residuals due to these uncorrected distortions are $\sim$5 mas for positions separated by $\sim$5–10$''$ (J. Lu, priv. comm.). We calibrated our photometry using the known 2MASS K_s magnitudes for each of our science targets; these absolute magnitudes are uncertain by $\sim$0.1-0.2 magnitudes due to the intrinsic variability of young stars (resulting from accretion or rotation).

6.3.3   (Sub)stellar and Companion Properties

Stellar properties can be difficult to estimate, particularly for young stars, since pre-main-sequence stellar evolutionary models are not well-calibrated. The model-predicted masses of young stars could be systematically uncertain by as much as 20% (e.g., Hillenbrand & White 2004), and estimates for individual stars could be uncertain by factors of 2 or more if their observed luminosities are biased by unresolved multiplicity or the intrinsic variability that young stars often display (from accretion or from rotational modulation of star spots). This suggests that any prescription for determining stellar properties should be treated with caution.

---

[1]http://www2.keck.hawaii.edu/realpublic/inst/nirc2/

We estimated the properties of all of our sample members using the methods described in Kraus & Hillenbrand (2007a). This procedure combines the 2 or 5 Myr isochrones of Baraffe et al.(1998) and Chabrier et al. (2000) with the temperature scales of Schmidt-Kaler (1982) and Luhman et al. (2003) to directly convert observed spectral types to masses. Relative properties (mass ratios q) for all binaries in our sample were calculated by combining these isochrones and temperature scales with the empirical NIR colors and K-band bolometric corrections of Kraus & Hillenbrand (2007c) to estimate q from the observed flux ratio ΔK.

For all binary systems, we have adopted the previously-measured (unresolved) spectral type for the brightest component and inferred its properties from that spectral type. This should be a robust assumption since equal-flux binary components will have similar spectral types and significantly fainter components would not have contributed significant flux to the original discovery spectrum. Projected spatial separations are calculated assuming the mean distance to the associations ($\sim$145 pc; de Zeeuw et al. 1999; Torres et al. 2009). If the total radial depth of each association is equal to its angular extent ($\pm 8°$ or ± 20 pc), then the unknown depth of each system within the association implies an uncertainty in the projected spatial separation of $\pm 14\%$. The systematic uncertainty due to the uncertainty in the mean distance of each association is negligible in comparison ($<2\%$).

6.4 Results

6.4.1 Candidate Companions and Detection Limits

Our search for sources in the speckle-dominated regime (at separations >1.5 times the PSF FWHM and extending to the edge of the detector; Section 6.3.1.1) yielded 45 candidate companions among the 78 young stars and brown dwarfs in our observed sample. All candidates within $<1''$ of the target sit well above the 5σ detection limit, so they all represent secure detections and do not seem to be spurious structures in the primary star's PSF. We also found numerous possible detections with significance
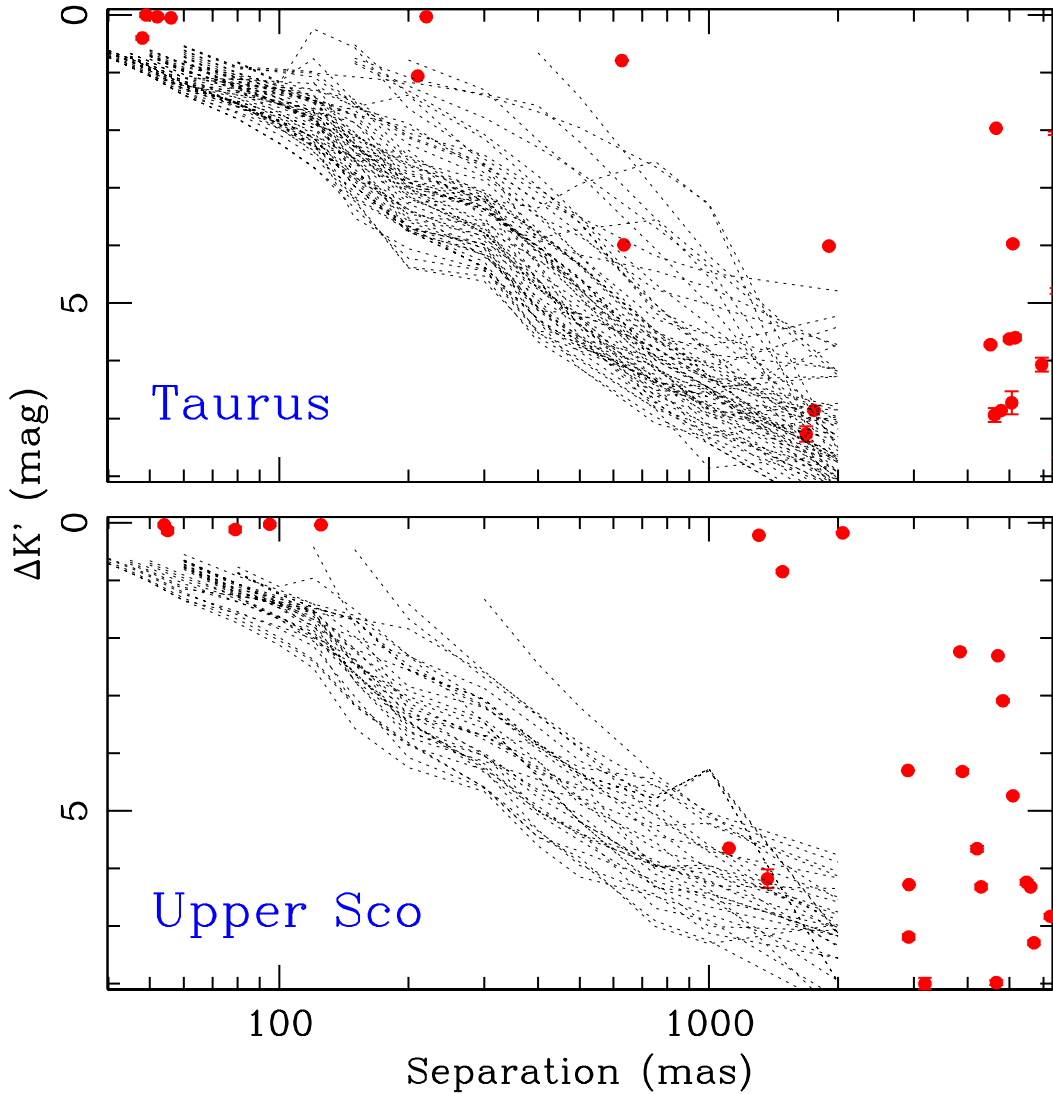
Figure 6.6 Separation and flux ratio for each of the candidate companions in our sample. The top panel shows our results for the 53 Taurus members in our sample, while the bottom panel shows our results for the 28 Upper Sco members. Red circles denote the candidate companions that we have detected, while dotted lines show the inferred detection limits for all sources. All detection limits converge to the read-noise limit at separations of $>2''$, so we do not extend the limits beyond that separation since the lines would obscure the faint sources detected at large separations.
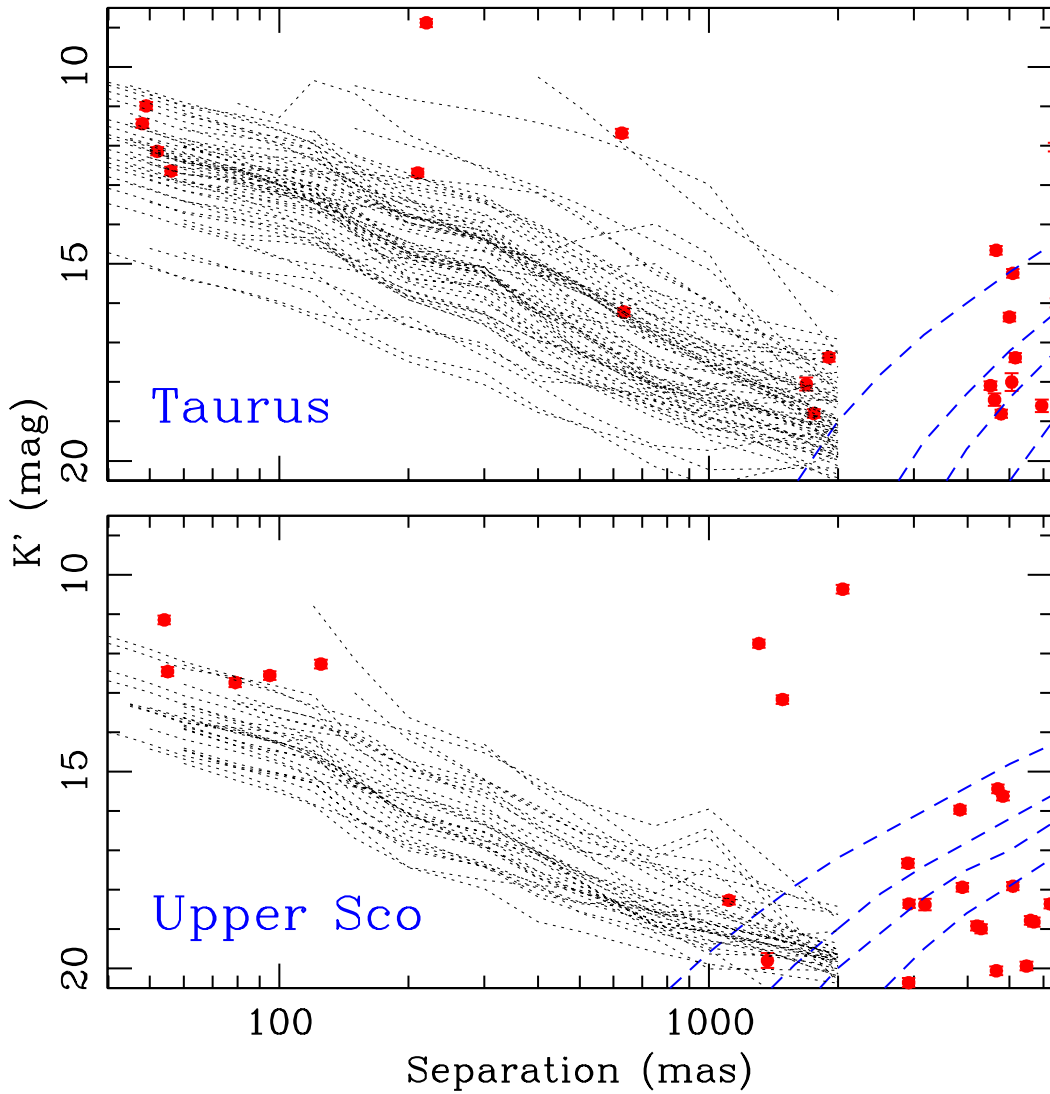
Figure 6.7 Separation and apparent magnitude $m_{K'}$ for each of the candidate companions in our sample. Red circles and dotted lines are defined as in Figure 6.6; blue dashed lines denote the limits above which we expect to find 1, 3, 5, or 10 background stars. We inferred these contamination rates using the star count models that we describe in Appendix B.

levels of 5–6σ in this regime, but as we described in Section 6.3.2.1, all of these possible detections appear to be spurious. Our corresponding search for sources in the core-dominated regime (at separations of order the PSF FWHM; Section 6.3.1.2) yielded 9 targets with PSF cores consistently elongated by >40%. Many targets had PSF elongations below this limit, but as we discussed above, most appear to be distorted due to observational effects and not the presence of a companion.

In Table 6.3, we list our survey's candidate companions and report their flux ratios, separations, and position angles. We also plot the flux ratio $\Delta K'$ and the candidate companion brightness K' as a function of separation in Figures 6.6 and 6.7, respectively. The vast majority of our wide-separation candidates are near the detection limits of our survey, in the brightness range where a real companion would fall below the deuterium-burning limit ($\sim$13 M_{Jup}), so we expect that almost all are unassociated field stars. However, a handful of planetary-mass companions have been identified around young stars and brown dwarfs (e.g., 2M1207b; Chauvin et al. 2004), so we must consider the possibility that some of these companions are analogs. We address the membership probabilities of these candidates in Section 6.4.2.

Of these 54 sources, 11 had already been identified as candidate binary companions by past survey efforts, so we note these past identifications in Table 6.3. Three of our candidate companions merit special attention. V410 X-ray3 AB was identified as a candidate binary in our previous HST/ACS multiplicity survey based on a marginal elongation of its PSF, but the best-fit separation was well inside the HST diffraction limit for the i' and z' filters. By contrast, the system is almost resolved in our K' observations, and corresponding JH images (in prep) clearly reveal V410 X-ray3 to be a genuine binary system. Two wide binary systems, USco 80 AB and UScoJ1607-2019 AB, were resolved to be hierarchical triples. USco 80 A is clearly resolved to be a close pair, while P02-083 B is marginally resolved.

We also note that six of these candidate companions were observed in two different observing runs. The intermediate-separation binary 2M0428+2714 and the wide pair 2M0455+3028 were observed at a second epoch because the first observation for each was significantly impacted by weather, while the other four sample members were

observed because each had a faint neighbor in close proximity that could have been an analog to the planetary-mass companion 2M1207b. We will discuss the relative motions of all targets with multi-epoch data in Section 6.5.3.

The other 26 members of our sample have no resolved neighbors within our detection limits. These detection limits, which we derived using the methods described in Section 6.3.1 and list in Table 6.4 (in terms of flux ratio ΔK) and Table 6.5 (in terms of mass ratio q), are extremely heterogeneous due to the wide range in observing conditions during our observing campaign. Some observations nearly achieve the expected limits for diffraction-limited images, while images from most of the other nights achieved significantly poorer conditions. We also note that our nominal detection limits for bound companions at wide separations was constrained by our followup efforts. We found many more faint candidates than we were able to follow up with second-epoch imaging, so we can not claim completeness beyond the maximum separation or flux ratio at which we have identified all of the field stars by testing for common proper motion.

Table 6.3.   Candidate Companions to Young Stars and Brown Dwarfs

Target	Epoch (JD-2450000)	N_{meas}	Sep (mas)	PA (deg)	$\Delta K'$ (mag)
2MASSJ04080782+2806280 B	4070	2	52±1	6.74±1.63	0.03±0.03
2MASSJ04152409+2910434 c1	4067	3	4520.9±0.3	0.29±0.01	5.72±0.02
2MASSJ04163911+2858491 B	4068	3	214±1	218.62±0.49	1.14±0.03
2MASSJ04163911+2858491 B	4089	5	210±1	219.38±0.22	1.06±0.01
2MASSJ04202555+2700355 c1	3728	2	4621±3	267.498±0.004	6.94±0.12
2MASSJ04230607+2801194 c1	4068	1	6443±3	291.63±0.02	4.79±0.05
2MASSJ04284263+2714039 B	3728	6	627±1	350.63±0.04	0.461±0.004
2MASSJ04284263+2714039 B	3772	6	627±1	350.56±0.02	0.79±0.01
2MASSJ04311907+2335047 c1	3728	6	644±1	118.22±0.03	3.973±0.003
2MASSJ04311907+2335047 c1	4067	10	634±1	117.7±0.02	3.99±0.01
2MASSJ04334291+2526470 c1	4068	3	1876±1	341.76±0.02	4.04±0.02
2MASSJ04334291+2526470 c1	4689	3	1903.1±0.4	341.83±0.01	4.01±0.02
2MASSJ04380084+2558572 c1	3728	2	6533±2	340.38±0.1	7.8±0.12
2MASSJ04403979+2519061 B	4070	5	49±2	270.96±0.74	0±0.01
2MASSJ04554046+3039057 c1	4068	1	5164±5	252.36±0.03	5.6±0.05
2MASSJ04554046+3039057 c2	4068	3	6891±1	38.2±0.02	5.84±0.01
2MASSJ04554757+3028077 B	3728	4	6368±4	115.74±0.01	1.92±0.04
2MASSJ04554757+3028077 B	3773	5	6379±1	115.8±0.01	2.05±0.03
2MASSJ04554970+3019400 c1	4067	1	7313±3	129.15±0.02	1.77±0.05
2MASSJ04554970+3019400 B	4067	4	56±1	13.48±0.72	0.05±0.02
2MASSJ04555289+3006523 c1	3772	2	5005±5	226.34±0.05	5.62±0.04
CFHT-Tau-14 c1	3773	6	1738±3	286.12±0.07	6.94±0.04
CFHT-Tau-14 c1	4089	4	1755±1	286.27±0.04	6.86±0.02
CFHT-Tau-14 c2	3773	4	4769±1	298.84±0.12	6.75±0.07
CFHT-Tau-14 c2	4089	3	4787.7±0.3	298.74±0.03	6.865±0.005
CFHT-Tau-16 c1	3728	2	8878±4	210.68±0.03	4±0.02
V410 X-ray 3 B	3728	6	49±1	340.71±0.3	0.35±0.04
V410 X-ray 3 B	3773	10	48±1	344.01±0.36	0.4±0.03
V928 Tau B	4068	3	220±3	292.92±0.09	0.03±0.01
DENIS-P-J161103.6-242642.9 c1	4187	4	5483±7	293.1±0.03	6.24±0.04
DENIS-P-J161916.5-234722.9 c1	4186	5	3844±10	24.92±0.28	2.18±0.04
DENIS-P-J161916.5-234722.9 c1	4187	3	3838.8±0.5	25.19±0.01	2.24±0.01
DENIS-P-J161916.5-234722.9 c2	4186	5	3891±2	265.75±0.02	4.3±0.01
DENIS-P-J161916.5-234722.9 c2	4187	4	3890±1	265.71±0.02	4.32±0.04
DENIS-P-J161916.5-234722.9 c3	4187	5	1368±6	332.25±0.21	6.18±0.16
SCH16111711-22171749 c1	4187	5	4207±2	344.41±0.02	5.66±0.05

Table 6.3 (cont'd)

Target	Epoch (JD-2450000)	N_{meas}	Sep (mas)	PA (deg)	$\Delta K'$ (mag)
SCH16121188-20472698 c1	3773	7	1093±1	44.59±0.07	5.76±0.03
SCH16121188-20472698 c1	3919	34	1107±4	44.92±0.05	5.76±0.02
SCH16121188-20472698 c1	4186	13	1113±3	43.73±0.05	5.65±0.01
SCH16131212-23050329 c1	4186	5	4703.5±0.2	157.78±0.02	2.31±0.02
SCH16131212-23050329 c2	4186	5	2905±0.2	329.9±0.01	4.3±0.01
SCH16151115-24201556 c1	4187	5	5100±1	141.03±0.01	4.74±0.02
SCH16151115-24201556 c2	4187	4	2917±13	222.74±0.04	7.19±0.05
SCH16253671-22242887 c1	4186	5	5604±10	219.34±0.03	6.32±0.02
SCHJ0359099+2009363 c1	3727	2	4660±1	264.275±0.003	1.965±0.005
SCHJ0359099+2009363 c2	3727	3	5953±2	99.284±0.004	6.07±0.12
SCHJ0434454+2308035 c1	4067	3	7769±1	38.35±0.01	7±0.01
SCHJ0523500+2435237 c1	3773	2	7861±1	16.49±0.02	5.36±0.03
SCHJ0536190+2242428 c1	3728	2	5095.5±0.2	157.109±0.002	3.97±0.02
SCHJ0536190+2242428 c1	3728	4	5065±2	192.24±0.04	6.73±0.2
SCHJ0537385+2428518 c1	3773	6	1684±8	152.84±0.14	7.27±0.13
SCHJ15582566-18260865 B	4186	8	95±1	253.28±0.2	0.03±0.03
SCHJ15582566-18260865 c1	4186	7	4833±4	304.09±0.02	3.09±0.03
USco 109 B	3773	2	4301±25	70.13±0.09	6.32±0.05
USco 55 B	3772	6	125±1	119±0.12	0.04±0.01
USco 66 B	3772	6	79±2	39.15±0.78	0.12±0.05
USco 80 A c1	4187	4	3183±14	23.1±0.04	8±0.1
USco 80 Ab	4187	4	54±1	100.59±0.67	0.04±0.03
USco 80 B c1	4187	4	2921±1	153.76±0.02	6.28±0.01
USco 80 B c2	4187	4	4664±7	302.33±0.14	7.98±0.04
USco-160702.1-201938 Ab	3772	6	55±2	271.63±1.08	0.14±0.05
USco-160702.1-201938 B	3772	6	1483±2	242.52±0.05	0.85±0.03
USco-160904.0-193359 B	3772	6	1307±1	322.88±0.03	0.22±0.01
USco-160904.0-193359 c1	3772	4	6231±5	219.84±0.02	6.83±0.04
USco-160904.0-193359 c2	3772	2	5708±10	152.49±0.05	7.29±0.04
USco-160908.4-200928 B	3773	4	2048±1	139.62±0.02	0.18±0.02

Table 6.4.   Companion Detection Limits

Target	$\Delta K'$ (mag) at $\rho=$ (mas)														
	40	45	50	60	80	100	120	150	200	300	400	500	750	1000	2000
2MASSJ04080782+2806280	...	...	...	...	...	...	...	0.84	1.32	2.07	2.79	3.51	5.01	5.88	7.56
2MASSJ04141188+2811535	...	...	...	0.55	0.93	0.97	1.01	1.07	1.17	1.37	1.57	2.21	3.52	4.31	6.25
2MASSJ04141188+2811535	...	0.67	0.81	1.09	1.19	1.29	1.39	2.24	3.07	3.73	4.23	4.88	6.34	6.76	7.74
2MASSJ04141188+2811535	0.66	0.81	0.97	1.28	1.5	1.73	1.96	2.51	3.71	3.97	5.12	5.69	6.39	6.92	7.28
2MASSJ04152409+2910434	0.71	0.87	1.03	1.35	1.6	1.86	2.12	2.54	2.45	3.52	4.6	5.39	6.29	7.1	8.06
2MASSJ04161885+2752155	...	...	...	0.68	1.1	1.37	1.63	2.09	2.6	3.05	3.78	4.34	5.46	6.25	7.94
2MASSJ04163911+2858491	...	...	...	...	...	...	...	...	0.78	1.3	2.17	2.77	4.06	5.03	7.7
2MASSJ04163911+2858491	...	...	0.77	1.03	1.27	1.51	1.74	1.6	1.39	2.59	3.91	4.75	6.09	6.9	8.57
2MASSJ04202555+2700355	...	...	0.68	0.93	1.32	1.7	2.08	2.48	3.18	3.7	4.69	5.27	6.61	6.53	8.17
2MASSJ04213460+2701388	...	0.74	0.89	1.18	1.34	1.5	1.66	2.53	3.56	3.99	4.76	5.25	6.42	6.77	8.09
2MASSJ04215450+2652315	...	...	...	0.81	1.27	1.36	1.46	1.87	2.68	3.23	3.91	4.16	4.44	4.72	5.77
2MASSJ04215450+2652315	...	...	0.7	0.96	1.25	1.55	1.84	2.73	3.41	3.85	4.75	5.2	5.77	6.32	6.27
2MASSJ04230607+2801194	...	...	0.61	0.85	1.08	1.3	1.53	2.06	2.74	3.17	3.76	4.31	5.51	6.25	8.05
2MASSJ04284263+2714039	...	...	0.7	0.96	1.24	1.53	1.81	2.52	3.26	3.21	3.35	2.93	2.54	3.3	8.37
2MASSJ04284263+2714039	0.66	0.81	0.97	1.28	1.5	1.73	1.96	2.81	3.46	3.65	3.87	3.72	3.56	4.55	8.41
2MASSJ04290068+2755033	0.62	0.76	0.91	1.21	1.59	1.97	2.35	3.19	3.74	4.16	5.13	5.18	5.78	6.31	6.85
2MASSJ04311907+2335047	...	...	...	0.62	1.02	1.21	1.4	2.04	2.97	3.37	4.03	4.77	5.91	6.01	7.3
2MASSJ04311907+2335047	...	0.74	0.89	1.18	1.39	1.61	1.82	2.67	3.59	4.06	5.33	5.77	6.24	6.97	6.74
2MASSJ04320329+2528078	0.62	0.76	0.91	1.21	1.44	1.67	1.9	2.13	2.85	3.2	4.35	5.43	6.7	7.44	8.75
2MASSJ04322329+2403013	...	...	0.77	1.03	1.29	1.54	1.79	2.74	3.28	3.78	4.74	5.36	6.53	7.15	8.57
2MASSJ04334291+2526470	...	...	...	0.53	0.9	0.94	0.98	1.54	2.13	2.62	3.44	4.18	5.28	5.55	6.18
2MASSJ04334291+2526470	0.64	0.79	0.94	1.24	1.54	1.84	2.14	3.02	4.08	4.61	5.46	5.7	6.22	6.53	7.02
2MASSJ04335245+2612548	0.73	0.9	1.06	1.39	1.68	1.97	2.27	2.44	2.35	3.37	4.09	4.75	5.62	5.75	5.22

Table 6.4 (cont'd)

Target	$\Delta K'$ (mag) at $\rho=$ (mas)														
	40	45	50	60	80	100	120	150	200	300	400	500	750	1000	2000
2MASSJ04380084+2558572	...	...	...	...	0.83	1.18	0.24	0.57	1.62	2.5	3.09	3.61	5.16	5.81	7.93
2MASSJ04400067+2358211	...	0.67	0.81	1.09	1.12	1.16	1.19	1.61	1.88	2.74	3.51	4.18	5.48	6.07	7.39
2MASSJ04403979+2519061	...	...	...	...	...	...	1.61	2.23	2.77	3.17	4.12	4.91	6.11	6.83	8.44
2MASSJ04442713+2512164	...	0.67	0.81	1.09	1.32	1.55	1.79	2.59	3.01	3.62	4.95	5.62	5.94	6.47	7.72
2MASSJ04552333+3027366	...	...	...	...	...	...	...	0.52	1.38	2.15	2.98	3.61	5.11	5.53	7.19
2MASSJ04554046+3039057	...	0.74	0.89	1.18	1.55	1.92	2.29	2.79	3.66	4.04	5.07	5.64	6.67	7.11	8.21
2MASSJ04554757+3028077	...	...	0.72	0.98	1.21	1.45	1.68	2.29	2.91	3.37	4.01	4.56	5.91	6.47	8.19
2MASSJ04554757+3028077	0.64	0.79	0.94	1.24	1.53	1.83	2.12	2.97	3.75	4.37	5.28	5.74	6.35	6.63	7.64
2MASSJ04554801+3028050	...	...	0.72	0.98	1.21	1.45	1.68	2.29	2.91	3.37	4.01	4.56	5.91	6.47	6.27
2MASSJ04554801+3028050	0.64	0.79	0.94	1.24	1.53	1.83	2.12	2.97	3.75	4.37	5.28	5.74	6.35	6.63	5.72
2MASSJ04554970+3019400	...	...	0.61	0.85	1.04	1.23	1.42	1.76	2.9	3.22	4.62	5.4	6.38	6.46	8.04
2MASSJ04555289+3006523	...	...	...	0.81	1.27	1.38	1.49	2.39	3.09	3.23	4.14	4.76	5.99	6.47	7.66
2MASSJ04555637+3049375	...	0.72	0.86	1.15	1.52	1.9	2.27	2.85	3.71	3.98	5.31	6.14	6.97	7.44	8.73
2MASSJ04574903+3015195	...	...	0.63	0.87	1.2	1.54	1.87	2.36	3	3.58	4.28	4.57	5.66	6.12	5.41
CFHT-Tau-10	...	...	...	...	0.82	1.16	0.76	1.5	2.45	3.1	3.85	4.34	5.49	5.89	6.14
CFHT-Tau-13	...	...	...	0.54	0.91	0.99	1.07	1.55	2.24	2.81	3.49	3.84	4.76	5.02	5.72
CFHT-Tau-14	0.62	0.76	0.91	1.21	1.54	1.86	2.19	3.16	3.72	4.28	5.51	5.96	6.82	7.25	7.9
CFHT-Tau-14	...	...	...	0.65	1.06	1.29	1.52	1.74	2.59	3.14	4.31	5.25	6.39	6.79	8.19
CFHT-Tau-16	...	...	...	...	0.82	1.16	1.32	1.47	2.11	2.58	3.25	3.51	4.18	4.47	4.79
CFHT-Tau-20	...	0.67	0.81	1.09	1.44	1.79	2.14	2.84	3.37	3.92	4.61	5.07	5.92	6.31	7.1
CFHT-Tau-9	...	...	...	0.61	1	1.24	1.48	1.72	1.96	2.61	3.23	3.79	5.01	5.81	7.32
DENIS-P-J161006.0-212744.6	...	...	0.66	0.91	1.29	1.68	2.06	2.46	3.07	3.58	4.35	4.56	5.05	5.7	6.17
DENIS-P-J161103.6-242642.9	...	...	...	0.77	1.22	1.4	1.58	2.47	3.31	3.7	4.14	4.88	5.54	6.3	6.35

Table 6.4 (cont'd)

Target	$\Delta K'$ (mag) at $\rho=$ (mas)														
	40	45	50	60	80	100	120	150	200	300	400	500	750	1000	2000
DENIS-P-J161452.6-201713.2	...	...	...	0.73	1.17	1.48	1.79	2.63	3.37	3.69	3.85	4.25	4.45	5.03	5.77
DENIS-P-J161916.5-234722.9	...	...	...	0.72	1.15	1.32	1.49	1.66	1.84	2.6	3.31	3.82	4.57	5.12	5.89
DENIS-P-J161916.5-234722.9	...	...	...	0.67	1.08	1.32	1.56	2.43	3.2	3.7	4.24	4.64	4.54	5.24	6.13
KPNO-Tau-10	...	0.72	0.86	1.15	1.55	1.96	2.37	3.07	3.66	4.4	5.49	5.54	6.6	6.95	7.76
KPNO-Tau-11	0.71	0.87	1.03	1.35	1.71	2.08	2.44	3.21	4.37	4.53	5.67	6.13	7.09	7.33	8.21
MHO-Tau-Tau-8	...	...	...	...	...	...	...	0.75	1.08	1.4	1.68	1.96	2.63	3.27	7.56
MHO-Tau-Tau-8	0.66	0.81	0.97	1.28	1.58	1.89	2.2	3.52	4.06	4.42	5.52	5.83	6.32	6.84	7.38
MHO-Tau-Tau-8	0.73	0.9	1.06	1.39	1.81	2.23	2.65	3.23	4.39	4.62	5.6	6	6.83	7.86	7.63
SCH15594802-22271650	...	...	...	...	0.77	1.11	0.96	1.51	2.3	3.1	3.9	4.32	5.43	5.63	6.5
SCH16044303-23182620	...	...	...	0.65	1.06	1.39	1.73	2.75	3.64	4.04	4.77	5.19	5.94	6.21	7.33
SCH16095991-21554293	...	...	...	0.55	0.93	1.17	1.41	1.98	2.84	3.21	3.82	4.36	5.26	5.22	6.06
SCH16111711-22171749	...	...	...	0.68	1.1	1.49	1.87	2.6	3.52	4.05	4.63	4.76	5.31	6.03	6.76
SCH16121188-20472698	...	0.69	0.84	1.12	1.38	1.64	1.9	2.64	3.44	4.28	4.92	5.44	5.94	6.24	7.02
SCH16121188-20472698	...	0.72	0.86	1.15	1.27	1.39	1.52	2.76	3.73	4.14	4.46	5.19	6.29	7.01	7.08
SCH16121188-20472698	...	...	...	0.75	1.19	1.44	1.68	2.45	3.02	3.48	4.4	5.18	6.33	6.43	7.17
SCH16131212-23050329	...	...	...	0.77	1.22	1.37	1.53	2.24	2.92	3.42	4.13	4.78	5.67	5.96	6.58
SCH16151115-24201556	...	...	0.74	1.01	1.33	1.64	1.96	2.73	3.47	4.24	5.01	5.39	5.86	6.35	8.53
SCH16183141-24195229	...	...	...	0.65	1.06	1.29	1.53	2.19	3.13	3.77	4.28	4.8	5.93	6.1	6.8
SCH16235158-23172740	...	...	...	...	0.86	1.22	1.41	1.61	2.3	3.47	4.42	5.18	5.97	6.01	7.36
SCH16252862-16585055	...	0.65	0.79	1.06	1.37	1.68	1.99	2.6	3.45	4.33	5.07	5.52	6.31	6.67	7.17
SCH16253671-22242887	...	...	...	0.81	1.27	1.41	1.55	1.69	2.48	3.18	3.94	4.48	6.01	6.42	7.17
SCHJ0359099+2009363	...	...	...	0.72	1.15	1.44	1.74	2.37	3.15	3.77	4.47	4.98	5.63	6.26	6.8
SCHJ0416272+2053093	...	0.74	0.89	1.18	1.54	1.89	2.25	2.89	3.77	4.12	5.08	5.58	6.8	7.15	8.19

Table 6.4 (cont'd)

Target	\Delta K' (mag) at \rho= (mas)														
	40	45	50	60	80	100	120	150	200	300	400	500	750	1000	2000
SCHJ0427074+2215039	...	...	...	0.72	1.15	1.31	1.48	1.65	2.52	2.87	3.72	4.36	5.62	6.1	7.7
SCHJ0434454+2308035	0.73	0.9	1.06	1.22	1.38	1.54	1.7	1.86	3.01	3.79	4.58	5.58	6.43	7.35	8.65
SCHJ0438586+2336352	...	...	...	0.79	1.24	1.26	1.28	1.58	2.05	2.43	3.01	3.51	4.66	5.37	7.08
SCHJ0438587+2323596	...	...	0.7	0.96	1.25	1.54	1.84	2.27	2.85	3.33	4.01	4.59	5.98	6.51	7.71
SCHJ0439016+2336030	0.62	0.76	0.91	1.21	1.52	1.83	2.14	2.77	3.37	4.2	4.9	5.39	6.12	6.86	7.02
SCHJ0439064+2334180	...	...	...	0.81	1.27	1.52	1.77	2.1	2.62	3.09	3.8	4.33	5.6	6.31	7.77
SCHJ0506466+2104298	0.68	0.84	1	1.31	1.55	1.78	2.02	2.98	3.66	4.16	5.08	5.72	6.51	6.57	8.01
SCHJ0516021+2214530	...	...	...	...	...	...	...	0.81	1.23	1.78	2.3	2.73	3.68	4.39	7.5
SCHJ0523500+2435237	...	...	0.66	0.91	1.1	1.28	1.47	2.27	3.14	3.78	4.72	5.23	6.14	6.56	7.14
SCHJ0536190+2242428	...	0.72	0.86	1.15	1.35	1.56	1.77	2.49	2.91	3.42	4.02	4.72	5.79	6.36	6.97
SCHJ0537385+2428518	0.73	0.9	1.06	1.39	1.8	2.22	2.63	3.36	4.22	4.44	5.28	5.85	6.73	7.3	6.97
SCHJ15582566-18260865	...	...	...	...	...	...	...	0.47	1.67	2.69	3.35	3.9	4.89	5.6	6.99
SCHJ16090451-22245259	...	...	...	0.79	1.24	1.43	1.63	2.37	3.34	4	4.68	5.07	6.1	6.51	7.95
SCHJ16095307-19481704	0.68	0.84	1	1.31	1.68	2.04	2.41	3.18	3.84	4.59	5.35	5.89	6.91	7.26	8.44
USco 109	...	...	0.7	0.96	1.29	1.63	1.96	2.38	3.61	4.18	5.02	5.4	5.97	5.94	6.9
USco 55	...	...	...	...	...	...	...	...	...	1.33	2.45	3.2	4.37	5.06	6.54
USco 66	...	...	...	...	...	...	...	...	1.41	2.58	3.34	3.93	5.09	5.72	7.11
USco 80 A	...	...	...	...	...	...	0.42	1.77	3.24	4.03	4.99	5.35	6.69	6.9	8.25
USco 80 B	0.62	0.76	0.91	1.21	1.6	1.99	2.38	3.14	3.82	4.59	5.46	5.81	7.01	7.31	6.97
USco-160702.1-201938	...	...	...	0.65	1.06	1.37	1.69	2	2.32	2.88	3.55	4.13	4.74	4.31	7.12
USco-160702.1-201938 B	...	...	...	0.65	1.06	1.44	1.81	2.19	2.56	3.2	3.88	4.41	4.93	4.28	7.12
USco-160904.0-193359 A	...	...	...	...	0.88	1.24	1.47	1.69	2.55	3.07	3.84	4.37	4.79	4.27	7.97
USco-160904.0-193359 B	...	...	...	...	0.88	1.24	1.47	1.69	2.55	3.07	3.84	4.37	4.79	4.27	7.97

Table 6.4 (cont'd)

Target	$\Delta K'$ (mag) at $\rho=$ (mas)														
	40	45	50	60	80	100	120	150	200	300	400	500	750	1000	2000
USco-160908.4-200928 A	0.71	0.87	1.03	1.35	1.74	2.13	2.53	3.57	4.25	4.67	5.61	6.15	6.48	6.8	7.56
USco-160908.4-200928 B	0.71	0.87	1.03	1.35	1.57	1.8	2.02	3.18	3.87	4.29	5.33	5.95	6.45	7.12	7.56
V410 X-ray 3	...	...	...	0.73	1.17	1.33	1.49	2.25	2.97	3.33	4.09	4.82	6.17	6.52	7.94
V410 X-ray 3	...	...	...	...	...	...	1.17	2.18	3.52	3.83	5	5.69	6.1	6.74	6.85
V928 Tau	...	...	...	...	...	...	...	...	...	...	0.66	1.42	3.04	4.18	6.19

Table 6.5.   Companion Detection Limits

Target	$q = M_s/M_p$ at $\rho=$ (mas)															M_{sec} (M_{Jup}) at $\rho=$ (mas)			
	40	45	50	60	80	100	120	150	200	300	400	500	750	1000	2000	500	750	1000	2000
2MASSJ04080782+2806280	1	1	1	1	1	1	1	0.463	0.281	0.176	0.122	0.084	0.024	0.016	0.008	26.6	7.7	4.9	2.5
2MASSJ04141188+2811535	1	1	1	0.694	0.558	0.547	0.537	0.521	0.495	0.442	0.406	0.294	0.099	0.062	0.028	27.9	9.4	5.9	2.6
2MASSJ04141188+2811535	1	0.646	0.598	0.516	0.489	0.463	0.439	0.289	0.138	0.083	0.064	0.047	0.027	0.022	0.015	4.5	2.5	2.1	1.4
2MASSJ04141188+2811535	0.664	0.609	0.564	0.481	0.434	0.387	0.334	0.245	0.084	0.074	0.043	0.034	0.026	0.021	0.018	3.2	2.5	2	1.7
2MASSJ04152409+2910434	0.682	0.633	0.589	0.501	0.439	0.377	0.25	0.198	0.209	0.102	0.062	0.046	0.032	0.022	0.011	2.8	1.9	1.4	0.7
2MASSJ04161885+2752155	1	1	1	0.642	0.512	0.444	0.395	0.313	0.23	0.14	0.081	0.061	0.038	0.028	0.013	5.8	3.6	2.6	1.2
2MASSJ04163911+2858491	1	1	1	1	1	1	1	1	0.481	0.352	0.227	0.166	0.053	0.032	0.011	24.4	7.8	4.8	1.6
2MASSJ04163911+2858491	1	1	0.484	0.408	0.357	0.315	0.277	0.3	0.333	0.183	0.065	0.037	0.021	0.015	0.007	5.5	3.1	2.3	1
2MASSJ04202555+2700355	1	1	0.511	0.436	0.348	0.284	0.237	0.194	0.1	0.075	0.038	0.029	0.017	0.018	0.009	4.9	2.9	3	1.5
2MASSJ04213460+2701388	1	0.492	0.45	0.377	0.344	0.316	0.291	0.189	0.081	0.058	0.037	0.029	0.019	0.016	0.009	4.3	2.7	2.4	1.4
2MASSJ04215450+2652315	1	1	1	0.488	0.341	0.324	0.308	0.248	0.179	0.144	0.109	0.098	0.088	0.078	0.042	2.3	2	1.8	1
2MASSJ04215450+2652315	1	1	0.528	0.397	0.343	0.295	0.252	0.175	0.134	0.112	0.077	0.062	0.042	0.023	0.025	1.4	1	0.5	0.6
2MASSJ04230607+2801194	1	1	0.667	0.586	0.519	0.459	0.413	0.318	0.166	0.13	0.082	0.062	0.037	0.028	0.012	5.9	3.5	2.6	1.2
2MASSJ04284263+2714039	1	1	0.504	0.429	0.363	0.311	0.267	0.19	0.096	0.099	0.092	0.15	0.188	0.094	0.009	25.3	31.6	15.9	1.5
2MASSJ04284263+2714039	0.52	0.47	0.427	0.356	0.315	0.279	0.25	0.161	0.086	0.077	0.068	0.074	0.081	0.041	0.008	12.4	13.7	7	1.3
2MASSJ04290068+2755033	0.701	0.505	0.464	0.391	0.283	0.225	0.185	0.127	0.102	0.087	0.059	0.057	0.044	0.032	0.019	1.6	1.2	0.9	0.5
2MASSJ04311907+2335047	1	1	1	0.743	0.598	0.53	0.37	0.257	0.137	0.114	0.087	0.065	0.041	0.039	0.017	2.6	1.6	1.6	0.7
2MASSJ04311907+2335047	1	0.701	0.648	0.542	0.371	0.331	0.292	0.161	0.103	0.086	0.051	0.043	0.035	0.023	0.027	1.7	1.4	0.9	1.1
2MASSJ04320329+2528078	0.666	0.614	0.564	0.484	0.43	0.388	0.346	0.307	0.157	0.129	0.06	0.038	0.023	0.017	0.007	3.6	2.1	1.6	0.6
2MASSJ04322329+2403013	1	1	0.691	0.594	0.502	0.343	0.297	0.155	0.118	0.096	0.066	0.05	0.03	0.019	-0.005	2	1.2	0.8	-0.2
2MASSJ04334291+2526470	1	1	1	0.584	0.43	0.401	0.392	0.295	0.223	0.182	0.133	0.097	0.059	0.05	0.028	1.8	1.1	0.9	0.5
2MASSJ04334291+2526470	0.549	0.501	0.4	0.345	0.296	0.252	0.222	0.156	0.101	0.082	0.053	0.045	0.027	0.016	-0.001	0.8	0.5	0.3	0
2MASSJ04335245+2612548	0.518	0.429	0.378	0.321	0.275	0.238	0.209	0.195	0.201	0.136	0.1	0.077	0.047	0.043	0.061	1.8	1.1	1	1.4
2MASSJ04380084+2558572	1	1	1	1	0.665	0.555	0.886	0.75	0.427	0.2	0.129	0.098	0.053	0.04	0.011	5.3	2.8	2.1	0.6
2MASSJ04400067+2358211	1	0.646	0.598	0.516	0.507	0.498	0.489	0.399	0.349	0.166	0.1	0.066	0.037	0.03	0.017	6.2	3.5	2.8	1.6
2MASSJ04403979+2519061	1	1	1	1	1	1	0.298	0.221	0.165	0.106	0.051	0.034	0.021	0.016	0.008	5.7	3.5	2.7	1.3
2MASSJ04442713+2512164	1	0.717	0.671	0.582	0.514	0.446	0.307	0.177	0.134	0.098	0.057	0.044	0.038	0.031	0.014	2.3	2	1.7	0.7
2MASSJ04552333+3027366	1	1	1	1	1	1	1	0.712	0.442	0.304	0.146	0.088	0.043	0.037	0.019	8.3	4.1	3.5	1.8
2MASSJ04554046+3039057	1	0.492	0.45	0.377	0.308	0.255	0.214	0.164	0.077	0.053	0.032	0.025	0.017	0.014	0.009	4.2	2.8	2.3	1.5
2MASSJ04554757+3028077	1	1	0.46	0.382	0.33	0.286	0.251	0.185	0.135	0.102	0.056	0.036	0.019	0.015	0.008	7.6	4	3.2	1.6
2MASSJ04554757+3028077	0.502	0.438	0.395	0.325	0.273	0.233	0.199	0.131	0.065	0.039	0.025	0.02	0.016	0.014	0.009	4.2	3.4	3	2
2MASSJ04554801+3028050	1	1	0.527	0.448	0.393	0.349	0.307	0.229	0.16	0.096	0.059	0.044	0.025	0.02	0.02	6.1	3.4	2.7	2.7
2MASSJ04554801+3028050	0.556	0.506	0.459	0.387	0.333	0.288	0.251	0.15	0.077	0.049	0.031	0.026	0.021	0.019	0.027	3.6	2.9	2.6	3.6

Table 6.5 (cont'd)

Target	$q = M_s/M_p$ at $\rho=$ (mas)															M_{sec} (M_{Jup}) at $\rho=$ (mas)			
	40	45	50	60	80	100	120	150	200	300	400	500	750	1000	2000	500	750	1000	2000
2MASSJ04554970+3019400	1	1	0.645	0.56	0.502	0.456	0.411	0.351	0.145	0.121	0.05	0.036	0.025	0.024	0.012	3.8	2.6	2.5	1.2
2MASSJ04555289+3006523	1	1	1	0.472	0.358	0.335	0.317	0.203	0.134	0.098	0.051	0.037	0.022	0.018	0.011	6.3	3.7	3.1	1.9
2MASSJ04555637+3049375	1	0.488	0.441	0.367	0.295	0.242	0.203	0.15	0.071	0.061	0.027	0.019	0.014	0.011	0.006	3.6	2.6	2.1	1.2
2MASSJ04574903+3015195	1	1	0.615	0.545	0.458	0.389	0.32	0.259	0.202	0.162	0.121	0.108	0.057	0.036	0.063	1.5	0.8	0.5	0.9
CFHT-Tau-10	1	1	1	1	0.497	0.405	0.514	0.339	0.211	0.112	0.067	0.05	0.029	0.025	0.022	6.3	3.7	3.1	2.8
CFHT-Tau-13	1	1	1	0.761	0.638	0.612	0.588	0.447	0.234	0.148	0.105	0.089	0.061	0.056	0.042	4.8	3.3	3	2.2
CFHT-Tau-14	0.746	0.692	0.638	0.53	0.344	0.285	0.213	0.124	0.098	0.079	0.048	0.04	0.025	0.018	0.007	1.6	1	0.7	0.3
CFHT-Tau-14	1	1	1	0.732	0.584	0.501	0.418	0.305	0.168	0.125	0.078	0.053	0.033	0.026	0.002	2.1	1.3	1	0.1
CFHT-Tau-16	1	1	1	1	0.487	0.401	0.368	0.335	0.21	0.164	0.124	0.113	0.087	0.077	0.066	3.2	2.5	2.2	1.9
CFHT-Tau-20	1	0.502	0.457	0.381	0.309	0.256	0.215	0.151	0.086	0.063	0.038	0.03	0.021	0.018	0.013	5.6	3.9	3.4	2.5
CFHT-Tau-9	1	1	1	0.566	0.444	0.387	0.343	0.302	0.272	0.193	0.105	0.074	0.035	0.026	0.014	9.3	4.5	3.2	1.8
DENIS-P-J161006.0-212744.6	1	1	0.768	0.682	0.589	0.501	0.429	0.361	0.278	0.23	0.169	0.156	0.128	0.097	0.08	4.3	3.5	2.6	2.2
DENIS-P-J161103.6-242642.9	1	1	1	0.737	0.611	0.566	0.523	0.366	0.263	0.225	0.189	0.138	0.102	0.06	0.058	2.6	1.9	1.1	1.1
DENIS-P-J161452.6-201713.2	1	1	1	0.747	0.625	0.548	0.478	0.344	0.257	0.226	0.211	0.18	0.165	0.129	0.089	3.4	3.1	2.5	1.7
DENIS-P-J161916.5-234722.9	1	1	1	0.75	0.623	0.583	0.48	0.504	0.471	0.339	0.254	0.21	0.155	0.124	0.09	6.9	5.1	4.1	2.9
DENIS-P-J161916.5-234722.9	1	1	1	0.767	0.638	0.583	0.529	0.367	0.265	0.22	0.178	0.151	0.157	0.119	0.081	4.9	5.1	3.9	2.6
KPNO-Tau-10	1	0.488	0.441	0.367	0.289	0.234	0.194	0.132	0.073	0.042	0.025	0.024	0.016	0.014	0.01	4.6	3	2.6	1.9
KPNO-Tau-11	0.502	0.454	0.41	0.342	0.282	0.237	0.197	0.099	0.045	0.042	0.025	0.021	0.014	0.013	0.009	3	2.1	1.9	1.3
MHO-Tau-Tau-8	1	1	1	1	1	1	1	0.591	0.49	0.416	0.364	0.319	0.218	0.118	0.015	33.6	23	12.4	1.6
MHO-Tau-Tau-8	0.625	0.57	0.523	0.445	0.38	0.329	0.281	0.102	0.067	0.056	0.035	0.03	0.025	0.02	0.016	3.2	2.7	2.1	1.7
MHO-Tau-Tau-8	0.595	0.545	0.496	0.419	0.344	0.277	0.216	0.121	0.056	0.05	0.033	0.029	0.02	0.013	0.015	3	2.1	1.4	1.5
SCH15594802-22271650	1	1	1	1	0.648	0.56	0.6	0.471	0.342	0.241	0.177	0.151	0.096	0.089	0.061	7	4.4	4.1	2.8
SCH16044303-23182620	1	1	1	0.512	0.401	0.352	0.302	0.199	0.135	0.115	0.087	0.074	0.055	0.049	0.03	5.1	3.8	3.4	2.1
SCH16095991-21554293	1	1	1	0.549	0.421	0.385	0.348	0.272	0.192	0.163	0.126	0.102	0.071	0.073	0.052	7.1	5	5	3.6
SCH16111711-22171749	1	1	1	0.671	0.562	0.475	0.35	0.259	0.174	0.142	0.114	0.108	0.086	0.064	0.054	5	4	3	2.5
SCH16121188-20472698	1	0.497	0.444	0.393	0.354	0.315	0.28	0.208	0.148	0.106	0.083	0.067	0.055	0.048	0.035	4.6	3.8	3.3	2.4
SCH16121188-20472698	1	0.488	0.435	0.388	0.37	0.351	0.333	0.198	0.128	0.111	0.098	0.074	0.047	0.032	0.034	5.1	3.3	2.2	2.3
SCH16121188-20472698	1	1	1	0.475	0.382	0.345	0.308	0.225	0.177	0.145	0.101	0.074	0.046	0.044	0.032	5.1	3.2	3.1	2.2
SCH16131212-23050329	1	1	1	0.469	0.378	0.355	0.331	0.246	0.185	0.149	0.111	0.087	0.061	0.054	0.041	6	4.2	3.8	2.9
SCH16151115-24201556	1	1	0.469	0.391	0.347	0.302	0.261	0.192	0.14	0.102	0.076	0.065	0.054	0.044	0.011	5.1	4.2	3.4	0.9
SCH16183141-24195229	1	1	1	0.512	0.401	0.366	0.331	0.25	0.168	0.128	0.106	0.087	0.055	0.051	0.038	6	3.8	3.6	2.6
SCH16235158-23172740	1	1	1	1	0.699	0.606	0.561	0.517	0.386	0.239	0.164	0.121	0.087	0.085	0.037	4	2.8	2.8	1.2
SCH16252862-16585055	1	0.772	0.725	0.643	0.571	0.5	0.441	0.339	0.242	0.17	0.127	0.104	0.074	0.062	0.043	3.4	2.4	2	1.4

6.4.2 Binary Systems and Field Stars

Companion searches must address the prospect of chance alignments with background stars, especially surveys with very deep detection limits. As we will describe in the next section, we have obtained multi-epoch astrometry for several candidates in order to test for common proper motion. However, we can use statistical arguments to determine which candidate companions require those followup observations. As we describe more fully in Appendix B, we have updated the Milky Way model of Bahcall & Soneira (1980) to predict star counts as a function of magnitude for the line of sight toward each of our targets; these models allow us to predict the field star contamination rate and thereby determine which companions have a significant probability of being background stars.

In Figure 6.7, we plot the joint magnitude-separation limits at which our models predict we should find 1, 3, 5, or 10 background stars among all the targets observed in that association. In both associations, our models predict that we should find <1 background star with $K < 15$ within $<5''$, which suggests that all of the bright sources we observe well inside this limit are genuine companions. This limit agrees with our estimate based on 2MASS source counts in the direction of Taurus and Upper Sco (Kraus & Hillenbrand 2007), which found that all neighbors down to the 2MASS 10σ limit ($K = 14.3$) could be assumed to be bound association members out to separations of 3-5$''$.

The status of our fainter candidates is not as clear. Our models predict that we should find only one background star with separation $\rho < 2''$ and brightness $K < 19$ in Taurus, so the candidates inside this limit all seem very promising as potential analogs to 2M1207b. The background star density is higher in the direction of Upper Sco since it lies in the direction of the galactic center, so even with our smaller sample size, we still expect 3 chance alignments with $\rho < 2''$ and $K < 19$. However, the star count models are not well-constrained at faint magnitudes since they are driven by the low-mass halo population at $K < 15$, so the contamination rate could be uncertain by a factor of at least 2-3. As such, it is prudent to measure common proper

Table 6.5 (cont'd)

Target	\(q = M_s/M_p\) at \(\rho=\) (mas)															\(M_{sec}\) (\(M_{Jup}\)) at \(\rho=\) (mas)			
	40	45	50	60	80	100	120	150	200	300	400	500	750	1000	2000	500	750	1000	2000
SCH16253671-22242887	1	1	1	0.485	0.405	0.381	0.357	0.332	0.243	0.181	0.131	0.108	0.058	0.048	0.035	6.6	3.5	3	2.1
SCHJ0359099+2009363	1	1	1	0.464	0.344	0.287	0.244	0.178	0.118	0.064	0.037	0.029	0.021	0.017	0.013	6.1	4.5	3.5	2.8
SCHJ0416272+2053093	1	0.48	0.432	0.36	0.292	0.242	0.204	0.148	0.068	0.054	0.03	0.024	0.015	0.013	0.008	4.5	2.8	2.4	1.6
SCHJ0427074+2215039	1	1	1	0.663	0.534	0.494	0.455	0.416	0.197	0.161	0.089	0.065	0.039	0.032	0.015	4.8	2.9	2.4	1.1
SCHJ0434454+2308035	0.494	0.446	0.401	0.367	0.334	0.309	0.284	0.261	0.142	0.071	0.041	0.026	0.018	0.013	0.007	4.3	3.1	2.1	1.1
SCHJ0438586+2336352	1	1	1	0.467	0.307	0.303	0.299	0.247	0.19	0.156	0.118	0.089	0.031	0.022	0.011	23.4	8.2	5.7	2.8
SCHJ0438587+2323596	1	1	0.647	0.567	0.486	0.425	0.366	0.287	0.16	0.114	0.074	0.056	0.032	0.026	0.015	4.7	2.7	2.2	1.3
SCHJ0439016+2336030	0.643	0.586	0.54	0.461	0.391	0.34	0.29	0.198	0.112	0.062	0.044	0.036	0.027	0.02	0.019	3.8	2.9	2.1	2
SCHJ0439064+2334180	1	1	1	0.673	0.53	0.457	0.329	0.254	0.17	0.129	0.091	0.073	0.044	0.033	0.009	3.4	2	1.5	0.4
SCHJ0506466+2104298	0.511	0.462	0.418	0.349	0.308	0.271	0.243	0.145	0.077	0.05	0.032	0.024	0.018	0.018	0.01	4.1	3	2.9	1.6
SCHJ0516021+2214530	1	1	1	1	1	1	1	0.457	0.346	0.258	0.2	0.16	0.072	0.042	0.011	30.4	13.7	8	2.1
SCHJ0523500+2435237	1	1	0.623	0.54	0.487	0.444	0.4	0.271	0.127	0.077	0.048	0.038	0.027	0.023	0.018	4.1	2.9	2.4	1.9
SCHJ0536190+2242428	1	0.464	0.418	0.344	0.301	0.268	0.24	0.168	0.136	0.094	0.055	0.033	0.02	0.016	0.013	7	4.2	3.4	2.7
SCHJ0537385+2428518	0.494	0.446	0.401	0.334	0.268	0.222	0.179	0.091	0.049	0.044	0.029	0.023	0.016	0.013	0.015	3.9	2.8	2.2	2.5
SCHJ15582566-18260865	1	1	1	1	1	1	1	0.605	0.299	0.195	0.148	0.117	0.08	0.06	0.034	9.1	6.2	4.7	2.6
SCHJ16090451-22245259	1	1	1	0.489	0.41	0.376	0.342	0.253	0.168	0.129	0.1	0.085	0.056	0.047	0.021	5.2	3.4	2.9	1.3
SCHJ16095307-19481704	0.49	0.436	0.393	0.349	0.298	0.253	0.22	0.159	0.119	0.09	0.066	0.053	0.035	0.03	0.013	4.1	2.7	2.3	1
USco 109	1	1	0.483	0.398	0.351	0.304	0.261	0.223	0.131	0.104	0.076	0.065	0.051	0.052	0.035	5	4	4.1	2.7
USco 55	1	1	1	1	1	1	1	1	1	0.296	0.186	0.137	0.083	0.064	0.035	14.5	8.8	6.8	3.7
USco 66	1	1	1	1	1	1	1	1	0.335	0.204	0.149	0.115	0.074	0.057	0.032	9	5.8	4.5	2.5
USco 80 A	1	1	1	1	1	1	0.736	0.243	0.074	0.053	0.036	0.03	0.018	0.016	0.009	11.5	6.8	6.2	3.6
USco 80 B	0.596	0.515	0.464	0.369	0.258	0.164	0.121	0.089	0.067	0.048	0.033	0.029	0.018	0.016	0.019	7.4	4.6	4.1	4.7
USco-160702.1-201938	1	1	1	0.602	0.397	0.284	0.227	0.202	0.176	0.139	0.105	0.082	0.064	0.076	0.025	11.3	8.7	10.4	3.4
USco-160702.1-201938 B	1	1	1	0.602	0.397	0.272	0.217	0.187	0.157	0.122	0.091	0.072	0.059	0.077	0.025	9.9	8	10.5	3.4
USco-160904.0-193359 A	1	1	1	1	0.476	0.359	0.296	0.235	0.113	0.092	0.066	0.053	0.045	0.056	0.012	13.5	11.3	14	3.1
USco-160904.0-193359 B	1	1	1	1	0.476	0.359	0.296	0.235	0.113	0.092	0.066	0.053	0.045	0.056	0.012	13.5	11.3	14	3.1
USco-160908.4-200928 A	0.543	0.479	0.424	0.329	0.221	0.132	0.106	0.071	0.055	0.047	0.031	0.026	0.023	0.02	0.015	6.5	5.7	5	3.7
USco-160908.4-200928 B	0.543	0.479	0.424	0.329	0.265	0.21	0.159	0.087	0.066	0.055	0.035	0.028	0.023	0.017	0.015	7	5.8	4.4	3.7
V410 X-ray 3	1	1	1	0.635	0.505	0.47	0.437	0.292	0.149	0.114	0.071	0.05	0.03	0.026	0.013	4.2	2.5	2.2	1.1
V410 X-ray 3	1	1	1	1	1	1	0.505	0.303	0.095	0.081	0.047	0.036	0.031	0.024	0.023	3	2.6	2	1.9
V928 Tau	1	1	1	1	1	1	1	1	1	1	0.574	0.295	0.082	0.046	0.01	186.3	51.7	29.2	6.4

motion for any candidate companion fainter than $K \sim 15$, especially since any genuine companion would have $M <$ 10-20 M_{Jup}, making it an extremely compelling discovery. The predicted background star contamination rate rises quickly for separations $>3''$, matching the many candidates we have discovered, so we provisionally adopt this separation as an outer limit at which it is worthwhile to test candidates for possible association.

Finally, multiplicity surveys in young clusters and associations must also consider chance alignments between two unbound young stars. These chance alignments are extremely difficult to distinguish from genuine binary systems since all association members are young, at similar distance, and comoving to very high precision. The only solution is to treat their probability in a statistical sense, which we have already done in our treatment of wider binary systems (Kraus & Hillenbrand 2008). We found that the probability of a chance alignment between two young association members is negligible for separations $<10''$, so we will proceed under the assumption that any pair of young stars constitutes a genuine binary system.

In Table 6.6, we list the mass ratios and component masses that we infer for the bound binary pairs in our sample. These properties were derived using the methods we describe in Section 6.3.3.

6.4.3   Testing for Common Proper Motion

Our detection limits extend far below the deuterium-burning limit for both associations, so our survey is potentially sensitive to analogs of 2M1207b, the intriguing ~ 5 M_{Jup} companion to a young brown dwarf in the TW Hya association. However, these deep limits will also include many background stars which must be considered as candidate companions. As we showed in the previous section, any candidate with a separation of $\rho < 3''$ must be considered as a candidate, but the expected rarity of planetary-mass companions suggests that we should follow up even candidates that are well inside this limit. The most efficient method of followup is to test for common proper motion by observing each candidate at multiple epochs; we have done this for
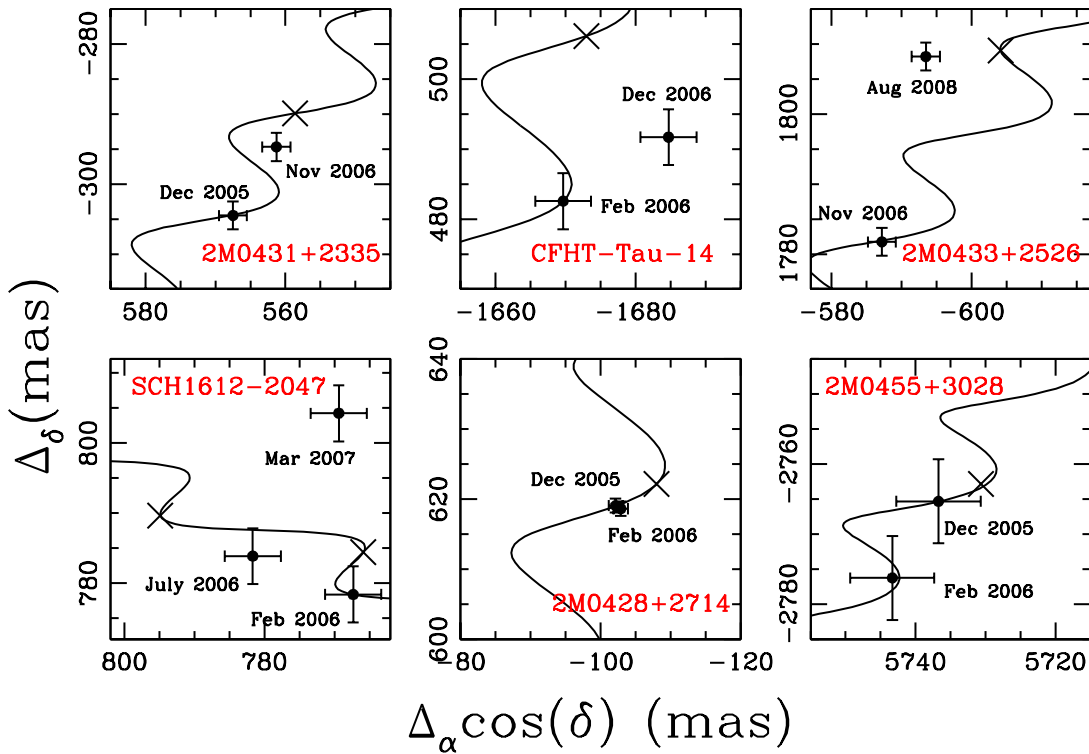
Figure 6.8 Multi-epoch astrometry for four candidates that could be faint planetary-mass companions, plus two secure binary systems. Filled circles denote the measurements and crosses denote expected followup-epoch positions for background stars. In each case, the solid line denotes the expected motion of a background star over time. The binary systems 2M0428+2714 and 2M0455+3028 have astrometry consistent with common proper motion, though the case of 2M0455+3028 shows that the error bars become significant with respect to yearly motion for separations of >5″. By contrast, none of the faint companions show common proper motion.

Table 6.6.   Binary System Properties

Target Name	Epoch (JD-2450000)	Proj. Sep. (AU)	q (M_s/M_p)	M_{prim} $(M_\odot)$	M_{sec} $(M_\odot)$
V410 X-ray 3 A-B	3773	49.9	0.77	0.08	0.062
V410 X-ray 3 A-B	3728	49.4	0.8	0.08	0.064
2MASSJ04403979+2519061 A-B	4070	39.3	1	0.16	0.16
2MASSJ04080782+2806280 A-B	4070	1	0.98	0.3	0.29
2MASSJ04554970+3019400 A-B	4067	2	0.95	0.1	0.095
2MASSJ04163911+2858491 A-B	4089	31.8	0.4	0.14	0.056
2MASSJ04163911+2858491 A-B	4068	31.7	0.38	0.14	0.054
V928 Tau A-B	4068	42.5	0.97	0.6	0.58
2MASSJ04284263+2714039 A-B	3728	50.8	0.6	0.16	0.095
2MASSJ04284263+2714039 A-B	3772	50.8	0.48	0.16	0.076
SCHJ0359099+2009363 A-c1	3727	38.3	0.22	0.2	0.043
2MASSJ04554757+3028077 A-B	3728	16.8	0.22	0.2	0.044
2MASSJ04554757+3028077 A-B	3773	16.8	0.21	0.2	0.041
2MASSJ04554970+3019400 A-c1	4067	18.7	0.28	0.1	0.028
USco 80 Aa-Ab	4187	14.6	0.97	0.36	0.35
USco-160702.1-201938 Aa-Ab	3772	39.4	0.91	0.13	0.12
USco 66 A-B	3772	5.7	0.89	0.074	0.066
SCHJ15582566-18260865 A-B	4186	36.7	0.98	0.074	0.072
USco 55 A-B	3772	17.3	0.97	0.1	0.097
USco-160904.0-193359 A-B	3772	46.8	0.84	0.24	0.2
USco-160702.1-201938 A-B	3772	35.2	0.5	0.13	0.064
USco-160908.4-200928 A-B	3773	20.2	0.87	0.24	0.21

four of the closest candidates in our sample.

In Figure 6.6, we show the multi-epoch astrometry for four of our candidates: 2M0431+2335, CFHT-Tau-14, 2M0433+2526, and SCH1612-2047. We also show similar results for two stellar binaries, 2M0428+2714 and 2M0455+3028, as a check of our astrometric calibration. In all cases, we also show the change in relative position that we would expect from a nonmoving background star due to the parallactic and proper motion of our target. None of our targets have well-measured parallaxes or proper motions, so we have adopted suitable measurements for other nearby (typically $<2^o$) association members. For 2M0431+2335, 2M0433+2526, and 2M0455+3028, we adopted the parallax (6.2 mas) and proper motion (+13.9, -15.4 mas yr^{-1}) measured for HP Tau/G2 by Torres et al. (2009). For CFHT-Tau-14 and 2M0428+2714, we adopted the parallax (7.8 mas) and proper motion (+8.9, -26.6 mas yr^{-1}) measured for for HD 283572 by Torres et al.(2007). Finally, for SCH1612-2047, we adopted the mean parallax (6.9 mas) and proper motion (-10, -25 mas yr^{-1}) for all high-mass Upper Sco members as measured by HIPPARCOS (de Zeeuw et al. 1999).

Our results suggest that none of the faint candidates are actually comoving companions. The candidate companions to 2M0431+2335 and 2M0433+2526 have relative motions close to those expected of a nonmoving background object. The relative motions of the candidate companions to CFHT-Tau-14 and SCH1612-2047 do not match comovement or nonmovement, suggesting that they are nearby field dwarfs. We also note that the three astrometric measurements for SCH1612-2047 do not match a simple straight line, suggesting that it might have a significantly different parallax as well as proper motion.

In contrast, the two epochs for 2M0428+2714 agree extremely well with comovement, matching to within <1 mas across a 1.5 month time baseline. This uncertainty is much smaller than the expected motion of a background star ($\sim$7 mas) and indicates that our other measurements across longer time baselines should also be free of systematic errors larger than this limit. The relative motion of 2M0455+3028 is also within $<1\sigma$ of zero, though the uncertainties are much larger because its separation is an order of magnitude larger than that of 2M0428+2714.

6.5 Characterizing Multiplicity at the Bottom of the IMF

The frequency and properties of multiple star systems are important indicators of star formation processes, and the extreme disparity between the binary populations of the VLM population and higher-mass stars could provide a powerful test of star formation models. However, most of the large multiplicity surveys in the VLM regime have been conducted for old systems in the field; constraints for young binary systems, especially those in dynamically primordial populations like Taurus and Upper Sco, are only now beginning to match the field surveys.

The archetypical concept of VLM multiplicity was established by a trio of high-resolution imaging surveys for nearby field targets. Burgasser et al. (2003), Close et al.(2003), and Bouy et al.(2003) all found that low-mass binaries are less com-
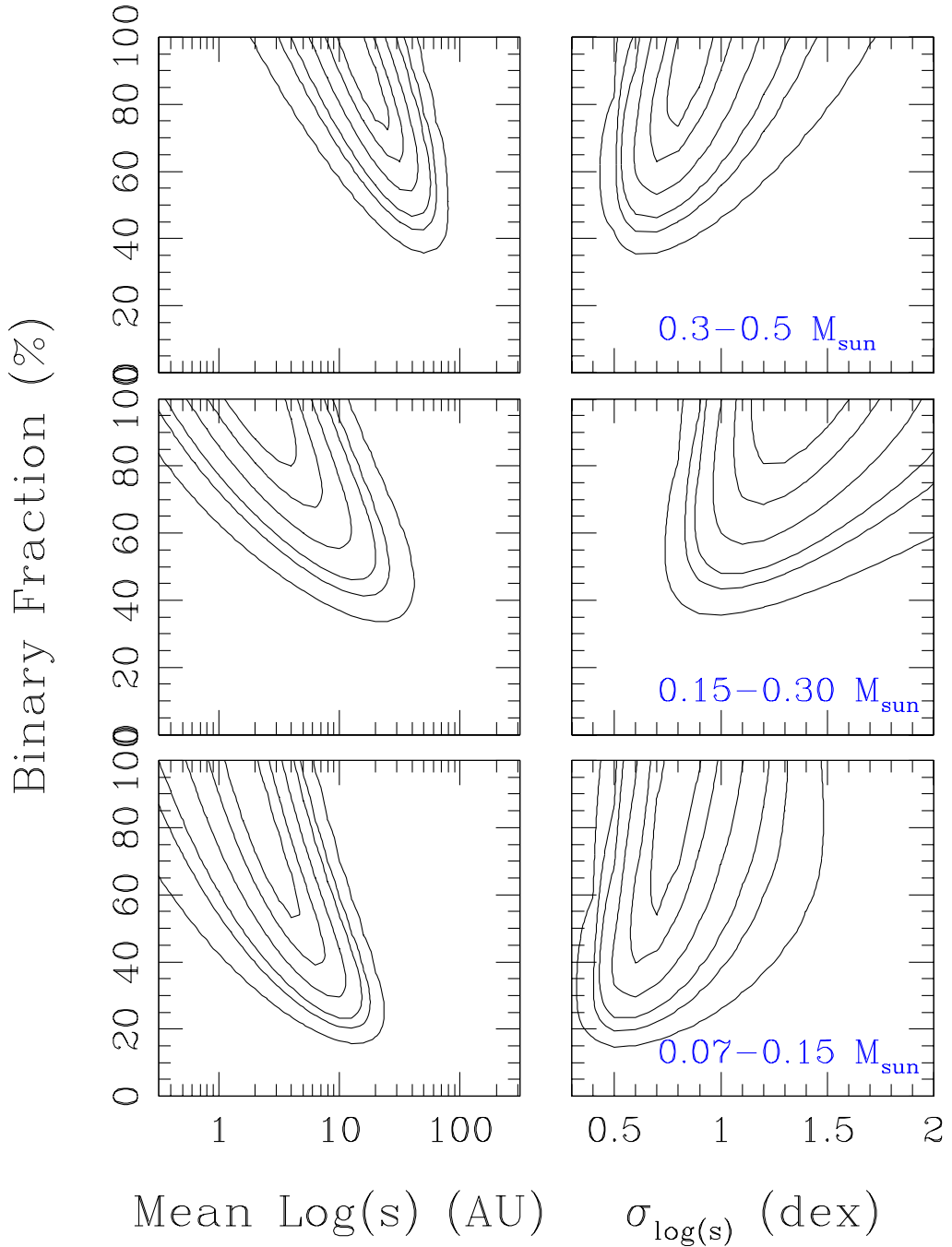
Figure 6.9 Posterior probability density functions for three mass ranges of stellar binaries in our sample. In each row, we plot the probability surface as projected onto the F-$\log(s)$ and F-$\sigma_{\log(s)}$ plane, showing contours that enclose total probability densities of 25%, 50%, 75%, 90%, 95%, and 99%.
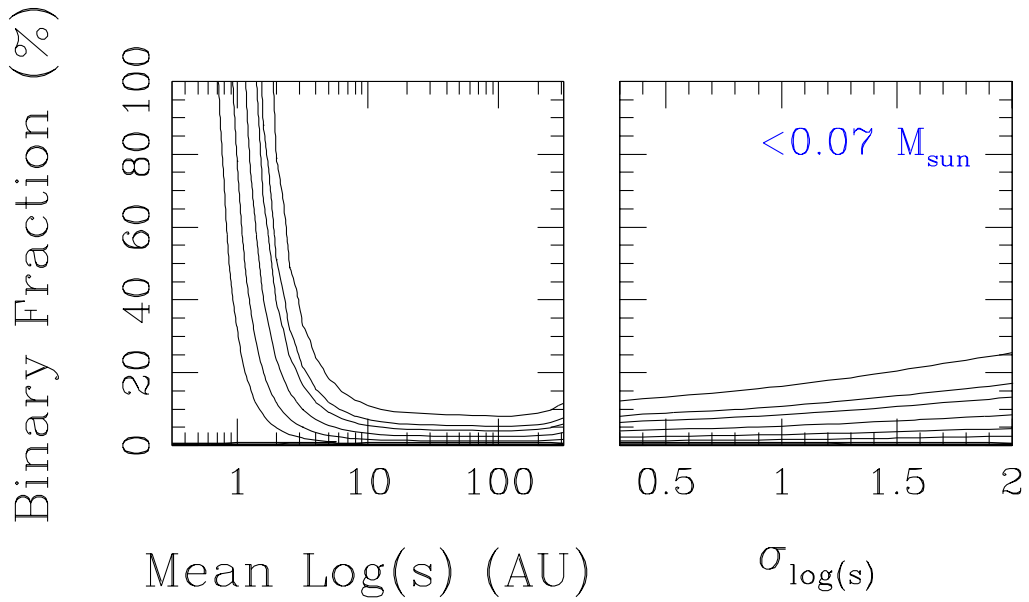
Figure 6.10 As in Figure 6.10, but for our substellar subsample. The posterior PDF can not be normalized, so we can not plot contours of enclosed total probability density or integrate across the unplotted parameters. We instead plot confidence contours on the probability surface for a null detection, and show cross-sections through the four-dimensional PDF at the most likely values inferred by the T dwarf multiplicity study of Burgasser et al.(2006): $\log(s) \sim 0.6$, $\sigma_{\log(s)} \sim 0.3$ dex, and $\gamma \sim 4.2$. We chose these parameters because the T dwarf sample studied by Burgasser et al. more closely matches our mass range than the full sample of MLT dwarfs studied by A07.
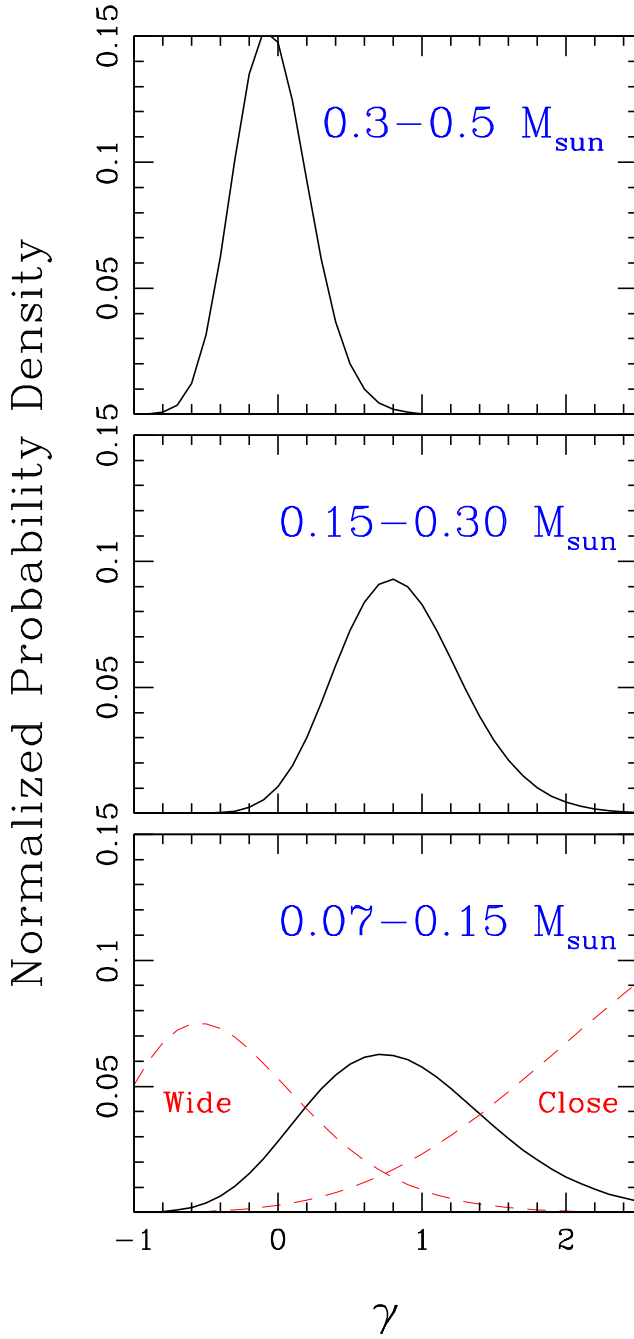
Figure 6.11 Posterior probability density functions for three mass ranges of stellar binaries in our sample. In each row, we plot the probability curve as projected onto the γ axis, denoting our confidence interval on the power-law exponent for the mass ratio distribution. As we discuss in the text, we also show separate fits in the 0.07-0.15 $M_\odot$ subsample for systems with separations of >25 AU and <25 AU; close binary systems have a mass ratio distribution that is strongly peaked at unity, while four of the five wider binary systems have mass ratios of <0.5.

mon ($f \sim$10-15% for separations of $\rho>$2-4 AU), more compact ($\rho<$10-20 AU), and more symmetric ($q >$0.7-0.8, or $M_{sec}\sim M_{prim}$) than the corresponding population of solar-type binaries studied by Duquennoy & Mayor (1991). The scarcity and tightly-bound nature of low-mass binaries led to suggestions that this indicated past strong dynamical interactions, perhaps consistent with the embryo ejection hypothesis for brown dwarf formation. However, the field population only allows an incomplete and muddled view of its primordial properties. The field represents a composite of many different formation environments, but probably dominated by stars formed in dense clusters (e.g., Lada & Lada 2003), so it is difficult to disentangle any environmental effects, especially those tied to primordial stellar density. Field brown dwarfs are also subject to a mass-age degeneracy, which makes it difficult to infer mass-dependent trends, and the steep mass-luminosity relation makes it difficult to identify companions which are much less massive than their primary stars.

These complications can be avoided by studying multiplicity in nearby star-forming regions and young associations. These populations have homogeneous and better-constrained initial conditions, their known age allows for a (model-dependent) resolution of the mass-age degeneracy, and their youth corresponds to a very shallow mass-luminosity relation that improves sensitivity to low-mass companions. The only tradeoff is that these populations are more distant than nearby field stars, imposing a resolution penalty against the discovery of binaries with small separations. Preliminary surveys have indicated that the field paradigm, with infrequent and tightly-bound binaries, is broadly consistent with several different formation environments. However, they also indicated a further dependence of separation and frequency on mass within the VLM and substellar regime, and these mass-dependent effects can only be explored with a large binary survey among targets with known ages.

6.5.1 Bayesian Inference and Binary Population Statistics

Binary population statistics are traditionally presented in terms of histograms of binary frequency versus separation or mass ratio, where the data are presented only for

a range where the survey is complete. The analytic form of the preferred model is then fit to these histograms in order to infer the population properties. This approach has the virtue of simplicity, but estimating the probability density function (PDF) for the model's scale parameters is often difficult, especially if there are covariances between parameters. This method also is manifestly inadequate for handling heterogeneous datasets. If different stars have different detection limits, such as from being observed with different methods or under different atmospheric conditions, then simple histograms can be constructed only by appealing to completeness corrections that are themselves poorly constrained.

A better solution for working with heterogeneous data is to adopt a Bayesian approach, where the scale parameters of the model are assigned a prior PDF and that PDF is modified by each observation. This method exploits Bayes' theorem:

$$P(\theta|O) \propto P(O|\theta)P(\theta) \tag{6.1}$$

where θ represents the "model" (a set of scale parameters describing the functional form), O represents the observation, $P(\theta|O)$ is the posterior PDF for the model (as a function of its parameters) given the data, $P(O|\theta)$ is the probability of obtaining an observation as a function of the model parameters, and $P(\theta)$ is the prior PDF for the model (again, as a function of its parameters). In cases with multiple observations, the posterior function for one observation is then used as the prior function for the next observation.

Allen et al.(2007, hereafter A07) developed the relevant techniques for applying Bayesian statistics to VLM multiplicity, and we have largely adopted their techniques. We specifically describe the binary population in terms of a binary fraction F, a power-law mass ratio distribution with exponent γ, and a log-normal separation distribution with mean $\log(s)$ and standard deviation $\sigma_{\log(s)}$. We have adopted the same Poisson likelihood function as A07, but we will use a moderately different set of prior distributions. A07 claimed that the optimal unbiased prior functions should be constant for γ and $\log(s)$ and inverse functions for F and $\sigma_{\log(s)}$ (proportional to $1/F$

and $1/\sigma_{\log(a)}$ respectively). However, the scale-independence arguments presented by A07 in justifying these inverse functions do not seem to apply, so we will instead use constant functions for the prior distributions for all parameters.

Another significant difference between our analysis and that of A07 is that we directly model the projected separation distribution, whereas A07 used the semimajor axis as a model parameter and then extrapolated a projected separation distribution using an assumed eccentricity distribution and randomly-distributed inclinations and phase angles. The eccentricity distribution for binary systems is still largely unconstrained for the separations and mass ranges that we consider, but most likely eccentricity distributions yield a separation distribution that is directly proportional to the semimajor axis distribution. As such, our results can be directly related to theoretical semimajor axis distributions once the eccentricity distribution is predicted by theory or measured by future surveys. We have also omitted the volume-completeness correction used by A07 to compensate for the overluminosity of similar-brightness binaries. The discovery surveys for most of our sample members were spatially limited, not flux- or volume-limited, so binary systems were equally likely to be detected. The high-resolution imaging techniques used in past surveys were themselves flux-limited, but we chose our LGSAO sample in part to compensate for this limit, so it should not significantly influence our results to invoke detections and detection limits from those past surveys where needed.

Our specific implementation of Bayesian analysis follows that of A07, defining two-dimensional functions of projected separation $\log(s)$ and mass ratio q that denote the number of observations sensitive to each set of $\log(s)$ and q (the "window function") and the corresponding number of companions with that set of parameters. We iterated our calculation over all mass ratios from 0 to 1 in steps of 0.01 and over all values of $\log(s)$ between 0.5 and 3.6 dex in steps of 0.1 dex.

Our own sample comprises the vast majority of available measurements in the VLM regime ($M < 0.15\ M_\odot$), but almost all of the measurements for higher-mass stars must be adopted from previous surveys. We have specifically adopted the detections and detection limits for all stars with $M < 0.5\ M_\odot$ for previous surveys of Taurus-

Auriga (Ghez et al. 1993; Simon et al. 1995; Konopacky et al. 2007; White et al. 2007), Upper Sco (Köhler et al. 2000), and Cha-I (Ahmic et al. 2007; Lafreniere et al. 2008a). In each case, we converted the measured angular separations (in mas) and flux ratios (in Δm) for their detections and detection limits into physical quantities (separations in AU and mass ratios) using the same methods that we applied to our own sample. This ensures a uniform set of inputs for our analysis, whereas each survey's inferred system properties were derived using different combinations of association distances/ages and pre-main sequence stellar evolutionary models.

Past studies have indicated that multiple star formation might be a mass-dependent process, so we have divided our sample into several bins. The stellar/substellar boundary represents a natural breaking point since it corresponds roughly to the M/L boundary for field objects, allowing for natural comparison to field samples. As we have indicated in our studies of solar-type multiplicity and wide multiplicity, systems with primary masses of >0.5 $M_\odot$ tend to have fundamentally different binary parameters, featuring a log-flat separation distribution and many very wide systems, so we have adopted this limit as the maximum for consideration in our sample. The desire for similar number statistics per bin therefore dictated four mass bins of similar width: <0.07 $M_\odot$, 0.07-0.15 $M_\odot$, 0.15-0.30 $M_\odot$, and 0.30-0.50 $M_\odot$. A more rigorous treatment might incorporate a mass dependence directly into our fit parameters (F, γ, $\log(s)$, and $\sigma_{\log(s)}$), but in the absence of any theoretical guidance on the functional form of this mass dependence, we will defer such analysis to a future study.

Our Bayesian analysis yields a PDF for all possible "models" that is defined across four dimensions, so we can not present the full results in a two-dimensional medium. However, any two parameters for which the covariance is small can be presented separately without discarding information. This independence allows us to instead present the results as a series of lower-dimensional surfaces, where PDF is integrated across the uncorrelated parameters in order to flatten its dimensionality. As we describe in the next section, our results can be described with a manageable number of two-dimensional or one-dimensional surfaces.

Finally, it is impossible to define a true PDF with only null detections, so we

can not use this analysis for the lowest-mass bin ($M < 0.07\ M_\odot$) since it includes no resolved binary systems. Our choice to use generic conjugate priors does not disallow arbitrarily extreme values, such as small mean separations or steep power laws. If we do not have enough constraints (i.e., detected binaries) to force the PDF to zero at all extrema of the scale parameters, then the integrated probability will diverge and render the PDF unnormalizeable. Since we can not estimate a well-defined probability for any particular set of parameters being "correct", we instead must settle for a weaker result: the probability that a given set of parameters would have yielded our null detection. This measurement is equally valid for ruling out parameter space, but does not carry any explicitly affirmative value; regions where the model is less improbable are not necessarily regions where the model is probable. The act of "flattening" the PDF to visualizable 1D or 2D figures is also not defined for this type of constraint, so in figures where the PDF for higher-mass bins is flattened, we will instead show a cross-section through the lowest-mass PDF where we adopt the field T dwarf parameters suggested by Burgasser et al.(2006): $\log(s)\sim0.6$, $\sigma_{\log(s)}\sim0.3$, and $\gamma\sim4.2$.

6.5.2 The Mass-Dependent Parameters of the Multiple Star Population

The four-dimensional posterior PDF for our Bayesian analysis can be flattened to present six two-dimensional probability surfaces and four one-dimensional probability curves, but to convey the useful conclusions, we only need surfaces for covarying parameters and curves for non-covarying parameters. For our results, we will present two probability surfaces (F versus $\log(s)$ and F versus $\sigma_{\log(s)}$) and one probability curve (γ).

In general, we found little covariance between γ and any other parameter, which is largely a result of the shallow mass-luminosity relation for young stars and brown dwarfs; at a given separation, most observations are either unable to detect any companions or sensitive to companions with almost all mass ratios. There is significant

covariance between the binary frequency F and the two parameters in the separation distribution, $\log(s)$ and $\sigma_{\log(s)}$. This degeneracy results from the inner working angle for most of the input datasets ($\sim$5-10 AU) being of similar order as the mean separation, since our measurements are consistent with a range of binary frequencies as long as an appropriate fraction of the companions are "hidden" inside the detection limit with a smaller mean separation and correspondingly wider standard deviation.

6.5.2.1 Frequencies and Separation Distributions for Stellar Multiplicity

In Figure 6.9, we show the PDFs for our three stellar-mass bins as projected onto the F-$\log(s)$ and F-$\sigma_{\log(s)}$ planes. In the two lower-mass bins (0.30-0.15 $M_\odot$ and 0.15-0.07 $M_\odot$), there is a significant degeneracy between the overall binary frequency and the mean separation, where a smaller mean separation is paired with a higher frequency. This degeneracy is unavoidable when fitting a normal distribution whose mean is near or outside the fitting region; the first derivative (i.e., the slope) of the distribution across the fitting region yields the standard deviation with little ambiguity, but distinguishing between the total amplitude of the curve and the distance (in standard deviations) to the mean requires measurements of both the number of measurements and the second derivative (i.e., the change in slope) across the fitting region. Measuring each successive derivative requires either more S/N or a wider fit regime. The highest-mass bin also shows some degeneracy with separation, but not to the same extent since its mean separation is outside of the typical inner working angles for many of the input surveys.

The F-$\log(s)$ locus in the highest-mass bin (0.3-0.5 $M_\odot$) is clearly distinct from the loci of the two lower bins (0.30-0.15 $M_\odot$ and 0.15-0.07 $M_\odot$), as its 90% confidence region does not overlap with the same regions for the other bins. This indicates that the mean separation and/or the binary frequency are significantly higher for 0.3-0.5 $M_\odot$ stars. The strong degeneracies seen for the lower-mass bins make it difficult to draw any strong conclusions, but it appears that the frequency and/or mean separation for binary systems declines from the 0.15-0.30 M_{sun} regime to the 0.07-0.15 $M_\odot$ regime. As we discuss below, this decline seems to continue in the

substellar bin, though our constraint on its relative magnitude in each parameter is even weaker since we only have a null detection for that mass bin. The F-$\sigma_{\log(s)}$ loci are not as easy to interpret; the middle locus is biased to a larger standard deviation, but this might be the result of having 4 probable binary systems with separations of >1000 AU; if some of these pairs of stars are actually chance alignments of unrelated association members, then removing them would reduce the standard deviation and the mean separation by a significant amount.

The frequency-separation degeneracy must be addressed before we can draw any stronger conclusions. The most direct solution would be to increase the number statistics in our existing program, yielding a better estimate of the high-order derivatives in the separation distribution. However, this endeavour would be very observationally expensive; simulations show that even doubling our sample would not decrease the length of the degenerate locus, only its width. A less direct solution would be to expand the range of separations over which the distribution is constrained, either by observing at higher resolution (sampling more of the core separation distribution) or by searching for spectroscopic binaries (constraining the other wing of the separation distribution). We suggest that an RV survey would be significantly cheaper since it can exploit the multiplexing of wide-field multi-object spectrographs, plus the separation-frequency degeneracy that results from an RV survey's outer working angle should be perpendicular to the degeneracy from imaging surveys' inner working angle. Such surveys are currently being pursued for nearby young populations like the sigma Ori cluster (Maxted et al. 2008) and the ONC (Tobin et al. 2009), and their results could be modeled with similar Bayesian techniques in order to produce constraints analogous to those shown in Figure 6.9. However, such a modeling effort is beyond the scope of the current work.

Finally, although Bayesian inference allows us to estimate the most general limits on the binary population, the degeneracies in those limits make it difficult to straightforwardly grasp the differences in our subsamples. We address this by forward-modeling from our four-dimensional PDF back into the range of separations and mass ratios where our observations could detection companions around most of our targets.

The net result of this extrapolation is to implement a minor correction for incompleteness, but rather than adopting one assumed form for the underlying distributions, we implicitly integrated the correction over all possible distributions, weighted by the probability for each distribution. To this end, we have integrated over the entire four-dimensional PDF of each mass subsample to extrapolate a the binary frequency at separations of 8–5000 AU and spanning all mass ratios of $0 < q < 1$. We find that in order of declining mass, our three subsamples (0.5-0.3 $M_\odot$, 0.30-0.15 $M_\odot$, and 0.15-0.07 $M_\odot$) have binary frequencies of $52\pm10\%$, $31\pm7\%$, and $17^{+7}_{-4}\%$ in this range of parameter space.

6.5.2.2 Limits on Substellar Multiplicity

As discussed above, we can not directly constrain the parameters of the substellar binary population because we did not discover any such binaries in our sample. However, we can estimate the probability of a null detection as a function of the four parameters in our model, ruling out a large portion of parameter space. In Figure 6.10, we show our null detection probability surfaces for the substellar mass bin in the F-$\log(s)$ and F-$\sigma_{\log(s)}$ planes. We can not integrate over the unplotted dimensions of our PDF since the integral diverges, so we instead show cross-sections for the most likely values as inferred by Burgasser et al.(2006): $\log(s)\sim0.6$, $\sigma_{\log(s)}\sim0.3$ dex, and $\gamma\sim4.2$. We chose these parameters because the T dwarf sample studied by Burgasser et al. more closely matches our mass range than the full sample of MLT dwarfs studied by A07.

We find that for the given values of $\sigma_{\log(s)}$ and γ, we can not rule out any mean separations <1 AU at >50% confidence. However, we can rule out combinations of increasing mean separation and decreasing binary frequency; if the mean separation is 2 AU, then the binary frequency is <10% at 50% confidence and <40% at 90% confidence. If the mean separation is 4 AU, which is the maximum value consistent with the results of Burgasser et al., then the corresponding frequency limits are <4% and <12%, respectively. Conversely, if the total binary frequency is ~20%, then the 50% and 90% confidence limits on the mean separation are 1.6 AU and 2.8 AU. The

corresponding probability surface for $\log(s)\sim0.6$ and $\gamma\sim4.2$ is strongly concentrated at low frequencies since this mean separation is very close to the inner working angle of our LGSAO survey, and therefore at least half of all companions should have been detectable.

In summary, all of these limits for the substellar regime are extremely discrepant with respect to the confidence intervals for the higher-mass subsamples, which indicates that the the mass-dependent tightening of binary systems continues into the substellar regime. There are no well-defined and observationally-supported models for how low-mass binary systems form, so it is difficult to infer the underlying justification for the continued decline of system separations and/or frequencies into the substellar regime. However, the trend for declining separations and frequencies in the field appears to be established at very early ages and must result directly from the formation process.

6.5.2.3 Mass Ratio Distributions

In Figure 6.11, we show the PDFs for our three stellar-mass bins as projected onto the γ axis; we do not show any results for the substellar-mass bin because our null detection does not yield a useful constraint on its mass ratio distribution. Unlike for Figures 6.9 and 6.10, we decided to project the PDF onto an axis instead of a plane in order to display our constraints on the mass ratio distribution. There is no significant covariance between our constraints on γ and those for other parameters, so this choice simplifies our presentation.

The 0.3-0.5 $M_\odot$ subsample has a best-fit slope of $\gamma= -0.04^{+0.21}_{-0.35}$, a value which is consistent with the linearly-flat mass ratio distribution found for higher-mass stars in young associations (e.g., Kraus et al. 2008; Kraus & Ireland in prep). By contrast, the 0.15-0.30 $M_\odot$ subsample has a steeper slope of $\gamma= +0.86^{+0.38}_{-0.48}$, a value intermediate between the flat slope of higher-mass stars and the typically very steep power laws ($\gamma\sim2$-4) seen for late-M stars and L/T brown dwarfs in the field.

Finally, the 0.07-0.15 $M_\odot$ subsample has a best-fit slope that is similar to the higher-mass bin, albeit with a very wide confidence interval, yielding $\gamma= 0.87^{+0.59}_{-0.68}$.

This result at first appears to contradict the overall trend for a steeping mass ratio distribution with declining mass that is seen in the field and would seem to lead from the 0.15-0.30 $M_\odot$ subsample. However, closer inspection of the sample suggests a possible resolution. Of the 7 binary systems in our combined sample with projected separations of <20 AU, all have mass ratios of >0.5. By contrast, of the 5 binary systems with projected separations of >25 AU (GG Tau B, CFHT-Tau-17, and CFHT-Tau-18 in Taurus, Hn 13 in Cha-I, and RXJ1558.1-2405b in Upper Sco), all but Hn 13 have a mass ratio of <0.5. The corresponding limits on the mass ratio power-law exponent are 4.6±2.0 in for the closer subset and -0.3±0.6 for the wider subset.

This trend is particularly intriguing because the five wider systems seem to approach or exceed the mass-maximum separation limit observed for field systems by Burgasser et al.(2003), who observed that for VLM binary systems in the field, there is a mass-dependent upper envelope to binary system separations, $a_{max} \sim 1400 M_{tot}^2$. The five systems have typical total masses of $\sim 0.15\ M_\odot$, corresponding to maximum "allowed" separations of ~ 30 AU. As such, they appear to unusual in both their separation and their mass ratio.

It is tempting to consider whether the markedly different mass function for wider VLM binary systems is a result of a different formation history. For example, wider binary systems most likely form earlier in the collapse of the progenitor molecular core. At these earlier stages, there is still more material left in the circumstellar envelope that might preferentially accrete onto the more massive binary component, driving the mass ratio further from unity. By contrast, close binary systems most likely form in the final stage of collapse, after much of the circumstellar envelope has been accreted into the central mass and little would remain for preferential accretion. Thus, if fragmentation tends to yield similar-mass components, then the epoch of fragmentation would dictate how far the mass ratio could evolve from unity. Since lower-mass binary systems also tend to have smaller separations, this would naturally lead to the trend for lower-mass binaries to have mass ratio distributions which are increasingly peaked at unity.

This model does not explain why these systems do not have analogs in the field, so we must appeal to a separate trend to justify their absence. Most of our sample is drawn from environments that are much less dense than typical star clusters; indeed, all of our targets are in loose associations that are unbound and should disperse within the next 10-50 Myr. By contrast, most stars form in denser clusters (Lada & Lada 2003) that are much more dynamically active and will ionize loosely-bound binary systems. For example, the separation distribution for solar-mass binary systems is truncated at separations of ∼300 AU in young clusters like the ONC (Köhler et al. 2006) and at ∼100 AU in older clusters like Praesepe (Patience et al. 2002; Kraus et al. in prep). VLM binary systems in Praesepe with equivalent binding energy would have separations a factor of ∼3 lower (∼30 AU). Therefore, these systems might have counterparts in denser clusters, but those counterparts could be disrupted into their component singleton stars before reaching the field.

Finally, we must consider a more prosaic explanation as well. All of our targets are distant, so we can not resolve binary systems closer than ∼5-10 AU. It is possible that our "unusually wide" binary systems are actually hierarchical multiples, where one component of the wide pair appears fainter (and thus less massive) because it is actually a close double comprised of two stars that each contain approximately half the mass of the primary. This would yield a total mass ratio close to unity in the wide pair, plus the higher total mass would allow for a correspondingly wider separation without violating the a_{max}-M_{tot} relation. Large field surveys are starting to uncover a significant number of the very rare systems that appear at first to violate this relation (e.g., Radigan et al. 2009, Dhital et al. 2009), but followup high-resolution imaging has shown that many of them are hierarchical triples or even quadruples (N. Law, priv. comm.).
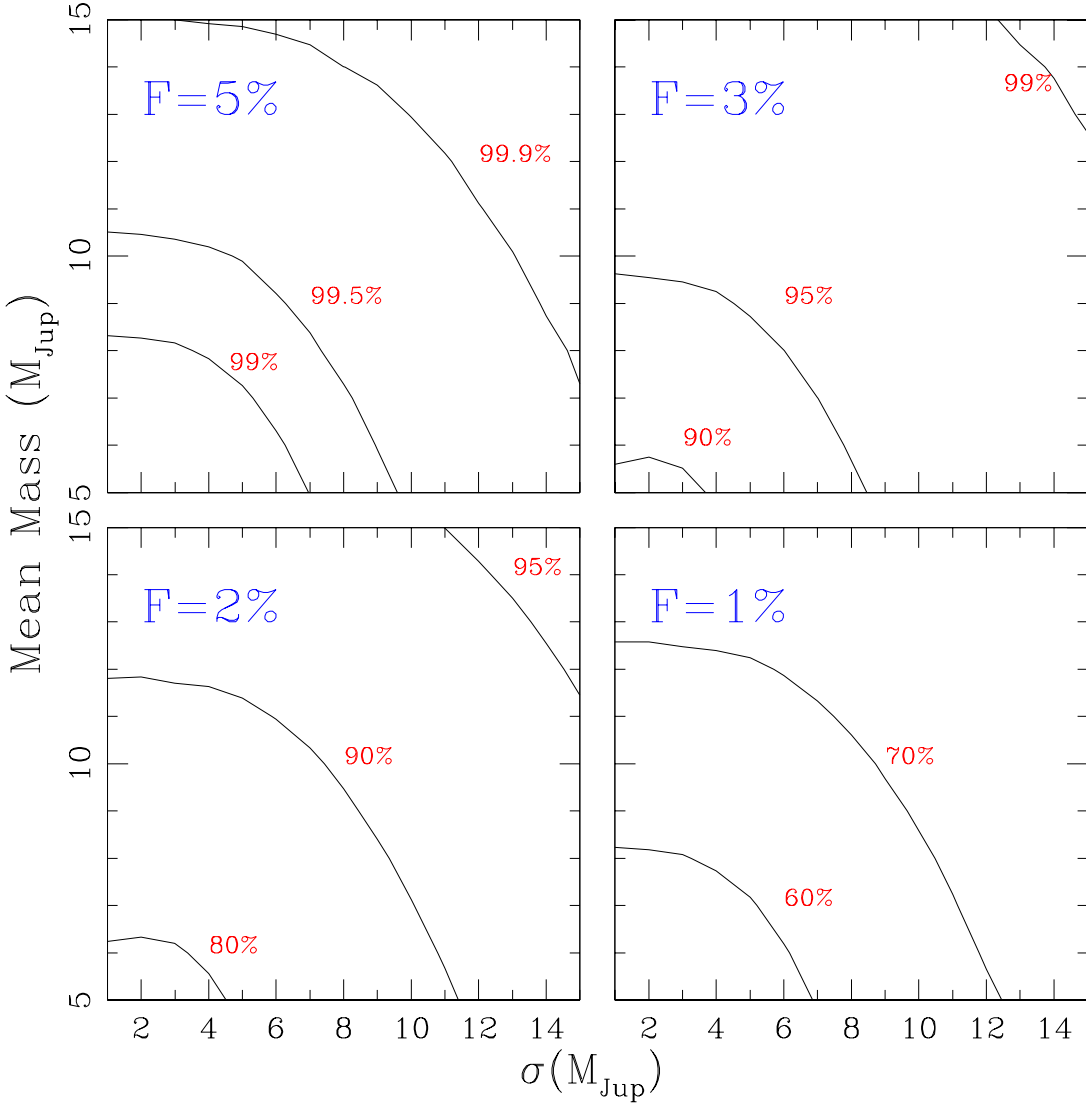
Figure 6.12 Confidence level at which our null detection rejects possible models for planetary-mass companions. Each panel denotes a different total frequency, while the model parameters are the mean μ and standard deviation σ (in M_{Jup}) for a Gaussian mass function. In each case, we assume a power-law separation distribution with slope $\beta = -1$; the separation distribution for higher-mass binary systems and the exoplanet separation distribution are both approximately log-flat, so we have chosen this value as a generic "most likely" power-law form. If we assume that the population mass function has a mean mass of $\sim 10\ M_{Jup}$ and a standard deviation in the mass of ~ 5 M_{Jup}, then our null detection rules out frequencies $F > 2\%$ at a confidence level of 90%.
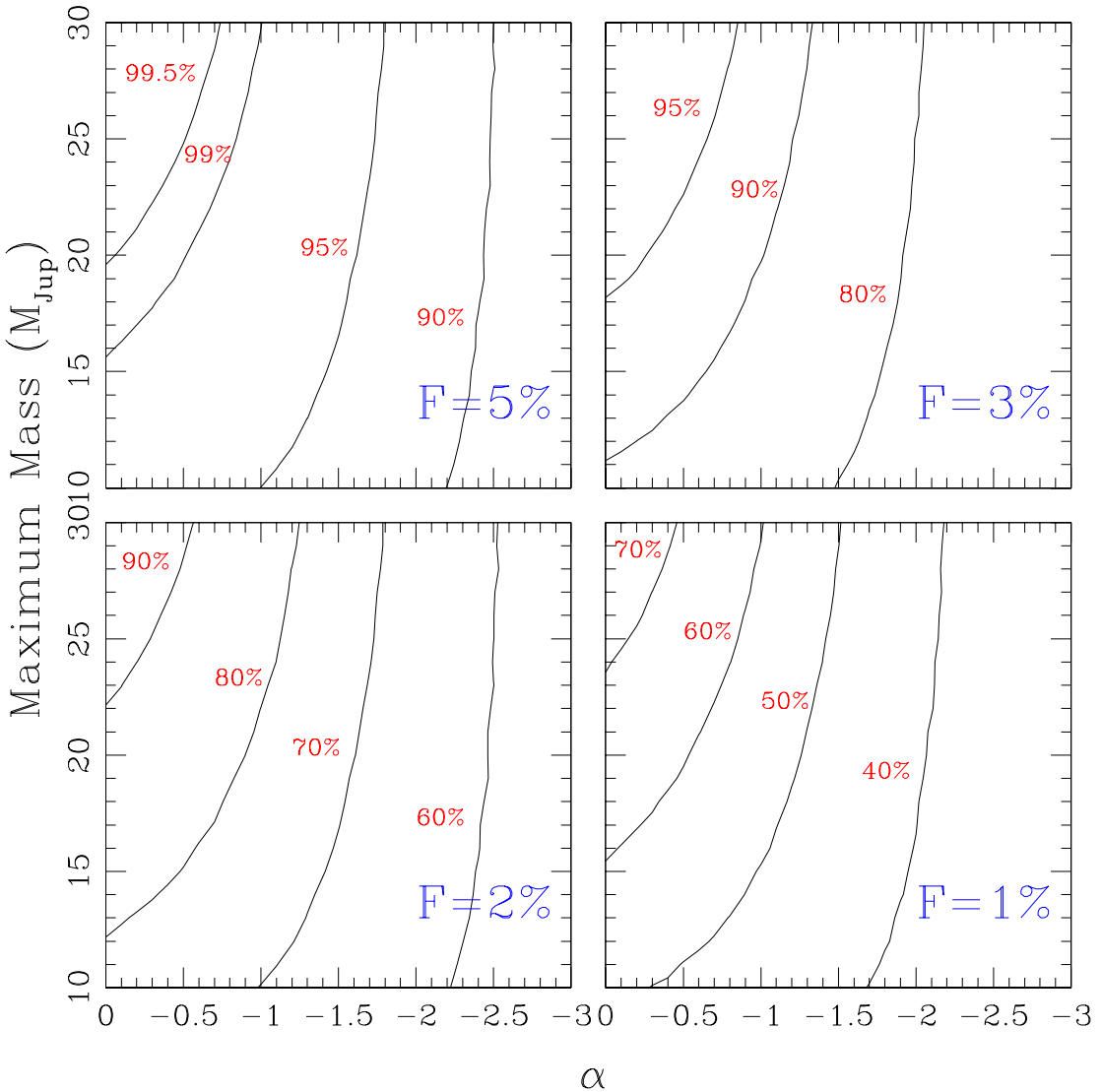
Figure 6.13 As for Figure 6.12, but for a power-law mass function with exponent α and maximum mass M (in M_{Jup}). We also assume the same log-flat separation distribution as in Figure 6.12. If we assume that the population mass function has a slope of $\alpha \sim -1$ and a maximum mass of 20 M_{Jup}, then our null detection rules out frequencies $F > 3\%$ at a confidence level of 90%.

6.6 The Frequency of Wide Planetary-Mass Companions

Over the past five years, direct imaging surveys for extrasolar planets have discovered a small but significant number of planetary-mass companions (PMCs) at >50 AU separations from their primaries. The prototypical system, 2M1207-3933, consists of a 4 M_{Jup} companion located ∼50 AU away from a 10 Myr old brown dwarf (Chauvin et al. 2004). Since its discovery, ∼5 other PMCs have also been reported, most of which orbit much higher-mass primaries (∼0.5–1.5 $M_\odot$; Luhman et al. 2006; Lafreniere et al. 2008b; Ireland & Kraus in prep). PMCs pose a significant challenge to existing models of planet and binary formation; their orbital radii are so large that the planet formation timescale (>100 Myr at 100 AU; Pollack et al. 1996) should be much longer than the typical protoplanetary disk dissipation timescale (∼3-5 Myr; Haisch et al. 2001; Hernández et al. 2007; Currie et al. 2009). However, their extreme mass ratios (q <0.01 for most, extending up to q ∼0.1 for 2M1207b) should be extremely improbable if they are drawn from typical binary mass ratio distributions; as we showed in the previous section, the projected separation for 2M1207b is also far wider than for most brown dwarf binaries.

Given the confirmed existence of wide PMCs, at least one improbable formation scenario must occur despite the contrary theoretical arguments. We can not directly measure their frequency or other population statistics because every known companion has been discovered either through serendipity or as part of a survey where the detection limits have not been reported. However, we can place a strong upper limit on the existence of PMCs around young low-mass stars and brown dwarfs in our sample.

In order to compute our upper limits, we must adopt an assumed form for the population. As in the last section, we will describe this population in terms of a frequency, a separation distribution, and a mass distribution. It is unclear what form these distributions should take, though, so we can only appeal to simple formation concepts to justify our choices. The core accretion model of planet formation

(e.g., Pollack et al. 1996) seems to be manifestly incapable of forming companions at separations of >50 AU , so we will not consider it. However, the gravitational instability model of planet formation (Boss 2001) could function if a small fraction of systems boast sufficiently massive, extended protostellar disks. Binary formation models could also function if some (currently unknown) process caused fragmentation to occur, yielding a mass with the opacity-limited minimum mass ($\sim$3–10 M_{Jup}; Low & Lynden-Bell 1976; Boss 1988; Boyd & Whitworth 2005) and then that mass did not continue to accrete out of the circumstellar envelope.

We suggest that the simplest separation distribution to consider is a power-law function, most likely with an exponent of $\sim$-1 (i.e., log-flat), that is truncated at an outer cutoff separation. The primordial separation distribution for solar-type binary companions seems to have a log-flat form (e.g., Kraus et al. 2008; Kraus & Hillenbrand 2008), and the log-normal distribution for normal substellar binaries already appears to be ruled out by the much wider separation of 2M1207b. The observed semimajor axis distribution for RV-discovered exoplanets is also approximately log-flat (Butler et al. 2006), and the existence of some very wide planets like Fomalhaut b and HR 8799 bcd suggests that the exoplanet distribution might not be truncated outside the snow line. Finally, several of the observed PMCs have projected separations of $\sim$200-300 AU (Luhman et al. 2006; Lafreniere et al. 2008b; Ireland et al., in prep), suggesting that any cutoff must lie outside this limit. Our current survey is limited to projected separations of <2.5″ (<300-400 AU) by background star confusion, so we assume that any cutoff falls outside our survey limit. We therefore can not constrain this cutoff, so we will instead account for our outer survey limit by explicitly only estimating the frequency of companions at separations <400 AU.

The best choice for a mass function is much less clear, but we suggest that two functional forms should be considered equally valid. If PMCs form out of a massive protoplanetary or protostellar disk, then they might have a mass function similar to the form inferred for RV planets: a power-law with a high-mass cutoff, perhaps with an exponent of $\alpha\sim$-1 and a cutoff of $\sim$20 M_{Jup}). If PMCs represented "failed" binary formation, then we might instead expect a mass function which is normally

distributed around the opacity-limited minimum mass ($\sim$10 M_{Jup}). Given that the handful of known PMCs seem to have masses of 5-15 M_{Jup}, we suggest that the standard deviation of such a distribution would be $\sim$5 M_{Jup}.

In the following subsections, we use Monte Carlo simulations to constrain the frequencies and/or scale parameters of these functional forms. We have discarded the more complex Bayesian analysis techniques of the previous section since they are not needed to interpret null detections, and instead simply simulate model populations and then convolve those populations with our detection limits to determine the probability that our survey would have yielded no detected companions. We must include a cautionary note: our analysis is tied to stellar and planetary evolutionary models that are almost completely unconstrained by data. All mass-related upper limits are therefore highly suspect until the models can be properly calibrated, especially since more recent models suggest significantly lower luminosities for young exoplanets than the older models did (e.g., Marley et al. 2007; Fortney et al. 2008), albeit only for the core accretion process that we have already dismissed.

6.6.1 Modeling the Population of Young Planets

As we described above, we expect that the planetary population over our range of interest will be described by a frequency, a separation distribution, and a mass function. We conduct an independent set of tests for each of the suggested mass functions, so our tests yield confidence limits for our null detection as a function of two common parameters (the frequency f and the separation distribution power-law exponent β) and two model-dependent parameters (the mass function power-law exponent α and high-end cutoff M_{max}, or else the mean mass M and its standard deviation σ_M).

There are no constraints on the eccentricity distribution for wide PMCs, so as for our binary analysis (Section 6.6), we directly model the projected separation distribution rather than invoking an eccentricity distribution and randomly-chosen inclination angles and true anomalies. Future comparison to formation models can then use each model's expected eccentricity distribution to directly match our results,

rather than first removing the effect of our adopted eccentricity distribution.

Our specific implementation uses a mass drawn from between 1 M_{Jup} and a modeled maximum mass and a projected separation drawn from between 25 and 400 AU. We do not directly model the planetary frequency f in our Monte Carlo routine because it can be added analytically. The inner separation limit corresponds to the maximum observed separation for most binary companions, while the outer separation limit is driven by our completeness in testing faint candidate companions for common proper motion. The minimum mass matches the maximum sensitivity of our survey. After conducting our simulations for a range of parameter values, we compiled a four-dimensional probability density function which corresponds to the probability that we would have detected a PMC, then extracted four-dimensional confidence surfaces which correspond to the 50%, 75%, 90%, 95%, and 99% probabilities that our observations actually would have found no wide PMCs.

6.6.2 Limits on the Population of Young Planets

It is difficult to present a set of four-dimensional confidence surfaces in a two-dimensional medium, so we have chosen to present a selection of two-dimensional slices where we fix one parameter to its most likely value, select several representative values for a second parameter, and plot each plane spanning the values of the final two parameters. Our detection limits are relatively deep and uniform across most of the separation range we model (>50 AU; >350 mas), so the slope of the separation distribution only changes our result by a modest amount. As such, we will fix this value to be log-flat ($\beta = -1$). The mass function parameters and the overall frequency are equally significant, but the effect of the overall frequency is easier to visualize in terms of the expected number of detection, so we will vary the frequency at a few fixed intervals, then fully plot the two mass-dependent parameters.

In the four panels of Figure 6.12, we present the joint confidence intervals for the parameters μ and σ (in M_{Jup}) in a Gaussian mass function. Each panel is fixed at a different overall companion frequency (1%, 2%, 3%, and 5%), and all are modeled

assuming a log-flat separation distribution. All values in the plotted parameter space are ruled out at >90% confidence for $F > 3\%$, at >75% for $F > 2\%$, and >50% for $F > 1\%$. Since the known wide PMCs have masses of 5-15 M_{Jup}, the "best" estimates for the mass function parameters might be $\mu = 10$ M_{Jup} and $\sigma = 5$ M_{Jup}; if we adopt these estimated values, then our results constrain the overall frequency of PMCs to be <3% with 96% confidence, <2% with 88% confidence, and <1% at 65% confidence.

In Figure 6.13, we show the corresponding results for a power-law mass function with slope α and high-mass cutoff M_{max} (in M_{Jup}). The overall constraints on the frequency are similar, though the range of parameter space shown includes some regions with lower-confidence limits than the corresponding frequencies for the gaussian mass function. We specifically find that all values are ruled out at >70% for $F > 3\%$, >50% for $F > 2\%$, and >30% for $F > 1\%$. If the "best" estimate for the mass function is described with parameters $\alpha = -1$ and $M_{max} = 20$ M_{Jup}, then our results constrain the overall frequency of PMCs to be <3% at 90% confidence, <2% at 79% confidence, and <1% at 54% confidence.

In general, the large number of observations which were sensitive to companions with masses of >5 M_{Jup} allow us to rule out mass functions with a shallow power law or a high mean mass unless the frequency is also quite low. The smaller number of LGSAO observations that were sensitive to masses of ~1-2 M_{Jup} also allow us to rule out a high frequency of companions in the Jovan mass regime, though we can not rule out frequencies as low as our constraints for massive Jovian analogs.

6.7   Conclusions

We have presented the results of a large-scale survey of multiplicity at the bottom of the IMF in several nearby young associations. We have confirmed the overall trend observed in the field for lower-mass binary systems to be less frequent and more compact, including a null detection for any substellar binary systems with separations wider than ~5-10 AU. In the stellar-mass regime, we confirm that the binary

frequency and binary separations decline between masses of 0.5 $M_\odot$ and 0.08 $M_\odot$, though a degeneracy between the binary frequency and the mean binary separation make it difficult to distinguish the degree of the decline in each parameter. We also confirm that the mass ratio distribution becomes progressively more concentrated at $q \sim 1$ for declining masses. However, we also note that a small number of systems appear to have unusually wide separations and low mass ratios for their system mass; this could indicate a secondary channel for low-mass binary formation, though unresolved high-order multiplicity could explain the unusual nature of some systems.

We also report a null detection for any planetary-mass companions like 2M1207 B or CHXR73 B in our survey or in any previous survey that was sensitive to such low masses. Depending on the functional form of the companion mass distribution, our null result suggests an upper limit on the companion frequency of $\sim 1\%$ at a 50% confidence level or ~ 2-3% at a 90% confidence level. All of the known planetary-mass companions have been discovered serendipitiously or in surveys which did not report their null detections, so it is difficult to draw any strong conclusions regarding the formation mechanism or properties of this rare class of objects.

Acknowledgements

Bibliography

Ahmic, M., Jayawardhana, R., Brandeker, A., Scholz, A., van Kerkwijk, M., Delgado-Donate, E., & Froebrich, D. 2007, ApJ, 671, 2074

Allen, P. 2007, ApJ, 668, 492

Bahcall, J. & Soneira, R. 1980, ApJ, 238, 17

Baraffe, I., Chabrier, G., Allard, F., & Hauschildt, P. 1998, A&A, 337, 403

Boss, A. 1988, ApJ, 331, 370

Boss, A. 2001, ApJ, 551, 167

Bouy, H. et al. 2003, AJ, 126, 1526

Bouy, H. et al. 2006, A&A, 451, 177

Boyd, D. & Whitworth, A. 2005, A&A, 430, 1059

Burgasser, A. et al. 2003, ApJ, 125, 850

Burgasser, A. et al. 2006, ApJS, 166, 585

Butler, R.P. et al. 2006, ApJ, 646, 505

Chabrier, G. et al. 2000, ApJ, 542, 464

Chauvin, G., Lagrange, A., Dumas, C., Zuckerman, B., Mouillet, D., Song, I., Beuzit, J., & Lowrance, P. 2004, A&A, 425, 29 395

Close, L. et al. 2003, ApJ, 587, 407

Correia, S., Zinnecker, H.;, Ratzka, T., & Sterzik, M. 2006, A&A, 459, 909

Currie, T., Lada, C., Plavchan, P., Robitaille, T., Irwin, J., & Kenyon, S. 2009, ApJ, 698, 1

de Zeeuw, P., Hoogerwerf, R., de Bruijne, J., Brown, A., & Blaauw, A. 1999, AJ, 117, 354

Dhital, S., West, A., Stassun, K., & Bochanski, J. 2009, in Cool Stars, Stellar Systems and the Sun 15, ed. E. Stempels (Melville, NY: AIP), 920

Duquennoy, A. & Mayor, M. 1991, A&A, 248, 485

Fischer, D. & Marcy, G. 1992, ApJ, 396, 178

Fortney, J., Marley, M., Saumon, D., & Lodders, K. 2008, ApJ, 683, 1104

Ghez, A., Neugebauer, G., & Matthews, K. 1993, AJ, 106, 2005

Ghez, A. et al. 2008, ApJ, 689, 1044

Goodwin, S. & Kroupa, P. 2007, in Protostars and Planets V, ed. B. Reipurth, D. Jewitt, & K. Keil (Tucson: Univ. Arizona Press), 133

Haisch, K., Lada, E., Piña, R., Telesco, C., & Lada, C. 2001, AJ, 121, 1512

Hillenbrand, L. & White, R. 2004, ApJ, 604, 741

Hernàndez, J. et al. 2007, ApJ, 662, 1067

Köhler, R. et al. 2000, A&A, 356, 541

Köhler, R., Petr-Gotzens, M., McCaughrean, M., Bouvier, J., Duchêne, G., Quirren-bach, A., & Zinnecker, H. 2006, A&A, 458, 461

Konopacky, Q. et al. Ghez, A., Rice, E., & Duchêne, G. 2007, ApJ, 663, 394

Kouwenhoven, M.B.N., Brown, A.G.A., & Kaper, L. 2007, A&A, 464, 581

Kraus, A., White, R., & Hillenbrand, L. 2005, ApJ, 633, 452

Kraus, A., White, R., & Hillenbrand, L. 2006, ApJ, 649, 306

Kraus, A., Ireland, M., Martinache, F. & Lloyd, J. 2008, ApJ, 679, 762

Kraus, A. & Hillenbrand, L. 2007, ApJ, 662, 413

Kraus, A. & Hillenbrand, L. 2007, ApJ, 664, 1167

Kraus, A. & Hillenbrand, L. 2007, AJ, 134, 2340

Kraus, A. & Hillenbrand, L. 2008, ApJ, 686, L111

Kraus, A. & Hillenbrand, L. 2009, ApJ, in press

Lada, C. & Lada, E. 2003, ARA&A, 41, 57

Lafreniere, D., Jayawardhana, R., Brandeker, A., Ahmic, M., & van Kerkwijk, M. 2008a, ApJ, 683, 844

Lafreniere, D., Jayawardhana, R., & van Kerkwijk, M. 2008b, ApJ, 689, L153

Leinert, C. et al. 1993, A&A, 278, 129

Low, C. & Lynden-Bell, D. 1976, MNRAS, 176, 367

Luhman, K. et al. 2003, ApJ, 593, 1093

Luhman, K. 2004, ApJ, 602, 816

Luhman, K. 2006, ApJ, 645, 676

Luhman, K. et al. 2006, ApJ, 649, 894

Marley, M., Fortney, J., Hubickyj, O., Bodenheimer, P., & Lissauer, J. 2007, ApJ, 655, 541

Maxted, P., Jeffries, R., Oliveira, J., Naylor, T., & Jackson, R. 2008, MNRAS, 385, 2210

Metchev, S. & Hillenbrand, L. 2009, ApJS, 181, 62

Monet, D. et al. 2003, AJ, 125, 984

Padgett, D., Brandner, W., Stapelfeldt, K., Strom, S., Terebey, S., & Koerner, D. 1999, AJ, 117, 1490

Patience, J. et al. 2002, AJ, 123, 1570

Pollack, J., Hubickyj, O., Bodenheimer, P., Lissauer, J., Podalak, M., & Greenzweig, Y. 1996, Icarus, 124, 62

Radigan, J., Lafreniere, D., Jayawardhana, R., & Doyon, R. 2009, ApJ, 698, 405

Schmidt-Kaler, Th., "Physical Parameters of the Stars", Landolt-Bornstein Numerical Data and Functional Relationships in Science and Technology, New Series, Group VI, Volume 2b, Springer-Verlag, Berlin, 1982

Simon, M. et al. 1995, ApJ, 443, 625

Skrutskie, M. et al. 2006, AJ, 131, 1163

Slesnick, C., Carpenter, J., & Hillenbrand, L.2006a, AJ, 131, 3016

Slesnick, C., Carpenter, J., Hillenbrand, L., & Mamajek, E. 2006b, AJ, 132, 2665

Slesnick, C., Hillenbrand, L., & Carpenter, J. 2008, ApJ, 688, 377

Stetson, P. 1987, PASP, 99, 191

Tobin, J., Hartmann, L., Furesz, G., Mateo, M., & Megeath, S. 2009, ApJ, 697, 1103

Torres, R., Loinard, L., Mioduszewski, A., & Rodrìguez, L. 2007, ApJ, 561, 1813

Torres, R., Loinard, L., Mioduszewski, A., & Rodrìguez, L. 2009, ApJ, 698, 242

White, R. & Ghez, A. 2001, ApJ, 556, 265

Wizinowich, P. et al. 2006, PASP, 118, 297

Chapter 7

The Coevality of Young Binary Systems

Abstract

Multiple star systems are commonly assumed to form coevally, so they provide the anchor for most calibrations of stellar evolutionary models. In this chapter, I study the binary population of the Taurus-Auriga association, using the component positions in an HR diagram, in order to quantify the frequency and degree of coevality in young binary systems. After identifying and rejecting the systems that are known to be affected by systematic errors (due to further multiplicity or obscuration by circumstellar material), we find that the overall dispersion in predicted relative binary ages, $\Delta \log \tau$, is 0.40 dex. For comparison, random pairs of Taurus members are coeval only to within 0.58 dex, indicating that Taurus binaries are indeed more coeval than the association as a whole. Based on the distribution of $\Delta \log \tau$, our sample appears to be composed of two populations, with $\sim 2/3$ appearing significantly more coeval ($\sigma_{\Delta \log \tau} \sim 0.16$ dex) and the other $\sim 1/3$ distributed in an extended tail with $\Delta \log \tau \sim 0.4$-0.9 dex. We suggest that the tail of the differential age distribution includes unrecognized hierarchical multiples, stars seen in scattered light, or stars with disk contamination; additional followup is required to rule out or correct for these explanations. We also find that the relative coevality of binary systems does

not depend significantly on the system mass, mass ratio, or separation, but any pair of Taurus members wider than $\sim10'$ (~0.7 pc) shows the full age spread of the association.

7.1   Introduction

Stellar evolutionary models are critical for interpreting astronomical observations, but they are not well-calibrated for pre-main sequence (PMS) stars. Such calibration requires the measurement of some or all of the fundamental stellar properties: age, mass, radius, luminosity, and effective temperature. Ages are notoriously difficult to estimate (Mamajek & Hillenbrand 2008; Hillenbrand 2009), though they can be inferred indirectly from a membership in a stellar population for which the mean age can be determined. Stellar masses and/or radii require orbital monitoring of eclipsing or visual binary systems. The known eclipsing binary systems sparsely sample parameter space due to their extreme rarity (e.g., Irwin et al. 2007; Stassun et al. 2007; Stempels et al. 2008), and most PMS visual binaries have only partial orbits because young stars are distant and any systems which can be spatially resolved necessarily have wide separations and corresponding long periods (Steffen et al. 2001; Duchêne et al. 2006), though a handful of short-period systems are bright enough for interometric techniques to be feasible (Boden et al. 2005; Schaefer et al. 2008). In contrast to ages, masses, and radii, the luminosities and temperatures of stars are straightforward to infer from single-epoch observations, so they offer the best near-term prospects for systematic calibration of stellar models. The procedure can also be inverted; given a star's luminosity and temperature, a theoretical model can be used to estimate its age and mass, plus its radius can be estimated directly from the Stefan-Boltzmann law.

The standard procedure for calibrating models with luminosities and temperatures is to place two or more nominally coeval stars on an HR diagram. These stars should trace an empirical isochrone sequence, and this sequence can be compared to theoretical isochrones in order to test their consistency with observations. HR

diagram analysis has provided many crucial insights into models of stellar interiors, atmospheres, and evolution (e.g., White et al. 1999; Luhman et al. 2003). There are many systematic astrophysical effects that can complicate this analysis, including unresolved multiplicity, obscuration from circumstellar material (i.e., an envelope or edge-on disk), and veiling from accretion (at blue wavelengths) or circumstellar disk emission (at near-infrared wavelengths). These effects can yield ages with errors of an order of magnitude or more, so the samples used in this analysis must be inspected closely to reject all contaminated stars. Additional physics, such as stellar activity or tidal inhibition of convection, could also play a role (Chabrier et al. 2007; Stassun et al. 2008).

The inverse procedure plays an important role in the study of binary systems (e.g., Hartigan et al. 1994; White & Ghez 2001; Hartigan & Kenyon 2003). It is commonly assumed that multiple star formation proceeds almost simultaneously, such that all stars in a bound multiple system are coeval. However, this assumption can be tested only by using the evolutionary models that require calibration, so any apparent disagreement between binary component ages could be due to non-coevality or errors in the models. Emerging evidence for several young eclipsing binary systems shows that their components appear non-coeval (e.g., Stassun et al. 2007, 2008), but the frequency and degree of noncoevality is still unclear.

In this chapter, we estimate the ages of a large sample of stringently vetted young binary systems in the Taurus association ($\tau \sim$1-2 Myr; $d \sim$145 pc) in order to test the system components' relative coevality and the validity of theoretical isochrones in matching empirical HR diagram sequences. In Section 7.2, we describe our sample of binary systems, and in Section 7.3, we describe the stellar models and analysis techniques used to infer stellar ages. In Section 7.4, we show an HR diagram with all our sample members and identify likely contaminants. In Section 7.5, we test the coevality of young binary systems by adopting model-predicted ages. Finally, in Sections 7.6 and 7.7, we test the evolutionary models using a large sample of likely single stars and using a subset of high-order multiple systems.

7.2 The Sample

The accurate determination of stellar parameters requires spatially- and/or spectrally-resolved observations that are not polluted by light from companions. Most binary systems in Taurus have separations smaller than the seeing limit, so we can only include association members that have been observed with HST, ground-based adaptive optics, or echelle spectrographs (distinguishing the components' spectra and relative fluxes). We list the observed properties of our sample members in Table 7.1, along with the references used to infer spectral types, extinctions, and fluxes.

The wide components that could be resolved in seeing-limited observations were drawn from the sample studied in our previous wide multiplicity survey (Kraus & Hillenbrand 2007a, 2009). Most of these stars had already been identified as Taurus members, so we drew their observed properties from previous work by Kenyon & Hartmann (1995), Duchêne et al.(1999), White & Basri (2003), White & Hillenbrand (2004), and Luhman (2004, 2006). All of these authors reported spectral types and extinctions, and we adopted NIR magnitudes from the 2MASS Point Source Catalog (Skrutskie et al. 2006) or from our own PSF fitting photometry of 2MASS atlas images (Kraus & Hillenbrand 2007a). The photometry for RW Aur AB and most of the Duchêne et al. sample was unreliable since the system separations fell near the 2MASS resolution limits, so we adopted total K fluxes from 2MASS and the K band flux ratios reported by White & Ghez (2001) or Correia et al.(2006).

The closer components that could be resolved with high-resolution imaging were drawn from several recent spectroscopic surveys. Most of the spectroscopic observations were obtained with HST/STIS by Hartigan & Kenyon (2003), but several systems were observed under good seeing by Duchêne et al.(1999). Individual systems were also studied by White et al. (1999) with STIS, or in our own survey of low-mass multiplicity with Keck laser guide star AO (LGSAO; Kraus et al., in prep). As before, we inferred NIR magnitudes from the total system fluxes reported in 2MASS and spatially resolved flux ratios reported by Leinert et al.(1993), White & Ghez (2001), Correia et al.(2006), and our LGSAO survey.

There are a small number of double-lined spectroscopic binaries that have been identified and studied in some detail in Taurus. We have added the well-known system UZ Tau Aab (Prato et al. 2002) to our sample, adopting their spectral types and inferred H band flux ratio. We also added the short-period spectroscopic binary V773 Tau Aab, which was studied with RV and interferometric monitoring by Boden et al.(2007) as part of their orbital monitoring program. The V773 Tau system also includes two faint companions at small separations and a wide brown dwarf companion; we do not include the close companions because they do not have spectral type determinations and because they are too faint to influence the observed properties of V773 Tau Aab, but we include the wide substellar companion. We also considered whether to include V826 Tau (Massarotti et al. 2005) and DQ Tau (Mathieu et al. 1997), but the only known flux ratio for V826 Tau is in the optical and there are no flux ratios reported for DQ Tau, so these systems could not be integrated with the rest of our sample.

Finally, most of the binary components in our sample have spatially resolved photometry in the K filter only. Inferring the component luminosities from such a red bandpass might introduce systematic errors in our estimated luminosities due to near-infrared excesses from circumstellar disks. In order to address this prospect, we have searched the literature to determine which stars are likely to host a warm disk; we summarize our assessments and the corresponding references in Table 7.1. We based these assessments, in order of priority, on 3-10 μm photometry (from Spitzer/IRAC or ground-based AO imaging), optical spectroscopic accretion signatures, 10-30 μm spectroscopy (from Spitzer/IRS), and finally on submm/mm photometry. In each case where sufficient data is available, we have concluded that the star either has a disk ("Y"), does not have a disk ("N"), or might have a disk (but the observations are not spatially resolved, so we can not determine which binary component(s) have one; "Y?"). We will address the significance of flux excesses from warm dust in Section 7.5.

Table 7.1.   Binary Sample: Observed and Inferred Properties

Name	RA	Dec (J2000)	Sep (mas)	Flux (mag)	SpT	A_V (mag)	T_{eff} (K)	M_{bol} (mag)	Warm Disk?	Refs
HBC 352	3 54 29.51	+32 03 01.4	8970±70	J=10.09	G0±2	0.9	6030±170	4.99	...	1, 2
HBC 353	3 54 30.17	+32 03 04.3	8970±70	J=10.45	G5±2	1.0	5770±100	5.41	...	1, 2
HBC 355	3 54 35.97	+25 37 08.1	6310±70	J=10.81	K0±2	0.5	5250±335	6.08	...	1, 3
HBC 354	3 54 35.56	+25 37 11.1	6310±70	J=11.80	K3±1	1.2	4750±155	7.05	...	1, 3
HBC 356	4 03 13.96	+25 52 59.8	1280±20	J=10.84	K3±1	0.7	4750±155	6.23	N	4, 5, 20
HBC 357	4 03 13.96	+25 52 59.8	1280±20	J=10.84	K3±1	0.7	4750±155	6.23	N	4, 5, 20
V773 Tau Aa	4 14 12.92	+28 12 12.4	SB	K=6.72	K2±1	1.8	4900±150	2.56	Y?	6, 20
V773 Tau Ab	4 14 12.92	+28 12 12.4	SB	K=7.27	K3±1.5	1.8	4750±200	3.25	Y?	6, 20
2M04141188	4 14 11.88	+28 11 53.5	23380±70	J=13.16	M6.25±0.25	1.0	2960±30	9.00	...	3, 7
FO Tau A	4 14 49.29	+28 12 30.6	152.5±2.9	K=8.87	M3.5±0.5	1.9	3340±75	5.53	Y	8, 9
FO Tau B	4 14 49.29	+28 12 30.6	152.5±2.9	K=8.87	M3.5±0.5	1.9	3340±75	5.53	Y	8, 9
DD Tau A	4 18 31.13	+28 16 29.0	555±10	K=8.45	M3.5±0.5	2.1	3340±75	5.08	Y	8, 9, 21
DD Tau B	4 18 31.13	+28 16 29.0	555±10	K=8.85	M3.5±0.5	2.9	3340±75	5.40	Y	8, 9, 21
FQ Tau A	4 19 12.81	+28 29 33.1	752±14	K=10.03	M3±0.5	2.0	3415±75	6.66	Y	8, 9, 21
FQ Tau B	4 19 12.81	+28 29 33.1	752±14	K=10.11	M3.5±0.5	1.8	3340±75	6.78	Y	8, 9, 21
LkCa 7 A	4 19 41.27	+27 49 48.5	1021±19	K=8.74	M0±0.5	0.2	3850±90	5.34	N	8, 9, 20
LkCa 7 B	4 19 41.27	+27 49 48.5	1021±19	K=9.37	M3.5±0.5	0.4	3340±75	6.20	N	8, 9, 20
FS Tau A	4 22 02.18	+26 57 30.5	227.6±7.1	K=8.33	M0±0.5	5.0	3850±90	4.40	Y	8, 9
FS Tau B	4 22 02.18	+26 57 30.5	227.6±7.1	K=10.43	M3.5±0.5	5.2	3340±75	6.72	Y	8, 9
Haro 6-5B	4 22 00.69	+26 57 33.3	19880±70	J=15.08	K5±2	10.0	4350±450	8.01	Y	10, 11
FV Tau A	4 26 53.53	+26 06 54.4	12081±9	J=9.92	K5±0.5	5.4	4350±135	4.11	Y	8, 9, 21
FV Tau/c A	4 26 54.41	+26 06 51.0	12081±9	K=9.00	M2.5±0.5	3.3	3485±75	5.46	N	8, 9, 21
FV Tau/c B	4 26 54.41	+26 06 51.0	713±1.8	K=11.21	M3.5±0.5	7.0	3340±75	7.30	Y	8, 9, 21

Table 7.1 (cont'd)

Name	RA	Dec (J2000)	Sep (mas)	Flux (mag)	SpT	A_V (mag)	T_{eff} (K)	M_{bol} (mag)	Warm Disk?	Refs
DF Tau A	4 27 02.80	+25 42 22.3	103±2	K=7.13	M2±0.5	0.6	3560±75	3.84	Y	5, 8
DF Tau B	4 27 02.80	+25 42 22.3	103±2	K=8.01	M2.5±0.5	0.8	3485±75	4.75	Y	5, 8
2M04284263 A	4 28 42.63	+27 14 03.9	621±7	K=10.85	M5±0.5	0.5	3125±75	7.84	Y?	7, 12, 23
2M04284263 B	4 28 42.63	+27 14 03.9	621±7	K=11.75	M5.5±0.5	0.5	3055±70	8.76	Y?	3, 7, 12, 23
UX Tau A	4 30 04.00	+18 13 49.4	5856±3	K=7.60	K2±1	0.2	4900±165	3.62	Y	1, 13, 21
UX Tau C	4 30 04.00	+18 13 49.4	2692±2	K=10.85	M5±0.5	0.1	3125±75	7.88	N	1, 13, 14, 21
FX Tau A	4 30 29.61	+24 26 45.0	890±17	K=8.33	M1±1	1.1	3705±145	4.91	Y	4, 9, 21
FX Tau B	4 30 29.61	+24 26 45.0	890±17	K=9.19	M4±1	1.1	3270±145	5.97	N	4, 9, 21
DK Tau A	4 30 44.25	+26 01 24.5	2360±1	K=7.36	K9±1	0.8	4060±250	3.66	Y?	4, 13, 22
DK Tau B	4 30 44.25	+26 01 24.5	2360±1	K=8.74	M1±1	0.8	3705±145	5.35	Y?	4, 13, 22
V927 Tau A	4 31 23.82	+24 10 52.9	267±6.8	K=9.31	M3±0.5	1.4	3415±75	6.00	N	8, 9, 23
V927 Tau B	4 31 23.82	+24 10 52.9	267±6.8	K=9.79	M3.5±0.5	0.9	3340±75	6.56	N	8, 9, 23
HL Tau	4 31 38.44	+18 13 57.7	23310±70	J=10.62	K5±1	7.4	4350±265	4.25	Y	10, 15
XZ Tau A	4 31 40.07	+18 13 57.2	300.6±1.3	K=8.36	M2±1	1.4	3560±145	4.98	Y	8, 9
XZ Tau B	4 31 40.07	+18 13 57.2	300.6±1.3	K=7.80	M3.5±0.5	1.4	3340±75	4.52	Y	8, 9
HK Tau A	4 31 50.57	+24 24 18.1	2342±61	K=8.64	M1±0.5	2.3	3705±75	5.08	Y	1, 9, 10, 23
HK Tau B	4 31 50.57	+24 24 18.1	2342±61	K=11.96	M1±0.5	2.3	3705±75	8.40	Y	1, 9, 10
V710 Tau A	4 31 57.79	+18 21 38.1	3224±3	K=9.38	M1±1	0.9	3705±145	5.98	Y	1, 13, 21
V710 Tau B	4 31 57.79	+18 21 38.1	3224±3	K=9.44	M3±1	0.9	3415±145	6.19	N	1, 13, 21
V710 Tau C	4 31 57.79	+18 21 38.1	28000±70	J=12.26	M3±0.5	0.9	3415±75	8.00	Y	1, 3, 16
GG Tau Aa	4 32 30.35	+17 31 40.6	10100±7	J=9.07	K7±1	0.7	4060±250	4.50	Y	13, 17, 21
GG Tau Ab	4 32 30.35	+17 31 40.6	250.2±2.6	J=9.95	M0.5±0.5	3.2	3775±75	4.87	Y	13, 17, 21
GG Tau Ba	4 32 30.35	+17 31 40.6	10100±7	J=11.28	M6±0.5	0.6	2990±65	7.24	Y	13, 14, 17, 21

Table 7.1 (cont'd)

Name	RA	Dec (J2000)	Sep (mas)	Flux (mag)	SpT	A_V (mag)	T_{eff} (K)	M_{bol} (mag)	Warm Disk?	Refs
GG Tau Bb	4 32 30.35	+17 31 40.6	1476.5±6.5	J=12.96	M7.5±0.5	0.0	2795±85	9.10	Y	13, 14, 17, 21
UZ Tau Aa	4 32 43.04	+25 52 31.1	SB	H=8.54	M1±1	1.5	3705±145	4.77	Y	1, 18, 22
UZ Tau Ab	4 32 43.04	+25 52 31.1	SB	H=9.36	M4±1	1.5	3270±145	5.73	Y	1, 18, 22
UZ Tau Ba	4 32 43.04	+25 52 31.1	3539.5±2.1	H=8.46	M2±0.5	0.6	3560±75	4.91	Y	8, 9, 21
UZ Tau Bb	4 32 43.04	+25 52 31.1	367.8±1	H=9.18	M3±0.5	1.8	3415±75	5.48	Y	8, 9, 21
GH Tau A	4 33 06.22	+24 09 34.0	311.1±1.3	K=8.66	M2±0.5	0.0	3560±75	5.44	Y	8, 9, 21
GH Tau B	4 33 06.22	+24 09 34.0	311.1±1.3	K=8.45	M2±0.5	0.5	3560±75	5.17	Y	8, 9, 21
IS Tau A	4 33 36.79	+26 09 49.2	222.8±2.4	K=8.82	M0±0.5	3.3	3850±90	5.08	Y	8, 9
IS Tau B	4 33 36.79	+26 09 49.2	222.8±2.4	K=10.72	M3.5±0.5	3.6	3340±75	7.19	N	8, 9
HN Tau A	4 33 39.35	+17 51 52.4	3142±1	K=8.51	K5±1	0.5	4350±265	4.82	Y?	1, 13, 20
HN Tau B	4 33 39.35	+17 51 52.4	3142±1	K=10.81	M4.5±1	0.5	3200±180	7.72	Y?	4, 13, 20
IT Tau A	4 33 54.70	+26 13 27.5	2416±8	K=8.12	K3±1	4.1	4750±155	3.84	Y?	4, 13, 22
IT Tau B	4 33 54.70	+26 13 27.5	2416±8	K=9.54	M4±1	4.1	3270±145	5.98	Y?	4, 13, 22
Haro 6-28 A	4 35 56.84	+22 54 36.0	647±12	K=10.12	M2±0.5	2.3	3560±75	6.64	Y?	8, 9, 24
Haro 6-28 B	4 35 56.84	+22 54 36.0	647±12	K=10.48	M3.5±0.5	1.9	3340±75	7.14	Y?	8, 9, 24
2M04414565	4 41 45.65	+23 01 58.0	12370±70	J=10.74	M3±0.5	0.0	3415±75	6.72	...	3, 16
2M04414489	4 41 44.89	+23 01 51.3	12370±70	J=14.42	M8.25±0.25	0.0	2630±78	10.56	...	3, 16, 19
LkHa332-G2 A	4 42 07.33	+25 23 03.2	234.1±4.5	K=8.38	M0.5±0.5	2.0	3775±75	4.82	N	8, 9, 22
LkHa332-G2 B	4 42 07.33	+25 23 03.2	234.1±4.5	K=9.16	M2.5±0.5	3.3	3485±75	5.61	N	8, 9, 22
V955 Tau A	4 42 07.77	+25 23 11.8	330.9±1.2	K=8.18	K7±0.5	2.8	4060±125	4.26	Y	8, 9, 21
V955 Tau B	4 42 07.77	+25 23 11.8	330.9±1.2	K=9.72	M2.5±0.5	2.3	3485±75	6.28	Y	8, 9, 21
UY Aur A	4 51 47.38	+30 47 13.5	878±17	K=7.68	M0±0.5	0.6	3850±90	4.24	Y	8, 9
UY Aur B	4 51 47.38	+30 47 13.5	878±17	K=8.44	M2.5±0.5	2.7	3485±75	4.96	Y	8, 9

7.3   Analysis

7.3.1   Inferred and Calculated Stellar Properties

Any comparison of observations to stellar evolutionary models requires the conversion of observed properties (spectral types, filtered magnitudes, and extinctions) into fundamental physical parameters (effective temperatures and bolometric luminosities). This process is accomplished by invoking a temperature scale, a set of bolometric corrections, a reddening law, and an estimated distance. Temperature scales directly relate spectral types to temperatures, and are typically calibrated with respect to a specific set of models in order to yield a consistent age for the cluster sequence in an HR diagram. Temperatures are also used to define intrinsic colors, from which an observed color can be used to infer the reddening and extinction. Bolometric corrections are temperature-dependent ratios of the flux in a filtered band to the full bolometric flux and are calibrated for nearby field stars that have been studied across the full range of wavelengths with significant contribution to the luminosity. Once the bolometric flux is known, the distance for a star then directly yields the bolometric luminosity.

We have adopted the temperature scale suggested by Luhman et al. (2003) for use in low-gravity young stars. For spectral types <M0, the temperature-SpT relation does not appear to be gravity-sensitive, so Luhman et al. use the temperature scale of Schmidt-Kaler (1982). For later spectral types, the effective temperatures of giants appear to be systematically hotter than those of dwarfs with identical spectral types (e.g., Leggett et al. 1996 versus Perrin et al. 1998; Richichi et al. 1998; van Belle et al. 1999). Since late-type (>M0) young stars have intermediate surface gravities, Luhman et al. define an intermediate temperature scale that makes the average cluster sequences of Taurus and IC348 internally coeval with respect to the NextGen models (Baraffe et al. 1998).

We have adopted the bolometric corrections that we previously described for use with field stars (Kraus & Hillenbrand 2007b). For spectral types <M0, we used the corrections suggested by Masana et al.(2006), while for M dwarfs, we used the

Table 7.1 (cont'd)

Name	RA	Dec (J2000)	Sep (mas)	Flux (mag)	SpT	A_V (mag)	T_{eff} (K)	M_{bol} (mag)	Warm Disk?	Refs
2M04554757	4 55 47.57	+30 28 07.7	6310±70	J=11.05	M4.75±0.25	0.0	3165±50	7.15	...	3, 7
2M04554801	4 55 48.01	+30 28 05.0	6310±70	J=13.19	M5.6±0.25	0.0	3045±35	9.31	...	3, 7
RW Aur A	5 07 49.54	+30 24 05.1	1417.5±3.4	K=7.25	K2±2	1.6	4900±330	3.11	Y	9, 10, 21
RW Aur B	5 07 49.54	+30 24 05.1	1417.5±3.4	K=8.82	K6±1	1.6	4350±265	5.01	Y	9, 10, 21

Note. — References: 1) Kenyon & Hartmann (1995), 2) Leinert et al.(1993), 3) Kraus et al.(in prep), 4) Duchêne et al.(1999), 5) White et al.(in prep), 6) Boden et al.(2007), 7) Luhman (2004), 8) Hartigan & Kenyon (2003), 9) White & Ghez (2001), 10) White & Hillenbrand (2004), 11) Krist et al.(1998), 12) Konopacky et al.(2007), 13) Correia et al.(2006), 14) White & Basri (2003), 15) Krist et al.(1995), 16) Kraus & Hillenbrand (2009), 17) White et al.(1999), 18) Prato et al.(2002), 19) Luhman (2006), 20) Furlan et al.(2006), 21) McCabe et al.(2006), 22) Hartmann et al.(2005), 23) Luhman et al.(2006), 24) Andrews & Williams (2005).

corrections of Leggett et al.(1992) and Leggett et al.(1996). Ideally, it would be good to verify whether these bolometric corrections are valid for young stars. However, we are not aware of any such tests having been attempted. We have implemented our extinction corrections using the interstellar reddening law of Schlegel et al. (1998), which stipulates that one magnitude of visual extinction corresponds to $A_J = 0.28$, $A_H = 0.18$, and $A_K = 0.11$; these values are consistent with the interstellar reddening law in the 2MASS filters suggested by Indebetouw et al.(2005). Reddening laws might vary in regions with extremely high density (Weingartner & Draine 2001; Román-Zúñiga et al. 2007), but most of our sample members are only moderately reddened. Analysis of 2MASS source counts and colors toward the Ophiuchus, Lupus, and Pipe Nebulae suggest that the interstellar reddening law is appropriate to extinctions of $A_V \sim 20$ or more (Lombardi et al. 2008).

We adopted a characteristic distance for all Taurus members of 145±15 pc. Recent high-precision parallax measurements with the VLBA (Lestrade et al. 1999; Loinard et al. 2007; Torres et al. 2007; Loinard et al. 2008) suggest that there might be a distance gradient of 165-125 pc in the east-west direction, though the discrepant distances of neighboring V773 Tau and Hubble 4 (148±5 pc versus 132.5±0.6 pc) suggest an overall scatter at any location of ~10-15 pc (10%). The luminosity uncertainty if we adopt the characteristic distance is only ~0.1-0.2 mag, which is similar to the uncertainty from dereddening and intrinsic variability, so attempting to extrapolating more precise distances from this suggestion of 3D structure is not likely to improve our results.

We should note that there is room for significant uncertainty in our inferred luminosities due to the intrinsic variability of young stars. Variability in Class III stars should be caused by spots, so its characteristic amplitude at near-infrared wavelengths should be no more than ~0.1 mag (e.g., Carpenter et al. 2002). However, the same survey showed that Class I-II stars occasionally vary by as much as 1-2 mag in the near infrared, and extreme classes of stars (such as FUor and EXor stars) can vary by even more. This suggests that an unusually young age for one binary component could be the result of variability in that component.

A star that is surrounded by circumstellar material could also appear systematically underluminous by several magnitudes if it possesses an edge-on disk or a massive circumstellar envelope. This star would then be seen only in scattered light, making it appear much older than its unobscured companion. These objects can be identified from high-resolution optical imaging since they will appear as nebulosity rather than as point sources.

Finally, the presence of veiling due to accretion (at blue wavelengths) or circumstellar dust emission (at red wavelengths) could bias the inferred luminosity of a binary component. Observations in the I filter are least sensitive to this veiling, so we have used photometry from the nearest redder filter. We would prefer to use J for all systems, but in most cases, the absence of suitable data forces us to use relative photometry in H or K.

We list the stellar properties that we inferred with these methods in Table 7.1. Each of the luminosity uncertainties listed above should contribute ~ 0.1 mag, so we have adopted a total statistical uncertainty of 0.3 mag. However, many of the uncertainties (such as for distance and extinction) should be correlated between binary components, so the uncertainty in their relative ages should be lower than our formal estimates. Our corresponding temperature uncertainties have been determined from the uncertainty in each star's spectral type.

7.3.2   Inferred Physical Stellar Parameters

Several sets of pre-main sequence evolutionary models have been developed in recent decades, but all of these models still face significant challenges in confronting observational constraints. Hillenbrand & White (2004) found that all models have difficulty matching the dynamical masses of young stars with $M <$1.2 $M_\odot$, a range which encompasses almost all of our sample. However, the Lyon models (Baraffe et al. 1998; Chabrier et al. 2000) seem to work best for low-mass stars, especially when using a mixing length of $\alpha=$ 1.0 and the revised temperature scale of Luhman et al.(2003). All models were found to reproduce the observed masses for stars with $M >$1.2 $M_\odot$,

though the Lyon models only extend to 1.4 $M_\odot$.

In light of these results, we have adopted a hybrid combination of the Lyon models for low-mass stars and the models of D'Antona and Mazzitelli (1997; DM97) for higher-mass stars. For masses ≤ 0.5 $M_\odot$, we use the mass-luminosity-temperature relations of the Lyon models with a mixing length of $\alpha = 1$. For masses ≥ 1.0 $M_\odot$, we use the corresponding relations of DM97. Finally, in the intermediate regime of 0.6-0.9 $M_\odot$, we adopt a weighted average of the luminosity and temperature predicted by each model in order to produce a smooth transition between the two sets of models. This choice does not provide any insight into the missing physics that are still required to bring the models into agreement, but it represents an acceptable compromise for estimating relative ages of a sample of young stars. The two sets of models converge at older ages, so our solution is only important for very young stars (<10 Myr).

These models report stellar luminosities and temperatures at quantized values of age and mass, so for each of our sample members, we have linearly interpolated between the four values of T_{eff} and M_{bol} around it in the HR diagram. The Lyon models also face a significant challenge with respect to very young stars since they are not defined for ages of <1 Myr, so for each star that falls above this isochrone and has a mass within the affected range (<1 $M_\odot$), we have linearly extrapolated its age from the four points below it in the HR diagram. These extrapolated ages should be regarded as much more uncertain than older ages, but the degree of error should be similar for stars with similar HR diagram positions, so only systems with disparate masses will be subject to the full systematic uncertainty.

In Table 7.2, we list the inferred mass and age for each star from our hybrid system and from the default Lyon and DM97 models. Several sample members illustrate the extreme difference in mass and age estimates for the two sets of models. For example, the inferred parameters of HN Tau A are $M = 1.35$ $M_\odot$ and $\log(\tau) = 6.85$ according to the Lyon models and $M = 0.65$ $M_\odot$ and $\log(\tau) = 6.05$ according to the DM97 models; our hybrid isochrones yield $M = 0.85$ $M_\odot$ and $\log(\tau) = 6.27$.

7.4 The HR Diagram

The overall population sequence in an HR diagram provides a valuable test of our choice of evolutionary models. If the association is nominally coeval, then it should trace a single recognizable sequence that is parallel to theoretical isochrones. Individual sample members that strongly deviate from the association sequence should also be examined for a systematic source of error such as erroneous membership, circumstellar material that blocks and scatters the stellar flux, or misclassification of spectral types.

In Figure 7.1, we show the HR diagram for all of our binary sample members. The cluster sequence seems to trace the 1-2 Myr isochrone, albeit with significant scatter due to the many sources of uncertainty and the unknown spread of stellar ages. We chose our models to yield a consistent age across the full mass range, so this agreement with the canonical age of Taurus is not surprising. However, many individual members fall unusually low; the 5 Myr isochrone appears to define the approximate lower limit for the observed scatter of the main body of members, as most of the stars below this isochrone are known to be anomalous. We describe these sources, as well as some potentially new anomalous stars, in the following paragraphs.

The warmest anomalous members (HBC 352-357) have been classified as Taurus members for several decades (e.g., Herbig & Bell 1988; Kenyon & Hartmann 1995). However, these stars are located at the far western edge of Taurus, well away from the central cloud cores, and their underluminosity has been recognized since their discovery. Few membership surveys have extended this far from the clouds, so it is unknown whether these stars are surrounded by a more extensive coeval population. Given their proximity to the Perseus complex, it seems plausible to speculate whether they are associated with that more distant, but similarly young population. Since both members of each binary pair seem to be equally anomalous, we choose to remove them from our sample for all subsequent analysis.

Three of the other binary companions are known to be seen only in scattered light due to the presence of an edge-on circumstellar disk. Stapelfeldt et al.(1998) used HST

and AO observations to show that the optical and NIR flux from HK Tau B comes from extended nebulosity, with no recognizable flux coming directly from the central star. Krist et al. (1995, 1998) found similar results from HST imaging of HL Tau and Haro 6-5B, respectively. HK Tau and Haro 6-5B appear significantly underluminous in our HR diagram since this reflected light only represents a small fraction of each star's total emitted flux. Surprisingly, HL Tau does not appear underluminous, which suggests that its luminosity might be dominated by scattered light in the optical and direct flux from the central star in the J band.

The binary component Haro 6-28 A sits just below the 5 Myr isochrone, so further analysis of its scattered-light properties might be worthwhile in the future. However, its companion Haro 6-28 B sits just above the 5 Myr isochrone, so inferred ages of the two components are mutually consistent. Barring a systematic uncertainty for the binary system, this consistency suggests that Haro 6-28 AB is genuinely one of the oldest systems in Taurus. [1]

Finally, two companions (V710 Tau C and L04-18) sit below the 5 Myr isochrone without any obvious explanation. Their optical spectra appear to be accurately classified (Luhman 2004; Kraus & Hillenbrand 2009), so a large error in temperature seems unlikely. They are associated with stars that appear youthful, so membership in a different population also does not explain their anomalously old apparent ages. V710 Tau C has not been observed at high spatial resolution, but it shows a very significant K band excess in 2MASS ($J - K \sim 2.2$), so it might possess an edge-on circumstellar disk. L04-18 appears as a point source in K band imaging with Keck LGSAO (Kraus & Hillenbrand, in preparation), so if the star is obscured, then the material is not sufficiently opaque as to block the star's light in the K band. The original discovery spectrum shows obvious signatures of youth (K. Luhman, priv. comm.), and the optical/NIR SED does not show any of the characteristic signs of an edge-on disk, so the explanation for its underluminosity is currently unknown.

---

[1] The 1.3mm excess found for Haro 6-28 by Andrews & Williams (2005) suggests that at least one component still possesses a circumstellar disk. As was demonstrated by Carpenter et al.(2006) for Upper Sco, massive circumstellar disks are relatively rare ($f \sim 5\%$) for ~ 0.3-0.5 $M_\odot$ stars by the age of ~ 5 Myr, though not as rare as for higher-mass stars.

In the following analysis, we will omit all of the HBC sources that have questionable membership. We will retain Haro 6-5B and HL Tau for a more in-depth study of high-order multiple systems, but will omit all three confirmed scattered light systems for testing coevality. We will retain Haro 6-28 A, V710 Tau C, and L04-18 since there is no conclusive evidence to suggest that they suffer a systematic bias.

7.5 The Coevality of Young Binary Systems

7.5.1 The Relative Ages of Binary Systems

The first step of our analysis is to determine whether binary systems appear more coeval than the association as a whole. The degree of coevality and the fraction of all systems that appear coeval or non-coeval will provide statistically significant context for the handful of eclipsing systems that appear non-coeval. An upper limit on the non-coevality of binary systems will also yield a constraint on the formation timescale for binary systems.

In Figure 7.2 (left), we show the same HR diagram as Figure 7.1, minus the objects we eliminated in the discussion above, where each of our binary pairs is connected by a line. The overall trend for binary pairs is to define lines that roughly parallel the theoretical isochrones, which suggests that the isochrones have the correct slope across the temperature range of our sample. However, some pairs are significantly less parallel than others, and some even seem to be perpendicular to the isochrones. This type of plot provides a summary of the underlying data, but it is hard to draw any firm conclusions regarding overall coevality or possible dependence of coevality on binary parameters. More detailed statistical analysis must be pursued using the inferred stellar ages, as has been concluded by past studies of binary ages (e.g Hartigan et al. 1994; White & Ghez 2001).

In Figure 7.3 (top), we show a histogram of the absolute difference in the logarithmic age, $\Delta \log \tau = |\log \tau_{prim} - \log \tau_{sec}|$, for each of our binary pairs. The RMS scatter in $\Delta \log \tau$ among our sample population is 0.40 dex and should encompass
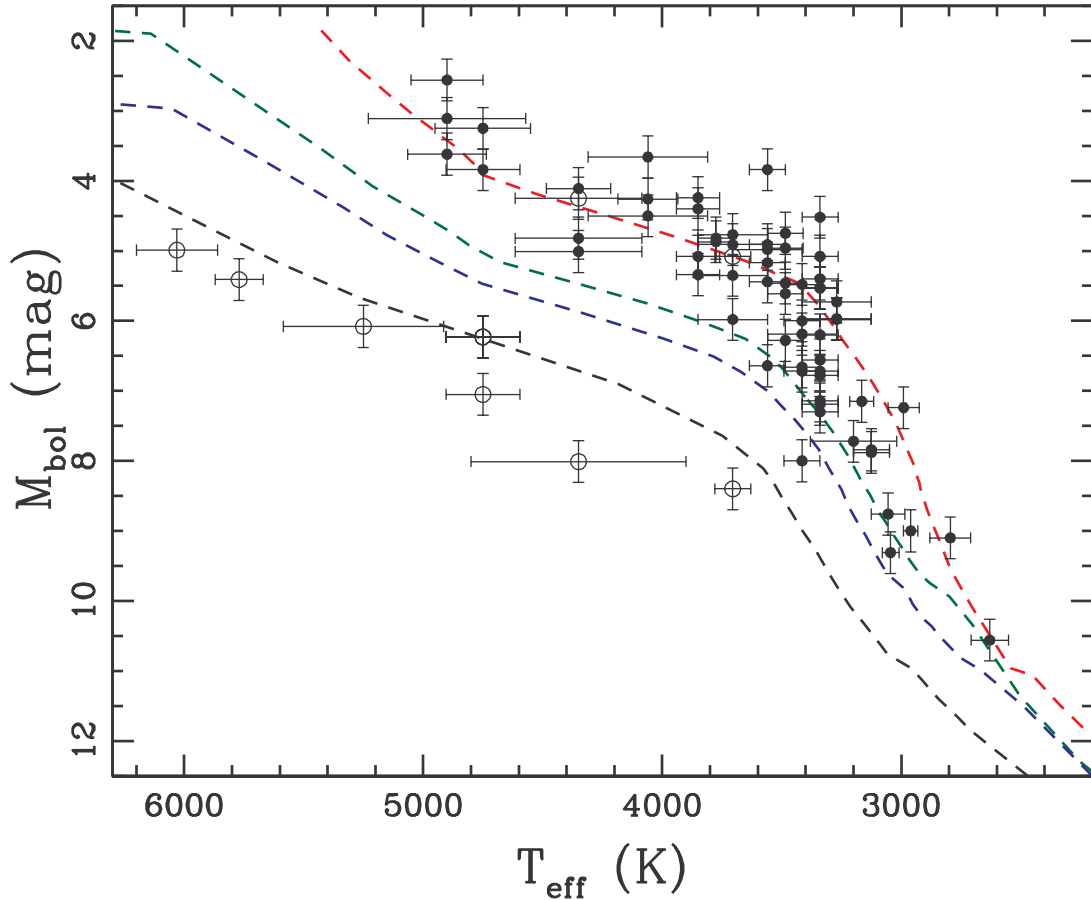
Figure 7.1 HR diagram for all components of all sample binaries. The binary components that we rejected (Section 7.4) are shown with open circles, while the rest of our sample is shown with filled circles. The dashed lines denote isochrones at 1 Myr (red), 5 Myr (green), 10 Myr (blue), and 50 Myr (black). Most Taurus members fall along the 1 Myr isochrone, but 10 fall below the 5 Myr isochrone. Three binary pairs that fall mutually below this limit might be associated with the more distant Perseus star-forming complex, while individual components that are associated with apparently young binary companions could be seen in scattered light or have incorrect spectral types.

all observational uncertainties as well as any intrinsic age spread for binary pairs. We have compared this scatter to that of the overall Taurus population by using a bootstrap Monte Carlo routine to simulate 10,000 populations where we pair each primary with another randomly-selected secondary. In Figure 7.3 (bottom), we show the distribution of all RMS scatter measurements for these simulated populations; only 14 realizations of our simulation ($\sim$0.15%) have RMS scatter of 0.40 dex or less, indicating that binaries are more coeval than the overall Taurus population at a significance of $\sim$3σ. The typical age differences for binary systems and for random pairs are similar to those measured by White & Ghez (2001); they used a similar sample, but estimated effective temperatures using dereddened $V - I$ photometry instead of spectral types.

As we describe in Section 7.3, the observational uncertainties for our sample also allow us to estimate the formal uncertainty in each binary component's age, and thus in the degree of coevality. These estimated uncertainties vary significantly across our sample, but the median, mean, and quadratic mean of these uncertainties (0.33, 0.42, and 0.48 dex in measured $\Delta \log \tau$, respectively) are all similar to the standard deviation for our sample. This strongly suggests that much of the total error budget is dominated by observational errors, and therefore that model-related errors and the true dispersion in relative ages for binary components are both $<<$0.40 dex.

However, we must also consider whether a single distribution is adequate for describing all binary systems. There are several effects that could bias one binary component's age by a significant amount (including unresolved additional multiplicity or the presence of an edge-on disk). We could expect a much narrower distribution centered close to zero and broadened by the observational errors (corresponding to unaffected binary systems) plus a secondary peak away from zero (for systems affected by unusual phenomena such as those mentioned above). The observed distribution seems to match our expectation, with most systems concentrated at $\Delta \log \tau <$0.3 dex and a secondary peak at $\Delta \log \tau \sim$0.6 dex. This peak includes the two systems that we deemed suspicious (V710 Tau C and L04-18) as well as DK Tau, which was suggested

to be a possible hierarchical triple by Jensen et al.(2004)[2]. If we omit the extended peak and compute the standard deviation of the binary age dispersion from only the first four bins of Figure 7.3 (top), we find a dispersion in $\Delta\log\tau$ of $\sim$0.16 dex, corresponding to a typical factor of 1.5 in relative age. This dispersion is actually lower than our estimated uncertainties for stellar ages, which suggests that we might have been too conservative in estimating observational uncertainties.

In light of this possible bimodality, it is worthwhile to return to Figure 7.2 and plot only the "coeval" sample ($\Delta\log\tau$<0.4 dex; center) and the "non-coeval" sample ($\Delta\log\tau$>0.4 dex; right). This division reveals a startling trend; among the "non-coeval" subsample, 11 of the 12 systems have a significantly younger primary star. As we show in Section 7.6, the model-derived ages in our sample's mass range do not show a mass-dependent trend, so the tendency for some binary primaries to appear younger must be either a genuine effect or a result of binary-specific systematic errors. Given the clear discrepancy with respect to the apparently coeval majority of our sample, we strongly suspect that systematic errors are to blame.

Amazingly, the fraction of apparently coeval binary systems in our sample (24/36) is identical to the fraction identified by the groundbreaking survey of Hartigan et al.(1994). In a sample of binary systems in Taurus and Orion (which included many Taurus binaries that we have rejected as hierarchical multiples), they found that 17/26 had $\Delta\log(L)$<0.24 dex, corresponding roughly to $\Delta\log\tau$<0.4 dex. On its face, this result suggests that all of the improvements in evolutionary models, spectral type assessments, and multiplicity surveys in the past 15 years have only served to cut the standard deviation in $\Delta\log\tau$ for coeval systems from 0.23 dex to 0.16 dex. However, there is one significant difference. All of our non-coeval systems possess apparently younger primaries, while all of the corresponding systems in the Hartigan et al. sample possess apparently older primaries. There is little overlap between our samples since many wide Taurus binaries have since been discovered to be hierarchical multiples, so one possible explanation is that our stringent multiplicity vetting simply

---

[2]Polarization measurements by Jensen et al. indicate that the component disks in DK Tau AB are misaligned, unlike most other double-disk systems in Taurus.

allows another systematic error to dominate.

There are three likely culprits for the systematic error that makes some systems appear non-coeval. First, the multiplicity fraction is higher among solar-type stars than lower-mass stars (Duquennoy & Mayor 1991; Fischer & Marcy 1992). If this trend also applies to the fragmentation of binary components into high-order multiples, then we might expect more binary primaries to be unresolved pairs (which would then appear to be a single overluminous star). Second, surveys of protoplanetary disks in binary systems have suggested that disks might be more likely to form or persist around the primary than the secondary (e.g., Monin et al. 2007). We determined most stellar luminosities from the K band flux, so a disk excess would have led to significant overestimation of those luminosities. Finally, the disks of high-mass stars boast more substantial NIR excesses than those of low-mass stars and brown dwarfs (e.g., Meyer et al. 1997 versus Liu et al. 2003), so the magnitude of the luminosity overestimate should also be larger for primaries than secondaries.

All of these explanations should be investigated and ruled out before an astrophysical explanation is considered. In particular, systematic effects from disks should be mitigated by estimating stellar luminosities using the least contaminated filter (J) and by modeling the circumstellar dust emission using $JHKL$ photometry so that any remaining excess can be subtracted. However, our preliminary disk census suggests that NIR excess contamination might play only a modest role in biasing relative binary ages (unless the disk directly obscures the central star, making it appear in scattered light; Section 7.4). Of the 24 pairs which appear coeval, 20 have at least one disk (where $\geq$4 are mixed pairs and $\geq$11 are double-disk systems). This presents little contrast to the 12 apparently non-coeval pairs, of which 9 have at least one disk (with $\geq$3 mixed pairs and $\geq$6 double-disk systems). The similar and nontrivial fractions of mixed pairs are difficult to explain if disk biases dominate, though double-disk systems could appear coeval if both binary components' luminosities are biased upward by the same amount.

Our results for binary pair age differences are consistent with the local and global star formation timescales that have been predicted by theoretical models. If most

binary systems in Taurus are coeval to within <0.16 dex (including observational uncertainties), then given its median age (1.8±0.2 Myr; Section 7.6), the formation times for binary components must differ by <0.7 Myr. The expected timescale for an individual protostar to collapse after achieving supercriticality is the dynamical timescale ($\sim$0.1-0.2 Myr; Shu et al. 1987); binary fragmentation is likely to occur during this collapse, so our limit is consistent with the predicted formation timescale.

In contrast, the timescale for global star formation is likely to be much longer, representing either the turbulent dissipation timescale ($\sim$1 Myr; Ballesteros-Paredes et al. 1999; Elmegreen 2000) or the ambipolar diffusion timescale ($\sim$3-10 Myr; Mouschovias 1976; Shu 1977). Our limit on the age dispersion of binary pairs is shorter than either timescale, while the overall age dispersion for unrelated pairs of stars is consistent with the ambipolar diffusion timescale, but only marginally with the turbulent dissipation timescale. We found a dispersion of $\sim$0.6 dex in $\Delta \log \tau$ for random pairs, corresponding to a dispersion in $\log \tau$ of $\sim$0.4 dex. For the median Taurus age of $\sim$1.8 Myr, this corresponds to a typical age range of 1-5 Myr.

Finally, if our results do reveal two distributions (one population that appears coeval and one that does not), then the number of systems in each distribution will allow a constraint on the fraction of binary systems that appear coeval. Of the 36 pairs of stars that we considered, 24 are coeval to within $\Delta \log \tau$<0.4 dex, while the other 12 have ages which are more discrepant. This suggests that $>67^{+7}_{-9}\%$ of all binary systems appear coeval with a dispersion of <0.16 dex. However, many of the non-coeval pairs could be affected by systematic errors while being genuinely coeval, so this fraction is a lower limit. More intensive study of the apparently non-coeval pairs should be a priority; as we discussed above, some stars (such as V710 Tau C and DK Tau A) already seem potentially erroneous and might be rejected from our sample based on additional followup observations.

Table 7.2.   Derived Ages and Masses

Name	M ($M_\odot$) (Adopted)	$\log(\tau)$ (yr) (Adopted)	M ($M_\odot$) (Lyon)	$\log(\tau)$ (yr) (Lyon)	M ($M_\odot$) (DM97)	$\log(\tau)$ (yr) (DM97)
HBC 352	...	>7.7	...	>7.7	...	>7.7
HBC 353	...	>7.7	...	>7.7	...	>7.7
HBC 355	...	>7.7	...	>7.7	...	>7.7
HBC 354	...	>7.7	...	>7.7	...	>7.7
HBC 356	$0.79^{+0.08}_{-0.03}$	$7.68^{+0.65}_{-0.27}$	...	>7.7	$0.79^{+0.09}_{-0.05}$	$7.56^{+0.52}_{-0.27}$
HBC 357	$0.79^{+0.08}_{-0.03}$	$7.68^{+0.65}_{-0.27}$	...	>7.7	$0.79^{+0.09}_{-0.05}$	$7.56^{+0.52}_{-0.27}$
V773 Tau Aa	$1.5^{+0.4}_{-0.3}$	$5.61^{+0.22}_{-0.21}$	$1.9^{+0.3}_{-0.2}$	$5.92^{+0.28}_{-0.27}$	$1.5^{+0.4}_{-0.3}$	$5.61^{+0.22}_{-0.21}$
V773 Tau Ab	$1.0^{+0.5}_{-0.1}$	$5.62^{+0.40}_{-0.24}$	$1.9^{+0.3}_{-0.3}$	$6.25^{+0.48}_{-0.31}$	$1.1^{+0.4}_{-0.4}$	$5.69^{+0.33}_{-0.35}$
2M04141188	$0.070^{+0.008}_{-0.007}$	$6.46^{+0.19}_{-0.19}$	$0.070^{+0.008}_{-0.007}$	$6.46^{+0.19}_{-0.19}$	$0.111^{+0.013}_{-0.014}$	$6.83^{+0.11}_{-0.12}$
FO Tau A	$0.4^{+0.10}_{-0.17}$	$5.86^{+0.21}_{-0.28}$	$0.40^{+0.10}_{-0.17}$	$5.86^{+0.21}_{-0.28}$	$0.19^{+0.03}_{-0.03}$	$5.20^{+0.54}_{-0.27}$
FO Tau B	$0.4^{+0.10}_{-0.17}$	$5.86^{+0.21}_{-0.28}$	$0.40^{+0.10}_{-0.17}$	$5.86^{+0.21}_{-0.28}$	$0.19^{+0.03}_{-0.03}$	$5.20^{+0.54}_{-0.27}$
DD Tau A	$0.43^{+0.13}_{-0.23}$	$5.63^{+0.23}_{-0.32}$	$0.43^{+0.13}_{-0.23}$	$5.63^{+0.23}_{-0.32}$	$0.18^{+0.03}_{-0.02}$	$4.85^{+0.27}_{-0.25}$
DD Tau B	$0.41^{+0.11}_{-0.19}$	$5.79^{+0.22}_{-0.29}$	$0.41^{+0.11}_{-0.19}$	$5.79^{+0.22}_{-0.29}$	$0.19^{+0.03}_{-0.02}$	$5.09^{+0.35}_{-0.26}$
FQ Tau A	$0.37^{+0.07}_{-0.05}$	$6.50^{+0.23}_{-0.20}$	$0.37^{+0.07}_{-0.05}$	$6.50^{+0.23}_{-0.20}$	$0.25^{+0.05}_{-0.03}$	$6.23^{+0.20}_{-0.16}$
FQ Tau B	$0.32^{+0.05}_{-0.05}$	$6.43^{+0.20}_{-0.19}$	$0.32^{+0.05}_{-0.05}$	$6.43^{+0.20}_{-0.19}$	$0.22^{+0.03}_{-0.03}$	$6.21^{+0.17}_{-0.15}$
LkCa 7 A	$0.67^{+0.04}_{-0.04}$	$6.28^{+0.21}_{-0.21}$	$0.96^{+0.09}_{-0.12}$	$6.61^{+0.19}_{-0.22}$	$0.42^{+0.07}_{-0.06}$	$5.91^{+0.23}_{-0.18}$
LkCa 7 B	$0.35^{+0.06}_{-0.07}$	$6.17^{+0.17}_{-0.22}$	$0.35^{+0.06}_{-0.07}$	$6.17^{+0.17}_{-0.22}$	$0.21^{+0.04}_{-0.03}$	$5.95^{+0.15}_{-0.47}$
FS Tau A	$0.66^{+0.03}_{-0.03}$	$5.67^{+0.20}_{-0.20}$	$1.06^{+0.10}_{-0.12}$	$6.06^{+0.22}_{-0.25}$	$0.32^{+0.05}_{-0.04}$	$5.16^{+0.42}_{-0.39}$
FS Tau B	$0.32^{+0.05}_{-0.05}$	$6.40^{+0.20}_{-0.19}$	$0.32^{+0.05}_{-0.05}$	$6.40^{+0.20}_{-0.19}$	$0.22^{+0.03}_{-0.03}$	$6.19^{+0.17}_{-0.15}$
Haro 6-5B	...	>7.7	...	>7.7	...	>7.7
FV Tau A	$0.83^{+0.06}_{-0.06}$	$5.85^{+0.19}_{-0.18}$	$1.54^{+0.15}_{-0.15}$	$6.38^{+0.32}_{-0.22}$	$0.56^{+0.10}_{-0.08}$	$5.61^{+0.20}_{-0.17}$
FV Tau/c A	$0.54^{+0.05}_{-0.07}$	$6.08^{+0.19}_{-0.18}$	$0.55^{+0.07}_{-0.07}$	$6.08^{+0.18}_{-0.19}$	$0.25^{+0.04}_{-0.04}$	$5.72^{+0.16}_{-0.59}$
FV Tau/c B	$0.30^{+0.07}_{-0.05}$	$6.67^{+0.26}_{-0.20}$	$0.30^{+0.07}_{-0.05}$	$6.67^{+0.26}_{-0.20}$	$0.23^{+0.04}_{-0.03}$	$6.48^{+0.22}_{-0.19}$
DF Tau A	$0.61^{+0.19}_{-0.01}$	$5.14^{+0.22}_{-0.24}$	$0.86^{+0.06}_{-0.10}$	$5.37^{+0.17}_{-0.16}$	$0.19^{+0.02}_{-0.02}$	$4.22^{+0.25}_{-0.24}$
DF Tau B	$0.65^{+0.05}_{-0.08}$	$5.74^{+0.15}_{-0.27}$	$0.65^{+0.05}_{-0.08}$	$5.74^{+0.20}_{-0.20}$	$0.22^{+0.03}_{-0.02}$	$4.83^{+0.28}_{-0.24}$
2M04284263 A	$0.16^{+0.04}_{-0.04}$	$6.50^{+0.16}_{-0.19}$	$0.16^{+0.04}_{-0.04}$	$6.50^{+0.16}_{-0.19}$	$0.17^{+0.02}_{-0.02}$	$6.52^{+0.20}_{-0.17}$
2M04284263 B	$0.098^{+0.025}_{-0.019}$	$6.62^{+0.34}_{-0.23}$	$0.098^{+0.025}_{-0.019}$	$6.62^{+0.34}_{-0.23}$	$0.148^{+0.025}_{-0.024}$	$6.91^{+0.19}_{-0.18}$
UX Tau A	$1.3^{+0.3}_{-0.4}$	$6.10^{+0.26}_{-0.30}$	$1.9^{+0.3}_{-0.3}$	$6.79^{+0.19}_{-0.42}$	$1.3^{+0.3}_{-0.4}$	$6.10^{+0.26}_{-0.30}$
UX Tau C	$0.16^{+0.04}_{-0.04}$	$6.51^{+0.16}_{-0.19}$	$0.16^{+0.04}_{-0.04}$	$6.51^{+0.16}_{-0.19}$	$0.17^{+0.02}_{-0.02}$	$6.54^{+0.20}_{-0.17}$
FX Tau A	$0.62^{+0.05}_{-0.03}$	$5.91^{+0.20}_{-0.19}$	$0.82^{+0.19}_{-0.15}$	$6.14^{+0.29}_{-0.27}$	$0.30^{+0.07}_{-0.06}$	$5.54^{+0.23}_{-0.59}$
FX Tau B	$0.28^{+0.16}_{-0.32}$	$5.90^{+0.33}_{-1.04}$	$0.28^{+0.16}_{-0.32}$	$5.90^{+0.33}_{-1.04}$	$0.18^{+0.06}_{-0.04}$	$5.41^{+0.56}_{-0.38}$
DK Tau A	$0.71^{+0.09}_{-0.06}$	$5.34^{+0.32}_{-0.36}$	$1.30^{+0.16}_{-0.22}$	$5.81^{+0.32}_{-0.36}$	$0.37^{+0.13}_{-0.12}$	$4.76^{+0.65}_{-0.51}$
DK Tau B	$0.61^{+0.06}_{-0.04}$	$6.17^{+0.22}_{-0.20}$	$0.78^{+0.18}_{-0.17}$	$6.38^{+0.29}_{-0.27}$	$0.35^{+0.08}_{-0.07}$	$5.81^{+0.21}_{-0.23}$
V927 Tau A	$0.42^{+0.07}_{-0.06}$	$6.21^{+0.19}_{-0.18}$	$0.42^{+0.07}_{-0.06}$	$6.21^{+0.19}_{-0.18}$	$0.24^{+0.04}_{-0.04}$	$5.93^{+0.15}_{-0.31}$
V927 Tau B	$0.33^{+0.05}_{-0.05}$	$6.32^{+0.20}_{-0.18}$	$0.33^{+0.05}_{-0.05}$	$6.32^{+0.20}_{-0.18}$	$0.22^{+0.03}_{-0.03}$	$6.12^{+0.15}_{-0.15}$
HL Tau	$0.83^{+0.11}_{-0.10}$	$5.93^{+0.24}_{-0.25}$	$1.53^{+0.21}_{-0.27}$	$6.51^{+0.35}_{-0.35}$	$0.57^{+0.21}_{-0.15}$	$5.68^{+0.33}_{-0.22}$

Table 7.2 (cont'd)

Name	M ($M_\odot$) (Adopted)	$\log(\tau)$ (yr) (Adopted)	M ($M_\odot$) (Lyon)	$\log(\tau)$ (yr) (Lyon)	M ($M_\odot$) (DM97)	$\log(\tau)$ (yr) (DM97)
XZ Tau A	$0.59^{+0.07}_{-0.04}$	$5.86^{+0.20}_{-0.23}$	$0.67^{+0.14}_{-0.12}$	$5.97^{+0.27}_{-0.28}$	$0.25^{+0.06}_{-0.05}$	$5.16^{+0.57}_{-0.36}$
XZ Tau B	$0.46^{+0.17}_{-0.30}$	$5.36^{+0.24}_{-0.36}$	$0.46^{+0.17}_{-0.30}$	$5.36^{+0.24}_{-0.36}$	$0.17^{+0.02}_{-0.01}$	$4.44^{+0.25}_{-0.25}$
HK Tau A	$0.62^{+0.03}_{-0.02}$	$6.01^{+0.19}_{-0.17}$	$0.80^{+0.10}_{-0.09}$	$6.24^{+0.2}_{-0.21}$	$0.32^{+0.05}_{-0.04}$	$5.69^{+0.15}_{-0.45}$
HK Tau B	...	>7.7	...	>7.7	...	>7.7
V710 Tau A	$0.62^{+0.09}_{-0.07}$	$6.57^{+0.24}_{-0.21}$	$0.73^{+0.15}_{-0.18}$	$6.74^{+0.26}_{-0.32}$	$0.43^{+0.12}_{-0.10}$	$6.21^{+0.31}_{-0.25}$
V710 Tau B	$0.40^{+0.14}_{-0.12}$	$6.29^{+0.32}_{-0.30}$	$0.40^{+0.14}_{-0.12}$	$6.29^{+0.32}_{-0.30}$	$0.24^{+0.10}_{-0.06}$	$6.01^{+0.22}_{-0.35}$
V710 Tau C	$0.35^{+0.07}_{-0.07}$	$7.24^{+0.21}_{-0.25}$	$0.35^{+0.07}_{-0.07}$	$7.24^{+0.21}_{-0.25}$	$0.29^{+0.05}_{-0.04}$	$7.06^{+0.24}_{-0.24}$
GG Tau Aa	$0.73^{+0.09}_{-0.08}$	$5.88^{+0.25}_{-0.30}$	$1.21^{+0.25}_{-0.22}$	$6.34^{+0.35}_{-0.33}$	$0.43^{+0.15}_{-0.12}$	$5.62^{+0.25}_{-0.57}$
GG Tau Ab	$0.64^{+0.03}_{-0.03}$	$5.93^{+0.19}_{-0.18}$	$0.91^{+0.10}_{-0.10}$	$6.23^{+0.20}_{-0.22}$	$0.33^{+0.05}_{-0.04}$	$5.59^{+0.18}_{-0.46}$
GG Tau Ba	$0.104^{+0.024}_{-0.020}$	$5.80^{+0.31}_{-0.51}$	$0.104^{+0.024}_{-0.020}$	$5.80^{+0.31}_{-0.51}$	$0.134^{+0.014}_{-0.012}$	$6.11^{+0.16}_{-0.44}$
GG Tau Bb	$0.044^{+0.011}_{-0.013}$	$5.63^{+0.61}_{-2.08}$	$0.044^{+0.011}_{-0.013}$	$5.63^{+0.61}_{-2.08}$	$0.062^{+0.021}_{-0.018}$	$6.56^{+0.14}_{-0.71}$
UZ Tau Aa	$0.62^{+0.05}_{-0.03}$	$5.83^{+0.19}_{-0.20}$	$0.84^{+0.18}_{-0.14}$	$6.06^{+0.29}_{-0.27}$	$0.29^{+0.07}_{-0.05}$	$5.27^{+0.43}_{-0.42}$
UZ Tau Ab	$0.26^{+0.20}_{-0.35}$	$5.76^{+0.38}_{-1.20}$	$0.26^{+0.20}_{-0.35}$	$5.76^{+0.38}_{-1.20}$	$0.17^{+0.06}_{-0.04}$	$5.20^{+0.67}_{-0.34}$
UZ Tau Ba	$0.59^{+0.05}_{-0.01}$	$5.81^{+0.19}_{-0.21}$	$0.68^{+0.07}_{-0.08}$	$5.93^{+0.19}_{-0.17}$	$0.25^{+0.04}_{-0.03}$	$5.09^{+0.53}_{-0.28}$
UZ Tau Bb	$0.49^{+0.07}_{-0.09}$	$5.98^{+0.18}_{-0.20}$	$0.49^{+0.07}_{-0.09}$	$5.98^{+0.18}_{-0.20}$	$0.22^{+0.04}_{-0.03}$	$5.33^{+0.53}_{-0.31}$
GH Tau A	$0.58^{+0.02}_{-0.05}$	$6.15^{+0.19}_{-0.20}$	$0.61^{+0.09}_{-0.07}$	$6.20^{+0.20}_{-0.18}$	$0.29^{+0.05}_{-0.04}$	$5.77^{+0.15}_{-0.47}$
GH Tau B	$0.58^{+0.02}_{-0.02}$	$5.98^{+0.20}_{-0.20}$	$0.64^{+0.08}_{-0.07}$	$6.07^{+0.18}_{-0.18}$	$0.27^{+0.04}_{-0.03}$	$5.50^{+0.29}_{-0.49}$
IS Tau A	$0.67^{+0.04}_{-0.03}$	$6.11^{+0.21}_{-0.20}$	$0.99^{+0.09}_{-0.12}$	$6.46^{+0.19}_{-0.21}$	$0.39^{+0.06}_{-0.05}$	$5.77^{+0.19}_{-0.18}$
IS Tau B	$0.30^{+0.06}_{-0.05}$	$6.62^{+0.25}_{-0.20}$	$0.30^{+0.06}_{-0.05}$	$6.62^{+0.25}_{-0.20}$	$0.23^{+0.04}_{-0.03}$	$6.42^{+0.21}_{-0.18}$
HN Tau A	$0.85^{+0.11}_{-0.10}$	$6.27^{+0.27}_{-0.25}$	$1.35^{+0.13}_{-0.16}$	$6.85^{+0.30}_{-0.34}$	$0.65^{+0.23}_{-0.18}$	$6.05^{+0.38}_{-0.32}$
HN Tau B	$0.20^{+0.13}_{-0.10}$	$6.59^{+0.45}_{-0.49}$	$0.20^{+0.13}_{-0.10}$	$6.59^{+0.45}_{-0.49}$	$0.19^{+0.07}_{-0.05}$	$6.54^{+0.33}_{-0.23}$
IT Tau A	$1.0^{+0.3}_{-0.1}$	$5.96^{+0.32}_{-0.21}$	$1.8^{+0.2}_{-0.2}$	$6.76^{+0.18}_{-0.39}$	$1.0^{+0.3}_{-0.3}$	$5.96^{+0.31}_{-0.32}$
IT Tau B	$0.28^{+0.15}_{-0.32}$	$5.90^{+0.33}_{-1.04}$	$0.28^{+0.15}_{-0.32}$	$5.90^{+0.33}_{-1.04}$	$0.18^{+0.06}_{-0.04}$	$5.42^{+0.55}_{-0.38}$
Haro 6-28 A	$0.52^{+0.07}_{-0.08}$	$6.80^{+0.21}_{-0.22}$	$0.52^{+0.07}_{-0.08}$	$6.80^{+0.21}_{-0.22}$	$0.35^{+0.07}_{-0.06}$	$6.45^{+0.24}_{-0.23}$
Haro 6-28 B	$0.30^{+0.06}_{-0.05}$	$6.60^{+0.24}_{-0.20}$	$0.30^{+0.06}_{-0.05}$	$6.60^{+0.24}_{-0.20}$	$0.23^{+0.04}_{-0.03}$	$6.39^{+0.21}_{-0.17}$
2M04414565	$0.37^{+0.08}_{-0.05}$	$6.54^{+0.24}_{-0.20}$	$0.37^{+0.08}_{-0.05}$	$6.54^{+0.24}_{-0.20}$	$0.25^{+0.05}_{-0.03}$	$6.26^{+0.21}_{-0.16}$
2M04414489	$0.027^{+0.006}_{-0.009}$	$6.47^{+0.44}_{-0.94}$	$0.027^{+0.006}_{-0.009}$	$6.47^{+0.44}_{-0.94}$	$0.022^{+0.007}_{-0.006}$	$6^{+0.82}_{-0.47}$
LkHa332-G2 A	$0.64^{+0.03}_{-0.02}$	$5.90^{+0.19}_{-0.18}$	$0.92^{+0.10}_{-0.10}$	$6.20^{+0.20}_{-0.21}$	$0.33^{+0.04}_{-0.04}$	$5.56^{+0.19}_{-0.50}$
LkHa332-G2 B	$0.52^{+0.05}_{-0.07}$	$6.15^{+0.19}_{-0.18}$	$0.52^{+0.07}_{-0.07}$	$6.15^{+0.19}_{-0.19}$	$0.26^{+0.05}_{-0.04}$	$5.81^{+0.14}_{-0.53}$
V955 Tau A	$0.72^{+0.05}_{-0.04}$	$5.73^{+0.22}_{-0.24}$	$1.24^{+0.11}_{-0.10}$	$6.20^{+0.22}_{-0.22}$	$0.41^{+0.07}_{-0.06}$	$5.51^{+0.15}_{-0.55}$
V955 Tau B	$0.45^{+0.08}_{-0.07}$	$6.46^{+0.23}_{-0.20}$	$0.45^{+0.08}_{-0.07}$	$6.46^{+0.23}_{-0.20}$	$0.28^{+0.06}_{-0.04}$	$6.12^{+0.20}_{-0.16}$
UY Aur A	$0.66^{+0.03}_{-0.02}$	$5.56^{+0.20}_{-0.20}$	$1.07^{+0.12}_{-0.12}$	$5.95^{+0.23}_{-0.25}$	$0.31^{+0.04}_{-0.04}$	$4.94^{+0.56}_{-0.31}$
UY Aur B	$0.62^{+0.05}_{-0.08}$	$5.84^{+0.15}_{-0.23}$	$0.62^{+0.08}_{-0.07}$	$5.84^{+0.19}_{-0.20}$	$0.22^{+0.03}_{-0.02}$	$4.99^{+0.43}_{-0.24}$
2M04554757	$0.20^{+0.03}_{-0.03}$	$6.27^{+0.17}_{-0.17}$	$0.20^{+0.03}_{-0.03}$	$6.27^{+0.17}_{-0.17}$	$0.17^{+0.02}_{-0.01}$	$6.22^{+0.14}_{-0.13}$
2M04554801	$0.092^{+0.008}_{-0.012}$	$6.96^{+0.76}_{-0.27}$	$0.092^{+0.008}_{-0.012}$	$6.96^{+0.76}_{-0.27}$	$0.133^{+0.015}_{-0.016}$	$7.13^{+0.16}_{-0.15}$
RW Aur A	$1.4^{+0.6}_{-0.7}$	$5.85^{+0.44}_{-0.53}$	$2.1^{+0.3}_{-0.5}$	$6.32^{+0.54}_{-0.42}$	$1.4^{+0.6}_{-0.7}$	$5.85^{+0.44}_{-0.53}$

Table 7.2 (cont'd)

Name	M ($M_\odot$) (Adopted)	$\log(\tau)$ (yr)	M ($M_\odot$) (Lyon)	$\log(\tau)$ (yr)	M ($M_\odot$) (DM97)	$\log(\tau)$ (yr)
RW Aur B	$0.86^{+0.11}_{-0.10}$	$6.40^{+0.26}_{-0.26}$	$1.26^{+0.14}_{-0.14}$	$6.96^{+0.29}_{-0.33}$	$0.69^{+0.24}_{-0.19}$	$6.19^{+0.39}_{-0.35}$
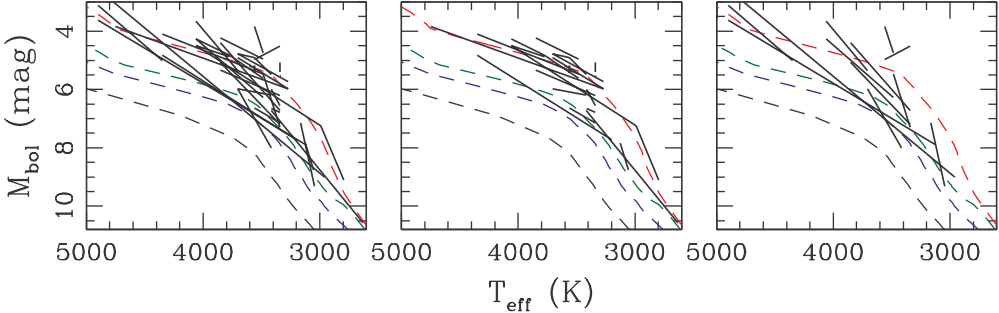
Figure 7.2 HR diagram for the binary pairs in our sample, where each pair is connected by a line. The left panel shows all systems, whereas following the text in Section 7.5.1, the other panels show only systems with $\Delta\log\tau<0.4$ dex (middle) and $\Delta\log\tau>0.4$ dex (right). The binary systems in our sample trace the approximate contours of stellar evolutionary models, suggesting that the overall trend is correct, but it is difficult to distinguish a trend in coevality from the full sample.

7.5.2 The Role of Binary Parameters in System Coevality

The detailed physics of multiple star formation are still poorly understood, so any apparent trends in the coevality of binary systems could yield valuable new constraints on theoretical models. The three binary properties that we can test for coevality are the component mass ratio, the total system mass, and the projected pair separation. The degree of coevality as a function of separation across the entire association could also constrain the large-scale star formation processes, so we will also analyze the coevality as a function of separation between all pairs of stars in our sample.

In Figure 7.4, we plot the difference in system age $|\Delta\log\tau|$ as a function of binary mass ratio. If binaries truly formed non-coevally, then we might expect the systems with the most extreme mass ratios to show the largest discrepancy in ages. However, the dispersion in $\Delta\log\tau$ for the five systems with $q < 0.3$ is 0.41 dex, similar to the overall dispersion for our full sample (0.40 dex). If we limit this analysis to only the apparently coeval population ($\Delta\log\tau<0.40$ dex), the dispersions are 0.17 dex and 0.16
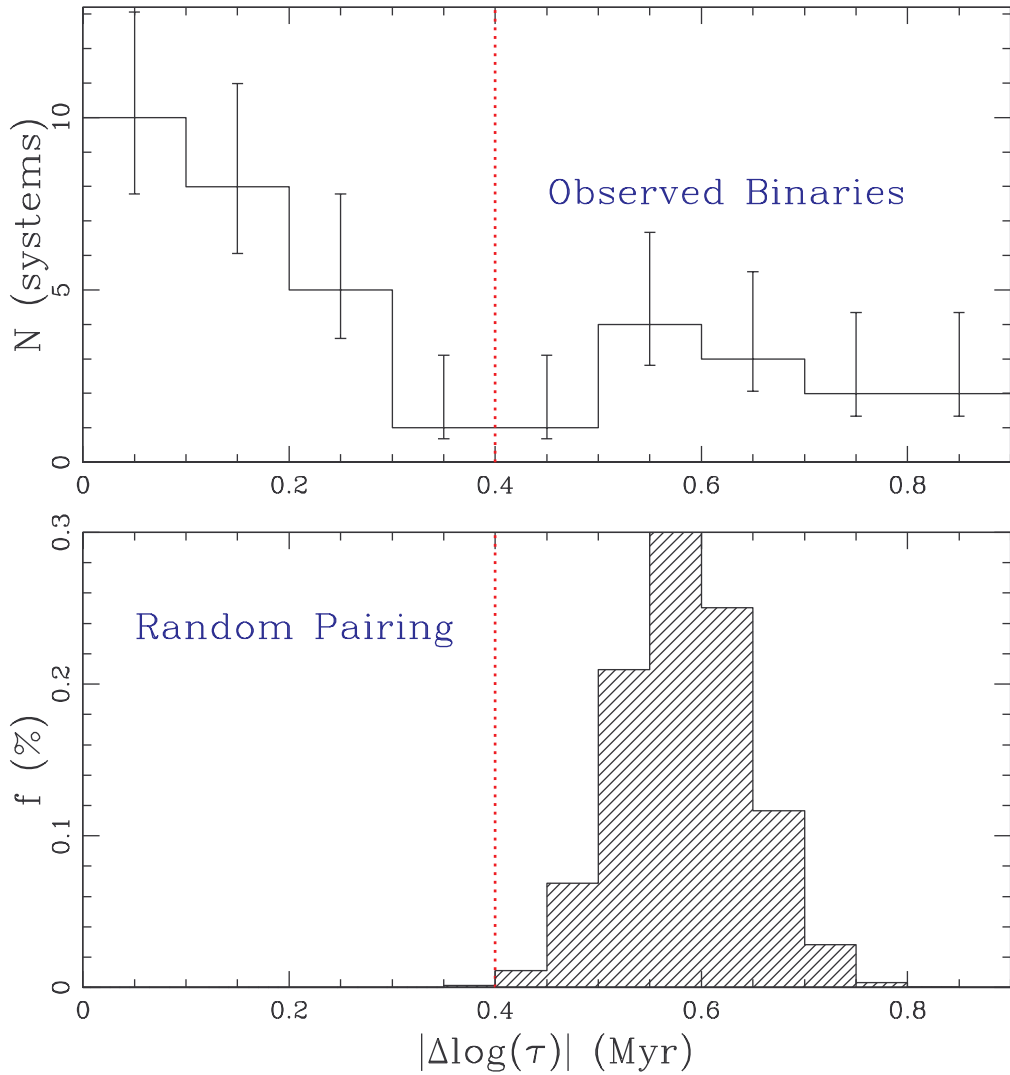
Figure 7.3 Top: Distribution of differences in logarithmic age, $\Delta \log \tau$, for all 36 pairs of stars in our sample. The RMS scatter in $\Delta \log \tau$, $\sigma = 0.40$ dex, is indicated by a red dotted line. Bottom: Distribution of RMS scatter for a set of 10,000 simulated binary populations that were constructed by randomly pairing primaries with secondaries. As before, we show the RMS scatter of our observed population with a red dotted line; only 14 of the 10,000 simulated populations have $\sigma < 0.40$ dex, indicating that our binary pairs are more coeval than Taurus at $\sim 3\sigma$ significance.

dex, respectively. This indicates that there is no strong trend for reduced coevality in these extreme systems. Hartigan et al.(1994) also found no such trend in their sample.

In Figure 7.5, we plot $|\Delta \log \tau|$ as a function of total system mass. Most of our sample spans only a limited mass range (0.7-1.5 $M_\odot$), but we see no evidence of a mass-dependent trend. Our sample includes only four systems with a total mass of <0.5 $M_\odot$, but we also see no significant trend for a higher scatter in ages. The dispersion (0.36 dex) is similar to that of the full sample, though almostly entirely dominated by one system (2M04554757+2M04554801). Our sample includes only two high-mass pairs, RW Aur AB and V773 Tau Aab, for which we measure age discrepancies of 0.55 dex and 0.01 dex, respectively.

In Figure 7.6, we plot $|\Delta \log \tau|$ as a function of system separation. If the separation of a binary system denotes the protostellar core size when fragmentation occurred, then wide systems must fragment at an earlier stage than closer systems. This suggests that wide binary pairs might fragment earlier and show a larger dispersion in apparent ages. However, as for the previous figures, this comparison does not indicate any significant role of separation in establishing the binary component ages. The inner and outer halves of the sample (divided at 800 AU) have dispersions of 0.37 dex versus 0.42 dex (for the full set) and 0.14 versus 0.18 dex (for the coeval subset). We conclude that binary systems of all separations are similar coeval to within our observed limits.

7.5.3   The Intracluster Coevality of Young Stars

The lack of a separation-dependent trend in differential age begs an important question. If binary pairs are similarly coeval with their associated components, but significantly more coeval than the association as a whole, then what is the form of the transition between these regimes? Are adjacent (but unassociated) Taurus members more coeval than distant members, or is the age spread similar across all spatial scales greater than the binary separation regime?
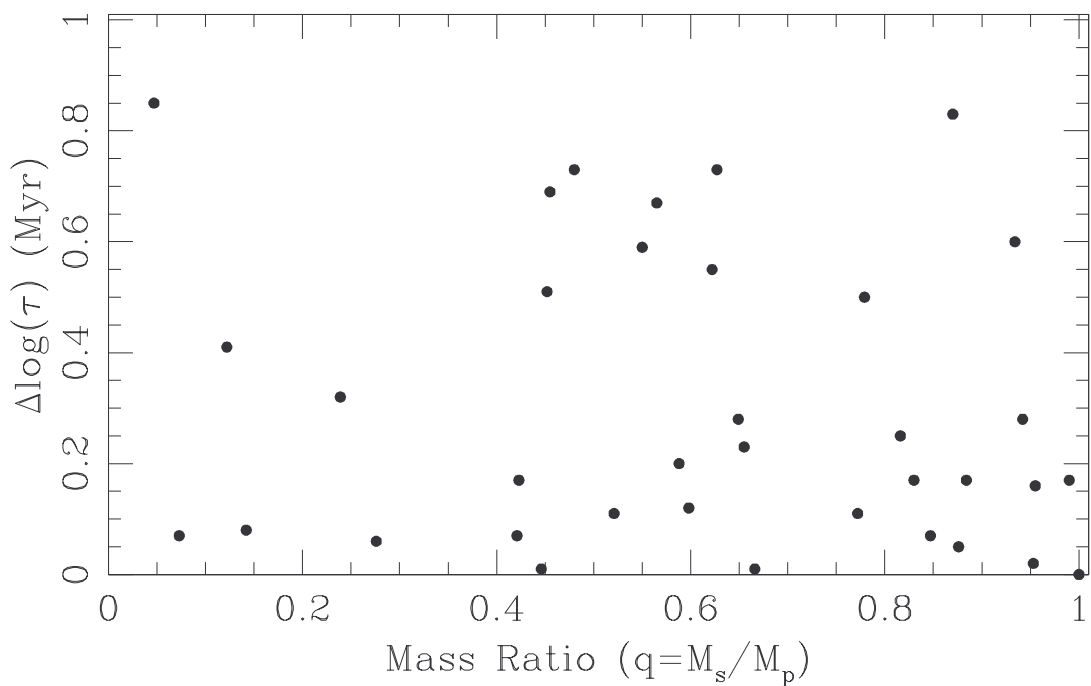
Figure 7.4 Difference in binary component age, $\Delta\log\tau$, as a function of binary mass ratio. We see no evidence of a trend with q, as the standard deviation in $\Delta\log\tau$ for $q < 0.3$ and for the full sample are the same for all pairs (0.41 dex versus 0.40 dex) and for the apparently coeval subset (0.17 versus 0.16 dex).
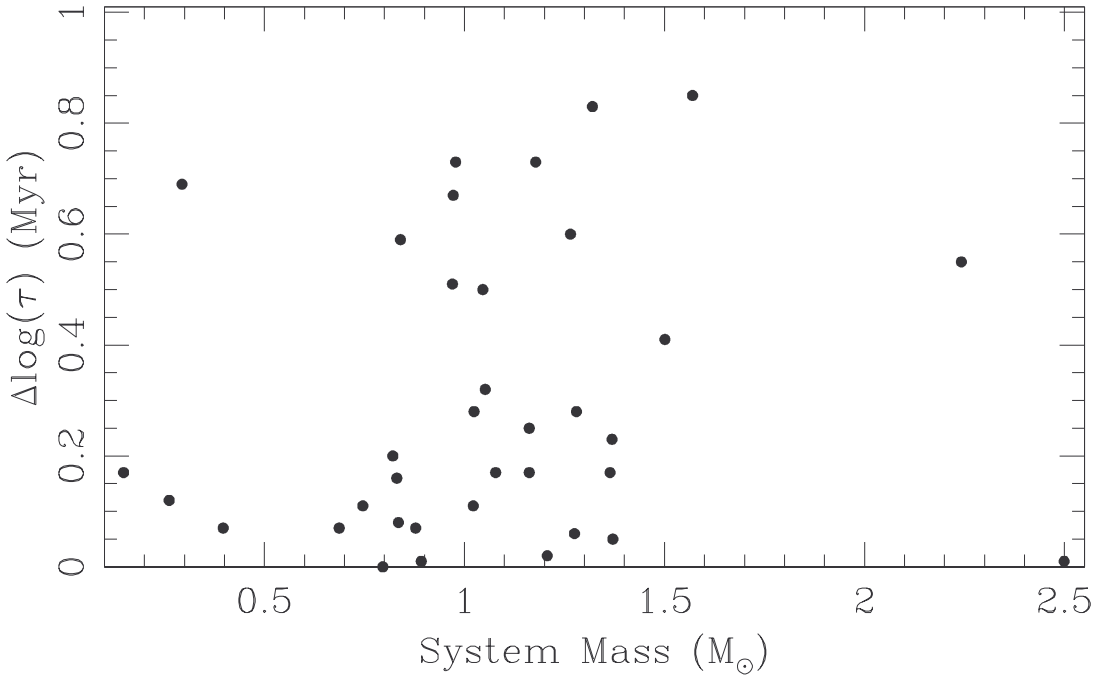
Figure 7.5 Difference in binary component age, $\Delta\log\tau$, as a function of system mass. We see no trend for low-mass systems to appear more discrepant, but are unable to test systems with $M > 1.5\ M_\odot$ and can only test a handful of systems with $M < 0.7\ M_\odot$.

In Figure 7.7, we address this question by plotting $|\Delta\log\tau|$ as a function of separation for all possible pairs of the primary and secondary stars in our binary sample. We can not draw any conclusions for separations of 30-1000″ (5000 AU to 0.7 pc) due to small number statistics, but the dispersion at larger separations (as indicated by the standard deviation in bins 0.5 dex wide) is consistently $\sim$0.6 dex across the entire separation range. This result suggests that the coevality we see for binary systems (Figure 7.6) is limited to scales of $<$0.7 pc, but we can not determine if this coevality is limited exclusively to binary systems since the binary regime is characterized by separations $<2'$ (Kraus & Hillenbrand 2008). This scatter is unlikely to result from any distance dispersion of Taurus members ($<$15 pc for members in similar parts of the cloud; Section 7.3.1) since it would yield a scatter of $<$0.2 mag in M_{bol} or $\sim$0.15 dex in $\log\tau$ (0.20-0.25 dex in $\Delta\log\tau$ for a pair of stars).

Our results all indicate that the properties of a binary system can play only a modest role in its formation timescale; even extreme systems (with very wide separa-
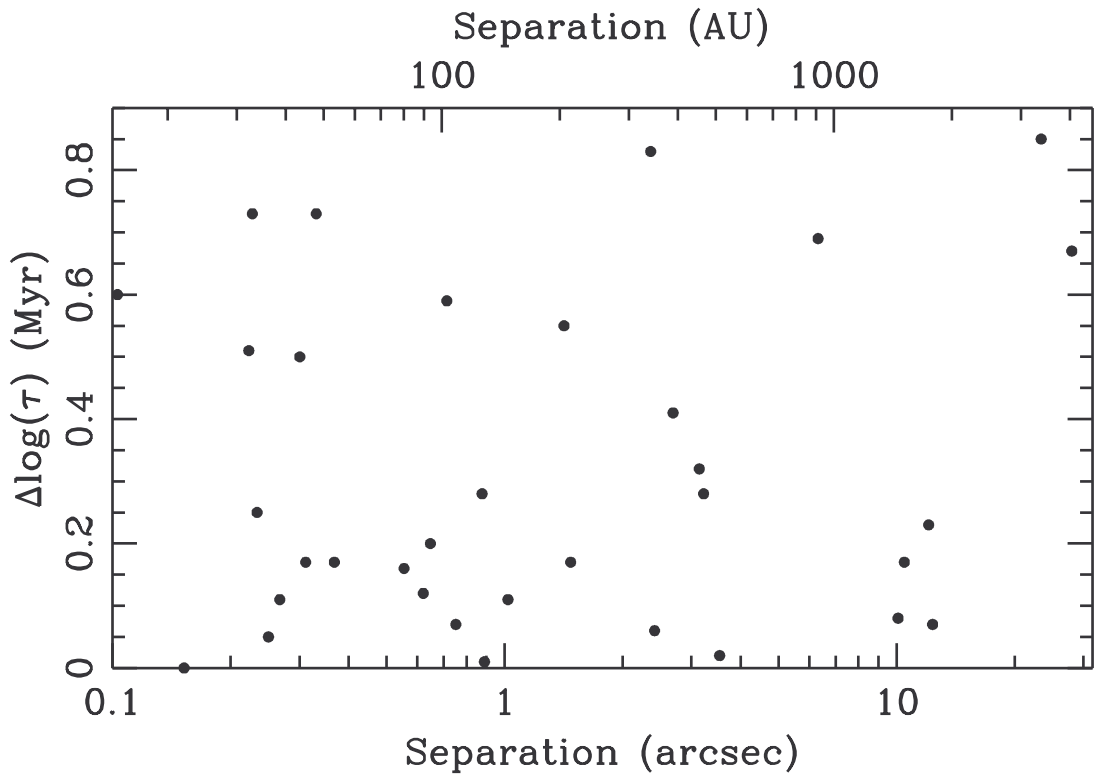
Figure 7.6 Difference in binary component age, $\Delta \log \tau$, as a function of binary separation. The standard deviations in $\Delta \log \tau$ for the inner and outer halves are 0.37 dex versus 0.42 dex (for the full set) and 0.14 dex versus 0.18 dex (for the coeval subset); in both cases, the inner and outer halves are divided at 800 AU. This indicates that binary systems of all separations are similarly coeval.
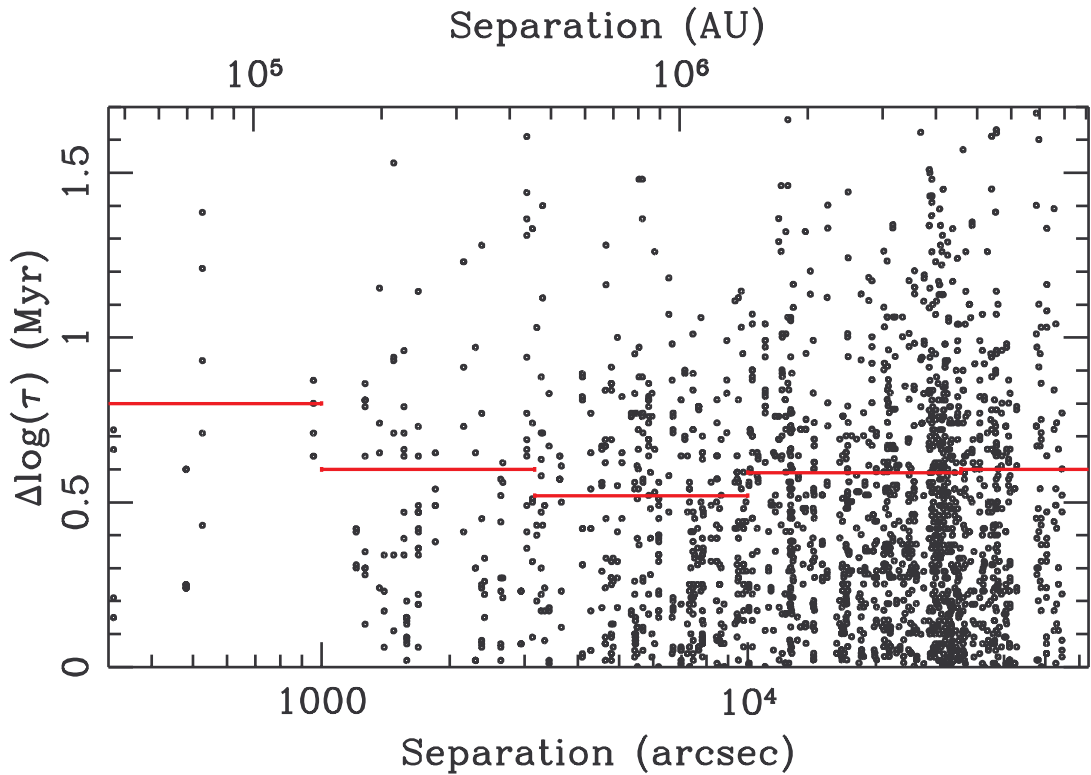
Figure 7.7 Difference in age as a function of (large-scale) separation for all possible pairs of Taurus members among our binary sample. We also show the dispersion for all pairs in bins 0.5 dex wide (red lines). The sample is insufficient for testing coevality on scales smaller than $\sim 1000''$ (0.7 pc), but all pairs on larger spatial scales have a dispersion of ~ 0.6 dex, the overall value of Taurus. This indicates that the coevality seen for binary systems is limited to smaller spatial scales, and perhaps only to binary systems themselves.

tions or disparate masses) appear similarly coeval on average. Conversely, unbound pairs of stars that are only modestly separated (~ 1 pc) show the full age dispersion of the association. These trends strongly indicate that binary coevality is a natural result of the binary formation process itself, not a reflection of any trend for star formation to occur simultaneously within larger regions of the natal molecular cloud.

7.6   The Single Stars in Taurus

The single stars of Taurus provide a useful check on the validity of our results, as well as providing their own constraints on its star formation history. In this section,

we compile a sample of all stars which have a significant probability of being single (based on nondetections with one or more high-resolution imaging techniques). We then place these single stars on an HR diagram and estimate their ages and masses. Finally, we investigate the dependence of apparent age on stellar mass and on location within the association.

7.6.1   Sample

We list our sample of apparently single stars in Table 7.3, including all of the references for our adopted parameters (singleness, spectral type, and extinction). We based our sample on the compilation of all Taurus members that we originally described in Kraus & Hillenbrand 2007a), and then we omitted all stars that did not have at least one observation at high angular resolution. We then searched the literature for spectral types, requiring uncertainties of ≤ 1 subclass for spectral types $>$K0 and ≤ 2 subclasses for earlier-type stars.

Most stars have only been surveyed for multiplicity to a separation limit of 50-100 mas (7-15 AU), so close binary systems still contaminate this sample. However, we do not expect any mass-dependent systematic biases. The binary fraction drops significantly with declining primary mass (e.g., Kraus et al. 2006, 2008), but much of that drop is seen among the wider binary systems (e.g., Kraus & Hillenbrand 2009) that would have fallen outside our required sensitivity limit of $<$15-20 AU.

We inferred the fundamental properties of these stars (luminosity and temperature, then age and mass) using the methods described in Section 7.3. We list these properties in Table 7.3.

7.6.2   The Ages of Single Taurus Members

In Figure 7.8, we show the HR diagram for our sample of single Taurus members. The composition of our single-star sample is significantly different from our binary sample, featuring many high-mass (>1 $M_{\odot}$) and low-mass (<0.3 $M_{\odot}$) members, but few members with intermediate masses. This difference in composition is driven

largely by selection biases since few binaries at either extremum of mass have spatially resolved spectra. High-mass binaries in Taurus tend to be hierarchical multiples with additional components, while low-mass binaries were difficult to observe with spectroscopy before the recent advent of laser guide star AO. As a result, we must be very cautious in comparing the bulk properties of both samples.

We also note that many members fall below our designated lower edge of the Taurus sequence (the 5 Myr isochrone) and might have erroneously low luminosities. Most of these members have not been well-studied (e.g., ITG33a and I04301+2608), so we can not reject them with certainty, but their presence as extreme outliers in our plots invites skepticism. Most of the highest-mass members (SpT≤K3; $M > 1$ $M_\odot$) also fall systematically below the 1-2 Myr isochrone. Few of our binary sample members fall in this mass range, but those that do are either obviously erroneous (the HBC stars) or appear genuinely young. We have no satisfactory explanation for this discrepancy between the single stars and binary components since an error in our methods or in the underlying models should affect both populations equally, but the small number of high-mass stars in our binary sample suggests that the single-star sample might provide a more reliable indication of the true empirical isochrone.

In Figure 7.9, we show the model-derived age as a function of model-derived mass for our sample of single stars. Most stars seem to track the median age of Taurus, but as we noted above, the highest-mass stars (>1 $M_\odot$) appear systematically older. The brown dwarfs of Taurus ($M < 0.7$ $M_\odot$) have very uncertain ages, so it is difficult to determine when they formed in relation to the stars. This uncertainty is driven by the physics of brown dwarf contraction, as isochrones at ages of <10 Myr follow similar tracks in the HR diagram. If we only consider members with masses of $\sim$0.07-0.9 $M_\odot$, then the median age of Taurus is $\log(\tau) = 6.25 \pm 0.05$ yr (1.8 ± 0.2 Myr).

Finally, in Figure 7.10, we show the spatial distribution of our single-star sample on the sky, with the position of each star color-coded according to its age, as well as the mean age for the eastern subgroup, southern subgroup, and the eastern and western halves of the central filaments. The eastern subgroup appears $\sim 4\sigma$ older than the other subgroups (3.2 Myr, versus 1.4-1.9 Myr); if this age difference is genuine,

then it suggests that star formation occurred first in Auriga, then in the rest of the association. However, this apparent age difference could also be a three-dimensional projection effect; the difference of ∼0.25 dex in mean age could be explained if the distance to Auriga stars were ∼15-20% larger than the mean distance to Taurus (∼170 pc versus ∼145 pc). Otherwise, there is no significant trend in the ages of Taurus members, suggesting that global star formation proceeded nearly simultaneously (to within <0.3 Myr).

Table 7.3. Single Star Sample: Observed Properties

Name	RA	Dec	J	SpT	A_V	T_{eff}	M_{bol}	M	$\log(\tau)$	Refs
	(J2000)		(mag)		(mag)	(K)	(mag)	$(M_\odot)$	(yr)	
L06-01	4 08 07.82	28 07 28.0	12.444	M3.75±0.25	1	3305±35	8.18	$0.25^{+0.03}_{-0.03}$	$7.04^{+0.16}_{-0.17}$	1, 2
LkCa1	4 13 14.14	28 19 10.8	9.635	M4±0.5	0	3270±70	5.66	$0.26^{+0.13}_{-0.2}$	$5.7^{+0.28}_{-0.32}$	3, 4
Anon1	4 13 27.23	28 16 24.8	8.83	M0±1	3.6	3850±178	3.59	$0.65^{+0.04}_{-0.03}$	$5.13^{+0.2}_{-0.21}$	3, 5, 6
L04-01	4 14 11.88	28 11 53.5	13.159	M6.25±0.25	0.7	2960±28	9.08	$0.069^{+0.008}_{-0.006}$	$6.5^{+0.19}_{-0.18}$	1, 7
FMTau	4 14 13.58	28 12 49.2	10.333	M0±1	1.9	3850±178	5.56	$0.68^{+0.09}_{-0.08}$	$6.42^{+0.23}_{-0.24}$	3, 4, 6
FNTau	4 14 14.59	28 27 58.1	9.469	M5±0.5	1.4	3125±70	5.23	$-0.2^{+0.2}_{-1.1}$ a	$4.2^{+0.97}_{-22.11}$ a	3, 8
CWTau	4 14 17.00	28 10 57.8	9.557	K3±1	1.9	4730±155	4.6	$1^{+0.22}_{-0.07}$	$6.39^{+0.29}_{-0.21}$	3, 6, 8
CIDA-1	4 14 17.61	28 06 09.7	11.727	M5.5±0.5	3	3060±68	7.02	$0.02^{+0.15}_{-0.23}$	$4.4^{+1.8}_{-3.98}$	9, 10, 11
MHO-1	4 14 26.40	28 05 59.7	11.522	M2.5±0.5	5.7	3490±73	5.9	$0.49^{+0.07}_{-0.07}$	$6.3^{+0.2}_{-0.18}$	6, 10, 12
FPTau	4 14 47.31	26 46 26.4	9.893	M4±0.5	0.2	3270±70	5.85	$0.27^{+0.11}_{-0.18}$	$5.82^{+0.26}_{-0.31}$	3, 4
CXTau	4 14 47.86	26 48 11.0	9.867	M2.5±0.5	0.8	3490±73	5.59	$0.53^{+0.05}_{-0.07}$	$6.15^{+0.19}_{-0.18}$	3, 4
KPNO-Tau-1	4 15 14.71	28 00 09.6	15.102	M8.5±0.25	0.4	2555±78	11.13	$0.023^{+0.01}_{-0.006}$	$6.75^{+0.4}_{-1.36}$	13, 14, 15
L06-02	4 15 24.09	29 10 43.4	13.683	M7±0.25	2	2880±33	9.27	$0.053^{+0.006}_{-0.005}$	$6.31^{+0.26}_{-0.26}$	1, 2
L04-02	4 16 12.10	27 56 38.6	12.265	M4.75±0.25	2	3160±38	7.81	$0.181^{+0.022}_{-0.023}$	$6.55^{+0.11}_{-0.14}$	7, 16
L06-03	4 16 18.85	27 52 15.5	12.546	M6.25±0.25	1	2960±28	8.39	$0.08^{+0.008}_{-0.008}$	$6.18^{+0.16}_{-0.16}$	1, 2
L06-04	4 16 39.11	28 58 49.1	12.717	M5.5±0.25	2.8	3060±38	8.07	$0.13^{+0.02}_{-0.03}$	$6.44^{+0.12}_{-0.18}$	1, 2
CYTau	4 17 33.73	28 20 46.9	9.827	M1±0.5	0.1	3705±73	5.64	$0.61^{+0.04}_{-0.02}$	$6.35^{+0.2}_{-0.2}$	3, 8
KPNO-Tau-10	4 17 49.55	28 13 31.9	11.892	M5±0.25	0	3125±33	8.02	$0.154^{+0.021}_{-0.021}$	$6.55^{+0.11}_{-0.13}$	1, 14, 17
V410-Xray1	4 17 49.65	28 29 36.3	11.021	M3.75±0.25	0.9	3305±35	6.78	$0.29^{+0.03}_{-0.02}$	$6.36^{+0.16}_{-0.14}$	6, 10, 18
V410-Anon13	4 18 17.11	28 28 41.9	12.958	M6±0.5	3.8	2990±63	8.02	$0.09^{+0.03}_{-0.02}$	$6.12^{+0.31}_{-0.25}$	6, 12, 15
KPNO-Tau-11	4 18 30.31	27 43 20.8	11.887	M5.5±0.25	0	3060±38	8.01	$0.13^{+0.02}_{-0.03}$	$6.42^{+0.12}_{-0.17}$	1, 17
KPNO-Tau-2	4 18 51.16	28 14 33.2	13.923	M7.5±0.25	0.4	2795±45	9.96	$0.04^{+0.007}_{-0.005}$	$6.71^{+0.13}_{-0.67}$	13, 14, 15
HBC376	4 18 51.70	17 23 16.6	10.03	K7±1	0	4060±250	5.66	$0.79^{+0.1}_{-0.13}$	$6.63^{+0.27}_{-0.26}$	3, 4

Table 7.3 (cont'd)

Name	RA	Dec	J	SpT	A_V	T_{eff}	M_{bol}	M	$\log(\tau)$	Refs
	(J2000)		(mag)		(mag)	(K)	(mag)	($M_\odot$)	(yr)	
I04158+2805	4 18 58.14	28 12 23.5	13.776	M6±1	8.6	2990±123	7.5	$0.1^{+0.07}_{-0.04}$	$5.91^{+0.45}_{-0.88}$	10, 19
KPNO-Tau-12	4 19 01.27	28 02 48.7	16.307	M9±0.25	0.5	2400±75	12.31	$0.032^{+0.007}_{-0.01}$	$7.46^{+0.23}_{-0.28}$	15, 17
V410-Xray5a	4 19 01.98	28 22 33.2	11.993	M5.5±0.5	2.6	3060±68	7.41	$0.14^{+0.04}_{-0.12}$	$6.2^{+0.17}_{-1.88}$	6, 10, 12
BPTau	4 19 15.84	29 06 26.9	9.096	K7±1	0.5	4060±250	4.59	$0.73^{+0.09}_{-0.08}$	$5.94^{+0.25}_{-0.29}$	3, 5
L04-04	4 20 25.55	27 00 35.5	12.858	M5.25±0.25	2	3095±33	8.42	$0.123^{+0.018}_{-0.014}$	$6.62^{+0.11}_{-0.11}$	1, 7
J2-157	4 20 52.73	17 46 41.5	11.616	M5.5±0.5	0	3060±68	7.74	$0.14^{+0.03}_{-0.04}$	$6.32^{+0.17}_{-0.35}$	3, 10
CFHT-Tau-19	4 21 07.95	27 02 20.4	13.853	M5.25±0.25	7.3	3095±33	7.95	$0.145^{+0.02}_{-0.018}$	$6.46^{+0.12}_{-0.13}$	14, 16
L04-05	4 21 34.60	27 01 38.8	11.897	M5.5±0.25	1.8	3060±38	7.53	$0.14^{+0.02}_{-0.05}$	$6.24^{+0.13}_{-0.73}$	7, 16
CFHT-Tau-10	4 21 46.31	26 59 29.6	13.824	M5.75±0.25	2	3020±35	9.38	$0.084^{+0.012}_{-0.012}$	$6.88^{+0.45}_{-0.22}$	1, 2
L06-05	4 21 54.50	26 52 31.5	15.535	M8.5±0.25	1	2555±78	11.4	$0.027^{+0.012}_{-0.009}$	$7.09^{+0.23}_{-0.85}$	1, 2
DETau	4 21 55.64	27 55 06.1	9.179	M2±0.5	0.6	3560±70	4.93	$0.59^{+0.04}_{-0.01}$	$5.82^{+0.19}_{-0.2}$	3, 8
RYTau	4 21 57.40	28 26 35.5	7.155	K1±1	1.8	5080±175	2.09	$2.1^{+0.6}_{-0.6}$	$5.61^{+0.28}_{-0.35}$	3, 8
HD283572	4 21 58.84	28 18 06.6	7.419	G5±2	0.4	5770±98	2.54	$2^{+0.4}_{-0.2}$	$6.62^{+0.1}_{-0.25}$	3, 5
CFHT-Tau-14	4 22 16.44	25 49 11.8	13.056	M7.75±0.25	0.5	2750±43	9.06	$0.036^{+1.12}_{-0.006}$	$4.19^{+1.12}_{-2.14}$	1, 2, 14
CFHT-Tau-21	4 22 16.76	26 54 57.1	11.581	M1.5±0.25	3	3630±38	6.63	$0.58^{+0.02}_{-0.03}$	$6.91^{+0.18}_{-0.18}$	2, 16
L06-18	4 23 06.07	28 01 19.4	12.242	M6.25±0.25	0	2960±28	8.36	$0.08^{+0.008}_{-0.008}$	$6.17^{+0.16}_{-0.16}$	1, 20
CFHT-Tau-9	4 24 26.46	26 49 50.4	12.884	M5.75±0.25	0.5	3020±35	8.86	$0.087^{+0.012}_{-0.01}$	$6.57^{+0.21}_{-0.17}$	1, 2
IPTau	4 24 57.08	27 11 56.5	9.779	M0±1	0.2	3850±178	5.47	$0.68^{+0.08}_{-0.08}$	$6.37^{+0.23}_{-0.24}$	3, 5
KPNO-Tau-3	4 26 29.39	26 24 13.8	13.319	M6±0.25	1.6	2990±30	8.98	$0.077^{+0.009}_{-0.008}$	$6.55^{+0.17}_{-0.17}$	13, 15
KPNO-Tau-13	4 26 57.33	26 06 28.4	11.28	M5±0.25	2.5	3125±33	6.71	$0.12^{+0.08}_{-0.07}$	$5.84^{+0.31}_{-0.51}$	10, 17
HBC388	4 27 10.56	17 50 42.6	8.786	K1±1	0.1	5080±175	4.2	$1.42^{+0.12}_{-0.13}$	$6.63^{+0.24}_{-0.26}$	3, 5
KPNO-Tau-4	4 27 28.00	26 12 05.3	15.001	M9.5±0.25	2.5	2245±80	10.46	$-0.015^{+0.011a}_{-0.006}$	$3.45^{+1.41}_{-0.58}$	13, 14, 15
L06-08	4 29 00.68	27 55 03.3	14.016	M8.25±0.25	0	2630±578	10.16	$0.02^{+0.13}_{-0.17}$	$4.46^{+3.38}_{-16.38}$	1, 2

Table 7.3 (cont'd)

Name	RA	Dec	J	SpT	A_V	T_{eff}	M_{bol}	M	$\log(\tau)$	Refs
	(J2000)		(mag)		(mag)	(K)	(mag)	$(M_\odot)$	(yr)	
KPNO-Tau-5	4 29 45.68	26 30 46.8	12.636	M7.5±0.25	0	2795±45	8.78	$0.043^{+0.008}_{-0.006}$	$4.77^{+1}_{-1.44}$	13, 15
IQTau	4 29 51.56	26 06 44.9	9.419	M0.5±0.5	1.3	3775±73	4.87	$0.64^{+0.03}_{-0.02}$	$5.93^{+0.19}_{-0.18}$	3, 5
CFHT-Tau-20	4 29 59.51	24 33 07.9	11.68	M5±0.25	2.2	3125±33	7.19	$0.18^{+0.02}_{-0.04}$	$6.21^{+0.15}_{-0.23}$	2, 16
KPNO-Tau-6	4 30 07.24	26 08 20.8	14.999	M8.5±0.25	0.9	2555±78	10.9	$0.021^{+0.007}_{-0.007}$	$5.98^{+0.99}_{-1.92}$	13, 14, 15
CFHT-Tau-16	4 30 23.65	23 59 13.0	14.958	M8.25±0.25	0	2630±578	11.1	$0.03^{+0.12}_{-0.11}$	$7^{+1.37}_{-11.4}$	1, 2
KPNO-Tau-7	4 30 57.19	25 56 39.5	14.522	M8.25±0.25	0	2630±578	10.66	$0.03^{+0.12}_{-0.14}$	$6.55^{+1.53}_{-14.43}$	13, 15
JH56	4 31 14.44	27 10 18.0	9.704	M0.5±0.5	1.1	3775±73	5.21	$0.64^{+0.03}_{-0.03}$	$6.13^{+0.2}_{-0.19}$	3, 10
MHO-9	4 31 15.78	18 20 07.2	11.214	M5±0.5	2.2	3125±70	6.73	$0.1^{+0.1}_{-0.4}$	$5.86^{+0.34}_{-6.59}$	6, 9, 10
L06-10	4 31 19.07	23 35 04.7	13.507	M7.75±0.25	0.5	2750±43	9.51	$0.036^{+0.005}_{-0.005}$	$5.28^{+0.9}_{-1.61}$	1, 2
MHO-4	4 31 24.06	18 00 21.5	11.657	M7±0.5	1	2880±70	7.53	$0.07^{+0.03}_{-0.02}$	$5.19^{+0.65}_{-1.44}$	6, 9, 15
CFHT-Tau-13	4 31 26.69	27 03 18.8	14.83	M7.5±0.25	0.5	2795±45	10.84	$0.049^{+0.011}_{-0.01}$	$7.14^{+0.27}_{-0.21}$	1, 2
LkHa358	4 31 36.13	18 13 43.3	12.797	M5.5±0.5	13.5	3060±68	5.18	$-0.9^{+1}_{-0.5}$ [a]	$-9.28^{+14.39}_{-8.92}$ [a]	3, 6, 10
HLTau	4 31 38.44	18 13 57.7	10.62	K5±1	7.4	4350±265	4.25	$0.83^{+0.11}_{-0.1}$	$5.93^{+0.24}_{-0.25}$	8, 19
J1-665	4 31 58.44	25 43 29.9	10.589	M5±0.5	1	3125±70	6.45	$0.1^{+0.1}_{-0.6}$	$5.55^{+0.5}_{-9.46}$	3, 10
L06-11	4 32 03.29	25 28 07.8	11.716	M6.25±0.25	0	2960±28	7.84	$0.089^{+0.008}_{-0.008}$	$5.95^{+0.16}_{-0.15}$	1, 2
L1551-51	4 32 09.27	17 57 22.8	9.7	K7±1	0	4060±250	5.33	$0.76^{+0.11}_{-0.11}$	$6.42^{+0.25}_{-0.26}$	3, 4, 6
Haro6-13	4 32 15.41	24 28 59.7	11.241	M0±0.5	11.9	3850±90	3.72	$0.653^{+0.018}_{-0.017}$	$5.22^{+0.2}_{-0.2}$	8, 19
MHO-5	4 32 16.07	18 12 46.4	11.073	M7±0.5	0.1	2880±70	7.18	$0.07^{+0.03}_{-0.02}$	$4.97^{+0.75}_{-1.63}$	6, 9, 15
CFHT-Tau-7	4 32 17.86	24 22 15.0	11.542	M5.75±0.25	0	3020±35	7.65	$0.12^{+0.02}_{-0.03}$	$6.21^{+0.13}_{-0.98}$	2, 10
MHO-6	4 32 22.11	18 27 42.6	11.709	M4.75±0.25	0.9	3160±38	7.57	$0.191^{+0.021}_{-0.021}$	$6.46^{+0.14}_{-0.16}$	6, 10, 13
L06-12	4 32 23.29	24 03 01.3	12.335	M7.75±0.25	0	2750±43	8.48	$0.037^{+0.006}_{-0.006}$	$2.76^{+1.44}_{-2.87}$	1, 2
MHO-7	4 32 26.28	18 27 52.1	11.113	M5.25±0.25	0.4	3095±33	7.12	$0.15^{+0.03}_{-0.08}$	$6.12^{+0.16}_{-0.99}$	6, 10, 13
FYTau	4 32 30.58	24 19 57.3	9.982	K7±1	3.5	4060±250	4.65	$0.74^{+0.09}_{-0.09}$	$5.98^{+0.25}_{-0.29}$	3, 4

Table 7.3 (cont'd)

Name	RA	Dec	J	SpT	A_V	T_{eff}	M_{bol}	M	$\log(\tau)$	Refs
	(J2000)		(mag)		(mag)	(K)	(mag)	$(M_\odot)$	(yr)	
FZTau	4 32 31.76	24 20 03.0	9.897	M0±1	3.6	3850±178	4.67	$0.66^{+0.06}_{-0.05}$	$5.84^{+0.24}_{-0.2}$	8, 13, 21
L1551-55	4 32 43.73	18 02 56.3	10.158	K7±1	0.7	4060±250	5.6	$0.78^{+0.11}_{-0.12}$	$6.59^{+0.27}_{-0.26}$	3, 22
KPNO-Tau-14	4 33 07.81	26 16 06.6	11.909	M6±0.25	3.1	2990±30	7.17	$0.11^{+0.01}_{-0.07}$	$5.77^{+0.16}_{-2.31}$	15, 17
V830Tau	4 33 10.03	24 33 43.4	9.322	K7±1	0.3	4060±250	4.87	$0.74^{+0.1}_{-0.09}$	$6.12^{+0.26}_{-0.27}$	3, 5
I04303+2240	4 33 19.07	22 46 34.2	11.103	M0.5±1	11.7	3775±163	3.67	$0.64^{+0.03}_{-0.03}$	$5.2^{+0.18}_{-0.19}$	10, 19
GITau	4 33 34.06	24 21 17.0	9.338	K6±1	0.9	4350±265	4.78	$0.85^{+0.11}_{-0.1}$	$6.25^{+0.27}_{-0.25}$	3, 8
DLTau	4 33 39.06	25 20 38.2	9.63	K7±1	1.7	4060±250	4.79	$0.74^{+0.09}_{-0.09}$	$6.07^{+0.25}_{-0.28}$	3, 4, 23
L06-13	4 33 42.91	25 26 47.0	14.639	M8.75±0.25	0	2475±78	10.78	$0.014^{+0.006}_{-0.007}$	$5.74^{+0.33}_{-1.48}$	1, 2
DMTau	4 33 48.72	18 10 10.0	10.442	M1±0.5	0	3705±73	6.28	$0.63^{+0.05}_{-0.04}$	$6.76^{+0.2}_{-0.2}$	3, 4
CITau	4 33 52.00	22 50 30.2	9.483	K7±1	1.8	4060±250	4.62	$0.74^{+0.09}_{-0.08}$	$5.96^{+0.25}_{-0.29}$	3, 8
JH108	4 34 10.99	22 51 44.5	10.596	M1±0.5	1.5	3705±73	6.03	$0.62^{+0.05}_{-0.04}$	$6.6^{+0.2}_{-0.2}$	3, 24
CFHT-Tau-1	4 34 15.27	22 50 31.0	13.739	M7±0.25	3.1	2880±33	9.02	$0.055^{+0.006}_{-0.005}$	$6.14^{+0.25}_{-0.27}$	15, 25
AATau	4 34 55.42	24 28 53.2	9.437	K7±1	0.5	4060±250	4.93	$0.74^{+0.1}_{-0.09}$	$6.16^{+0.26}_{-0.27}$	3, 4
HOTau	4 35 20.20	22 32 14.6	11.201	M0.5±0.5	1.1	3775±73	6.69	$0.69^{+0.04}_{-0.06}$	$7.1^{+0.23}_{-0.22}$	3, 24
DNTau	4 35 27.37	24 14 58.9	9.135	M0±0.5	1.9	3850±90	4.37	$0.66^{+0.03}_{-0.03}$	$5.65^{+0.2}_{-0.2}$	5, 19
KPNO-Tau-8	4 35 41.84	22 34 11.6	12.945	M5.75±0.25	0.5	3020±35	8.92	$0.086^{+0.011}_{-0.01}$	$6.6^{+0.24}_{-0.17}$	13, 15
KPNO-Tau-9	4 35 51.43	22 49 11.9	15.475	M8.5±0.25	0	2555±78	11.62	$0.033^{+0.011}_{-0.013}$	$7.24^{+0.25}_{-0.43}$	13, 15
HPTau-G2	4 35 54.15	22 54 13.5	8.104	G0±2	2.1	6030±170	2.67	$1.83^{+0.07}_{-0.07}$	$6.75^{+0.04}_{-0.05}$	3, 4
CFHT-Tau-2	4 36 10.39	22 59 56.0	13.759	M7.5±0.25	2	2795±45	9.34	$0.041^{+0.007}_{-0.005}$	$5.68^{+0.63}_{-1.03}$	13, 15
LkCa14	4 36 19.09	25 42 59.0	9.34	M0±1	0	3850±178	5.1	$0.67^{+0.07}_{-0.06}$	$6.12^{+0.24}_{-0.22}$	3, 4
CFHT-Tau-3	4 36 38.94	22 58 11.9	13.727	M7.75±0.25	1	2750±43	9.59	$0.036^{+0.004}_{-0.005}$	$5.46^{+0.86}_{-1.53}$	13, 15
L04-07	4 38 00.84	25 58 57.2	11.537	M7.25±0.25	0.6	2840±43	7.51	$0.059^{+0.01}_{-0.01}$	$4.72^{+0.52}_{-1.82}$	7, 16
GMTau	4 38 21.34	26 09 13.7	12.802	M6.5±0.5	2	2935±55	8.38	$0.074^{+0.015}_{-0.013}$	$6.07^{+0.25}_{-0.38}$	9, 11, 15

Table 7.3 (cont'd)

Name	RA (J2000)	Dec	J (mag)	SpT	A_V (mag)	T_{eff} (K)	M_{bol} (mag)	M ($M_\odot$)	$\log(\tau)$ (yr)	Refs
DOTau	4 38 28.58	26 10 49.4	9.473	M0±1	2.6	3850±178	4.5	$0.66^{+0.06}_{-0.05}$	$5.73^{+0.23}_{-0.2}$	3, 8
CS9	4 39 01.60	23 36 03.0	11.335	M6±0.25	0	2990±30	7.45	$0.1^{+0.01}_{-0.03}$	$5.89^{+0.25}_{-1.02}$	1, 11, 26
CIDA-13	4 39 15.86	30 32 07.4	12.684	M3.5±0.5	0.4	3340±73	8.59	$0.25^{+0.05}_{-0.05}$	$7.31^{+0.22}_{-0.23}$	10, 27
LkCa15	4 39 17.80	22 21 03.5	9.423	K5±1	0.6	4350±265	4.93	$0.85^{+0.11}_{-0.1}$	$6.35^{+0.26}_{-0.26}$	3, 4
CFHT-Tau-4	4 39 47.48	26 01 40.8	12.172	M7±0.25	3	2880±33	7.48	$0.068^{+0.012}_{-0.007}$	$5.16^{+0.39}_{-0.36}$	13, 15, 25
I04370+2559	4 40 08.00	26 05 25.4	12.409	M4.75±0.25	10	3160±38	5.75	$-0.05^{+0.13a}_{-0.09}$	$5.24^{+0.35}_{-0.6}$	2, 10
I04385+2550	4 41 38.82	25 56 26.8	11.85	M0.5±0.5	10.2	3775±73	4.83	$0.64^{+0.03}_{-0.02}$	$5.91^{+0.19}_{-0.18}$	10, 19
CIDA-7	4 42 21.02	25 20 34.4	11.399	M4.75±0.25	1	3160±38	7.22	$0.199^{+0.021}_{-0.023}$	$6.29^{+0.16}_{-0.15}$	2, 10
DPTau	4 42 37.70	25 15 37.5	11	M0±1	6.3	3850±178	5.02	$0.67^{+0.07}_{-0.06}$	$6.07^{+0.24}_{-0.22}$	4, 19
GOTau	4 43 03.09	25 20 18.8	10.712	M0±1	1.2	3850±178	6.15	$0.72^{+0.09}_{-0.11}$	$6.81^{+0.26}_{-0.25}$	3, 4
L04-13	4 44 27.13	25 12 16.4	12.191	M7.25±0.25	0	2840±43	8.33	$0.054^{+0.008}_{-0.008}$	$5.37^{+0.41}_{-1.22}$	7, 16
DQTau	4 46 53.05	17 00 00.2	9.511	M0±1	1	3850±178	5	$0.67^{+0.07}_{-0.06}$	$6.06^{+0.24}_{-0.22}$	3, 4
DRTau	4 47 06.21	16 58 42.8	8.844	K7±1	3.2	4060±250	3.59	$0.7^{+0.09}_{-0.06}$	$5.29^{+0.32}_{-0.36}$	3, 5, 23
DSTau	4 47 48.59	29 25 11.2	9.466	K5±1	0.3	4350±265	5.06	$0.86^{+0.11}_{-0.11}$	$6.44^{+0.25}_{-0.26}$	3, 4
GMAur	4 55 10.98	30 21 59.5	9.343	K3±1	0.1	4730±155	4.88	$1.02^{+0.16}_{-0.08}$	$6.58^{+0.26}_{-0.23}$	3, 4
L04-14	4 55 23.33	30 27 36.6	13.066	M6.25±0.25	0	2960±28	9.19	$0.068^{+0.007}_{-0.006}$	$6.56^{+0.19}_{-0.19}$	1, 7
LkCa19	4 55 36.96	30 17 55.3	8.868	K0±2	0	5250±335	4.27	$1.35^{+0.19}_{-0.16}$	$6.84^{+0.27}_{-0.38}$	3, 4
L04-15	4 55 40.46	30 39 05.7	12.713	M5.25±0.25	0.3	3095±33	8.76	$0.11^{+0.015}_{-0.011}$	$6.72^{+0.22}_{-0.1}$	1, 7
L04-16	4 55 45.35	30 19 38.9	11.442	M4.75±0.25	0	3160±38	7.54	$0.192^{+0.02}_{-0.021}$	$6.44^{+0.14}_{-0.16}$	7, 16
L04-19	4 55 49.70	30 19 40.0	12.811	M6±0.25	0	2990±30	8.92	$0.078^{+0.009}_{-0.008}$	$6.52^{+0.17}_{-0.17}$	1, 7
L04-20	4 55 52.89	30 06 52.3	11.644	M5.25±0.25	0	3095±33	7.76	$0.152^{+0.019}_{-0.018}$	$6.4^{+0.12}_{-0.13}$	1, 7
L04-21	4 55 56.37	30 49 37.5	12.002	M5±0.25	0.4	3125±33	8.03	$0.154^{+0.021}_{-0.021}$	$6.56^{+0.11}_{-0.13}$	1, 7
SUAur	4 55 59.38	30 34 01.6	7.2	G2±2	0.9	5860±115	2.11	$2.3^{+0.3}_{-0.3}$	$6.39^{+0.19}_{-0.21}$	3, 8

7.7 The Coevality of Triple and Quadruple Systems

High-order multiple systems are a critical tool for constraining stellar evolutionary models. If these multiple systems form coevally, then they provide a simultaneous test of the models at three or more masses. This feature was exploited by White et al.(1999) to constrain models with the well-known quadruple system GG Tau and to infer the best set of models to use for low-mass stars (the Lyon models) as well as to establish the best temperature scale for young stars (Luhman et al. 2003). We now extend this analysis to a quadruple system (UZ Tau), a quadruple that is part of a sextuple system (V955 Tau + LkHa332/G2), three components each of two systems that are not yet completely characterized (FV Tau and V773 Tau), and three triple systems (FS Tau, V710 Tau, and HL Tau/XZ Tau), plus we replicate the analysis of White et al.(1999) for GG Tau to provide context.

As we show in Figure 7.11, all three of the quadruple systems appear to have consistent ages. The consistency of GG Tau is partly a result of its previous role in calibrating stellar models and temperature scales, but UZ Tau appears to be almost coeval and similarly consistent. Three components of V955 Tau + LkHa332/G2 also fall along the 1 Myr isochrone, but V955 Tau B has an inferred age of $\sim$3 Myr. This is $\sim 2\sigma$ away from a consistent age, but among 12 components, we would expect $\sim$0.6 outliers at $> 2\sigma$.

Dynamical masses are available in the literature for the UZ Tau Aab and GG Tau Aab pairs and can be compared to those inferred from the HR diagram. The consistency is mixed. Guilloteau et al.(1999) found from the circumbinary disk kinematics that the total system mass for GG Tau Aab is 1.28±0.07 $M_\odot$; the total mass predicted by theoretical models (1.37 $M_\odot$) agrees to within $\sim$7%. By contrast, Prato et al. (2002) reported dynamical masses for UZ Tau Aa and Ab of 1.02±0.06 $M_\odot$ and 0.29±0.03 $M_\odot$, while the masses predicted by theoretical models are 0.61 and 0.30 $M_\odot$. The secondary mass agrees very well, but the discrepancy in the primary mass is very puzzling because its position in the HR diagram is virtually identical to

Table 7.3 (cont'd)

Name	RA	Dec (J2000)	J (mag)	SpT	A_V (mag)	T_{eff} (K)	M_{bol} (mag)	M ($M_\odot$)	$\log(\tau)$ (yr)	Refs
L04-22	4 57 49.03	30 15 19.5	15.774	M9.25±0.25	0	2325±78	11.91	$0.016^{+0.011}_{-0.005}$	$6.54^{+0.76}_{-0.55}$	1, 7
V836Tau	5 03 06.60	25 23 19.7	9.915	K7±1	1.7	4060±250	5.08	$0.75^{+0.1}_{-0.1}$	$6.26^{+0.26}_{-0.26}$	4, 19
CIDA-8	5 04 41.40	25 09 54.4	10.917	M3.5±0.5	3	3340±73	6.09	$0.36^{+0.06}_{-0.08}$	$6.13^{+0.17}_{-0.23}$	3, 10
CIDA-10	5 06 16.75	24 46 10.2	10.795	M4±0.5	0.5	3270±70	6.68	$0.27^{+0.04}_{-0.04}$	$6.25^{+0.19}_{-0.2}$	3, 10
RX05072+2437	5 07 12.07	24 37 16.4	10.137	K6±0.5	0.9	4350±133	5.56	$0.9^{+0.04}_{-0.06}$	$6.77^{+0.25}_{-0.22}$	10, 13, 27
CIDA-12	5 07 54.97	25 00 15.6	11.42	M4±0.5	0.8	3270±70	7.22	$0.26^{+0.04}_{-0.04}$	$6.51^{+0.19}_{-0.2}$	3, 10

[a]Some systems which sit extremely high or low in the HR diagram exceed the limits of the models and have nonphysical derived quantities (i.e., negative masses).

Note. — References: 1) Kraus et al.(in prep), 2) Luhman (2006), 3) Kenyon & Hartmann (1995), 4) Leinert et al.(1993), 5) Tanner et al.(2007), 6) Luhman (2000), 7) Luhman (2004), 8) Ghez et al.(1993), 9) White & Basri (2003), 10) White et al.(in prep), 11) Herczeg & Hillenbrand (2008), 12) Briceño et al.(1998), 13) Briceño et al.(2002), 14) Guieu et al.(2005), 15) Kraus et al.(2006), 16) Konopacky et al.(2007), 17) Luhman et al.(2003), 18) Strom & Strom (1994), 19) White & Hillenbrand (2004), 20) Luhman et al.(2006), 21) Hartigan et al.(1994), 22) Sartoretti et al.(1998), 23) Hartigan et al.(1995), 24) Simon et al.(1995), 25) Martín et al.(2001), 26) Slesnick et al.(2006), 27) Briceño et al.(1999).
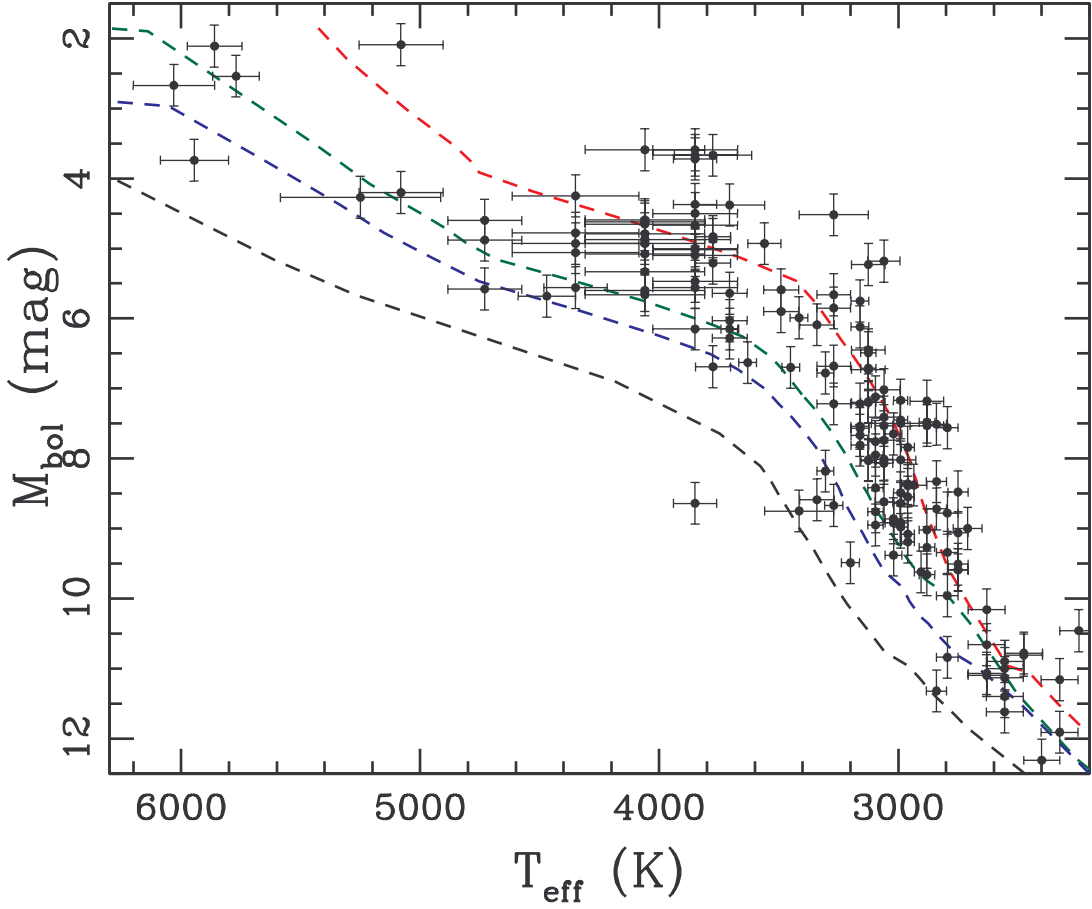
Figure 7.8 HR diagram for all members of our single star sample. The dashed lines denote isochrones at 1 Myr (red), 5 Myr (green), 10 Myr (blue), and 50 Myr (black). Most Taurus members fall along the 1-2 Myr isochrone, but many fall significantly below that level, perhaps due to the presence of an edge-on disk, undiscovered binary companion, erroneous observations. The highest-mass stars (>1 $M_\odot$) also fall systematically below the 1-2 Myr isochrone, suggesting either that the models might not be calibrated correctly in this regime or that these stars formed earlier in Taurus.
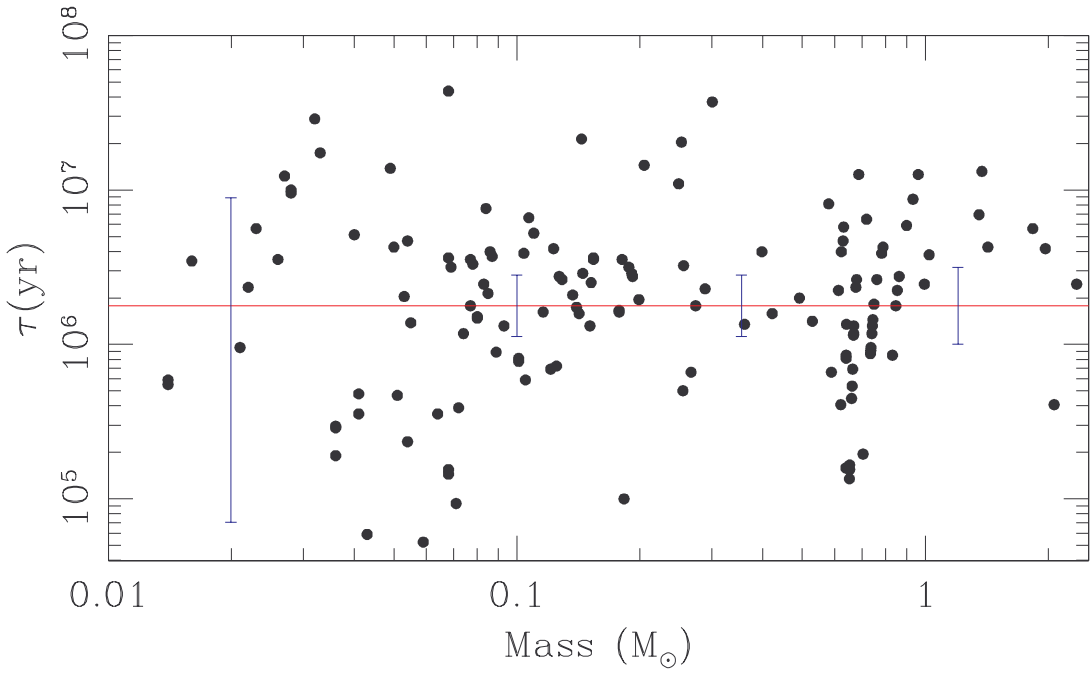
Figure 7.9 Age as a function of mass for all members of our single star sample. We also show the model-derived median age of Taurus (1.8 Myr; red line) as determined from our sample, plus representative error bars at four different masses (blue). The mass-dependent age of our sample tracks the overall median age except at the high-mass end ($>1\ M_\odot$), where stars appear older, and at the low-mass end ($<0.07\ M_\odot$), where the uncertainties become very large.
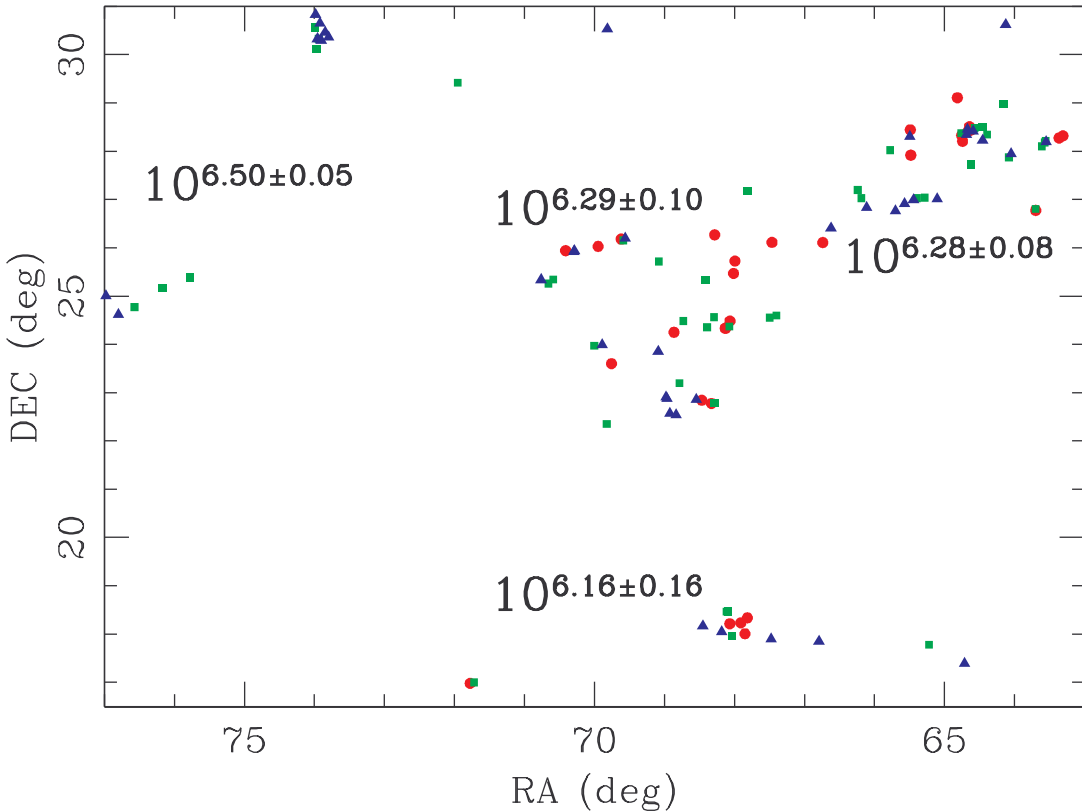
Figure 7.10 Spatial distribution for all members of our single star sample in the mass range that is well-calibrated (0.07-0.9 $M_\odot$), color-coded by age (red circles: <1 Myr; green squares: 1-3 Myr; blue triangles: >3 Myr). We also show the mean age for the eastern subgroup, southern subgroup, and the eastern and western halves of the core regions. The eastern subgroup appears $\sim 4\sigma$ older than the other subgroups (3.2 Myr, versus 1.4-1.9 Myr) and contains no stars with an apparent age of <1 Myr, but otherwise there is no apparent pattern in the ages of Taurus members.

that of GG Tau Ab, which has excellent consistency between observations and theory. Prato et al. explored the possible sources of this discrepancy in much greater detail, so we simply note its existence as proof that HR diagram analysis plays a critical, but incomplete role in constraining stellar evolutionary models. A full study of evolutionary models must include their dynamical masses (e.g., Schaefer et al. 2008), not just their temperatures and luminosities. Truly precise tests will also require direct measurement of radii (Stassun et al. 2008) rather than indirect estimates from the Stefan-Boltzmann law and the observed luminosity and temperature.

None of the three-component tests in our sample provide the same consistency seen among the quadruple systems, though as we described in Section 7.3, the two largest discrepancies are likely to be systematic. The edge-on disk host Haro 6-5B sits very far below the Taurus sequence, unlike FS Tau AB, while V710 Tau C might also be seen in scattered light. HL Tau is also seen in scattered light in the optical, but our inferred age based on its J magnitude seems consistent with that of XZ Tau AB, suggesting that the central star of HL Tau might dominate its luminosity in the NIR. FS Tau A and FS Tau B also appear moderately discrepant, sitting 1.5σ on either side of the 1 Myr isochrone. FV Tau Aa and FV Tau Ba have very consistent ages, but FV Tau Bb sits somewhat lower in the HR diagram; the only spatially resolved spectrum for FV Tau Bb is very noisy, so the apparent underluminosity could actually indicate that it has a later spectral type (M5.0-M5.5 rather than M3.5).

7.8 Summary

We have studied the binary population of the Taurus-Auriga association in order to quantify the frequency and degree of noncoevality in young binary systems. After identifying and rejecting the systems that are known to be affected by systematic errors (such as further multiplicity or obscuration by circumstellar material), we have found that the overall dispersion in the relative binary ages, $\Delta\log\tau$, is 0.40 dex, while random pairs of Taurus members only coeval to within 0.58 dex. This indicates that Taurus binaries are indeed more coeval than the association as a whole.
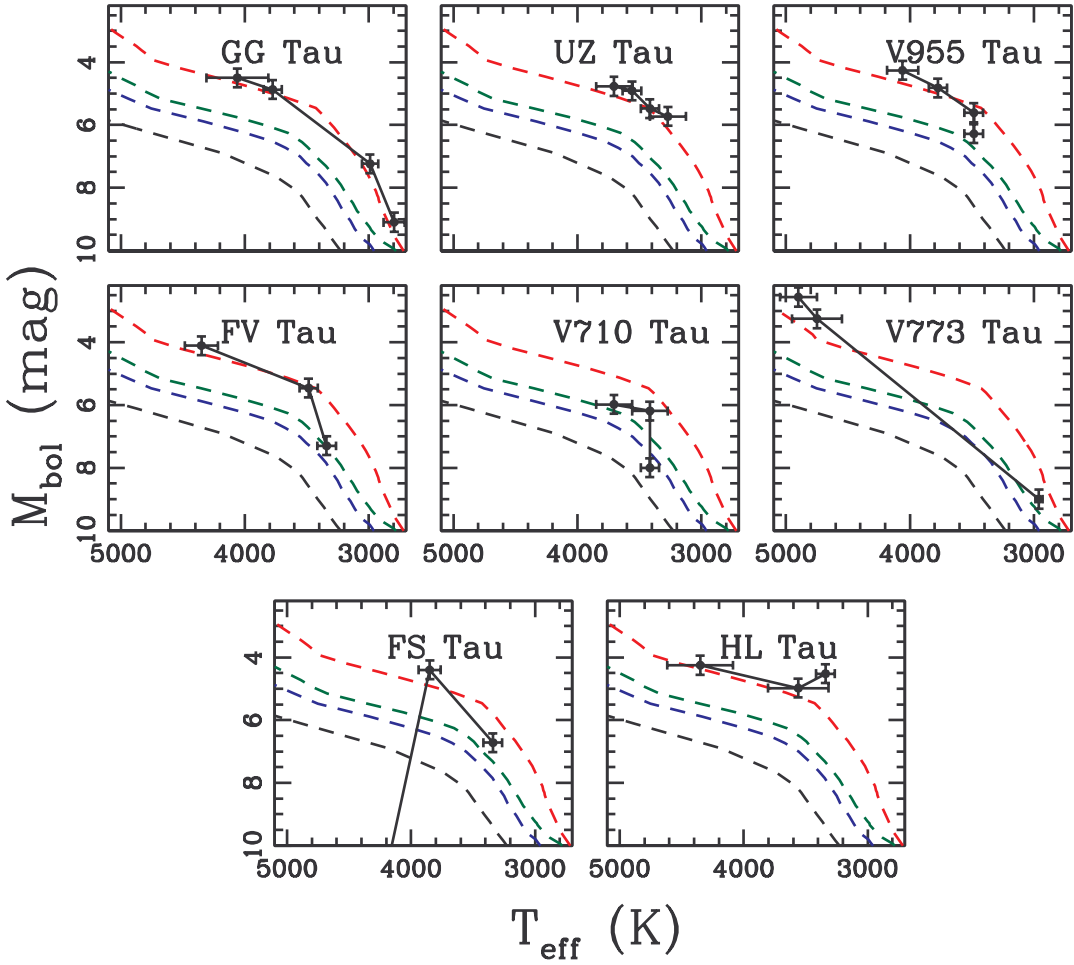
Figure 7.11 HR diagrams showing the components of eight hierarchical multiple systems. The four components of GG Tau and UZ Tau appear to be coeval, plus the components of V955 Tau might be coeval. However, as we describe in the text, the other five systems all have one or more components that disagree significantly. This could be due to errors in determining their luminosity (stars seen in scattered light only or which host a circumstellar disk) or temperature (incorrect spectral types).

Further inspection suggests that our sample is comprised of two populations, with $\sim 2/3$ appearing to be coeval binaries with a dispersion of $\sigma_{\Delta \log \tau} \sim 0.16$ dex and the other $\sim 1/3$ appearing to be systematically offset from coevality by ~ 0.6 dex. We suggest that this non-coeval population is comprised mainly of unrecognized hierarchical multiples, stars seen in scattered light, or stars with NIR disk excesses; identifying any truly non-coeval systems will require additional followup to rule out or correct for these explanations. The full age dispersion of our sample is ~ 1 dex, which suggests that a binary system tends to form in a very short period of time relative to the global star formation timescale for Taurus.

Finally, we found that the relative coevality of binary systems does not depend significantly on the system mass, mass ratio, or separation. However, any pair of Taurus members wider than $\sim 10'$ (~ 0.7 pc) shows the full age spread of the association. This suggests that the enhanced coevality is seen only for binary systems and not for neighboring stars that formed from separate protostellar cores. The apparent coevality of a large fraction of our sample is also an implicit endorsement of pre-main sequence isochrones; any mass-dependent error in ages would cause systems with unequal mass ratios to appear less coeval, and we see no such trend to within the uncertainties in our results.

Acknowledgements

Bibliography

Andrews, S. & Williams, J. 2005, ApJ, 631, 1134

Ballesteros-Paredes, J., Hartmann, L., & Vázquez-Semadeni, E. 1999, ApJ, 527, 285

Baraffe, I., Chabrier, G., Allard, F. & Hauschildt, P.H. 1998, A&A, 337, 403

Boden, A. et al. 2005, ApJ, 635, 442

Boden, A. et al. 2007, ApJ, 670, 1214

Briceño, C., Hartmann, L., Stauffer, J., & Martín, E. 1998, AJ, 115, 2074

Briceño, C., Calvet, N., Kenyon, S., & Hartmann, L. 1999, AJ, 118, 1354

Briceño, C. et al. 2002, ApJ, 580, 317

Carpenter, J., Hillenbrand, L., Skrutskie, M., & Meyer, M. 2002, AJ, 124, 1001

Carpenter, J., Mamajek, E., Hillenbrand, L., & Meyer, M. 2006, ApJ, 651, 49

Chabrier, G., Baraffe, I., Allard, F., & Hauschildt, P. 2000, ApJ, 542, 464

Chabrier, G., Gallardo, J., & Baraffe, I. 2007, A&A, 472, 17

Correia, S., Zinnecker, H., Ratzka, Th., & Sterzik, M. 2006, A&A, 459, 909

D'Antona, F. & Mazzitelli, I. 1997, MmSAI, 68, 807

Duchêne, G., Monin, J.-L., Bouvier, J., & Menard, F. 1999, A&A, 351, 954

Duchêne, G., Beust, H., Adjali, F., Konopacky, Q., & Ghez, A. 2006, A&A, 457, 9

Duquennoy, A. & Mayor, M. 1991, A&A, 248, 485

Elmegreen, B. 2000, ApJ, 530, 277

Fischer, D. & Marcy, G. 1992, ApJ, 396, 178

Furlan, E. et al. 2006, ApJS, 165, 568

Ghez, A., Neugebauer, G., & Matthews, K. 1993, AJ, 106, 2005

Guieu, S. et al. 2005, A&A, 446, 485

Guilloteau, S., Dutrey, A., & Simon, M. 1999, A&A, 348, 570

Hartigan, P., Strom, K., & Strom, S. 1994, ApJ, 427, 961

Hartigan, P., Edwards, S., & Ghandour, L. 1995, ApJ, 452, 736

Hartigan, P. & Kenyon, S. 2003, ApJ, 583, 334

Hartmann, L. et al. 2005, ApJ, 629, 881

Herbig, G. & Bell, K. 1988, Lick Obs. Bull., 1111, 1

Herczeg, G. & Hillenbrand, L. 2008, ApJ, 681, 594

Hillenbrand, L. & White, R. 2004, ApJ, 604, 741

Hillenbrand, L. 2009, arXiv:0812:1261

Indebetouw, R. et al. 2009, ApJ, 619. 931

Irwin, J. et al. 2007, MNRAS, 380, 541

Jensen, E., Mathieu, R., Donar, A., & Dullighan, A. 2004, ApJ, 600, 789

Kenyon, S. & Hartmann, L. 1995, ApJS, 101, 117

Konopacky, Q., Ghez, A., Rice, E., & Duchêne, G. 2007, ApJ, 663, 394

Kraus, A., White, R., & Hillenbrand, L. 2006, ApJ, 649, 306

Kraus, A., Ireland, M., Martinache, F., & Lloyd, J. 2008, ApJ, 679, 762

Kraus, A. & Hillenbrand, A. 2007a, ApJ, 662, 413

Kraus, A. & Hillenbrand, A. 2007b, ApJ, 664, 1167

Kraus, A. & Hillenbrand, L. 2008, ApJ, 686, 111

Kraus, A. & Hillenbrand, L. 2009, ApJ, in press

Krist, J. et al. 1995, BAAS, 187, 4413

Krist, J. et al. 1998, ApJ, 501, 841

Leggett, S. 1992, ApJS, 82, 351

Leggett, S., Allard, F., Berriman, G., Dahn, C., & Hauschildt, P. 1996, ApJS, 104, 117

Leinert, Ch. et al. 1993, A&A, 278, 129

Lestrade, J.-F. et al. 1999, A&A, 344, 1014

Liu, M., Najita, J., & Tokunaga, A. 2003, AJ, 585, 372

Loinard, L. et al. 2007, ApJ, 671, 546

Loinard, L., Torres, R., Mioduszewski, A., & Rodriguez, L. 2008, arXiv:0804.4016

Lombardi, M., Lada, C., & Alves, J. 2008, A&A, 489, 143

Luhman, K. 2000, ApJ, 544, 1044

Luhman, K., Stauffer, J., Muench, Al, Rieke, G., Lada, E., Bouvier, J., & Lada, C. 2003, ApJ, 593, 1093

Luhman, K. 2004, ApJ, 617, 1216

Luhman, K. 2006, ApJ, 645, 676

Luhman, K., Whitney, B., Meade, M., Babler, B., Indebetouw, R., Bracker, S., & Churchwell, E. 2006b, ApJ, 647, 1180

Mamajek, E. & Hillenbrand, L. 2008, ApJ, 687, 1264

Martín, E., Dougados, C., Magnier, E., Menard, F., Magazzu, A., Cuillandre, J., & Delfosse, X. 2001, ApJ, 561, 195

Masana, E., Jordi, C., & Ribas, I. 2006, A&A, 540, 735

Massarotti, A., Latham, D., Torres, G., Brown, R., & Oppenheimer, B. 2005, AJ, 129, 2294

Mathieu, R., Stassun, K., Basri, G., Jensen, E., Johns-Krull, C., Valenti, J., & Hartmann, L. 1997, AJ, 113, 1841

McCabe, C., Ghez, A., Prato, L., Duchêne, G., Fischer, R., & Telesco, C. 2006, ApJ, 636, 932

Meyer, M., Calvet, N., & Hillenbrand, L. 1997, ApJ, 114, 288

Monin, J.-L., Clarke, C., Prato, L., & McCabe, C. 2007, in Protostars and Planets V, ed. B. Reipurth, D. Jewitt, & K. Keil (Tucson: Univ. Arizona Press), 395

Mouschovias, T. 1976, ApJ, 206, 753

Perrin, G., Coude Du Foresto, V., Ridgway, S., Mariotti, J.-M., Traub, W., Carleton, N., & Lacasse, M. 1998, A&A, 331, 619

Prato, L., Simon, M., Mazeh, T., Zucker, S., & McLean, I. 2002b, ApJ, 579, 99

Richichi, A., Ragland, S., Fabbroni, L. 1998, A&A, 330, 578

Román-Zúñiga, C., Lada, C., Muench, A., & Alves, J. 2007, ApJ, 664, 357

Sartoretti, P., Brown, R., Latham, D., & Torres, G. 1998, A&A, 334, 592

Schaefer, G., Simon, M., Prato, L., & Barman, T. 2008, AJ, 135, 1659

Schlegel, D., Finkbeiner, D., & Davis, M. 1998, ApJ, 500, 525

Schmidt-Kaler, Th., "Physical Parameters of the Stars", Landolt-Bornstein Numerical Data and Functional Relationships in Science and Technology, New Series, Group VI, Volume 2b, Springer-Verlag, Berlin, 1982

Shu, F. 1977, ApJ, 214, 488

Shu, F., Adams, F., & Lizano, S. 1987, ARA&A, 25, 23

Simon, M. et al. 1995, ApJ, 443, 625

Skrutskie, M. et al. 2006, AJ, 131, 1163

Slesnick, C., Carpenter, J., Hillenbrand, L., & Mamajek, E. 2006, AJ, 132, 2665

Stapelfeldt, K., Krist, J., Menard, F., Bouvier, J., Padgett, D., & Burrows, C. 1998, ApJ, 502, 65

Steffen, A. et al. 2001, AJ, 122, 997

Stempels, H., Hebb, L., Stassun, K., Holtzman, J., Dunstone, N., Glowienka, L., & Frandsen, S. 2008, A&A, 481, 747

Stassun, K., Mathieu, R., & Valenti, J. 2007, ApJ, 664, 1154

Stassun, K., Mathieu, R., Cargile, P., Aarnio, A., Stempels, E., & Geller, A. 2008, Nature, 453, 1079

Strom, K. & Strom, S. 1994, ApJ, 424, 237

Tanner, A. et al. 2007, PASP, 119, 747

Torres, R., Loinard, L., Mioduszewski, A., & Rodriguez, L. 2007, ApJ, 671, 1813

van Belle, G. et al. 1999, AJ, 117, 521

White, R., Ghez, A., Reid, I.N., & Schultz, G. 1999, ApJ, 520, 811

White, R. & Ghez, A. 2001, ApJ, 556, 265

White, R. & Basri, G. 2003, ApJ, 582, 1109

White, R. & Hillenbrand, L. 2004, ApJ, 616, 998

Weingartner, J. & Draine, B. 2001, ApJ, 548, 296

Chapter 8

Lessons for the Future

Multiplicity studies encompass a tremendous number of observing techniques, target populations, and binary parameters. My thesis has concentrated on slices of this parameter space, partly to isolate regions of maximum interest and partly because those slices were easiest to measure or offered the best prospect for exclusivity. In this chapter, I synthesize my conclusions from all of these targeted studies into a set of observational "lessons" regarding multiple star formation. To preemptively summarize, these lessons are:

1. The primordial binary frequency is strongly mass dependent, matching the overall trend seen in the field. However, the detailed features of field binary systems represent a combination of primordial effects and the different levels of dynamical evolution that occur in different natal environments. The primordial frequency as a function of logarithmic separation is also nearly constant, suggesting that much of the frequency dependence is rooted in the absence of wide binary companions in low-mass systems.

2. The mass-dependent maximum separation of binary systems that is seen in the field appears to be a primordial feature, and the functional form of the mass dependence suggests that it is tied to a critical binding energy. The primordial separation distribution for solar-type stars is log-flat; the log-normal distribution in the field most likely is a consequence of mixing dynamically primordial stars (from sparse associations) with dynamically evolved stars that have had

the outermost binary companions stripped while still in their natal cluster. At masses $<0.3\ M_\odot$, characteristic binary separations decline with declining mass, but the exact form of the separation distribution is still uncertain.

3. The mass ratio distribution for solar-type stars is linear-flat, but similar-mass binary systems become increasingly more probable at primary masses of <0.3 $M_\odot$. There are some systems that do not follow this trend, but unidentified hierarchical multiplicity could explain their existence.

4. Dynamical interactions can not be used to explain any observed properties for young binary systems in the sparse associations that I have studied, especially for substellar binaries where there are few systems wider than $\sim$5–10 AU. However, the majority of stars are thought to form in denser clusters where the interaction timescale for wide binary systems is similar to the cluster disruption timescale, so most wide binaries seen in the field must come from sparse regions like Taurus and Upper Sco.

5. At intermediate separations (5–500 AU), I found a small number of companions around the stellar/substellar boundary. However, I found no companions less massive than $\sim$80–100 M_{Jup}, despite detection limits that in many cases extended as low as 7–10 M_{Jup}. My limit on the substellar companion frequency is still too weak for strong conclusions, but there is no evidence that the brown dwarf desert does not exist in this separation range.

6. My survey did not find any 2M1207b analogs, but my results suggest that they occur with a frequency of $<2\%$ at $\sim$90% confidence or $<1\%$ at $\sim$50% confidence. These limits depend somewhat on the functional form of their separation distribution and mass function, but I have constructed two plausible models that both yield similar limits.

7. My results show that at least $\sim$2/3 of all binary systems appear significantly more coeval ($\sigma_{\Delta\log(\tau)}\sim$0.15 dex) than randomly paired association members ($\sigma_{\Delta\log(\tau)}\sim$0.6 dex for any pairs wider than $\sim$1 pc). Many of the apparently

non-coeval pairs are probably affected by systematic errors such as unresolved multiplicity or the presence of a protoplanetary disk, so the true frequency of highly coeval pairs is probably much closer to unity. The age dispersion across Taurus as a whole appears to be a genuine feature, suggesting that star formation has been occuring for at least the past 3–5 Myr.

It is my hope that these lessons will guide future observational and theoretical studies of multiple star formation, and of star formation as a whole.

8.1 The Mass-Dependent Outcome of Multiple Star Formation

Observations in the field have demonstrated a clear mass dependence in the properties of binary systems; higher-mass binaries are more frequent, wider, and less likely to have equal-mass companions than their lower-mass counterparts. My results have confirmed that the overall trends are primordial outcomes of the formation process, but many of the specific characteristics differ, suggesting that part of the field population underwent evolution before leaving its natal environment.

My survey of solar-type stars in Chapter 5 confirmed the overall result found by earlier surveys: the binary frequency in sparse young associations is indeed significantly higher than for the field ($35^{+5}_{-4}\%$ just for separations of 6–435 AU, and likely $>70\%$ across all separations). However, the binary frequency does not seem to decline smoothly with mass. As I showed in Chapter 6, the binary frequency is $>60\%$ for stars extending down to $\sim 0.3\ M_\odot$; the frequency then seems to decline precipitously below this mass limit. My results in Chapter 4 show that the only strong mass-dependent trend among stars spanning masses of 0.3–3.0 $M_\odot$ is among the widest binary systems (>500 AU).

The binary frequency per logarithmic unit of separation does not show a strong dependence on mass, with a total frequency of $\sim 15\%$–20% per decade of separation. This constant frequency suggests an alternate view of binary formation, indicating

that perhaps there is a critical cloud size (or binding energy) required either for star formation or specifically for binary formation, but after this density limit is reached, binary formation is indeed independent of mass. I discuss the possible source of the observed M-a_{max} relation in the next section.

8.2 The Separation Distribution and Characteristic Length Scales

Binary systems in the field have been observed to follow a relation between the system mass M and the maximum possible binary separation a_{max}; as I discuss in Chapter 4, my sample largely follows this trend. The functional form of this trend is $a_{max} \propto M^2$ for masses <0.4 $M_\odot$ (Burgasser et al. 2003), so the envelope corresponds to a constant binding energy at all masses. As I discuss below, dynamical interactions do not seem to explain the critical binding energy for binary survival. However, the critical separation and mass ($\sim$200 AU for a pair of 0.2 $M_\odot$ stars) correspond to a circular Keplerian velocity that is roughly equivalent to the sound speed (c_s $\sim$200 m/s). Thus, the limit suggests that even if cores larger than the critical size can condense, the overdensities that fragment out to become binary companions (which likely find their original in transsonic or supersonic turbulence) might have sufficiently different velocities as to be unbound from each other.

The overall separation distribution for young solar-mass stars is significantly different from that observed in the field. Numerous surveys have suggested that the field distribution is unimodal and log-normal, with a mean at $\sim$30 AU. In contrast, my results in Chapters 2, 4, and 5 show that the separation distribution for solar-mass stars is approximately log-flat over at least 3.5 decades of separation (5–20,000 AU). As I will describe below, this distinction is a nuanced indication that dynamical interactions play a role in binary evolution; the stars that I am observing will escape to the field intact, but stars in dense, gravitationally bound clusters would have a higher probability of undergoing at least one interaction before escaping to the field. The

log-normal separation distribution observed for the field thus indicates the relative contributions of stars from environments of different characteristic densities.

The uniformity of the separation distribution for solar-mass binaries is quite surprising; as I described in the introduction, binary formation should occur through very different processes at very large and very small separations. The presence of a discontinuity in binary properties near the expected transition point ($\sim$100 AU) would confirm this expectation. The lack of a discontinuity does not necessarily disprove the expectation, but it does argue that both modes yield similar results despite the very different evolutionary paths.

For wide ($>>$100 AU) binary systems that are expected to fragment during or just after freefall collapse, the semimajor axis of the binary system should depend on the characteristic size of the core when fragmentation occurred and the location within the core where the critical overdensity was reached. The rate of collapse along the rotational axis is determined only by the amount of thermal and turbulent support, and thus is independent of the rotational energy, while collapse along the equatorial plane would be opposed by rotational energy and would occur more slowly. Fragmentation should occur once a local overdensity is sufficiently flattened to become Jeans critical. The detailed results of this process should depend on the distribution of overdensities in a collapsing core, which in turn depends on the turbulent power spectrum on small scales. One possible experiment for theorists would be to invoke varying degrees of rotation and turbulence in order to replicate the log-flat distribution of radii at which overdensities become Jeans critical.

For close ($<$100 AU) binary systems that are expected to form via disk fragmentation, the semimajor axis should depend on the radius at which fragmentation occurs and the subsequent migration of the binary companion. The structure of these disks is still largely unconstrained, so detailed predictions regarding the radius of initial fragmentation are not possible. Any companion that forms via disk instability should be large enough to open a gap immediately, so subsequent migration should proceed via the Type II mechanism (Lin & Papaloizou 1985) and carry the companion inward. This suggests that binary companions must initially form at separations of $>$20 AU.

The migration timescale depends on the primary and companion masses (being much longer for similar-mass companions) so it will depend on the accretion history of the system. For example, if the mass ratio is ∼1:100, then the migration timescale in a disk which is massive (∼10 times the Minimum-Mass Solar Nebula) and has a viscosity parameter of $\alpha \sim 10^{-3}$ will be ∼10^5 yr at 1 AU and ∼5×10^5 yr at 25 AU (Ida & Lin 2004). Increasing the mass ratio by a factor of 10 will lengthen the migration timescale by a factor of 10, effectively freezing the companion at the location where significant accretion occurred. This suggests that accretion history sets the final location of a companion, with the migration distance depending on the length of time before significant accretion occurs.

The form of the separation distribution for very low-mass stars and brown dwarfs is not firmly constrained; as I showed in Chapter 6, it could be a log-normal function with a single-parameter family of possible means and standard deviations. However, only a small part of the separation distribution is well studied, so an equally plausible form could be a log-flat distribution, like that seen for solar-type stars, that is truncated by the maximum separation limit that I discussed above. The first solution that should be pursued is to analyze RV data for similar-mass objects in order to constrain the inner wing of the separation distribution, breaking the degeneracy of the single-parameter family of solutions. It might be worthwhile to increase the sample size in order to further study the separation distribution at very low masses, but this (observationally expensive) option should only be pursued after an RV study casts further light on the topic.

8.3 The Mass Ratio Distribution and Implications for Accretion Histories

The mass ratio distribution that I have measured for solar-type stars differs from the distribution measured for field stars by Duquennoy & Mayor (1991), with a linear-flat distribution rather than one that rises toward low mass ratios. However, their result

relied on a substantial completeness correction; if their correction was an overestimate, then the results could be more consistent. Otherwise, the mass ratio distributions that I have seen in different mass ranges largely agree with the field. The flat mass ratio distribution inferred by Fischer & Marcy (1992) matches mine for the 0.3–0.5 $M_\odot$ regime, and the tendency toward equal-mass companions in the very low-mass regime also matches numerous field results (e.g., Allen 2007).

As with the the separation distribution, the similarity of the mass ratio distributions for very wide companions and very close companions is not necessarily expected. Fragmentation out of a collapsing cloud is a very different process from fragmentation in a disk. However, if disk fragmentation occurred promptly after the formation of the central protostar, then the total amount of mass remaining in the envelope could be similar in either case; if so, then one might expect the accretion histories to be similar.

The relation between the binary mass ratio distribution and expected accretion history has not been modeled in detail. For close pairs that share a common envelope, mass should preferentially accrete onto the companion since it is higher in the potential well; this trend is seen for moderately older binaries that are still accreting from a circumbinary disk (e.g., Jensen et al. 2007). If the companion initially fragments with negligible mass compared to the primary, then this trend predicts that the companion mass is equivalent to the total envelope mass left at the time of fragmentation; if the envelope was more massive than the primary, then competitive accretion would drive the mass ratio to unity and subsequent accretion would fall in similar amounts on both components. This accretion overflow might explain the population of binary "twins" among close binary systems.

For wider binary pairs, the cloud should split into two separate core/envelope systems. However, the details of this process are not clear. If all mass fell to whichever core was closer, then wide binary pairs should have higher-mass primaries and lower-mass secondaries than closer pairs. However, there is no evidence that this is the case. More detailed observations of Class 0 binary systems (e.g., Duchêne et al 2007) should cast light on this process.

The preponderance of similar-mass binaries in the very low-mass regime seems counterintuitive as compared to the model for close solar-type binaries; if the remaining envelope mass sets the companion mass, then low-mass systems (which feature sparse, low-mass envelopes) should have many companions that form as the envelope is being exhausted. However, if most disk fragmentation occurs early, then perhaps the majority of mass is still contained in the envelope at that epoch. Very low-mass binaries could then be subject to the accretion overflow that might explain the twin population for higher masses. These low-mass systems likely have their maximum disk mass at very early ages (when the envelope has not yet begun to deplete), so this explanation seems plausible, if largely untested. The fission process suggested by Goodwin et al.(2007), where H_2 dissociation softens the equation of state and encourages fragmentation, might also preferentially lead to similar mass ratios since the pre-fission core would achieve bilateral symmetry in the final stages of the freefall collapse process when dynamical timescales are short.

8.4   The Role of Dynamical Interactions in Binary Evolution

As I show in Chapter 2, the overall velocity dispersion in these regions is quite low ($\sim$200 m/s in Taurus, and $\sim$1 km/s in Upper Sco). Given the low stellar density, the corresponding interaction timescale is much longer than each region's lifetime. Even for binary systems with an interactional cross-section radius of 10^4 AU, the interaction timescale in Taurus is $>10^{12}$ yr. As such, dynamical interactions can not be used to explain any observed properties for young binary systems, especially for substellar binaries where there are few systems wider than $\sim$5–10 AU. All of the binary systems that I have studied should escape into the field population intact, and past theoretical modeling has already indicated that dynamical interactions are insigificant for field binaries with separations <20,000 AU (Weinberg et al. 1987), so all of my targets should have analogs in the field population.

My results do not necessarily indicate that dynamical interactions are unimportant in shaping the total binary population of the Milky Way field. Most of the binary systems that I have observed are in sparse associations that will disintegrate promptly, merging with the field population in the very near future. However, the majority of stars are thought to form in denser clusters (e.g., Lada & Lada 2003) where the interaction timescale for wide binary systems is similar to the cluster disruption timescale; the same 10^4 AU binary system would have an interaction timescale of $\sim 10^6$ AU in the core of the ONC, and so it should have already been disrupted. In fact, multiplicity surveys of the ONC suggest that the binary population at separations of >200 AU has been destroyed within the ~ 1–2 Myr since most stars have formed (Reipurth et al. 2007).

As I discussed above, this trend indicates that the separation distribution seen in the field is a composite of all possible star-formation modes, weighted by the cluster mass function (i.e., the number of stars that form in each mode). If the cluster mass function is relatively flat, then the field could contain as many stars that formed in Westerlund 1 analogs as in Taurus analogs, and the binary population among those stars would have suffered severe dynamical stripping before it joined the field. A future goal for theorists should be to decompose the field binary population into its component eigenpopulations, directly constraining the historical cluster mass function of the Milky Way; a preliminary attempt at this by Patience et al. (2002) has suggested that $\sim 1/3$ of all stars form in Taurus analogs and the other $\sim 2/3$ form in dense clusters, but more recent binary surveys have yielded much more precise statistics for a variety of populations.

8.5 The Extent and Aridity of the Brown Dwarf Desert

The brown dwarf desert has been confirmed with little remaining ambiguity by radial velocity exoplanet searches (Grether & Lineweaver 2006), but the evidence at wider

separations is less clear and partly depends on the definition of a "desert" (Metchev & Hillenbrand 2009). Since migration is expected to play a role in both planet and binary formation at separations of <3–5 AU, the RV desert might say more about migration processes than about formation processes. The frequency of extremely low-mass binary companions to solar-mass stars offers a significant constraint on the binary formation process, and especially on the rate of fragmentation near the end of the envelope accretion phase, especially since companions with moderately higher masses are quite common.

As I described in Chapter 5, my survey results are still somewhat uncertain due to small number statistics and suffer from the same ambiguity as surveys for wider companions. At separations of 5–500 AU, I found a small number of companions around the stellar/substellar boundary. However, I found no companions less massive than $\sim$80–100 M_{Jup}, despite detection limits that in many cases extended as low as 7–10 M_{Jup}. An extension of the flat mass ratio distribution seen for higher-mass companions indicated that only 1–2 genuinely substellar companions were expected, but a factor of $\sim$2–4 increase in the sample size would yield a much stronger detection of the brown dwarf desert. Some of my ongoing observational programs are aimed at expanding the sample to this degree.

8.6 The Frequency and Properties of Planetary-Mass Companions

A very small population of apparently planetary-mass companions has been found around nearby young stars and brown dwarfs, indicating that companions with extremely low mass ratio can form in rare cases. These companions pose a significant challenge to existing models of planet and binary formation; their orbital radii are so large that the planet formation timescale (>100 Myr at 100 AU; Pollack et al. 1996) should be much longer than the typical protoplanetary disk dissipation timescale ($\sim$3–5 Myr; Haisch et al. 2001; Hernández et al. 2007; Currie et al. 2009). However,

their extreme mass ratios ($q <0.01$ for most, extending up to $q \sim 0.1$ for 2M1207b) should be extremely improbable if they are drawn from typical binary mass ratio distributions that I describe in Chapters 4, 5, and 6. The projected separation of 2M1207b (~ 50 AU; Chauvin et al. 2004) is also far wider than for most brown dwarf binaries.

My survey did not find any 2M1207b analogs, but my results suggest that they occur with a frequency of <2% at $\sim 90\%$ confidence or <1% at $\sim 50\%$ confidence. This limits depend somewhat on the functional form of their separation distribution and mass function, so I have derived my limits using two plausible mass functions: a Gaussian distribution around the opacity-limited minimum mass (inspired by binary formation models), and a power-law mass function with an upper cutoff (inspired by planet formation models). Both cases yield similar limits.

Given the extreme rarity of these companions, assembling a statistically significant sample will be a daunting challenge. However, as I and my collaborators will describe in followup work to my survey from Chapter 5, the frequency of wide planetary-mass companions to solar-type stars might be higher. We have already discovered two such companions in Upper Sco and are continuing our search in Taurus and Ophiuchus.

8.7 Binary Coevality and the Timescale for (Multiple) Star Formation

Some observations of low-mass eclipsing binaries have found apparently non-coeval pairs, though additional physics (like stellar activity and different magnetic field strengths) could make coeval pairs appear to have different ages (Stassun et al. 2007, 2008). This discrepancy can only be addressed with a large survey to determine if most binaries are truly coeval. The degree of coevality also places some constraints on the binary formation process, and age determinations can be useful in studying the overall star formation history of a region as well.

In Chapter 7, I inferred the ages of a large sample of Taurus binaries based on

their positions in an HR diagram. My results show that at least $\sim 2/3$ of all binary systems appear significantly more coeval ($\sigma_{\Delta\log(\tau)} \sim 0.15$ dex) than randomly paired association members ($\sigma_{\Delta\log(\tau)} \sim 0.6$ dex for any pairs wider than ~ 1 pc). Many of the apparently non-coeval pairs are probably affected by systematic errors such as unresolved multiplicity or the presence of a protoplanetary disk, so the true frequency of highly coeval pairs is probably much closer to unity. At the median age of Taurus, the observed scatter corresponds to an age spread within binary systems of <0.7 Myr. However, this scatter includes all remaining observational errors; even systems younger than ~ 1 Myr show a similar spread in logarithmic age, so the underlying genuine age spread for binary systems (and hence the characteristic duration of stellar assembly) is almost certainly <0.3 Myr.

Since binary systems appear significantly more coeval than random pairs of association members, the random uncertainties in ages are most likely less than the binary age spread. If so, the high scatter across the entire association must indicate a genuine age spread and not an observed uncertainty, and thus star formation must have occurred for at least the past 3–5 Myr. This large age spread suggests that the quicker star formation rate of the turbulent fragmentation models might not be relevant, though updated versions that incorporate magnetic fields decrease the star formation efficiency and could extend the total star-forming lifetime of clouds to match my results. The ages of single stars support the existence of a genuine age spread. Members at the eastern edge of Taurus appear systematically older than at the western edge, indicating that star formation might have begun at the east and spread westward. This trend matches the ongoing star formation in the Pipe Nebula (Lada et al. 2008), where young stars have already formed at one tip, but the remainder of the cloud consists of starless cores. This intriguing similarity suggests that the Pipe Nebula and Taurus might be close analogs, but merely separated in age by ~ 3–5 Myr.

Finally, since many of my targets were drawn from surveys in the literature, the shape of the age distribution could be biased by the selection processes of those surveys. However, a future program to study a uniform sample of all binary systems

might offer the first robust measurement of the star formation history in a star-forming region.

Bibliography

Allen, P. 2007, ApJ, 668, 492

Burgasser, A. et al. 2003, ApJ, 125, 850

Chauvin, G., Lagrange, A., Dumas, C., Zuckerman, B., Mouillet, D., Song, I., Beuzit, J., & Lowrance, P. 2004, A&A, 425, 29

Currie, T., Lada, C., Plavchan, P., Robitaille, T., Irwin, J., & Kenyon, S. 2009, ApJ, 698, 1

Duchêne, G., Bontemps, S., Bouvier, J., André, P., Djupvik, A., & Ghez, A. 2007, A&A, 476, 229

Duquennoy, A. & Mayor, M. 1991, A&A, 248, 485

Fischer, D. & Marcy, G. 1993, ApJ, 396, 178

Goodwin, S. & Kroupa, P. 2007, in Protostars and Planets V, ed. B. Reipurth, D. Jewitt, & K. Keil (Tucson: Univ. Arizona Press), 133

Grether, D. & Lineweaver, C. 2006, ApJ, 640, 1051

Haisch, K., Lada, E., Piña, R., Telesco, C., & Lada, C. 2001, AJ, 121, 1512

Hernàndez, J. et al. 2007, ApJ, 662, 1067

Ida, S. & Lin, D. 2004, ApJ, 616, 567

Jensen, E. et al. 2007, AJ, 134, 241

Lada, C. & Lada, E. 2003, ARA&A, 41, 57

Lada, C., Muench, A., Rathborne, J., Alves, J., & Lombardi, M. 2008, ApJ, 672, 410

Lin, D. & Papaloizou, J. 1985, in Protostars and Planets II, ed. D. Black & M.S. Mathews (Tucson, AZ: Univ. Arizona Press), 981

Metchev, S. & Hillenbrand, L. 2009, ApJS, 181, 62

Patience, J. et al. 2002, AJ, 123, 1570

Pollack, J., Hubickyj, O., Bodenheimer, P., Lissauer, J., Podalak, M., & Greenzweig, Y. 1996, Icarus, 124, 62

Reipurth, B., Guimarães, M., Connelley, M., & Bally, J. 2007, AJ, 134, 2272

Stassun, K., Mathieu, R., & Valenti, J. 2007, ApJ, 664, 1154

Stassun, K., Mathieu, R., Cargile, P., Aarnio, A., Stempels, E., & Geller, A. 2008, Nature, 453, 1079

Weinberg, M., Shapiro, S., & Wasserman, I. 1987, ApJ, 312, 367

Chapter 9

The Path Forward

Over the course of my thesis, I have tested numerous aspects of the reigning ideas regarding (multiple) star formation. Many of these concepts have withstood my scrutiny, but I have also cast significant doubt on some and convincingly debunked several more. In any field, these changes would require theorists to evaluate the new state of knowledge and adjust their models accordingly. However, the statistical characterization of multiple star formation already has far outpaced the corresponding theoretical progress, so it worthwhile to consider which observational programs warrant further effort or should be allowed to lie entirely fallow.

In the low-mass binary regime, the major open question is whether a significant number of unidentified binary systems lie within the detection limits of direct imaging. Some progress could be made with larger imaging samples, especially using new techniques like aperture-masking interferometry that increase the effective resolution of the telescope. However, it seems preferable to approach this unexplored parameter space from the inside out, using large radial velocity surveys. Radial velocity surveys are subject to an outer working limit, whereas imaging surveys are subject to an inner working limit, so the degeneracy between higher frequencies and smaller mean separations that results from pure imaging constraints would be decisively broken by adding radial velocity constraints.

In the solar-mass binary regime, the inner working limits of direct-imaging surveys (especially those that exploit aperture-masking interferometry and/or concentrate on nearest regions) are now approaching the outer working limits of RV surveys. Once

the first generation of young-star RV planet-search programs release their results, solar-type binary formation in regions like Taurus will be fully characterized. However, there is no similarly complete study of denser clusters like the ONC, so it is unclear whether different environments yield different primordial binary parameters. Ongoing RV surveys and better exploitation of existing HST imaging data should significantly narrow this gap, especially for the close binary systems that should remain dynamically pristine and primordial even in very dense cluster environments.

Finally, for all masses of primary stars, the properties of extremely low-mass companions are still poorly constrained. The frequency, separation distribution, and mass function for wide planetary-mass companions (50–500 AU; 5–20 M_{Jup}) are almost completely unconstrained, and my results indicate that extremely large surveys will be required to amass a significant sample of companions. However, this type of program can be pursued using mid-sized telescopes (in the 4m and 6m classes) where large surveys are feasible, so there are excellent prospects for continued progress in studying this rare and intriguing class of objects.

Appendix A

The Provenance and Properties of Northern Sco-Cen

A.1 Proper Motions of Young Stars

Photometric criteria are usually insufficient for identifying members of stellar populations. As we show in Section A.3, near-infrared color cuts allow us to reject only $\sim$50-90% of background and foreground contaminants. Any further increase in the rejection rate of our survey would require either spectroscopic observations (to test for lithium or signatures of low surface gravity, both indicators of youth) or astrometric observations (to measure proper motions and test for kinematic association). Performing spectroscopic observations can be a resource-intensive undertaking, but astrometric data are now commonly available from all-sky surveys.

The largest astrometric database currently available is the USNO-B catalogue (Monet et al. 2003), which computed proper motions from the Palomar Observatory Sky Surveys of the mid-1950s and early 1980s. These observations were originally performed using wide-field photographic plates, and the USNO team digitally scanned these plates and computed photometry and astrometry for every source. The faint limit for photometry is $\sim R = 19 - 20$, and astrometry is available for most sources brighter than $R = 17 - 18$. Typical proper motion uncertainties are $\sim$2-3 mas yr^{-1} in each axis for bright stars and $<$10-15 mas yr^{-1} for faint stars.

Since the USNO-B catalogue is the result of an automated photometric/astrometric pipeline, individual measurements are subject to some uncertainties like distortions in the plate scale and centroid errors due to diffraction spikes from nearby bright stars. There are also some design issues which limit its utility. For example, objects with no proper motion information (such as from detection in only one epoch) are reported to have proper motions of 0 mas yr^{-1}, but all objects which have motions within 1σ of zero are also rounded to 0 mas yr^{-1}. Thus, it is impossible to determine whether a measurement of 0 mas yr^{-1} corresponds to a bad measurement or a genuine detection of small proper motion. Finally, most stars within $<10''$ of a brighter object do not have proper motion measurements available, so USNO-B astrometry is only potentially useful in studying wide companions.

In Figure A.1, we present a plot of the fraction of confirmed Upper Sco members as a function of magnitude which possess any USNO-B proper motion measurement (dashed line) and a measurement which lies within 15 mas yr^{-1} of the mean association value ($\sim3\sigma$ for bright sources; solid line). The maximum fraction of confirmed members which are identified as kinematic members is only $\sim2/3$, and this fraction declines rapidly for faint targets ($K > 12$). This suggests that using existing proper motions to select candidate binary companions would introduce significant incompleteness in the resulting statistics, so we have chosen to omit this data from our selection criteria. However, these proper motion measurements are useful as a test of our selection process, so we list the USNO-B proper motions for each candidate companion in Table 4.5. Those objects with consistent proper motions could be high-priority candidates for spectroscopic followup or more detailed astrometric followup. We also list the proper motions of each primary star in our sample in Table 4.2.

A.2 The Kinematics of Northern Sco-Cen

The young stars of the Sco-Cen complex are divided into three subgroups: Upper Scorpius, Upper Centaurus-Lupus, and Lower-Centaurus Crux. These three subgroups are spatially distinct on the sky, but there is some overlap along the border
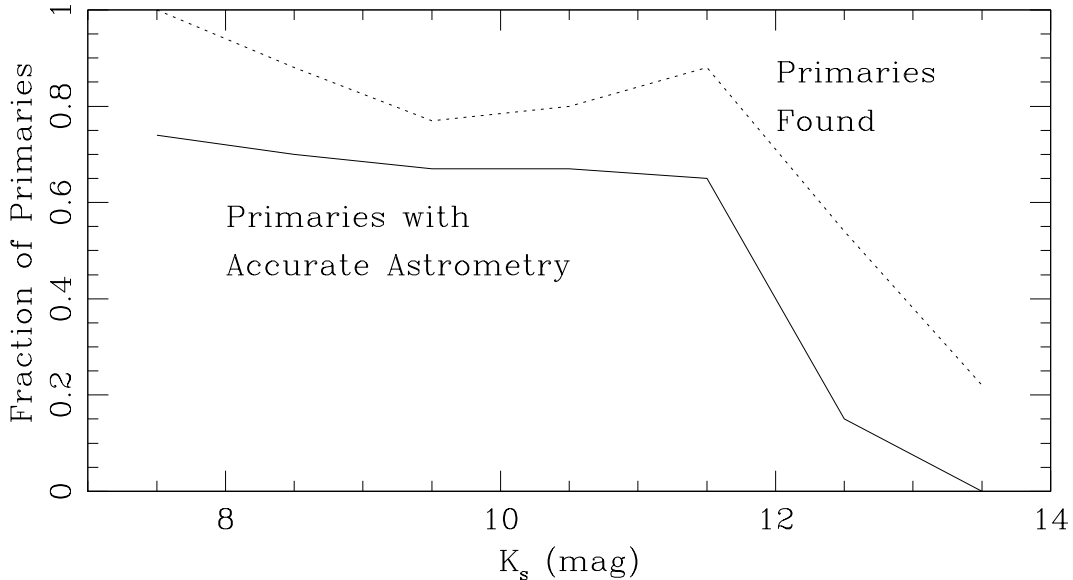
Figure A.1 A plot of the fraction of confirmed Upper Sco members as a function of magnitude which possess proper motion measurements in USNO-B (dashed line) and measurements which lie within 15 mas yr^{-1} of the mean association value (solid line). The maximum fraction of members which could be recovered by kinematic selection criteria is only $\sim 2/3$, and this declines rapidly for faint targets ($K > 12$).

between populations. This can lead to ambiguities in assigning stars to their appropriate population. For example, the stars of USco-B lie on the border between Upper Scorpius and Upper-Centaurus Lupus. It is not known which group they are associated with, or if they form another distinct population. The color-magnitude sequences for each subgroup are not distinct due to their similar age and distance, so photometry does not provide a reliable diagnostic of subgroup membership. However, studies of the high-mass stars of Sco-Cen (e.g., de Zeeuw et al. 1999) have found that the space velocities of each subgroup differ by ~ 2–3 km s^{-1}. This difference is not measurable in the proper motions of individual stars, but it might be detected as a difference in the mean proper motion for a population.

In Figure A.2, we present proper motion diagrams for USco members which have previously been assigned to USco-A or USco-B by Brandner et al.(1996) and Kohler et al.(2000). The mean proper motions for each subgroup are not directly comparable due to projection effects, but given the small radial velocity of USco-A (-4.6 km s^{-1}; de Zeeuw et al. 1999) and the locations of the association centers (16h, -22° for

USco-A; 15.5h, -31° for USco-B), the difference in proper motions should be no more than 2-3 mas yr^{-1} and the vectors should be almost parallel. We find that the proper motion of USco-B (33.2 mas yr^{-1}) is significantly higher than that of USco-A (22.3 mas yr^{-1}), and the vectors diverge by $\sim$15 degrees.

This result suggests not only that it is appropriate to consider USco-A and USco-B separately for statistical purposes, but that it might be prudent to question the relationship between USco-B and the rest of Sco-Cen. The difference in space velocities between USco-B and the other nearby Sco-Cen subgroups ($\sim$10 km s^{-1}) is far higher than that between the major subgroups. However, any further investigation is beyond the scope of this work.

We also conclude that the kinematic information lacks sufficient precision to distinguish the subgroup membership of individual stars and identify the boundary between the regions. Indeed, it is likely that there is no precise dividing line. The spatial distribution of these objects on the celestial sphere is only a projection of their three-dimensional distribution, so it is quite likely that the projected two-dimensional distributions overlap. This suggests that any difference between these two populations could be averaged out by cross-contamination. However, the distinct proper motions apparent in Figure A.3 imply that most of the stars have been classified in the appropriate group.

A.3 The Nature of Upper Scorpius B

The distinct binary properties observed for USco-A and USco-B suggest that it might be prudent to reconsider the nature of USco-B. The Sco-Cen complex consists primarily of three kinematically associated OB associations: Lower Centaurus-Crux, Upper Centaurus-Lupus, and Upper Scorpius. The ρ Oph dark cloud complex is also associated with Sco-Cen (specifically with USco), and the Lupus dark clouds could be kinematically associated, but the evidence of is not yet conclusive. LCC and UCL appear to be $\sim$5-10 Myr older than USco, which in turn is $\sim$5 Myr older than ρ Oph. This has been cited as evidence (e.g., Mamajek et al. 2002; Sartori et al. 2003) that
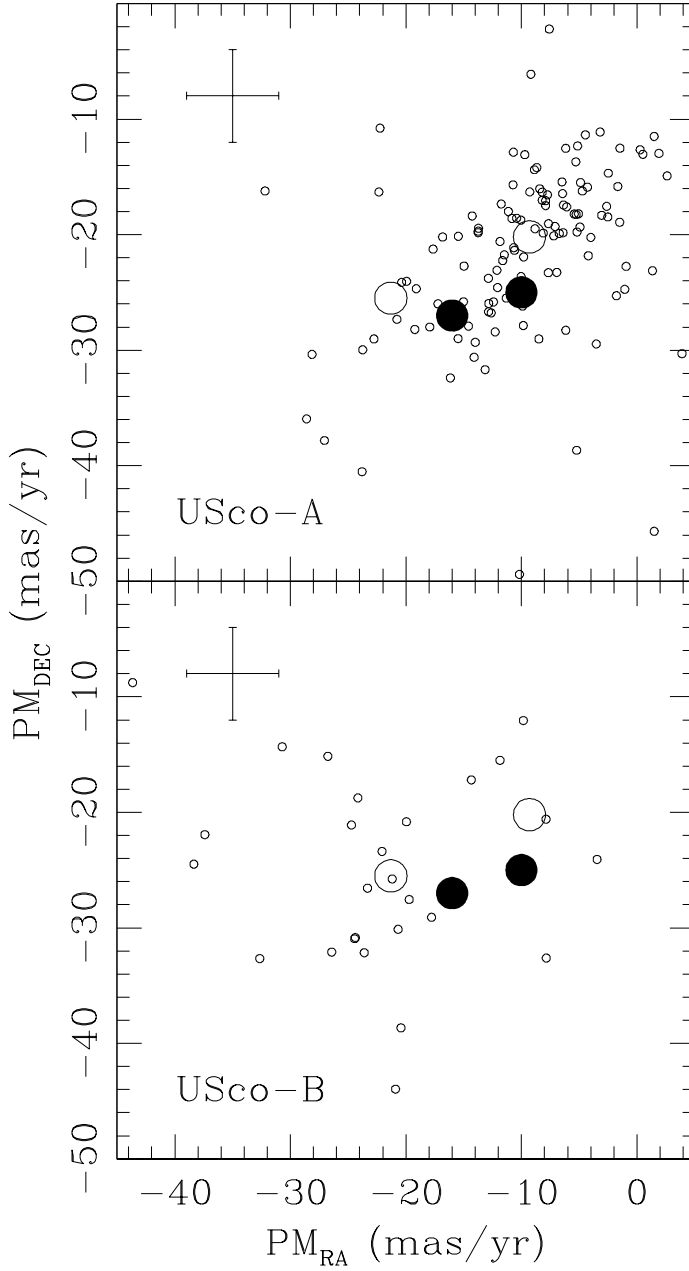
Figure A.2 Proper-motion diagrams for Sco-Cen members brighter than $K = 10$ which have been previously assigned to either USco-A or USco-B. The large filled circles denote the regional proper motions for Upper Sco (-10,-25) and UCL (-16,-27) as determined by HIPPARCOS for early-type members (de Zeeuw et al. 1999). The large open circles denote regional proper motions for USco-A (-9.3,-20.2) and USco-B (-21.3,-25.5) as determined from our data. The typical uncertainties for individual measurements are shown with error bars in the upper left corner; the scatter for USco-A appears to be consistent with these uncertainties, but the scatter for USco-B is significantly larger. The uncertainties in the mean values are $\sim$0.5 mas yr^{-1} for USco-A and $\sim$1.5 mas yr^{-1} for USco-B.

triggered star formation is occurring in Sco-Cen. The implication is that supernovae originating from the highest-mass members of UCL triggered star formation in USco, and in turn one or more supernovae in USco triggered star formation in ρ Oph. Since the ages of UCL and LCC are somewhat uncertain, it is unclear whether they are coeval or one triggered star formation in the other.

USco-B is located on the border between UCL and USco, in a region largely bereft of high-mass stars. Its age and distance are difficult to assess since there are no high-mass members which might possess HIPPARCOS distances, but the association's color-magnitude sequences lie slightly lower than USco-A and are consistent with the slightly larger distance and older age of UCL. However, its kinematics appear to be marginally inconsistent with the OB subgroups of Sco-Cen, with a spatial velocity which differs by $\sim$10 km s^{-1}. Finally, its binary properties are inconsistent with the one OB association which has been extensively studied (USco-A); no comparison is possible with UCL since there have been no large-scale surveys for new low-mass members.

The absence of high-mass stars and high wide binary frequency in USco-B are much more consistent with low-density T associations. This suggests that perhaps USco-B is an older analogue to the ρ Oph or Lupus clouds: an association consisting primarily of low-mass stars whose formation was triggered by supernovae in UCL, much as the current star formation in ρ Oph was triggered by supernovae in USco, but which is not directly associated. Unfortunately, it will be difficult to test this assertion. Any primordial gas in USco-B has been dispersed, either consumed in star formation or swept away by supernovae and stellar winds, so it only consists of an unbound association of pre-main-sequence stars. The low galactic latitude of USco-B also results in significant contamination from background stars, which will confuse any photometric surveys that attempt to identify these stellar members of the association.

Bibliography

Brandner, W. et al. 1996, A&A, 307, 121

de Zeeuw, P. et al. 1999, AJ, 117, 354

Kohler, R. et al. 2000, A&A, 356, 541

Mamajek, E., Meyer, M., & Liebert, J. 2002, AJ, 124, 1670

Monet, D. et al. 2003, AJ, 125, 984

Sartori, M. et al. 2003, A&A, 404, 913

Appendix B

A Model for Star Counts in the K Band

Abstract

I describe an updated version of the Milky Way models of Bahcall & Soneira (1980) that is suitable for predicting source counts as a function of apparent magnitude in the K band, $N(K)$, for an arbitrary location on the sky.

B.1 Introduction

The use of star count models was pioneered by Bahcall & Soneira (1980) in order to study the structure of the Milky Way. Their procedure invoked a simple two-component model of the galaxy (composed of a disk and a spheroid) to characterize the density of stars as a function of position in the galaxy. The integrated luminosity function along any sightline through this distribution would then yield the number of stars as a function of magnitude for that location on the celestial sphere. The model has since been updated to include two disk components, the thin and thick disks (e.g., Gilmore & Reid 1983)), as well as separate components for the bulge and halo (e.g., Jackson et al. 2002).

Bahcall & Soneira originally used observational star counts in order to determine the scale heights and scale radii for each component of the galaxy. However, this process can also be inverted; given an adopted luminosity function and a set of scale

heights and scale radii, it is possible to predict the number of stars per magnitude for any arbitrary position on the sky. We have developed an updated version of the Bahcall & Soneira models in order to predict faint source counts in our K band observations, characterizing the rate of background star contamination.

B.2   An Updated Model

We adopted our K-band luminosity functions from several sources in the literature. We directly invoked the well-known K-band luminosity function for field giants as described by Mamon & Soneira (1982). The luminosity function for field dwarfs has only been measured in other filters, so we invoked the V-band luminosity function for A-K dwarfs from Reid et al. (2002), the J-band luminosity function for M0-M6 dwarfs from Reid et al. (2003), and the J-band luminosity function for M7-L8 dwarfs from Cruz et al. (2007). In each case, we used the magnitude-SpT relations of Kraus & Hillenbrand (2007) and the color-SpT relations of Bessell & Brett (1988) to calculate the corresponding K-band luminosity function.

The scale parameters for Milky Way structural distributions, and even the functional forms themselves, have been updated numerous times since Bahcall & Soneira derived their original estimates. We have chosen to characterize the two disk components using exponential scale heights and scale radii and the halo using a power-law scale exponent and an oblate axis ratio. We did not fit the bulge because its triaxial distribution is still somewhat uncertain and because all of our targets are $>20^o$ from the Galactic Center. Thus, the resulting functional form is:

$$\rho(R, Z) = \rho(R_\odot, 0) \times \left(\exp \left(\frac{R_\odot - R}{L_{thin}} - \frac{Z}{H_{thin}} \right) + f_{thick} \exp \left(\frac{R_\odot - R}{L_{thick}} - \frac{Z}{H_{thick}} \right) + \right.$$

$$f_{halo} \left(\frac{R_\odot}{\sqrt{R^2 + (Z/q)^2}} \right)^{n_{halo}}$$

where R and Z are cylindrical Galactocentric coordinates, $R_\odot$ is the solar Galactocentric radius, f_x denotes the normalized density of each component in the solar

neighborhood (relative to the thin disk), L_x denotes a scale radius, H_x denotes a scale height, q_{halo} is the oblate axis ratio for the halo, and n_{halo} is the power law exponent for the halo.

The parameters for the disks and halo were estimated most recently by Jurić et al.(2008), using positions and photometric distances for stars from the Sloan Digital Sky Survey to directly fit the three-dimensional distributions of stars. Based on the distribution of disk M dwarfs, they found that the two disk components have scale heights of $H_{thin} = 300$ pc and $H_{thick} = 900$ pc and corresponding scale radii of $L_{thin} = 2600$ pc and $L_{thick} = 3600$ pc; the normalized density of thick disk stars in the solar neighborhood is $f_{thick} = 0.12$. Based on the distribution of main-sequence turnoff stars, they found that the halo has an axis ratio of $q_{halo} = 0.64$, a radial power-law exponent of $n_{halo} = -2.8$, and a normalized local density of $f_{halo} = 5 \times 10^{-3}$.

However, we found from comparisons to 2MASS that the parameters of Jurić et al.(2008) yielded a radial gradient in thin disk density that was too steep, overestimating the density of thin disk stars toward the Galactic center and underestimating the density toward the Galactic anticenter. Based on observations at very high galactic latitudes, we found that their parameters also overestimated the number of thick disk stars. Older studies (e.g., Siegel et al. 2001; Chen et al. 2001) have found that a larger thin disk scale radius (similar to the thick disk, $\sim$3600 pc) and a lower fraction of thick disk stars in the solar neighborhood ($\sim$0.06) produce acceptable fits for other datasets. These values also fit our data, so we have adopted them instead.

Finally, we accounted for dust obscuration by assuming that the dust density approximately traces the thin disk; this result is roughly consistent with observations of nearby edge-on disk galaxies (e.g., Bianchi et al. 2007). The total integrated extinction along a sightline (in magnitudes) is then proportional to the total integrated dust density. We normalized the extinction by assuming that dust causes one magnitude of V band extinction per kiloparsec in the Solar neighborhood, (0.11 magnitude of K band extinction, based on the reddening law of Schlegel et al. 1998). All of our science targets are at intermediate galactic latitudes ($15^o < |b| < 30^o$), so the total effect is <0.5 mag in all cases.

We did not include the effect of residual molecular cloud material around our science targets because extinction measurements from the literature only include foreground obscuration, not background obscuration. The IRAS extinction maps of Schlegel et al.(1998) would provide rough estimates, but the obscuring material is usually patchy on scales smaller than the IRAS resolution, so any correction would be very uncertain. We prefer to overestimate source counts for all targets (a conservative error) rather than to risk underestimating source counts for some. This problem does not affect most Upper Sco members because its natal gas and dust has already dispersed.

B.3 Results

In Figure B.1, we plot the predicted K band source counts as a function of magnitude for five sightlines that correspond to nearby stellar populations. We find that the integrated density of all stars brighter than $K = 20$ varies quite significantly, from 48 arcmin^{-2} on the eastern edge of Upper Sco to 1.2 arcmin^{-2} in the middle of Coma Berenices. We also show the observed 2MASS source counts for a 1° field surrounding each sight line; in all cases, our predictions agree with 2MASS predictions down to its 10σ detection limit ($K = 14.3$). Finally, we also show the K band galaxy source counts as determined from numerous extragalactic surveys (e.g., Cimatti et al. 2002). Galaxies only contribute significantly in Upper Sco at $K > 21$, but they are a significant source of background contamination for lower-density fields (e.g., $K > 17$ in Taurus). However, the galaxy size-brightness relations of Trujillo et al.(2004) suggest that most galaxies in our brightness range ($K < 21$) have sizes of > 100 mas, so we can screen any galaxy that is sufficiently well detected to be obviously extended.

Bibliography

Bahcall, J. & Soneira, R. 1980, ApJ, 238, 17

Bessell, M. & Brett, J. 1988, PASP, 100, 1134
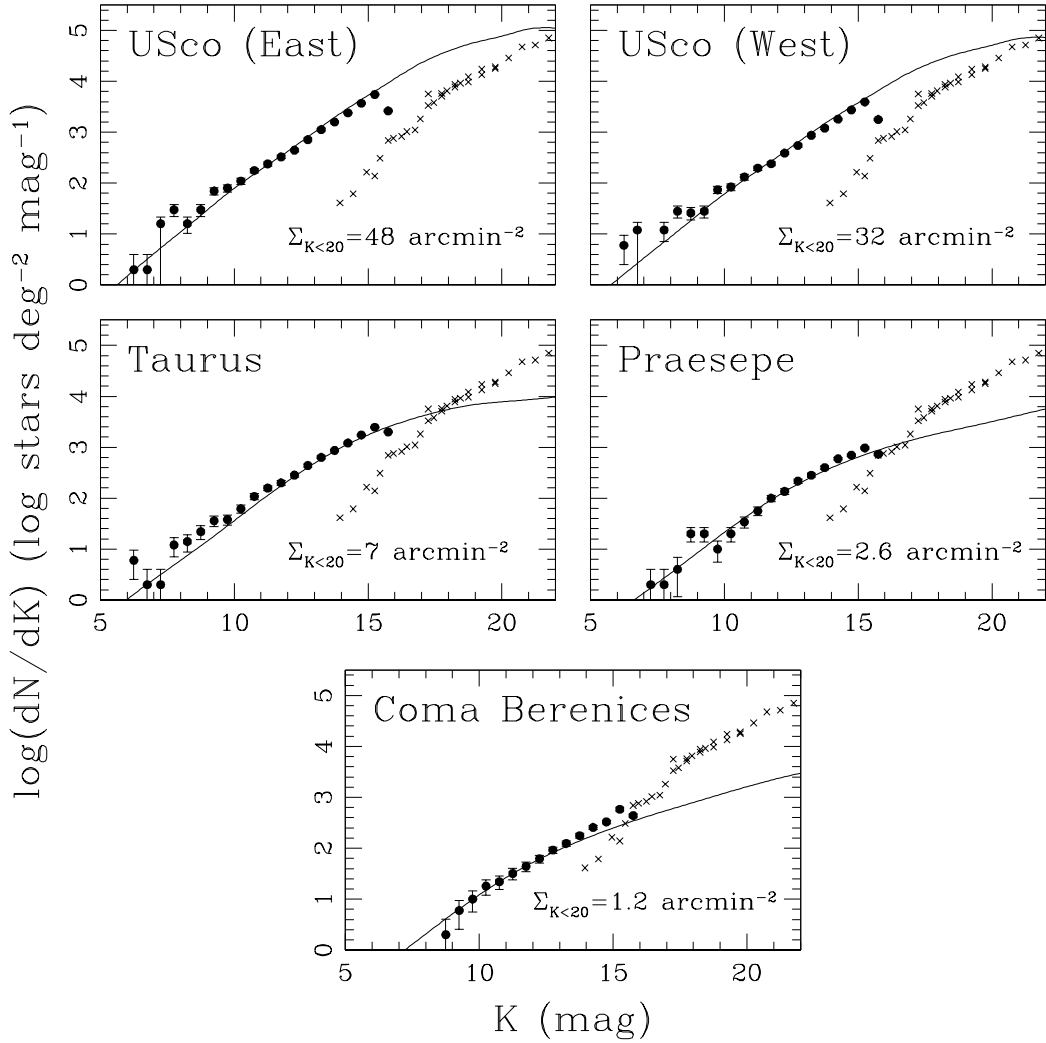
Figure B.1 K-band source counts for five sightlines corresponding to nearby clusters or associations: eastern Upper Sco (16:00:00, -22:00:00), western Upper Sco (16:20:00, -22:00:00), Taurus (4:30:00, +25:00:00), Praesepe (8:40:00, +22:00:00), and Coma Berenices (12:30:00, +26:00:00). The solid line shows the predicted source counts from our model, filled circles show the empirical source counts for that sightline from 2MASS, and crosses show galaxy source counts as summarized by Cimatti et al.(2003). Our model shows excellent agreement with 2MASS; the empirical source counts diverge at faint magnitudes for Praesepe and Coma Ber because background galaxies dominate over Milky Way stars at $K > 15$.

Bianchi, S. 2007, A&A, 471, 765

Chen, B. et al. 2001, ApJ, 553, 184

Cimatti, A. et al. 2002, A&A, 392, 395

Cruz, K. et al. 2007, AJ, 133, 439

Gilmore, G. & Reid, N. 1983, MNRAS, 202, 1025

Jackson, T., Ivezic̀, Z., & Knapp, G. 2002, MNRAS, 337, 749

Jurìc, M. et al. 2008, ApJ, 673, 864

Kraus, A. & Hillenbrand, L. 2007, AJ, 134, 2340

Mamon, G. & Soneira, R. 1982, ApJ, 255, 181

Reid, I.N., Gizis, J. & Hawley, S. 2002, AJ, 124, 2721

Reid, I.N. et al. 2003, AJ, 126, 3007

Schlegel, D., Finkbeiner, D., & Davis, M. 1998, ApJ, 500, 525

Siegel, M., Majewski, S., Reid, I., & Thompson, I. 2002, ApJ, 578, 151

Trujillo, I. et al. 2004, ApJ, 604, 521

Appendix C

The Stellar Populations of Praesepe and Coma Berenices

Abstract

We present the results of a stellar membership survey of the nearby open clusters Praesepe and Coma Berenices. We have combined archival survey data from the SDSS, 2MASS, USNOB1.0, and UCAC-2.0 surveys to compile proper motions and photometry for $\sim$5 million sources over 300 deg^2. Of these sources, 1010 stars in Praesepe and 98 stars in Coma Ber are identified as candidate members with probability >80%; 442 and 61 are identified as high-probability candidates for the first time. We estimate that this survey is >90% complete across a wide range of spectral types (F0 to M5 in Praesepe, F5 to M6 in Coma Ber). We have also investigated the stellar mass dependence of each cluster's mass and radius in order to quantify the role of mass segregation and tidal stripping in shaping the present-day mass function and spatial distribution of stars. Praesepe shows clear evidence of mass segregation across the full stellar mass range; Coma Ber does not show any clear trend, but low number statistics would mask a trend of the same magnitude as in Praesepe. The mass function for Praesepe ($\tau \sim$600 Myr; $M \sim$500 $M_\odot$) follows a power law consistent with that of the field present-day mass function, suggesting that any mass-dependent tidal stripping could have removed only the lowest-mass members (<0.15 $M_\odot$). Coma

Ber, which is younger but much less massive ($\tau \sim 400$ Myr; $M \sim 100~M_\odot$), follows a significantly shallower power law. This suggests that some tidal stripping has occurred, but the low-mass stellar population has not been strongly depleted down to the survey completeness limit ($\sim 0.12~M_\odot$).

C.1 Introduction

Star clusters are among the most powerful and versatile tools available to stellar astronomy. Nearby clusters serve as prototypical populations for studying many diverse topics of stellar astrophysics, including star formation, stellar structure, stellar multiplicity, and circumstellar processes like planet formation (e.g., Patience et al. 2002; Bouy et al. 2006; Muench et al. 2007; Stauffer et al. 2007; Siegler et al. 2007); star clusters are uniquely sensitive to the physics of these processes due to their uniform and well-constrained age, distance, and metallicity. Open clusters are also thought to be the birthplaces of most stars, so the formation, evolution, and disruption of clusters establish the environment of star formation and early stellar evolution. Two of the nearest open clusters are Praesepe and Coma Berenices. Praesepe is a rich ($N \sim 1000$ known or suspected members), intermediate age (~ 600 Myr) cluster at a distance of 170 pc (Hambly et al. 1995a), while Coma Ber is younger and closer (~ 400 Myr; 90 pc) and much sparser ($N \sim 150$; Casewell et al. 2006).

Praesepe has been the target of numerous photometric and astrometric membership surveys over the past century; part of the reason for its popularity is that its proper motion is relatively distinct from that of field stars (-36.5,-13.5 mas yr^{-1}), simplifying the identification of new members. Its high-mass stellar population was identified early in the last century by Klein-Wassink (1927), and subsequent surveys extended the cluster census to intermediate-mass stars (Artyukhina 1966; Jones & Cudworth 1983). The M dwarf stellar population was first identified by Jones & Stauffer (1991). A later survey by Hambly et al.(1995a) extended this work to a fainter limit and a larger fraction of the cluster, producing a cluster census that is still used for most applications (e.g., Allen & Strom 1995; Holland et al. 2000; Kafka

& Honeycutt 2006). There have been additional surveys to identify cluster members, but they have been prone to contamination from field stars (Adams et al. 2002) or based purely on photometry with no astrometric component (Pinfield et al. 1997; Chappelle et al. 2005).

Coma Ber, in contrast, has been largely neglected in surveys of nearby open clusters. The cluster would be an ideal population for many studies due to its proximity (second only to the Hyades) and intermediate age between the Pleiades (125 Myr) and Hyades or Praesepe ($\sim$600 Myr), but its members are difficult to distinguish from field stars because it has a proper motion (-11.5, -9.5 mas yr^{-1}) which is significantly lower than that of Praesepe. It is also a much sparser cluster than Praesepe, and its few members are projected over a much larger area of the sky. Its high-mass stellar population has been known for many decades (Trumpler 1938), but only a handful of additional members have been confirmed (Artyunkhin 1966; Argue & Kenworthy 1969; Bounatiro 1993; Odenkirchen et al. 1998); many candidate members have been identified, but a large fraction of them have been shown to be unrelated field stars (e.g., Jeffries 1999; Ford et al. 2001). One survey for low-mass stars was conducted recently by Casewell et al.(2006), who used 2MASS photometry and USNO-B1.0 astrometry to identify 60 candidate members extending well into the M dwarf regime ($\sim$0.30 $M_\odot$). This survey discovered many candidate members with spectral types of late G and early M, but as we will discuss later, significant contamination from field stars rendered it completely insensitive to K dwarf members and diluted its other discoveries with a significant number of nonmembers.

In this paper, we combine the photometric and astrometric results of several wide-field imaging surveys to compile a full stellar census of Praesepe and Coma Ber. This census is both wider and deeper than any previous proper motion survey, extending to near the substellar boundary. Our results for Praesepe allow us to fully characterize the structure and dynamical evolution of this prototypical cluster, while our results for Coma Ber unveil a new benchmark stellar population that is closer than any cluster except the Hyades and that fills a poorly-studied age range. In Section C.2, we describe the all-sky surveys that contribute to our cluster census, and in Section

C.3, we describe the photometric and astrometric analysis techniques that we used to identify new members. We summarize our new catalog of cluster members in Section C.4. Finally, in Section C.5, we analyze the structure and properties of each cluster.

C.2 Data Sources

In this survey, we worked with archival data from several publicly available surveys: SDSS, 2MASS, USNO-B1.0, and UCAC2. In each case, we extracted a portion of the source catalogue from the data access websites. We worked with circular areas of radius 7° centered on the core of each cluster (8h40m, $+20^o$ and 11h24m,$+26^o$, respectively); for both clusters, this radius is approximately twice the estimated tidal radius (Hambly et al. 1995a; Casewell et al. 2006).

C.2.1 SDSS

The Sloan Digital Sky Survey (SDSS; York et al. 2000) is an ongoing deep optical imaging and spectroscopic survey of the northern galactic cap. The most recent data release (DR5; Adelman-McCarthy et al. 2007) reported imaging results in five filters ($ugriz$) for 8000 deg^2, including the full areas of Praesepe and Coma Ber. The 10σ detection limits in each filter are $u = 22.0$, $g = 22.2$, $r = 22.2$, $i = 21.3$, and $z = 20.5$; the saturation limit in all filters is $m \sim 14$. The typical absolute astrometric accuracy is $\sim$45 mas RMS for sources brighter than $r = 20$, declining to 100 mas at $r = 22$ (Pier et al. 2003); absolute astrometry was calibrated with respect to stars from UCAC2, which is calibrated to the Inertial Coordinate Reference Frame (ICRS).

The default astrometry reported by the SDSS catalog is the r band measurement, not the average of all five filters. However, the residuals for each filter (with respect to the default value) are available, so we used these residuals to construct a weighted mean value for our analysis. We adopted a conservative saturation limit of $m \sim 15$ in all filters, even though the nominal saturation limit is $m \sim 14$, because we found that many photometric measurements were mildly saturated for $14 < m < 14.5$. We also neglect measurements which are flagged by the SDSS database as having one or

more saturated pixels. Finally, we removed all sources which did not have at least one measurement above the nominal 10σ detection limits. Any cluster members fainter than this limit will not have counterparts in other catalogs, and the presence of excess sources can complicate attempts to match counterparts between datasets.

C.2.2 USNO-B1.0

The USNO-B1.0 survey (USNOB; Monet et al. 2003) is a catalogue based on the digitization of photographic survey plates from five epochs. For fields in the north, including both Praesepe and Coma Ber, these plates are drawn from the two Palomar Observatory Sky Surveys, which observed the entire northern sky in the 1950s with photographic B and R plates and the 1990s with photographic B, R, and I plates; we follow standard USNOB nomenclature in designating these observations $B1$, $R1$, $B2$, $R2$, and $I2$.

The approximate detection limits of the USNOB catalog are $B \sim 20$, $R \sim 20$, and $I \sim 19$, and the observations saturate for stars brighter than $V \sim 11$. The typical astrometric accuracy at each epoch is ~ 120 mas, albeit with a significant systematic uncertainty (up to 200 mas) due to its uncertain calibration into the the ICRS via the unpublished USNO YS4.0 catalog. As we describe in Section C.3.2, we have recalibrated the USNOB astrometry at each epoch using UCAC2 astrometry; this step reduces the systematic uncertainty.

C.2.3 2MASS

The Two-Micron All-Sky Survey (2MASS; Skrutskie et al. 2006) observed the entire sky in the J, H, and K_s bands over the interval of 1998-2002. Each point on the sky was imaged six times and the coadded total integration time was 7.8s, yielding 10σ detection limits of $K = 14.3$, $H = 15.1$, and $J = 15.8$. The saturation levels depend on the seeing and sky background for each image, but are typically $J < 9$, $H < 8.5$, and $K_s < 8$. However, the NIR photometry is typically accurate to well above these saturation limits since it was extrapolated from the unsaturated PSF wings. The

typical astrometric accuracy attained for the brightest unsaturated sources ($K \sim 8$) is $\sim$70 mas. The absolute astrometry calibration was calculated with respect to stars from Tycho-2; subsequent tests have shown that systematic errors are typically <30 mas (Zacharias et al. 2003).

C.2.4   UCAC2

The astrometric quality of all three of the above surveys could be compromised for bright, saturated stars, so proper motions calculated from those observations could be unreliable. Many of the brightest stars are saturated in all epochs, so we have no astrometry with which to compute proper motions. We have addressed this problem by adopting proper motions for bright stars as measured by the Second USNO CCD Astrograph Catalog (UCAC2; Zacharias et al. 2004).

UCAC2 was compiled from a large number of photographic sky surveys and a complete re-imaging of the sky south of $\delta \sim 40^o$. UCAC2 is not complete since many resolved sources (double stars and galaxies) were rejected. However, most sources between $R = 8$ and $R = 16$ should be included. The typical errors in the reported proper motions are $\sim$1-3 mas yr^{-1} down to $R = 12$ and $\sim$6 mas yr^{-1} to $R = 16$. We have adopted UCAC2 proper motions in cases where we were unable to calculate new values or where the UCAC2 uncertainties are lower than the uncertainties for our values.

C.2.5   Known Members of Praesepe

There have been many previous surveys to identify members of Praesepe, so we have compiled a list of high-confidence cluster members that can be used to test our survey procedures (Section C.3) and determine the completeness of our survey (Section C.4.2). We have not done the same for Coma Ber since there are far fewer high-confidence members (<50). However, the brightness ranges are similar enough that the detection efficiencies should be similar for both clusters.

We drew our high-confidence Praesepe sample from the proper motion surveys of

Jones & Cudworth (1983), Jones & Stauffer (1991), and Hambly et al. (1995a). We also included the high-mass stars identified by Klein-Wassink (1927) which possessed updated astrometry in the survey by Wang et al. (1995). We required each member of our high-confidence sample to have been identified with $\geq 95\%$ probability of membership by at least one survey, and to not have been identified with $<80\%$ probability by any other survey; a total of 381 sources met these requirements.

C.2.6   Stellar SED Library

There is no single source in the literature that describes all of the SED data that we require, so we compiled a preliminary set of models from a heterogeneous set of empirical observations. We then optimized these models by comparing the color-magnitude sequences to the single-star sequence of our high-confidence Praesepe sample (Section C.2.5).

Luminosities and optical colors for our high-mass and intermediate-mass stellar models (spectral types B8 to K7) were based on the absolute UBV magnitudes of Schmidt-Kaler (1982), which we converted to SDSS absolute magnitudes using the color transformations of Jester et al.(2005). We then used the optical-NIR colors ($V - K$, $J - K$, and $H - K$) of Bessell and Brett (1988) to estimate JHK absolute magnitudes, and converted these values to the 2MASS filter system using the NIR color transformations of Carpenter (2001). We estimated absolute bolometric magnitudes for each model using the bolometric corrections of Masana et al.(2006).

For M dwarfs (M0-L0), we based our models on the fourth-order polynomial relation of absolute JHK versus spectral type described by Cruz et al. (2007); they only explicitly defined this relation for spectral types later than M6, so we used 2MASS observations of stars in the CNS3 catalog (Gliese & Jahreiss 1991) and the 8 pc sample (Reid et al. 2002) to estimate the appropriate polynomial relation for M0-M5 stars. We combined these results with the $r - i$, $i - z$, and $z - J$ colors of West et al. (2005) and the $u - g$ and $g - r$ colors of Bochanski et al.(2007). We estimated absolute bolometric magnitudes using the bolometric corrections of Leggett (1992)

and Leggett et al.(2002).

Finally, we optimized our set of spectral type models by comparing theoretical color-color and color-magnitude sequences to the empirical color-color and color-magnitude sequences of our sample of high-confidence Praesepe members. We found that the absolute magnitudes of our models differed from the empirical sequence at spectral types F2-F8 and at the K/M boundary, so we adjusted these absolute magnitudes to match the empirical sequences. We did not find any need to adjust the colors of any model, which suggests that any discrepancies are a result of the bolometric corrections.

In Table C.1, we list our final set of spectral type models. Our fitting routine subsamples this model grid by linearly interpolating to predict values for intermediate spectral types; our final grid of models (491 in all) proceeds from B8 to L0 in steps of 0.1 subclasses, following the recent nomenclature trend to proceed directly from K5 to K7 to M0, not using subclasses K6, K8, or K9.

For high-mass stars ($\leq$F2), we directly adopted masses from the models of Schmidt-Kaler (1982). For lower-mass stars, we adopted effective temperatures for each model using the dwarf temperature scales of Schmidt-Kaler (1982) (for spectral types $\leq$M0) and Luhman (1999) (for spectral types >M0). We then combined these T_{eff} values with the 500 Myr isochrones of Baraffe et al.(1998) to estimate stellar masses. The appropriate mixing length has been found to change with mass (Yildiz et al. 2006), so for masses >0.6 $M_\odot$, we used the models with a mixing length of H_P. For masses <0.6 $M_\odot$, we used the models with a mixing length of 1.9 H_P.

Several studies (e.g., Hillenbrand & White 2004; Lopez-Morales 2007) have found that theoretical models can underpredict masses, so these values should be considered with some caution. The most uncertain mass range is <0.5 $M_\odot$. Observational calibrations suggest that the models underpredict masses by ~10-20% in the mass range of 0.2-0.5 $M_\odot$, and the models are almost completely uncalibrated for lower masses. We have addressed this problem by increases the masses of M1 stars by 5%, M2 stars by 10%, and later-type stars by 20%; these adopted values are more consistent with the observations (e.g., Lacy 1977; Delfosse et al. 1999; Creevy et al.

Table C.1.   Stellar SEDs

SpT	M_u	M_g	M_r	M_i	M_z	M_J	M_H	M_K	M_{bol}	T_{eff}	M $(M_\odot)$
B8	0.32	-0.39	-0.04	0.34	0.62	0.01	0.10	0.11	-1.00	11900	3.8
A0	1.58	0.47	0.72	1.04	1.28	0.54	0.58	0.56	0.30	9520	2.9
A2	2.41	1.22	1.39	1.65	1.87	1.12	1.15	1.12	1.10	8970	2.4
A5	3.14	1.88	1.95	2.15	2.32	1.53	1.52	1.48	1.75	8200	2.0
A7	3.47	2.21	2.23	2.40	2.55	1.75	1.71	1.66	2.08	7580	1.8
F0	3.94	2.77	2.68	2.79	2.90	2.10	2.01	1.96	2.61	7200	1.6
F2	4.23	3.10	2.96	3.04	3.13	2.32	2.20	2.14	2.89	6890	1.5
F5	5.01	3.90	3.68	3.69	3.74	2.85	2.67	2.61	3.61	6440	1.25
F8	5.76	4.60	4.29	4.26	4.28	3.31	3.08	3.01	4.24	6200	1.17
G0	6.09	4.89	4.52	4.44	4.44	3.53	3.27	3.20	4.47	6030	1.11
G2	6.35	5.07	4.65	4.54	4.51	3.64	3.38	3.30	4.60	5860	1.06
G5	6.78	5.40	4.92	4.79	4.74	3.86	3.56	3.48	4.89	5770	1.04
G8	7.55	6.03	5.50	5.32	5.25	4.31	3.95	3.86	5.30	5570	0.98
K0	8.08	6.38	5.77	5.55	5.45	4.49	4.10	4.00	5.69	5250	0.90
K2	8.89	6.94	6.23	5.94	5.80	4.80	4.35	4.24	6.08	4900	0.82
K4	9.90	7.62	6.77	6.40	6.20	5.08	4.56	4.43	6.55	4590	0.75
K5	10.36	7.98	7.03	6.59	6.35	5.20	4.64	4.51	6.68	4350	0.70
K7	11.27	8.59	7.45	6.90	6.58	5.46	4.85	4.70	6.89	4060	0.63
M0	12.46	9.90	8.50	7.83	7.46	6.04	5.37	5.18	7.60	3850	0.59
M1	13.00	10.47	9.00	8.12	7.64	6.33	5.68	5.47	7.97	3680	0.54
M2	13.66	11.36	9.76	8.73	8.15	6.73	6.09	5.86	8.44	3510	0.42
M3	14.55	12.37	10.77	9.44	8.74	7.31	6.68	6.44	9.09	3350	0.29
M4	15.83	13.55	11.99	10.48	9.64	8.10	7.49	7.22	9.92	3180	0.20
M5	17.38	15.22	13.67	11.76	10.71	9.08	8.47	8.16	11.01	3010	0.15
M6	18.71	16.56	14.99	12.98	11.88	10.15	9.50	9.16	12.06	2840	0.12
M7	19.74	17.82	16.21	13.94	12.68	10.76	10.08	9.69	12.70	2720	0.11
M8	21.05	19.40	17.60	14.83	13.21	11.19	10.46	10.03	13.13	2600	0.102
M9	21.72	19.93	18.19	15.38	13.69	11.49	10.73	10.26	13.43	2400	0.088
L0	22.33	20.98	18.48	15.85	14.01	11.76	10.96	10.44	13.69	2200	0.078

2005; Lopez-Morales & Ribas 2005).

We list all of the adopted values of M and T_{eff} in Table C.1.

C.3   Data Analysis

Cluster surveys typically identify candidate members using a combination of photometric and astrometric data. All cluster members have the same age, distance, and spatial velocity, so they follow the same color-magnitude sequence and have the same proper motion. This allows for the efficient rejection of all nonmembers which do not meet both criteria.

In the following subsections, we describe our procedure for applying these tests. First, we use SED fitting for our photometric data (spanning 0.3-2.3 μm) to estimate the temperatures and luminosities of all $\sim$5 million sources, and then we calculate a

weighted least-squares fit of our time-series astrometric data to calculate the corresponding proper motions. After deriving both sets of results, we then cut the overwhelming majority of sources which do not follow the cluster photometric sequence. Finally, we examine the (much smaller) list of remaining sources and determine membership probabilities based on the level of agreement between individual candidate astrometry (proper motion and radius from cluster center) and the corresponding distributions for the cluster and for background stars.

We chose to apply the cuts in this order specifically because the final membership probabilities are based on the astrometric properties and not the photometric properties, but inverting the order of the cuts would not affect our final results. Both sets of tests were crucial in narrowing the list of candidates. Of the $\sim10^6$ sources in each cluster for which we measured proper motions, $\sim10^5$ would have been selected by a purely kinematic test and $\sim10^4$ would have been selected by a purely photometric test.

C.3.1 SED Fitting

We base our photometric analysis on the merged results from 2MASS and SDSS, which yield measurements in 8 filters ($ugrizJHK$) for each source. We do not use the photometric results reported by USNOB because they are much more uncertain (~0.25 mag) and do not introduce any new information beyond that reported by SDSS. We also note that many high-mass sources were saturated in one or more filters, so they had fewer than 8 photometric measurements available; the highest-mass stars were saturated in all five SDSS filters, leaving only JHK photometry.

Candidate cluster members traditionally have been selected by photometric surveys which measure magnitudes in several bandpasses and then estimate each star's intrinsic properties (bolometric flux and temperature) using its observed properties (magnitudes and colors). Candidate members are then selected from those stars which fall along the cluster sequence (as defined by known members and by theoretical models) on color-magnitude diagrams. However, this method suffers from serious
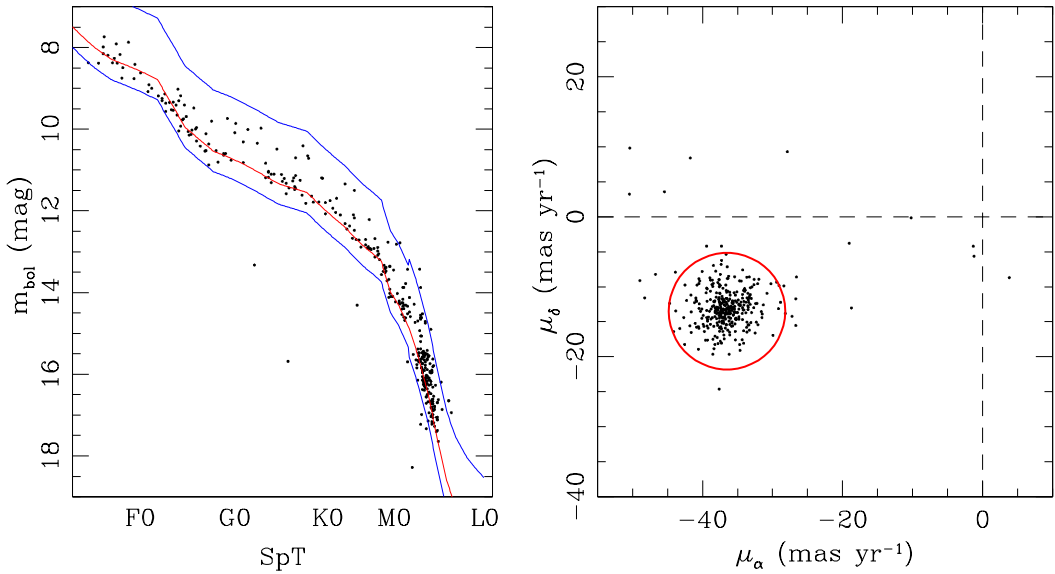
Figure C.1 HR and proper motion diagrams for our high-confidence sample of Praesepe members. For the HR diagram, we plot the cluster single-star sequence (red) and the selection range for identifying new members (blue). In the proper motion diagram, we plot a circle of radius 8 mas yr^{-1} (approximately 2σ for a typical M4 member) centered at the mean cluster proper motion.

flaws. A single magnitude is typically taken as a proxy for flux, which places excessive weight on that bandpass and underweights other bandpass(es) in the survey. If there are more than two bandpasses, motivating the use of multiple CMDs, then color-magnitude selection also neglects the covariance between measurements, artificially inflating the uncertainty in an object's intrinsic properties. Finally, the use of many CMDs introduces significant complexity in the interpretation and communication of results.

We have addressed these challenges by developing a new method for photometric selection of candidate members. Instead of using many different combinations of color and magnitude as proxies for stellar flux and temperature, we have used an SED fitting routine to estimate directly each star's intrinsic properties, then selected candidate members based on their positions in the resulting HR diagram. This method is not vulnerable to the flaws of individual color-magnitude selection since it uses all data simultaneously and uniformly, and since we can implement it as a least-squares minimization, it significantly reduces the uncertainty in the final results.
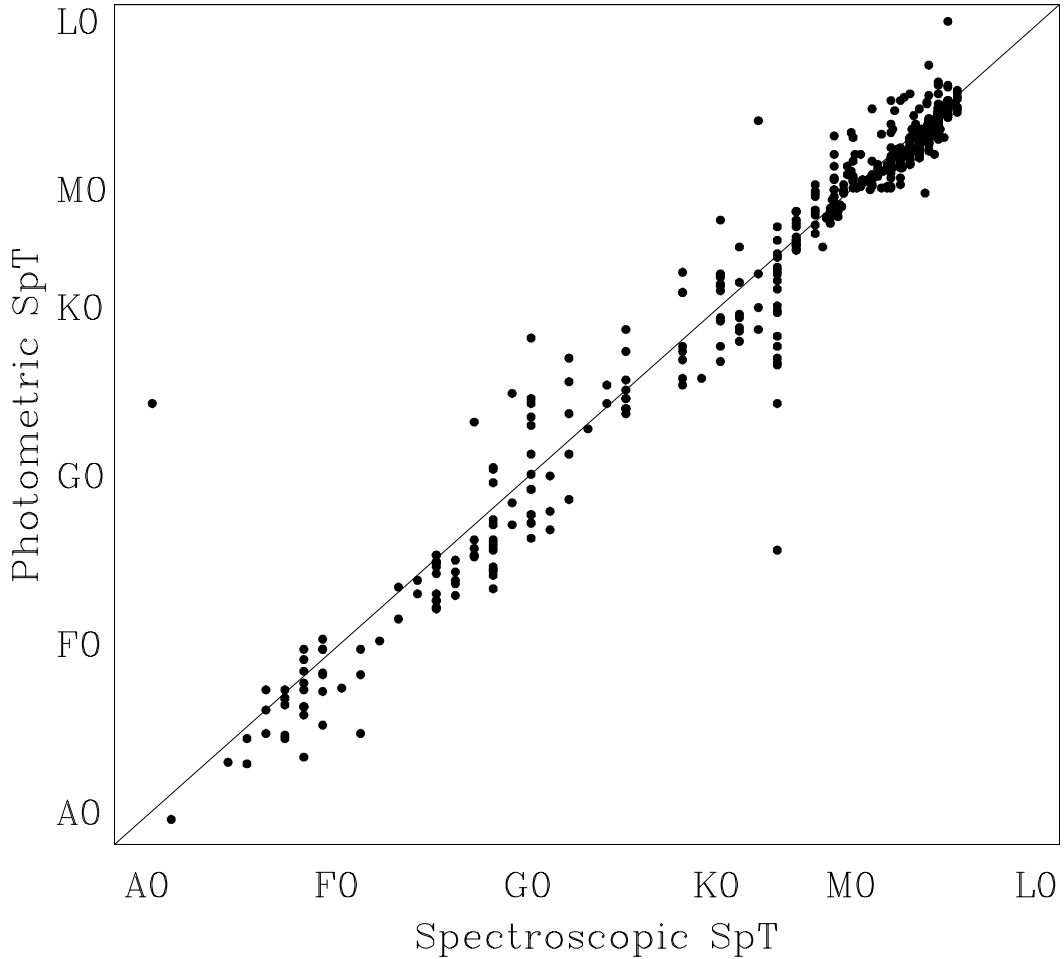
Figure C.2 A comparison of our photometric spectral type determinations to spectroscopic determinations for 632 candidate Praesepe members in the literature. The small excess of points below the relation at spectral type K3 are all drawn from the spectroscopic survey of Adams et al. (2002), which observed spectra in a red wavelength range that contained no diagnostics for distinguishing FGK stars. The A0 star that we misclassified (KW 552) is an Algol-type eclipsing binary, so the 2MASS photometry may have been obtained during primary eclipse; we did not use any SDSS photometry in its SED fit because it was all saturated. If this is the case, our derived spectral type corresponds to an unknown combination of light from the primary and secondary. The K2 star that we misclassified (KW 572) was biased by saturated SDSS photometry which was not flagged.

Specifically, for each star we calculated the χ^2 goodness of fit for the system of eight equations:

$$M_i - m_i = DM$$

where m_i is the observed magnitude in filter i, M_i is the absolute magnitude in filter i for the SED model being tested, and DM is the distance modulus, which was estimated from a weighted least-squares fit across all filters. This system ignores the effects of reddening, but this should be minimal for both clusters. Taylor (2006) found a reddening value for Praesepe of $E(B-V) = 27 \pm 4$ mmag, while Feltz (1972) found a value for the Coma Ber region of $E(B-V) = 0 \pm 2$ mmag.

We tested a library of 491 stellar SEDs which spanned a wide range of spectral types: B8 to L0, in steps of 0.1 subclasses. We describe the SED library and its construction in more detail in Section C.2.6. We rejected potentially erroneous observations by rejecting any measurement that disagreed with the best-fit SED by more than 3σ, where σ is the photometric error reported by the SDSS or 2MASS, and then calculating a new fit. The model which produced the best χ^2 fit over the 8 filters was adopted as the object spectral type, and the corresponding value of DM was added to the model's absolute bolometric magnitude to estimate the apparent bolometric flux. The uncertainties in the spectral type and distance modulus were estimated from the 1σ interval of the χ^2 fit for each object.

In the left panel of Figure C.1, we plot an H-R diagram for our high-confidence sample of Praesepe members. The red line shows the field main sequence at the distance of Praesepe (Section C.2.6), and the blue lines show the upper and lower limits that we use for identifying cluster members. For stars earlier than M2, these limits are set 0.5 magnitudes below and 1.5 magnitudes above the main sequence to allow for the width of the cluster sequence (due to errors, the finite depth of the cluster, and the existence of a multiple-star sequence). The late main sequence is nearly vertical in the HR diagram, which suggests that uncertainties in spectral type will be more important than uncertainties in flux for broadening the cluster sequence.

We account for this by extending the selection range for spectral types $\geq$M2 to 0.7 magnitudes below and 1.7 magnitudes above the field main sequence. Most of the 15 outliers have fluxes or spectral types that are biased by one or more photometric measurements which appear to be erroneous by less than 3σ, causing them to fall just outside our selection range. However, four sources appear to have colors and magnitudes that are genuinely inconsistent with the cluster sequence.

In Figure C.2, we plot our photometric spectral type against previously-measured spectroscopic spectral types for 632 candidate Praesepe members (Ramberg 1938; Bidelman 1956; Corbally & Garrison 1986; Abt 1986; Williams et al. 1994; Allen & Strom 1995; Adams et al. 2002; Kafka & Honeycutt 2006). The two sets of spectral types agree systematically to within <2 subclasses; the dispersion in the relation is ~3 subclasses for early-type stars (A0-G0) and <1 subclass for later-type stars (G0-M6). This dispersion represents the combined dispersions of both our measurements and those in the literature, so it represents an upper limit on the statistical uncertainties in our spectral type estimate. Most of the early-type stars were classified by Ramberg (1938) and Bidelman (1956), so the larger scatter could be a result of their older, less precise observing techniques. However, our SED-fitting routine rejected most of the SDSS photometry for these sources since it was saturated, so some of the uncertainty may be a result of using only 2MASS JHK photometry.

When applied to our full source list, our photometric selection criteria identify 11,999 candidate members of Praesepe and 2,034 candidate members of Coma Ber. As we demonstrate in the Section C.3.2 and C.3.3, the vast majority of these sources are probably background stars since they have proper motions inconsistent with cluster membership.

C.3.2 Proper Motions

Kinematic measurements are a key tool in identifying members of stellar populations. Internal cluster velocity dispersions are typically much lower than the dispersion of field star velocities, so stellar populations generally can be distinguished from the

Table C.2.   Astrometric Recalibration Offsets

Cluster/Epoch	Δ_α	Δ_δ
Praesepe B1	+42	+97
Praesepe R1	+49	+104
Praesepe B2	+10	-75
Praesepe R2	-2	-78
Praesepe I2	-11	-119
Coma Ber B1	-16	+55
Coma Ber R1	-21	+80
Coma Ber B2	-132	-58
Coma Ber R2	-96	-64
Coma Ber I2	-118	-93

Note. — Offsets are measured in mas. The typical uncertainty for each offset, as estimated from the standard deviation of the mean, is ∼3-5 mas.

field star population by their uniform kinematics. The measurement of tangential kinematics, via proper motions, is also an efficient method since it can be applied to many cluster members simultaneously using wide-field imaging. Many recent efforts have employed various combinations of all-sky surveys in order to systematically measure proper motions of both clusters and field stars; USNOB is itself a product of such analysis, and Gould & Kohlmeier (2004) produced an astrometric catalog for the overlap between USNOB and SDSS Data Release 1. However, there has been no systematic attempt to combine all available catalogs using a single algorithm to produce a single unified set of kinematic measurements.

Before calculating proper motions for our survey, our first step was to recalibrate the five epochs of USNOB astrometry into the ICRS. The densest reference system that is directly tied to the ICRS is UCAC2, which we already cross-referenced with our dataset, so we used all of its sources with high-precision astrometry ($\sigma_\mu<4$ mas yr^{-1}) as calibrators. For each USNOB epoch, we projected the simultaneous UCAC2 positions of all calibrators using modern (epoch 2000) UCAC2 astrometry and proper motions, then determined the median offset between the predicted UCAC2 values and the observed USNOB values. These offsets were then added to each USNOB source to bring its astrometry into the ICRS. We list these mean offsets in Table C.2; each

offset was typically calculated from ~3000 sources, and the standard deviation of the mean for each offset was ~3-5 mas. The median offsets were small ($<$150 mas), so the net change in our calculated final proper motions is $<$3 mas yr^{-1}.

After we recalibrated all surveys into the same reference system, we used a weighted least-squares fit routine to calculate the proper motion of each object based on all available astrometry for unsaturated detections. Our algorithm tested the goodness of each fit and rejected all outliers at $> 3\sigma$; most of these outliers were found in the photographic survey data, not in 2MASS or SDSS.

In the right panel of Figure C.1, we plot a proper motion diagram for our high-confidence sample of Praesepe members. The mean cluster proper motion (-36.5,-13.5 mas yr^{-1}) is denoted by a red circle with a radius of 8 mas yr^{-1} (twice the typical 1σ uncertainty for the M4 members in our high-confidence sample). We found that 326 of our 381 high-confidence members fall within this limit, and most of the early-type stars (which have much smaller errors) form a much tighter distribution. Most of the outliers appear to be biased by erroneous first-epoch positions that can not be rejected at a 3σ level by our fitting routine. These early epochs are not significantly more prone to erroneous measurements than later photographic measurements, but they change the resulting proper motion by a larger amount since their time baseline with respect to all other measurements is so long.

Our subsequent kinematic analysis (Section C.3.3) has retained all photometric candidates with proper motions within 20 mas yr^{-1} (5σ for low-mass candidates) of each cluster's mean proper motion; we set this limit to be much larger than the cluster distribution so that we would also retain enough field stars to determine their density in proper motion space. We found that 2611 of our 11999 photometric candidates in Praesepe and 645 of our 2034 photometric candidates in Coma Ber fell within this limit.

We removed a small number of sources (44 from Praesepe and 4 from Coma Ber) that had highly uncertain proper motions ($\sigma>$10 mas yr^{-1}) because we could not have accurately assessed their membership. The astrometry was typically more uncertain for these few sources because there were few or no detections in USNOB. We also

visually inspected the SED for any source with a poor photometric fit ($\chi_\nu^2 > 10$) and rejected two sources near Coma Ber which were only selected due to saturated SDSS photometry that had not been flagged.

Finally, we visually inspected the color-composite SDSS image of each source using the SDSS batch image service.[1] We found that 8 sources in Praesepe and 31 sources in Coma Ber were resolved background galaxies, so we removed them from further consideration. These galaxies were split roughly evenly between bright ($r \sim 14-16$) sources with K star colors and faint ($r \sim 19$) galaxies with red riz colors and no ug or JHK detections; in all cases, the apparent proper motion was caused by a large scatter in the photometric centroids. The SDSS database also includes a morphological classification of whether each object is a star or galaxy that is likely to be more sensitive than visual inspection, but we have found that saturated stars and marginally resolved binaries are often classified as galaxies by the SDSS pipeline, so we chose not to use this parameter in rejecting likely galaxies.

C.3.3 Identification of Cluster Members

Our photometric and astrometric selection criteria do not perfectly reject field stars, so we expect that some fraction of our candidates will actually be interlopers and not cluster members. Many surveys quantify the level of contamination by studying one or more control populations, selected from a nearby volume of kinematic or spatial parameter space. The membership probability for a set of stars is then represented by the fractional excess in the candidate population with respect to the control population. However, this choice ignores all information about the spatial or proper motion distribution of the candidates, treating these distributions as constant within the selection limits. A more rigorous approach should take these non-constant probability density functions into account, giving highest membership probability to those candidates that are closest to the cluster center and have proper motions closest to the mean cluster value.

---

[1]http://cas.sdss.org/dr5/

To this end, we have adopted the maximum likelihood method of Sanders (1971) and Francic (1989) to distinguish cluster members and field stars among the candidates that meet our photometric and kinematic selection criteria. This method explicitly fits the spatial and kinematic distributions of all candidates with two separate probability density functions, $\Phi = \Phi_c + \Phi_f$, corresponding to cluster members and field interlopers. The method then assigns a membership probability to each star based on the values of each distribution for that location in parameter space, $P_{mem} = \Phi_c/(\Phi_c + \Phi_f)$.

Following some of the refinements of Francic (1989), we chose to fit the cluster spatial distribution with an exponential function and the cluster proper motion distribution with a gaussian function:

$$\Phi_c(\mu_\alpha, \mu_\delta, r) = \frac{N_c e^{-r/r_0}}{2\pi^2 r_0^2 \sigma^2} e^{\frac{1}{2\sigma^2}((\mu_\alpha - \mu_{\alpha,m})^2 + (\mu_\delta - \mu_{\delta,m})^2)}$$

Where the quantities N_c (the total number of cluster stars), r_0 (the scale radius), and σ (the standard deviation of the cluster proper motion distribution) were determined from the fit. We adopted the mean proper motions of each cluster, $(\mu_{\alpha,m}, \mu_{\delta,m}) = (-36.5, -13.5)$ mas yr^{-1} (Praesepe) and $(-11.5, -9.5)$ mas yr^{-1} (Coma Ber), from the literature; these results match UCAC2 values for known high-mass cluster members.

We evaluated the option of fitting the cluster spatial distribution with a mass-dependent King profile (King 1962), but we found that the function produced a poor fit at large separations. High-mass stars in particular are more centrally concentrated than a King profile would predict. By contrast, an exponential radial density profile can accurately match the outer density profile at the cost of moderately overestimating the central density. We decided that it is more important to accurately predict the spatial structure of the outer cluster, where cluster members are less numerous and harder to distinguish from field stars, so we chose to use the exponential profile.

We chose to fit the field spatial distribution with a constant function since the density of field stars does not vary significantly at these high galactic latitudes. In a departure from previous convention, we also chose to fit the field proper motion

distribution with a constant function. As we show in Figures C.4 and C.5, the proper motion distribution of field stars is not easily parametrized with a single function. However, the distribution varies only on scales much larger than the astrometric precision for typical mid-M candidates ($\sim$4 mas yr^{-1}). If we consider a small region of parameter space, then the distribution should be roughly constant. Thus, the field probability density function we have adopted is:

$$\Phi_f = \frac{N_{total} - N_c}{A_{SP} A_{PM}}$$

Where N_{total} is the total number of stars (field and cluster), N_c is the number of cluster stars, A_{SP} represents the total spatial area of our survey on the sky (a circle with radius 7°), and A_{PM} represents the total area of proper motion parameter space from which we selected candidates (a circle with radius 20 mas yr^{-1}). The proper motion criterion was chosen to be much larger than the typical uncertainty in cluster proper motions ($\sim$5σ for the faintest stars) while being small enough that an assumption of a constant field distribution is approximately valid.

Both clusters are old enough for mass segregation to have occurred, plus the astrometric uncertainties depend significantly on brightness, so we expect that the spatial and kinematic distributions will show a significant mass dependence. We have accounted for this by dividing each cluster sample into spectral type bins and fitting these bins independently. As we describe in Section C.5, this choice also offers a natural system for quantifying the mass-dependent properties of each cluster. Our parametrization of the cluster spatial and proper motion distributions provides direct measurements of the cluster mass function (via N_c), the astrometric precision (via σ), and the effects of mass segregation (via r_0).

Finally, we determined confidence intervals for each value via a bootstrap Monte Carlo routine. This method creates synthetic datasets by drawing with replacement from the original dataset; for each bin we constructed 100 synthetic datasets with the same number of total members, re-ran our analysis for each set, and used the distribution of results to estimate the standard deviations of the fit parameters.

Table C.3.   Cluster Fit Parameters

SpT	N_c	N_{tot}	r_0 (deg)	σ (mas yr^{-1})
Praesepe				
A-F	89±9	248	0.45±0.04	1.36±0.10
G	69±8	236	0.49±0.05	1.65±0.14
K0.0-K3.9	72±9	212	0.66±0.09	3.44±0.36
K4.0-K7.9	102±9	247	0.71±0.06	3.34±0.16
M0.0-M1.9	127±9	283	0.71±0.04	2.85±0.16
M2.0-M2.9	90±10	243	0.92±0.10	3.03±0.23
M3.0-M3.9	202±12	440	0.71±0.03	3.01±0.17
M4.0-M4.9	249±15	514	0.87±0.04	4.69±0.28
M5.0-M5.9	40±6	94	0.80±0.10	6.30±0.66
M6.0-M6.9	15±6	42	0.98±0.38	7.00±1.93
Coma Ber				
A-F	17±3	25	1.19±0.24	1.22±0.19
G	13±3	31	1.06±0.16	1.19±0.18
K	40±13	413	1.58±0.17	3.91±0.89
M0.0-M2.9	24±5	50	1.33±0.12	4.58±0.58
M3.0-M5.9	36±6	78	1.46±0.12	5.07±0.58
M6.0-M8.9	3±2	15	1.62±0.55	4.63±1.26

In Table C.3, we summarize the parameter fits. We found in both clusters that the fits for spectral types >M6 predicted marginally significant values of N_c, a result we attribute to our nondetection of most late-type members. We therefore will not use those parameters in our analysis of the mass-dependent cluster properties. However, in the interest of completeness, we will still report any candidates which have high membership probabilities. Some of these stars have already been identified as candidates by previous surveys (e.g., IZ072; Pinfield et al. 2003), so they may be worthy of consideration in future studies. We also found extremely high contamination rates for K stars in Coma Ber; this is a natural result of its low proper motion, which causes confusion with background K giants. There are few high-probability K-type members identified for Coma Ber, but the fits for bulk properties (N_c, r_0, and σ) are statistically significant.

C.4 Results

C.4.1 New Cluster Members

Based on our kinematic and photometric selection procedures, we identified 1130 candidate members of Praesepe and 149 candidate members of Coma Ber with membership probabilities of $\geq$50%; 1010 and 98 of these candidates have membership probabilities of >80%. Of these high-probability candidates, 76 and 50 are newly-identified as proper-motion candidates, while 568 and 37 have been classified as high-probability (>80%) candidates in at least one previous survey and 366 and 11 were previously identified with lower probability (see references in Section C.1). In Tables C.4 and C.5, we list all candidate members with P_{mem} >50%. We also list their derived stellar properties, proper motions, membership probabilities, cross-identifications with previous surveys, and spectroscopically determined spectral types. In Figure C.3, we plot a histogram of the number of candidates as a function of P_{mem} for each cluster; a majority of candidates have membership probabilities of >90% or <10%, suggesting that most of these candidates are being unambiguously identified.

To demonstrate the impact of our selection techniques, in Figure C.4 we plot an HR diagram for all stars near Praesepe which fall within 2σ of the mean cluster proper motion (left) and a proper motion diagram for all stars which passed our photometric selection criteria (right). In both cases, the distribution of cluster members can be visually distinguished from the underlying distribution of field stars. However, there is also significant overlap between cluster members and field stars, indicating that both tests were necessary. The proper motion test was a far better discriminant against field stars, a result of Praesepe's high and distinct proper motion; the photometric criteria accepted 11,999 sources, but only 1,932 stars fell within 2σ of the cluster's mean proper motion.

Based on the HR diagram, it appears that most field stars with consistent proper motions are nearby dwarfs; this is not surprising since few distant stars will have the large transverse velocities required to match the angular velocity of Praesepe. Based on the proper motion diagram, it appears that the interlopers which pass our

Table C.4.   Candidate Members of Praesepe

ID	SpT	m_{bol} (mag)	μ_α	μ_δ (mas yr^{-1})	σ_μ	P_{mem} (%)	Previous ID[a]
2MASS J08374071+1931064	A8.0±3.2	8.17±0.02	-34.8	-12.5	0.7	99.9	KW 45 (A9; Abt 1986)
2MASS J08430594+1926153	F9.5±3.2	9.74±0.01	-36.6	-13.8	0.9	99.9	KW495 (F8; Ramberg 1938)
2MASS J08393837+1926272	K1.5±1.0	12.10±0.01	-33.0	-9.6	1.9	99.2	KW198 (K3; Allen & Strom 1995)
2MASS J08325566+1843582	K3.3±0.5	12.63±0.01	-38.1	-12.1	3.0	97.1	JS 17
2MASS J08380730+2026557	M1.5±0.1	14.59±0.01	-41.4	-13.2	3.0	99.5	
2MASS J08455917+1915127	M3.5±0.1	15.56±0.01	-41.8	-11.0	2.7	96.6	AD 3470 (M4; Adams et al. 2002)
2MASS J08410334+1837159	M6.8±0.2	17.47±0.01	-37.3	-14.2	4.0	96.5	IZ072 (M4.5; Adams et al. 2002)

Note. — The full version of Table C.4 is published as an online-only table in AJ.

[a]The survey by Adams et al.(2002) used standard 2MASS names for their sources. We already provide these names in the first column, so we have labelled the sources as AD $NNNN$ (where $NNNN$ represents the number of the entry in their results table) in the interest of brevity.

photometric criteria are split evenly between stationary sources (such as halo giants) and moving sources with larger, randomly distributed proper motions (disk dwarfs that occupy the same physical volume as Praesepe). We also note that a clear binary sequence can be seen for early-type stars in the HR diagram, but it blends with the sigle-star sequence for late-type stars ($>$M0).

In Figure C.5, we plot similar HR and proper motion diagrams for the stars of Coma Ber. The cluster's HR sequence and proper motion distribution are not as visually distinctive since the cluster population is smaller, but the combination of kinematics and photometry still allow for the efficient identification of candidate members. Unlike for Praesepe, the photometric test was a better discriminant (accepting 2,034 sources) than the proper motion test (21,264 sources); this is a result of the cluster's lower distance (which places it higher in the HR diagram relative to the field star population) and much smaller proper motion (which allows more contamination from nonmoving background sources).

The HR diagram for Coma Ber (which shows kinematically selected sources) includes a recognizeable giant branch and many faint (distant) early-type stars, both classes which typically have small proper motions. The proper motion diagram, which shows photometrically selected stars, includes far fewer sources than Praesepe; again, these are split between nonmoving background giants and nearby disk dwarfs. A probable binary sequence can also be seen for Coma Ber, though it is not as visually distinctive as for Praesepe.
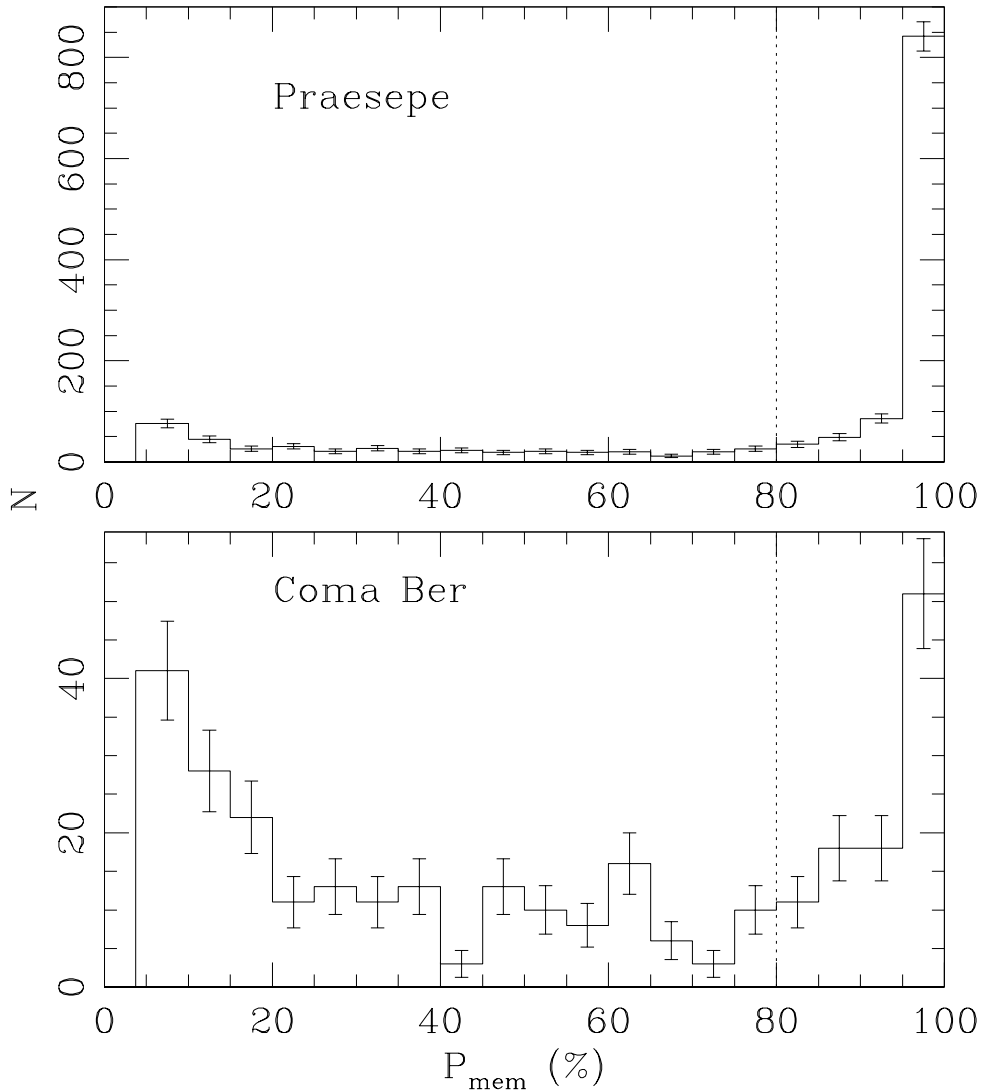
Figure C.3 The number of candidate members with membership probability P_{mem} for Praesepe (top) and Coma Ber (bottom). Most of the Coma Ber candidates with $20\% < P_{mem} < 80\%$ are K stars, corresponding to the large number of candidates which we cannot conclusively distinguish as either K dwarf members or background K giant contaminants. The vertical dashed line denotes our suggested limit ($P_{mem} > 80\%$) for identifying high-confidence cluster members.

Table C.5.   Candidate Members of Coma Ber

ID	SpT	m_{bol} (mag)	μ_α	μ_δ (mas yr^{-1})	σ_μ	P_{mem} (%)	Previous ID[a]
2MASS J12230841+2551049	F9.7±2.9	8.97±0.01	-10.0	-8.5	0.7	100.0	Tr 97 (F8; Abt & Levato 1977)
2MASS J12272068+2319475	G7.9±1.5	9.91±0.01	-11.6	-8.8	0.7	99.6	CJD 6 (K0; SIMBAD)
2MASS J12262402+2515430	K2.8±0.5	11.55±0.02	-15.9	-6.1	1.7	84.9	
2MASS J12225942+2458584	K5.4±0.7	10.86±0.02	-8.7	-12.3	0.9	89.5	
2MASS J12241088+2359362	M2.2±0.1	14.03±0.01	-9.9	-9.4	2.7	98.1	CJD 46
2MASS J12163730+2653582	M2.6±0.1	14.04±0.01	-7.8	-10.9	3.0	97.6	CJD 45

Note. — The full version of Table C.5 is published as an online-only table in AJ.

[a]The survey by Casewell et al.(2006) did not give explicit names for their sources, so we have labelled the sources as CJD NN (where NN represents the number of the entry in their results table).
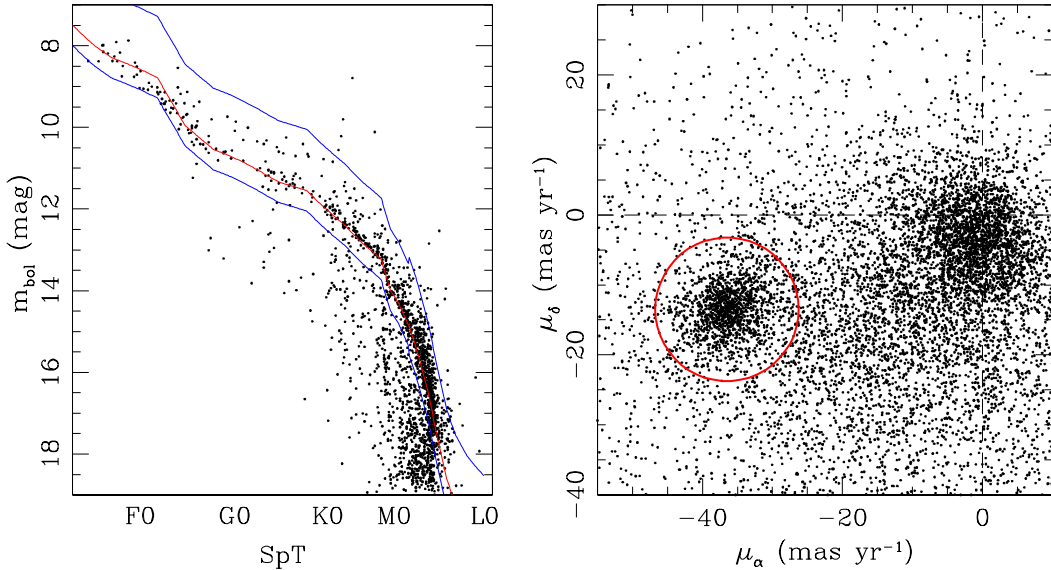
Figure C.4 Left: An HR diagram for all objects which have proper motions within 8 mas yr^{-1} of the mean value for Praesepe. The field main sequence at the distance of Praesepe is shown with a red line; the blue lines outline our photometric selection limits. We identified few candidate members of Praesepe fainter than $m_{bol} = 17.5$. The possible sequence below and blueward of this point is not a genuine feature, but is instead a result of the large number of background early-mid M dwarfs with similar proper motions. These stars are spatially uniformly distributed, which also argues that they are not associated with the cluster. Right: A proper motion diagram for all objects which fall within our photometric selection limits. The red circle outlines the 2σ limit for a low-mass (M5) Praesepe member.
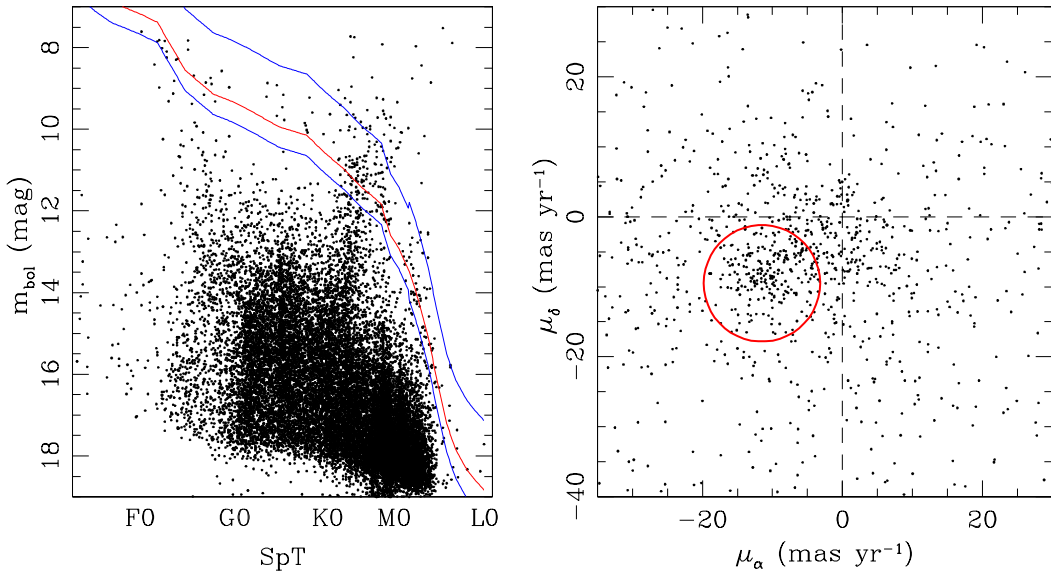
Figure C.5 As in Figure 4, but for Coma Ber.

C.4.2 Completeness

As we describe in Section C.2.5, there have been several previous surveys which identified a large number of high-confidence Praesepe members. The resulting sample of 381 members, comprising all stars which have been identified at $\geq 95\%$ confidence in one survey and at no lower than $<80\%$ confidence by any others, can test the completeness of our proposed member list.

Of the 381 known member stars, 22 were too bright to have proper motions in UCAC2, so they were immediately excluded from our cluster survey. This suggests that most of the brightest, highest-mass stars in either cluster would not have been identified with our technique. Of the 359 stars which were not rejected due to lack of data, 330 were identified as members with $>80\%$ confidence; the corresponding total completeness is 87%. We found that 15 stars were rejected for having inconsistent photometry and 24 were rejected for having inconsistent proper motions. Of the 15 stars rejected based on their photometry, 10 also possessed discrepant proper motions, suggesting that these sources are probably not genuine members of Praesepe and raising our completeness above 90%.

In Figure C.6, we plot the completeness as a function of spectral type for mem-

bers of Praesepe. We project that our survey is >90% complete for spectral types F0 to M5, declining to 0% completeness for spectral types ≤A5 and ≥M7. The incompleteness for early-type stars is a result of the bright limit of UCAC2 data, while the incompleteness for late-type stars is a result of the detection limits for USNOB and 2MASS, which are reached nearly simultaneously for stars on the Praesepe and Coma Ber cluster sequences. The low-mass limit is also consistent with the results we summarize in Table C.3 since we found no members with late M spectral types. We project that the 90% completeness limits should be marginally later (F5 and M6) for Coma Ber since it is closer and its members are brighter; the completeness is also lower for K stars due to contamination from background K giants.

These results are mostly consistent with our comparison to individual surveys. In Praesepe, we find excellent agreement in comparing our list of high-probability candidates with those of Jones & Stauffer (1991) and Hambly et al.(1995a); approximately 90% of each survey's high-confidence ($P_{mem} > 80\%$) candidates were also identified as high-confidence candidates by our survey. We find less overlap with the Praesepe survey of Adams et al.(2002) and the Coma Ber survey of Casewell et al.(2006). Of the candidates which Adams et al. identify as "high confidence" ($P_{mem} > 20\%$ and $r < 4^o$), we only recovered 483 of 724 in our list of high-probability candidates. Casewell et al. used a moderately mass-dependent threshold, varying between $60\% < P_{mem} < 90\%$, to identify 60 new candidate members. Of these stars, we only recover 22.

For both of these surveys, much of the contamination can be traced to the use of 2MASS JHK photometry in the color-selection procedures. The K,$J - K$ color-magnitude sequence for dwarfs is nearly vertical for spectral types M0-M6, so it is difficult to distinguish a moderately brighter foreground star or moderately fainter background star from a genuine cluster member. We found that most of the unrecovered candidates were background M0-M2 stars that fall below the cluster sequence in our HR diagrams. For the survey by Casewell et al., we also found that the recovery fraction was exceptionally low (∼20%) among K stars. We attribute this to contamination from background K giants, which affected both their survey and ours.
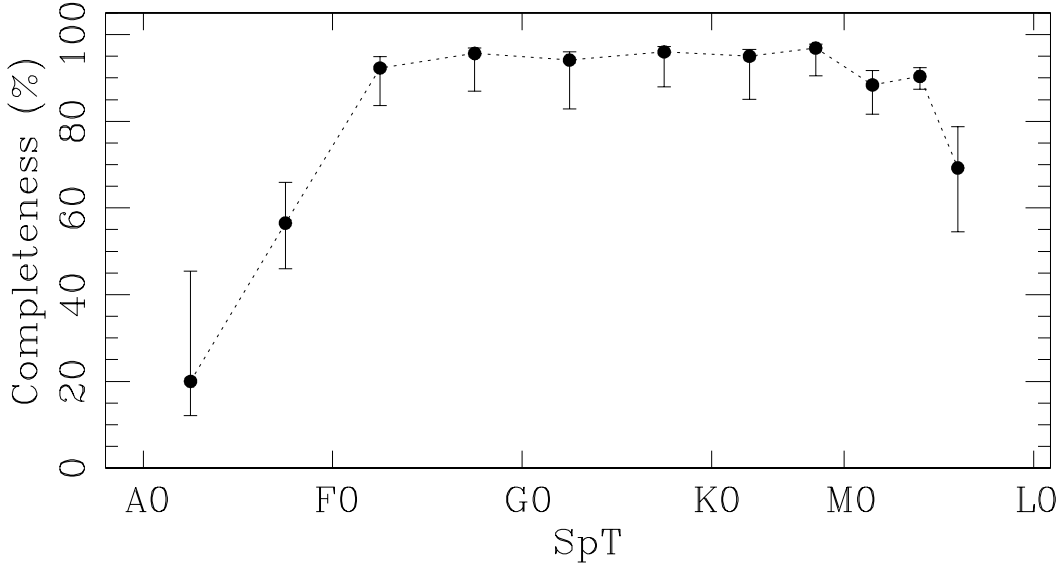
Figure C.6 Completeness as a function of spectral type for our high-confidence sample of Praesepe members. The high-mass cutoff is a result of image saturation, while the low-mass cutoff is a result of nondetection by 2MASS and USNOB. We expect similar results for Coma Ber, but given that its members are ∼1.5 magnitudes brighter, the 90% completeness range will shift to later spectral types (F5-M6).

We were able to identify only 13 of the ∼40 estimated K star members with high (>80%) confidence (Tables C.5 and C.3, respectively), suggesting that there should be only marginal overlap. Many of the candidates from the survey by Casewell et al. appear to be likely cluster members that were only identified at lower confidence ($50\% < P_{mem} < 80\%$) by our survey. However, most of their remaining candidates appear to have proper motions more consistent with nonmovement than comovement, suggesting that they are background giants.

C.5   The Structure and Evolution of Praesepe and Coma Ber

Open clusters are thought to be the birthplaces of most stars, so cluster evolution plays a key role in setting the environment for early stellar evolution. Present-day cluster properties can be used to determine their past history and extrapolate their future lifetime; the three most important sets of properties are the spatial structure
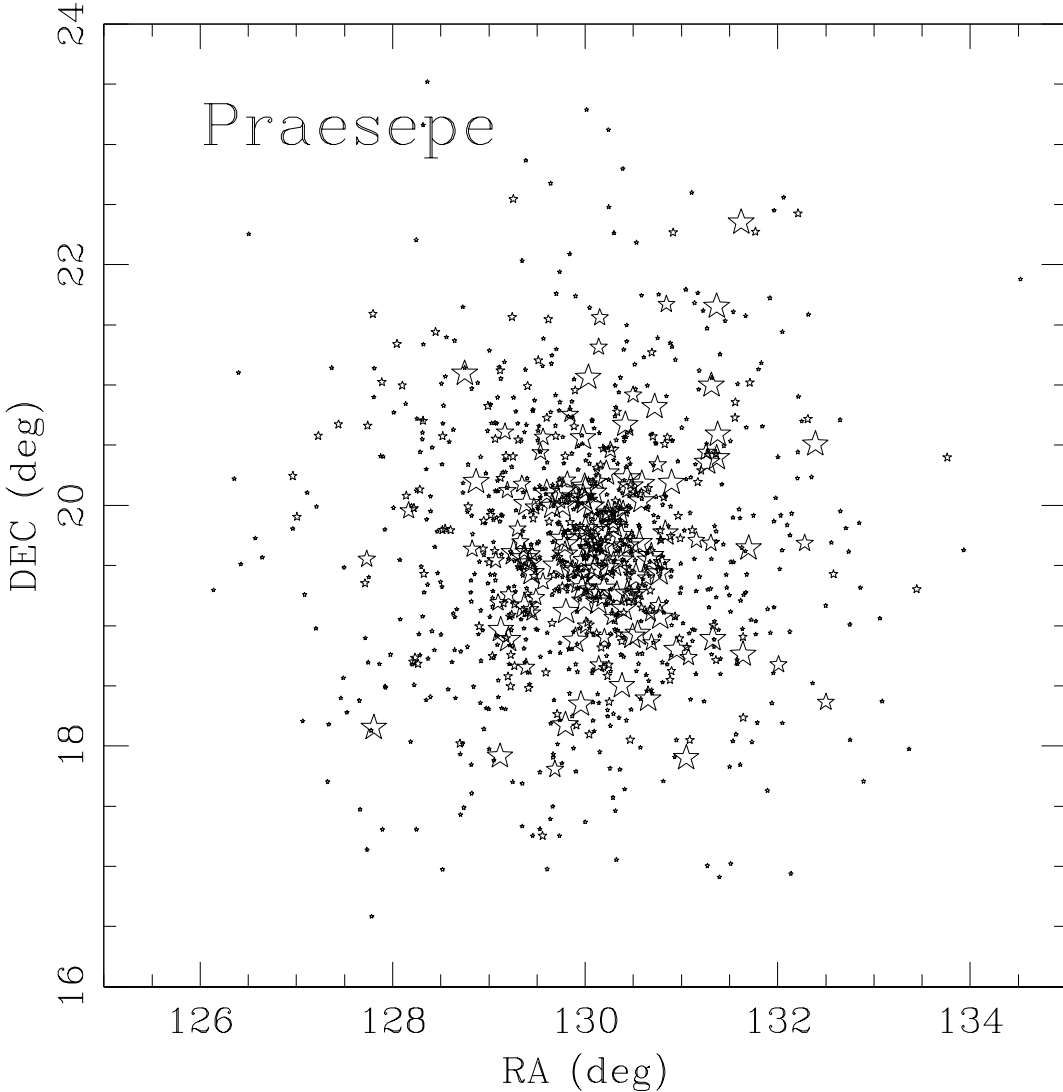
Figure C.7 The spatial distribution of high-probability ($P_{mem} > 80\%$) members of Praesepe. The points are scaled to decreasing size for A-F, G, K, and M stars.

(as inferred from mass segregation), the cluster's stellar mass function, and the total cluster mass.

C.5.1 Radial Distributions and Mass Segregation

In Figures C.7 and C.8, we plot the spatial distribution of all high-probability candidate members of Praesepe and Coma Ber. In each plot, we have scaled the points to decreasing sizes for A-F, G, K, and M stars. These figures clearly illustrate the radial density profile of each cluster. However, it is perilous to infer cluster properties
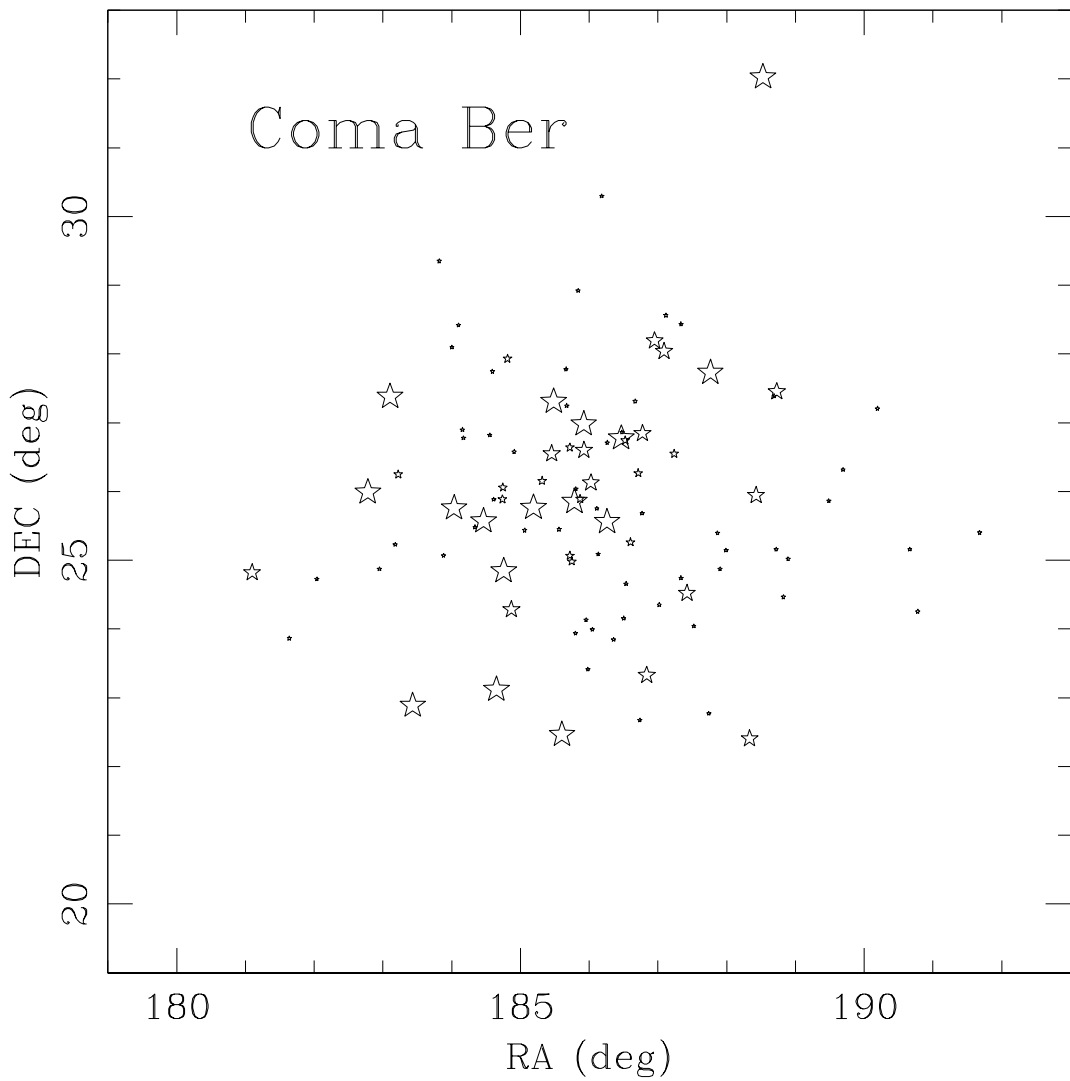
Figure C.8 As in Figure 6, but for Coma Ber.

directly from the distribution of individual stars. The surface density as a function of radius, $\Sigma(r)$, is biased in our sample because each star's radial distance is factored into its membership probability.

Ideally, cluster properties should be estimated using an unbiased method. Our parametric determination of the e-folding scale radius r_0 provides a natural diagnostic for quantifying the radial distribution and mass segregation of each cluster. This quantity allows us to study these properties without dependence on potentially biased measurements for individual stars, plus we can avoid arbitrary choices like the selection of a cutoff in P_{Mem}.

In Figure C.9, we plot the mass-dependent function $r_0(M)$ for Praesepe (top) and Coma Ber (bottom). The uncertainties and upper limits were derived using the Monte Carlo methods described in Section C.3.3. As we described in Section C.4.2, the completeness of our sample drops for spectral types later than M5 in Praesepe and M6 in Coma Ber, so we do not plot results below these limit. In Praesepe, the scale radius increases significantly across the full mass range, following the power law $r_0 \propto M^{-0.25 \pm 0.06}$, which indicates the clear presence of mass segregation. Coma Ber shows no clear trend to indicate mass segregation, but the result is more uncertain: $r_0 \propto M^{-0.10 \pm 0.09}$. We expect Coma Ber to be less segregated than Praesepe due to its younger age and lower stellar density, but a trend with the same slope as in Praesepe is inconsistent by only $<2\sigma$.

C.5.2   Mass Functions

The present-day mass function provides an important test of the evolutionary state of each cluster, assuming clusters form with a common initial mass function. Dynamical evolution (mass segregation and tidal stripping) will preferentially remove low-mass cluster members, so evolved clusters should show large deficits of low-mass stars. The mass function is defined as $\Psi(M) = dN/dM$, such that $\Psi(M)$ is the number of stars with masses in the interval $(m, m + dm)$. We have constructed mass functions using the spectral type intervals defined in Section C.3.3, where the number of stars is the
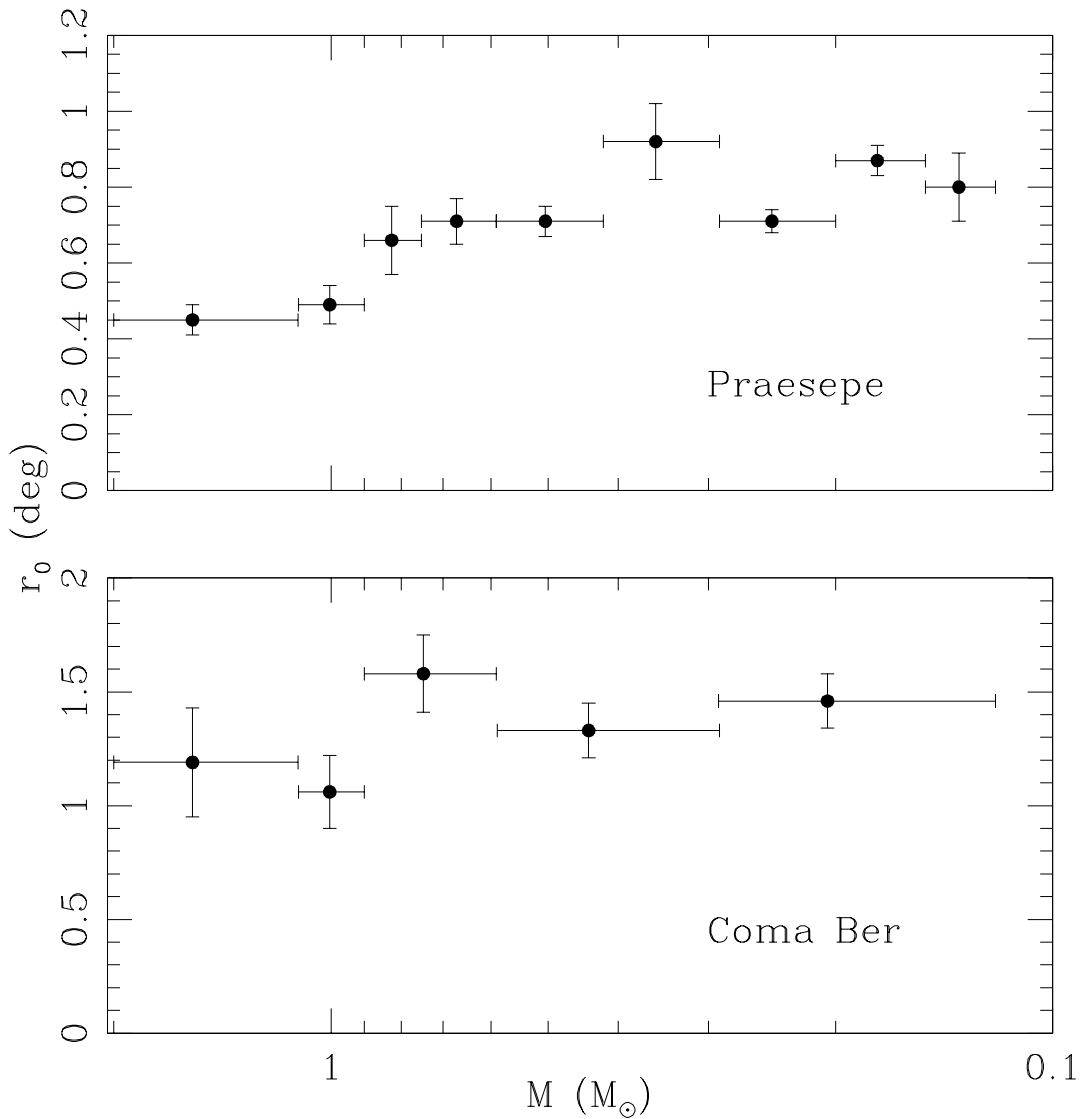
Figure C.9 Scale radius $r_0(M)$ for each cluster. The scale radius in Praesepe clearly increases with decreasing mass, indicating the presence of mass segregation. The corresponding trend for Coma Ber is inconclusive due to low number statistics.

quantity N_c determined in our fitting routine. These mass bins have uneven width, so we normalized each value to represent the number of stars per interval 0.1 $M_\odot$.

In Figure C.10, we plot the cluster mass functions for Praesepe (top) and Coma Ber (bottom). Each function can be fit with a single power law, $\Psi \propto M^{-\alpha}$, where $\alpha = 1.4 \pm 0.2$ for Praesepe and $\alpha = 0.6 \pm 0.3$ in Coma Ber. Both power laws are significantly shallower than a Salpeter IMF ($\alpha = 2.35$), but the Praesepe power law agrees well with the present-day mass function for nearby field stars ($\alpha = 1.35 \pm 0.2$ for 1.0-0.1 $M_\odot$; Reid et al. 2002). Previous studies of the mass function for young clusters and unbound associations have also found similar slopes in this mass range ($\alpha \sim 1.25 \pm 0.25$; Hillenbrand 2004 and references therein).

Neither cluster has a sharp decline in the number of low-mass members within the mass range of our sample. Chappelle et al.(2005) found that the Praesepe mass function may drop sharply just below the limit of our survey (<0.12 $M_\odot$), which could denote the effect of tidal stripping of low-mass members, but we can not confirm or disprove this result. The shallower power law of the Coma Ber mass function suggests that some of its low-mass members may have been removed, but it appears that any limit for the total depletion of cluster members must lie below ~ 0.12 $M_\odot$ as well.

C.5.3 Cluster Masses and Tidal Radii

We have derived the total masses of each cluster by integrating the mass functions that we described in the previous section. Since these mass functions do not include high-mass stars, we have manually added the masses of known high-mass cluster members which were not identified in our survey, comprising $\sim 1/3$ of the total mass. We identified the missing Praesepe members using our high-confidence cluster sample (Section C.2.5), plus the five evolved giant members identified by Klein-Wassink (1927), while the corresponding members of Coma Ber were identified from the original member list of Trumpler et al.(1938).

We have not included any of the candidate Coma Ber members suggested by subsequent surveys (Bounatiro 1993; Odenkirchen et al. 1998) since it has been
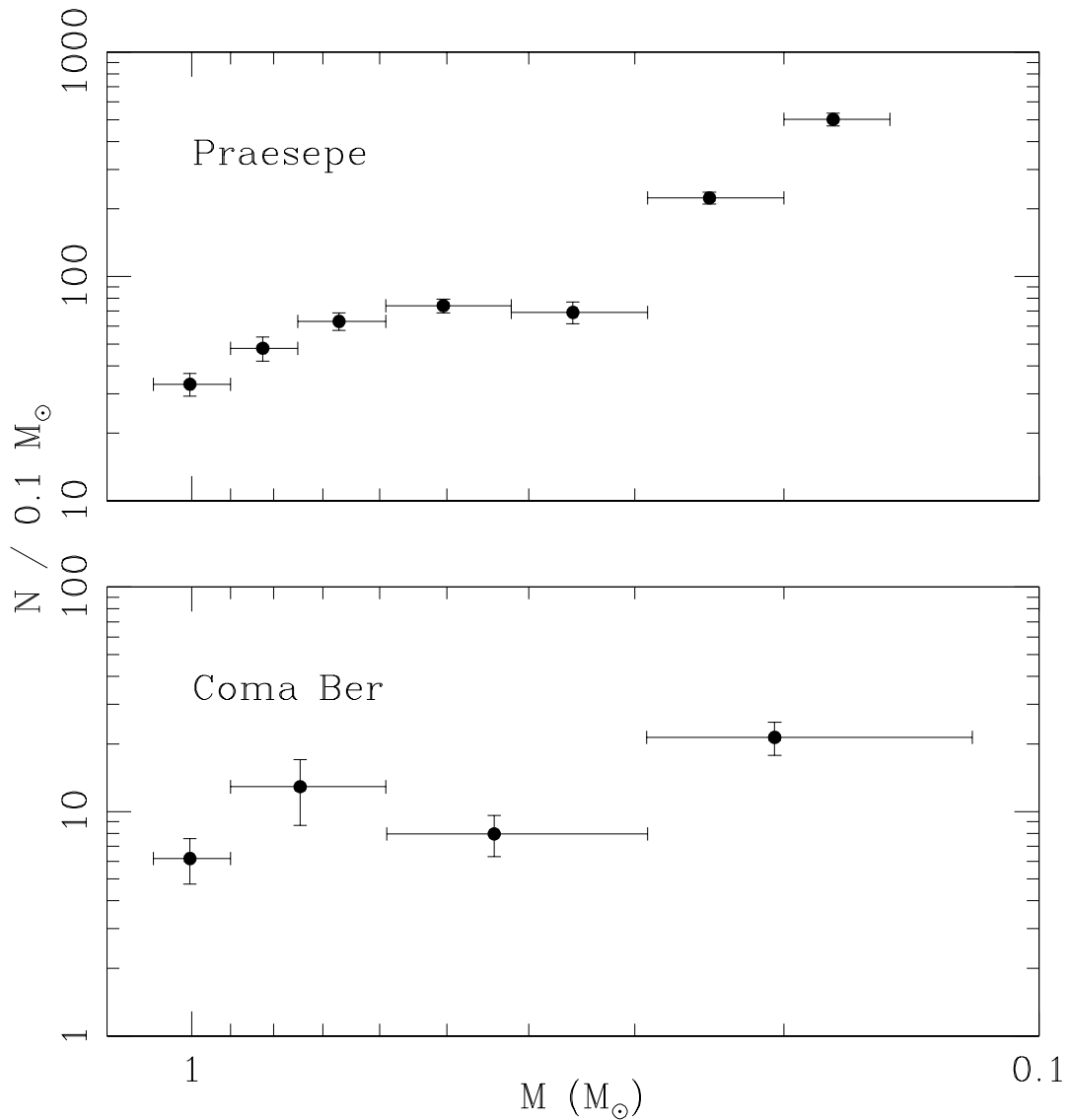
Figure C.10 Mass functions, $\Psi(M) = dN/dM$, for Praesepe and Coma Ber. We derived these results from our best-fit values for $N_c(M)$, as described in Section C.3.3 and Table C.3; each spectral type bin corresponds to a different width in mass, so we normalized all bins to report the number of stars per 0.1 $M_\odot$.

suggested that a significant fraction of these candidates may be spurious (Ford et al. 2001). We also did not attempt to include any substellar or near-substellar members of Praesepe or Coma Ber since they are not thought to comprise a significant fraction of the cluster mass (e.g., Chappelle et al. 2005).

Based on this analysis, we estimate that the total stellar populations for Praesepe and Coma Ber consist of 1050 ± 30 stars earlier than M5 and 145 ± 15 stars earlier than M6, respectively. The corresponding total masses are 550 ± 40 $M_\odot$ and 112 ± 16 $M_\odot$. Given these cluster masses, we can also estimate the tidal radius of each cluster:

$$r_t = [\frac{GM_c}{4A(A-B)}]^{1/3}$$

(King 1962), where A and B are the Oort constants ($A = 14.4$ km s^{-1} kpc^{-1}; $B = -12.0$ km s^{-1} kpc^{-1}; Kerr & Lynden-Bell 1986). We derive estimated tidal radii of 11.5 ± 0.3 pc (3.5 ± 0.1^o) for Praesepe and 6.8 ± 0.3 pc (4.3 ± 0.2^o) for Coma Ber. In both cases, these radii are approximately half the radius of our search area (7°). This suggests that our survey should be spatially complete for all bound members.

Finally, we note that all of these results are likely to be marginally underestimated due to unresolved stellar multiplicity. Given the typical binary frequency found for open clusters ($\sim$30%; Patience et al. 2002) and the mean mass ratio for binaries ($\sim$0.3-0.7), the magnitude of this mass underestimate should be $\sim$20%. We will address this problem in a future publication that specifically studies stellar multiplicity in both clusters.

C.6   Summary

We have combined archival survey data from the SDSS, 2MASS, USNOB1.0, and UCAC-2.0 surveys to calculate proper motions and photometry for $\sim$5 million sources in the fields of the open clusters Praesepe and Coma Ber. Of these sources, 1010 stars in Praesepe and 98 stars in Coma Ber have been identified as candidate members with probability >80%; 442 and 61, respectively, are newly identified as high-probability

candidates for the first time. We estimate that this survey is >90% complete across a wide range of spectral types (F0 to M5 in Praesepe, F5 to M6 in Coma Ber).

We have also investigated each cluster's mass function and the stellar mass dependence of their radii in order to quantify the role of mass segregation and tidal stripping in shaping the present-day mass function and spatial distribution. Praesepe shows clear evidence of mass segregation, but if significant tidal stripping has occurred, it has affected only members near and below the substellar boundary (<0.15 $M_{\odot}$). Low number statistics make it difficult to quantify the level of mass segregation in Coma Ber. The shallower slope of its mass function suggests that some mass loss has occurred, but any mass limit for total depletion of the cluster population must fall below the limit of our survey.

Acknowledgements

Bibliography

Abt, H. 1986, PASP, 98, 307

Abt, H. & Levato, H. 1977, PASP, 89, 29

Adams, J., Stauffer, J., Monet, D., Skrutskie, M., & Beichman, C. 2001, AJ, 121, 2053

Adams, J., Stauffer, J., Skrutskie, M., Monet, D., Portegies Zwart, S., Janes, K., & Beichman, C. 2002, AJ, 124, 1570

Adelman-McCarthy, J. et al. 2007, ApJS, 172, 634

Allen, L. & Strom, K. 1995, AJ, 109, 1379

Argue, A. & Kenworthy, C. 1969, MNRAS, 146, 479

Artyukhina, N. 1955, TrSht, 26, 3

Artyukhina, N. 1966, TrSht, 34, 181

Baraffe, I., Chabrier, G., Allard, F. & Hauschildt, P. 1998, A&A, 337, 403

Bessell, M. & Brett, J. 1988, PASP, 100, 1134

Bidelman, W. 1956, PASP, 68, 318

Bochanski, J., West, A., Hawley, S., & Covey, K. 2007, AJ, 133, 531

Bounatiro, L. 1993, A&AS, 100, 531

Bouy, H. et al. 2006, ApJ, 637, 1056

Carpenter, J. 2001, AJ, 121, 3160

Casewell, S., Jameson, R., & Dobbie, P. 2006, MNRAS, 365, 447

Chappelle, R., Pinfield, D., Steele, I., Dobbie, P., & Magazzu, A. 2005, MNRAS, 361, 1323

Corbally, C., & Garrison, R. 1986, AJ, 92, 90

Creevey, O. et al. 2005, ApJ, 625, 127

Cruz, K. et al. 2007, AJ, 133, 439

Delfosse, X., Forveille, T., Mayor, M., Burnet, M., & Perrier, C. 1999, A&A, 344, 897

Feltz, K. 1972, PASP, 84, 497

Ford, A., Jeffries, R., James, D., & Barnes, J. 2001, A&A, 369, 871

Francic, S. 1989, AJ, 98, 888

Gliese, W. & Jahreiss, H. 1991, Astronomical Data Center CD-ROM: Selected Astronomical Catalogs, Vol. I, Preliminary Version of the Third Catalogue of Nearby Stars (Greenbelt: NASA)

Gould, A. & Kohlmeier, J. 2004, ApJS, 152, 103

Hambly, N., Steele, I., Hawkins, M., & Jameson, R. 1995, A&AS, 109, 29

Hambly, N., Steele, I., Hawkins, M., & Jameson, R. 1995, MNRAS, 273, 505

Hillenbrand, L. 2004, in The Dense Interstellar Medium in Galaxies, ed. S. Pfalzner et al.(Berlin: Springer), 601

Hillenbrand, L. & White, R. 2004, ApJ, 604, 741

Holland, K., Jameson, R., Hodgkin, S., Davies, M., & Pinfield, D. 2000, MNRAS, 319, 956

Jeffries, R. 1999, MNRAS, 304, 821

Jester, S. et al. 2005, AJ, 130, 873

Jones, B. & Cudworth, K. 1983, AJ, 88, 215

Jones, B. & Stauffer, J. 1991, AJ, 102, 1080

Kafka, S. & Honeycutt, R. 2006, AJ, 132, 1517

Kerr, F. & Lynden-Bell, D. 1986, MNRAS, 221, 1023

King, I. 1962, AJ, 67, 471

Klein-Wassink, W. 1927, Publ. Kapteyn Astron. Lab. Groningen, No. 41

Lacy, C. 1977, ApJ, 218, 444

Leggett, S. 1992, ApJS, 82, 351

Leggett, S. et al. 2002, ApJ, 564, 452

Lopez-Morales, M. 2007, ApJ, 660, 732

Lopez-Morales, M. & Ribas, I. 2005, ApJ, 631, 1120

Luhman, K. 1999, ApJ, 525, 466

Masana, E. et al. 2006, A&A, 450, 735

Monet, D. et al. 2003, AJ, 135, 984

Muench, A., Lada, C., Luhman, K., Muzerolle, J., & Young, E. 2007, AJ, 134, 411

Odenkirchen, M., Soubiran, C., & Colin, J. 1998, New Astronomy, 3, 583

Patience, J., Ghez, A., Reid, I., & Matthews, K. 2002, AJ, 123, 1570

Pier, J., Munn, J., Hindsley, R., Hennessy, G., Kent, S., Lupton, R., Ivezic, Z. 2003, AJ, 125, 1559

Pinfield, D., Hodgkin, S., Jameson, R., Cossburn, M., & von Hippel, T. 1997, MNRAS, 287, 180

Pinfield, D., Dobbie, P., Jameson, R., Steele, I., Jones, H., & Katsiyannis, A. 2003, MNRAS, 342, 1241

Ramberg, J. 1938, StoAn, 13, 9

Reid, I.N., Gizis, J., Hawley, S. 2002, AJ, 124, 2721

Sanders, W. 1971, A&A, 14, 226

Schmidt-Kaler, Th., "Physical Parameters of the Stars", Landolt-Bornstein Numerical Data and Functional Relationships in Science and Technology, New Series, Group VI, Volume 2b, Springer-Verlag, Berlin, 1982

Siegler, N. et al. 2007, ApJ, 654, 580

Skrutskie, M. et al. 2006, AJ, 131, 1163

Stauffer, J. et al. 2007, ApJS, 172, 663

Stephenson, C.B. 1986, AJ, 91, 144

Taylor, B. 2006, AJ, 132, 2453

Trumpler, R. 1938, LicOB, 18, 167

Upgren, A. 1962, AJ, 67, 37

Upgren, A. 1963, AJ, 68, 194

Wang, J., Chen, L., Zhao, J., & Jiang, P. 1995, A&AS, 113, 419

West, A., Walkowicz, L., & Hawley, S. 2005, PASP, 117, 706

Williams, S., Stauffer, J., Prosser, C., & Herter, T. 1994, PASP, 106, 817

Yildiz, M., Yakut, K., Bakis, H., & Noels, A. 2006, MNRAS, 368, 1941

York, D. et al. 2000, AJ, 120, 1579

Zacharias, N., McCallon, H., Kopan, E., Cutri, R. 2003, IAUJD, 16, 43

Zacharias, N., Urban, S., Zacharias, M., Wycoff, G., Hall, D., Monet, D., & Rafferty,
    T. 2004, AJ, 127, 3043

Appendix D

USco1606-1935: An Unusually Wide Low-Mass Triple System?

Abstract

We present photometric, astrometric, and spectroscopic observations of USco160611.9-193532 AB, a candidate ultrawide ($\sim$1600 AU), low-mass (M_{tot} $\sim$0.4 $M_\odot$) multiple system in the nearby OB association Upper Scorpius. We conclude that both components are young, comoving members of the association; we also present high-resolution observations which show that the primary is itself a close binary system. If the Aab and B components are gravitationally bound, the system would fall into the small class of young multiple systems which have unusually wide separations as compared to field systems of similar mass. However, we demonstrate that physical association can not be assumed purely on probabilistic grounds for any individual candidate system in this separation range. Analysis of the association's two-point correlation function shows that there is a significant probability (25%) that at least one pair of low-mass association members will be separated in projection by $<15''$, so analysis of the wide binary population in Upper Sco will require a systematic search for all wide systems; the detection of another such pair would represent an excess at the 98% confidence level.

D.1 Introduction

The frequency and properties of multiple star systems are important diagnostics for placing constraints on star formation processes. This has prompted numerous attempts to characterize the properties of nearby binary systems in the field. These surveys (e.g., Duquennoy & Mayor 1991; Fischer & Marcy 1992; Close et al. 2003; Bouy et al. 2003; Burgasser et al. 2003) have found that binary frequencies and properties are very strongly dependent on mass. Solar-mass stars have high binary frequencies ($>60\%$) and maximum separations of up to $\sim 10^4$ AU. By contrast, M dwarfs have moderately high binary frequencies (30-40%) and few binary companions with separations of more than ~ 500 AU, while brown dwarfs have low binary frequencies ($\sim 15\%$) and few companions with separations >20 AU.

The mass-dependent decline in the maximum observed binary separation has been described by Reid et al.(2001) and Burgasser et al.(2003) with an empirical function which is exponential at high masses ($a_{max} \propto 10^{3.3 M_{tot}}$) and quadratic at low masses ($a_{max} \propto M_{tot}^2$). The mechanism that produces the mass dependence is currently unknown; N-body simulations show that the empirical limit is not a result of dynamical evolution in the field (e.g., Burgasser et al. 2003; Weinberg et al. 1987) since the rate of disruptive stellar encounters is far too low. This suggests that the limit must be set early in stellar lifetimes, either as a result of the binary formation process or during early dynamical evolution in relatively crowded natal environments. Surveys of nearby young stellar associations have identified several unusually wide systems (Chauvin et al. 2004; Caballero et al. 2006; Jayawardhana & Ivanov 2006; Luhman et al. 2006, 2007; Close et al. 2007), but not in sufficient numbers to study their properties in a statistically meaningful manner.

We have addressed this problem by using archival 2MASS data to systematically search for candidate wide binary systems among all of the known members of three nearby young associations (Upper Sco, Taurus-Auriga, and Chamaeleon-I; Kraus & Hillenbrand 2007). Our results broadly agree with the standard paradigm; there is a significant deficit of wide systems among very low-mass stars and brown dwarfs as

compared to their more massive brethren. However, we did identify a small number of candidate wide systems. One of these candidates is [PBB2002] USco160611.9-193532 (hereafter USco1606-1935), a wide (10.87″; 1600 AU) pair of stars with similar fluxes and colors. The brighter member of the pair was spectroscopically confirmed by Preibisch et al.(2002) to be a young M5 star. The fainter member fell just below the flux limit of their survey.

In this paper, we describe our photometric, astrometric, and spectroscopic followup observations for USco1606-1935 and evaluate the probability that the system is an unusually wide, low-mass binary. In Section D.2, we describe our observations and data analysis methods. In Section D.3, we use these results to establish that both members of the pair are young and co-moving, and that the primary is itself a close binary. Finally, in Section D.4 we address the possibility that the pair is not bound, but a chance alignment of young stars, by analyzing the clustering of pre-main-sequence stars in Upper Sco.

D.2 Observations and Data Analysis

Most binary surveys, including our discovery survey, identify companions based on their proximity to the primary star and argue for physical association based on the (usually very low) probability that an unbound star would have been observed in chance alignment. However, the probability of contamination is much higher for very wide systems like USco1606-1935, so we decided to pursue additional information in order to confirm its multiplicity and further characterize its system components. In this section, we describe our followup efforts: a search of publicly available databases to obtain additional photometry and astrometry, acquisition of intermediate-resolution spectra to measure the secondary spectral type and test for signatures of youth, and acquisition of high-resolution images to determine if either component is itself a tighter binary and to test for common proper motion.

D.2.1 Archival Data

We identified USco1606-1935 AB as a candidate binary system using archival data from 2MASS (Skrutskie et al. 2006). The binary components are bright and clearly resolved, so we were able to retrieve additional photometry and astrometry from several other wide-field imaging surveys. We collated results for the binary components themselves and for nearby field stars from 2MASS, the Deep Near Infrared Survey (DENIS; Epchtein et al. 1999), United States Naval Observatory B1.0 survey (USNO-B; Monet et al. 2003), and the SuperCOSMOS Sky Survey (SSS; Hambly et al. 2001). The DENIS and 2MASS source catalogues are based on wide-field imaging surveys conducted in the optical/NIR (IJK and JHK, respectively) using infrared array detectors, while the USNO-B and SSS source catalogues are based on independent digitizations of photographic plates from the First Palomar Observatory Sky Survey and the ESO Southern-Sky Survey.

D.2.1.1 Photometry

After evaluating the data, we decided to base our analysis on the JHK magnitudes measured by 2MASS and the photographic I magnitude of USNO-B (hereafter denoted $I2$, following the nomenclature of the USNO-B catalog, to distinguish it from Cousins I_C). We chose these observations because their accuracy can be directly tested using the independent IJK magnitudes measured by DENIS; this comparison shows that the fluxes are consistent within the uncertainties. We do not directly use the DENIS observations because they are not as deep as the other surveys. We adopted the photometric uncertainties suggested in each survey's technical reference.

D.2.1.2 Astrometry

As we describe in Section D.3.3, there appear to be large systematic differences in the astrometry reported by the USNO-B and SSS source catalogs. These surveys represent digitizations of the same photographic plates, so these systematic discrepancies suggest that at least one survey introduces systematic biases in the digitization and

calibration process. Given the uncertainty in which measurements to trust, we have chosen to disregard all available photographic astrometry and only use results from 2MASS and DENIS.

Our discovery survey already measured 2MASS relative astrometry for each filter directly from the processed atlas images, so we have adopted those values. We extracted DENIS astrometry from the source catalog, which contains the average positions for all three filters. Both surveys quote astrometric uncertainties of 70-100 mas for stars in the brightness range of our targets, but that value includes a significant systematic term resulting from the transformation to an all-sky reference frame. We have conducted tests with standard binary systems of known separation which suggest that relative astrometry on angular scales of $<1'$ is accurate to $\sim$40 mas, so we adopt this value as the astrometric uncertainty for each survey.

D.2.2 Optical Spectroscopy

We obtained an intermediate-resolution spectrum of USco1606-1935 B with the Double Spectrograph (Oke & Gunn 1982) on the Hale 5m telescope at Palomar Observatory. The spectrum presented here was obtained with the red channel using a 316 l/mm grating and a 2.0″ slit, yielding a spectral resolution of $R \sim$1250 over a wavelength range of 6400-8800 angstroms. Wavelength calibration was achieved by observing a standard lamp after the science target, and flux normalization was achieved by observation of the spectrophotometric standard star Feige 34 (Massey et al. 1988). The spectrum was processed using standard IRAF[1] tasks.

Our field and young spectral type standards were drawn from membership surveys of Upper Sco and Taurus by Slesnick et al.(2006a, 2006b) which used identical instrument settings for the spectroscopic confirmation of photometrically selected candidate members.

---

[1]IRAF is distributed by the National Optical Astronomy Observatories, which are operated by the Association of Universities for Research in Astronomy, Inc., under cooperative agreement with the National Science Foundation.

D.2.3 High-Resolution Imaging

We observed USco1606-1935 A and B on February 7, 2006 (JD=2453773) using laser guide star adaptive optics (LGSAO; Wizinowich et al. 2006) on the Keck-II telescope with NIRC2 (K. Matthews, in prep), a high spatial resolution near-infrared camera. The seeing was average to poor ($>1''$) for most of the observing run, but the system delivered nearly diffraction-limited correction in K' (60 mas FWHM) during the period of these observations. The system performance was above average given the low elevation (34 degrees; 1.8 airmasses), most likely due to the proximity and brightness of the tip-tilt reference star ($R = 14.2$, $d = 14''$).

Images were obtained using the K' filter in both the narrow and wide camera modes. The pixel scales in these modes are 9.942 mas pix^{-1} (FOV=10.18$''$) and 39.686 mas pix^{-1} (FOV=40.64$''$). All wide-camera observations were centered on the close Aab binary. The A and B components were too wide to fit reasonably into a single narrow-camera exposure, so we took separate exposure sequences centered on each. We obtained four wide-camera exposures of the AB system, seven narrow-camera exposures of A, and four narrow-camera exposures of B; the total integration times for each image set are 80s, 175s, and 100s, respectively. Each set was produced with a 3-point box dither pattern that omitted the bottom-left position due to higher read-noise for the detector in that quadrant. Single exposures were also taken at the central position.

Our science targets are relatively bright, so all observations were taken in correlated double-sampling mode, for which the array read noise is 38 electrons/read. The read noise is the dominant noise term for identifying faint sources, yielding 10σ detection limits of $K \sim 19.2$ for the wide camera observations, $K \sim 18.8$ for the narrow-camera observations centered on component A, and $K \sim 18.3$ for the narrow-camera observations centered on component B; the detection limits for B are slightly shallower due to the shorter total integration time. The data were flat-fielded and dark- and bias-subtracted using standard IRAF procedures. The images were distortion-corrected using new high-order distortion solutions (P. Cameron, in prep)

that deliver a significant performance increase as compared to the solutions presented in the NIRC2 pre-ship manual[2]; the typical residuals are $\sim$4 mas in wide camera mode and $\sim$0.6 mas in narrow camera mode. We adopt these systematic limits as the uncertainty in astrometry for bright objects; all faint objects ($K \sim$16-18) have larger uncertainties ($\sim$10 mas) due to photon statistics.

We measured PSF-fitting photometry and astrometry for our sources using the IRAF package DAOPHOT (Stetson 1987), and specifically with the ALLSTAR routine. We analyzed each frame separately in order to estimate the uncertainty in individual measurements and to allow for the potential rejection of frames with inferior AO correction; our final results represent the mean value for all observations in a filter.

In the wide-camera observations, we produced a template PSF based on the B component and the field star F1 (see Section D.3.1 and Figure D.1), both of which appear to be single sources. In the narrow-camera observations centered on A or B, the science target was the only bright object detected in our observations, so there was not a separate source from which to adopt a template PSF. We could have adopted a template PSF from another set of observations, but the AO correction usually varies significantly between targets since it is very sensitive to the seeing, elevation, laser return, and tip-tilt separation and brightness. We found that no other target in our survey provided a good PSF match.

We addressed this issue for the Aab binary pair by developing a procedure to reconstruct the single-source PSF directly from the observations of the binary system. Our algorithm begins with a preliminary estimate of the single-source PSF, then iteratively fits both components of the binary system with the estimated PSF and uses the synthetic PSF to subtract the best-fit estimate of the secondary flux. This residual image (which is dominated by the primary flux distribution) is then used to fit an improved estimate of the single-source PSF.

DAOPHOT characterizes an empirical PSF in terms of an analytical function and a lookup table of residuals, so we first iterated the procedure using a purely

---

[2]http://www2.keck.hawaii.edu/realpublic/inst/nirc2/

analytical function until it converged, then added a lookup table to the estimated PSF and iterated until its contents also converged. Observations of single stars suggested that the penny2 function (a Gaussian core with Lorentzian wings) would provide the best analytic fit, so we chose it as our analytic function. Four iterations of the fitting process were required for the analytic function to converge and 3 iterations were required for the lookup table to converge. Our algorithm does not work for the B component because it appears to be single, so we adopted the average synthetic single-source PSF from analysis of the Aab system to perform PSF fitting and verify that it is single.

We calibrated our photometry using 2MASS K magnitudes for the A and B components and the nearby field star F1 (Section D.3). The 2MASS observations were conducted using the K_s filter rather than K', but the theoretical isochrones computed by Kim et al.(2005) for the K_s and K' systems differ by <0.01 magnitudes for objects in this color range; this is much smaller than other uncertainties in the calibration. Carpenter (2001) found typical zero point shifts of <0.03 magnitudes between 2MASS K_s and several standard K bandpasses, all of which are more distinctly different from K_s than K', which also demonstrates that the zero point shift between K_s and K' should be negligible.

The calibration process could introduce systematic uncertainties if any of the three calibration sources are variable, but based on the small deviation in the individual calibration offsets for each source (0.03 mag), variability does not appear to be a significant factor. We tested the calibration using DENIS K magnitudes and found that the two methods agree to within 0.01 mag, albeit with a higher standard deviation (0.12 mag) for DENIS.
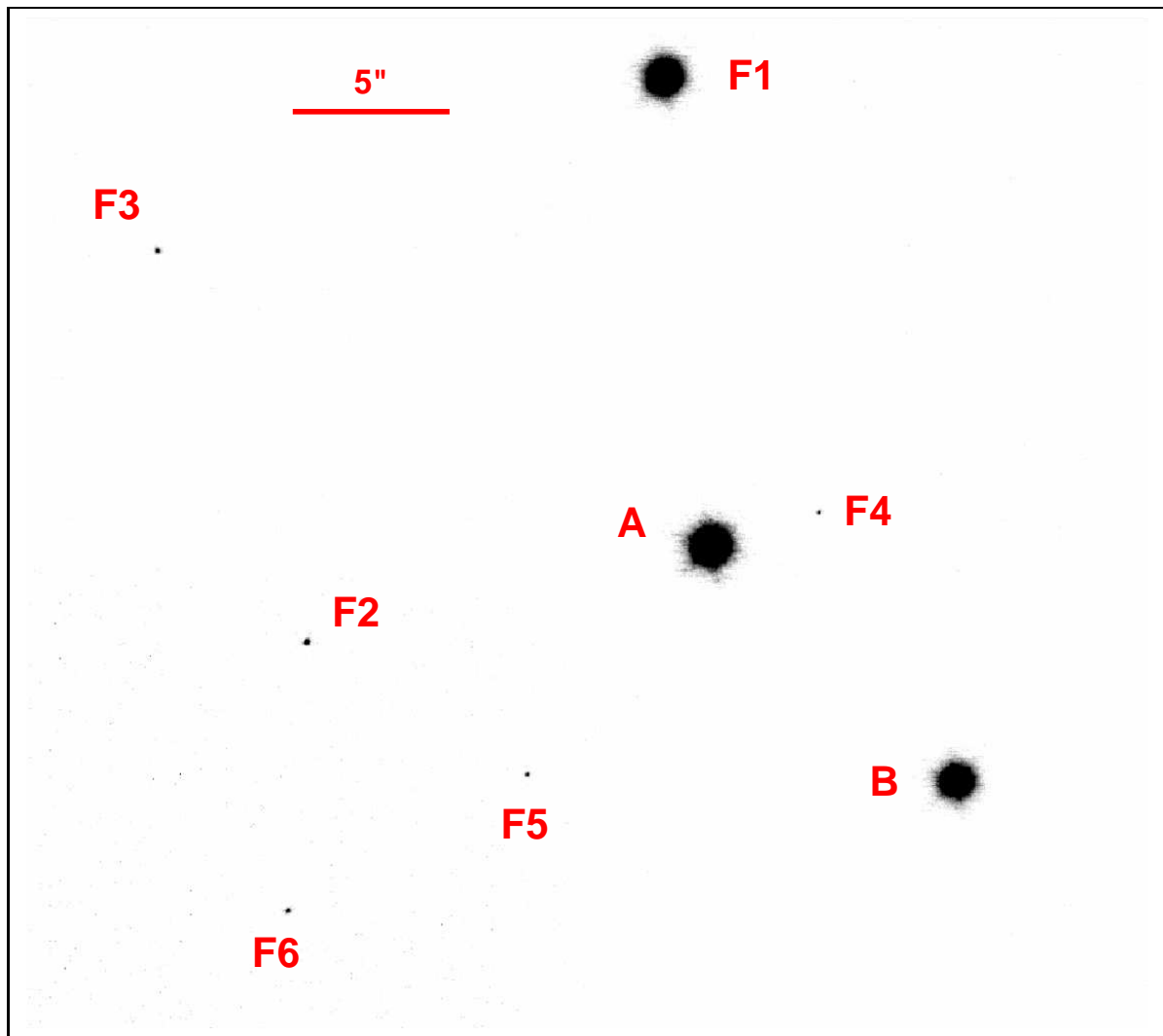
Figure D.1 The field surrounding USco1606-1935. The A and B components are labeled, as are 6 apparent field stars. The separation between the Aa and Ab components is too small to be apparent in this image.

Aa+Ab   Aa   Ab   B (single)

Δ_δ (mas)

+100

0

−100

+100   0   −100   +100   0   −100   +100   0   −100   +100   0   −100

Δ_α (mas)
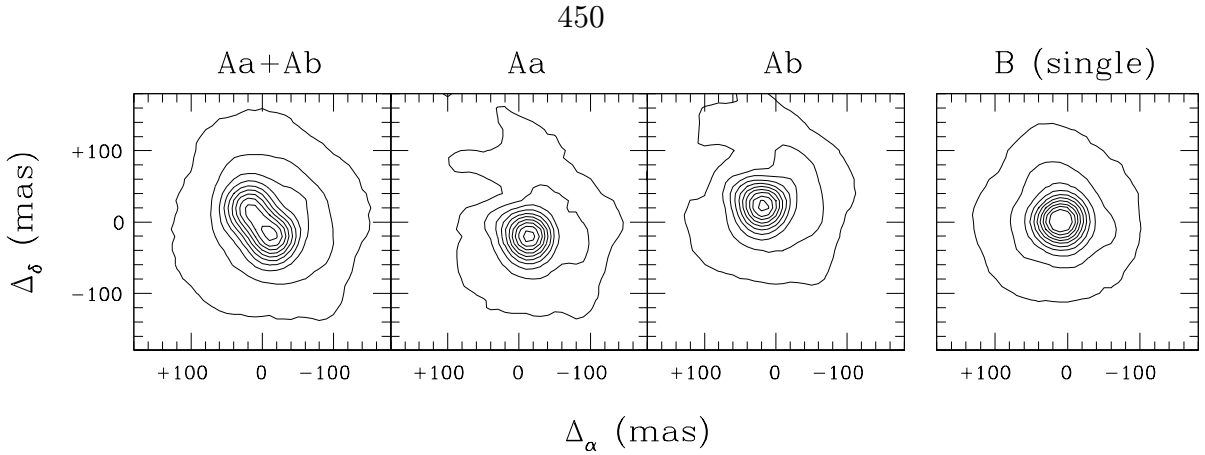
Figure D.2 Contour plots showing our LGSAO observations of USco1606-1935. The first panel shows an original exposure for the Aab pair, the second and third panels show Aa and Ab after subtracting best-fit values for the other component, and the last panel shows an original exposure for B. The contours are drawn at 5% to 95% of the peak pixel values.

D.3 Results

D.3.1 Images

In Figure D.1, we show a NIRC2 wide-camera image of the field surrounding USco1606-1935. The A and B components are labeled, as are 6 apparent field stars (named F1 through F6) which we use as astrometric comparison stars. We found counterparts for the first three field stars in existing survey catalogues: F1 was detected by all four sky surveys, F2 was detected by DENIS, USNO-B, and SSS, and F3 was detected only by USNO-B and SSS.

In Figure D.2, we show individual contour plots drawn from NIRC2 narrow-camera images of the A and B components. These high-resolution images show that USco1606-1935 A is itself composed of two sources; we designate these two components Aa and Ab. We do not possess any direct diagnostic information to determine if Aa and Ab are physically associated, but there are only two other bright sources in the field of view. If the source count is representative of the surface density of bright ($K < 15$) sources along the line of sight, the probability of finding an unbound bright source within <100 mas of the A component is only $\sim 10^{-5}$. Thus, we consider Aa and Ab to comprise a physically bound binary system.

Table D.1. Coordinates and Photometry

Name	RA[a]	DEC[a]	K_{LGS}[b]	K_{2MASS}[b]	H[b]	J[b]	$I2$[b]
A	16 06 11.99	-19 35 33.1	11.04	11.02	11.35	12.01	14.1
Aa	-	-	11.71	-	-	-	-
Ab	-	-	11.88	-	-	-	-
B	16 06 11.44	-19 35 40.5	11.74	11.78	12.32	13.00	14.9
F1	16 06 12.09	-19 35 18.3	11.51	11.50	11.62	12.27	13.5
F2	16 06 12.90	-19 35 36.1	16.32	-	-	-	17.8
F3	16 06 13.23	-19 35 23.7	16.66	-	-	-	18.7
F4	16 06 11.75	-19 35 32.0	17.43	-	-	-	-
F5	16 06 12.40	-19 35 40.3	17.28	-	-	-	-
F6	16 06 12.94	-19 35 44.6	16.97	-	-	-	-

Note. — Photometry is drawn from our observations (K_{LGS}), 2MASS (JHK_{2MASS}), and the USNO-B1.0 catalogue ($I2$).

[a]Coordinates are derived from the 2MASS position for USco1606-1935 A and the relative separations we measure using LGSAO. The absolute uncertainty in the 2MASS position with respect to the International Coordinate Reference System (ICRS) is $<0.1''$.

[b]Photometric uncertainties are $\sim$0.03 mag for LGSAO and 2MASS photometry and $\sim$0.25 mag for USNO-B1.0 photometry.

D.3.2 Photometry

Photometric data are generally sufficient to reject most nonmember interlopers because association members follow a bright, well-defined cluster sequence in color-magnitude diagrams and most field stars will fall below or bluer than the association sequence. In Table D.1, we summarize the observed and archival photometry for each source in the NIRC2 wide-camera images. In Figure D.3, we show three color-magnitude diagrams (K versus $J - K$, $H - K$, and $I2 - K$) for our observed sources and for all spectroscopically confirmed members of Upper Sco (as summarized in Kraus & Hillenbrand 2007).

The colors and magnitudes for USco1606-1935 B are consistent with the known members of Upper Sco, which supports the assertion that it is an association member. B is located marginally above and redward of the mean cluster sequence in the (K,$J - K$) and (K,$H - K$) diagrams; if this result is genuine and not a consequence of the photometric uncertainties, it could be a consequence of differential reddening, a K band excess associated with a hot disk, or the presence of an unresolved tight binary companion. However, B does not appear to be as red in DENIS data ($J - K = 0.98$),
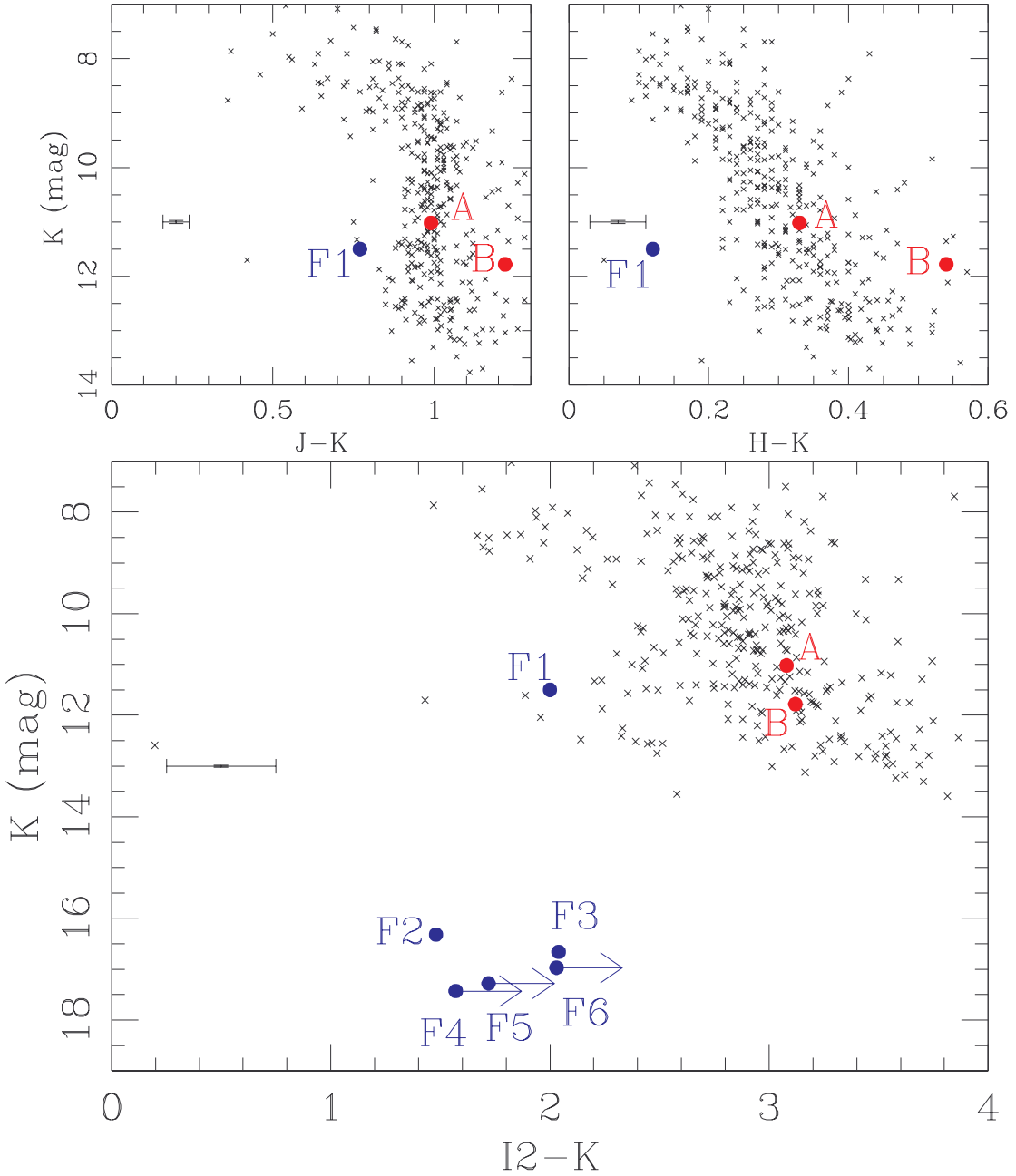
Figure D.3 Color-magnitude diagrams showing all spectroscopically confirmed members of Upper Sco (black crosses), the A and B binary components (red), and the other six objects detected in our LGSAO images (blue). The NIR CMDs (top) demonstrate that F1 lies significantly below the association sequence, and therefore is an unrelated field star. The optical-NIR CMD (bottom) supports this identification and demonstrates that F2 and F3 are also field stars that lie below the association sequence. We measure formal upper limits only for stars F4-F6, but marginal R band detections in the POSS plates suggest that F4 and F6 are also field stars. Typical uncertainties are plotted on the left edge of each plot.

which suggests that the 2MASS result may not be genuine.

The three sources for which we have colors (F1, F2, and F3) all sit below the Upper Sco member sequence in the $(K, I2-K)$ color-magnitude diagram. Some USco members also fall marginally blueward of the association sequence in $(K, I2 - K)$; we can find no correlation with location, multiplicity, or other systematic factors, so this feature may be a result of intrinsic variability between the epochs of K and $I2$. This result suggests that the $(K, I2 - K)$ CMD is not sufficient for ruling out the membership of F1. However, F1 also sits at the extreme blueward edge of the association sequence in $(K, J-K)$ and is clearly distinct from the association sequence in $(K, H - K)$. We therefore judge that all three sources are unassociated field star interlopers.

We do not possess sufficient information to determine whether these three stars are field dwarfs in the Milky Way disk or background giants in the Milky Way bulge; the unknown nature of these sources could complicate future efforts to calculate absolute proper motions because comparison to nonmoving background giants is the best way to establish a nonmoving astrometric frame of reference. As we will show in Section D.3.3, F1 possesses a small total proper motion (<10 mas yr^{-1}), so it may be a distant background star. Its 2MASS colors ($J - H = 0.65$, $H - K = 0.12$) place it on the giant sequence in a color-color diagram, but reddened early-type stars with spectral type $<$M0 can also reproduce these colors.

We are unable to measure colors for the stars F4, F5, and F6 because they were detected only in our LGSAO observations. However, visual inspection of the digitized POSS plates via Aladdin (Bonnarel et al. 2000) found possible R band counterparts to F4 and F6 that were not identified by USNO-B. If these detections are genuine and these two sources fall near the USNO-B survey limit ($R \sim 20 - 21$), their colors ($R - K \sim 3 - 4$ or $I2 - K \sim 2 - 3$) are too blue to be consistent with association membership.
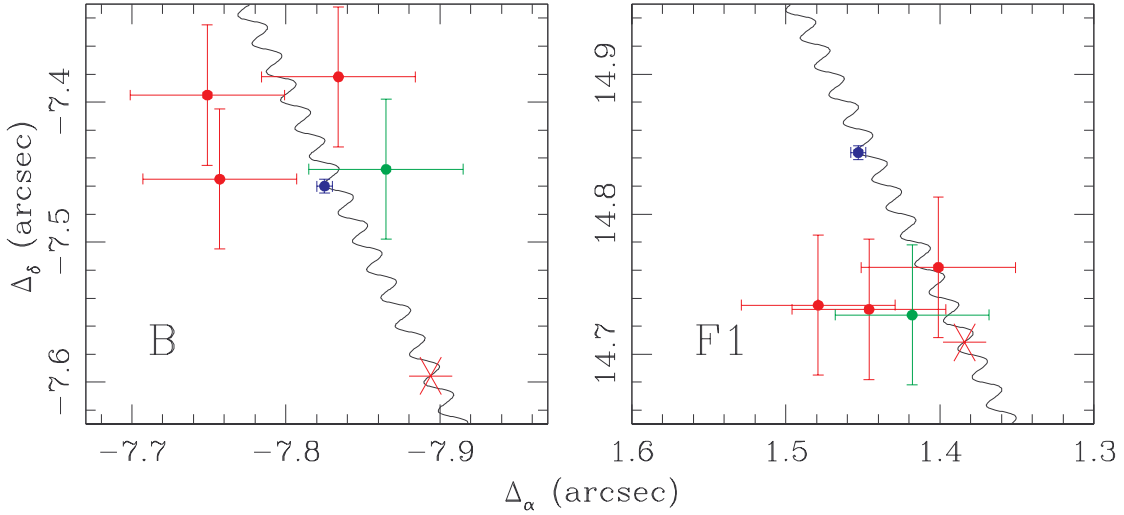
Figure D.4 Relative separations from the A component to the B component (left) and the field star F1 (right) for our LGSAO data and archival 2MASS/DENIS data. The blue circles denote LGSAO data, the red circles denote 2MASS data for each filter (J, H, and K), and the green circles denote the average DENIS values for all three filters (IJK). The black line shows the expected relative astrometry as a function of time for a stationary object, and the predicted archival astrometry values for the non-moving (background) case are shown on these curves with red asterisks. The results for component B are consistent with common proper motion; the results for F1 are inconsistent with common proper motion and suggest that the total proper motion is small, denoting a probable background star.

Table D.2.   Relative Astrometry

	LGSAO K (JD=2453773)		2MASS K (JD=2451297)		2MASS H (JD=2451297)		2MASS J (JD=2451297)		DENIS IJK (JD=2451332)	
	Δ_α	Δ_δ	Δ_α	Δ_δ	Δ_α	Δ_δ	Δ_α	Δ_δ	Δ_α	Δ_δ
Aa	-0.0132	-0.0149	-	-	-	-	-	-	-	-
Ab	+0.0201	+0.0266	-	-	-	-	-	-	-	-
B	-7.825	-7.460	-7.757	-7.455	-7.749	-7.395	-7.834	-7.382	-7.865	-7.448
F1	+1.453	+14.844	+1.401	+14.762	+1.446	+14.732	+1.479	+14.735	+1.418	+14.728
F2	+12.839	-3.017	-	-	-	-	-	-	_a	_a
F3	+17.571	+9.370	-	-	-	-	-	-	-	-
F4	-3.438	+1.056	-	-	-	-	-	-	-	-
F5	+5.805	-7.224	-	-	-	-	-	-	-	-
F6	+13.385	-11.540	-	-	-	-	-	-	-	-

Note. — The zero-point for all coordinate offsets is the photocenter of the unresolved Aab system. The relative astrometric uncertainties for 2MASS and DENIS results are ~40 mas; uncertainties for the LGSAO results are ~5 mas for bright objects and ~10 mas for faint objects.

[a] F2 was marginally detected in i by DENIS, but the astrometry is not sufficiently precise to be useful in calculating its proper motion.

D.3.3   Astrometry

The standard method for confirming physical association of candidate binary companions is to test for common proper motion. This test is not as useful for young stars in associations because other (gravitationally unbound) association members have similar proper motions to within $<$2-3 mas yr^{-1}. However, proper motion analysis can still be used to eliminate nearby late-type field stars and background giants that coincidentally fall along the association color-magnitude sequence but possess distinct kinematics.

In Table D.2, we summarize the relative astrometry for the three system components and for the field stars F1-F6 as measured with our LGSAO observations and archival data from 2MASS and DENIS. All offsets are given with respect to the photocenter of the unresolved Aab system; Aa and Ab have similar fluxes and do not appear to be variable in any of these measurements (Section D.2.3), so this zero point should be consistent between different epochs. We evaluated the possibility of including astrometric data from older photographic surveys like USNO-B and SSS, but rejected this idea after finding that the two surveys reported very large (up to 1$''$) differences in the separation of the A-B system from digitization of the same photographic plates. We calculated relative proper motions in each dimension by averaging the four first-epoch values (2MASS and DENIS; Table D.2), then comparing the result to our second-epoch observation obtained with LGSAO. We did not attempt a least-squares fit because the 2MASS values are coeval and the DENIS results were measured only 35 days after the 2MASS results.

In Figure D.4, we plot the relative astrometry between A and B and between A and F1 as measured by 2MASS, DENIS, and our LGSAO survey. We also show the expected relative motion curve if B or F1 are nonmoving background stars and A moves with the mean proper motion and parallax of Upper Sco, (μ_α,μ_δ)=(-9.3,-20.2) mas yr^{-1} and π=7 mas (de Zeeuw et al. 1999; Kraus & Hillenbrand 2007). The total relative motion of B over the 6.8 year observation interval is $(+24\pm25,-40\pm25)$ mas; the corresponding relative proper motion is $(+3.5\pm3.7,-5.9\pm3.7)$ mas yr^{-1}, which

is consistent with comovement to within $<2\sigma$. This result is inconsistent with the hypothesis that B is a nonmoving background star at the 8σ level.

The relative motion of F1 is $(+17\pm25,+105\pm25)$ mas or $(+2.5\pm3.7,+15.4\pm3.7)$ mas yr^{-1}, which is inconsistent with comovement at the 4σ level. The absolute proper motion of F1, assuming A moves with the mean proper motion of Upper Sco, is $(-7\pm4,-5\pm4)$ mas yr^{-1}, which is consistent with nonmovement to within $<2\sigma$. The implication is that F1 is probably a distant background star, either a giant or a reddened early-type star.

D.3.4 Spectroscopy

The least ambiguous method for identifying young stars is to observe spectroscopic signatures of youth like lithium or various gravity-sensitive features. Spectroscopic confirmation is not strictly necessary in the case of USco1606-1935 since we confirmed common proper motion for the A-B system, but a spectral type is also useful in constraining the physical properties of the secondary, so we decided to obtain an optical spectrum.

In the top panel of Figure D.5, we plot our spectrum for B in comparison to three standard field dwarfs with spectral types of M4V-M6V. We qualitatively find that the standard star which produces the best fit is GJ 866 (M5V). The M4V and M6V standards do not adequately fit either the overall continuum shape or the depths of the TiO features at 8000 and 8500 angstroms, so the corresponding uncertainty in the spectral type is <0.5 subclasses.

In the bottom panel of Figure D.5, we plot a restricted range of the spectrum (8170-8210 angstroms) centered on the Na-8189 absorption doublet. The depth of the doublet is sensitive to surface gravity (e.g., Slesnick et al. 2006a, 2006b); high-gravity dwarfs possess very deep absorption lines, while low-gravity giants show almost no absorption. We also plot standard stars of identical spectral type (M5) spanning a range of ages. The depth of the B component's Na 8189 doublet appears to be consistent with the depth for a member of USco (5 Myr), deeper than that of a
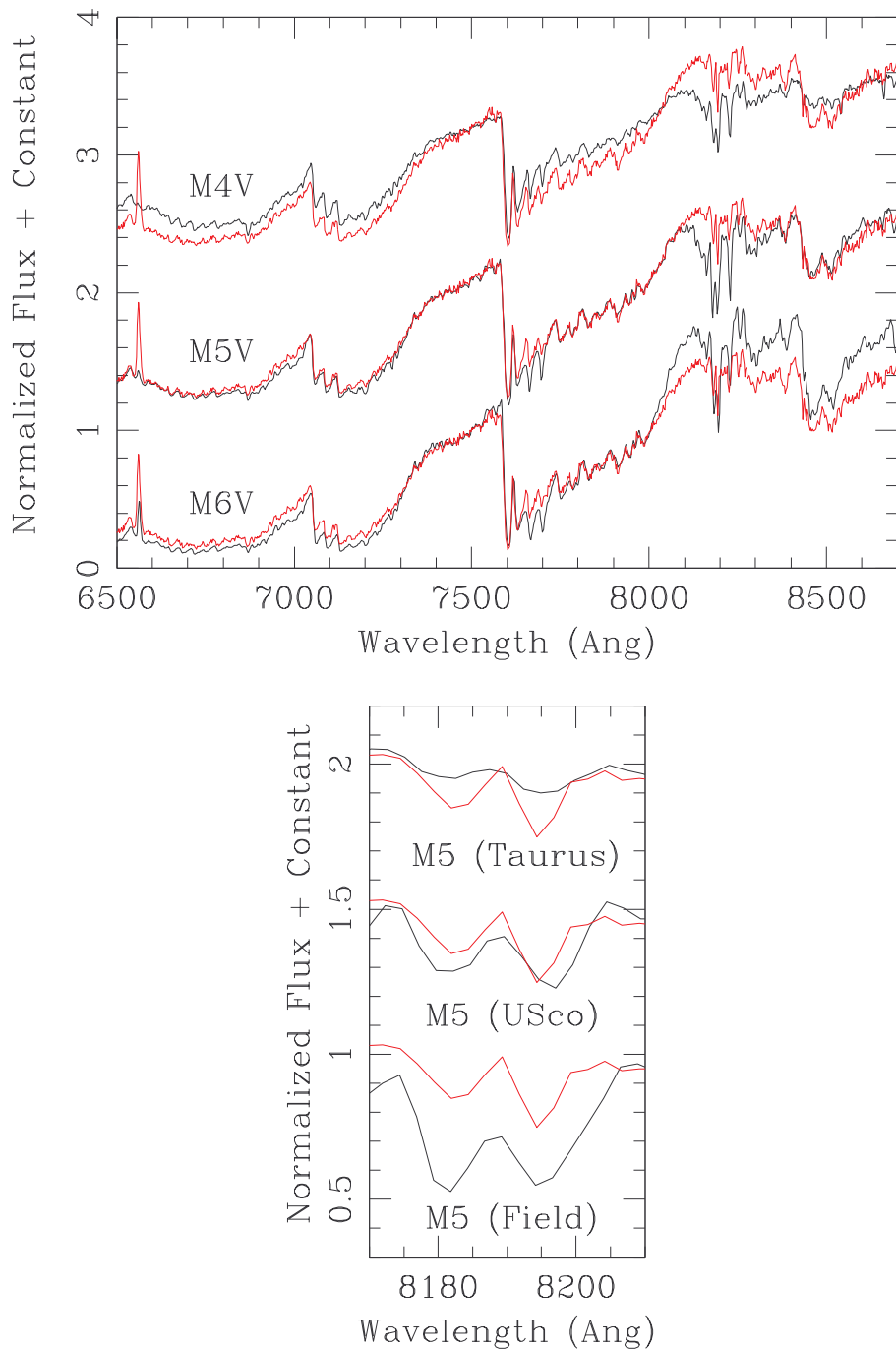
Figure D.5 The spectrum of USco1606-1935 B (red) as compared to a set of standard stars drawn from the field and from the young Taurus and Upper Sco associations. The overall continuum shape is best fit by a field standard with spectral type M5; the spectrum around the Na doublet at 8189 angstroms is better fit by an intermediate-age (5 Myr) M5 than a young (1-2 Myr) or field M5, suggesting that the B component is also intermediate-aged.

Table D.3. Binary Properties

Property	Aa-Ab	A-B
Measured		
Sep (mas)	53.2±1.0	10874±5
PA (deg)	38.7±1.0	226.45±0.03
ΔK (mag)	0.17±0.05	0.70±0.05
a_{proj} (AU)	7.7±1.2	1600±200
Inferred		
q	0.88±0.05	0.53±0.08
SpT_{Prim}	M5±0.5	M5+M5.2(±0.5)
SpT_{Sec}	M5.2±0.5	M5±0.5
M_{Prim}	0.14±0.02	0.26±0.04
M_{Sec}	0.12±0.02	0.14±0.02

Note. — The center of mass for the Aa-Ab pair is unknown, so we calculate all A-B separations with respect to the K band photocenter.

Taurus member (1-2 Myr), and shallower than that of a field star, which confirms that the B component is a pre-main sequence member of Upper Sco.

We have quantified our analysis by calculating the spectral indices TiO-7140, TiO-8465, and Na-8189, which measure the depth of key temperature- and gravity-sensitive features (Slesnick et al. 2006a). We find that $TiO_{7140} = 2.28$, $TiO_{8465} = 1.23$, and $Na_{8189} = 0.92$; all three indices are consistent with our assessment that B is a young M5 star which has not yet contracted to the zero-age main sequence.

D.3.5 Stellar and Binary Properties

In Table D.3, we list the inferred stellar and binary properties for the Aa-Ab and A-B systems, which we estimate using the methods described in Kraus & Hillenbrand (2007). This procedure calculates component masses by combining the 5 Myr isochrone of Baraffe et al.(1998) and the M dwarf temperature scale of Luhman et al.(2003) to directly convert observed spectral types to masses. Relative properties (mass ratios q and relative spectral types) are calculated by combining the Baraffe isochrones and Luhman temperature scale with the empirical NIR colors of Bessell & Brett (1998) and the K-band bolometric corrections of Leggett et al.(1998) to estimate q and ΔSpT from the observed flux ratio ΔK.

We have adopted the previously measured spectral type for A (M5; Preibisch et al. 2002) as the type for component Aa, but the inferred spectral type for Ab is only 0.2 subclasses later, so this assumption should be robust to within the uncertainties ($\sim$0.5 subclasses). The projected spatial separations are calculated for the mean distance of Upper Sco, 145$\pm$2 pc (de Zeeuw et al. 1999). If the total radial depth of Upper Sco is equal to its angular extent ($\sim$15° or $\sim$40 pc), then the unknown depth of USco1606-1935 within Upper Sco implies an uncertainty in the projected spatial separation of $\pm$15%. The systematic uncertainty due to the uncertainty in the mean distance of Upper Sco is negligible ($<$2%).

D.4 Is USco1606-1935 AB a Binary System?

The unambiguous identification of pre-main sequence binaries is complicated by the difficulty of distinguishing gravitationally bound binary pairs from coeval, comoving association members which are aligned in projection. Most traditional methods used to confirm field binary companions do not work in the case of young binaries in clusters and associations because all association members share common distances and kinematics (to within current observational uncertainties), so the only remaining option is to assess the probability of chance alignment. We address this challenge by quantifying the clustering of PMS stars via calculation of the two-point correlation function (TPCF) across a wide range of angular scales (1$''$ to $>$1 degree). This type of analysis has been attempted in the past (e.g., Gomez et al. 1993 for Taurus; Simon 1997 for Ophiuchus, Taurus, and the Trapezium), but these studies were conducted using samples that were significantly incomplete relative to today.

The TPCF, $w(\theta)$, is defined as the number of excess pairs of objects with a given separation θ over the expected number for a random distribution (Peebles 1980). The TPCF is linearly proportional to the surface density of companions per star, $\Sigma(\theta) = (N_*/A)[1 + w(\theta)]$, where A is the survey area and N_* is the total number of stars. However, it is often easier to evaluate the TPCF via a Monte Carlo-based definition, $w(\theta) = N_p(\theta)/N_r(\theta) - 1$, where $N_p(\theta)$ is the number of pairs in the survey
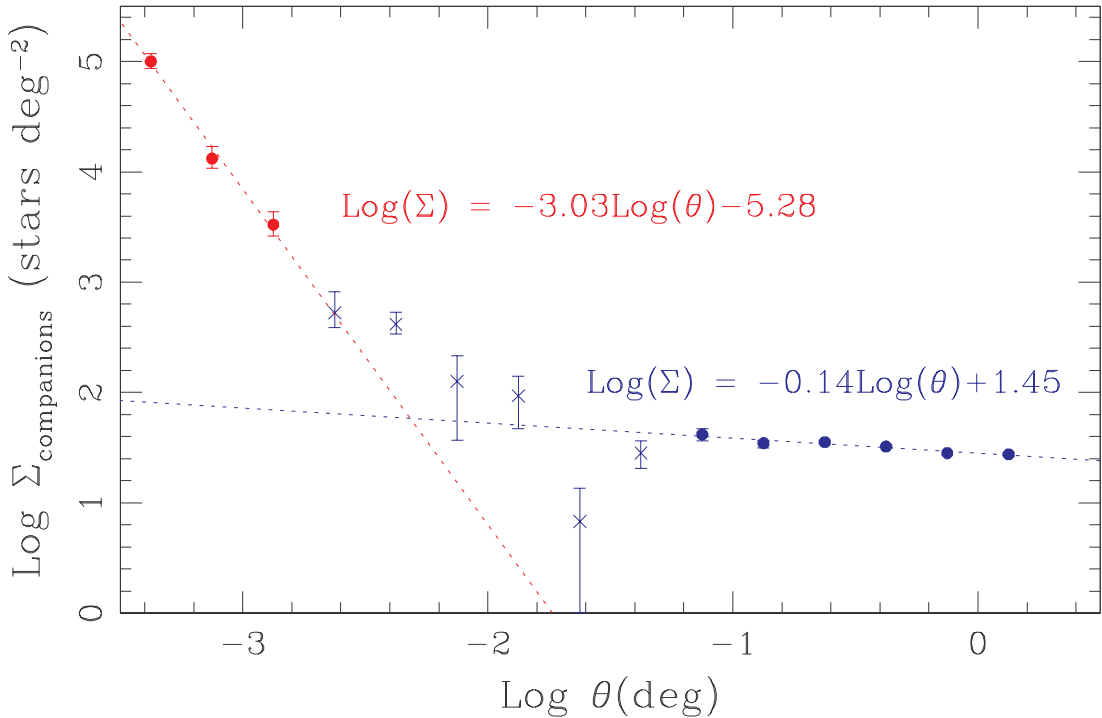
Figure D.6 The surface density of companions as a function of separation for young stars and brown dwarfs in Upper Sco. Red symbols denote results from our wide-binary survey using 2MASS (Kraus & Hillenbrand 2007) and blue symbols denote data for all spectroscopically confirmed members in two fields surveyed by Preibisch et al.(2002). The data appear to be well-fit by two power laws (dashed lines) which most likely correspond to gravitationally bound binaries and unbound clusters of stars that have not yet completely dispersed from their formation environments. The data points which were used to fit these power laws are denoted with circles; other points are denoted with crosses.

area with separations in a bin centered on θ and $N_r(\theta)$ is the expected number of pairs for a random distribution of objects over the same area (Hewett 1982). The advantage of this method is that it does not require edge corrections, unlike direct measurement of $\Sigma(\theta)$. We adopted this method due to its ease of implementation, but we report our subsequent results in terms of $\Sigma(\theta)$ since it is a more intuitive quantity.

The current census of Upper Sco members across the full association is very incomplete, so we implemented our analysis for intermediate and large separations ($\theta > 6.4''$) using only members located in two heavily-studied fields originally observed by Preibisch et al.(2001, 2002; the 2df-East and 2df-West fields). The census of members in these fields may not be complete, but we expect that it is the least incomplete. The census of companions at smaller separations ($1.5''$-$6.4''$) has been uniformly studied for all spectroscopically confirmed members (Kraus & Hillenbrand 2007), so we have maximized the sample size in this separation range by considering the immediate area around all known members, not just those within the Preibisch fields. Our survey was only complete for mass ratios $q > 0.25$, so we do not include companions with mass ratios $q < 0.25$.

These choices might lead to systematic biases if the Preibisch fields are still significantly incomplete or if the frequency and properties of binary systems show intra-association variations, but any such incompleteness would probably change the result by no more than a factor of 2-3. As we will subsequently show, $\Sigma(\theta)$ varies by 4 orders of magnitude across the full range of θ. The well-established mass dependence of multiplicity should not affect our results since the mass function for the Preibisch fields is similar to that seen for the rest of the association.

In Figure D.6, we plot $\Sigma(\theta)$ for Upper Sco, spanning the separation range $-3.5 < log(\theta) < 0.25$ ($1.14''$ to 1.78 deg). We have fit this relation with two power laws, one which dominates at small separations (<15-$30''$) and one at larger separations. We interpret the two segments, following Simon (1997), to be the result of gravitationally-bound binarity and gravitationally unbound intra-association clustering, respectively. We fit the binary power law to the three lowest-separation bins ($log(\theta) < -2.75$) because this is the separation range over which we possess uniform multiplicity data.

The cluster power law was fit to the six highest-separation bins ($log(\theta) > -1.25$) because those bins have the smallest uncertainties. Bins corresponding to intermediate separations seem to follow the two power laws.

We found that the slope of the cluster power law (-0.14±0.02) is very close to zero, which implies that there is very little clustering on scales of <1 deg. This result is not unexpected for intermediate-age associations like Upper Sco; given the typical intra-association velocity dispersion ($\sim$1 km s^{-1}) and the age (5 Myr), most association members have dispersed $\sim$5 pc (2 deg) relative to their formation point, averaging out structure on smaller spatial scales. Simon (1997) found that the slopes for Taurus, Ophiuchus, and the ONC are steeper, suggesting that more structure is present on these small scales at young ages ($\sim$1-2 Myr). The slope of the binary power law (-3.03±0.24) is much steeper than the cluster regime. The separation range represented is much larger than the peak of the binary separation distribution ($\sim$30 AU for field solar-mass stars; Duquennoy & Mayor 1991), so the steep negative slope corresponds to the large-separation tail of the separation distribution function. The two power laws seem to cross at separations of $\sim$15-30″ (a_{proj} $\sim$2,500–5,000 AU), though this result depends on the sample completeness in the binary and cluster regimes. We interpret this to be the maximum separation range at which binaries can be identified.

If we extrapolate the cluster power law into the separation regime of the binary power law, we find that the expected surface density of unbound coincidentally aligned companions is $\sim$60 deg^{-2}. Given this surface density, there should be $\sim$1 chance alignment within 15″ among the 366 spectroscopically confirmed members of Upper Sco. Among the 173 known late-type stars and brown dwarfs (SpT≥M4) for which this separation range is unusually wide, the expected number of chance alignments with any other member is 0.5. If the mass function of known members is similar to the total mass function, approximately half ($\sim$0.25 chance alignments) are expected to occur with another low-mass member. Therefore, we expect $\sim$0.25 chance alignments which might be mistaken for a low-mass binary pair.

The probability that one or more such chance alignments actually exists for a

known low-mass USco member is 25% (based on Poisson statistics), which suggests that the nature of a single candidate wide pair like USco1606-1935 AB can not be unambiguously determined. If any more pairs can be confirmed, then they would represent a statistically significant excess. The corresponding probability of finding 2 chance alignments of low-mass members is only 2%. As we have described in our survey of wide multiplicity with 2MASS (Kraus & Hillenbrand 2007), we have identified at least three additional candidate ultrawide systems in Upper Sco, so spectroscopic and astrometric followup of these candidate systems is a high priority.

D.5   Summary

We have presented photometric, astrometric, and spectroscopic observations of USco1606-1935, a candidate ultrawide ($\sim$1600 AU), low-mass ($M_{tot} \sim$0.4 $M_\odot$) hierarchical triple system in the nearby OB association Upper Scorpius. We conclude that the ultrawide B component is a young, comoving member of the association, and show that the primary is itself a close binary system.

If the Aab and B components are gravitationally bound, the system would join the growing class of young multiple systems which have unusually wide separations as compared to field systems of similar mass. However, we demonstrate that binarity can not be assumed purely on probabilistic grounds. Analysis of the association's two-point correlation function shows that there is a significant probability (25%) that at least one pair of low-mass association members will be separated by $<15''$, so analysis of the wide binary population requires a systematic search for all wide binaries. The detection of another pair of low-mass members within $15''$ would represent an excess at the 98% confidence level. In principle, binarity could also be demonstrated by measuring common proper motion with precision higher than the internal velocity scatter of the association; given the astrometric precision currently attainable with LGSAO data (<1 mas), the test could be feasible within <5 years.

Acknowledgements

Bibliography

Baraffe, I., Chabrier, G., Allard, F., & Hauschildt, P. 1998, A&A, 337, 403

Bessell, M. & Brett, J. 1988, PASP, 100, 1134

Bonnarel, F. et al. 2000, A&AS, 143, 33

Bouy, H., Brandner, W., Martin, E., Delfosse, X., Allard, F., & Basri, G. 2003, AJ, 126, 1526

Burgasser, A. et al. 2003, ApJ, 125, 850

Caballero, J., Martin, E., Dobbie, P., & Barrado y Navascues, D. 2006, A&A, 460, 635

Carpenter, J. 2001, AJ, 121, 2851

Chauvin, G., Lagrange, A., Dumas, C., Zuckerman, B., Mouillet, D., Song, I., Beuzit, J., & Lowrance, P. 2004, A&A, 425, 29

Close, L., Siegler, N., Freed, M., & Biller, B. 2003, ApJ, 587, 407

Close, L. et al. 2007, ApJ, 660, 1492

de Zeeuw, P., Hoogerwerf, R., de Bruijne, J., Brown, A., & Blaauw, A. 1999, AJ, 117, 354

Duquennoy, A. & Mayor, M. 1991, A&A, 248, 485

Epchtein, N. et al. 1999, A&A, 349, 236

Fischer, D. & Marcy, G. 1992, ApJ, 396, 178

Gomez, M., Hartmann, L., Kenyon, S., & Hewett, R. 1993, AJ, 105, 1927

Hambly, N. et al. 2001, MNRAS, 326, 1279

Hewett, P. 1982, MNRAS, 201, 867

Jayawardhana, R. & Ivanov, V. 2006, Science, 313, 1279

Kim, S., Figer, D., Lee, M., & Oh, S. 2005, PASP, 117, 445

Kraus, A. & Hillenbrand, L. 2007, ApJ, 662, 413

Leggett, S., Allard, F., & Hauschildt, P. 1998, ApJ, 509, 836

Luhman, K., Stauffer, J., Muench, Al, Rieke, G., Lada, E., Bouvier, J., & Lada, C. 2003, ApJ, 593, 1093

Luhman, K., Whitney, B., Meade, M., Babler, B., Indebetouw, R., Bracker, S., & Churchwell, E. 2006, ApJ, 649, 1180

Luhman, K., Allers, K., Jaffe, D., Cushing, M., Williams, K., Slesnick, C., & Vacca, W. 2007, ApJ, 659, 1629

Massey, P., Strobel, K., Barnes, J., & Anderson, E. 1988, ApJ, 328, 315

Monet, D. et al. 2003, AJ, 125, 984

Oke, B. & Gunn, J. 1982, PASP, 94, 586

Peebles, J. 1980, The Large Scale Structure of the Universe (Princeton: Princeton Univ. Press)

Preibisch, T., Guenther, E., & Zinnecker, H. 2001, AJ, 121, 1040

Preibisch, T., Brown, A., Bridges, T., Guenther, E., & Zinnecker, H. 2002, AJ, 124, 404

Reid, I., Gizis, J., Kirkpatrick, J., & Koerner, D. 2001, AJ, 121, 489

Simon, M. 1997, ApJ, 482, 81

Skrutskie, M. et al. 2006, AJ, 131, 1163

Slesnick, C., Carpenter, J., & Hillenbrand, L. 2006a, AJ, 131, 3016

Slesnick, C., Carpenter, J., Hillenbrand, L., & Mamajek, E. 2006b, AJ, 132, 2665

Stetson, P. 1987, PASP, 99, 191

Weinberg, M., Shapiro, S., & Wasserman, I. 1987, ApJ, 312, 367

Wizinowich, P. et al. 2006, PASP, 118, 297